Acta Physica Hungarica

VOLUME 65, NUMBER 1, 1989

EDITOR-IN-CHIEF

I. KOVÁCS

EDITORIAL BOARD

Z. BAY, R. GÁSPÁR, I. GYARMATI, N. KÜRTI,
K. NAGY, L. PÁL, P. SZÉPFALUSY, I. TARJÁN,
B. TELEGDI, L. TISZA, E. WIGNER

Akadémiai Kiadó, Budapest

ACTA PHYS. HUNG. APAHAQ 65 (1) 1–134 (1989) HU ISSN 0231–4428

ACTA PHYSICA HUNGARICA

A JOURNAL OF THE HUNGARIAN ACADEMY OF SCIENCES

EDITED BY
I. KOVÁCS

Acta Physica publishes original papers on subjects in physics. Papers are accepted in English, French, German and Russian.

Acta Physica is published in two yearly volumes (4 issues each) by

AKADÉMIAI KIADÓ
Publishing House of the Hungarian Academy of Sciences
H-1054 Budapest, Alkotmány u. 21

Subscription information

Orders should be addressed to

KULTURA Foreign Trading Company
1389 Budapest P.O. Box 149

or to its representatives abroad.

Acta Physica Hungarica is abstracted/indexed in Chemical Abstracts, Current Contents–Physical, Chemical and Earth Sciences, Mathematical Reviews, Science Abstracts, Physics Briefs, Risk Abstracts

© Akadémiai Kiadó, Budapest

ACTA PHYSICA HUNGARICA

EDITORIAL BOARD

Z. BAY, R. GÁSPÁR, I. GYARMATI, N. KÜRTI, K. NAGY, L. PÁL,
P. SZÉPFALUSY, I. TARJÁN, B. TELEGDI, L. TISZA, E. WIGNER

EDITOR-IN-CHIEF

I. KOVÁCS

VOLUME 65

AKADÉMIAI KIADÓ, BUDAPEST
1989

CONTENTS
Volume 65

ELEMENTARY PARTICLES AND FIELDS

Higgs gravitational vacuum in the gauge gravitation theory. *G. Sardanashvily* and *B. Ikhlov* 79
Painlevé property and Bäcklund transformation of SU(2) Yang–Mills–Higgs system. *B. V. Baby* 435

NUCLEAR AND HIGH ENERGY PHYSICS

Measurement of the fission cross-section ratio for $^{237}NP/^{235}U$ around 14 MeV neutron energies. *L. Desdin, S. Szegedi* and *J. Csikai* 271
New data for $^{12}C(p,\gamma)^{13}N$ radiative capture process: note on an anomaly in thick target measurements. *Á. Z. Kiss, E. Koltay* and *E. Somorjai* 277
Low energy alpha scattering on ^{62}Ni. *Z. Máté, S. Szilágyi, L. Zolnai, A. Bredbacka, M. Brenner, K. M. Källman* and *P. Manngard* 287
Nuclear structure of ^{116}In. *T. Fényes* and *Zs. Dombrádi* 295
On the role of anti-bound states in the RPA description of the giant monopole resonance. *T. Vertse, P. Curutchet, R. J. Liotta* and *J. Bang* 305
What happened to the iron in the Sun? *G. Marx* and *D. S. P. Dearborn* 315
Searching for monopoles in Lake Baikal. *G. V. Domogatsky, P. Kakas, S. Fehér* and *D. Kiss* . 323
Dirac particle in a periodic field. *I. Lovas* and *L. Molnár* 331

ATOMIC AND MOLECULAR PHYSICS

The hyperfine interaction parameter $\rho(0)$ calculated by the $X\alpha$ method with ab initio self-consistent exchange parameter. *Á. Nagy* 55
Ab initio method for treatment of spatially extended systems, Parts I–III. *E. Kapuy, C. Kozmutza* and *Zs. Ozoróczy* 85
Study of the convoy electron production from solids with hydrogenic Ni-ions. *J. Kemmler, O. Heil, H. Rothard, K. Kroneberger, S. Lencinas, K. O. Groeneveld, C. Biedermann* and *I. A. Sellin* 135
On the cross sections for electron transfer, ejection, and excitation in coincidence with a hole in a specific shell. *R. L. Becker* 141
Depth profiling by ion-beam analysis. *K. Ishii* and *S. Morita* 151
Electronegativities and hardnesses of several atoms and ions calculated with the $X\alpha$ method having self-consistent parameter α. *R. Gáspár* and *Á. Nagy* 159
Wave function effects in K-shell ionization. *T. Mukoyama* 165
Relativistic phenomena in atomic and chemical physics: opportunities for studies with synchrotron radiation. *B. Crasemann* 171
High-resolution electron spectroscopy of radioactive samples using the ESA12 electrostatic spectrometer. *V. Brabec, O. Dragoun, N. Dragounová, J. Novák, M. Fišer, A. Kovalik* and *M. Ryšavý* 183
Ejected electrons at backward angles from He and Ne by He^{2+} impact. *Gy. Szabó, Á. Kövér* and *L. Gulyás* 195
L-shell ionization and L X-ray emission induced by antiprotons. *L. Sarkadi* 201
Resolution and detection of weak X-ray lines using a Si (Li) detector combined with absorbers. *T. Papp* and *J. Pálinkás* 209

An experimental method for resolution calibration of electron spectrometers. *L. Kövér, J. Tóth* and *A. Itoh* 217
Study of the chemical shift of K X-ray lines with a home-built X-ray crystal spectrometer. *I. Török* 225
The reduction of the systematic error caused by the nuclear background in high resolution electron spectroscopy of high-energy ion–atom collisions. *I. Kádár, S. Ricz, B. Sulik, D. Varga* and *J. Végh* 229
An apparatus for low energy atomphysical experiments and the first results. *L. Szótér, J. Macsuga, B. Palásthy* and *G. Vitéz* 239
On the energy dependence of the electron shake processes. *E. Vatai* 257
Ab initio theoretical study of the structures and stabilities of the $LiBeH_3$, Li_2BeH_4 and $LiBe_2H_5$ molecules. *I. Tamássy-Lentei* and *J. Szaniszló* 265
Rotational analysis of the $A^6\Sigma - X^6\Sigma$ transition of chromium monofluoride. *V. M. Dubov, D. V. Tschechovskoy, E. A. Shenyavskaya* and *I. Kovács* 411
Spectrum of atomic electrons ionised by an intense field. *P. Kálmán* 425
Effect of hydrogen bonding on the polarization of fluorescence of 4-methyl-7-hydroxy coumarin. *R. Giri, S. S. Rathi, M. K. Machwe* and *V. V. S. Murti* 431

FLUIDS, PLASMAS AND ELECTRIC DISCHARGES

Influence of electrode temperature and auxiliary discharge on the electrical breakdown in helium. *M. M. Pejović* and *M. K. Radović* 19
An application of the governing principle of dissipative processes to eigenvalue problem of hydro–thermodynamics. *Nguyen Huyen Tung* 69

OPTICS

Investigation of electric field distribution in Z-cut KDP Q-switch modulator crystals. *R. Sh. Alnayli, Cs. Kuti, J. S. Bakos* and *I. Tóth* 395

CONDENSED MATTER

Electron bombardment induced conductivity in crystalline anthracene. *M. Saleh* 3
The kinetics of growth and the morphological instability of zinc single crystals. *D. Iwanov* 11
Electron–phonon interaction in thin films. *J. Kierul* and *L. Wojtczak* 25
Electron–phonon interaction in transition metals. *J. Kierul* 33
Theoretical analysis of the Einstein relation in degenerate ternary chalcopyrite semiconductors in the presence of an arbitrarily oriented quantizing magnetic field. *M. Mondal, K. P. Ghatak* and *A. K. Das* 43
Аппроксимация зонной сртуктуры полупроводников IV группы. В. А. Филиков, В. Н. Гордеев, В. А. Лигачев и О. Е. Акимов 367
On superfluid ^3He–^4He mixtures in magnetic fields. *R. Gonczarek* 381
Calculation of electron density and surface energy by variation method. *A. Iskander* and *L. Orosz* 391
Characteristics of laser-heated titanium in a nitrogen atmosphere. *L. Nánai, I. Hevesi, B. S. Luk'yanchuk, E. M. Morozova, A. S. Rogachev, A. V. Simakhin, N. M. Sukonkhina* and *G. A. Shafeev* 405

CLASSICAL AND APPLIED PHYSICS

Analytic solution for combined forced and free convection from a non-isothermal wedge. *S. Antony Raj* 59
On the stability of shear flow. *Nguyen Thi Bang Van* 109
On the flow of the corotational Jeffrey body in circular pipes. *Nguyen Thi Bang Van* 115

ASTROPHYSICS

Can the creation of matter in the early universe stall inflation? *C. Wolf* 123

INTERDISCIPLINARY

The problem of anomalous near surface diffusion. *J. Giber, S. Kristyán* and *P. Deák* 335
Gaia hypothesis and atmospheric aerosol. *E. Mészáros* 343
Are lymphocytes excitable cells? *S. Damjanovich, M. Balázs* and *J. Szöllősi* 349
Measurement of oxide-layer thickness of internal granules in high-purity aluminium. *S. Takács, F. Ditrói* and *I. Mahunka* 355
A study of third harmonic mode acceleration for the MGC. *Z. Kormány, I. Szücs, A. Valek* and *J. Vámosi* 359

ERRATUM 441

BOOK REVIEWS 125, 443

CONTENTS

ELEMENTARY PARTICLES AND FIELDS

Higgs gravitational vacuum in the gauge gravitation theory. *G. Sardanashvily* and *B. Ikhlov* 79

ATOMIC AND MOLECULAR PHYSICS

The hyperfine interaction parameter $\rho(0)$ calculated by the $X\alpha$ method with ab initio self-consistent exchange parameter. *Á. Nagy* 55

Ab initio method for treatment of spatially extended systems, Parts I-III. *E. Kapuy, C. Kozmutza* and *Zs. Ozoróczy* 85

FLUIDS, PLASMAS AND ELECTRIC DISCHARGES

Influence of electrode temperature and auxiliary discharge on the electrical breakdown in helium. *M.M. Pejović* and *M.K. Radović* 19

An application of the governing principle of dissipative processes to eigenvalue problem of hydro-thermodynamics. *Nguyen Huyen Tung* 69

CONDENSED MATTER

Electron bombardment induced conductivity in crystalline anthracene. *M. Saleh* 3

The kinetics of growth and the morphological instability of zinc single crystals. *D. Iwanov* 11

Electron-phonon interaction in thin films. *J. Kierul* and *L. Wojtczak* 25

Electron-phonon interaction in transition metals. *J. Kierul* 33

Theoretical analysis of the Einstein relation in degenerate ternary chalcopyrite semiconductors in the presence of an arbitrarily oriented quantizing magnetic field. *M. Mondal, K.P. Ghatak* and *A.K. Das* 43

CLASSICAL AND APPLIED PHYSICS

Analytic solution for combined forced and free convection from a non-isothermal wedge. *S. Antony Raj* 59

On the stability of shear flow. *Nguyen Thi Bang Van* 109

On the flow of the corotational Jeffrey body in circular pipes. *Nguyen Thi Bang Van* .. 115

ASTROPHYSICS

Can the creation of matter in the early universe stall inflation? *C. Wolf* 123

BOOK REVIEWS 125

Acta Physica Hungarica 65 (1), pp. 3–9 (1989)

ELECTRON BOMBARDMENT INDUCED CONDUCTIVITY IN CRYSTALLINE ANTHRACENE

M. SALEH

Department of Physics, Bahauddin Zakariya University
Multan, Pakistan

(Received 8 August 1986)

A study of the electron-bombardment induced conductivity at room temperature in crystalline anthracene was made using the drift method. The observed low gain (≈ 10) for the current induced by the electron beam is attributed to the short recombination lifetimes $\approx 10^{-8}$s and the low quantum efficiency ($\approx 4\%$) of pair production. These results are explained on the basis of a simple photoconductor model. The values for the drift mobilities normal to the 'ab' crystallographic plane viz., $\mu_e = 0.37$ and $\mu_h = 0.98$ cm^{2}s^{-1}V^{-1} agree well with other published values.

1. Introduction

A considerable number of discrepancies in the measurement of quantum yield under different modes of excitation has been reported by various investigators. Kepler and Merrifield [1] state that 10^{-8} carriers are produced per square centimetre for total photon flux of 10^{14} cm^2 in a $1\mu s$ pulse, from which one deduces a quantum efficiency of about $10^{-4}\%$, but no explanation is given of the method they used to calculate the number of excited carriers. Raman et al [2] estimate a quantum efficiency of the order of $10^{-2}\%$. Batt et al [3] have reported that the quantum yield for single-photon bulk generation of charge carriers remains relatively constant at about $10^{-2}\%$ for photons over the energy range from 4.2 eV to about 6 eV. Geacintov and Pope [4] using uv, found yields of the order 0.4% of energy absorbed. This yield is an order of magnitude greater than that reported for X-ray excitation [5], at least an order of magnitude greater than that obtained for intrinsic excitation with red light or near uv [6] both involving exciton–exciton processes and also for intrinsic excitation with uv [7,8] ascribed to band-to-band transitions. However, regardless of which value is correct, it is quite obvious that the quantum efficiency for carrier production is very low.

The work reported here is aimed at studying the electron bombardment induced conductivity in crystalline anthracene at room temperature using the drift method essentially pioneered by Spear [9,10], and to explain the observed low gain (induced current/bombarding current) on the basis of a simple photoconductor model.

2. Experimental

2.1 Anthracene crystals

Anthracene crystals were grown from the vapour phase, after the method of Sloan [11], under a vacuum of less than 6.7×10^{-4} Nm^{-2}, following intensive purification efforts, including liquid column chromatography, sublimation and zone refining [12]. The apparatus used for zone-refining was a Sloan–McGowan zone-refiner, manufactured to the pattern of the original refiner designed by Sloan especially for anthracene [13]. The crystal growth vessel was part of the zone-refining assembly, so that it was possible to exclude oxygen from the anthracene from the time it was introduced to the zone-refining steps [12].

All crystals for use were checked as single crystals by observing the extinction between cross polaroids under a polarizing microscope. Typical crystal thicknesses were between 200–250 μm and had surfaces of 1 cm × 1 cm, which were 'ab' planes.* The crystals were equipped with evaporated aluminium electrodes on two opposite faces and the subsequent mounting was carried out as described by Saleh [14].

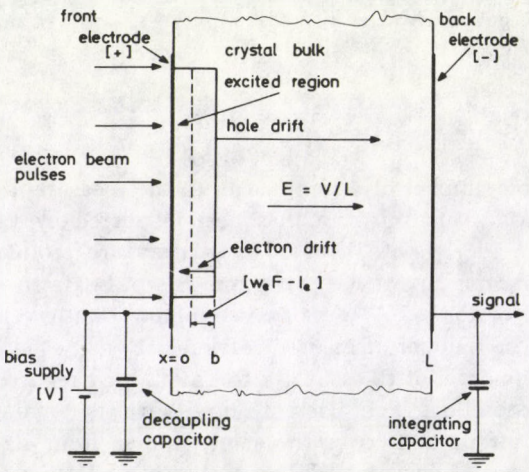

Fig. 1. Schematic arrangement for the measurement of transit time of positive carriers in an anthracene crystal

2.2. Basis of experiment

The experiment performed was essentially to irradiate the crystal specimen through a thin conducting electrode with a short pulse of electrons of energy between

*The orientation of the planes was kindly checked by Professor J. W. Jeffery of the Crystallography Department, Birkbeck College, University of London, London. U. K.

20 and 60 keV, and to record the transient charges induced on the opposite electrode for various applied electric field strengths in the crystal specimen (see Fig. 1). The bombarding electron pulses may be envisaged as generating electron-hole pairs in the region penetrated, and the subsequent drift of these carries as inducing charges on the electrodes. A bias field is essential not only to produce the drift, but also to prevent immediate recombination.

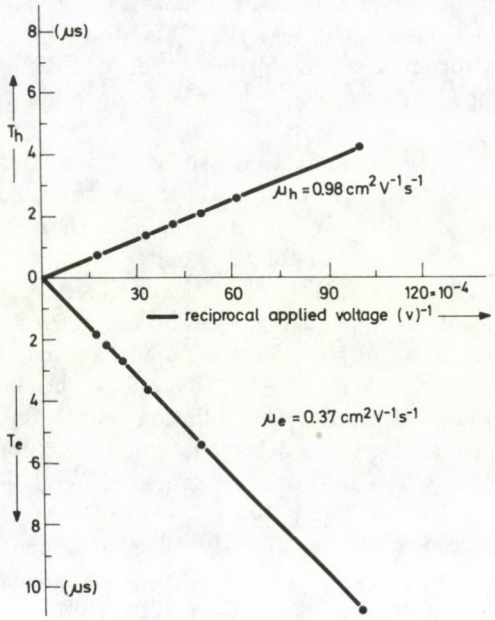

Fig. 2. Electron and hole transit time vs reciprocal applied voltage at 293 K for specimen No.12.12, thickness 200 μm

In the present experiments precautions were taken to avoid space charge effects such as those discussed by Saleh and Zafar [15]. The bombarding dose never exceeded 2.5×10^{-14} C (1.5×10^7 electrons per cm^2), and the bias was regularly reversed as explained by Saleh and Zafar [15]. The induced conductivity transient may thus be treated analytically in terms of the drift of a sheet of charge across a parallel plate capacitor on which the field is uniform. When the back electrode is at a positive potential V with respect to the front electrode , the end of the ramp (the "knee") corresponds to the electron transit time; when the back electrode is negative, the knee marks the hole transit time. Provided the field is uniform, i.e., space charge is negligible, the carrier mobility is given by $\mu = L^2/TV$. T was always found inversely proportional to V, thus confirming the assumption of a uniform field as shown in Fig. 2.

3. Results and interpretation

Following the procedure described above, the values found for the electron and hole mobilities in anthracene single crystals at room temperature are $\mu_e = 0.37$ $cm^2s^{-1}V^{-1}$ and $\mu_h = 0.98$ $cm^2s^{-1}V^{-1}$, respectively (Fig. 2). These values agree well with those given by Kepler [16], Bogus [17], Sansal and Schott [18], and Saleh [12,19].

Figure 3 shows the electron and hole charge collected as function of bias field and primary electron energy for specimen No.12.12 (representative of a group of specimens). Curves for primary energies of 50, 55 and 60 keV are indistinguishable. The absence of saturation implies that in the bombarded region the recombination current far exceeds the drift current. A simple photoconductor model is used to explain these results.

It is assumed that (i) the excitation can be regarded as uniform in a layer o....x....b (Fig.1) where $b << L$, the crystal thickness; (ii) the longer of the carrier recombination lifetimes in this region is much shorter than the pulse duration so that a steady state may be assumed for the greater part of the pulse; there is no injection of space charge at the bombarded electrode (see Section 2.2).

Let the direction of the applied bias field be as shown in Fig.1. Then during electron bombardment, the entire free electron population may be regarded as being displaced to the left by a distance $(w_eF - l_e)$, where w_e is the electron recombination mean free path per unit field and l_e the diffusion length for electrons, provided $w_eF > l_e$. This displacement creates a layer in which recombination may be neglected and which represents the predominant source of free holes. To this degree of approximation the hole charge Q_0^+ crossing unit area of the plane at 'b' to the right during electron bombardment, and eventually collected at the back electrode, is

$$Q_0^+ = q_0 w_e(F - l_e/w_e), \tag{1}$$

where q_0 is the total charge of either sign excited by the bombarding beam per cm^3 per pulse. If the voltage V is reversed, electron charge Q_0^- per unit area is collected and, therefore,

$$Q_0^- = q_0 w_h(F - l_h/w_h), \tag{2}$$

where w_h and l_h are the hole recombination mean free path and diffusion length, respectively.

Applying Eq. (1) or (2) to Fig.3, it is found that the intercept on the F-axis is $F_h^{'} = l_e/w_e$ or $F_e^{'} = l_h/w_h$, giving

$$w_{e,h} = kT/e(F_{h,e}^{'})^2. \tag{3}$$

This simple model fails when $F \leq F_{h,e}^{'}$ as there is then no layer in which recombination may be neglected, and also when $F > (b + l_{h,e})/w_{h,e}$ in which case the electrons liberated by electron bombardment are exhausted from the entire bombarded region and Q_0^+ or Q_0^+ should saturate at the value $q_0 b$. This could not be

observed at bias field up to 25 kV cm^{-1}. The crystal specimens break down at higher field strengths; this could be due to an intensive local field build up in the exhaustion region under these conditions.

Figure 3 shows that at constant bias field the charge drawn out of the bombarded region tends to saturate with primary electron energy; this is in confirmation with the idea that the charge originates from the end of this region. However, when the bombarding energy is reduced which in turn reduces the penetration depth 'b' a superlinear dependence of Q_0^+ or Q_0^- on F is obtained. A superlinear dependence of charge on field in anthracene excited by light has been reported by several investigators [2,7,20].

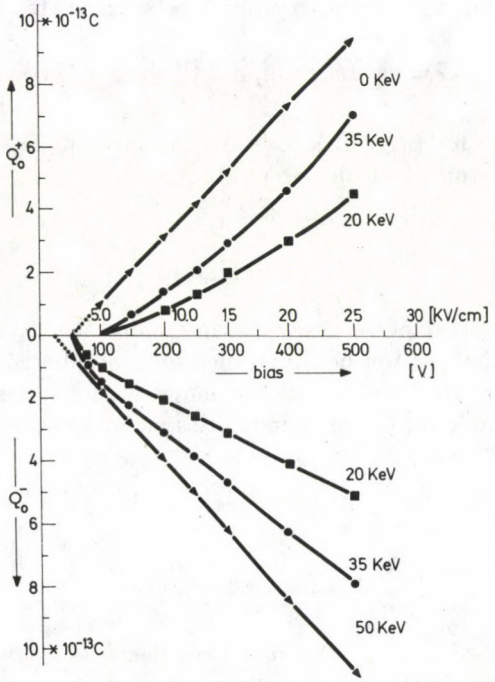

Fig. 3. Field dependence of electron and hole induced charge at 293 K. Specimen No.12.12, thickness 200 μm, $Q_b = 2.5 \times 10^{-14}$C/pulse

Therefore, applying this model to Fig. 3, the following approximate values are obtained,

$$w_h = 1.6 \times 10^{-8}\text{cm}^2V^{-1}, \qquad w_e = 0.4 \times 10^{-8}\text{cm}^2V^{-1},$$
$$\tau_h = 1.6 \times 10^{-8}\text{s}, \qquad \tau_e = 1.1 \times 10^{-8}\text{s}.$$

$\tau_{h,e}$ are the recombination lifetimes; $\tau_{h,e} = w_{h,e}/\mu_{h,e}$ where $\mu_{h,e}$ are the drift mobilities. Also from the slope of the straight lines in Fig. 3 and with the known value of $w_{h,e}, q_0$ can be calculated. Therefore, the quantum efficiency of pair production is given by the relation:

$$\eta = (q_0/Q_b) \cdot E_{h,e}/(\overline{dE_b/dx}),$$

where Q_b is the charge deposited by the electron beam through 1 cm^2 of surface to form a free carrier pair, and $(\overline{dE_b/dx})$ the average rate of energy lost by a bombarding electron per cm path. Substituting $E_{h,e}$ =5 eV [20], $(\overline{dE_b/dx}) = 2\times10^7$ eV cm^{-1} [21], in the above equation, quantum efficiency η of pair production of the order of 4% is obtained and, therefore, an estimate of the current gain 'G' which is expected in such thin anthracene crystals can be calculated by the formula:

$$G = \eta\,[(\overline{dE_b/dx})/E_{h,e}]\,(w_h + w_e)F.$$

Taking half the value for (dE_b/dx) to allow for incomplete excitation and F = 10 kV cm^{-1}, $G \approx 16$ which is of the order observed.

4. Conclusions

The field dependence of the collected charge and the small gain (≈ 10) for the current induced by the electron beam is, therefore, attributed to the short recombination lifetimes of $\approx 10^{-8}$ and a quantum efficiency for carrier pair production of $\approx 4\%$. The values found for the drift mobilities normal to the 'ab' crystallographic plane viz., $\mu_e = 0.37$ and $\mu_h = 0.98$ cm^{2}s^{-1}V^{-1} agree well with other published values.

Acknowledgement

The author wishes to thank the Chairman, Department of Physics, Birkbeck College, University of London, London for providing him with the facilities for conducting the experimental work. The author also acknowledges the Central Research Fund of the University of London for the provision of a zone melter.

References

1. R.G. Kepler and R.E. Merrifield, J. Chem. Phys., *40*, 1173, 1964.
2. R. Raman, L. Azarraga and S.P. McGlynn, J. Chem. Phys., *41*, 2516, 1964.
3. R.H. Batt, C.L. Braun and J.F. Horning, Appl. Opt. Suppl., *3*, 20, 1969.
4. N. Geacintov and M. Pope, J. Chem. Phys., *54*, 3884, 1966.
5. R.G. Kepler, and F.N Coppage, Phys. Rev., *151*, 610, 1966.
6. H. Bauser, Naturwiss., *54*, 505, 1967.

7. G. Castro and J.F. Horning, J. Chem. Phys., *42*, 1459, 1965.
8. R.F. Chaiken and D.R. Kearns, J. Chem. Phys., *45*, 3966, 1966.
9. W.E. Spear, Proc. Phys. Soc., *B70*, 669, 1957.
10. W.E. Spear, J. Non-Cryst. Solids, *1*, 197, 1969.
11. G.J Sloan, Molec. Cryst., *2*, 323, 1967.
12. M. Saleh, Japanese Journal of Applied Phys., *17*, No. 6. (June), 1978.
13. G.J. Sloan and N.H. McGown, Rev. Sci. Instr., *34*, 60, 1963.
14. M. Saleh and M.S. Zafar, Acta Phys. Hung., *45*, 233, 1978.
15. M. Saleh and M.S. Zafar, Acta Phys. Hung., *60*, 161, 1986.
16. R.G. Kepler, Organic Semiconductors, p.1. The Macmillan Co., New York, 1962.
17. C. Bogus, Z. Physik, *207*, 281, 1967.
18. B. Sansal and M. Schott, Solid State Commun., *8*, 1499, 1970.
19. M. Saleh, J. Phys. C: Solid State Phys., *9*, 4165, 1976.
20. I. Nakada and Y. Ishihara, J. Phys. Soc. (Japan), *19*, 695, 1964.
21. W. Ehrenberg and D.E.N. King, Proc. Phys. Soc. (London), *81*, 751, 1963.

Acta Physica Hungarica 65 (1), pp. 11–17 (1989)

THE KINETICS OF GROWTH AND THE MORPHOLOGICAL INSTABILITY OF ZINC SINGLE CRYSTALS*

D. IWANOV

Institute of Physical Chemistry, Bulgarian Academy of Sciences
1040 Sofia, Bulgaria

(Received 16 October 1986)

The effect exerted by diffusion upon the kinetics and morphological stability of zinc single crystals during growth from vapour phase in the presence of argon is studied. The shift of the basal face in normal direction and the growth of the edge of the same face as a function of time is checked at constant temperature and constant supersaturation at high vacuum or argon pressure 666-33330 Pa. Linear and parabolic dependences of the crystal size R as a function of the time t, respectively of the length of the basal edge a as a function of the time as well as the kinetic critical size R_k, respectively a_k are established. In agreement with the isotropic theory of Chernov and Cahn, zinc single crystals with sizes R smaller than R_k grow in a kinetic regime, while those with sizes R larger than R_k grow in a diffusion regime. It is shown that the results of the kinetic investigations are in good agreement with data obtained by morphological studies.

Introduction

The rate of crystal growth generally depends on the transport of matter within the bulk of the parent phase and the elementary processes upon the surface of the crystals. The consideration of the surface processes only during growth in vacuum and the retention of the polyhedral form has been shown by Kaischew, Stranski et al [1, 2]. The predominant effect of bulk diffusion has been studied by Chernov [3] and Cahn [4]. Nanev and Iwanov [5, 6] have established that during the growth of zinc single crystals from a vapour phase in the presence of hydrogen and argon, when a certain size is surpassed, a depression appears upon the smooth basal face. The transition from polyhedral to skeleton growth hitherto has been mainly investigated by a morphological approach. The present paper is aimed at the confirmation that diffusion in a vapour phase affects not only the morphological stability, but also the kinetics of crystal growth.

Experimental

The kinetic and morphological investigations were carried out with zinc single crystals prepared by the method of Stranski and Kaischew, described earlier [2, 5].

*Paper presented at the HCCG-4 Conference, Budapest, 22-25 July 1986.

By this method the single crystals are obtained in a glass ampoule from a molten droplet using a furnace with a cooling finger. A constant temperature difference ΔT between the furnace and the finger determined the supersaturation σ. The zinc single crystals were grown in a vapour phase at a constant temperature of the furnace $T = 400°C$, $\Delta T = 20°C$ ($\sigma = 0.6$) in the presence of highly purified argon at the following pressure : 666, 1333, 6666, 13332, 19998 and 33330 Pa.

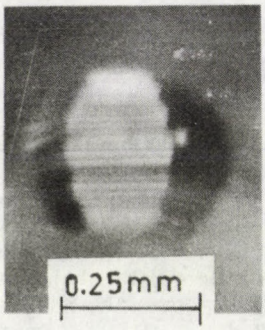

Fig. 1. Zinc single crystal grown in the presence of argon, $P_{Ar} = 1333$ Pa

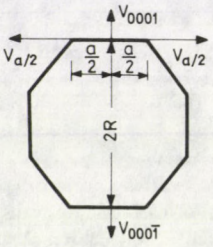

Fig. 2. Schematic representation of zinc single crystal

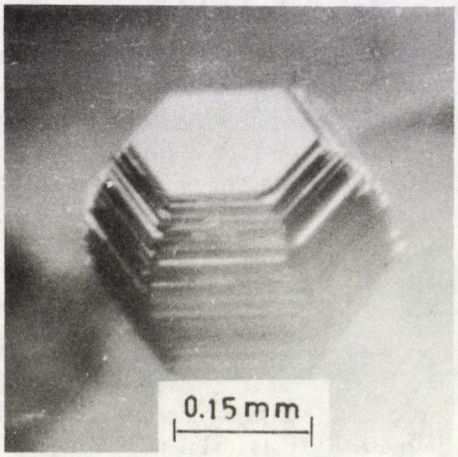

Fig. 3. Zinc single crystal with a smooth basal face

The kinetic studies included the measurement of the shift of the basal face in normal direction as a function of the time t [7]. The measurements were carried out as the single crystals lay with one of their prismatic faces upon the glass ampoule and the two {0001} faces were positioned laterally (Fig.1). Thus the distance between the two opposite basal edges $2R$ was measured (Fig.2).

At each pressure of argon used in the experiments, as well as at vacuum $1.33 \cdot 10^{-4}$ Pa, we carried out 10–15 separate measurements using crystals with sizes within the range $R = 0.4 \cdot 10^{-2}$ to $3.5 \cdot 10^{-2}$ cm. Under the same experimental conditions we carried out 10 to 20 separate measurements of the growth of the edge of the basal face a as a function of time t [8]. In the latter case the {0001} face was situated on the upper side of the single crystals (Fig.3). The size a had the same values as that of R. Simultaneous measurements were made of the change of R and a with time t using identical crystals (Fig.2).The morphological observations of the {0001} face were also carried out simultaneously with the measurements of the increase of the edge length a as a function of the time t [8].

Results and discussion

It has been established that the size R of small zinc single crystals increases linearly with the time t (Fig.4).

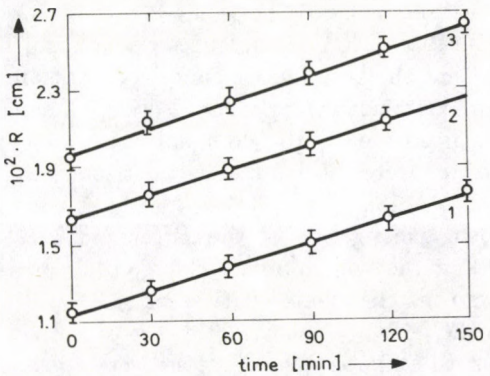

Fig. 4. The size R as a function of the time t of three zinc single crystals 1, 2, 3, grown at $P_{Ar} = 1333$ Pa. The error bar shows the accuracy of the measurements

The linear relationships show that the growth rate is constant. A crystal dimension region exists, where the linear $R(t)$ relationship is transformed into a non-linear one. The non-linear $R(t)$ curves were approximated to $R^2 = a_1 + b_1 t$ -type parabolas, where a_1 and b_1 are constants. Fig.5 shows the relationship between R^2 and t at $P_{Ar} = 6666$ Pa.

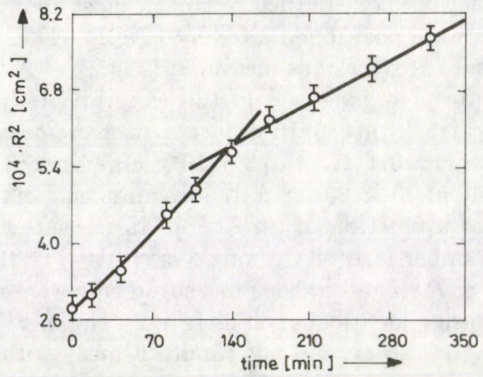

Fig. 5. R^2 as a function of the time t of a zinc single crystal, grown at $P_{Ar} = 6666$ Pa. The intersection point of the curves determines the critical size R_k

It can be noted that the last 5 points are well fixed on a straight line, confirming that the $R(t)$ relationship in this region is parabolic. All graphical relationships comprising two regions displayed an abrupt transition. From the intersection point of the two separate curves of a given graph the kinetic critical size R_k was determined [7] (Fig.5). When the initial size of zinc single crystal R_0 was larger than the critical size R_k, only parabolic $R(t)$ dependences were obtained. It follows from the parabolic relationship that the growth rate is not constant and depends on the size R. Under high vacuum conditions only linear $R(t)$ dependences were obtained, i.e. the single crystal growth proceeded at a constant rate.

Similar relationships were obtained when the size a was plotted with the time t : linear and parabolic $a(t)$ [8].

The simultaneous investigation of the $R^2(t)$ and $a^2(t)$ relationships established that both curves at the same moment change their initial shape into a linear one. This result shows that the kinetic critical sizes R_k and a_k [8] fix an identical transition moment in the growth of the {0001} face of the zinc single crystals.

The results from the kinetic investigations were considered by applying the isotropic theory of Chernov [3] and Cahn [4]. According to the theory, the growth of a spherical crystal from an unstirred solution under diffusion transport conditions proceeds in two stages, depending on the value of the radius R : kinetic and diffusion. The kinetic regime is characterized by a constant rate of growth and a linear increase of the size R with time t. During a diffusion regime the growth rate is not constant and depends on the crystal size R. Under this growth regime the radius of the sphere R changes with time t according to a parabolic relation.

In agreement with the isotropic theory [3,4], we accept that the size R of the zinc single crystals is the radius of the sphere, inscribed between the two basal faces (Fig. 2).

The results from the kinetic investigations were compared with the basic conclusions of the isotropic theory. The observed linear $R(t)$ and $a(t)$ relationships and the constant growth rate suggest that the small size zinc single crystals grow in a kinetic regime. The establishment of parabolic $R(t)$ and $a(t)$ relationships and rates dependent on the size R show that larger single crystals grow in a diffusion regime. Consequently, the transition between the two growth modes begins at the kinetic critical size R_k and a_k, respectively.

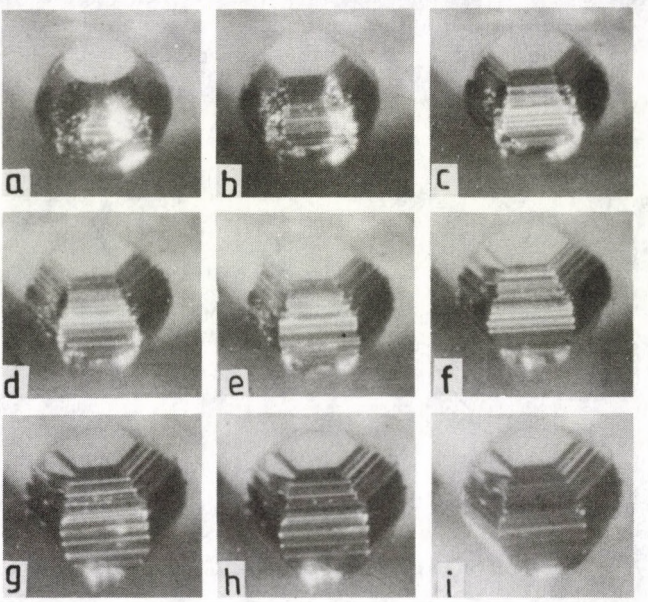

Fig. 6. Consecutive growth stages of a zinc single crystal at $P_{Ar} = 13332$ Pa, magnification 25 X

Table I

Values of V, β, D, R_k and R_{th}

P_{Ar} [10^3 Pa]	V [10^{-7} cm/s]	β [cm/s]	D [cm^2/s]	R_k [10^{-2} cm]	R_{th} [10^{-2} cm]
0.666	16 ± 3.5	191.38	4.72 ± 1.0	3.00 ± 0.35	2.46
1.333	10 ± 2.0	119.61	1.79 ± 0.5	2.60 ± 0.30	1.49
6.666	6 ± 1.5	71.77	0.77 ± 0.3	1.90 ± 0.35	1.07
13.332	2.9 ± 0.4	34.68	0.41 ± 0.2	1.65 ± 0.35	1.18
19.998	2.6 ± 0.9	31.10	0.248 ± 0.05	1.50 ± 0.20	0.79
33.330	1.6 ± 0.4	19.13	0.088 ± 0.05	< 0.78	0.46

The values of the growth rate V and the kinetic coefficient β were calculated by using the basic relationships of the isotropic theory and the slopes of the $R(t)$ curves, while the parabolic $R(t)$ graphs served for the evaluation of the diffusion coefficient D [7]. The V and β values characterize the growth mode during predominant surface processes, while D values are relevant when diffusion is the rate determining factor. Data of V, β and D are presented in Table I. The calculated data of V and D are not in agreement with literature data given by Parker et al [9] for V in vacuum and Redko and Kosinar [10] in the case of D.

The theoretical critical size R_{th} when the transition from kinetic to diffusion regime begins was calculated from the ratio between the values of D and β. The comparison of the values of the critical sizes R_k and R_{th} (Table I) shows that the agreement between theoretical and experimental data is fairly good. The R_k data represent the first experimental proof of the isotropic theory [3,4].

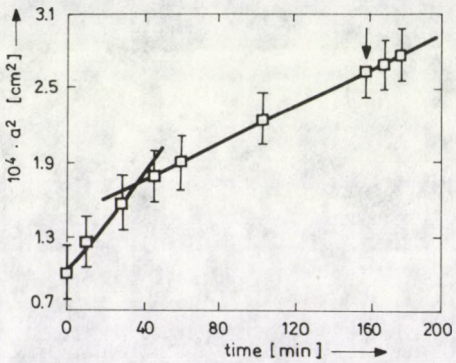

Fig. 7. a^2 as a function of the time t of a zinc single crystal shown in Fig. 6

We presume that during the transition from a kinetic to a diffusion regime of growth, surface changes occur upon the basal face. This presumption was checked by carrying out simultaneous kinetic and morphological studies using the same crystal. The zinc single crystals were oriented so as to fix the {0001} face on the top, as shown in Fig. 3. A similar orientation offered a possibility to measure the growth of the edge of the basal face a with time t, simultaneously observing the changes upon the surface of the face. At the moment when a depression appeared upon the basal face, we determined the observed morphological size a_m. Fig. 6 provides an illustration of consecutive growth of a zinc single crystal. The comparison between the plotted $a^2(t)$ dependence (Fig. 7) and Fig. 6 shows that the size a_k corresponds to Figs. 6c, 6d while a visible depression is not formed until Fig. 6g. The vertical arrow shows the moment when the size a_m is attained. It can be noted that the sizes a_k and a_m do not coincide. In fact this discrepancy is fictitious, since at the moment

of transition from a kinetic to a diffusion regime, the morphological stability of the face is disturbed. However, at the magnifications we used in the investigations, the microscopic changes upon the basal face were invisible. Only after the crystal was grown and the surface changes became macroscopic we were able to check the morphological size a_m.

Conclusion

The investigation of zinc single crystal growth in the presence of argon shows that as a result of the effect of diffusion in the vapour phase, when a certain size of the crystals is reached, a transition from kinetic to diffusion regime begins and the morphological stability is lost.

The author is indebted to Dr. St. Stojanov and Prof. A. A. Chernov for helpful discussions.

References

1. R. Kaischew and I.N. Stranski, Z. phys. Chem., *B 26*, 100, 1934.
2. R. Kaischew, Chr. Nanev, phys. stat. sol., *10*, 779, 1965.
3. A. A. Chernov, Kristallografiya, *16*, 842, 1971.
4. J. Cahn, in Proc. Int. Conf. Cryst. Growth, Boston 1966, ed. H. S. Peiser, Pergamon Press, Oxford, 1967, p.681.
5. Chr. Nanev and D. Iwanov, J. Cryst. Growth, *3/4*, 530, 1968.
6. Chr. Nanev and D. Iwanov, Cryst. Res. Technol., *17*, 575, 1982.
7. D. Iwanov and A. A. Chernov, to be published.
8. D. Iwanov, to be published.
9. R. I. Parker and L. M. Kusner, J. Chem. Phys., *35*, 1345, 1961.
10. T. P. Redko and I. Kosinar, Czech. J. Phys., *B30*, 1293, 1980.

Acta Physica Hungarica 65 (1), pp. 19–23 (1989)

INFLUENCE OF ELECTRODE TEMPERATURE AND AUXILIARY DISCHARGE ON THE ELECTRICAL BREAKDOWN IN HELIUM

M.M. PEJOVIĆ

Faculty of Electronic Engineering
18001, Niš, Yugoslavia

and

M.K. RADOVIĆ

Philosophical Faculty, P.F. 92,
18001, Niš, Yugoslavia

(Received in revised form 30 October 1986)

The influence of electrode temperature and the auxiliary discharge on the statical breakdown voltage and the electrical breakdown time delay in helium-filled diodes has been investigated. It was shown that the statical breakdown voltage decreased about 20 % with increasing the temperature of electrodes up to 450°C. With increasing the temperature, the time delay decreased, too, and the current of discharge increased. The results show that time delay decreased with increasing the current of the auxiliary discharge. It was found that these changes are the result of the presence of metastables in helium which can initiate the electrical breakdown by releasing the electrons from the cathode.

1. Introduction

It is known that, when the cathode is heated to a high temperature, the intensive thermoelectric emission has influence on the breakdown. Some investigations [1,2] showed that there is some influence on the breakdown when the electrode temperature is below 400°C. This influence was investigated by the breakdown time delay measurements method.

Recent investigations [2,3,4,5] showed that in the case of a long period of breakdown delay the dominant role in initiating the electrical breakdown was played by metastable atoms or molecules in the gases. The metastables can release the electrons from the cathode and initiate the electrical breakdown in gases [6]. This effect was used for studying the influence of electrode temperature and auxiliary discharge on the electrical breakdown in helium.

2. Experiment

A specially designed tube with two loop-formed electrodes was used, given schematically in [7]. The loops were made of 0.4 mm diameter tungsten wires with a thermocouple brazed to the central part of the electrode, where the highest temperature is expected. Corresponding feed-throughs were provided. The thermocouple was calibrated after mounting and then the whole set-up was completed. Before filling the tube it was baked, evacuated to 10^{-7} mbar and simultaneously heated to 450°C. In this case the tube was filled with helium of 40 mbar with an oxygen impurity content less than 1 ppm (Matheson Co.).

Before measuring the electrodes were conditioned in the way described in [4]. Measurements were done at the main diode of a gap length of 2 mm. The gap length of the auxiliary diode was 4 mm.

The measurements of electrical breakdown time delay t_d were carried out by an electronic timer as described in [1]. The measurements of static DC breakdown voltage U_s are described in [8]. In this case the main diode was irradiated with ^{60}Co with an activity 28 MBq.

3. Results and discussion

The static breakdown voltage as a function of electrode temperature for the main diode is given in Fig. 1 with curves a and b. From that Figure it can be seen that U_s decreases with increasing the electrode temperature.

To determine the thermoelectric emission of the cathode, we calculated the thermoelectric emission current density using the Richardson–Dushmans expression [9]. The calculated value of the thermoelectric emission current density for the experimental conditions at 450°C is about $10^{21}\,\mathrm{A}\cdot\mathrm{m}^{-2}$. On the basis of this result it is obvious that the influence of thermoelectric emission can be neglected. It seems that the static breakdown voltage depends only on the temperature of the gas.

Fig.1, curve c, gives the electrical breakdown time delay as a function of the cathode temperature t. The applied voltage was 1180 V. The passive time τ (time between two successive measurements during the voltage on the diode is zero) was 10 s. After 10 s passive time all ions can be considered as recombined while only one part of metastables is deexcited. From curve c it can be seen that with increasing the cathode temperature from 20 to 450°C the time delay decreased about one order of magnitude.

Metastables impacting the cathode release secondary electrons. The number of the released secondary electrons is proportional to the number of metastable states impacting the cathode in unit time:

$$N_s = \gamma_m \frac{N_m \cdot \bar{v}}{4}, \tag{1}$$

where γ_m is the coefficient of secondary emission of electrons under bombardment with metastables, N_m is the concentration of metastables in the gap and $\bar{v}$ is their thermal velocity.

The gas pressure p rises with heating the electrode, $p = p(T)$, T being the gas temperature in the interelectrode space. Taking into account a relatively small gap length of 2 mm the cathode temperature can be considered approximately equal to the gas temperature in the interelectrode space. The concentration N_m changes as $p(T)/kT$, while $\bar{v}$ rises as $C \cdot \sqrt{T}$. Then:

$$N_s(T) \sim \gamma_m \frac{p(T)}{kT} \cdot C \cdot \sqrt{T} \sim C_1 \cdot \frac{p(T)}{\sqrt{T}}. \tag{2}$$

Exp.(2) shows that when $p(T)$ rises faster than $\sqrt{T}$, then $N_s(T)$ rises with temperature.

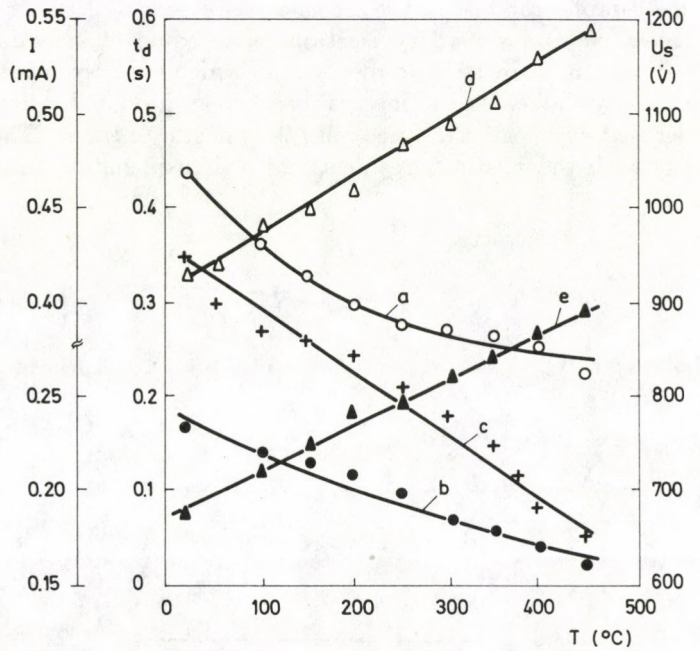

Fig. 1. Static breakdown voltage U_s, time delay t_d and discharge current I as a function of temperature T of electrodes:

a–U_s when cathode was heated
b–U_s when anode was heated
c–t_d when cathode was heated
d–I when cathode was heated
e–I when anode was heated

Fig.1, curves d and e, give the glow current as a function of the electrode temperature. The applied voltage for cathode heating was 1180 V and for anode heating was 910 V. From Fig.1, curves d and e, one can see that the current of glow discharge increased no matter whether cathode or anode was heated.

Fig.2 gives the time delay as a function of passive time of the diode. The measurements were carried out for the cases when there were glow discharges on the auxiliary diode with currents of 10^{-6} A (curve a) and 10^{-3} A (curve b). We presume that the curves a and b are the results of diffusion of the metastable helium atoms from the auxiliary discharge. In the stationary state there is a steady concentration of metastables in the electrode gap of the main diode which, by striking the cathode, gives the steady number of secondary electrons per time unit.

In the afterglow regime the concentration of metastable atoms in the main diode was created in the previous discharge and decreased by the exponential law [10]. These metastables can release the secondary electrons by striking the cathode, too, so the total yield of secondary electrons is the sum of secondary electrons released from the cathode by striking metastables which were produced in the main and in the auxiliary diode. As the integral breakdown probability depends on the number of released electrons, the time delay is opposite to them. The increase of the time delay with the τ is in agreement with this explanation (see curve a in Fig.2).

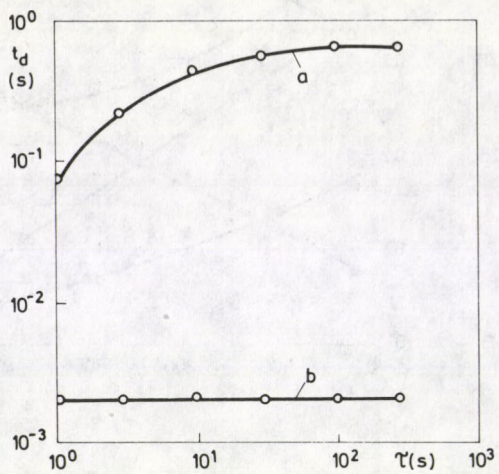

Fig. 2. Time delay t_d as a function of passive time τ. Current in the auxiliary diode:

$a - I = 10^{-6}$ A

$b - I = 10^{-3}$ A

When the current in the auxiliary discharge is 1 mA, the created concentration of metastable atoms is enough to establish the steady concentration in the

main diode space, which is higher than the concentration of metastables from the main discharge for the passive times used in this work (1 – 300 s). So the curve b does not depend on τ.

There are, of course, other factors which can ionize the gas such as photons produced in the auxiliary discharge, cosmic and radioactive rays. We presume that, in our experimental conditions, the effect of metastable atom diffusion from auxiliary to main diode was dominant.

4. Conclusion

The results of this work show that there is a change of breakdown conditions in helium for the electrode temperature from 20°C to 450°C no matter that there is no thermoelectric emission from the cathode. The curves a and b in Fig.1 are similar to the curve given by Nagata et al [11] for heating air and nitrogen at a pressure of 1 bar. That indicates that decreasing of the breakdown voltage with increasing the cathode temperature up to 450°C is the result of heating the surrounding gas in the diode.

With gas temperature increasing, the thermal velocity of the metastable atoms in helium afterglow increased. So the probability of secondary electron releasing from the cathode and the breakdown probability increased, too. In that way the time delay of the electrical breakdown decreased. This explanation is in agreement with the curve c in Fig.1.

It is also shown (Fig.1, curves d and e) that the discharge current increased no matter whether cathode or anode was heated.

Fig.2 shows that the number of metastables which generate on the distance of 15 cm in the auxiliary diode can arrive by diffusion through the 10 mm diameter tube and they can have a great influence on the breakdown in the main diode.

References

1. Dj.A. Bošan and M.M. Pejović, J.Phys.D:Appl.Phys., *12*, 1699, 1979.
2. M.M. Pejović and Dj.A. Bošan, J.Phys.D:Appl.Phys., *14*, 693, 1981.
3. M.M. Pejović, B.J. Mijović and Dj.A. Bošan, J.Phys.D:Appl. Phys., *16*, L149, 1983.
4. M.M. Pejović, B.J. Mijović and Dj.A. Bošan, J.Phys.D:Appl. Phys., *17*, 351, 1984.
5. Dj.A. Bošan, M.K. Radović and Dj.M. Krmpotić, J.Phys.D:Appl. Phys., *19*, 2343, 1986.
6. D.V. Razevig and M.V. Sokolova, Raschat nachal'nyh i razrayadnyh gazovy promedzutkov, Energya, Moskva, 1977.
7. Dj.A. Bošan and M.M. Pejović, Acta Phys. Hung., *59*, 239, 1986.
8. B.J. Mijovic and M.M. Pejović, Contributed papers of XXVIII Yugosl.Conf. for ETAN, Split, II.243, 1984.
9. I. Slivkov, V. Mihaylov, N. Sidorov and A. Nastyuha, Elektrichesky proboi i razryad v vakuume, Atomizdat, Moskva, 1966.
10. W. Wieme and J. Lenaerts, Physica, *98C*, 229, 1980.
11. M. Nagata, I. Miyachi and Y. Yokoi, 5th Int. Conf. on the Gas Discharges, Liverpool, 316, 1978.

Acta Physica Hungarica 65 (1), pp. 25–32 (1989)

ELECTRON – PHONON INTERACTION IN THIN FILMS*

J. KIERUL and L. WOJTCZAK

Department of Solid State Physics, Institute of Physics, University of Lódź
90-238 Lódź, Poland

(Received 7 January 1987)

The electron–phonon interaction decoupling scheme in thin films is considered. The decoupled Green functions satisfy the equations containing the additional interaction terms calculated in a self-consistent way for the local quantities such as the mean square displacements of atoms and the occupation numbers of electrons. In particular, the appearance of these additional terms of the mass operator character allows us to expect that the electron phonon interaction is responsible for the stable structure of films.

1. Introduction

The electron–phonon interaction plays an important role in determining both the electron and phonon properties of transition metals. The purpose of the present paper is to extend the theory of the electron – lattice coupling to the case of thin films in order to describe the surface effects and their influence on electron and phonon properties. The generalized theory describing these properties for bulk samples and based on the double-time Green function technique was proposed in [1,2] and seems to be the most convenient approach to be extended to metallic thin films.

Usually, the electron–phonon interaction is considered for the Hamiltonian consisting of three parts: phonon and electron as well as electron–phonon coupling terms. The self-consistent theory of phonons is well developed in terms of the double-time Green function technique [3,4] and applied to thin films in pseudoharmonic approximation [5]. The electronic Hamiltonian is chosen in the Hubbard model form which turned out to be sufficient for the explanation of many features of the electron system, although the application of the double-time Green functions to thin films has even been given for a more general form of the Hamiltonian [6]. Thus, the descriptions of free electrons and free phonons refer to known formulations mentioned above and the present paper deals will the description of the electron–lattice coupling term appearing in thin films. Our approach is based on the preliminary results for bulk bodies discussed in the case of linear approximation with respect to the ion displacement operators as well as the electron occupation numbers. The methods are based on the molecular field decoupling scheme [7] or a more advanced decoupling procedure [8]. The different ways for the electron–phonon interaction representation can be discussed as particular cases of the generalized version proposed in [1,2]. Therefore, we apply this version in order to extend it for thin films and surface regions.

*This paper was supported by the program CPB 01.08

2. The electron – phonon coupling model

We consider the model of a thin film with the Hamiltonian consisting of anharmonic terms of the ion–ion interaction and non-linear terms in the ion–electron interaction as well as the Hubbard model of electrons. The Hamiltonian of the model reads then [1,2]

$$H = H_{\mathrm{e}} + H_{\mathrm{ph}} + H_{\mathrm{eph}} \tag{1}$$

with

$$H_{\mathrm{e}} = \sum_{j\nu j'\nu'} \sum_{\sigma} t_{j\nu,j'\nu'} a^{+}_{j\nu\sigma} a_{j'\nu'\sigma} + \sum_{\nu j} U_{\nu} n_{\nu j\uparrow} n_{\nu j\downarrow}, \tag{2}$$

$$H_{\mathrm{ph}} = \sum_{\nu j} \frac{P^2_{\nu j}}{2M_{\nu}} + \Phi(u_{\nu j}), \tag{3}$$

$$H_{\mathrm{eph}} = \sum_{\nu j\nu' j'} \sum_{\sigma} S_{\nu j\nu' j'}(u) a^{+}_{\nu j\sigma} a_{\nu' j'\sigma}, \tag{4}$$

where $(j,\nu),(j'\nu')$ denote the sites of the lattice according to the Valenta model of a thin film [9, see also 5,6], i.e. j, j' are the site numbers in the monoatomic layer parallel to the surface and ν, ν' label the atomic layers. The functions Φ and S are analytical functions of the displacement operators.

For the sake of simplicity we assume that only one kind of atoms is considered and all parameters of the model have the translational symmetry in the plane of a film. The functions $S(u)$ are chosen so that

$$\left\langle S_{j\nu,j'\nu'}(u) \right\rangle = 0. \tag{5}$$

If the condition (5) is not observed we simply can include $\left\langle S_{j\nu,j'\nu'}(u) \right\rangle$ to the electronic term of the Hamiltonian and redefine the hopping parameters.

The Hamiltonian (1) is of the general form and follows directly from the general considerations reported in [1] under the assumption that the electron interaction term takes the Hubbard form.

Let us remark that the model (1) is a generalization of both the Hubbard model and the Barisic–Lubbe–Friedel model [10] which is known in literature.

3. Electron Green function

We use the double-time thermodynamic Green functions [7]. In order to calculate the electron Green function we use the mixed representation of electron states:

$$\begin{aligned} a^{+}_{k,\nu\sigma} &= \frac{1}{\sqrt{N}} \sum_{j} e^{ikR_j} a^{+}_{j\nu\sigma}, \\ a_{k\nu\sigma} &= \frac{1}{\sqrt{N}} \sum_{j} e^{-ikR_j} a_{j\nu\sigma}, \end{aligned} \tag{6}$$

where k is a two-dimensional Bloch vector and N is the number of layers. The equations of motion for the electron Green function

$$G^{\sigma}_{\mu\nu k} = \ll a_{\mu k\sigma} | a^{+}_{\nu k\sigma} \gg_{\omega} \tag{7}$$

have the following form:

$$\omega G^{\sigma}_{\mu\nu k} = \delta_{\mu\nu} + \sum_{\mu'} \epsilon_{\mu\mu' k} G^{\sigma}_{\mu'\nu k} + U_{\mu} n_{\mu\bar{\sigma}} G^{\sigma}_{\mu\nu k} + \sum_{\mu'} \ll S_{\mu\mu' k}(u) a_{\mu' k\sigma} | a^{+}_{\Psi k\sigma} \gg . \tag{8}$$

We employ the Hartree–Fock approximation in the electron interaction term:

$$n_{\mu\bar{\sigma}} = \frac{1}{N} \sum_{q} \langle n_{\mu q\bar{\sigma}} \rangle . \tag{9}$$

The Fourier-transformed parameters of the Hamiltonian are

$$\epsilon_{\mu\mu' k} = \sum_{j} t_{\mu j, \mu' j'} e^{-ik(R_j - R_{j'})} \tag{10}$$

and a similar expression can be written for $S_{\mu\mu' k}(u)$.

We define the irreducible Green functions as in [1,2,4]:

$$\ll u_1 \dots u_n a | a^{+} \gg = \sum_{m=0}^{n} \binom{n}{m} \langle u_{m+1} \dots u_n \rangle \ll u_1 \dots u_m a | a^{+} \gg^{\mathrm{irr}} . \tag{11}$$

Introducing the Taylor expansion of $S_{\mu\mu' k}(u)$:

$$S_{\mu\mu' k}(u) = \sum_{p=0}^{\infty} \frac{1}{p!} \sum_{1 \dots p} S^{1 \dots p}_{\mu\mu' k} u_1 \dots u_p \tag{12}$$

we define the renormalized expansion coefficients

$$\tilde{S}^{1 \dots p}_{\mu\mu' k}(u) = \sum_{R=0}^{\infty} \frac{1}{R!} \sum_{1 \dots R} S^{1 \dots p 1 \dots l}_{\mu\mu' k} \langle u_1 \dots u_l \rangle \tag{13}$$

and the renormalized electron–phonon interaction functions:

$$\tilde{S}_{\mu\mu' k}(u) = \sum_{p=0}^{\infty} \frac{1}{p!} \sum_{1 \dots p} \tilde{S}^{1 \dots p}_{\mu\mu' k} u_1 \dots u_p . \tag{14}$$

By means of the last function and by employing the technique of differentiating over the second time-variable [1,2,4,8] we arrive at the following expression for the electron Green function

$$G^{\sigma}_{\mu\nu k} = G^{0\sigma}_{\mu\nu k} + \sum_{\mu'\nu'} G^{0\sigma}_{\mu\mu' k} K_{\mu'\nu' k} G^{0\sigma}_{\nu'\nu k}, \tag{15}$$

where the zero-order Green function is given by

$$\sum_{\nu} [(\omega - U_{\mu} n_{\mu\bar{\sigma}})\delta_{\mu\nu} - \epsilon_{\mu\nu k}]\, G^{0\sigma}_{\nu\mu' k} = \delta_{\mu\mu'} \tag{16}$$

and the scattering operator has the following form

$$K_{\mu\nu k} = \sum_{\mu'\nu'} \ll \tilde{S}_{\mu\mu' k}(u) a_{\mu' kG} | \tilde{S}_{\nu'\nu k}(u) a^{+}_{\nu' k\sigma} \gg^{\mathrm{irr}} . \tag{17}$$

In order to get an expression for the electron Green function of the form of Dyson equation we have to introduce the proper parts of the irreducible Green functions. The proper parts obey the equations:

$$\ll u_1 \ldots u_n a | u_1 \ldots u_m a^{+} \gg^{ir} = \ll u_1 \ldots u_n a | u_1 \ldots u_m a^{+} \gg^{p} +$$

$$+ \sum \ll u_1 \ldots u_n a | B_{\nu k} \gg^{p} G^{0}_{\nu\nu' k} \ll A_{\nu' k} | u_1 .. u_m a^{+} \gg^{ir}, \tag{18}$$

where the following abbreviations have been employed:

$$B_{\nu k} = \sum_{\nu'} \tilde{S}_{\nu'\nu k}(u) a^{+}_{\nu' k\sigma}, \tag{19}$$

$$A_{\nu k} = \sum_{\nu'} \tilde{S}_{\nu\nu' k}(u) a_{\nu' k\sigma}. \tag{20}$$

Making use of (18) and (15–17) we obtain for the electron Green function

$$G^{\sigma}_{\mu\nu k} = G^{0\sigma}_{\mu\nu k} + \sum_{\mu'\nu'} G^{0\sigma}_{\mu\mu' k} M_{\mu'\nu' k} G^{\sigma}_{\nu'\nu k} \tag{21}$$

and the self-energy operator M is the proper part of the scattering operator:

$$M_{\mu\nu k} = \ll A_{\mu k} | B_{\nu k} \gg^{p} . \tag{22}$$

Thus the calculation of the electron Green function is equivalent to the calculation of the proper part of the irreducible Green function as in the case of bulk materials. The equation (21) can be also written down as

$$\sum_{\nu} [\delta_{\mu\nu}(\omega - U_{\mu} n_{\mu\bar{\sigma}}) - \epsilon_{\mu\nu k} - M_{\mu\nu k}] G_{\nu\mu' k} = \delta_{\mu\mu'} \tag{23}$$

and the problem of finding the thin film Green function is turned into an $N \times N$ matrix problem.

4. Phonon Green functions

By means of a procedure similar to that employed above we introduce the renormalized anharmonic potential parameters and irreducible Green functions. The renormalized ion – ion interaction parameters are as follows [4]:

$$\tilde{\Phi}^{1\ldots p} = \sum_{n=0}^{\infty} \frac{1}{n!} \sum_{1\ldots n} \left(\Phi^{1\ldots p\,1\ldots n} \langle u_1 \ldots u_n \rangle + \sum_{i\nu j\mu\sigma} S^{1\ldots p\,1\ldots n}_{i\nu,j\nu} \langle u_1 \ldots u_n a^{+}_{i\nu\sigma} a_{j\mu\sigma} \rangle \right). \tag{24}$$

We see that the electronic part of energy is also included. This means that our starting point in calculating phonon properties is the adiabiatic approximation. The renormalized anharmonic potential is defined

$$\tilde{\Phi}(u) = \sum_{n=3}^{\infty} \frac{1}{n!} \sum_{1\ldots n} \tilde{\Phi}^{1\ldots n} u_1 \ldots u_n. \tag{25}$$

We also define the renormalized electron–phonon part of the Hamiltonian:

$$\tilde{H}_{\text{eph}} = \sum_{i\nu,j\mu,\sigma} \tilde{S}_{i\nu,j\mu}(u) a^{+}_{i\nu\sigma} a_{j\mu\sigma}. \tag{26}$$

The phonon Green function is defined as

$$D^{\beta\alpha}_{i\nu,j\mu} = \ll u^{\beta}_{i\nu} | u^{\alpha}_{j\mu} \gg, \tag{27}$$

where $\alpha, \beta = x, y, z$. We also introduce the Fourier transform of the phonon Green function:

$$D^{\beta\alpha}_{\nu\mu k} = \sum_{j} e^{-ik(R_j - R_m)} D^{\beta\alpha}_{\nu n, m\mu}. \tag{28}$$

Repeating for the phonon Green function the procedure anologous to that for electrons we finally arrive at the formula for the phonon Green function [4]:

$$\sum_{\mu\beta} \left(M_\nu \omega^2 \delta_{\nu\mu}\delta_{\alpha\beta} - \tilde{\Phi}^{\alpha\beta}_{\nu\mu} - \Pi^{\alpha\beta}_{\nu\mu k} \right) D^{\beta\gamma}_{\mu\nu' k} = \delta_{\nu'\nu}\delta_{\gamma\alpha}, \tag{29}$$

where the following notation is introduced

$$\tilde{\Phi}^{\alpha\beta}_{\nu\mu k} = \sum_{j} e^{-ik(R_j - R_m)} \tilde{\Phi}^{\alpha\beta}_{\nu n, m\mu}, \tag{30}$$

$$\Pi^{\alpha\beta}_{\nu,\mu k} = \sum_{j} e^{-ik(R_j - R_m)} \Pi^{\alpha\beta}_{\nu n, m\mu}, \tag{31}$$

and the self-energy operator appearing in (31) can be expressed [4] as:

$$\Pi^{\alpha\beta}_{\nu n,\mu m} = \ll \frac{\partial\tilde{\Phi}}{\partial u_{\nu n\alpha}} + \frac{\partial\tilde{H}_{eph}}{\partial u_{\nu n\alpha}} \middle| \frac{\partial\tilde{\Phi}}{\partial u_{\mu m\beta}} + \frac{\partial\tilde{H}_{eph}}{\partial u_{\mu m\beta}} \gg. \tag{32}$$

The equations (22–23) and (29–32) are exact but intractable. They may serve, however, as a convenient point of departure for the self-consistent system of approximate equations. In the next Section we discuss the simplest of the possible approximations applied to the full system of equations.

5. Self consistent decoupling scheme

The simplest approximation consisting in renormalization of parameters is the pseudoharmonic approximation applied to phonons in thin films in [5] and HF approximation applied to electrons in thin films in [6]. In our case we have to find not only the renormalized potential parameters but the renormalized hopping integrals as well. The formulas are completely analogous however and we only give the expressions for the hopping integrals [1,2]:

$$\tilde{S}_{\mu m,\nu n}(l) = \sum_{n=0}^{\infty} \frac{1}{n!} \left(\frac{1}{2}\overline{u^2(l)}\right)^n S^{(2n)}_{\mu m,\nu n}(l), \tag{33}$$

where the so-called leading term approximation is applied and

$$u^2(l) = \frac{\langle [\bar{l}(\bar{u}_{\mu m} - \bar{u}_{\nu n})]^2 \rangle}{l^2} \tag{34}$$

is the parameter describing relative displacements of the neighbouring ions, depending on the localization of the ions with respect to the surface of the film. Here we assume that the parameters S are functions of distance of the ions. In order to find $u^2(l)$ we should calculate the phonon Green function.

In order to find the self-energy operators M (22) and Π (32) we apply the approximation in which the proper correlation functions are replaced by the products of simpler correlations functions. The approximation was applied in the case of alloys in the paper [9] where, however, no anharmonic effects were included. We limit ourselves to the first non-vanishing terms in the expressions (22) and (32).

For the correlation functions we write

$$\left\langle u^{\alpha}_{\mu i}(t) a_{\nu k\sigma}(t) u^{\beta}_{\mu' i'} a^{+}_{\nu' k'\sigma} \right\rangle^{p} \simeq \left\langle u^{\alpha}_{\mu i}(t) u^{\beta}_{\mu' i'} \right\rangle \left\langle a_{\nu k\sigma}(t) a^{+}_{\nu' k'\sigma} \right\rangle, \tag{35}$$

$$\left\langle a^{+}_{\mu k\sigma}(t) a_{\nu k'\sigma}(t) a^{+}_{\mu' l\sigma} a_{\nu' l'\sigma} \right\rangle^{p} \simeq \left\langle a^{+}_{\mu k\sigma}(t) a_{\nu' l'\sigma} \right\rangle \left\langle a_{\nu k'\sigma}(t) a^{+}_{\mu' l\sigma} \right\rangle. \tag{36}$$

Making use of the spectral representations of the Green functions [7] we obtain the following expressions:

$$\begin{aligned} M_{\mu'\nu' q}(\omega) = \int \frac{d\omega_1 d\omega_2 [1 + g(\omega_2) N(\omega_2) - f(\omega_1)]}{\omega - \omega_1 - \omega_2} \times \\ \times \frac{1}{\pi^2 N} \sum_{\alpha\beta} \sum_{\mu\nu k} [\tilde{S}^{\alpha}_{\mu'\nu k}\ Im\ G_{\nu\mu k}(\omega_1)\ Im\ D^{\alpha\beta}_{\mu' \mu q-k}(\omega_2) \tilde{S}^{\beta}_{\mu\nu' q} + \\ - \tilde{S}^{d}_{\mu'\nu q}\ Im\ G_{\nu\mu q-k}(\omega_1)\ Im\ D^{\alpha\beta}_{\nu\mu k}(\omega_2) \tilde{S}^{\beta}_{\mu\nu' q} + \\ - \tilde{S}^{\alpha}_{\mu'\nu k}\ Im\ G_{\nu\mu k}(\omega_1)\ Im\ D^{\alpha\beta}_{\mu'\nu' q-k}(\omega_2) \tilde{S}^{\beta}_{\mu\nu' k} + \\ + \tilde{S}^{\alpha}_{\mu'\nu q}\ Im\ G_{\nu\mu k}(\omega_1)\ Im\ D^{\alpha\beta}_{\nu\nu' q-k}(\omega_2) \tilde{S}^{\beta}_{\mu\nu' k}], \end{aligned} \tag{37}$$

where $g(\omega)N(\omega), f(\omega)$ are the Bose and Fermi functions, respectively; $\alpha, \beta = x, y, z$ and $\tilde{S}^{\alpha}_{\mu\nu k}$ are interaction parameters:

$$\tilde{S}^{\alpha}_{\mu\nu k} = \sum_{j} e^{-ik(R_j - R_n)} \partial_{\alpha} \tilde{S}_{\mu m, \nu n}. \tag{38}$$

For the phonon self-energy operator we have:

$$\begin{aligned} \Pi^{\alpha\beta}_{\nu\mu k}(\omega) = \int \frac{d\omega_1 d\omega_2 [f(\omega_2) - f(\omega_1)]}{\omega + \omega_2 - \omega_1} \times \\ \times \frac{1}{\pi^2 N} \sum_{\rho\tau q} [\tilde{S}^{\alpha}_{\nu q k-q} \tilde{S}^{\beta}_{\tau\mu q} \; Im\, G_{\nu\tau q}(\omega_1) \; Im\, G_{\rho\mu k-q}(\omega_2) + \\ + \tilde{S}^{\alpha}_{\nu\rho q} \tilde{S}^{\beta}_{\tau\mu q} \; Im\, G_{\rho\tau q}(\omega_1) \; Im\, G_{\nu\mu k-q}(\omega_2) + \\ + \tilde{S}^{\alpha}_{\nu\rho q} \tilde{S}^{\beta}_{\tau\mu k-q} \; Im\, G_{\nu\tau k-q}(\omega_2) \; Im\, G_{\rho\mu q}(\omega_1) + \\ - \tilde{S}^{\alpha}_{\nu\rho k-q} \tilde{S}^{\beta}_{\tau\mu k-q} \; Im\, G_{\nu\mu q}(\omega_1) \; Im\, G_{\rho\tau k-q}(\omega_2)]. \end{aligned} \tag{39}$$

The system of equations (23), (37–39), (29) enables us to calculate the electron and phonon Green functions, provided that we have some input Green functions. Thus the procedure is selfconsistent and at every stage of the calculations we have to know only the electron and phonon Green functions [7] and [27]. All the other Green functions are, by means of the decoupling (35–36), expressed by these two functions. For practical calculations the iteration procedure can be applied to Eq.(29) with the input functions in (39) given by (16) and to Eq.(23) with the input functions in (37) given by (16) and (29).

6. Discussion

The decoupling procedure leads to the description of phonon and electron properties by the effective independent quasi-particles whose corresponding Green functions are determined by the Eq.(23) and Eq.(29), respectively. It means that the thermodynamic properties of the system with the electron–lattice interaction can be calculated by the energy eigenvalues of these effective quasi-particles instead of those of non-interacting electrons and phonons. That difference in the calculations is very important for thin films, or more generally, for systems with restricted dimensions, and essential for the explanations of physical reasons of finite samples stability. We discuss this problem in the case of the mean square displacement of atoms which is referred to the imaginary part of the phonon Green functions [5].

The analysis of the mean square displacement of atoms in thin films in connection with the melting phenomenon [11] shows that the mean square displacement diverges in ideal films for temperatures different from zero when the zero energy eigenvalue is included. This physically incorrect result is confirmed by the considerations of the Debye–Waller factor in thin films [12] when the harmonic approximation is taken into account. The application of the pseudoharmonic approach

does not eliminate this difficulty [5]. In order to obtain the convergent value of the mean square displacement the interaction with the substrate was used [11] or some additional effective surface anisotropy was introduced.

In the light of these considerations we can see from the Eq.(29) that the terms $\tilde{\Phi}^{\alpha\beta}_{\nu\mu k}$ do not assure the discussed convergence, because they are of pseudoharmonic character. However, the same Eq.(29) shows that the expression $\Pi^{\alpha\beta}_{\nu\mu k}$ plays the role of an additional anisotropy field appearing in a natural way as the influence of the electron–lattice interaction.

According to the expression (39) this field is described by the electron Green functions which should be found with the mean square displacements in the self-consistent way. In this manner we can expect explanation of the physical origin of the conditions in which the mean square displacement of atoms in systems with restricted dimensions is convergent. The assurance of this convergence is equivalent to the statement that the electron–phonon interaction can be treated as responsible for the stable structure of small limited crystals and crystalline films. In the case of a convergent expression for the mean square displacement of atoms we can only determine the temperature of stability for the crystalline phase [5] and the melting temperature with its dependence on the film thickness [11].

Besides the above discussions of a quite fundamental question the present paper brings a generalized decoupling scheme for electron and phonon Green functions which can be applied to various practical calculations concerning surface phenomena. For this purpose the fumctions $\Phi(u)$ and $S(u)$ in their analytical forms are required. The first function takes one of the well known lattice potential curves. The second one is expressed by the hopping integral on the basis of the Slater orbitals and usually evaluated by exponential functions. Confining our considerations to the linear term for $R(u)$ we are on the approximation level reported in [8]. The advantage of the generalization is then particularly evident in (37) where we can see the influence of lattice vibrations on the electron energy spectrum via the mean square displacements even in the case of harmonic force constants when the linear approximation does not lead to this dependence.

References

1. L. Wojtczak, Bull. Soc. Sci. et Letters Łódź, Recherches sur les deformations, No 11, Vol. XXXV, 6, 1985.
2. J. Kierul, Doctor Thesis, University of Łódź, Łódź, 1986.
3. N.M. Plakida, T. Siklós, Phys. Stat. Sol. *33*, 103, 1969.
4. T. Siklós, The Thermodynamic Green's Functions Method in the Self-Consistent Phonon Theory of Anharmonic Crystals, Hungarian Academy of Sciences, Preprint KFKI-1981-43, Budapest, 1981.
5. J. Zimnicki, Acta Phys. Hung., *38*, 27, 1975.
6. L. Valenta and L. Wojtczak, Czech. J. Phys., *B30*, 1025, 1980.
7. D.N. Zubarev, Usp. Fiz. Nauk., *71*, 71, 1960.
8. K.I. Wysokinski, A.L. Kuziemsky, Phys. Stat. Sol.,/b/*113*, 409, 1982.
9. L. Valenta, Phys. Stat. Sol., *2*, 112, 1962.
10. S. Barisic, J. Lubbe and J. Friedel, Phys. Rev. Lett., *25*, 919, 1970.
11. L. Wojtczak, Phys. Stat. Sol., *23*, K163, 1967.
12. J. Dlouha, Czech. J. Phys., *B16*, 495, 1966.

Acta Physica Hungarica 65 (1), pp. 33–42 (1989)

ELECTRON – PHONON INTERACTION IN TRANSITION METALS

J. KIERUL

Department of Solid State Physics, Institute of Physics, University of Łódź
90-238 Łódź, Poland

(Received 7 January 1987)

The generalized Hubbard model including the interaction of electrons with anharmonic phonons is considered. The self-consistent system of equations for the electron and phonon Green functions is obtained and several approximations valid for non-uniform materials are discussed.

1. Introduction

The electron – phonon interaction is well-known to play an important role in the description of transition metals, transition metal alloys and compounds. Thermal expansion, specific heat, stability of crystal structure etc. cannot be treated without taking into account of the electron – phonon interaction.

The purpose of the paper is to develop the general self-consistent theory of interacting electrons and phonons capable of including anharmonic effects and non-uniformity of material. The theory makes use of the ideas of the self-consistent phonon theory of Plakida and Siklós [2 – 4] and extends them to the present case. For the model Hamiltonian of the type discussed in [1] we obtain the general system of equations for the electron and phonon Green functions. In this paper we develop the general theory and postpone the specific numerical applications to another paper.

The model used is described in Section 2. Sections 3 and 4 deal with the problem of calculating electron and phonon Green functions. Section 5 is devoted to the discussion of various approximations to the full system of equations. Section 6 discusses briefly the results and possible applications of the theory.

2. Model Hamiltonian

We consider the generalized Hubbard model with the electron – phonon interaction included. Specifically, the Hamiltonian reads:

$$H = H_{\mathrm{e}} + H_{\mathrm{ph}} + H_{\mathrm{eph}}, \tag{1}$$

$$H_{\mathrm{e}} = \sum_{ij\sigma} t_{ij}^{o} a_{i\sigma}^{+} a_{j\sigma} + \sum_{i\sigma} \varepsilon_{i\sigma} n_{i\sigma} + \sum_{i} U_i n_{i\sigma} n_{i\bar{\sigma}}, \tag{2}$$

$$H_{\mathrm{ph}} = \sum_{i} \frac{P_i^2}{2M_i} + \Phi(u), \tag{3}$$

$$H_{\mathrm{eph}} = \sum_{ij\sigma} T_{ij}(u) a_{i\sigma}^{+} a_{j\sigma}, \tag{4}$$

where $\alpha_{i\sigma}(a_{i\sigma}^{+})$ is the annihilation (creation) operator of an electron on the site i; t_{ij}^{o}, ε_i, U_i are the usual parameters of the Hubbard model; P_i, u_i are the momentum and displacement operators respectively, and M_i is the mass of the ion on the site i; $\Phi(u)$, $T_{ij}(u)$ are the analytical functions of displacements. The derivation and discussion of the Hamiltonian was presented in [2]. We do not assume the ionic potential to be harmonic and do not assume any specific form of the functions $T_{ij}(u)$ either. The model we consider is a generalization of the Barisic – Lubbe – Friedel (BLF) model known in the literature and extensively used in many problems [5 – 10]. If the $T_{ij}(u)$ is linear in displacements we return to the original BLF model:

$$T_{ij}(u) = \sum_{\alpha=x,y,z} \Gamma_{ij}^{\alpha}(u_i^{\alpha} - u_j^{\alpha}), \tag{5}$$

in fact our model is still more general as it is capable of describing the deformation-dependent changes of not only the hopping parameters but also the electronic energies as well ($T_{ij}(u)$ for $i = j$). And last but not least all functions of sites need not be translationally invariant. The model should thus be valid for disordered, non-uniform and low-dimensional systems. For the disordered media the problem of averaging over configuration arises. This particular problem is beyond the scope of the paper.

3. Electron Green functions

We apply the Plakida – Siklós self-consistent phonon theory to the present case of the electron – phonon interaction. We make use of the two-time thermodynamic Green functions [10] defined for the electron operators as:

$$G_{ij}^{\sigma}(t - t') = \ll a_{i\sigma} | a_{j\sigma}^{+} \gg = -i\theta(t - t') \left\langle [a_{i\sigma}(t), a_{j\sigma}^{+}(t')]_{+} \right\rangle, \tag{6}$$

where $[\ldots]_{+}$ means anticommutator and $\langle \ldots \rangle$ thermodynamic averaging. We introduce the irreducible Green functions:

$$\ll u_1 \ldots u_n a | a^{+} \gg = \sum_{m=0}^{n} \binom{n}{m} \langle u_{m+1} \ldots u_n \rangle \ll u_1 \ldots u_m a | a^{+} \gg^{\mathrm{irr}}. \tag{7}$$

The functions $T_{ij}(u)$ are analytical and have an expansion

$$T_{ij}(u) = \sum_{p=0}^{\infty} \frac{1}{p!} \sum_{1\ldots p} T_{ij}^{1\ldots p} u_1 \ldots u_p. \tag{8}$$

We define also the renormalized coefficients $\tilde{T}_{ij}^{1\ldots p}$:

$$\tilde{T}_{ij}^{1\ldots p} = \sum_{k=0}^{\infty} \frac{1}{k!} \sum_{1\ldots k} T_{ij}^{1\ldots p\,1\ldots k} \langle u_1 \ldots u_k \rangle \tag{9}$$

and the renormalized interaction functions:

$$\tilde{T}_{ij}(u) = \sum_{p=0}^{\infty} \frac{1}{p!} \sum_{1\ldots p} \tilde{T}_{ij}^{1\ldots p} u_1 \ldots u_p. \tag{10}$$

We also assume that t_{ij}^{o}, ε_i have such values that

$$\langle T_{ij}(u) \rangle = 0. \tag{11}$$

The last condition means that we choose our electronic Hamiltonian in a special way taking an advantage of the arbitrariness of the functions $T_{ij}(u)$. Thus the parameters t_{ij}^{o}, ε_i are temperature and pressure dependent and the electronic Hamiltonian becomes an effective Hamiltonian modified by the interaction with phonons [1]. For the electron–electron interaction term we use the Hartree–Fock approximation as is widely accepted in the literature.

Writing down the equations of motion and proceeding in analogy with [2–4] we obtain for the electron Green function:

$$G_{ij}^{\sigma} = G_{ij}^{0\sigma} + \sum_{m,n} G_{m}^{0\sigma} K_{mn} G_{nj}^{0\sigma}, \tag{12}$$

where

$$(G^{0\sigma})_{ij}^{-1} = (\omega - \varepsilon_i - U_i \langle n_{i\bar{\sigma}} \rangle)\delta_{ij} - t_{ij}^{o} \tag{13}$$

and the scattering matrix is given by:

$$K_{mn} = \ll \sum_{j} \tilde{T}_{mj}(u) a_{j\sigma} | \sum_{l} \tilde{T}_{in}(u) a_{i\sigma}^{+} \gg^{\mathrm{irr}} \equiv \ll A_{m\sigma} | B_{n\sigma} \gg^{\mathrm{irr}}. \tag{14}$$

In order to get the Dyson form of equation (12) we define proper parts of irreducible Green functions as follows:

$$\ll u_1 \ldots u_n a | u_1 \ldots u_m a^{+} \gg^{\mathrm{irr}} = \ll u_1 \ldots u_n a | u_1 \ldots u_m a^{+} \gg^{\mathrm{irr},p} +$$

$$+\sum_{mm'} \ll u_1 \ldots u_n a|B_{m\sigma} \gg^{\mathrm{irr},p} G^{0\sigma}_{mm'} \ll A_{m'\sigma}|u_1 \ldots u_m a^+ \gg^{\mathrm{irr}} . \qquad (15)$$

Making use of these equations the expression for the electron Green function takes the form

$$G^{\sigma}_{ij} = G^{0\sigma}_{ij} + \sum_{mn} G^{0\sigma}_{im} \sum_{mn} G^{\sigma}_{nj}, \qquad (16)$$

$$\sum_{mn} = K^{(p)}_{mn}. \qquad (17)$$

The self-energy operator $\sum$ is equal to the proper part of the scattering operator K. The above expressions are exact. The approximations used for connecting $K^{(p)}$ with the electron and phonon Green functions are discussed in Section 5 below.

4. Phonon Green functions

We define the phonon Green function as

$$D_{\alpha\beta}(t-t') = \ll u_\alpha(t)|u_\beta(t') \gg = -i\theta(t-t')\langle [u_\alpha(t), u_\beta(t')]_- \rangle, \qquad (18)$$

where α, β run over phonon degrees of freedom and $[\ldots]_-$ means the commutator. We introduce the irreducible phonon Green functions

$$\ll u_1 \ldots u_n|u \gg = \sum_{m=l}^{n} \binom{n}{m} \langle u_{m+1} \ldots u_n \rangle \ll u_1 \ldots u_m|u \gg^{\mathrm{irr}} . \qquad (19)$$

As the phonon Green functions are coupled with the mixed Green functions we need to define also the irreducible mixed Green function:

$$\ll u_1 \ldots u_n a^+ a|a \gg = \sum_{m=0}^{n} \binom{n}{m} \langle u_{m+1} \ldots u_n \rangle \ll u_1 \ldots u_m a^+ a|u \gg^{\mathrm{irr}} +$$

$$+ \sum_{m=1}^{n} \binom{n}{m} \langle u_{m+1} \ldots u_n a^+ a \rangle \ll u_1 \ldots u_m|u \gg^{\mathrm{irr}} . \qquad (20)$$

The potential energy function Φ is analytical, its Taylor expansion reads:

$$\tilde{\Phi}(u) = \sum_{p=0}^{\infty} \frac{1}{p!} \sum_{1\ldots p} \phi^{1\ldots p} u_1 \ldots u_p. \qquad (21)$$

We also need to define the renormalized expansion coefficients

$$\tilde{\Phi}^{1\ldots p} = \sum_{n=0}^{\infty} \frac{1}{n!} \sum_{1\ldots n} (\phi^{1\ldots p\,1\ldots n} \langle u_1 \ldots u_n \rangle + \sum_{ij\sigma} T^{1\ldots p\,1\ldots n}_{ij} \langle u_1 \ldots u_n a^+_{i\sigma} a_{j\sigma} \rangle) \qquad (22)$$

and the renormalized potential energy function is defined as:

$$\tilde{\phi}(u) = \sum_{n=3}^{\infty} \frac{1}{n!} \sum_{1\ldots n} \tilde{\phi}^{1\ldots n} u_1 \ldots u_n. \tag{23}$$

One should note that the renormalized potential includes the effect of the electron – phonon interaction in the adiabatic approximation. The renormalized potential does not contain quadratic terms because such terms are used to define zero order phonon Green function

$$(D^{-1})_{\alpha}\beta = M_{\alpha}\omega^2\delta_{\alpha\beta} - \tilde{\phi}_{\alpha\beta}. \tag{24}$$

Thus our starting Green functions contain some effects of the phonon–phonon and electron – phonon interaction.

The further developement of calculations is formally similar to the case of the spin – phonon interaction investigated in [12]. We make use of the relations

$$\langle [u_1 \ldots u_n, P_{\alpha}] \rangle^{\text{irr}} = 0, \tag{25}$$

$$\langle [u_1 \ldots u_n a^{+} a, P_{\alpha}] \rangle^{\text{irr}} = 0, \tag{26}$$

which can be proved by the help of the definitions (19–20) of the irreducible Green functions. Proceeding again in a way analogous to [2–4] we arrive at the following expression for the phonon Green function:

$$D_{\alpha\beta} = D^0_{\alpha\beta} + \sum_{\gamma\delta} D^0_{\alpha\gamma} K_{\gamma\delta} D^0_{\delta\beta}, \tag{27}$$

where the scattering matrix is given by the formula:

$$K_{\gamma\delta} = \ll \frac{\partial\tilde{\phi}}{\partial u_{\gamma}} \left| \frac{\partial\tilde{\phi}}{\partial u_{\delta}} \right. \gg^{\text{irr}} + \ll \frac{\partial\tilde{\phi}}{\partial u_{\gamma}} \left| \frac{\partial\tilde{H}_{\text{eph}}}{\partial u_{\delta}} \right. \gg +$$

$$+ \ll \frac{\partial\tilde{H}_{\text{eph}}}{\partial u_{\gamma}} \left| \frac{\partial\tilde{\phi}}{\partial u_{\delta}} \right. \gg^{\text{irr}} + \ll \frac{\partial\tilde{H}_{\text{eph}}}{\partial u_{\gamma}} \left| \frac{\partial\tilde{H}_{\text{eph}}}{\partial u_{\delta}} \right. \gg^{\text{irr}}, \tag{28}$$

where formal partial derivatives of the operator functions $\tilde{\phi}$ (23) and $\tilde{H}_{\text{eph}}$ are taken. The latter function is defined in terms of the renormalized electron – phonon interaction as

$$\tilde{H}_{\text{eph}}(u) = \sum_{ij\sigma} \tilde{T}_{ij}(u) a^{+}_{i\sigma} a_{j\sigma}. \tag{29}$$

The equations (27) can be transformed to the Dyson form if we introduce proper parts of the irreducible Green functions. These proper parts have to fulfil the

equations:

$$\ll C|D \gg^{\text{irr}} = \ll C|D \gg^{\text{irr.p}} + \sum_{\gamma,\delta} \ll C \left| \frac{\partial \tilde{\phi}}{\partial u_\gamma} + \frac{\partial \tilde{H}_{\text{eph}}}{\partial u_\gamma} \right. \gg^{\text{irr.p}} D^0_{\gamma\delta} \cdot$$

$$\cdot \ll \left. \frac{\partial \tilde{\phi}}{\partial u_\delta} + \frac{\partial \tilde{H}_{\text{eph}}}{\partial u_\delta} \right| D \gg^{\text{irr}}, \tag{30}$$

where C, D stand for products of phonon coordinates and/or a^+a. We obtain eventually the following expressions for the phonon Green function

$$D^{-1}_{\alpha\beta} = (D^0)^{-1}_{\alpha\beta} - \Pi_{\alpha\beta}, \tag{31}$$

$$\Pi_{\alpha\beta} = K^p_{\alpha\beta}. \tag{32}$$

The electron (16,17) and phonon (31,32) Green functions are thus given in terms of the proper parts of the irreducible Green functions and the renormalized interaction parameters.

We also may express the averages of products of operators by the proper parts. Using the equation of motion in the Green function technique [10] and the equation (30) we arrive at the formula

$$\ll C|u_\beta \gg^{\text{irr}} = \sum_\gamma \ll C \left| \frac{\partial \tilde{\phi}}{\partial u_\gamma} + \frac{\partial \tilde{H}_{\text{eph}}}{\partial u_\gamma} \right. \gg^{\text{irr.p}} D_{\gamma\beta}, \tag{33}$$

where the notation is the same as in (30). The Green function on the left side is in a usual way connected with cumulant averages [2–4], all average values can be obtained by the help of the cumulant ones. We see that the electron and phonon Green functions as well as the averages of products of operators are expressed by the proper parts of the irreducible Green functions.

The equations up to this stage were exact but the system of equations is open. In order to close it we need some approximations. Such approximations are discussed below.

5. Approximations

In the self – consistent phonon theory the most general approximation called the second order of the theory [2–4] consists in the factorization of the higher correlation functions:

$$\left\langle u_1(t) \dots u_n(t) a(t) u_{1'} \dots u_{n'} a^+ \right\rangle^{p,\text{irr}} \simeq \delta_{nn'} n! \prod_{i=1}^{n} \left\langle u_i(t) u_{i'} \right\rangle \left\langle a(t) a^+ \right\rangle. \tag{34}$$

Employing now the spectral representation for the Green function one obtains for the electron self – energy operator given by (17) the expression as follows:

$$\sum_{mn}(E) = \int \frac{d\omega}{2\pi} \frac{1+e^{-\beta\omega}}{E-\omega+i0^+} \int dt e^{i\omega t} \sum \langle a_{m'\sigma}(t) a^+_{n'\sigma} \rangle \cdot$$

$$\cdot \sum_{n=1}^{\infty} \frac{1}{n!} \left(\sum_{\alpha\beta} \langle u_\alpha(t) u_\beta \rangle \, \partial_\alpha \partial'_\beta \right)^n \left\langle \tilde{T}_{mm'}(x_\alpha + u_\alpha) \right\rangle \left\langle \tilde{T}_{n'n}(x'_\beta + u_\beta) \right\rangle \Big|_{x=0}, \quad (35)$$

where ∂, ∂' are acting on $\tilde{t}(x)$, $\tilde{t}(x')$, respectively. The similar approximation can be used for the other correlation functions:

$$\langle u_1(t) \dots u_n(t) u_{1'} \dots u_{n'} \rangle^{p,\mathrm{irr}} \simeq \delta_{nn'} n! \prod_{i=1}^{n} \langle u_i(t) u_{i'} \rangle, \quad (36)$$

$$\langle u_1(t) \dots u_n(t) a^+(t) a(t) u_{1'} \dots u_{n'} \rangle^{p,\mathrm{irr}} \simeq 0, \quad (37)$$

$$\langle u_1(t) \dots u_n(t) u_{1'} \dots u_{n'} a^+ a \rangle^{p,\mathrm{irr}} \simeq 0, \quad (38)$$

$$\langle u_1(t) \dots u_n(t) a^+(t) a(t) u_{1'} \dots u_{n'} a^+ a \rangle^{p,\mathrm{irr}} = \delta_{nn'} n! \prod_{i=1}^{n} \langle u_i(t) u_i \rangle \langle a^+(t) a(t) a^+ a \rangle^{\mathrm{irr}}. \quad (39)$$

The approximation above is formally analogous to the approximation applied in [12] to the case of the Heisenberg model interacting with phonons. The phonon self-energy is the sum of two terms:

$$\Pi_{\alpha\beta} \simeq \ll \frac{\partial\tilde{\phi}}{\partial u_\alpha} \Big| \frac{\partial\tilde{\phi}}{\partial u_\beta} \gg^{p,\mathrm{irr}} + \ll \frac{\partial\tilde{H}_{\mathrm{eph}}}{\partial u_\alpha} \Big| \frac{\partial\tilde{H}_{\mathrm{eph}}}{\partial u_\beta} \gg^{p,\mathrm{irr}}. \quad (40)$$

The first term on the right hand side of (40) is the usual result of the self-consistent phonon theory and the second one describes the influence of electrons on the phonon spectrum. Employing (36–39) one obtains:

$$\ll \frac{\partial\tilde{\phi}}{\partial u_\alpha} \Big| \frac{\partial\tilde{\phi}}{\partial u_\beta} \gg^{p,\mathrm{irr}}_{E} = \int \frac{d\omega}{2\pi} \frac{1-e^{-\alpha\omega}}{E-\omega+i0^+} \cdot$$

$$\cdot \int dt e^{i\omega t} \sum_{n=2}^{\infty} \frac{1}{n!} \left(\sum_{\alpha'\beta'} \langle u_{\alpha'}(t) u_{\beta'} \rangle \, \partial_{\alpha'} \partial_{\beta'} \right)^n \cdot$$

$$\cdot \left\langle \frac{\partial}{\partial x_\alpha} \left(\tilde{\phi} + \tilde{H}_{\mathrm{eph}} \right)(x+u) \right\rangle \left\langle \frac{\partial}{\partial x_\beta} \left(\tilde{\phi} + \tilde{H}_{\mathrm{eph}} \right)(x+u) \right\rangle \Big|_{x=0}, \quad (41)$$

$$\ll \frac{\partial \tilde{H}_{\text{eph}}}{\partial u_\alpha} \Bigg| \frac{\partial \tilde{H}_{\text{eph}}}{\partial u_\beta} \gg_E^{\text{p,irr}} = \int \frac{d\omega}{2\pi} \frac{1 - e^{-\beta\omega}}{E - \omega + i0^+} \cdot$$

$$\cdot \int dt e^{i\omega t} \sum_{ij\sigma} \left\langle a_{i\sigma}^+(t) a_{j\sigma}(t) a_{i'\sigma}^+ a_{j'\sigma} \right\rangle^{\text{irr}} \cdot \sum_{n=0}^{\infty} \frac{1}{n!} \left(\sum_{\gamma\delta} \langle u_\gamma(t) u_\delta \rangle \, \partial_\gamma \partial_\delta \right)^n \cdot$$

$$\cdot \left\langle \frac{\partial}{\partial x_\gamma} \tilde{T}_{ij}(x+u) \right\rangle \left\langle \frac{\partial}{\partial x_\delta} \tilde{T}_{i'j'}(x+u) \right\rangle \Bigg|_{x=0} . \tag{42}$$

The full system of equations is now closed but rather untractable. One may introduce further simplifications to the equations (35, 40–42) leading to the pseudoharmonic approximation.

In the pseudoharmonic approximation the phonon – phonon interaction is taken into account only by renormalization of potential parameters. The average values of products of phonon operators are equal

$$\langle u_1 \dots u_{2n+1} \rangle \simeq 0,$$

$$\langle u_1 \dots u_{2n} \rangle = \sum \langle u_{i_1} u_{i_2} \rangle \dots \langle u_{i_{2n-1}} u_{i_{2n}} \rangle , \tag{43}$$

where the sum runs over all the divisions of the set of indices $\{1, \dots, 2n\}$ into two-element subsets. The average value of the arbitrary function of displacements is equal to

$$\langle f(u) \rangle = \exp \left(\frac{1}{2} \sum \langle u_\alpha u_\beta \rangle \, \partial_\alpha \partial_\beta \right) \langle f(x+u) \rangle \Big|_{x=0} . \tag{44}$$

In the Eq. (40) only the second term survives in the pseudoharmonic approximation and we have the formula for the phonon self-energy operator:

$$\Pi_{\alpha\beta}^0(E) = \int \frac{d\omega}{2\pi} \frac{1 - e^{-\beta\omega}}{E - \omega + i0^+} \int dt e^{i\omega t} \sum_{ij\sigma} \sum_{i'j'\sigma'} \left\langle a_{i\sigma}^+(t) a_{j'\sigma} \right\rangle \left\langle a_{j\sigma}(t) a_{i'\sigma}^+ \right\rangle \cdot$$

$$\cdot \left\langle \frac{\partial}{\partial x_\alpha} \tilde{T}_{ij}(x+u) \right\rangle \left\langle \frac{\partial}{\partial x_\beta} \tilde{T}_{i'j'}(x+u) \right\rangle \Bigg|_{x=0} . \tag{45}$$

In order to obtain this expression we have to keep only the $n = 0$ term in (42) and to factorize the electron correlation function. The phonon Green function is now given by

$$D^{-1} = (D^0)^{-1} - \Pi^0, \tag{46}$$

$$(D^0)_{\alpha\beta}^{-1} = M\omega^2 \delta_{\alpha\beta} - \tilde{\phi}_{\alpha\beta}, \tag{47}$$

where the renormalized potential parameters in (47) are to be obtained by the pseudoharmonic expression (44). The derivatives of the hopping parameters are

also meant to be averaged by means of (44). Employing the spectral representation one obtains for (45):

$$\Pi^0_{\alpha\beta}(E) = \int \frac{d\omega}{E - \omega + i0^+} \int d\omega_1 \left[f(\omega_1) - f(\omega + \omega_1)\right] \cdot$$

$$\cdot \sum_{ij} \sum_{i'j'} \left(-\frac{1}{\pi}\, Im\, G^{\sigma}_{j'i}(\omega_1)\right) \left(-\frac{1}{\pi}\, Im\, G^{\sigma}_{ji'}(\omega + \omega_1)\right) \left\langle \frac{\partial \tilde{T}_{ij}}{\partial u_\alpha} \right\rangle \left\langle \frac{\partial \tilde{T}_{i'j'}}{\partial u_\beta} \right\rangle, \quad (48)$$

where $f(\omega)$ is the Fermi – Dirac function. The equations (46–48) give the phonon function expressed by means of the electron function. Retaining only the $n = 1$ term in (35) one obtains the electron Green function

$$G^{-1} = (G^0)^{-1} - \Sigma^0, \quad (49)$$

$$\Sigma^0_{mn\sigma}(E) = \int \frac{d\omega}{E - \omega + i0^+} \int d\omega_1 \left[N(\omega_1) + f(\omega + \omega_1)\right] \cdot$$

$$\cdot \sum_{m'n'} \sum_{\alpha\beta} \left(-\frac{1}{\pi}\, Im\, G^{\sigma}_{m'n'}(\omega + \omega_1)\right) \left(-\frac{1}{\pi}\, Im\, D_{\beta\alpha}(\omega_1)\right) \left\langle \frac{\partial \tilde{T}_{mm'}}{\partial u_\alpha} \right\rangle \left\langle \frac{\partial \tilde{T}_{n'n}}{\partial u_\beta} \right\rangle, \quad (50)$$

where $N(\omega)$ is the Bose–Einstein function. The above expression closes the system of equations (46–50). This system reduces for the case of harmonic phonons and BLF model of interaction to the equations considered in [10] for transition metal alloys.

The system of equations (46–50) can thus be viewed as the generalization of the procedure employed in [10].

6. Discussion

The self-consistent phonon theory [2–4] proved to be a useful tool in describing physical phenomena in various models of phonon sytems. It was also applied to the case of localized spins interacting with phonons see e.g. [12]. It is a purpose of this paper to apply it also to the electron – phonon interaction and to obtain a framework for various approximations to be used in this physical situation.

The most general approximation given by the factorization of the proper parts of irreducible correlation functions (34) cannot usually be employed in actual computations except, possibly, very simple models. There is, however, a wide range of approximations to the expressions (35), (41), (42). Even the simplest one given by (46–50) improves the approximations considered in the literature [1, 10].

The important feature of the theory is also the fact that all the equations are formulated in real space, which enables the applications to small particles, thin films and other systems with surface. The anharmonic effects near the surface

are greater and are included from the beginning. The theory gives the unified picture of electrons and phonons mutually interacting in transition metal and can be expected to deal with the problems of structural stability, thermal expansion and magnetostriction. The specific numerical applications of the theory will be the subject of another paper

The paper has been done in the framework of the Problem 01.08B1.8. The author thanks Prof. L. Wojtczak for his suggesting of the problem and valuable discussions.

References

1. L. Wojtczak, Bull. Soc. Sci. et Lettres Łódź, Recherches sur les deformations, No 11, Vol. XXXV, 6, 1985.
2. N.M. Plakida and T. Siklós, Acta Phys. Hung., *25*, 17, 1968.
3. N.M. Plakida and T. Siklós, Acta Phys. Hung., *45*, 37, 1978.
4. T. Siklós, The Thermodynamic Green's Function Method in the Self-Consistent Phonon Theory of Anharmonic Crystals, Hung. Acad. of Sciences preprint KFKI-1981-43, Budapest, 1981.
5. S. Barisic, I. Lubbe and J.Friedel, Phys. Rev. Lett., *25*, 919, 1970.
6. J. Ashkenazi, M. Dacorogna and M. Peter, Sol. St. Comm., *29*, 181, 1979.
7. J.C. Van Hay, J. Phys. C *10*, L337, 1977.
8. H. Azizi, J. Phys., F *5*, 2307, 1975.
9. S. Barisic, Phys. Rev., *B5*, 932, 941, 1972.
10. K.I. Wysokinski and A.L. Kuzemsky, Phys. Stat. Sol. /b/, *113*, 409, 1982.
11. D.N. Zubarev, Usp. Fiz. Nauk, *71*, 71, 1960.
12. H. Konwent and N.M. Plakida, Acta Phys.Pol., *A47*, 589, 1975.

Acta Physica Hungarica 65 (1), pp. 43–54 (1989)

THEORETICAL ANALYSIS OF THE EINSTEIN RELATION IN DEGENERATE TERNARY CHALCOPYRITE SEMICONDUCTORS IN THE PRESENCE OF AN ARBITRARILY ORIENTED QUANTIZING MAGNETIC FIELD

M. MONDAL, K.P. GHATAK* and A.K. DAS**

Department of Physics, University College of Science and Technology
Calcutta-700009, India

(Received 30 January 1987)

An attempt is made to investigate theoretically the Einstein relation for the diffusivity–mobility ratio of the electrons in ternary chalcopyrite semiconductors at low temperatures on the basis of a newly derived dispersion relation of the conduction electrons in the presence of an arbitrarily-oriented quantizing magnetic field for the more general case which occurs from the consideration of the various types of anisotropies in the energy spectrum. It is found, taking degenerate n–$CdGeAs_2$ as an example, that the above ratio oscillates in a periodic manner with the orientation of the magnetic field with respect to the c-axis. The ratio shows an oscillatory magnetic field dependence, as expected since the origin of the oscillations in the Einstein's relation is the same as that of the Shuvnikov–de Hass oscillations and also increases with increasing electron concentration as expected in degenerate semiconductors. The corresponding well-known results for isotropic two-band Kane model, both in the presence and absence of magnetic quantization, are also obtained from the expressions derived.

Introduction

In recent years, there has been considerable interest in studying the physical features of degenerate semiconductors having non-parabolic energy bands obeying Kane's dispersion relation under magnetic quantization [1,2]. The band non-parabolicity has been observed to influence many of these features resulting in special properties of these semiconductors. It is well-known that [3,4] the performance of the semiconductor devices at the device terminals and the speed of operation of the modern switching semiconductor devices are significantly influenced by the degree of carrier degeneracy present in these devices. The simplest method of analyzing semiconductor devices taking into account the degeneracy of the bands is to use the Einstein relation to express the performance at the device terminals and the switching speed in terms of carrier concentration. Moreover, the relation for the diffusivity – mobility ratio of the carriers in semiconductors (hereafter referred

*Department of Electronics and Telecommunication Engineering, Faculty of Engineering and Technology, University of Jadavpur, Calcutta–700032, INDIA

**Kalidhan Institution, 20A & B, Southern Avenue, Calcutta-7000026

widely used parameters of carrier transport in semiconductors. Furthermore, in recent years the connection of the Einstein relation with the velocity auto-correlation function [5], its relation with the screening of the carriers in semiconductors [6] and the different modifications of the DMR under various physical conditions have extensively been investigated [7-14]. Nevertheless, it appears from the literature that the DMR in degenerate n-type ternary chalcopyrite semiconductors has yet to be theoretically studied in the presence of an arbitrarily oriented quantizing magnetic field for the more difficult case which occurs from the consideration of various types of anisotropies in the energy spectrum. The more so, since these semiconductors are being increasingly used as non-linear optical materials [15] and light-emitting diodes [16]. Incidentally, Rowe and Shay [17] have demonstrated that the quasi-cubic model [18] can be used to explain the observed splitting and symmetry properties in the conduction and the valence bands at the zone centre of these materials. The s-like conduction band is singly degenerate and the p-like valence band is triply degenerate. The latter splits into sub-bands because of the spin–orbit splitting and crystal-field interactions. Incidentally, Kildal [19,20] proposed an $E - \mathbf{k}$ dispersion relation of the carriers in the same semiconductor, according to which the conduction band corresponds to a single ellipsoid of revolution at the zone centre in k-space together with the assumptions of isotropic momentum-matrix element and isotropic spin–orbit splitting parameters, respectively. In what follows, we shall generalize the Kildal's model [19,20] by incorporating the anisotropies in the two above mentioned band-parameters in the presence of an arbitrarily oriented quantizing magnetic field. We shall then derive the electron statistics and the DMR, respectively, by formulating the density-of-state function under arbitrary magnetic quantization. This will make our analysis a generalized one because we can derive the corresponding well-known expressions for the isotropic two band Kane model both in the presence and absence of magnetic quantization, respectively, from our generalised expression for ternary chalcopyrite semiconductors in the presence of an arbitrarily oriented quantizing magnetic field. We shall investigate theoretically the effects of the orientation of the quantizing magnetic fields, the strength of the magnetic field and the electron concentration on the same ratio, taking degenerate n-$CdGeAs_2$, as an example.

Theoretical background

The DMR of the electrons in semiconductors in the presence of magnetic quantization can, in general, be expressed [10] as

$$\left(\frac{D}{\mu}\right)_B = \frac{1}{e} n_0 \Big/ \frac{dn_0}{dE_{FB}} , \tag{1}$$

where n_0 is the electron concentration, e is the electron charge and E_{FB} is the Fermi energy in the presence of an arbitrarily oriented quantizing magnetic field (B) as measured from the edge of the conduction band in the absence of any quantization.

It appears then that the derivation of DMR using Eq. (1) requires an expression of the electron statistics under magnetic quantization which in turn is determined by the corresponding electron energy spectrum. The form of the $\mathbf{K} \cdot \mathbf{p}$ matrix for ternary chalcopyrite semiconductors can be expressed, following Kildal [19], as

$$H = \begin{bmatrix} H_1 & H_2 \\ H_2^+ & H_1 \end{bmatrix}, \tag{2}$$

where

$$H_1 \equiv \begin{bmatrix} E_g & P_{\|}k_z & 0 & 0 \\ P_{\|}k_z & (\delta + \frac{1}{3}\Delta_{\|}) & \frac{\sqrt{2}}{3}\Delta_{\perp} & 0 \\ 0 & \frac{\sqrt{2}}{3}\Delta_{\perp} & -\frac{2}{3}\Delta_{\|} & 0 \\ 0 & 0 & 0 & 0 \end{bmatrix}, H_2 \equiv \begin{bmatrix} 0 & 0 & f_{,-} & f_{,+} \\ 0 & 0 & 0 & 0 \\ -f_{,-} & 0 & 0 & 0 \\ f_{,+} & 0 & 0 & 0 \end{bmatrix},$$

E_g is the bandgap, $P_{\|}$ and $P_{\perp}$ are the momentum-matrix elements $\|$ and $\perp$ to the c-axis, respectively, δ is the crystal field splitting parameter, $\Delta_{\|}$ and $\Delta_{\perp}$ are the spin-orbit splitting parameters $\|$ and $\perp$ to the c-axis, respectively, $f_{\pm} \equiv \frac{P_{\perp}}{\sqrt{2}}(k_x \pm ik_y)$ and $i \equiv \sqrt{-1}$.

Thus, neglecting the contribution of the higher bands and the free electron energy, the diagonalization of the above matrix leads to the generalized expression of the dispersion relation in bulk specimens of ternary chalcopyrite semiconductors as

$$\gamma(E) = f_1(E)K_s^2 + f_2(E)K_z^2, \tag{3}$$

where E is the energy as measured from the edge of the conduction band in the absence of any quantization, $k_s^2 \equiv k_x^2 + k_y^2$ and the other symbols are defined in the Appendix. Thus, in the presence of an arbitrarily oriented quantizing magnetic field B the modified electron energy spectrum can be written as

$$\gamma(E) = A_{,\pm}(n, E, \Theta) + a(E, \Theta)(k_z')^2, \tag{4}$$

where $n(\equiv 0, 1, 2, \ldots)$ is the Landau quantum number, $k_z'(\equiv k_z \cos\Theta + k_x \sin\Theta)$ is the direction of application of the quantizing magnetic field B which makes an angle Θ with z–axis and lies in the $k_x k_z$ plane. Besides, the functions $A_{\pm}(n, E, \Theta)$ and $a(E, \Theta)$ are defined in the Appendix. Thus, using Eq. (4) the density-of-states function under arbitrary magnetic quantization can be expressed as

$$N_B(E) = \frac{eB}{4\pi^2\hbar} \sum_{n=0}^{n_{max}} [\gamma(E) - A_{,\pm}(n, E, \Theta)]^{-1/2} [a(E, \Theta)]^{1/2} \cdot$$

$$\left[\{a(E, \Theta)\}^{-1}\{\gamma'(E) - C_{,\pm}(n, E, \Theta)\} - a(E, \Theta)^{-2} b(E, \Theta) \cdot \{\gamma(E) - A_{\pm}(n, E, \Theta)\}\right]. \tag{5}$$

Combining (5) with the Fermi–Dirac occupation probability factor, the electron statistics in ternary chalcopyrite semiconductors can be written after considerable mathematics as

$$n_0 = \frac{eB}{2\pi^2\hbar}\sum_{n=0}^{n_{max}}[\phi(E_{FB}) + \beta(E_{FB})]. \tag{6}$$

Thus, differentiating equation (6) with respect to E_{FB} and using Eq. (1), the generalized expression of the DMR in n-type degenerate ternary chalcopyrite semiconductors under arbitrary magnetic quantization can be expressed as

$$\left(\frac{D}{\mu}\right) = \frac{1}{e}\left[\sum_{n=0}^{n_{max}}\{\phi(E_{FB}) + \beta(e_{FB})\}\right]\left[\sum_{n=0}^{n_{max}}\psi(E_{FB}) + p(E_{FB})\right]^{-1}. \tag{7}$$

Incidentally, under the conditions $\Delta_{\|} = \Delta_{\perp} = \Delta$ (the isotropic spin orbit splitting parameter), $\delta = 0$, $m_{\|}^* = m_{\perp}^* = m^*$ (the isotropic effective electron mass at the edge of the conduction band) and $P^2 \equiv \frac{\hbar^2 E_g(E_g+\Delta)}{2m^*(E_g+\frac{2}{3}\Delta)}$ the Eqs. (3) and (4) assume the forms

$$\frac{E(E+E_g)(E+E_g+\Delta)}{(E+E_g+\frac{2}{3}\Delta)} = P^2k^2 \tag{8}$$

and

$$\frac{(E+E_g)E(E+E_g+\Delta)}{(E+E_g+\frac{2}{3}\Delta)} = P^2k_z^2 + \frac{2eB}{\hbar}(n+\frac{1}{2})P^2 \pm (eB\Delta P^2/3\hbar)\left(E+E_g+\frac{2}{3}\Delta\right)^{-1} \tag{9}$$

which are the well-known dispersion relations for three-band Kane model both in the absence and presence of magnetic quantization [21]. Therefore, under the conditions as stated above, the Eqs. (5), (6) and (7) assume the forms

$$N_B(E) = (eB/4\pi^2\hbar P)\sum_{n=0}^{n_{max}} L_{,\pm}(E), \tag{10}$$

$$n_0 = \frac{eB}{2\pi^2\hbar P}\sum_{n=0}^{n_{max}}[R_{\pm}(E_{FB}) + S_{,\pm}(E_{FB})] \tag{11}$$

and

$$\left(\frac{D}{\mu}\right)_B = \frac{1}{e}\left[\sum_{n_0}^{n_{max}}\{R_{\pm}(E_{FB} + S_{\pm}(E_{FB})\}\right]\left[\sum_{n=0}^{n_{max}}\chi_{,\pm}(E_{FB}) + J_{,\pm}(E_{FB})\right]^{-1}. \tag{12}$$

where the notations are defined in the Appendix.

Under the conditions $\Delta \longrightarrow \infty$ and $\alpha E_{FB} << 1$, the Eqs. (8) to (12) assume the well-known [2] forms:

$$E(I+\alpha E) = (\hbar^2k^2/2m^*), \qquad \alpha \equiv 1/Eg, \tag{13}$$

$$E(I+\alpha E)=(n+\frac{1}{2})\hbar\omega_0+\frac{\hbar^2k_z^2}{2m^*}\pm\frac{1}{2}K_0B_0 \text{ where } K_0\equiv e\hbar/3m_0, \tag{14}$$

$$N_B(E)=\pi\hbar\omega_0\left(\frac{2m^*}{h^2}\right)^{3/2}\sum_{n=0}^{n_{max}}(1+2\alpha E)\left[E(1+\alpha E)-\left(n+\frac{1}{2}\right)\hbar\omega_0\pm\frac{1}{2}K_0B\right]^{-1/2}, \tag{15}$$

$$n_0=[N_c\hbar\omega_0/2K_BT]\sum_{n=0}^{n_{max}}\left\{\left[1+\alpha\left(n+\frac{1}{2}\right)\hbar\omega_0\right]^{-1/2}\left[\frac{3}{4}\alpha K_BT.F_{\frac{1}{2}}(\eta')+\left(1+\frac{3}{2}\alpha b\right)F_{-\frac{1}{2}}(\eta')\right]\right\} \tag{16}$$

and

$$\left(\frac{D}{\mu}\right)_B=\frac{k_BT}{e}\left[\frac{\sum_{n=0}^{n_{max}}\left\{\left[\frac{3}{4}\alpha k_BTF_{\frac{1}{2}}(\eta')+\left(1+\frac{3}{2}\alpha b\right)F_{-\frac{1}{2}}(\eta')\right]\left[1+\alpha\left(n+\frac{1}{2}\right)\hbar\omega_0\right]^{-1/2}\right\}}{\sum_{n=0}^{n_{max}}\left\{\left[\frac{3}{4}\alpha k_BTF_{-\frac{1}{2}}(\eta')+\left(1+\frac{3}{2}\alpha b\right)F_{-\frac{3}{2}}(\eta')\right]\left[1+\alpha\left(n+\frac{1}{2}\right)\hbar\omega_0\right]^{-1/2}\right\}}\right], \tag{17}$$

where

$$\omega_0\equiv\frac{eB}{m^*},\quad \eta'\equiv\frac{E_{FB}-b}{k_BT},\quad b\equiv\frac{(n+\frac{1}{2})\hbar\omega_0\pm\frac{1}{2}K_0B}{1+\alpha(n+\frac{1}{2})\hbar\omega_0}$$

and $F_j(\eta')$ is the one-parameter Fermi–Dirac integral of order j as defined by Blakemore [22]. Eq. (17) was derived for the first time by Nag and Chakravarti [9].

Finally it may be noted that under the condition $B\longrightarrow 0$, the Eqs (5), (6), (7), (10), (11), (12), (15), (16) and (17) assume the following forms

$$N_0(E)=\frac{1}{3\pi^2}\left[\frac{3\gamma'(E)\sqrt{\gamma(E)}}{2f_1(E)\sqrt{f_2(E)}}-\frac{f_1'(E)\gamma^{3/2}(E)}{f_1^2(E)\sqrt{f_2(E)}}-\frac{1}{2}\frac{f_2'(E)\gamma^{3/2}(E)}{f_1(E)f_2^{3/2}(E)}\right], \tag{18}$$

$$n_0=(3\pi^2)^{-1}[V(E_{F0})+\rho(E_{F0})], \tag{19}$$

$$\left(\frac{D}{\mu}\right)_0=\frac{1}{e}[V(E_{F0})+\rho(E_{F0})][V'(E_{F0})+\rho'(E_{F0})]^{-1}, \tag{20}$$

$$N_0(E)=(2\pi^2P^3)\tau'(E)\sqrt{\tau(E)}, \tag{21}$$

$$n_0=(3\pi^2P^3)^{-1}\left[g(E_{F0})+f(E_{F0})\right], \tag{22}$$

$$\left(\frac{D}{\mu}\right)_0=\frac{1}{e}\left[g(E_{F0})+f(E_{F0})\right]\left[g'(E_{F0})+f'(E_{F0})\right]^{-1}, \tag{23}$$

$$N_0(E)=4\pi(2m^*/h^2)^{3/2}(1+2\alpha E)\sqrt{E(1+\alpha E)}, \tag{24}$$

$$n_0=N_c\left[F_{\frac{1}{2}}(\eta_0)+\frac{15\alpha k_BT}{4}F_{\frac{3}{2}}(\eta_0)\right] \tag{25}$$

and

$$\left(\frac{D}{\mu}\right)_0 = \frac{k_B T}{e}\left[\frac{F_{\frac{1}{2}}(\eta_0) + \frac{15}{4}\alpha k_B T F_{\frac{3}{2}}(\eta_0)}{F_{-\frac{1}{2}}(\eta_0) + \frac{15}{4}\alpha k_B T F_{\frac{1}{2}}(\eta_0)}\right], \tag{26}$$

where E_{F0} is the Fermi energy in the absence of magnetic quantization $\eta_0 \equiv E_{F0}/k_B T$ and the other symbols are defined in the Appendix. It may be mentioned in this context that the Eqs (24) to (26) are already well-known in the literature [2].

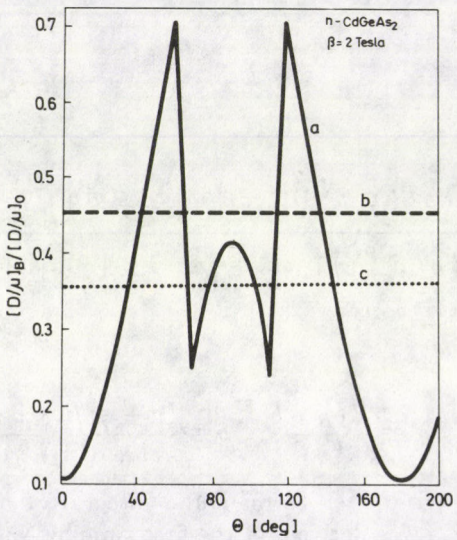

Fig. 1. Plot of the normalized DMR as a function of the orientation of the quantizing magnetic field at 4.2K in degenerate n-$CdGeAs_2$ by using (a) the proposed dispersion relation, (b) three-band Kane model and (c) two-band Kane model corresponding to $n_0 = 2.2 \times 10^{22}$ m^{-3} and $B = 2T$

Results and discussion

Using Eqs (6), (7), (19) and (20) together with the parameters [20, 21]: $m_{\|}^* = 0.030\ m_0, m_{\perp}^* = 0.039\ m_0, \Delta_{\|} = 0.34$eV, $\Delta_{\perp} = 0.36$eV, $\delta = -0.21$eV and $E_g = 0.57$eV , we have plotted $(D/\mu)_B/(D/\mu)_0$ versus Θ (neglecting magnetic freeze out and spinsplitting effects) at 4.2 K as shown in Fig 1 corresponding to the given values of the electron concentration and the quantizing magnetic field, respectively.

Besides, using the Eqs (11), (12), (22) and (23) as are appropriate for three-band Kane model and also taking the Eqs (16), (17), (25) and (26) which are valid for two-band Kane model we have further plotted the normalized DMR according to both models, respectively, in the same Figure for the purpose of comparison. Using the same parameters as used in obtaining Fig. 1, we have also plotted the

$(D/\mu)_B/(D/\mu)_0$ as functions of the reciprocal quantizing magnetic field and the electron concentration as shown in Figs 2 and 3, respectively, in which the simplified limiting cases of three and two band Kane models have again been considered.

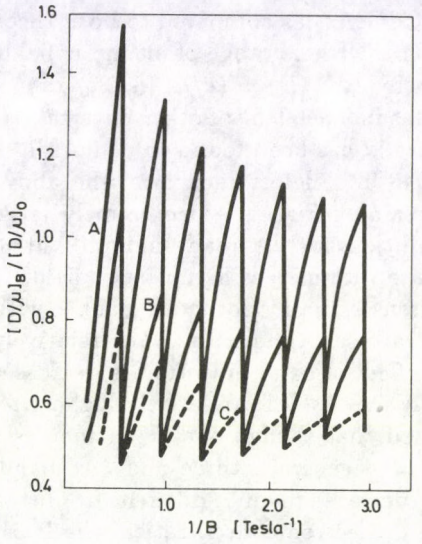

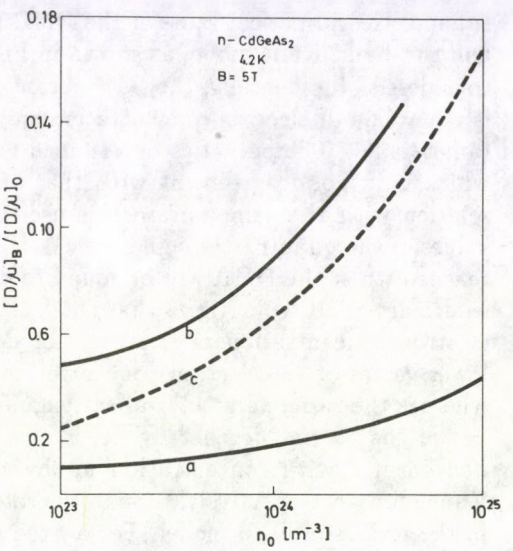

Fig. 2. Plot of the normalized DMR as a function of reciprocal quantizing magnetic field at 4.2K in degenerate n-$CdGeAs_2$ by using (a) the proposed dispersion relation, (b) three-band Kane model and (c) two-band Kane model corresponding to $n = 2.2 \times 10^{22} m^{-3}$ and $\Theta = 60^0$

Fig. 3. Plot of the normalized DMR as a function of electron concentration in degenerate n-$CdGeAs_2$ by using (a) the proposed dispersion relation, (b) three-band Kane model and (c) two-band Kane model corresponding to $B = 5T$ and $\Theta = 70^0$

It appears from plot *a* of Fig. 1 that the DMR in n-$CdGeAs_2$ is a periodic function of the orientation of the quantizing magnetic field. It is also apparent from the same Figure that the DMR exhibits spiky variation corresponding to specified values of Θ when the magnetic quantum number changes from one fixed value to another. The ratio increases at a high rate in a monotonous manner with increasing angles of orientation of the quantizing magnetic field up to $\Theta = 60^0$, beyond which the ratio suddenly drops to a lower value due to the change in magnetic quantum number. Moreover, between $\Theta = 70^0$ to 90^0 the ratio increases with Θ and from $\Theta = 90^0$ the repetition of the whole process starts again. In the absence of anisotropies the DMR turns out to be independent of the angle of orientation of the quantizing magnetic field since the basic dispersion relation becomes spherical instead of being ellipsoidal. Thus the DMR for both the three and two-band Kane's model becomes independent of Θ as shown in Fig. 1.

It appears from Fig. 2 that the DMR oscillates with reciprocal quantizing magnetic field. The oscillatory dependence is due to the crossing over of the Fermi

level by the subbands in steps, resulting in a successive reduction in the number of occupied Landau levels as the magnetic field is increased. For each coincidence of a Landau level with the Fermi level, these would be a discontinuity in the density-of-states function resulting in peak of oscillations and the origin of the oscillations in DMR is the same as that of the SdH oscillations. Besides, the band anisotropies enhance the numerical value of the DMR in n-$CdGeAs_2$ as compared to both three and two-band Kane model as shown in Fig. 2 in the whole range of magnetic fields considered. Incidentally, the SdH period given by $\Delta'(1/B) = (e/h)\ (8/3n_0\sqrt{\pi})^{2/3}$ is a function of electron concentration only and is independent of other physical parameters [2]. The period as determined graphically has been found to be 0.41 T^{-1} which is in good agreement with that of 0.3945 T^{-1} determined from the above relation with the same parameters used in obtaining Fig. 2. At extremely large values of the quantizing magnetic field, the conditions for the quantum limit will be reached when the DMR will be found to decrease with increasing magnetic field. It is also apparent from Fig. 3 that the DMR increases in a monotonous manner with electron concentration as expected for degenerate semiconductors. For relatively lower values of the electron concentration the effect of band anisotropies decreases whereas the same parameter affects significantly the DMR for relatively higher values of the carrier degeneracy. It is again noted that though the DMR increases non-linearly with concentration in the cases of degenerate three and two-band Kane models, respectively, though the rates of increase are quite different from that in the proposed band model. For a fixed value of electron concentration, the DMR of the electrons according to generalized dispersion relation is smaller as compared to the plots of band c as shown in Fig. 3 in the whole range of concentrations considered. Our calculation is valid only under the conditions of carrier degeneracy since under non-degenerate electron concentration the DMR is independent of impurity concentration and rises with temperature in a linear fashion. The classical value of the DMR (k_BT/e) is equal to 0.36 meV at 4.2K.

The DMR will, in general, be anisotropic in the presence of a quantizing magnetic field. It appears then that for investigating the DMR under magnetic quantization, we have to determine the element D_{zz}/μ_{zz} of the corresponding tensor as a function of B. Thus, the DMR defined here refers to the direction of the application of the magnetic field. The peaks in Figs 1 and 2 would increase in number with decreasing amplitudes if the spin-splitting term were included in the dispersion relation. Though the effects of collision broadening are usually small at low temperatures, the sharpness of the oscillatory spikes would be reduced by their influence. Moreover, the many body effects, the variation of the diffusion constant and the formation of band-tails in degenerate semiconductors have not been considered in this simplified theoretical formulation. It may be remarked that the basic qualitative features of this paper would not be altered to any significant extent even after the above modifications.

In recent years the mobility of the electrons in semiconductors under magnetic quantization has been extensively investigated, but the diffusion constant (a very important device parameter which cannot be easily experimentally determined) of such semiconductors has relatively been less studied. Thus the theoretical results of

our paper will be useful in determining the diffusion constants even for parabolic energy bands both in the presence and absence of quantizing magnetic field. Though the experimental verification of the basic content of our paper is not available to the best of our knowledge, the importance of the DMR in semiconductor physics is already well-known. Incidentally, it may be noted in this context that since the available noise power is directly proportional to the DMR as discussed elsewhere [11], the experimental results on the thermal noise of degenerate semiconductors will provide an experimental check for the predictions of the above ratio and also a technique for probing the band structure in degenerate semiconductors. Finally, it may be stated that the basic purpose of the present paper is not solely to demonstrate the influence of an arbitrarily oriented quantizing magnetic field on the DMR in ternary chalcopyrite semiconductors having non-parabolic and non-standard energy bands, but also to formulate the corresponding density-of-states function since the various transport and other phenomena in semiconductors and the analytical formulation of different important physical parameters are based on the density-of-states function in such materials.

Appendix

The functions $\gamma(E)$, $f(E)$, $f_2(E)$, $A_\pm(n,E,\Theta)$, $a(E,\Theta)$, $G(E)\gamma'(E)$, $C_\pm(n,E,\Theta)$, $l(E,\Theta)$, $\phi(E_{FB})$, $\beta(E_{FB})$, $\psi(E_{FB})$, $\rho(E_{FB})$, $L_\pm(E)$, $R_\pm(E_{FB})$, $S_\pm(E_{FB})$, $x_\pm(E_{FB})$, $J_\pm(E_{FB})$, $V(E_{F0})$, $\rho(E_{F0})$, $V'(E_{F0})$, $\rho'(E_{F0})$, $\tau(E)$, $\tau'(E)$, $J(e_{F0})$, $f(E_{F0})$, $g'(E_{F0})$ and $f'(E_{F0})$ are defined as follows:

$$\gamma(E) = E(E+E_g)\left[(E+E_g)(E+E_g+\Delta_\parallel)+\delta\left(E+E_g+\frac{2}{3}\Delta_\parallel\right)+\frac{2}{9}(\Delta_\parallel^2-\Delta_\perp^2)\right], \tag{1}$$

$$f_1(E) = \hbar^2 E_g(E_g+\Delta_\perp)\left[2m_\perp^*\left(E_g+\frac{2}{3}\Delta_\perp\right)\right]^{-1}\left[\delta\left(E+E_g+\frac{1}{3}\Delta_\parallel\right)+\right.$$
$$\left.+(E+E_g)\left(E+E_g+\frac{2}{3}\Delta_\parallel\right)+\frac{1}{9}(\Delta_\parallel^2-\Delta_\perp^2)\right], \tag{2}$$

$$f_2(E) = \hbar^2 E_g(E_g+\Delta_\parallel)\left[2m_\parallel^*\left(E_g+\frac{2}{3}\Delta_\parallel\right)\right]^{-1}\left[(E+E_g)\times\left(E+E_g+\frac{2}{3}\Delta_\parallel\right)\right], \tag{3}$$

$$A_\pm(n,E,\Theta) = \frac{2eB}{\hbar}\left(n+\frac{1}{2}\right)[G(E)\{G(E)\cos^2\Theta+f_2(E)\sin^2\Theta\}]^{1/2}-$$
$$-E(E+E_g)\left[\frac{2}{9}(\Delta_\parallel^2-\Delta_\perp^2)\right]\pm\frac{eB\hbar E_g}{6}\left[\frac{(E_g+\Delta_\perp)}{m_\perp^*\,(E_g+\frac{2}{3}\Delta_\perp)}\right]^{1/2}$$
$$\left[\left(E+E_g+\delta+\frac{\Delta_\parallel^2-\Delta_\perp^2}{3\Delta_\perp}\right)^2\frac{\Delta_\parallel^2\cos^2\Theta(E_g+\Delta_\perp)}{m_\perp^*\,(E_g+\frac{2}{3}\Delta_\perp)}+\right.$$

$$+\frac{(E+E_g)^2\Delta_\perp^2\sin^2\Theta(E_g+\Delta_\parallel)}{m_\parallel^*\,(E_g+\tfrac{2}{3}\Delta_\parallel)}\Bigg]^{1/2} \tag{4}$$

$$a(E,\Theta)=G(E)f_2(E)[G(E)\cos^2\Theta+f_2(E)\sin^2\Theta]^{-1}, \tag{5a}$$

$$G(E)=f_1(E)+\left[\frac{\hbar^2E_g}{18m_\perp^*}(\Delta_\parallel^2-\Delta_\perp^2)\frac{(E_g+\Delta_\perp)}{(E_g+\tfrac{2}{3}\Delta_\perp)}\right], \tag{5b}$$

$$\gamma'(E)=[E(E+E_g)]^{-1}\gamma(E)(2E+E_g)+E(E+E_g)(2E+2E_g+\delta+\Delta_\parallel), \tag{6}$$

$$C_\pm(n,E,\Theta)=\frac{eB}{\hbar}(n+\frac{1}{2})[G(E)\{G(E)\cos^2\Theta+f_2(E)\sin^2\Theta\}^{-1/2}\times$$

$$\times\{2\cos^2\Theta G(E)G'(E)+G'(E)f_2(E)\sin^2\Theta+G(E)f_2'(E)\sin^2\Theta\}-$$

$$-(2E+E_g)\left[\frac{2}{9}(\Delta_\parallel^2-\Delta_\perp^2)\right]\pm\frac{eB\hbar E_g}{6}\left[\frac{(E_g+\Delta_\perp)}{m_\perp^*\,(E_g+\tfrac{2}{3}\Delta_\perp)}\right]^{1/2}\Bigg[\Bigg(E+E_g+$$

$$+\delta+\frac{\Delta_\parallel^2-\Delta_\perp^2}{3\Delta_\perp}\Bigg)^2\frac{\Delta_\parallel^2\cos^2\Theta(E_g+\Delta_\perp)}{m_\perp^*\,(E_g+\tfrac{2}{3}\Delta_\perp)}+\frac{(E+E_g)^2\Delta_\perp^2\sin^2\Theta(E_g+\Delta_\parallel)}{m_\parallel^*\,(E_g+\tfrac{2}{3}\Delta_\parallel)}\Bigg]^{-1/2}$$

$$\left[\left(E+E_g+\delta+\frac{\Delta_\parallel^2-\Delta_\perp^2}{3\Delta_\perp}\right)\frac{\Delta_\parallel^2\cos^2\Theta(E_g+\Delta_\perp)}{m_\perp^*\,(E_g+\tfrac{2}{3}\Delta_\perp)}+\frac{(E+E_g)\Delta_\perp^2\sin^2\Theta(E_g+\Delta_\perp)}{m_\parallel^*\,(E_g+\tfrac{2}{3}\Delta_\parallel)}\right], \tag{7}$$

$$b(E,\Theta)=a(E,\Theta)\left[\frac{-G'(E)\cos^2\Theta-f_2'(E)\sin^2\Theta}{G(E)\cos^2\Theta+f_2(E)\sin^2\Theta}+\frac{G'(E)}{G(E)}+\frac{f_2'(E)}{f_2(E)}\right], \tag{8}$$

$$\phi(E_{FB})=[\gamma(E_{FB})-A_\pm(n,E_{FB},\Theta)]^{1/2}[a(E_{FB},\Theta)]^{-1/2}, \tag{9}$$

$$\beta(E_{FB})=\sum_{\gamma=1}^{S}2(K_BT)^{2\gamma}\left[1-2^{1-2\gamma}\right]\mathcal{G}(2\gamma)\frac{d^{2\gamma}}{dE_{FB}^{2\gamma}}[\phi(E_{FB})], \tag{10}$$

$$\psi(E_{FB})=\frac{1}{2}[\phi(E_{FB})]^{-1}\left[\{a(E,\Theta)\}^{-1}\{\gamma'(E)-C_\pm(n,E,\Theta)\}-\right.$$

$$\left.-\,l(E,\Theta)a^{-2}(E,\Theta)\{\gamma(E)-A_\pm(n,E,\Theta)\}\right]|_{E=E_{FB}}, \tag{11}$$

$$b\,(E_{FB})=\frac{d}{dE_{FB}}[\beta(E_{FB})], \tag{12}$$

$$L_\pm(E)=\Bigg[\tau(E)-2eB\hbar^{-1}\left(n+\frac{1}{2}\right)P^2$$

$$\pm eB\Delta P^2\left\{3\hbar\left(E+E_g+\frac{2}{3}\Delta\right)\right\}^{-1}\Bigg]^{-1/2}\bar{\Psi}_\pm(E), \tag{13}$$

$$R_\pm(E_{FB})=$$

$$=\left[\tau(E)-2eB\hbar^{-1}\left(n+\frac{1}{2}\right)P^2\pm eB\Delta P^2\left\{3\hbar\left(E+E_g+\frac{2}{3}\Delta\right)\right\}^{-1}\right]^{1/2}\Bigg|_{E=E_{FB}} \tag{14}$$

$$S_{\pm}(E_{FB}) = \sum_{\gamma=1}^{S} 2(K_B T)^{2\gamma}(1 - 2^{1-2\gamma})\mathcal{G}(2\gamma)\frac{d^{2\gamma}}{dE_{FB}^{2\gamma}}[R \pm (E_{FB})], \tag{15}$$

$$\kappa_{\pm}(E_{FB}) = \frac{1}{2}L_{\pm}(E_{FB}), \tag{16}$$

$$J_{\pm}(E_{FB}) = \frac{d}{dE_{FB}}[S_{\pm}(E_{FB})], \tag{17}$$

$$V(E_{F0}) = [\gamma(E_{F0})]^{3/2}\left[f_1(E_{F0})\sqrt{f_2(E_{F0})}\right]^{-1}, \tag{18}$$

$$\rho(E_{F0}) = \sum_{\gamma=1}^{S} 2(K_B T)^{2\gamma}(1 - 2^{1-2\gamma})\mathcal{G}(2\gamma)\frac{d^{2\gamma}}{dE_{F0}^{2\gamma}}[V(E_{F0})], \tag{19}$$

$$V'(E_{F0}) = \left[\frac{3}{2}\frac{\gamma'(E)\sqrt{\gamma(E)}}{f_1(E)\sqrt{f_2(E)}} - \frac{f_1'(E)\gamma^{3/2}(E)}{f_1^2(E)\sqrt{f_2(E)}} - \frac{1}{2}\frac{f_2'(E)\gamma^{3/2}(E)}{f_1(E)f_2^{3/2}(E)}\right]\Bigg|_{E=E_{FG}}, \tag{20}$$

$$\rho'(E_{F0}) = \frac{d}{dE_{F0}}[\rho(E_{F0})], \tag{21}$$

$$\tau(E) = E(E + E_g)(E + E_g + \Delta)\left(E + E_g + \frac{2}{3}\Delta\right)^{-1}, \tag{22}$$

$$\tau'(E) = \tau(E)\left[E^{-1} + (E + E_g)^{-1} + (E + E_g + \Delta)^{-1} - \left(E + E_g + \frac{2}{3}\Delta\right)^{-1}\right], \tag{23}$$

$$g(E_{F0}) = [\tau(E_{F0})]^{3/2}, \tag{24}$$

$$f(E_{F0}) = \sum_{\gamma=1}^{S} 2(K_b T)^{2\gamma}(1 - 2^{1-2\gamma})\mathcal{G}(2\gamma)\frac{d^{2\gamma}}{dE_{F0}^{2\gamma}}[g(E_{F0})], \tag{25}$$

$$g'(E_{F0}) = \frac{3}{2}\sqrt{\tau(E_{F0})}\tau'(E_{F0}), \tag{26}$$

$$f'(E_{F0}) = \frac{d}{dE_{F0}}[f(E_{F0})], \tag{27}$$

where

$$G'(E) \equiv f_1'(E), f_1'(E) \equiv \left[\hbar^2 E_g(E_g + \Delta_{\perp})\left\{2m_{\perp}^{*}\left(E_g + \frac{2}{3}\Delta_{\perp}\right)\right\}^{-1}\right] \times$$

$$\times \left[2E + 2E_g + \delta + \frac{2}{3}\Delta_{\perp}\right],$$

$$f_2'(E) \equiv \left[2m_{\parallel}^{*}\left(E_g + \frac{2}{3}\Delta_{\parallel}\right)\right]^{-1} \times \hbar^2 E_g(E_g + \Delta_{\parallel})\left(2E + 2E_g + \frac{2}{3}\Delta_{\parallel}\right), \mathcal{G}(2\gamma)$$

is the zeta function of order $2r$, r is the set of real positive integers and

$$\bar{\Psi}_{\pm}(E) \equiv \left[\tau'(E) \pm \frac{1}{3}\frac{eB\Delta P^2}{\hbar}\left(E + E_g + \frac{2}{3}\Delta\right)^{-2}\right].$$

References

1. E.O. Kane. J. Phys. Chem. Solids, *1*, 249, 1957.
2. B.R. Nag, Electron Transport in Compound Semiconductors, Springer Verlag, Berlin, Heidelberg, 1980 and the references cited therein.
3. G.D. Hatchel and A.E. Ruchli, I.E.E.E. Trans. on *ED 15*, 437, 1968.
4. T.I. Kamins and R.S. Muller, Solid State Electronics, *10*, 423, 1967.
5. G.G. Emch, J. Math. Phys., *14*, 1775, 1973.
6. R. Kubo, J. Math. Soc. Japan, *12*, 570, 1957.
7. K.M. Van Vliet and A. Vander Zeil, Solid State Electronics, *20*, 931, 1977.
8. H. Kroemer, I.E.E.E. Trans. on *ED 25*, 850, 1980.
9. B.R. Nag and A.N. Chakravarti, Phys. Stat. Sol. (a), *22*, K153, 1974.
10. B.R. Nag, A.N. Chakravarti and P.K. Basu, Phys. Stat. Sol. (a), *68*, K75, 1981.
11. B.R. Nag and A.N. Chakravarti, Phys. Stat. Sol. (a), *67*, K113, 1981.
12. P.T. Landsberg, Eur. J. Phys., *2*, 213, 1981.
13. M. Mondal and K.P. Ghatak, Phys. Stat. Sol. (b), *122*, K93, 1984.
14. S.N. Biswas and K.P.Ghatak, Proc. S.P.I.E. Quantum Well and Superlattice Physics – Int. Opt. Soc. Eng. (U.S.A.) *792*, 239, 1987;
    M. Mondal and K.P. Ghatak, J. Phys. C., Solid State, 1986. (to be published).
15. D.S. Chemla, P.J. Kupeck, D.S. Robertson and R.C. Smith, Opt. Commun., *3*, 29, 1971.
16. J.L. Shay, K.J. Backman, E. Buchler and J.H. Wernick, Appl. Phys. Letts., *23*, 226, 1973.
17. J.W. Rowe and J.L. Shay, Phys. Rev., *3B*, 451, 1971.
18. J.J. Hopfield, J. Phys. Chem. Solids., *15*, 97, 1960.
19. H. Kildal, Phys. Rev., *10B*, 5082, 1974.
20. J.L. Shay and J.W. Wernick, Ternary Chalcopyrite Semiconductors Growth, Electronic Properties and Applications, Pergamon Press, London, 1975.
21. R. Dornhaus and G. Nimtz, in Springer Tracts in Modern Physics, *76*, 1, 1976.
22. J.S. Blackmore, Semiconductor Statistics, Pergamon Press, London, 1962.

Acta Physica Hungarica 65 (1), pp. 55–58 (1989)

THE HYPERFINE INTERACTION PARAMETER $\rho(0)$ CALCULATED BY THE $X\alpha$ METHOD WITH AB INITIO SELF-CONSISTENT EXCHANGE PARAMETER

Á. NAGY

Institute of Theoretical Physics, Kossuth Lajos University
4010 Debrecen, Hungary

(Received 17 February 1987)

The total electronic density at the nucleus for atoms has been calculated by the $X\alpha$ method with ab initio exchange parameter α_{SCF}. Calculations have been done for a few atoms with the exchange parameter 2/3, 1 and α_{HF}, too. It has been found that the values obtained with α_{HF} and α_{SCF} show the best agreement with the Hartree–Fock data.

Introduction

Since the $X\alpha$ method was proposed by Slater [1], it has been a fascinating question how to select the value of α. In 1974 Gáspár [2] suggested a method of calculating an ab initio exchange parameter α. In a recent article [3] a comparison has been made between the Hartree–Fock and $X\alpha$ orbitals studying the expectation values of some powers of the radius. It has been found that the $X\alpha$ orbitals calculated with the SCF exchange parameters well approximate the HF ones.

There is another parameter which is very sensitive to the accuracy of the wave function. The Mössbauer isomer shift is proportional to the total electronic density at the nucleus

$$\rho(0) = \sum_i n_i |u_i(0)|^2, \tag{1}$$

where n_i is the occupation number of the orbital u_i. The sum includes only the s orbitals. There are a few $X\alpha$ studies on the hyperfine interactions [4], however systematic investigation is still lacking. Here, only the parameter $\rho(0)$ for light atoms has been determined by the $X\alpha$ method having SCF exchange parameter α. For a few cases, calculations have been done using several values of α, including 1, 2/3, α_{HF} and α_{SCF}. It has been found that the results obtained with α_{HF} and α_{SCF} are the best ones in approximating the HF values.

The method

Here the method is briefly reviewed. For details we refer to [2]. The derivation of the theory is based on the free-electron gas model. The exchange parameter suggested by Slater [1]($\alpha = 1$) can be obtained averaging the exchange potential

over the whole Fermi sphere. An average over a layer with a thickness of ϵ near the Fermi surface and $\epsilon \to 0$, gives the value of 2/3 for the exchange parameter. This is the Gáspár, Kohn–Sham [5] case. The average suggested by Gáspár [2] is between these extreme ones: it is over a layer containing $\nu_\uparrow$ electrons in the unit volume near the Fermi surface. The exchange parameter for the orbital j is given by

$$\alpha_j = \frac{1}{1-\eta_j^3}\left\{1 - \frac{1}{2}\eta_j - \frac{1}{2}\eta_j^3 + \frac{1}{4}(\eta_j^2 - 1)^2 \ln\left|\frac{1+\eta_j}{1-\eta_j}\right|\right\}, \tag{2}$$

where

$$\eta_j = (1 - \frac{\nu_\uparrow^j}{\rho_\uparrow}). \tag{3}$$

$\nu_\uparrow^j$ is the charge density of the orbital j and $\rho_\uparrow$ is the total electron density of electrons with spin up. An average over the shells leads to the exchange parameter

$$\alpha = \frac{\sum_j n_j \alpha_j}{\sum_j n_j}, \tag{4}$$

where n_j is the occupation number of the shell j. Solving the one-electron $X\alpha$ equations, this exchange parameter can be calculated self-consistently. That is why the term of self-consistent exchange parameter α_{SCF} is used.

Results and discussion

The value of $\rho(0)$ has been calculated by the $X\alpha$ method for several atoms. In Tables I–III the electronic density of orbitals at the nucleus $n_i|u_i(0)|^2$ are also presented. Hartree–Fock data [6] are also shown for comparison. The $X\alpha$ calculations have been carried out using several values of α. Tables I–III include the results obtained with the exchange parameter 2/3, 1 α_{HF} and α_{SCF}. While there is considerable difference between the HF and $X\alpha$ values for the orbitals — $n_i|u_i(0)|^2$ — there is agreement between the values of $\rho(0)$ obtained by the $X\alpha$ and HF methods. It suggests that the $X\alpha$ method — as it is expected — should be a better approximation for the atom as a whole than for the individual orbitals. The best agreement between the $X\alpha$ and HF results has been found for the exchange parameters α_{SCF} and α_{HF}. As it is well known α_{HF} is the value of α for which the total $X\alpha$ energy is equal to the HF one [6]. Table IV includes the values $\rho(0)$ of several atoms calculated by the HF and $X\alpha$ methods with self-consistent exchange parameters. The difference between them is about 0.2–0.3 per cent except for very small atomic numbers ($Z = 3 - -5$).

On the basis of these results it can be concluded that the $X\alpha$ method with self-consistent exchange parameter α_{SCF} provides sufficiently good electronic density.

Table I
Values of $\rho(0)$ of Ne calculated by the HF [6] and $X\alpha$ methods with exchange parameters 2/3, 1, α_{HF} and α_{SCF}

Orbital	HF	$X\alpha$			
		$\alpha = \frac{2}{3}$	$\alpha = 1$	α_{HF}	α_{SCF}
1*s*	587.535	581.319	597.203	597.194	585.403
2*s*	32.400	32.910	34.815	34.815	33.372
total	619.935	614.229	632.018	632.009	618.775

Table II
Values of $\rho(0)$ of Ar calculated by the HF [6] and $X\alpha$ methods with exchange parameters 2/3, 1, α_{HF} and α_{SCF}

Orbital	HF	$X\alpha$			
		$\alpha = \frac{2}{3}$	$\alpha = 1$	α_{HF}	α_{SCF}
1*s*	3527.724	3508.710	3559.603	3517.202	3516.218
2*s*	284.369	278.766	289.248	280.476	280.283
3*s*	27.772	31.101	32.743	31.353	31.327
total	3839.865	3818.577	3881.594	3829.031	3827.828

Table III
Values of $\rho(0)$ of Kr determined by the HF [6] and $X\alpha$ methods with exchange parameters 2/3, 1, α_{HF} and α_{SCF}

Orbital	HF	$X\alpha$			
		$\alpha = \frac{2}{3}$	$\alpha = 1$	α_{HF}	α_{SCF}
1*s*	28871.115	28800.648	29005.201	28824.191	28816.290
2*s*	2858.533	2830.345	2873.074	2835.335	2833.611
3*s*	460.166	458.334	470.859	459.757	459.295
4*s*	46.688	54.591	57.944	54.968	54.846
total	32236.502	32143.918	32407.078	32174.251	32164.042

Table IV
The total electron density at the atomic nucleus of atoms determined by the HF and the $X\alpha$ methods applying the self-consistent exchange parameter α_{SCF}

Z	HF	$X\alpha$
3	13.815	13.570
4	35.388	34.993
5	71.923	72.459
6	127.461	128.183
7	205.973	206.576
8	311.668	311.819
9	448.331	447.911
10	619.935	618.775
11	833.776	829.071
12	1093.744	1090.142
13	1402.875	1397.100
14	1765.646	1759.724
15	2186.363	2179.276
16	2669.519	2660.927
17	3219.247	3208.992
18	3839.865	3827.828
19	4538.725	4520.746
20	5319.719	5299.928
21	6182.441	6163.075
22	7133.395	7112.034
23	8177.116	8153.576
24	9318.062	9291.944
25	10560.309	10531.749
26	11908.955	11877.441
27	13367.667	13332.907
28	14940.899	14902.792
29	16632.956	16591.480
30	18448.022	18403.162
31	20397.625	20546.315
32	22480.511	22426.314
33	24701.383	24643.206
34	27064.951	27001.915
35	29575.097	29507.450
36	32236.502	32164.042

References

1. J.C. Slater, Phys. Rev., *81*, 385, 1951.
2. R. Gáspár, Acta Phys. Hung., *35*, 213, 1974.
3. R. Gáspár and Á.Nagy, Acta Phys. Hung., *53*, 247, 1982.
4. S.K. Lie, D.M.S. Esquivel and D. Guenzburger, Chem. Phys. Lett., *57*, 458, 1978.
5. R. Gáspár, Acta Phys. Hung., *3*, 263, 1954; W. Kohn and L.I. Sham, Phys Rev., *140A*, 1133, 1965.
6. C. Froese- Fischer, Atomic Data, *4*, 301, 1972.

Acta Physica Hungarica 65 (1), pp. 59–68 (1989)

ANALYTIC SOLUTION FOR COMBINED FORCED AND FREE CONVECTION FROM A NON-ISOTHERMAL WEDGE

S. ANTONY RAJ

Department of Mathematics, Presidency College
Madras - 600 005, India

(Received 3 March 1987)

The variational principle developed by Gyarmati embodying the principles of thermodynamics of irreversible processes is employed to investigate the combined forced and free convection flow over a non-isothermal wedge. The velocity and temperature functions are assumed as simple third order polynomial and the variational principle is formulated. The effect of buoyancy force on local heat transfer and skin friction is studied over different parametric values of Reynolds number, Grashof number, Prandtl number, wedge parameter and wall temperature exponent. The comparison of results with known solution establishes the fact that the accuracy is remarkable.

1. Introduction

The effect of buoyancy forces on flow and heat transfer is usually ignored when a forced convection flow over a heated or cooled surface is studied. However, neglecting buoyancy effects cannot be justified, since, under certain circumstances the buoyancy forces considerably influence the flow and temperature fields despite the presence of forced convection flow. In such combined forced and free convection flows, the relative effect of free convection is the greater, the larger the temperature difference between the surface and the fluid and the lower the forced convection velocity. With high velocity forced motion the effect of free convection becomes negligible.

The aim of this investigation is to study the buoyancy effects in flow over a non-isothermal wedge using some of the recent developments in thermodynamics of irreversible processes and to obtain a rapid analytical solution to the boundary layer flow and heat transfer with the help of a variational technique based on the governing principle of dissipative processes. Since in boundary layer flows the irreversible processes of momentum and heat transfer occur inside a very thin layer near the surface of the body, the natural and appropriate manner of studying these non-equilibrium processes is by using the technique developed on irreversible thermodynamics.

2. The Governing Equations of the system

Let us consider the system of steady, two-dimensional and laminar fluid flow of constant transport coefficients over a non-isothermal wedge whose included angle is $\pi\beta$. The external flow velocity U_∞ and the surface temperature T_0 satisfy the power law

$$U_\infty = ax^m \qquad \text{and} \qquad T_0 - T_\infty = bx^n, \tag{1}$$

where U_∞ is determined by the inviscid potential flow. The coordinate axes along x and y directions are considered along and perpendicular to the surface, respectively. The equations of conservation of mass, momentum and energy are

$$\begin{aligned} &u_x + v_y = 0 \text{ (mass)}, \\ &uu_x + vu_y = \gamma u_{yy} + U_\infty U_\infty' + gB(T - T_\infty)\sin(\pi\beta/2) \\ &\qquad + \left[\int_y^\infty gB(T - T_\infty)\cos(\pi\beta/2)dy\right]_x \text{ (momentum)}, \\ &uT_x + vT_y = \alpha T_{yy} \text{ (energy)}, \end{aligned} \tag{2}$$

if viscous dissipation is disregarded. These equations are obtained with the usual boundary layer approximations and with the assumption that all fluid properties are constants except the density which is allowed to vary with the temperature. A further approximation called "Boussinesq approximation" restricts the effect of variable density to the formation of buoyant-force terms. Thus the density, except in the buoyant-force terms will be considered external flow density ρ_∞ and the density in the buoyant force terms is expressed in linear relation to temperature as

$$\rho = \rho_\infty[1 - B(T - T_\infty)], \tag{3}$$

where B is the expansivity considered as small constant quantity.

The conservation equations (2) satisfy the boundary conditions

$$\begin{aligned} &y = 0; \qquad u = 0, \qquad T = T_0(x), \\ &y \longrightarrow \infty; \quad u \longrightarrow U_\infty, \quad T \longrightarrow T_\infty. \end{aligned} \tag{4}$$

3. Variational formulation of the problem

Gyarmati formulated the Governing Principle of Dissipative Processes (GPDP) which describes the evolution of irreversible processes in space and time. The principle is written in its energy picture [1–3]

$$\delta \int_V [T\sigma - \Psi^* - \Phi^*]dV = 0, \tag{5}$$

where the integration is taken over the volume V of the system.

Since balance equations play a fundamental role in the formulation of GPDP, we write the governing equations of motion (2) in the following balance forms:

$$\begin{aligned}
\nabla \cdot \vec{V} &= 0, \\
\rho_\infty (\vec{V} \cdot \nabla)\vec{V} + \nabla \cdot \overline{\overline{P}} &= gB\rho_\infty (T - T_\infty)\sin(\pi\beta/2) \\
&\quad + \left[\int_y^\infty gB\rho_\infty (T - T_\infty)\cos(\pi\beta/2)dy \right]_x , \\
\rho_\infty C_p (\vec{V} \cdot \nabla)T + \nabla \cdot \vec{J}_q &= 0.
\end{aligned} \tag{6}$$

Here the pressure tensor $\overline{\overline{P}}$ can be decomposed as [3]

$$\overline{\overline{P}} = P\overline{\overline{\delta}} + \overset{\circ}{\overline{\overline{P}}}^{vs}, \tag{7}$$

where p is the hydrostatic pressure and $\overset{\circ}{\overline{\overline{P}}}^{vs}$ is the viscous part of the pressure tensor whose trace is zero. The constitutive relations connecting the independent forces and fluxes for the present two-dimensional problem are

$$P_{12} = -L_s \frac{\partial u}{\partial y}, \qquad J_q = -L_\lambda \frac{\partial \ln T}{\partial y}, \tag{8}$$

where P_{12} is the only component of $\overset{\circ}{\overline{\overline{P}}}^{vs}$ and J_q is the energy flux. L_s is equal to the coefficient of viscosity μ while $L_\lambda = \lambda T$, where λ is the conductivity. In the energy picture, the proper state variable is $\ln T$ instead of T. The energy dissipation for this problem is

$$T\sigma = -J_q \frac{\partial \ln T}{\partial y} - P_{12}\frac{\partial u}{\partial y}. \tag{9}$$

The dissipation potentials in energy picture are

$$\begin{aligned}
\psi^* &= T\psi = \frac{1}{2}\left[L_\lambda \left(\frac{\partial \ln T}{\partial y} \right)^2 + L_s \left(\frac{\partial u}{\partial y} \right)^2 \right], \\
\phi^* &= T\phi = \frac{1}{2}\left[R_\lambda J_q^2 + R_s P_{12}^2 \right].
\end{aligned} \tag{10}$$

Here $L_\lambda = R_\lambda^{-1}$ and $L_s = R_s^{-1}$.

Using (9) and (10) we formulate the principle (5) in the form:

$$\begin{aligned}
\delta \int_0^l \int_0^\infty \Bigg[&- J_q \frac{\partial \ln T}{\partial y} - P_{12}\frac{\partial u}{\partial y} - \frac{L_\lambda}{2}\left(\frac{\partial \ln T}{\partial y} \right)^2 - \\
&- \frac{L_s}{2}\left(\frac{\partial u}{\partial y} \right)^2 - \frac{J_q^2}{2L_\lambda} - \frac{P_{12}^2}{2L_s} \Bigg] dy\, dx = 0,
\end{aligned} \tag{11}$$

in which l is the characteristic length of the wedge.

Let us assume the following third order polynomial functions for flow and temperature fields inside their respective boundary layers

$$u/U_\infty = 3y/d_1 - 3y^2/d_1^2 + y^3/d_1^3 (y < d_1), \quad u = U_\infty (y \geq d_1)$$

and

$$(T - T_\infty)/(T_0 - T_\infty) = 1 - 3y/2d_2 + y^3/2d_2^3 (y < d_2), \quad T = T_\infty (y \geq d_2), \tag{12}$$

which satisfy the conditions

$$\begin{aligned} &y = 0 \ : u = 0 \text{ (no-slip)}, && T = T_0, \ T_{yy} = 0, \\ &y = d_1 : u = U_\infty, && u_y = 0 \text{ or } P_{12} = 0 \text{ (smooth-fit)}, \ u_{yy} = 0, \\ &y = d_2 : T = T_\infty, && T_y = 0 \text{ or } J_q = 0 \text{ (smooth-fit)}. \end{aligned} \tag{13}$$

The quantities d_1 and d_2 are the extent of the hypothetical hydrodynamical and thermal boundary layer thicknesses, respectively. These unknowns are determined from our variational analysis.

The velocity and temperature polynomial functions (12) and the conditions (13) are used in the balance equations (6) and on integration with respect to y with the help of smooth-fit conditions, the fluxes P_{12} and J_q for $P \geq 1$ are obtained, respectively as given by Eqs (A-1)-(A-2) of the Appendix. Using the expressions of P_{12} and J_q along with the velocity and temperature functions (12) the variational principle (11) is formulated. After carrying out the integration with respect to y the variational principle is obtained as

$$\delta \int_0^l L(d_1, d_2, d_1' d_2') dx = 0. \tag{14}$$

The explicit form of the above variational principle is given by Eq. (A-3) of the Appendix. The variation is carried out with respect to the independent parameters d_1 and d_2. The Euler–Lagrange equations corresponding to these variational parameters are

$$\frac{d}{dx}\left(\frac{\partial L}{\partial d_{1,2}'}\right) - \frac{\partial L}{\partial d_{1,2}} = 0, \tag{15}$$

respectively. The Eqs (15) are found as nonlinear second order ordinary differential equations in d_1 and d_2 whose coefficients are functions of R, K, L and n. Here

$$\begin{aligned} &R = U_\infty x/\gamma \quad \text{(Reynolds number)}, \\ &G = gB(T_0 - T_\infty)x^3/\gamma^2 \quad \text{(Grashof number)}, \\ &K = G/(R^{5/2}) \quad \text{(buoyancy parameter)} \end{aligned}$$

and

$$L = \pi m/(m+1).$$

The Eqs (15) are solved numerically for the simultaneous solution of d_1 and d_2.

4. Discussion of results

The results which may be of greatest practical interest are the heat transfer and shear stress characteristics of the problem. We observe that the local heat transfer from the wall to the fluid may be calculated from Fourier's law $q = -\lambda(\partial T/\partial y)_y = 0$ and the skin friction is obtained by applying the Newtonian shear law $\tau = \mu(\partial u/\partial y)_{y=0}$. It is customary to rephrase the heat transfer and skin friction results in terms of dimensionless coefficients as are given by

$$Nu = \sqrt{\gamma x/U_\infty (T_0 - T_\infty)^2}(J_q/L_\lambda)$$

and

$$\tau^* = \sqrt{\gamma x/U_\infty^3}(-P_{12}/L_s). \tag{16}$$

It is well-known that the Grashof number is the controlling parameter in the case of free convection flows while the Reynolds number is the controlling parameter for forced convection flows. Hence the buoyancy parameter K is of fundamental importance in combined forced and free convection flows. For small values of K forced convection predominates and free convection becomes negligible. When K assumes large values, forced convection has little influence while the flow is controlled by free convection.

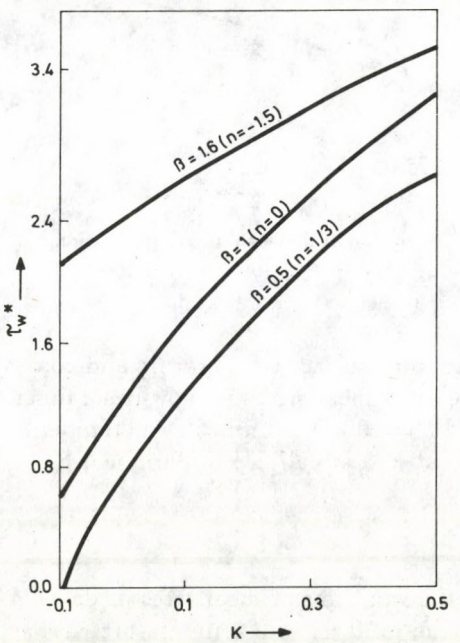

Fig 1. Dimensionless skin friction vs buoyancy parameter K for $P = 0.7$ and $R = 100$ (constant surface temperature)

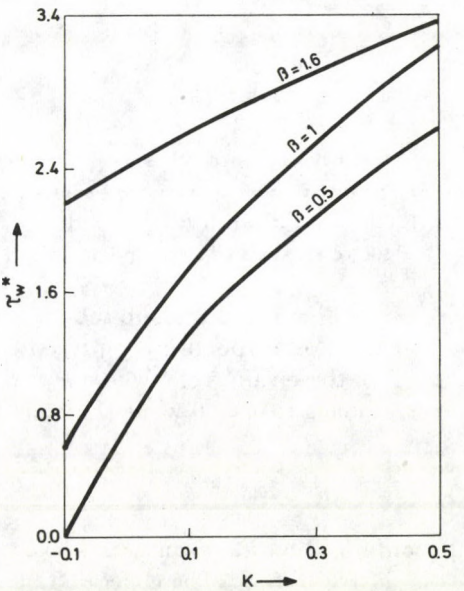

Fig 2. Dimensionless skin friction vs buoyancy parameter K for $P = 0.7$ and $R = 100$ (constant surface heat flux)

When the surface is heated, that is, $T_0 - T_\infty > 0$ then $K > 0$ and the flow experiences a favourable pressure gradient. The adjacent boundary layer flow is accelerated and with the increasing of K, the hydrodynamical and thermal boundary layer thicknesses decrease while the local heat transfer and skin friction values increase with respect to their values in non-buoyant case. On the other hand when the surface is cooled, then $K < 0$ and the boundary layer flow is decelerated . In this case a flow separation occurs since the forced and free convection act in opposite directions. That is, the condition for the boundary layer separations from the wedge surface is met when the flow tends to reverse at the interface. This phenomenon occurs when $(\partial u/\partial y)_{y=0} = 0$ at a certain negative value of K. For instance, in the case of $\beta = 0.5$, $n = 0$, and $R = 100$, the boundary layer is separated for $P = 0.7$, 1 and 3 at $K = -0.0952, -0.1007$ and -0.1322 respectively. These values clearly indicate that the separation is delayed with the increase of Prandtl number. It is also found that the separation is delayed with the increase of wall temperature exponent n. For, when $\beta = 0.5$, $R = 100$ and $P = 1$, the separations occur at $K = -0.1007$ and -0.1039 when $n = 0$ and $n = 1/3$, respectively.

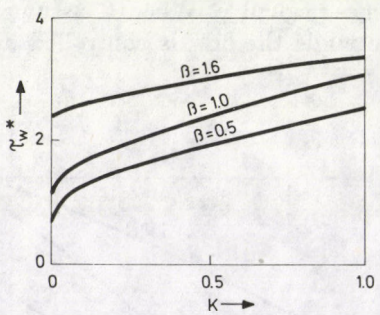

Fig 3. Variation of dimensionless skin friction with K when $P = 100$ and $R = 100$ (constant surface temperature)

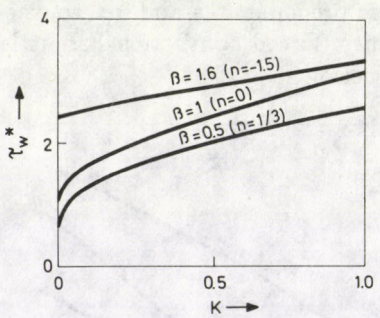

Fig 4. Variation of dimensionless skin friction with K when $P = 100$ and $R = 100$ (constant surface heat flux)

In Figs 1 and 2 where the cases of constant surface temperature and constant heat flux are, respectively, represented, the local shear stress is shown as a function of K for three values of β where $P = 0.7$ and $R = 100$. The uniform wall temperature corresponds to $n = 0$ while the constant heat flux situation is determined by

$$m + 2n = 1. \tag{17}$$

From Figs 1 and 2 it can be observed that the vanishing of shear stress is delayed by the increase in β. The general trends for the uniform wall temperature case seem to be repeated for the constant heat flux case. In Figs 3 and 4 the effect of K on high Prandtl number fluid ($P = 100$) is studied for constant surface temperature and constant surface heat flux cases, respectively. It is shown that the skin friction

values increase with K in the case of heating. The buoyancy force has a similar effect on local heat transfer as on shear stress. Figures 5 and 6 give the local Nusselt number curves for $P = 0.7$ and 100, respectively, when the surface temperature is uniform.

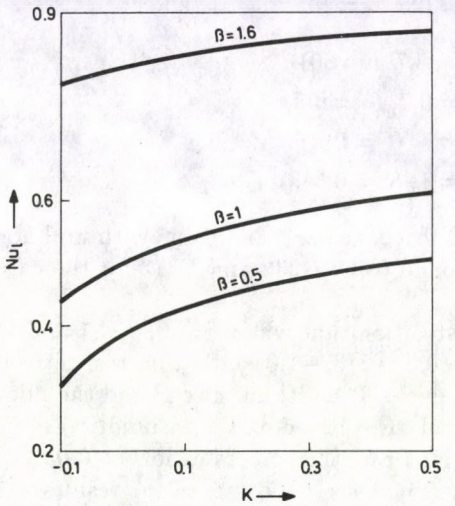

Fig 5. Local Nusselt number as a function of K ($P = 0.7$, $R = 100$, $n = 0$)

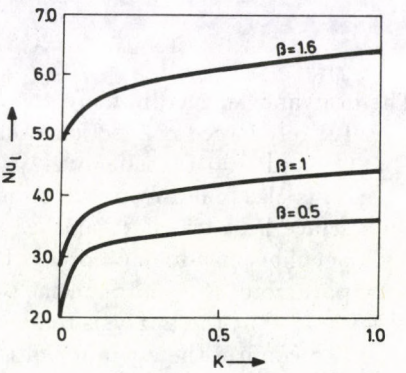

Fig 6. Local Nusselt number as a function of K ($P = 100$, $R = 100$, $n = 0$)

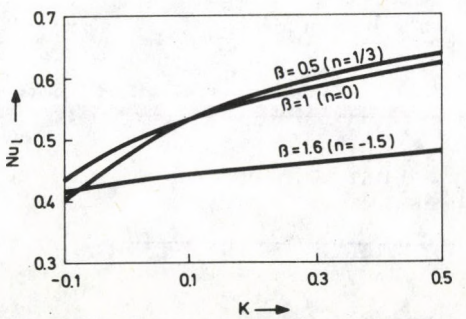

Fig 7. Buoyancy effect on local Nusselt number when $P = 0.7$, $R = 100$ and surface heat flux is constant

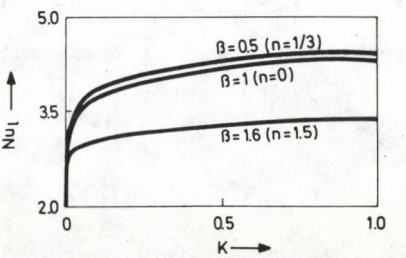

Fig 8. Buoyancy effect on local Nusselt number when $P = 100$, $R = 100$ and local heat flux is constant

The case of constant heat flux along the wedge is studied in Figs 7 and 8. In general, it follows that, when $K < 0$, the effect of buoyancy is to decrease the skin friction and heat transfer. It is also evident that the vanishing of local heat flux occurs at

a position beyond the point of zero skin friction. The inspection of Figs 1 and 5 reveals the fact that the skin friction is more strongly affected by buoyancy forces than is the heat transfer. This is due to the reason that the direct effect of buoyancy is an additional force in the momentum balance. It is also found that lower Prandtl number fluids are more sensitive to buoyancy effects. To illustrate this fact, let us choose the parametric values $R = 100$, $K = 0.5$, $n = 0$ and $\beta = 0.5$. For this case,

$$\begin{aligned} Nu_l &= 0.3840 \ (P = 0.7, K = 0), \\ &= 0.5114 \ (P = 0.7, K = 0.5), \\ &= 0.4397 \ (P = 1, K = 0), \\ &= 0.5777 \ (P = 1, K = 0.5). \end{aligned} \tag{18}$$

The bouyancy effects, namely, the ratios of heat transfer to its value with no buoyancy (purely forced convection value) are found to be 1.332 and 1.313 for the cases $P = 0.7$ and $P = 1$, respectively.

It is also found from the present investigation that when $\beta = 0$, 0.5, 1 and 1.6 the surface heat transfer vanishes at $n = -0.5, -2/3, -1.0$ and -2.5, respectively. This peculiar phenomenon occurs for any value of Prandtl number P and the buoyancy parameter K. Although the present analysis is based on the assumption $P \geq 1$ it is found that the analysis remains valid for Prandtl numbers as low as 0.05.

To confirm the accuracy of the present analysis, we compare the results with series solution of Sparrow and Minkowycz [4] when $\beta = 0$ and $P = 0.7$ in Table I.

Table I
Comparison of present results with Sparrow and Minkowycz solution ($P = 0.7$, $\beta = 0$)

K	Local Nusselt number		Skin friction	
	Ref. [4]	Present method	Ref. [4]	Present method
0.01	0.2963	0.3042	0.3493	0.3562
0.05	0.3106	0.3116	0.4182	0.4268
0.1	0.3284	0.3204	0.5043	0.5049

It is quite evident from Table I that the present values of local heat transfer and skin friction are in good agreement with known solution.

Acknowledgement

The author acknowledges gratefully the encouragements and suggestions of Prof. P. Singh of I.I.T., Kanpur.

Appendix

The velocity and temperature functions (12) are substituted in the momentum and energy balance equations (6) and on integration with respect to y with the help of the smooth-fit boundary conditions, the momentum and energy fluxes P_{12} and J_q are obtained, respectively. Their expressions are

$$\begin{aligned}-P_{12}/L_s =&U_\infty/d_1 + (mU_\infty^2/\gamma x)[53d_1/160 - y + 3y^3/2d_1^2 - 3y^4/2d_1^3\\ &+ 3y^5/4d_1^4 - y^6/4d_1^5 + y^7/28d_1^6] + (U_\infty^2 d_1'/\gamma)[9/160 - 3y^3/2d_1^3\\ &+ 3y^4/d_1^4 - 9y^5/4d_1^5 + 3y^6/4d_1^6 - 3y^7/28d_1^7] + (gBd_1/\gamma)(T_0 - T_\infty)\\ &[\sin(\pi\beta/2)(1/2 - 1/4\Delta + 1/40\Delta^3 - y/d_1 + 3y^2/4d_1d_2 - y^4/8d_1d_2^3\\ &+ (nd_2/x)\cos(\pi\beta/2)(3/16 - 1/6\Delta + 1/16\Delta^2 - 1/240\Delta^4 - 3y/8d_1\\ &+ y^2/2d_1d_2 - y^3/4d_1d_2^2 + y^5/40d_1d_2^4) + d_2'\cos(\pi\beta/2)(3/16\\ &- 1/16\Delta^2 + 1/80\Delta^4 - 3y/8d_1 + y^3/4d_1d_2^2 - 3y^5/40d_1d_2^4)], \qquad \text{(A-1)}\end{aligned}$$

$$\begin{aligned}-J_q/L_\lambda =&(U_\infty/\alpha)(T_0 - T_\infty)[(3d_1'/2)\{\Delta^2/5 - \Delta^3/6 + 3\Delta^4/70\\ &- y^3/2d_1^2d_2 + y^4/2d_1^3d_2 + (3y^5/10)(1/d_1^2d_2^3 - 1/2d_1^4d_2) - y^6/3d_1^3d_2^3\\ &+ 3y^7/28d_1^4d_2^3\} + d_2'\{-3\Delta/5 + 3\Delta^2/8 - 3\Delta^3/35 + 3y^3/2d_1d_2^2\\ &- 9y^4/8d_1^2d_2^2 + (y^5/10)(3/d_1^3d_2^2 - 9/d_1d_2^4) + 3y^6/4d_1^2d_2^4\\ &- 3y^7/14d_1^3d_2^4\} + (nd_2/x)\{-3\Delta/10 + \Delta^2/8 - 3\Delta^3/140 + 3y^2/2d_1d_2\\ &- y^3(3/2d_1d_2^2 + 1/d_1^2d_2) + y^4(9/8d_1^2d_2^2 + 1/4d_1^3d_2) + (3y^5/10)(1/d_1d_2^4\\ &- 1/d_1^3d_2^2) - y^6/4d_1^2d_2^4 + y^7/14d_1^3d_2^4\} + (3md_2/2x)\{-\Delta/5 + \Delta^2/12\\ &- \Delta^3/70 + y^3/2d_1d_2^2 - y^4/4d_1^2d_2^2 + y^5(1/20d_1^3d_2^2 - 3/10d_1d_2^4) + y^6/6d_1^2d_2^4\\ &- y^7/28d_1^3d_2^4\}]. \qquad \text{(A-2)}\end{aligned}$$

Here $\Delta = d_2/d_1$. We assumed $P \geq 1$ while obtaining the above flux expressions.

The principle (11) is formulated with the help of flux expressions (A-1) and (A-2), and the velocity and temperature profiles (12). After integration with respect to y and simplification we get the GPDP as

$$\delta \int_0^l [L_s\{(U_\infty^3/\gamma)[md_1(0.1241071)/x + d_1'(0.03482143)] - (0.4)u_\infty^2/d_1$$
$$- (U_\infty^4/\gamma^2)[m^2 d_1^3(0.00971555)/x^2 + d_1'^2 d_1(0.000812449) + md_1' d_1^2$$
$$(0.00528494)/x] + (U_\infty d_1/\gamma)gB(T_0 - T_\infty)[\sin(\pi\beta/2)(0.25 - 0.175/\Delta$$
$$+ 0.02142857/\Delta^3) + (nd_2/x)\cos(\pi\beta/2)(0.09375 - 0.1166667/\Delta + 0.05/\Delta^2$$
$$- 0.003720238/\Delta^4) + d_2' \cos(\pi\beta/2)(0.09375 - 0.05/\Delta^2 + 0.01116071/\Delta^4)$$
$$- (gB/2\gamma)(T_0 - T_\infty)[\sin(\pi\beta/2)(mU_\infty^2 d_1^3/\gamma x)(0.07569444 - 0.0514881/\Delta$$
$$+ 0.006083604/\Delta^3) + \sin(\pi\beta/2)(U_\infty^2 d_1' d_1^2/\gamma)(0.02291667 - 0.01696429/\Delta$$
$$+ 0.002165855/\Delta^3) + (nd_2/x)\cos(\pi\beta/2)(mU_\infty^2 d_1^3/\gamma x)(0.02838542$$
$$- 0.0343254/\Delta + 0.01441085/\Delta^2 - 0.00104432/\Delta^4) + (nd_2/x)\cos(\pi\beta/2)$$
$$(U_\infty^2 d_1' d_1^2/\gamma)(0.00859375 - 0.01130952/\Delta + 0.004981737/\Delta^2$$
$$- 0.000378944/\Delta^4) + d_2' \cos(\pi\beta/2)(mU_\infty^2 d_1^3/\gamma x)(0.02838542 - 0.01441085/\Delta^2$$
$$- 0.06604645\Delta^5 + 0.01643814\Delta^6 - 0.001770105\Delta^7)$$
$$+ (md_2' d_2^2/x)(0.1850649\Delta^2 - 0.2055804\Delta^3 + 0.09906968\Delta^4$$
$$- 0.02301339\Delta^5 + 0.00236014\Delta^6) + (mnd_2^3/x^2)(0.06777597\Delta^2$$
$$- 0.06322917\Delta^3 + 0.02636801\Delta^4 - 0.005436282\Delta^5$$
$$+ 0.0005004371\Delta^6)]\}]dx = 0. \qquad \text{(A-3)}$$

References

1. I. Gyarmati, Z.Phys.Chemie, *239*, 133 1968.
2. I. Gyarmati, Ann.Phys., *23*, 353, 1969.
3. I. Gyarmati, Non-Equilibrium Thermodynamics, Field Theory and Variational Principles, Springer-Verlag, Berlin, 1970.
4. E. M. Sparrow and W. J. Minkowycz, Int.J.Heat Mass transfer, *5*, 505, 1962.

Acta Physica Hungarica 65 (1), pp. 69–78 (1989)

AN APPLICATION OF THE GOVERNING PRINCIPLE OF DISSIPATIVE PROCESSES TO EIGENVALUE PROBLEM OF HYDRO-THERMODYNAMICS

NGUYEN HUYEN TUNG

Institute of Physics, Technical University of Hanoi
*Hanoi, Vietnam**

(Received 12 March 1987)

Gyarmati's principle is applied to study the temperature distribution of the fluid flow in a pipe, due to sudden change in wall temperature. It is found that the approximate results obtained in the paper are quite close to the exact ones and the dual field method is quite fit for the case of eigenvalue problem of hydro-thermodynamics.

1. Introduction

The main aim of the present analysis is to apply the dual field method to obtain the solution of the Graetz problem. It is well-known that the dual field method is based on the Governing Principle of Dissipative Processes (GPDP) which has been developed by Gyarmati [1 – 6]. The GPDP in its most general form is written as

$$\delta \int_v [\sigma - \psi - \phi] dV = 0, \tag{1}$$

where σ denotes the entropy production of system, ψ and ϕ are local dissipation potentials. This principle describes the evolution of dissipative processes at any instant of time under constraints when the general balance equations

$$\rho \dot{a}_i + \nabla \mathbf{I}_i = \sigma_i \qquad (i = 1, 2 \ldots) \tag{2}$$

are satisfied. Here ρ is the density of the continuum, $\bar{I}_i$ is the substantial current density and σ_i is the source of a_i quantity per unit volume and unit time. The entropy production σ is a bilinear function of f independent currents $\mathbf{I}_k$ and the conjugate dissipative forces $\mathbf{X}_k$, defined as gradients of thermostatic parameters $\gamma_k / \mathbf{X}_k \equiv \nabla \gamma_k /$:

$$\sigma(\mathbf{I}, \mathbf{X}) = \sum_{k=1}^{f} \mathbf{I}_k \cdot \mathbf{X}_k \geq 0. \tag{3}$$

*Present address: Institute of Physics, Technical University of Budapest, Hungary

In the traditional Onsager theory the fluxes are linear functions of the forces:

$$\mathbf{I}_i = \sum_{k=1}^{f} L_{ik}\mathbf{X}_k \qquad \text{or} \qquad X_i = \sum_{k=1}^{f} R_{ik}\mathbf{I}_k, \tag{4}$$

where the coefficients L_{ik} are conductivities while R_{ik} are resistances. These coefficients satisfy the Onsager relation:

$$L_{ik} = L_{ki} \qquad \text{and} \qquad R_{ik} = R_{ki} \tag{5}$$

and their matrices are mutually reciprocals of one another, i. e.,

$$\sum_{m=1}^{f} L_{im}L_{mk} = \sum_{m=i}^{f} R_{im}R_{mk} = \delta_{ik}. \tag{6}$$

The local dissipation potentials ψ and ϕ are defined as [1–3]:

$$\psi = \frac{1}{2}\sum_{i,k=1}^{f} L_{ik}\mathbf{X}_i\mathbf{X}_k \geq 0; \qquad \psi = \frac{1}{2}\sum_{i,k=1}^{f} R_{ik}\mathbf{I}_i\mathbf{I}_k \geq 0. \tag{7}$$

Evidently, in the linear Onsager theory the relation

$$\psi = \phi = \frac{1}{2}\sigma \tag{8}$$

is valid. The principle (1) now can be written as:

$$\delta \int_v \left[\sum \mathbf{I}_i \cdot \mathbf{X}_i - \frac{1}{2}\sum L_{ik}\mathbf{X}_i\mathbf{X}_k - \frac{1}{2}\sum R_{ik}\mathbf{I}_i \cdot \mathbf{I}_k\right] dv = 0, \tag{9}$$

but this variational principle (9) is operative if and only if the balance equations (2) are regarded as auxiliary conditions and for their variations the following restriction holds:

$$\delta(\rho\dot{a}_i - \sigma_i) = -\delta\nabla \cdot \mathbf{I}_i = -\nabla\delta\mathbf{I}_i \qquad (i = 1, 2, \ldots f). \tag{10}$$

Thereby it is remarkable that the simultaneous variation of the principle with respect to forces and fluxes leads to the universal form of Gyarmati's principle which is a genuine variational principle of irreversible processes. However, the restricted variations of the principle with respect to one of these two independent functions give two partial forms of the principle. The variation with respect to currents (i. e. $\delta\mathbf{I} \neq 0$ but $\delta\mathbf{X} = 0$) yields the flux representation of the principle which is equivalent to Lagrangian thermodynamics of Biot [7]. On the other hand, the variation of the principle with respect to forces (i. e. $\delta\mathbf{I} = 0$, $\delta\mathbf{X} \neq 0$) results in the force representation of the principle which is equivalent to the local potential method of Glansdorff and Prigogine [8].

In this paper we employ the dual field method to get the solution of the Graetz problem for the case of the flow of a liquid in a circular tube. Recently Singh and Srivastava [10] applied this method to solve the problem for the case of the fluid flow inside two parallel semi-infinite plates. We shall show that the method is quite a fit for the eigenvalue problem of hydro-thermodynamics.

2. Formulation of the problem

Let us consider the problem of developing temperature profile in tube due to a sudden change in the wall temperature. We neglect the dissipation due to viscosity and axial heat conduction. In this case, the equation of balance of energy has the following simple form:

$$v\frac{\partial T}{\partial Z} = \frac{\alpha}{r}\frac{\partial}{\partial r}\left(r\frac{\partial T}{\partial r}\right), \tag{11}$$

where $\alpha = \frac{K}{\rho C_p}$ is the thermal diffusivity of the fluid. The velocity distribution $v(r,z)$ is assumed known. In this case $v = 2\bar{v}\left(1 - \frac{r^2}{r_0^2}\right)$ where $\bar{v}$ is mean velocity and r_0 is the tube radius. The equation (11) is written in cylindrical polar coordinates r, θ, z. Moreover, we assume that the fluid temperature is uniform until the sudden change is reached, after which $T = T(r,z)$ with the wall conditions $T(r_0,z) = T_w$. In our case, the proper boundary conditions for (11) are

$$\begin{aligned} z \leq 0, &\qquad T = T_0 \\ z > 0, &\qquad T(r_0,z) = T_w. \end{aligned} \tag{12}$$

Now, including dimensionless variables for this problem

$$\theta = \frac{T_w - T}{T_w - T_0}; \quad x = \frac{r}{r_0}, \quad y = \frac{z}{d_0 \cdot P_e}, \tag{13}$$

where $d_0 = 2r_0$, $P_e = R_e \cdot P_r$ is the Peclet number, R_e is the Reynolds number, P_r is the Prandtl number. Equation (11) and condition (12) become

$$\frac{\partial \theta}{\partial y} = \frac{2}{x(1-x^2)}\frac{\partial}{\partial x}\left(x\frac{\partial \theta}{\partial x}\right), \tag{14}$$

and

$$\theta(x,o) = 1, \qquad \theta(1,y) = 0, \tag{15}$$

respectively. Let us suppose that:

$$\theta(x,y) = f(x) \cdot g(y) \tag{16}$$

and substituting (16) into (14), we obtain:

$$\frac{g'}{2g} = \frac{xf'' + f'}{x(1-x^2)f} = -\lambda^2 = \text{const.} \tag{17}$$

Here, the $g(y)$ function has the solution

$$g = c \cdot \exp\left(-2\lambda^2 y\right) \qquad \text{where} \qquad C = \text{constant}. \tag{18}$$

On the other hand the function $f(x)$ satisfies the equation:

$$\frac{1}{x(1-x^2)}\frac{\partial}{\partial x}\left(x\frac{\partial f}{\partial x}\right)+\lambda^2 f=0, \tag{19}$$

with the boundary conditions

$$f(1)=0 \qquad \text{and} \qquad f(0)=1. \tag{20}$$

It is obvious that for equation (9) λ^2 and $f(x)$ are eigenvalue and eigenfunction, respectively. We can write $f(x)$ as in [9]:

$$f_{(x)}^{(n)}=\sum_{i=1}^{n} b_i\varphi_i(x), \tag{21}$$

where $\varphi_i(x)$ is a set of trial functions satisfying the condition (20), and b_i are the coefficients which must be determined by the variational principle. Then, we seek for the sequence of approximate temperature field $T^{(n)}$ as:

$$T^{(n)}=T_w-(T_w-T_0)\theta^{(n)}, \tag{22}$$

where

$$\theta^{(n)}=\frac{T_w-T^{(n)}}{T_w-T_0}=\sum_{j=1}^{n} B_j^{(n)} f_j^{(n)}(x)\exp\left[-2\lambda_j^2 y\right]. \tag{23}$$

By virtue of (4) and (22) we can write

$$\mathbf{I}_g=L_g\mathbf{X}_g=-L_g\frac{\partial T^{(n)}}{\partial x}. \tag{24}$$

The entropy production of system is given by

$$\sigma^{(n)}=-\mathbf{I}_g^{(n)}\frac{\partial T^{(n)}}{\partial x}; \tag{25}$$

while the dissipation potentials are

$$\psi^{(n)}=\frac{L_g}{2}\left(\frac{\partial T^{(n)}}{\partial x}\right)^2; \qquad \phi^{(n)}=\frac{1}{2L_g}\mathbf{I}_g^{(n)}. \tag{26}$$

Evidently, the Gyarmati principle in our case gets the form

$$\delta\int_v\left[-\mathbf{I}_g^{(n)}\frac{\partial T^{(n)}}{\partial x}-\frac{L_g}{2}\left(\frac{\partial T^{(n)}}{\partial x}\right)^2-\frac{1}{2L_g}\mathbf{I}_g^{(n)^2}\right]dv=0. \tag{27}$$

For the sake of simplicity indices are neglected.

The driving force of the system is $\frac{\partial T}{\partial x}$ hence we take T as basic quantity and $\mathbf{I}_g$ is substituted by another temperature T^* which is related to $\mathbf{I}_g$ through the following approximate constitutive law:

$$\mathbf{I}_g = -L_g \frac{\partial T^*}{\partial x}, \tag{28}$$

where

$$T^* = T_w - (T_w - T_0)\theta^* \tag{29}$$

is the so-called temperature dual field [9,10]. Assuming that the axial heat conduction is neglected we can write

$$\theta^* = g \cdot f^*, \tag{30}$$

where g is defined by (18) and f^* is the function of x. Now the principle (27) becomes

$$\delta \int_0^1 \left[\left(\frac{\partial f}{\partial x}\right)\left(\frac{\partial f^*}{\partial x}\right) - \frac{1}{2}\left(\frac{\partial f}{\partial x}\right)^2 - \frac{1}{2}\left(\frac{\partial f^*}{\partial x}\right)^2 \right] x dx = 0 \tag{31}$$

In our case, from the equation of balance of energy, the following equation

$$\frac{1}{x(1-x^2)} \frac{\partial}{\partial x}\left(x \frac{\partial f^*}{\partial x}\right) = -\lambda^2 f; \tag{32}$$

is valid with the boundary condition

$$\left.\frac{\partial f^*}{\partial x}\right|_{x=0} = 0. \tag{33}$$

By the functions $f(x)$ and $g(y)$ we can write $\theta(x, y)$ as

$$\theta = \sum_{j=1}^{\infty} B_j f_j(x) \exp(-2\lambda_j^2 y). \tag{34}$$

3. Eigenvalues

We select the set of trial functions $\varphi_k(x)$ in the form:

$$\varphi_k(x) = \left(1 - \frac{3}{2}x^2 + \frac{x^4}{2}\right)^k. \tag{35}$$

It is obvious that in this form $\varphi_k(x)$ satisfies the condition (20) and

$$f_j^{(n)} = \sum_{k=1}^{n} b_k^{(j)} \left(1 - \frac{3}{2}x^2 + \frac{x^4}{2}\right). \tag{36}$$

Then $f_j^{(n)}(x)$ has the form of the fourth-degree polynomial function. At first, we consider the problem in the force representation and of the lowest approximation, i. e. $n = 1$. The variational principle (31) reduces to the form

$$\delta \int_0^1 \left[f' f^{*\prime} - \frac{1}{2} f'^2 \right] x dx = 0 \tag{37}$$

and

$$f^{(n)}(x) = f^{(1)}(x) = b\left(1 - \frac{3}{2}x^2 + \frac{x^4}{2}\right). \tag{38}$$

Now, from (32), we get

$$f'^{(1)*} = -b^* \lambda^2 \left(\frac{x}{2} - \frac{5}{8}x^3 + \frac{x^5}{3} - \frac{x^7}{16}\right), \tag{39}$$

where b is variational parameter which is determined. Substituting $f'^{(1)}$ and $f'^{(1)*}$ from (38) and (39) into (37) and integrating with respect to x from 0 to 1, we have

$$\delta \left[0.1020833 \lambda^2 b b^* - 0.75000 \cdot \frac{1}{2} b^2 \right] = 0. \tag{40}$$

After variation with respect to b only, and putting $b^* = b$, we get

$$(0.1020833\lambda^2 - 0.7500)b = 0. \tag{41}$$

If the Eq. (41) has a nontrivial solution, then

$$\lambda^2 = 7.34694 \qquad \text{and} \qquad \lambda = 2.71052 \tag{42}$$

where λ is the eigenvalue.

In the next approximation, i. e. if $n = 2$, we can write

$$f^{(2)} = b_1 \left(1 - \frac{3}{2}x^2 + \frac{x^4}{2}\right) + b_2 \left(1 - \frac{3}{2}x^2 + \frac{x^4}{2}\right)^2, \tag{43}$$

and $f'^{(2)*}$ is obtained as

$$\begin{aligned} f'^{(2)*}(x) = \lambda^2 \Bigg[& b_1^* \left(\frac{x^7}{16} - \frac{x^5}{3} + \frac{5}{8}x^3 - \frac{x}{2}\right) + \\ & + b_2^* \left(\frac{x^{11}}{48} - \frac{7}{40}x^9 + \frac{19}{32}x^7 - \frac{25}{24}x^5 + x^3 - \frac{x}{2}\right) \Bigg]. \end{aligned} \tag{44}$$

By variation with respect to force only, the variational principle (37) yields a set of linear equations in b_1 and b_2, i. e.

$$\begin{aligned} G_{11}b_1 + G_{12}b_2 &= 0, \\ G_{21}b_1 + G_{22}b_2 &= 0; \end{aligned} \tag{45}$$

where

$$G_{11} = 0.1020833\lambda^2 - 0.75000; \qquad G_{22} = 0.0635169\lambda^2 - 0.5869048$$

$$G_{12} = G_{21} = 0.0783482\lambda^2 - 0.5583334. \tag{46}$$

Of course, the eigenvalues must be determined so that the determinant vanishes i. e.

$$G_{11}G_{22} - G_{12}^2 = 0; \tag{47}$$

which yields an equation of fourth degree

$$0.34558\lambda^4 - 20.06202\lambda^2 + 12844244 = 0. \tag{48}$$

The positive solutions of (48) are

$$\begin{aligned} \lambda_1^2 &= 7.32703, & \lambda_1 &= 2.70685, \\ \lambda_2^2 &= 50.72616, & \lambda_2 &= 7.12223. \end{aligned} \tag{49}$$

In the flux representation, the Gyarmati principle (31) takes the form:

$$\delta \int_0^1 \left[f' f'^* - \frac{1}{2} f'^{*2} \right] x dx = 0 \tag{50}$$

and the variation is taken only with respect to the quantities with asterisk.

Let us estimate the first eigenvalue. From (38), (39) and the variational principle (5) it is easy to get

$$\lambda^2 = 7.31828; \qquad \lambda = 2.70523. \tag{51}$$

For the next approximation, $n = 2$, the variational principle yields the set of algebraic equations, that are linear and homogeneous in the constants b_1, b_2:

$$\begin{aligned} G_{11}^* b_1 + G_{12}^* b_2 &= 0, \\ G_{21}^* b_1 + G_{22}^* b_2 &= 0; \end{aligned} \tag{52}$$

where

$$G_{11}^{*} = \lambda^2(0.1020833 - 0.0139491\lambda^2); \quad G_{22}^{*} = \lambda^2(0.0635169 - 0.0083765\lambda^2);$$
$$G_{12}^{*} = G_{21}^{*} = \lambda^2(0.0783422 - 0.0107623\lambda^2). \tag{53}$$

The system (52) has a nontrivial solution when

$$G_{11}^{*}G_{22}^{*} - G_{12}^{*} = 0, \tag{54}$$

which yields the algebraic equation

$$0.10152\lambda^4 - 54.67342\lambda^2 + 34.55731 = 0. \tag{55}$$

The positive solutions of the equation (55) are

$$\begin{aligned} \lambda_1^2 &= 7.31398, \qquad \lambda_1 = 2.70444; \\ \lambda_2^2 &= 46.54084, \qquad \lambda_2 = 6.82208. \end{aligned} \tag{56}$$

These values of λ are good as compared with the exact values of those which are given by Brown in [11]: $\lambda_1 = 2.704$ and $\lambda_2 = 6.66$.

4. The eigenfunctions

To determine the approximate eigenfunctions associated with each of the eigenvalues, we must find the values $b_k^{(j)}$ in (36). For the sake of simplicity, the value of each constant will be selected so that $f_j^{(n)}(x)$ be equal to one at $r = 0$. From (45) and (52) we can compute only the ratio of b_1 and b_2, i. e.:

$$\begin{aligned} \lambda_1 &= 2.70444, \qquad b_2^{(1)} = 0.163\, b_1^{(1)} \\ \lambda_2 &= 6.82208; \qquad b_2^{(2)} = -1.2948\, b_1^{(2)}. \end{aligned} \tag{57}$$

From the condition (20) and (57) we get

$$b_1^{(1)} = 0.8598, \qquad b_2^{(1)} = 0.1402$$

and

$$b_1^{(2)} = -3.3917, \qquad b_2^{(2)} = 4.3917. \tag{58}$$

For determining $\theta(x, y)$ we must find $B_j^{(n)}$ in the expression (23). From (15) we have:

$$\sum_{j=1}^{n} B_j^{(n)} f_j^{(n)}(x) = 1 \qquad n = 1, 2, 3 \ldots, \tag{59}$$

where (in the case $n = 2$)

$$f_1^{(2)}(x) = 0.8598\left(1 - \frac{3}{2}x^2 + \frac{x^4}{2}\right) + 0.1402\left(1 - \frac{3}{2}x^2 + \frac{x^4}{2}\right)^2;$$

and

$$f_2^{(2)}(x) = -33917\left(1 - \frac{3}{2}x^2 + \frac{x^4}{2}\right) + 4.3917\left(1 - \frac{3}{2}x^2 + \frac{x^4}{2}\right)^2. \tag{60}$$

Multiplying both sides of (59) by $f_K^{(n)}(x)$ and taking the so-called "cup-mixing" values of this between the limits of 0 and 1, we get the set of linear equations for $B_j^{(n)}$ as

$$\sum_{j=1}^{n} A_{kj}^{(n)} B_j^{(n)} = C_k^{(n)}, \tag{61}$$

where

$$A_{kj}^{(n)} \quad \frac{\int_0^1 f_k^{(n)} f_j^{(n)} x(1-x^2)dx}{\int_0^1 x(1-x^2)dx}, \tag{62}$$

and

$$C_k^{(n)} = \frac{\int_0^1 f_k^{(n)} x(1-x^2)dx}{\int_0^1 x(1-x^2)dx}, \quad k, j = 1, 2 \ldots n. \tag{63}$$

With $f_j^{(n)}(x)$ determined in (60) the set of equations (61) becomes

$$\begin{aligned} 0.09560309B_1^{(2)} - 0.00000031B_2^{(2)} &= 0.13969958, \\ -0.00000031B_1^{(2)} + 0.06533620B_2^{(2)} &= -0.04630550, \end{aligned} \tag{64}$$

the solutions of which are

$$B_1^{(2)} = 1.4612428, \qquad B_2^{(2)} = -0.7086897. \tag{65}$$

Thus, an approximation for the temperature distribution is determined.

To evaluate this approximation, let us determine the "cup-mixing" temperature that would be observed if the fluid at an axial position was permitted to flow into an insulated cup and come to equilibrium

$$T_m = \frac{\int_0^1 Tx(1-x^2)dx}{\int_0^1 x(1-x^2)dx}. \tag{66}$$

From (23) we can show that

$$\frac{T_m - T_w}{T_w - T_0} \cong 4 \sum_{j=1}^{n} B_j^{(n)} f_j^{(n)*}(1). \exp(-2\lambda_j^2 y). \tag{67}$$

$$\frac{T_m - T_w}{T_0 - T_w} = 0.81654 \exp\left(-\frac{2(2.70444)^2 z}{d_0 \cdot P_e}\right) + 0.13124 \exp\left(-\frac{2(6.82208)^2 z}{d_0 \cdot P_e}\right). \tag{68}$$

The equation (68) relates the mean fluid temperature to the axial position z. At $z = 0$ our approximation is in error by 5.2 per cent. For comparison we have chosen the first two terms given by Brown numerically [11]:

$$\frac{T_m - T_w}{T_0 - T_w} = 0.82 \exp\left(-\frac{(2.7)^2}{2r_0}\frac{\alpha}{\bar{v}}\frac{z}{r_0}\right) + 0.098 \exp\left(-\frac{(6.66)^2}{2r_0}\frac{\alpha}{\bar{v}}\frac{z}{r_0}\right). \tag{69}$$

For large values of $z/y \geq 0.05/$ the Eq. (68) yields results different from those which would be calculated from (69) by approximately 0.48%. It is obvious that at the position very near to the inlet the Eq. (68) gives results better than those obtained by (69).

As a general conclusion we can state that, by applying the dual field method based on the Governing Principle of Dissipative Processes, we have found solutions to a very difficult computational problem. The result can be improved by taking trial functions $\varphi_i(x)$ of higher order or by taking more variational parameters in $f_j^{(n)}(x)$.

References

1. I. Gyarmati, Non-Equilibrium Thermodynamics, Field Theory and Variational Principle, Springer-Verlag, Berlin, 1970.
2. I. Gyarmati, Ann. Phys., *23*, 353, 1969.
3. J. Verhás, Z. Phys. Chemie, *249*, 119, 1972.
4. J. Verhás, Ann. Phys., 7, 189, 1983.
5. H. Farkas, J. Non-Equilib. Thermodyn., *1*, 117, 1976.
6. H. Farkas, Int. J. Engng. Sci., *13*, 1035, 1975.
7. M.A. Biot, Variational Principles in Heat Transfer, Oxford University Press, 1970.
8. P. Glansdorff and I. Prigogine, Thermodynamic Theory of Structure, Stability and Fluctuation, Wiley, Interscience, London, 1971.
9. A. Stark, Ann. Phys., 7, 53, 1974.
10. P. Singh and K. Srivastava, Acta Phys. Hung., *45*, 201, 1978.
11. R.S. Schechter, The Variational Method in Engineering, McGraw Hill, New York, 1967.

Acta Physica Hungarica 65 (1), pp. 79–84 (1989)

HIGGS GRAVITATIONAL VACUUM IN THE GAUGE GRAVITATION THEORY

G. SARDANASHVILY and B. IKHLOV

Physics Faculty of Moscow University
117234, Moscow, USSR

(Received 27 March 1987)

The Higgs–Goldstone nature of a gravitational field responsible for spontaneous breaking of space-time symmetries is examined. The Higgs matter vacuum is suggested to be the source of the Higgs gravitational vacuum.

The geometric nature of gravity as a metric field was established by Einstein's General Relativity. The physical specification of gravity as a Higgs–Goldstone type field is now clarified due to the gauge gravitation theory [1,2].

Higgs–Goldstone fields are parts and parcels of most contemporary gauge unified models. One makes use of these classical fields to model the non-invariant vacuum in quantum field theory.

Not long ago one used to treat the vacuum in quantum field theory as an empty state, e.g. described by Fock's vacuum. However, this turned out to be relevant as a rule only for free systems. This led to the introduction of the notion of "physical" vacuum. By contrast to the "bare" Fock's vacuum, "physical" vacuum possesses certain nonvanishing physical characteristics, and, therefore, this vacuum appears to be non-invariant under some symmetries. Real particles and fields can interact with such a vacuum.

In algebraic quantum theory [3] the criterion of non-invariant vacuum is the non-invariance of a positive definite form f on an operator B^*-algebra A of physical variables, i. e.

$$f'(a) = f(g(a)) \neq f(a), \qquad a \in A, \qquad g \in G.$$

Such a form defines the representation of A in the Hilbert space

$$H_f = \overline{A/N_f}, \quad N_f = \{a \in A : f(a^*a) = 0\}$$

possessing the cyclic vacuum vector

$$| >= 1_A/N_f, H_f = \overline{A}| >, f(a) =< a >_f,$$

where 1_A is the approximative unit of the algebra A, and $\overline{A|}>$ is the completion of $A|>$ with respect to the norm $<\zeta|\zeta>=<a^*a>=f(a^*a)$ [4]. Non-invariance of the form $f' \neq f$ entails non-invariance of the vacuum $|>\neq|>'$.

In the quantum field theory a form f is composed by Green's functions defined by the generating functional

$$Z = N^{-1}\int [dq] \exp(iS(q)).$$

Green's functions, being vacuum expectation values of chronological products of quantum field operators q, can be represented as correlation functions $<T(q^*q)>= f(q^*q)$ of classical fields q. This enables one to replace the algebra of quantum fields by the enveloping algebra of classical fields $W = \bigoplus_h(\bigoplus_h E)/J$, where E is a vector space of classical fields, and J is the ideal generated by elements $q\otimes q' - (-1)^a q'\otimes q$ ($a = 0$ for bosons, and $a = 1$ for fermions)[5]. If E is a Hilbert space, $\overline{W}$ is a B^*-algebra.

Green's functions are invariant under a global group G of transformations of matter fields q if the action functional of these fields is G-invariant (which is not true for a gauge group $G(X)$ and for the chiral γ_5-symmetry). Therefore, to break G-invariance of the action $S(q)$ insert a term describing the interaction of q with some classical Higgs–Goldstone field σ into S. Then, the action S becomes G-covariant as a functional of fields q (i.e. $S'(q',\sigma') = S(q',\sigma') = S(q,\sigma)$), and

$$f_\sigma(a'(q_i)) = f_\sigma(a(q_i')) = N^{-1}\int [dq_i]a(q_i')\exp(iS(q_i,\sigma)) =$$

$$= N^{-1}\int [dq_i']a(q_i')\exp(iS(q_i',\sigma')) = f_{\sigma'}(a(q_i)),$$

where $a(q_i)\in W$ consists of some tensor products of basis elements q_i of the Hilbert space E. In general $f_\sigma \neq f_{\sigma'}$, and vacua $|>_\sigma$ and $|>_{\sigma'}$ are non-equivalent. Since the action $S(\varphi,\sigma)$ is G-covariant, the symmetry breaking caused by a Higgs–Goldstone field is spontaneous [5].

In the fibre bundle description a Higgs–Goldstone field σ is represented by a global section of the fibre bundle in the quotient space G/H [6, 7, 8]. By the well known theorems [9] there is an atlas ψ^σ of this bundle such that field functions σ_i take on values in the centre of the quotient space G/H, i. e. σ is reduced to the H-invariant Higgs component relative to ψ^σ whereas Goldstone components of σ are removed.

In practice, σ_0 is a H-invariant point of some vector space V. A field $\sigma(x)$ takes on values in the quotient space $G/H = G\sigma_0 \subset V$, i. e.

$$\sigma(x) = \exp(\tau^\alpha(x)I_\alpha)\sigma_0 \approx \sigma_0 + \sigma'(x), \sigma' = \tau^\alpha I_\alpha(\sigma_0),$$

where τ^α and I_α are parameters and generators of the symmetry group G, σ_0 is a H-invariant Higgs component of σ, and σ' is a Goldstone component of σ. In

the case of internal symmetries a Goldstone field fails to be a dynamical quantity because one can always remove σ' by a gauge choice.

A pseudo-Riemannian metric g makes an action functional $S(q,g)$ convariant under the group $GL(4,R)$.Consequently, a gravitational field makes Green's functions and the vacuum of matter fields q non-invariant under space-time transformations. Moreover, forms f_η and f_g define generally non-equivalent representations of the algebra W and, consequently, non-equivalent vacua.

Since the algebraic quantum field theory is far from the satisfactory completion, we illustrate this proposition within the framework of the quantum field theory in two Euclidean dimensions [10]. Let q be a scalar field on R^2, and

$$S = \int \frac{i}{2}(-\partial_i q^* \partial_i q - m^2 q^2) d^2x.$$

Let E be a Hilbert space of generalized functions whose Fourier images $q(p)$ are ordinary functions with the finite norm

$$\| q \|^2 = f(q^*q) = < q^*q > = \int q^2(p)(p^2 + m^2)^{-1} d^2p.$$

We consider $g = 2\eta$. Then

$$f_g(q^*q) = q^2(p)(p^2 + m^2/2)^{-1} d^2p \neq f(q^*q), \qquad q \in E. \tag{1}$$

If f and f_g define equivalent representations, there must exist such an element $b \in H_f, < b^*b > = 1$ that

$$< q^*q >_g = < b^*q^*qb > = < q^*b >< b^*q > + < q^*q >$$

[4]. However, in the case of fields q (such that the relation $< b^*q > \neq 0$, i.e. $< q^*q >_g = < q^*q >$ holds) a subspace of a countable Hilbert dimension is formed. This is in contradiction to relation (1), and vacua $| >$ and $| >_g$ are non-equivalent.

Thus, there are important reasons to treat a pseudo-Riemannian metric g as a Higgs–Goldstone field. In the fibre bundle description this metric is defined as a global section g of the fibre bundle B of pseudo-Euclidean bilinear forms in tangent spaces over a space-time manifold X^4. The bundle B is associated with the tangent bundle $T(X)$ possessing the structure group $GL^+(4,R)$, and this is isomorphic to the fibre bundle in quotient spaces $GL^+(4,R)/\mathrm{SO}(3,1)$. The global section h of the quotient bundle, which is isomorphic to g, describes a gravitational field in the tetrad form. By the theorems mentioned above for a global section h of the quotient bundle to exist, the possibility of contraction the structure group $GL^+(4,R)$ of the tangent bundle to the Lorentz group is necessary and sufficient. It means the existence of an atlas $\psi^g = \{U_i, \psi_i^g\}$ of $T(X)$ such that all transition functions of ψ^g are elements of the Lorentz gauge group, and all metric functions $g_i = \psi_i^g \cdot g$ coincide with the Minkowski metric η relative to ψ^g.

A metric g as well as a standard Higgs–Goldstone field possess the SO(3,1)-invariant Higgs component η and Goldstone components, i. e. a gravitational field identified with deviations of g from η. However, in contrast to Goldstone fields of internal symmetries, a Goldstone gravitational field cannot be removed by any gauge transformation. The reason lies in the fact that space-time transformations alter also derivatives ∂_μ as basis elements of tangent spaces, which include tetrad functions $\partial_a = h_a^\mu \partial_\mu$ relative to the nonholonomic reference frame ψ^g where $g_i = \eta$ [2,7].

The Higgs–Goldstone treatment of a gravitational field poses the question on the existence of the Higgs gravitational vacuum.

Although a non-invariant vacuum modelled by a Higgs field is part and parcel of the contemporary gauge unified theory, the physical nature of such a vacuum still remains unclear. The viewpoint many authors accept is that a non-invariant vacuum is sui generis a condensate by analogy with the Cooper condensate, and it Higgs field is described by constructing an effective action [11,12,13].

For example, let $\{q^A\}$ be Dirac fermions endowed with indices $\{A = 1, 2\}$ of internal symmetries G, whose G-invariant Lagrangian

$$L = q^*(i)q + K/2(q_a^{A^*} q_B^a)(q_b^{B^*} q_A^b) \tag{2}$$

includes the interaction term of the Ivanenko–Heisenberg nonlinear type which is responsible for the appearance of the condensate.

Lagrangian (2) can be linearized by inserting a collective field σ in the generating functional

$$Z = N^{-1} \int [dq^*][dq][d\sigma] \exp\left(i \int L' d^4x\right),$$
$$L' = q^*(i\gamma\partial + \hat{\sigma})q + Tr\hat{\sigma}^2/2K, \tag{3}$$

where σ' are components of the 2×2 matrix $\hat{\sigma}$ acting on indices A. Lagrangian (2) is reconstructed by integration of Z over the field σ. Lagrangian (3) of fields q is G-covariant due to the field σ. Then, if σ contains a classical component $\sigma_0 \neq 0$ fermion Green's functions and the vacuum fails to be G-invariant, i. e. spontaneous symmetry breaking takes place. Thereby, a collective field σ plays the role of a Higgs–Goldstone field.

Integration of Z over fermion fields results in the effective action of the field σ

$$S_{\text{eff}} = -iTr\ln(i\gamma\partial + \hat{\sigma}) + \int Tr\hat{\sigma}^2 d^4x/2K.$$

Then, a classical Higgs component σ_0 is defined as a stable solution of the equation $\delta S_{\text{eff}}/\delta\sigma = 0$.

Let us examine a constant solution σ_0 such that $Tr\hat{\sigma}_0 = 0$, $\det\hat{\sigma}_0 < 0$. Then the equation for σ_0 reads

$$\sigma_A^B/K + i\int 4\sigma_A^B(p^2 + \det\hat{\sigma})^{-1}d^4p = \sigma_A^B/K + 4\pi^2\sigma_A^B \det\hat{\sigma}[-\gamma + \\ +2/(4-n) - \ln(-\det(\hat{\sigma})/\mu^2)] = 0, \quad (4)$$

where the dimensional regularization is applied. This equation admits the non-zero stable solution ($-\det\hat{\sigma}_0 = M^2$, $\sigma_{0A}^B < 0$, $M^2 \to \infty$ when $n \to 4$) identified with the vacuum Higgs field.

The method of constructing an effective action can be applied also in gravitation theory [14,15]. Let us consider the fermion field q^A in the vacuum Higgs field σ_0 satisfying equation (4) and in a gravitational field g. Its Lagrangian reads

$$L = q^*(i\gamma D + \hat{\sigma}_0)q - K^{-1}M^2.$$

Following the standard procedure [15], one obtains the effective gravitation Lagrangian

$$L_g = (4\pi)^{n/2}(-\gamma + 2/(4-n) - \ln(M^2/\mu^2))(2M^4/n(n-2) + \\ + M^2R/12(n-2) + a_2) - M^2/K, \quad (5)$$

where a_2 denotes quadratic terms in the gravitation curvature R. Substitution of the solution M^2 of the Eq. (4) into Lagrangian (5) results in

$$L_g = ((4\pi)^{n/2}M^2/2\pi^2 n(n-2)K - M^2/K) + \\ + (4\pi)^{n/2}R/(48\pi^2(n-2)K) + (4\pi)^{n/2}a_2/(4\pi^2 K M^2).$$

When $n = 4 (M^2 \to \infty)$ the effective gravitation Lagrangian takes on the familiar Hilbert–Einstein form $L_g = R/6K$.

Note the following properties of the above effective gravitation Lagrangian due to the Higgs field σ_0 obeying Higgs vacuum equation (4). (i) Since $M^2 \to \infty$ the effective Lagrangian includes no quadratic terms in the curvature, i. e. this is the Hilbert Lagrangian of classical Einstein gravity. (ii) The effective Lagrangian L_g possesses no cosmological term because if such one is generated by vacuum polarization it is compensated by the identical term of the Higgs field Lagrangian. In our opinion, this may contribute to explaining the very small value of the cosmological constant one observes now. (iii) The gravitational constant in the effective Lagrangian L_g is finite, and this is connected to the coupling constant of the fermion–fermion interaction of the Ivanenko–Heisenberg non-linear spinor theory type.

As a consequence, the semiclassical equations for a Higgs gravitational field g_0 take on the familiar form of Einstein's equations of the general relativity

$$R_{\mu\nu} - g_{\mu\nu}R/2 = 6K < T_{\mu\nu} >,$$

where $T_{\mu\nu}$ is the energy-momentum tensor of the "ordinary" matter, so that one cannot exclude the coincidence of g with a familiar classical gravitational field.

References

1. G. Sardanashvily, Phys. Lett., *75A*, 257, 1980.
2. D. Ivanenko and G. Sardanashvily, Lett. Nuovo Cim., *30*, 220, 1981.
3. G. Emch, Algebraic Methods in Statistical Mechanics and Quantum Field Theory, John Wiley and Sons Inc., N. Y. - London, 1972.
4. J. Dixmier, Les C*-algèbres et leurs représentations, Gauthier - Villars Edition, Paris, 1969.
5. D. Ivanenko, P. Pronin and G. Sardanashvily, Gauge Gravitation Theory, Moscow Univ. Press, Moscow, 1985.
6. A. Trautman, Czech, J. Phys., *29B*, 107, 1979.
7. D. Ivanenko and G. Sardanashvily. Phys. Rep., *94*, 1, 1983.
8. L. Nikolova and V. Rizov, Rep. Math. Phys., *20*, 287, 1984.
9. S. Kobayashi and K. Nomizu, Foundation of differential geometry, Int. Publ. J. Wiley and Sons, N. Y. – London – Sydney, 1963.
10. B. Simon, The $P(\varphi)_2$ Euclidean (Quantum) Field Theory, Princeton Univ. Press, Princeton, 1974.
11. C. Bender, F. Cooper and G. Guralnik, Ann Phys., *109*, 165, 1977.
12. S. Kawati and H. Miyata, Phys. Rev., *23D*, 3010, 1981.
13. K. Sinha, Praman-J. Phys., *25*, 467, 1985.
14. S. Adler, Rev. Mod. Phys., *54*, 729, 1982.
15. N. Birrell and P. Davies, Quantum Field in Curved Space, Cambridge Univ. Press, Cambridge–London–N. Y., 1982.

Acta Physica Hungarica 65 (1), pp. 85–92 (1989)

AB INITIO METHOD FOR TREATMENT OF SPATIALLY EXTENDED SYSTEMS I VANISHING ATOMIC TWO-ELECTRON INTEGRALS

E. KAPUY

Quantum Theory Group, Physics Institute, Technical University
1521 Budapest, Hungary
and
Department of Theoretical Physics, József Attila University
Szeged, Hungary

and

C. KOZMUTZA and ZS. OZORÓCZY

Quantum Theory Group, Physics Institute, Technical University
1521 Budapest, Hungary

(Received 31 March 1987)

The possibility of the calculation of molecular properties on ab initio level for extended systems is investigated in a series of papers.

In the first Part the effect of the magnitude of basis function exponents as well as that of the threshold on the number of vanishing two-electron integrals is studied.

1. Introduction

In spite of the availability of fast computers during the past years, the computations of ab initio wavefunctions for molecules with more than 40 atoms are still not existing. The good determination of the total energy and other molecular properties requires an a) appropriate basis set, the b) ab initio method as well as c) correlation calculations. In order to get results by HF method and beyond for systems with a hundred of basis functions it is necessary to overcome certain special problems. Several attemps have already been made in this direction (see [1] and references therein, the molecular fragments [2] and the SAMO [3] methods etc.), also CI calculations [4,5] . The problem can simply be summarized in terms of computation: a very large amount of real numbers are to be produced, stored and handled. It is clear that this work requires a satisfactory program organization, and a largest, fastest possible computer (with an enormous central memory). It is evident, on the other hand, that while the systems to be treated can be increasing up to the infinity, the possibilities have their restrictions (more or less depending also on special circumstances).

Our opinion is the following. The calculation on "any extended system" is possible by using a) adequate program organization, b) step by step work and c) a reasonably large computer (i.e. a minicomputer of today's standard). We have already pointed out that ab initio and correlation calculations can be carried out on medium size molecules using basis sets including also polarization functions when the above requirements are fulfilled [6 – 9] . In a series of papers we will deal with the extension of our method toward the determination of wavefunctions of more and more extended molecules. The ab initio method is used throughout, while the correlation corrections will be calculated by the many-body perturbation theory (MBPT). In the first three parts of the series we will deal with the problem of the selection of the vanishing two-electron integrals (as is well known, their increasing number with increasing system can help to reduce the total number of matrix elements to be handled).

Table I

Study of two-electron integrals as to their order of magnitude within a two-center group (the distance between the centers is 12 a.u.). A minimal basis set is used, with 5 functions on each center, the exponent was taken 0.22; the total number of two-electron integrals in this case is 1300 (i.e. 1217+83, see below)

Centers and orbitals			Magnitude of integrals
BABA	all		10^{-15}
BBBA	any		$10^{-10} - 10^{-12}$
BAAA	any		$10^{-10} - 10^{-12}$
BBAA	$iijj$		$10^{-1} - 10^{-2}$
	$iijk$		$10^{-2} - 10^{-4}$
	$ijkl$		$10^{-3} - 10^{-6}$
			Vanishing integrals
Due to the C_{2v} symmetry			854
BABA	"pure exchange"		121
BBBA	"Coulomb-exchange"		121
BAAA	"Coulomb-exchange"		121
		Total:	1217
			Non-vanishing integrals
BBAA	$iijj$		25
	$iijk$		30
	$ijkl$		28
		Total:	83

In this paper it is described how the number of vanishing two-electron integrals depends on different parameters, namely the effects of
a/ the spatial symmetry,
b/ the exponents of basis functions and
c/ the magnitude of the threshold is investigated viz. increasing system size. The C_nH_{2n+2} series, the normal saturated hydrocarbons were taken for the study, with n = odd. All molecules were supposed to have C_{2v} symmetry.

2. The effect of spatial symmetry

It is well known that when the system studied belongs to a molecular point group, a certain number of two-electron integrals will vanish [10,11]. It is evident, therefore, that the search for zero integrals due to the large internuclear distances in the system is reasonable only within the non-redundant integral blocks. These calculations have been performed for the studied C_nN_{2n+2} systems. Let us first see, for the sake of simplicity, a two-center integral block (with internuclear distance 12 a.u.)(see Table I). The magnitudes of integrals are zero for certain integral types, while they are ranging from 10^{-1} to 10^{-12} for the non-vanishing ones. As to the effect of the presence of the C_{2v} molecular symmetry, 854 integrals (from the total of 1300) vanish due to the three symmetry operations. The remainder ones — as the internuclear distance between the two centers is very large — belong to a well-defined type, the so-called Coulomb's type (i.e. both functions of left-hand side are on the one, while the other two functions are on the other center, respectively). The dependence of the magnitude of integrals from the type of the given integral will be discussed in detail in Part II in this series. Now we return to the question, how the number of vanishing integrals depends on the function of exponents of the Gaussian primitives.

3. Dependence on the basis function exponents

It is evident that the larger are the exponents of basis functions, the smallest is the intermolecular distance where the two-electron integral vanishes (at a given threshold). The intermolecular distance is trivial for a two-center group, but it is not so for the three and four-center groups. That is the reason, why these groups will be discussed separately.

Let us see now the two-center integral groups.

A well-known basis set, the STO-3G minimal one [12] was chosen for the study. Namely the smallest exponents from the primitive Gaussians within each contracted set are the following: 0.17 for the hydrogen while 0.22 for the carbon atoms. Due to the C_{2v} symmetry, a rather large number of integrals vanish for a C-C two center group. The remainder ones are only slowly vanishing with enlarging intermolecular distance (see Table II). It is remarkable that the total number of vanishing integrals does not depend much on the type of the atoms present in the

two-center group. This follows from the fact that the smallest exponents determine the smallest distance where the integrals "begin" to vanish, and there are not too large differences between the values (0.2 ± 10%). This statement is generally valid, as usually within each basis set (the well-known ones, as 6–31G, 6—31G* etc.), the smallest exponents for each atom are ranging around the above value.

Table II
Zero integrals due to the symmetry as well as the distribution of the remainder ones viz. enlarging distances for some two-center groups

Distance in a.u. between centers 1 and 2	Zero integrals due to the symmety	Vanishing integrals
$\alpha_1 = 0.17, \alpha_2 = 0.22$		
2.07	36	-
7.81	-	6
12.23	-	76
8.76	36	12
13.47	36	63
9.42	-	95
	Total should be:	110
$\alpha_1 = 0.17, \alpha_2 = 0.17$		
8.14	-	1
14.13	-	3
	Total should be:	4
$\alpha_1 = 0.22, \alpha_2 = 0.22$		
2.88	536	16
4.71	854	29
7.26	536	170
14.13	854	363
11.89	636	572
	Total should be:	1300

One can thus conclude that the number of vanishing two-electron integrals does not depend much on the type of the centers.

A similar conclusion could be drawn for the three-center as well as for the four-center groups. The three-center groups have been investigated with various atoms (i.e. with different numbers of H or C atoms). The results show (see Table III) that the integrals vanish with increasing internuclear distance in a similar manner as it was observed for the two-center groups.

Table III
Zero integrals due to the symmetry as well as the distribution of the remainder ones viz. enlarging distances for some three-center groups

Distance in a.u.between centers 1,2 and 1,3, resp.		Vanishing integrals
Both D_{12} and D_{13} are varied $\alpha_1 = \alpha_2 = \alpha_3 = 0.22$	(Zero integrals due to the symmetry are:1284)	
2.88		142
7.26		1272
11.89		1686
	Total should be:	3000
D_{12}=2.07, D_{13} is varied $\alpha_1 = 0.22$, $\alpha_2 = \alpha_3 = 0.17$		
7.81		1
8.76		5
12.23		42
13.47		55
	Total should be:	60
D_{12}=3.38, D_{13} is varied $\alpha_1 = \alpha_2 = \alpha_3 = 0.17$		
9.07		1
12.50		4
13.67		5
	Total should be:	6
Both D_{12} and D_{13} are varied $\alpha_1 = \alpha_2 = \alpha_3 = 0.17$		
8.14		3
8.82		4
12.45		6
	Total should be:	6

The values obtained for the four-center groups are presented in Table IV. The results show that in the case when each internuclear distance between the four-center is larger than 12 a.u., all of the two-electron integrals will vanish. This result is in agreement with those presented in Table I: all integrals, except those of the Coulomb-type (and this type does not exist within a four-center group), are zero when the internuclear distance between two atoms is about 12 a.u. From the results

it follows a general conclusion: when the smallest exponents within the basis set are about 0.2, the two-electron integrals (with the exception of the Coulomb-type ones) will vanish when the internuclear distances between each atom-pair (present in the groups) are larger than 12 a.u. This result can help to omit the calculation of a certain number of integrals within a spatially extended system.

Table IV
Distribution of the vanishing and non-vanishing integrals viz. enlarging distances for some four-center groups

D_{12}=3.38 a.u., distances between centers 1,3 and 1,4, resp. are varied in a.u.	$\alpha_1 = \alpha_2 = 0.17$ $\alpha_3 = \alpha_4 = 0.22$	Vanishing integrals
4.07		9
7.80	Total should be: 75	43
12.23		75
D_{12}=2.07 a.u., D_{13} and D_{14} are varied	$\alpha_1 = \alpha_3 = \alpha_4 = 0.17$ $\alpha_2 = 0.22$	
4.07		1
7.80	Total should be: 15	7
12.23		15
D_{12}=3.38 a.u., D_{13} and D_{24} are varied	$\alpha_1 = \alpha_2 = 0.17$ $\alpha_3 = \alpha_4 = 0.22$	
8.14		1
8.82	Total should be: 3	2
12.45		3
D_{12}=2.07 a.u., D_{13} and D_{14} are varied	$\alpha_1 = \alpha_3 = \alpha_4 = 0.22$ $\alpha_2 = 0.17$	
2.88		23
7.26	Total should be: 375	297
11.89		375

4. Dependence on the threshold

All results obtained earlier have been calculated by comparing the integral values to a certain threshold. It is evident, therefore, that the results depend on the magnitude of this latter: namely the larger is the threshold, the larger is the number of vanishing two-electron integrals. We do not want to discuss here the problem of how to choose an appropriate threshold for ab initio calculations, which has already been studied in several works (see [1], e.g.). Here we present the results obtained for the C_nH_{2n+2} chain, by using the standard bond lengths as given in our earlier papers [6–9]. The four-center groups were taken for the investigation of the effect of the magnitude of the threshold, as it was shown above, the type of the integrals are the same within these groups, so the effect can simply be demonstrated. The

hydrocarbon series for the C_5H_{12} (i.e. m=5+12=17 and $\binom{m}{4} = 2380$, see first line in Table V) up to the $C_{21}H_{44}$ system was studied, for each molecule , where the number of the carbon atoms is odd.

Table V
Vanishing four-center groups, using different orders of magnitude for the threshold

Number of groups in the system	Threshold is equal to $1.0 \cdot 10^{-8}$	Threshold is equal to $1.0 \cdot 10^{-12}$
2 380	0	0
8 855	357	0
23 751	3 969	232
52 360	16 182	3 224
101 270	43 584	14 936
178 365	94 059	43 995
292 825	176 787	98 888
455 126	302 244	190 322
677 040	482 202	330 069

The results show that the number of vanishing integrals (here the totally vanishing four-center groups are given) depends much on the threshold used: the larger is the system, the larger is the difference. For the $C_{21}H_{44}$ molecule, e.g. more than 71% of the four-center groups vanish when a threshold of 10^{-8}, while only 49% when a threshold of 10^{-12} was used. It would be advantageous, of course, to choose a largest possible threshold. For ab initio calculations, however, the results in total energy etc. are much influenced by the small (in absolute value) integrals as well. For completeness we mention that we use in our ab initio calculations a threshold of 10^{-12}.

5. Conclusion

The dependence of the magnitude of the two-electron integrals on the basis function exponents and the threshold was investigated for variously extended molecules. It was pointed out that it is possible to find a common internuclear distance for each of two-, three- and four-center groups (using the same basis set), where the two-electron integrals "begin" to vanish. The results obtained for the normal saturated hydrocarbons are presented.

References

1. P. Carsky and M. Urban, Lecture Notes in Chemistry, *16*, Springer Verlag, Berlin, 1980.
2. D. Spangler and R.E. Christoffersen, Int. J. Quant. Chem., *17*, 1075, 1980.
3. B. J. Duke, B. O'Leary, J. Chem. Phys., *79*, 3424, 1983.
4. M. Yoshimine, J. Comp. Phys., *11*, 449, 1973.
5. N.C. Handy, Chem. Phys. Letters, *74*, 280, 1980.
6. C. Kozmutza, Theoret. Chim. Acta Berl., *60*, 53, 1981.
7. F. Bartha, E. Kapuy and C. Kozmutza: J. Mol. Structure (THEOCHEM), *122*, 205, 1985.
8. C. Kozmutza: J. Mol. Structure (THEOCHEM), *123*, 391, 1985.
9. F. Bartha, E. Kapuy and C. Kozmutza, Acta Phys Hung., *58*, 219, 227, 1985; *59*, 333, 339, 347, 1986.
10. R. Ahlrichs, Theoret, Chim. Acta Berl., *33*, 157, 1974.
11. C. Kozmutza, Zs. Ozoróczy, J. Comp. Chem., 7, 494, 1986.
12. W.J. Hehre, R.F. Stewart and J.A. Pople, J. Chem. Phys., *51*, 2657, 1969.

Acta Physica Hungarica 65 (1), pp. 93–99 (1989)

AB INITIO METHOD FOR TREATMENT OF SPATIALLY EXTENDED SYSTEMS II GROUPING OF ATOMIC TWO-ELECTRON INTEGRALS

E. KAPUY

Quantum Theory Group, Physics Institute, Technical University
1521 Budapest, Hungary
and
Department of Theoretical Physics, József Attila University
Szeged, Hungary

and

C. KOZMUTZA and ZS. OZORÓCZY

Quantum Theory Group, Physics Institute, Technical University
1521 Budapest, Hungary

(Received 31 March 1987)

In this Part of the series the possibility of a simple grouping of two-electron integrals according to the internuclear distance is investigated.

1. Introduction

In the first paper of this series we discussed, how the magnitude of two-electron integrals depends on the different internuclear distances (of the nuclei, to whom the basis functions belong, present in the given integral) [1]. It was pointed out that the integrals vanish, if the exponent of basis function is large enough and/or the nuclei are far from each other. The number of actually vanishing two-electron integrals depends also on the threshold used.

From the results one could see that it is possible to distribute the two-electron integral groups into vanishing and non-vanishing ones viz. increasing internuclear distances. This holds for all of two-, three- and four-center integral groups. In this part we present that it is possible to go further: not only a whole group can be eliminated, but a certain number of two-electron integrals are vanishing (provided some requirements are fulfilled) within the totally non-vanishing groups as well. This possibility is due to the different types of integrals, as it will be pointed out below.

2. Various types of two-electron integrals

Supposing that certain conditions exist, i.e. the magnitude of exponent and/or the internuclear distance allow it, the two-electron integrals vanish. It is evident, when that integral of a given (two-, or three-, or four-center) group is zero, which contains the smallest exponent for each function present in the integral, the total group can be eliminated. This fact was used in the first Part of this series for dropping the whole two-electron integral groups.

Table I
Reordering of types within the two-center blocks

	List of types within a block		New list for a threshold check
1.	BBBA	PC:	BBAA
	BAAA		BBA2A1
	BABA		B2A1AA
	BBAA		B2BA2A1
2.	BA2BA1	CE:	BBBA
	BBA2A1		B2B1B2A
	BA1A2A1		B2B2B1A
	BA2A1A1		B2B1B1A
	BA2A2A1		B2AB1B2
	BA1A2A2		B3B2B1A
3.	B2B1B2A		B3B1B2A
	B2B2B1A		B3AB2B1
	B2AB1A		BAAA
	B2B1AA		BA1A2A1
	B2B1B1A		BA2A1A1
	B2AB1B1		BA2A2A1
4.	BA3A2A1		BA1A2A2
	BA2A3A1		BA3A2A1
	BA1A3A2		BA2A3A1
5.	B2B1A2A1	PE:	BA1A3A2
	B2A2B1A1		BABA
	B2A1B1A2		BA2BA1
6.	B3B2B1A		B2AB1A
	B3B1B2A		B2A2B1A1
	B3AB2B1		B2AB1A2

It is clear, however, that the magnitude of integrals depends on some further characteristics, too. Namely, the type of the integrals as well as the quantum number

of the functions influence the value obtained (beside the magnitude of exponents and the internuclear distances).

Table II
Reordering of types within the three-center blocks

	List of types within a block		New list for a threshold check
1.	CBCA	CE:	CCBA
	CCBA		C2C1BA
	CABA		CABB
	CBAA		CAB2B1
	CBBA		CBAA
	CABB		CBA2A1
2.	CBA2A1	PE:	CBCA
	CA2BA1		C2BC1A
	CA1BA2		C2AC1B
3.	CB2B1A		CABA
	CB1B2A		CA2BA1
	CAB2B1		CA1BA2
4.	C2C1BA		CBBA
	C2BC1A		CB2B1A
	C2AC1B		CB1B2A

As to the angular momentum quantum number of functions, it has not much effect on the calculated values. That is the reason why simply the s-type overlaps are taken as a measure of the magnitude of several two-electron integrals [2].

Let us now see, what is meant by the type of a two-electron integral. As pointed out in detail in [3], the types of an integral group are different for the one-, two-, three- and four-center ones. It was shown that here are 25 types for the two-, 15 types for the three- while only 3 types for the four-center groups. The one-center groups are not dealt with here as the magnitude of integrals of these groups does not depend on the internuclear distance.

As it was shown in detail in [3,4], the types of integrals within the groups were chosen in such a way that the construction of supermatrix P in the SCF procedure should be the easiest possible as well as without any special memory requirements. This order of types is presented here for the two- and three-center groups in the first column of Table I and Table II, respectively. The four-center groups are not discussed in detail, as their order of (only three) types will remain the same (see also later). The order of types for two-center and three-center groups shows (see the Tables) that they do depend rather differently on the internuclear distance. Let us see, e.g., the first four types of two-center groups: the integrals of the BBBA

and BAAA types will vanish slower with increasing internuclear distance ($\bar{BA}$) than those of the BABA type, while the integrals belonging to the BBAA type change the slowest with increasing distance. It is clear that this latter type can be called "Coulomb's type" as the integrals of this type change with internuclear distance as the Coulomb potential does. Similarly, the BAAA and BBBA types can be called "Coulomb's exchange type" while the BABA one is a "pure exchange" type. From the above it clearly follows that first the integrals of "pure exchange" type (abbreviated PE) are vanishing with increasing internuclear distance, they will be followed by the "Coulomb's exchange" type (CE). The two-electron integrals of "pure Coulomb's" type (PC) can be said to be "never" vanishing ones (for medium size molecules).

A similar situation holds for the three-center groups (see Table III, first column). By using the same notation as above, the CBCA, CABA, CBBA types can be called PE types while the CCBA, CBAA and CABB are the CE types. It is a very important fact that there are no integrals which belong to the "pure Coulomb" type within the three-center groups. From this it clearly follows that the three-center groups can totally be vanishing much faster than the two-center groups do. This is encouraging, as the number of three-center groups are increasing faster with increasing size of the system than those of the two-center groups. Let us now see the four-center groups. There are only three different types within these groups and all of these, the DCBA, DBCA and DACB types, respectively, are "pure Coulomb's" (PC) types. From this it clearly follows that the four-center integrals — whose numbers are the fastest increasing when the system becomes larger — will vanish the fastest (compared to the two-, and three-center integral groups).

3. Coulomb exchange (CE) types of integrals

One can thus see that it is worthwhile distributing the integrals within each group into different types (from the point of view of their behaviour viz. increasing internuclear distances). This distribution is interesting especially for the two- and three-center groups (the four-center ones belong to the same type, as presented above).

The reordering of two-electron integrals of the two-center groups is presented in Table I (second column). One can see that while the integrals of only four types belong to the PC types, those of 16 types are CE ones while those of 5 types are PE types. Similarly, the reordering of three-center integral types show that the integrals of 6 types are CE ones, while those of 9 types are PE ones. This result indicates that with increasing internuclear distances more integrals of the three-center groups will vanish than of the two-center groups. The exact number of two-electron integrals vanishing, on the other hand, does depend on the basis set actually used, namely, it is not evident whether the number of integrals of CE types (B3AB2B1, BA1A3A2 etc.) is larger or smaller than that of PE types (B2A2B1A1, e.g.). Let us now first see the two-electron integrals of CE types. The STO-3G basis set [5] was used for the study, where 5 or 1 contracted basis functions belong to the given centers.

Those types which contain the same number of two-electron integrals are separated by a line (see Table I and Table II, first column). From this point of view there are 6 different sub-groups for the two-centers while only 4 for the three-center groups. The results are presented in Table III and Table IV for the two- and three-center groups, respectively.

Table III
Distribution of integrals within the two-center blocks (using a minimal basis set)

		1.	2.	3.	4.	5.	6.
	PC	1	-	-	-	-	-
1/1	CE	2	-	-	-	-	-
	PE	1	-	-	-	-	-
	PC	5	-	10	-	0	-
5/1	CE	10	-	40	-	30	-
	PE	5	-	10	-	0	-
	PC	25	50	50	0	0	100
5/5	CE	50	200	200	150	150	0
	PE	25	50	50	0	0	200

		1/1	5/1	5/5
	PC	1	15	225
	CE	2	80	750
	PE	1	15	325

The values obtained for the CE type show that there are always more integrals belonging to this type than those to the PE type in the case of two-center groups. The results, on the other hand, do depend on the number of basis functions present on the given centers, too: there are exactly twice as many integrals of CE type than those of PE one for a HH two-center group, e.g., much more integrals belong to the CE types than to the PE one in case of a OH, NH etc. group. The number of vanishing integrals does depend, of course, on the basis function exponents. A model calculation (a chain of X_9Y_{20}, where X and Y was chosen as C,N,O,F and H respectively) shows (see Table V) that the number of vanishing integral groups does not depend much on the exponents within a common basis set.

A similar situation holds for the three-center groups (see Table IV). One can see here also that the number of integrals belonging to the CE or PE type, respectively, does depend on the number of basis functions on the centers present in the given group. It is still valid, on the other hand, that more integrals belong

to the PE type than to the CE type for the three-center group (except the HHH group, where their numbers are equal).

Table IV
Distribution of integrals within the three-center blocks
(using a minimal basis set)

		1.	2.	3.	4.
1/1/1	CE	3	-	-	-
	PE	3	-	-	-
5/1/1	CE	15	10	-	-
	PE	15	20	-	-
5/5/1	CE	75	50	50	-
	PE	75	100	100	-
5/5/5	CE	375	250	250	250
	PE	375	500	500	500

	1/1/1	5/1/1	5/5/1	5/5/5
CE	3	25	175	1125
PE	3	35	275	1875

4. Pure exchange (PE) types of integrals

This type has already been discussed partly in the above Section. The results demonstrated in Table III and Table IV, respectively, show that the number of vanishing integrals is really increasing when going from the two-center to three-center groups, as more integrals (within a given group) belong to the PE type than to the CE type. This trend is still further increasing when looking at the four-center groups: the total amount of two-electron integrals belongs to the so-called PE types and, therefore, these are expected to vanish the fastest with increasing internuclear distances.

5. Conclusion

In this paper the possibility of the distribution of two-electron integrals within each of two-, three- and four-center groups was discussed in order to drop them

when enlarging the system. It was pointed out that it is easy to separate the two- and three-center groups into parts which do behave themselves differently with increasing internuclear distance. This separation is possible independently of the number of basis functions used. All of the integrals of four-center groups belong to the same type. The distribution of two-electron integrals into three different types (PC, CE and PE, respectively) allow an easy elimination of vanishing integrals when the system becomes larger and larger.

Table V

The number of vanishing integrals as it depends on the basis function exponent. The exponents were taken from the STO-3G basis set. The first four rows in the Table refer to the smaller exponents on C, N, O and F, respectively, while in the second four rows the larger exponents were used. The last four rows contain the results obtained by using both exponents on the corresponding heavy atoms. The H exponent was the same, 0.179926, throughout.

	Two-center	Three-center	Four-center
CH	115	174	232
NH	115	218	344
OH	122	304	480
FH	122	428	866
CH	165	835	3538
NH	165	855	3740
OH	165	869	4576
FH	165	873	4604
CC	169	1007	4203
NN	203	1565	6972
OO	231	1969	9803
FF	243	2359	12411

References

1. E.Kapuy, C. Kozmutza and Zs. Ozoróczy, Acta Phys. Hung., *65*, 85, 1989.
2. R. Ahlrichs, Theoret. Chim. Acta Berl., *33*, 157, 1974.
3. C. Kozmutza, Theoret. Chim. Acta Berl., *60*, 53, 1981.
4. F. Bartha, E. Kapuy and C. Kozmutza, Acta Phys. Hung., *58*, 219, 227, 1985; *59*, 333, 339, 347, 1986.
5. W.J. Hehre, R.F. Stewart and J.A. Pople, J. Chem. Phys., *51*, 2657, 1969.

Acta Physica Hungarica 65 (1), pp. 101–108 (1989)

AB INITIO METHOD FOR TREATMENT OF SPATIALLY EXTENDED SYSTEMS III VANISHING INTEGRALS OF THE C_9H_{20} SYSTEM

E. KAPUY

Quantum Theory Group, Physics Institute, Technical University
1521 Budapest, Hungary
and
Department of Theoretical Physics, József Attila University
Szeged, Hungary

and

C. KOZMUTZA and ZS. OZORÓCZY

Quantum Theory Group, Physics Institute, Technical University
1521 Budapest, Hungary

(Received 31 March 1987)

In this Part the C_9H_{20} system (and similar chains) are investigated. It is pointed out that it is easy to determine the number of vanishing two-electron integrals in advance.

1. Introduction

In the first two papers of this series [1,2] the variation of the magnitude of two-electron integrals was investigated. The dependence of the magnitude of integrals was studied on the basis function exponent as well as on the internuclear distance. It was pointed out that not only some two-, three- and four-center integral groups can be eliminated as a whole, but certain parts of integral groups can also be disregarded (when the magnitude of basis functions and/or the distance between the centers allows it. The effect of spatial symmetry has already been discussed in details elsewhere [3,4]. As to the role of the threshold used it has also been demonstrated in [1]: we concluded there that 10^{-12} threshold is taken in our calculations throughout. Let us now return to the investigation of the number of vanishing integral groups due to the enlarging molecular system. While in the first two papers we have dealt with the effects in general, in this paper we chose a rather extended molecule, on which the effects above will be discussed. According to our previous works, a medium sized system from the C_nH_{2n+2} chain is used for the study. The C_9H_{20} molecule (with C_{2v} symmetry) has already been calculated by our ab initio program package [5]. Model geometry was taken (with CC=2.884 a.u., CH=2.067 a.u.) and tetrahedral angles for the computation. The notation of centers (the number of carbon atoms

are the "measure" of the length of the chain, the hydrogen pairs connected to the given carbon atoms have, therefore, the neighbour serial numbers) for the C_9H_{20} system are presented in the Figure. The carbon atoms lie in the xz plane, the chain is extended in the z direction.

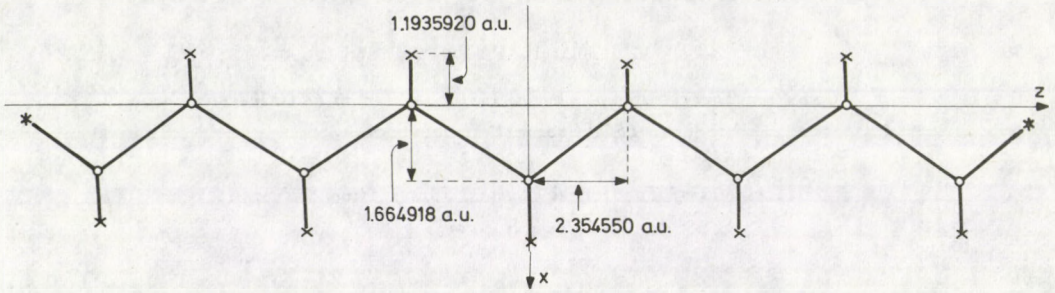

Fig. 1. The chain of C_9H_{20}. The 0 are the Carbon atoms, with serial numbers 1,4,7,10,13,16,19,22 and 26, respectively. The hydrogen atoms are denoted by X (two at each place) and by * (at the end of the chain)

Due to the C_{2v} spatial symmetry, there is a certain number of redundant integral groups. We do not deal in this paper with the symmetry, therefore, the number of vanishing integral groups will be investigated compared to the total (and not to the non-redundant) ones.

According to the previous papers, the totally vanishing groups will be presented as well as the vanishing types within the given groups. The results of computation are given for the two-, three- and four-center groups separately.

In order to get more insight into the effect of the increase of the molecular system, not only the vanishing groups for the C_9H_{20} system are investigated, but those for all systems "shorter" than the C_9H_{20} are presented as well. This study can simply be carried out according to the serial numbers of the carbon atoms (see also later). The well-known STO-3G-basis set [6] was used, by taking into account the basis function exponents for the carbon (0.222290 and 3.53053) as well as for the hydrogen (0.179926) atoms. As in the previous papers, the total groups are regarded as vanishing ones, when the product of overlaps (by using the above exponents) is smaller than the threshold (10^{-12}).

2. Vanishing two-center integrals and groups

The results are presented in Table I. The values obtained are given for each center and for each type separately, namely they are tabulated in the following way.

The column of "Type CE" collects those groups in which all integrals of "Coulomb-exchange" type vanish, i.e. BBBA or BAAA or B2B1B1A etc. ones (see Part II). The results are presented for the chain up to 29 atoms. When looking at the Figure, one can easily follow, how the increase of the system results in the increasing number of vanishing groups. Let us see now the subgroups which are marked α_1/α_H, α_2/α_H and α_1/α_2, respectively. There are two reasons, why the calculations have been carried out by using different basis function exponents. It

is known that the whole group will vanish (only the CE type is here investigated, i.e. all integrals belonging to this type will be zero), when the product of overlaps composed from the smallest exponents is small enough.

Table I

Vanishing two-center groups for the C_9H_{20} system, when using different orbital exponents $\alpha_1 = 0.22229$, $\alpha_2 = 3.53053$, $\alpha_H = 0.179926$, respectively. The total number is 406

Centers	Type CE			Type PE		
	$\frac{\alpha_1}{\alpha_H}$	$\frac{\alpha_2}{\alpha_H}$	$\frac{\alpha_1}{\alpha_2}$	$\frac{\alpha_1}{\alpha_H}$	$\frac{\alpha_2}{\alpha_H}$	$\frac{\alpha_1}{\alpha_2}$
4.					1	1
5.					0	0
6.					0	0
7.		1	1		2	2
8.		0	0		0	0
9.		0	0		0	0
10.		2	2		3	3
11.		0	0		0	0
12.		0	0		0	0
13.		3	3		6	6
14.		0	0		1	1
15.		0	0		1	1
16.		4	6	3	9	9
17.		0	1	3	4	4
18.		0	1	3	4	4
19.		7	9	6	12	12
20.		1	2	6	7	7
21.		1	2	6	7	7
22.	3	10	12	9	15	15
23.	1	2	5	9	10	10
24.	1	2	5	9	10	10
25.	3	5	7	9	11	13
26.	7	14	16	13	19	19
27.	5	6	9	13	14	14
28.	5	6	9	13	14	14
29.	7	9	11	13	15	17
Total	32	73	101	115	165	169

From this point of view when using the STO-3G basis set, the first column (under heading α_1/α_H) is relevant, as showing the vanishing subgroups (i.e. the integrals of CE type). There are, on the other hand, many integrals, which contain the larger exponents of the basis set. These are presented in the second column (carbon and hydrogen) and the third column (those groups, which would vanish, if all integrals included only the two exponents of the carbon atoms). It is evident that no more integrals, than the given ones in the third subgroup can be discarded from the CE types (when using basis STO-3G basis set). These calculations were performed with different exponents also in order to have a survey of what we could expect

Table II
Vanishing three-center integral blocks for the C_9H_{20} system, when using different orbital exponents (the total number is 3654, the exponents are as given in Table II)

Centers	Type CE			Type PE		
	$\frac{\alpha_1}{\alpha_H}$	$\frac{\alpha_2}{\alpha_H}$	$\frac{\alpha_1}{\alpha_2}$	$\frac{\alpha_1}{\alpha_H}$	$\frac{\alpha_2}{\alpha_H}$	$\frac{\alpha_1}{\alpha_2}$
7.					1	1
8.					0	0
9.					0	0
10.					3	3
11.					0	0
12.					0	0
13.	0	1	1		6	8
14.	0	0	0		0	1
15.	0	0	0		0	1
16.	0	3	3		21	23
17.	0	0	0		5	6
18.	0	0	0		6	7
19.	0	6	6		47	49
20.	0	0	0		13	16
21.	0	0	0		15	18
22.	0	10	12	3	88	96
23.	0	0	1	1	40	47
24.	0	0	1	2	43	52
25.	0	1	1	10	53	80
26.	0	19	23	31	166	186
27.	0	1	3	34	98	116
28.	0	1	3	29	105	125
29.	0	3	3	54	125	172
Total		45	57	174	835	1007

when using larger exponents (i.e. another basis set), than these minimal ones in the STO-3G set. All of above statements discussed for the "Coulomb-exchange" type are valid for the "pure Coulomb" type. The integrals vanishing of this type, i.e. the BABA or B2AB1A or BA2BA1 etc., were also calculated by using different basis function exponents. The results are presented (under heading Type PE) for the two-center groups also in Table I. Two conclusions could be drawn looking at the values. First, the number of vanishing groups is always larger for the type PE than for CE. This simply follows from the definition of the types (discussed in detail in Part II of this series). Second, taking into acount that a whole group (except the PC types, see Part II) vahishes, when the integrals belonging both to the CE as well as to the PE types vanish, it is enough to look only at the values obtained for the type CE: these show the number of those groups which vanish for both types.

It is worthwhile, however, to make a separation within the groups, as the number of vanishing integrals belonging to the PE types is large, and they are increasing rather fast with the enlarging molecular system.

3. Vanishing three-center integrals and groups

The results obtained for the three-center vanishing two-electron integrals in the case of C_9H_{20} are presented in Table II.

The values can be interpreted in a similar way (as the headings and the subgroups are the same, see the Tables). There are, however, some remarkable differences between the results obtained for the two- and the three-center groups, respectively. These are summarized as follows.

A smaller number vanish from the three-center groups than from the two-center ones, which simply follows from the fact that there are three different internuclear distances in the three-center groups, while only one distance for the two-center groups which are responsible for the magnitude of integrals. It is less probable that all of the three distances (CA, BA and CB, respectively) of a three-center group are large enough simultaneously to decrease the magnitude of integrals below the given threshold.

Another difference, on the other hand, makes it easier to find the vanishing groups from the three-center groups than those from the two-center groups. This is due to the fact that there are no PC (pure Coulomb's) type integrals within the former groups. From this it follows that all groups within the three-center ones, in which the integrals of the CE type vanish will totally be vanishing as well.

It should also be mentioned that in the case of three-center groups it is still more worthwhile to distribute the integrals into types in order to drop them when the internuclear distance allows it. This can be seen in Table II: there is a large number of groups which vanish for the PE, but not for the CE type. The PE type collects all integrals of types CABA, CBBA, CBCA etc. It is expected that only integrals of CABA type, e.g. vanish (as both CA and BA distances are large enough), while the C and B centers are rather close to each other (i.e. the CBBA, CBCA etc. types will not vanish). From this is follows that not only the various types but the different subgroups should be taken into account as well within the groups for the three-center groups. The partitioning into subgroups (CABA, CBBA etc.) can be done in a similar way as into types (see Part I and Part II of this series).

4. Vanishing four-center integrals and groups

The results obtained for the vanishing four-center groups are presented in Table III. It is remarkable that a much smaller portion of groups can be eliminated as vanishing ones from the four-center groups, than was the case for the two- or three-center groups. It is evident, as there are more internuclear distances which should be small enough (at the same time) to make the integrals zero. All vanishing

four-center groups — similarly to the two- and three-center ones — have been calculated by using different basis function exponents (see Table III). It is helpful, however, that all integrals within the four-center groups belong to the pure (PE) type, therefore, it is rather easy to select the totally vanishing groups. Inspite of this, it is worthwhile to distribute the groups into three parts, namely DCBA, DBCA and DACB. It is advantageous as many integrals, e.g., belonging to the DCBA type, could vanish while those of DBCA type will not be zero at the same time (due to the different internuclear distances between the D, C, B and A centers, respectively).

5. Conclusion

In this paper the vanishing two-, three- and four-center integral groups for the C_9H_{20} system were presented. As the calculations include the results obtained for the increasing chain continuously up to the 29 centers, it is easy to compare the values (i.e. the number of vanishing groups) for each center, separately.

Table III
Vanishing four-center integral blocks for the C_9H_{20} system, when using different orbital exponents (the total number is 23751, the exponents are as given in Table II)

Centers	Type PE		
	$\frac{\alpha_1}{\alpha_H}$	$\frac{\alpha_2}{\alpha_H}$	$\frac{\alpha_1}{\alpha_2}$
10.		1	3
11.		0	1
12.		0	1
13.		16	22
14.		3	4
15.		3	4
16.		62	74
17.		11	13
18.		15	17
19.		179	197
20.		45	48
21.		56	59
22.	1	408	434
23.	0	125	142
24.	1	152	169
25.	4	196	279
26.	43	930	1000
27.	39	370	459
28.	54	426	520
29.	90	540	757
Total	232	3538	4203

Table IV
Integral blocks for the C_9H_{20} system, divided into different regions (see also text)

Two-center	Ins/Outs	$Outs_1/Outs_2$
CC	7	1
CH	35	6
HH	42	9

Three-center	Ins/Outs	$Ins/Outs_1/Outs_2$	$Outs_1/Outs_2$
CCC	21	7	0
CCH	182	56	3
CHH	448	147	12
HHH	315	126	9

Four-center	Ins/Outs	$Ins/Outs_1/Outs_2$	$Outs_1/Outs_2$
CCCC	35	21	0
CCCH	462	245	0
CCHH	1876	994	3
CHHH	2891	1659	10
HHHH	1379	945	3

The results show that the number of vanishing two-center groups is relatively the largest: for the PE type, e.g., they vanish, if between the carbon centers the distance corresponds to 5 times the CC bond lengths ($\approx$ 14.4 a.u.). The same distance is 16.0 a.u. for the three-centers while also $\approx$5 times the CC lengths for the four-center groups, (using the smallest exponents). The increase of the number of vanishing groups with the extension of the chain, on the other hand, is the fastest for the four-center groups. One can thus see that it is easy to establish for a molecule like C_9H_{20}, how many integral groups will vanish due to the large internuclear distances. There is still an "open question". It is interesting to see, how the number of vanishing groups depends on the increase of a chain like the C_nH_{2n+2} one. The results are presented in Table IV and V. The inside part ("Ins") includes the atoms belonging to the C_7H_{16} molecule, while the outside parts ("$Outs_1$" and "$Outs_2$") are those of increments (CH_2 groups) on both sides of C_7H_{16} up to C_9H_{20}. The total groups for all two-, three- and four-center groups are given in Table IV, the vanishing ones are presented in Table V (when using the smallest exponents). The results show that there is not much difference between the groups, i.e. their vanishing number

does not depend on the type of the atoms (CCH or CHH, e.g.). The number of vanishing groups, on the other hand, does differ much for the various regions. This will be the subject of one of our following works.

Table V

Vanishing integral blocks when going from a smaller to a larger system (the $C_7H_{16} \rightarrow C_9H_{20}$ was taken)

Two-center	Ins/Outs	$Outs_1/Outs_2$
CC	3	1
CH	15	6
HH	18	9
Total	36	16
From	84	16

Three-center	Ins/Outs	$Ins/Outs_1/Outs_2$	$Outs_1/Outs_2$
CCC	0	2	0
CCH	2	16	3
CHH	7	40	12
HHH	2	36	9
Total	16	94	24
From	966	336	24

Four-center	Ins/Outs	$Ins/Outs_1/Outs_2$	$Outs_1/Outs_2$
CCCC	0	0	0
CCCH	1	10	0
CCHH	2	46	3
CHHH	1	52	10
HHHH	0	26	3
Total	4	134	16
From	6580	3864	52

References

1. E. Kapuy, C. Kozmutza and Zs. Ozoróczy, Acta Phys. Hung., *65*, 85, 1989.
2. E. Kapuy, C. Kozmutza and Zs. Ozoróczy, Acta Phys. Hung., *65*, 93, 1989.
3. F. Bartha, E. Kapuy and C. Kozmutza, J. Mol. Structure (THEOCHEM), *122*, 305, 1985.
4. C. Kozmutza, Zs. Ozoróczy, J. Comput. Chem., *7*, 494, 1986.
5. R. Daudel, E. Kapuy and C. Kozmutza, J. Mol. Structure (THEOCHEM) (submitted).
6. W.J. Hehre, R.F. Stewart and J.A. Pople, J. Chem. Phys., *51*, 2657. 1969.

Acta Physica Hungarica 65 (1), pp. 109–113 (1989)

ON THE STABILITY OF SHEAR FLOW

NGUYEN THI BANG VAN

Institute of Physics, Technical University
1521 Budapest, Hungary

(Received 8 April 1987)

We prove that the shear flow of the corotational Jeffrey body is unstable if the shear stress function is decreasing at the actual shear rate.

Introduction

Recently Verhás [1] published a paper in which corotational Jeffrey model was derived with thermodynamic argumentation. It was also shown that the corotational Jeffrey body behaves like a plastic material if the material constants are suitable. The cited paper analyses the plastic flow in details for uniaxial traction and compression, and concludes that plastic behaviour is due to some kinds of rotations and the sudden changes in flow are in close connection with the stability of the stationary solution of the governing differential equations. The rather similar case of simple shear flow is only mentioned by Verhás. Here we give the stability analysis of the simple shear flow in details.

We follow the notation of [1] but the stationarity will not be presupposed. The constitutive equation for the extra stress reads:

$$\tau_t \overset{\circ}{\mathbf{t}}{}^v + \mathbf{t}^v = 2\eta(\overset{\circ}{\mathbf{d}} + \tau_d \overset{\circ\circ}{\mathbf{d}}) \qquad \tau_t > \tau_d > 0, \quad \eta > 0, \tag{1}$$

where $\overset{\circ}{\mathbf{d}}$ stands for the symmetric part of the velocity gradient, $\overset{\circ\circ}{\mathbf{d}}$ its corotational time derivate:

$$\overset{\circ\circ}{\mathbf{d}} = \frac{d\overset{\circ}{\mathbf{d}}}{dt} + (\mathbf{v}\ \mathrm{grad})\overset{\circ}{\mathbf{d}} + \overset{\circ}{\mathbf{d}}\vec{\omega} - \vec{\omega}\overset{\circ}{\mathbf{d}}.$$

Here $\mathbf{t}^v$ is the extra stress defined by

$$\mathbf{t} = -p\delta + \mathbf{t}^v,$$

where $\mathbf{t}$ is Cauchy's stress, p the scalar pressure, δ is the unit tensor. The notation $\overset{\circ}{\mathbf{t}}{}^v$ means the corotational time derivative of the extra stress:

$$\overset{\circ}{\mathbf{t}}{}^v = \frac{d\mathbf{t}^v}{dt} + (v\ \mathrm{grad})\mathbf{t}^v + \mathbf{t}^v\vec{\omega} - \vec{\omega}\mathbf{t}^v,$$

Above, $\vec{\omega}$ stands for the skew symmetric part of the velocity gradient. The quantities τ_t, τ_d and η are material constants.

The picture of the simple shear in a Cartesian frame is given by:

$$v_1 = \kappa(t)x_2, \qquad v_2 = v_3 = 0.$$

The matrices of the tensors in Eq. (1) are:

$$\overset{\circ\circ}{\mathrm{d}} = \frac{\kappa(t)}{2}\begin{bmatrix}0 & 1 & 0\\ 1 & 0 & 0\\ 0 & 0 & 0\end{bmatrix}, \quad \omega = \frac{\kappa(t)}{2}\begin{bmatrix}0 & 1 & 0\\ -1 & 0 & 0\\ 0 & 0 & 0\end{bmatrix},$$

$$\overset{\circ}{\mathrm{d}} = \frac{1}{2}\frac{d\kappa}{dt}\begin{bmatrix}0 & 1 & 0\\ 1 & 0 & 0\\ 0 & 0 & 0\end{bmatrix} + \frac{\kappa^2}{2}\begin{bmatrix}-1 & 0 & 0\\ 0 & 1 & 0\\ 0 & 0 & 0\end{bmatrix}$$

and

$$\overset{\circ}{\mathrm{t}}{}^v = \begin{bmatrix} \dfrac{dt^v_{11}}{dt} - \kappa t^v_{12}; & \dfrac{dt^v_{12}}{dt} + \dfrac{\kappa}{2}(t^v_{11} - t^v_{22}); & \dfrac{dt^v_{13}}{dt} - \dfrac{\kappa}{2}t^v_{23} \\ \dfrac{dt^v_{12}}{dt} + \dfrac{\kappa}{2}(t^v_{11} - t^v_{22}); & \dfrac{dt^v_{22}}{dt} + \kappa t^v_{12}; & \dfrac{dt^v_{23}}{dt} + \dfrac{\kappa}{2}t^v_{13} \\ \dfrac{dt^v_{13}}{dt} - \dfrac{\kappa}{2}t^v_{23}; & \dfrac{dt^v_{23}}{dt} + \dfrac{\kappa}{2}t^v_{13}; & \dfrac{dt^v_{23}}{dt} \end{bmatrix}.$$

When substituting them into Eq. (1), we get a matrix equation which is equivalent to the next system of component equations:

$$\begin{aligned}
&\text{a)}\tau_t t^v_{11} - \tau_t\kappa t^v_{12} + t^v_{11} = -\eta\tau_d\kappa^2,\\
&\text{b)}\tau_t t^v_{12} + \tau_t\frac{\kappa}{2}(t^v_{11} - t^v_{22}) + t^v_{12} = \eta(\tau_d\dot{\kappa} + \kappa),\\
&\text{c)}\tau_t t^v_{13} - \tau_t\frac{\kappa}{2}t^v_{23} + t^v_{13} = 0,\\
&\text{d)}\tau_t t^v_{23} + \tau_t\frac{\kappa}{2}t^v_{13} + t^v_{23} = 0,\\
&\text{e)}\tau_t t^v_{22} + \tau_t\kappa t^v_{12} + t^v_{22} = \eta\tau_d\kappa^2,\\
&\text{f)}\tau_t t^v_{33} + t^v_{33} = 0.
\end{aligned} \tag{2}$$

The stationary solution is given in (1) and it reads:

$$\begin{aligned}
&t^v_{13} = t^v_{23} = t^v_{33} = 0,\\
&t^v_{12} = \eta\kappa\frac{1 + \tau_d\tau_t\kappa^2}{1 + \tau_t^2\kappa^2} = \tau(\kappa),\\
&t^v_{11} = -t^v_{22} = \frac{\eta(\tau_t - \tau_d)\kappa^2}{1 + \tau_t^2\kappa^2} = \sigma(\kappa).
\end{aligned} \tag{3}$$

Then the condition for stationarity is that the $\kappa(t)$ function be constant. Another question is whether the stationary solution is stable or not and in what circumstances. If the shear rate is given, it is not hard to show that the stationary solution of the system of equations (2) is stable. On the other hand the value of κ can be hardly fixed in an experiment. As, for example, in the gap of Couette viscometer, the average value of κ can be controlled and at the same time the shear stress is nearly uniform throughout the gap. For this reason it seems more realistic to examine the stability of the stationary states belonging to a given shear stress τ. It does not mean that the stress tensor is given as the other components of $\mathbf{t}$ can vary with time. In the following, the stability of the solution given in Eq. (3) will be studied when $t^v_{12} = \tau$ =constant and all the other components of the tensor as well as the shear rate are functions of time.

The stability of the stationary flow

The solution of Eq.$(2)_f$ is always

$$t^v_{33} = c \exp\left(-\frac{t}{\tau_t}\right).$$

So it is clear that the stationary solution $t^v_{33} = 0$ is stable and consequently $t^v_{11} + t^v_{22} = 0$ is also a stable relation because the trace of the extra stress is zero.

From Eqs $(2)_c$ and $(2)_d$ we conclude to the characteristic equation

$$\begin{bmatrix} \tau_t p + 1 & -\tau_t \frac{\kappa}{2} \\ \tau_t \frac{\kappa}{2} & \tau_t p + 1 \end{bmatrix} = 0,$$

which has the complex roots

$$p_{1,2} = -\frac{1}{\tau_t} \pm i\frac{\kappa}{2}.$$

The real part of them is negative so the solutions

$$t^v_{12} = t^v_{23} = 0$$

are also stable in any case.

To analyse the stability of the shear rate and the normal stresses, we introduce the following notations:

$$\begin{aligned} t^v_{11} &= -t^v_{22} = \sigma + \sigma_*(t); & \sigma &= \sigma(\kappa_0); \\ t^v_{12} &= \tau; & \tau &= \tau(\kappa_0); \\ \kappa &= \kappa_0 + \kappa_*(t), \end{aligned} \tag{4}$$

where κ_0 is the stationary shear rate and $\kappa_*(t)$ and $\sigma_*(t)$ are supposed to be small as they describe the deviation from stationarity. Up to now we have made use of Eqs $(2)_c, (2)_d$ and $(2)_f$. Moreover, the Eqs $(2)_a, (2)_e$ and $(2)_f$ are not independent. To carry out our test, $(2)_a$ $(2)_b$ are at our disposal. With the notations (4) they read:

$$\begin{aligned} \tau_t \frac{d\sigma_*}{dt} - \tau_t \kappa_* \tau + \sigma_* &= -2\eta\tau_d \kappa_0 \kappa_*, \\ \tau_t \kappa_0 \kappa_* + \tau_t \sigma \kappa_* &= \eta \left(\tau_d \frac{d\kappa_*}{dt} + \kappa_* \right). \end{aligned} \tag{5}$$

When deriving these equations we made use of the presumptions that σ_* and κ_* were small and the higher powers of them were neglected. The characteristic equation of the system of Eq. (5) is

$$\begin{vmatrix} \tau_t p + 1 & 2\eta\tau_d \kappa_0 - \tau_t \tau \\ \tau_t \kappa_0 & \eta_t \sigma - \eta - \eta\tau_d p \end{vmatrix} = 0$$

or

$$\eta\tau_t\tau_d p^2 + (\eta\tau_d + \eta\tau_t - \tau_t^2\sigma)p + \eta - \tau_t\sigma - \tau_t^2\kappa_0\tau + 2\eta\tau_t\tau_d\kappa_0^2 = 0.$$

The conditions for the real part of both roots to be negative are

$$\eta\tau_d + \eta\tau_t - \tau_t^2\sigma > 0$$

and

$$\eta - \tau_t\sigma - \tau_t^2\kappa_0\tau + 2\eta\tau_t\tau_d\kappa_0^2 > 0 \tag{6}$$

as the coefficient of p^2, i. e. $\eta\tau_t\tau_d$ is positive. The first condition is always satisfied, because

$$\sigma\tau_t^2 = \frac{\eta\tau_t^2(\tau_t - \tau_d)}{\frac{1}{\kappa_0^2} + \tau_t^2} < \frac{\eta\tau_t^2(\tau_t - \tau_d)}{\tau_t^2} = \eta(\tau_t - \tau_d) < \eta(\tau_t + \tau_d).$$

Here we made use of the stationary value of the normal stress σ given by Eq. (3). A similar treatment with the second condition leads to the condition

$$\frac{\eta}{1 + \tau_t^2\kappa_0^2}[\tau_t^3\tau_d\kappa_0^4 + (3\tau_t\tau_d - \tau_t^2)\kappa_0^2 + 1] > 0. \tag{7}$$

It is interesting to evaluate the derivative of the shear stress function with respect to the shear rate:

$$\frac{d\tau(\kappa)}{d\kappa} = \frac{\tau_t^3\tau_d\kappa^4 + (3\tau_t\tau_d - \tau_t^2)\kappa^2 + 1}{(1 + \tau_t^2\kappa^2)^2}. \tag{8}$$

Notice that the numerator in Eq. (8) is the same as the quantity in square brackets in condition (7) while all the other multipliers and divisors are positive. This means that the stability condition (7) is satisfied if and only if the shear stress function is increasing at the given shear rate. So we can reformulate the condition of stability. We can say that the increasing sections of the shear stress function are stable while the decreasing section, if it exits at all, is unstable.

References

1. J. Verhás, Acta Mechanica (Vienna), *53*, 125, 1984.
2. J. Verhás, Thermodynamics and Rheology (in Hungarian), Technical Publishing House, Budapest, 1985.
3. I. Gyarmati, Non-equilibrium Thermodynamics, Field Theory and Variational Principles, Springer, Berlin, Heidelberg, New York, 1970.
4. S.R. de Groot and P. Mazur, Non-equilibrium Thermodynamics, North-Holland Publ. Co., Amsterdam, 1962.
5. L.S. Pontryagin, Ordinary Differential Equations, Akadémiai Kiadó, (Publishing House of Hungarian Academy of Sciences) Budapest, 1972.
6. M. Slemrod, Shear Flows of Non-linear Viscoelastic Fluids, in: Trends in Applications of Pure Mathematics to Mechanics, Ed. by E. Kröner and K. Kirchgassner, Springer, Berlin, Heidelberg, New York, Tokyo, 1986.
7. J. Verhás, Int. J. Heat Mass Transfer, *30*, 1001, 1987.

Acta Physica Hungarica 65 (1), pp. 115–121 (1989)

ON THE FLOW OF THE COROTATIONAL JEFFREY BODY IN CIRCULAR PIPES

NGUYEN THI BANG VAN

Institute of Physics, Technical University
1521 Budapest, Hungary

(Received 8 April 1987)

The Poiseuille flow of the corotational Jeffrey body is dealt with. The unstable section of its shear stress function leads to plastic behaviour. The pressure drop is plotted against the volume of the fluid passing a cross section of a tube in unit time.

Introduction

Recently the problem raised by the decreasing section of the shear stress function shown in Fig. 1 was studied by several authors [1,2]. Verhás [2] showed that the corotational Jeffrey body with suitable parameters has such a shear stress function.

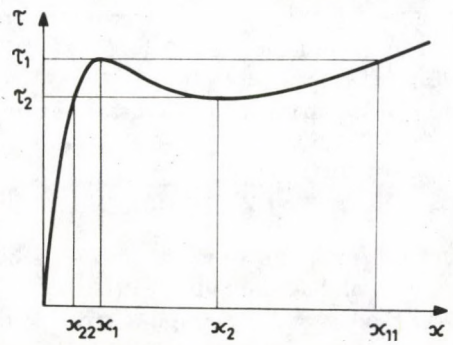

Fig. 1

Jeffrey's body is the simplest version of the viscoelastic bodies in the framework of Onsager's irreversible thermodynamics. Verhás stated that the decreasing section of the shear stress function explains plastic properties, which he studied under uniaxial traction and in simple shear flow. In this paper, we analyse the flow through a tube with circular cross section. In a previous paper [3], we found that the stationary

flow belonging to the decreasing section of the shear stress function is unstable. It means that in the case of a shear stress to which three different shear rates belong, the middle one cannot be realized but the two others can, according to the deformation history of the moving particle. We study two limiting cases. The first one occurs if the entrance section of the tube is wide enough, while the second one does if the entrance section is narrow. The real cases are between the two limits. The phenomenon resembles hysteresis, but a real hysteresis cannot be expected as the fluid continuously leaves the tube and fresh fluid flows into it. Some hysteric phase changes are realistic in Couette viscometers but investigation of them is out of our present purposes.

The shear stress function

We put the shear stress function of the corotational Jeffrey body in the form

$$\tau = \eta \frac{1 + \tau_d \tau_t \kappa^2}{1 + \tau_t^2 \kappa^2} \kappa, \quad 0 < \tau_d < \tau_t, \tag{1}$$

where τ is the shear stress, κ the shear rate, τ_t, τ_d and η are material coefficients. If $\tau_t/\tau_d > 9$ this function has a decreasing section to which unstable stationary states belong as it was shown in [3]. Let κ_1 denote the beginning of the decreasing section and κ_2 the end. The shear stresses belonging to them are τ_1 and τ_2, respectively. With increasing shear stresses, up to τ_1, the shear rate also increases slowly, crossing τ_1 the shear rate jumps over κ_{11}, which is the shear rate with the same stress as belonging to κ_1. When the shear stress decreases so does the shear rate, continuously, down to κ_2 and then jumps below κ_{22}. The consequences of this phenomenon are investigated in pipes.

The shear stress in them varies with the distance from the axis of the tube

$$\tau = \frac{\Delta p}{2l} r = \frac{\tau_m}{R} r. \tag{2}$$

Here Δp is the pressure difference between the two ends of the pipe, l its length, τ_m the maximal shear stress and R the radius of the tube.

The volume of the fluid passing through a cross section of the pipe in unit time is given by

$$Q = \int_0^R 2\pi r V(r) dr, \tag{3}$$

where $V(r)$ is the velocity. Integrating by part, we get:

$$Q = [r^2 V(r)]_0^R - \int_0^R \pi r^2 \frac{dV}{dr} dr = -\pi \int_0^R r^2 \frac{dV}{dr} dr. \tag{4}$$

Introducing the shear rate

$$\kappa = -\frac{dV}{dr}$$

and making use of Eq.(2) we obtain the equation

$$Q = \pi \int_0^R \kappa r^2 dr = \pi \frac{R^3}{\tau_m^3} \int_0^{\tau_m} \kappa \tau^2 d\tau. \tag{5}$$

To evaluate the last integral is the easiest if we substitute the $\tau = \tau(\kappa)$ function that corresponds to the velocity distribution in the tube:

$$Q = \frac{\pi R^3}{\tau_m^3} \int_0^{\tau_m} \kappa \tau^2 \frac{d\tau}{d\kappa} d\kappa = \frac{\pi R^3}{2\tau_m^3} \int_0^{\tau_m} \tau^2 \frac{d\tau}{d\kappa} d(\kappa^2). \tag{6}$$

When evaluating the integral, we have to keep in mind that the function (1) can be applied in the stable section only, so $\frac{d\tau}{d\kappa}=0$ is substituted between κ_1 and κ_{11} when the stress increases or between κ_{22} and κ_2 if the stress decreases.

The evaluation of the integral

Setting forth to evaluate the integral (6), we determine the derivative

$$\frac{d\tau}{d\kappa} = \eta \frac{\tau_d \tau_t^3 \kappa^4 + (3\tau_d \tau_t - \tau_t^2)\kappa^2 + 1}{(1 + \tau_t^2 \kappa^2)^2}. \tag{7}$$

Making use of this and introducing the notations

$$x = \tau_t^2 \kappa^2, \quad t = \tau_t^2 \kappa_m^2, \quad t_1 = \tau_t^2 \kappa_1^2, \quad t_2 = \tau_t^2 \kappa_2^2,$$

$$t_{11} = \tau_t^2 \kappa_{11}^2, \qquad t_{22} = \tau_t^2 \kappa_{22}^2, \tag{8}$$

$$X = \frac{2\tau_t}{\pi R^3} Q, \quad y = \frac{\tau_t}{\eta} r, \quad Y = \frac{\tau_t}{\eta} \tau_m = \frac{\tau_t R}{2\eta} \frac{\Delta p}{l}, \quad z = \frac{l}{\xi} = \frac{\tau_d}{\tau_t},$$

we get:

$$Y = \sqrt{t} \frac{1 + zt}{1 + t} \tag{9}$$

and

$$X = \frac{1}{Y^3} \int_0^t f(x) dx, \tag{10}$$

where

$$f(x) = \begin{cases} 0 & \text{between the ends of the jumps,} \\ x = \dfrac{(1+zx)^2[zx^2+(3z-1)x+1]}{(1+x)^4} & \text{elsewhere.} \end{cases} \tag{11}$$

This rational fraction is decomposed into partial fractions:

$$x\frac{(1+2x)^2[zx^2+(3z-1)x+1]}{(1+x)^4} = ax+b+\frac{c}{1+x}+\frac{d}{(1+x)^2}+\frac{e}{(1+x)^3}+\frac{f}{(1+x)^4}.$$

Here

$$\begin{aligned} a &= z^3, \\ b &= z^2 - z^3, \\ c &= -2z^3 + 3z^2 - z, \\ d &= 8z^3 - 15z^2 + 8z - 1, \\ e &= -7z^3 + 17z^2 - 13z + 3, \\ f &= 2z^3 - 6z^2 + 6z - 2. \end{aligned}$$

The indefinite integral is

$$I(x) = a\frac{x^2}{2} + bx + c\ln(1+x) - \frac{d}{1+x} - \frac{e}{2(1+x)^2} - \frac{f}{3(1+x)^3},$$

where the arbitrary constant is omitted.

Finally, for the case of increasing stress we get:

$$X = \begin{cases} \dfrac{1}{Y^3}(I(t) - I(0)), & \text{if } t < t_1, \\ \dfrac{1}{Y^3}(I(t) - I(0) + I(t_1) - I(t_{11})), & \text{if } t > t_{11}, \end{cases}$$

and for decreasing stress

$$X = \begin{cases} \dfrac{1}{Y^3}(I(t) - I(0)), & \text{if } t < t_{22}, \\ \dfrac{1}{Y^3}(I(t) - I(t_2) + I(t_{22}) - I(0)), & \text{if } t > t_2. \end{cases}$$

As it can be seen from the notations (8) the quantity X is proportional to the volume passing through the cross section of the tube in unit time, while Y varies with the pressure drop, so we have got the function joining them in parametric form. We did the computation for a few particular values of τ_t/τ_d numerically and

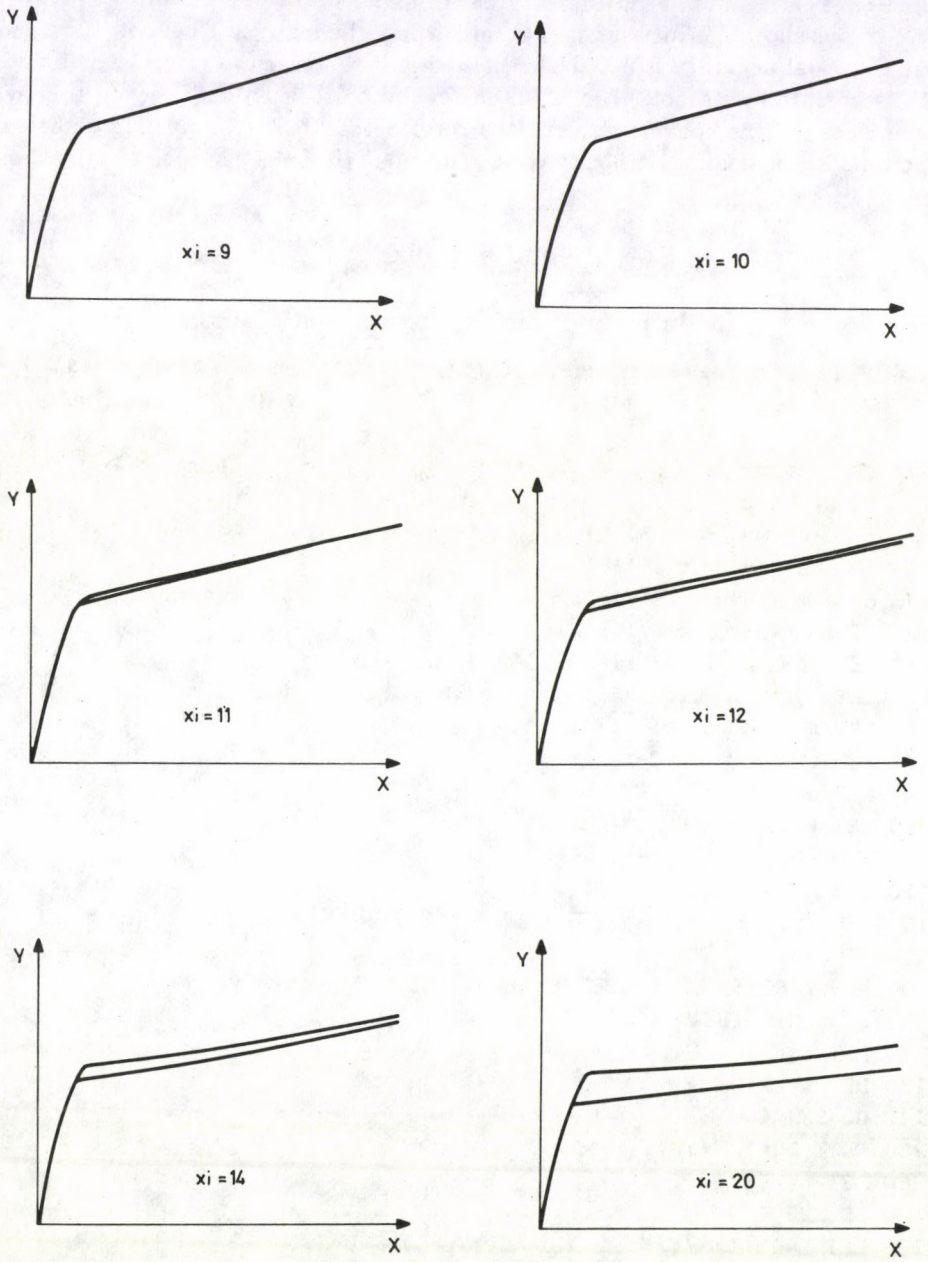

Figs. 2–7

plotted Y against X in Figs 2–7. The graphs in the pictures resemble those of a Bingham body. We can conclude by saying that the body with a shear stress function (1) is found to be viscoplastic during experiments with capillary equipment. The graphs show that measurements can display the material constants τ_t, τ_d and η but the usual accuracy is not sufficient to decide whether the viscometric function (1) is acceptable or not. Nevertheless, numerical calculations — together with experience — are convincing that the corotational Jeffrey body is a sufficiently good model for dealing with extruders and some other plastic processing machines.

Appendix

Basic program for the computations

```
10>DEF FN I(x)=(x*a/2+b)*x+c*LN (1+x)-((f/3/(1+x)+e/2)/(1+x)+d)/(1+x)
20 INPUT "xi=";xi
30 LET z=1/xi
40 LET a=z*z*z
50 LET b=z*z-a
60 LET c=z*(z*(-2*z+3)-1)
70 LET d=z*(z*(8*z-15)+8)-1
80 LET e=z*(z*(-7*z+17)-13)+3
90 LET f=z*(z*(2*z-6)+6)-2
100 LET t1=(xi-3-SQR(xi*(xi-10)+9))/2
110 LET t2=xi-3-t1
120 LET t11=4*t1/(t1-1)/(t1-1)
130 LET t22=4*t2/(t2-1)/(t2-1)
140 LET out=0
150 LET t=.1
160 PLOT 0,0
170 LET t=t*1.03
180 IF t>t1 AND t<t11 THEN LET t=t11
190 GO SUB 350
200 LET X=80*I/Y/Y/Y: LET p=180*Y: GO SUB 430
210 IF out=0 THEN GO TO 170
220 LET out=0
230 LET t=t2
240 GO SUB 400
250 PLOT 80*I/Y/Y/Y,180*Y
260 LET t=t*1.1
270 GO SUB 400
280 LET X=80*I/Y/Y/Y: LET p=180*Y: GO SUB 430
290 IF out=0 THEN GO TO 260
```

```
300 PRINT AT 18,12;"xi=";xi
310 PLOT 0,175:  DRAW 0,-175:  DRAW 223,0
330 REM **********************
340 STOP
350 LET Y=SQR t*(1+t/xi)/(1+t)
360 LET I=FN I(t)-FN I(0)
370 IF t<t1 THEN RETURN
380 LET I=I-FN I(t11)+FN I(t1)
390 RETURN
400 LET Y=SQR t*(1+t/xi)/(1+t)
410 LET I=FN I(t)-FN I(0)-FN I(t2)+FN I(t22)
420 RETURN
430 IF X>223 OR p>175 THEN LET out=1:  RETURN
440 LET X0=PEEK 23677
450 LET p0=PEEK 23678
460 PLOT X,P
470 DRAW X0-X,p0-p
480 PLOT X,p
490 RETURN
```

References

1. M. Slemrod, Shear Flows of Non-linear Viscoelastic Fluids, in: Trends in Applications of Pure Mathematics to Mechanics , Ed. by E. Kröner and K. Kirchgassner, Springer, Berlin, Heidelberg, New York, Tokyo, 1986.
2. J. Verhás, Acta Mechanica (Vienna), *53*, 125, 1984.
3. Nguyen thi bang Van, Acta Phys. Hung., *65*, 109, 1989.
4. J. Verhás, Thermodynamics and Rheology (in Hungarian) Technical Publishing House, Budapest, 1985.
5. I. Gyarmati, Non-equilibrium Thermodynamics. Field Theory and Variational Principles, Springer, Berlin, Heidelberg, New-York, 1970.
6. S.R. de Groot and P. Mazur, Non-equilibrium Thermodynamics, North-Holland Publ.Co., Amsterdam, 1962.
7. J. Verhás, Periodica Polytechnica (Budapest), *21(4)*, 319, 1977.
8. J. Verhás, Periodica Polytechnica (Budapest), *25*, 53, 1981.

Acta Physica Hungarica 65 (1), pp. 123–124 (1989)

CAN THE CREATION OF MATTER IN THE EARLY UNIVERSE STALL INFLATION ?

C. WOLF

Department of Physics, North Adams State College
North Adams, MA. 01247 U. S. A.

(Received in revised form 14 April 1987)

It is argued that the dominant creation of matter in the very early universe can stall and delay the period of inflation suggesting that inflation might inseparably be related to the conservative phase or phase when the relation $T^{\mu\nu}{}_{;\nu} = 0$ rigorously applies.

There has been some speculation that nature might enjoy a non-conservative dynamics wherein the relation $T^{\mu\nu}{}_{;\nu} = 0$ does not apply ($T^{\mu\nu}$ = energy momentum tensor of matter). Rastall [1] suggested that a violation of the local relation $T^{\mu\nu}{}_{;\nu} = 0$ cannot be ruled out by experiment and Smalley [2] has shown how Brans–Dicke theory can be modified to accommodate a non-conservative gravitational theory. Barber [3] has suggested two variations of general relativity that violate the energy conservation principle with the second alternative presenting no serious conflict with the equivalence principle. From a quantum point of view a non-conservative theory or a term such that $T^{\mu\nu}{}_{;\nu} = \lambda R'^{\mu}(\lambda = \text{ const.})$, where $R'^{\mu} \neq 0$ might result from gravitational anomalies in the quantum domain and might leave their classical effect in a phenomenological way as pointed out by Dittrich [4]. In a previous paper [5] we have discussed cosmological consequences of a five-dimensional theory that violated the conservation law $T^{\mu\nu}{}_{;\nu} = 0$ and found that inflation was permitted only at a rate that was different from the general relativistic result and depended on the constant in the equation $T^{\mu\nu}{}_{;\nu} = \lambda R'^{\mu}$; the weakness in the five-dimensional theory was that the fifth dimension also inflated leading to an unrealistic cosmology [5]. In this brief note we show that if creation dominates the early universe, that inflation is wiped out, thus suggesting that if creation from gravitational curvature is effective in the pre-G. U. T. era, then it might lead to a stalling effect, perhaps giving reason why we are able to treat $V(\varphi), [V(\varphi) =$ Higgs field effective potential] in the G.U.T. potential as homogeneous as perhaps due to the homogenizing property possessed by the early universe prior to inflation.

We start by writing the modified Einstein equation as

$$R_{\mu\nu} + \frac{1}{2} R g_{\mu\nu} = -kT_{\mu\nu} + (T_{\mu\nu})_s, R_{\mu\nu} = R^{\lambda}_{\mu\nu\lambda}, \tag{1.1}$$

where $k = \frac{8\pi G_4}{C^4}$, $R^{\lambda}_{\mu\nu\beta}$ = curvature tensor, $g_{\mu\nu}$ = metric, $R = R_{\mu\nu} g^{\mu\nu}$, $(T_{\mu\nu})_s$ = non-conservative source energy momentum tensor. Taking the divergence of Eq. (1.1) we have

$$R^{\mu\nu}{}_{;\nu} + \left(\frac{1}{2} R g^{\mu\nu}\right)_{;\nu} = -kT^{\mu\nu}{}_{;\nu} + (T^{\mu\nu})_{s;\nu}, \tag{1.2}$$

letting $T^{\mu\nu}{}_{;\nu} = \lambda R^{,\mu}$ and $R^{\mu\nu}{}_{;\nu} = \left(\frac{1}{2}Rg^{\mu\nu}\right)_{;\nu}$ by the Bianchi identities we have

$$(T_s^{\mu\nu})_{;\nu} = R^{,\mu} + k\lambda R^{,\mu},$$

since $g^{\mu\nu}{}_{;\nu} = 0$ this equation is statisfied, by

$$T_s^{\mu\nu} = (1 + k\lambda)Rg^{\mu\nu}, \tag{1.3}$$

since $[(1 + k\lambda)Rg^{\mu\nu}]_{;\nu} = (1 + k\lambda)R_{,\nu}g^{\mu\nu} = (1 + k\lambda)R^{,\mu}$. Eq. (1.1) becomes

$$R_{\mu\nu} + \frac{1}{2}Rg_{\mu\nu} = -kT_{\mu\nu} + (1 + k\lambda)Rg_{\mu\nu}. \tag{1.4}$$

Taking the trace of Eq. (1.4) and resubstituting for R we have

$$R_{\mu\nu} = -kT_{\mu\nu} + \frac{k}{2}\left(\frac{1 + 2k\lambda}{1 + 4k\lambda}\right)Tg_{\mu\nu}. \tag{1.5}$$

For $T_{\mu\nu} = V_0 g_{\mu\nu} + (T_{\mu\nu})_{\text{matter}}$ where $(T_{\mu\nu})_{\text{vac}} = V_0 g_{\mu\nu}$ is the energy momentum tensor of the false vacuum, we have for the trace of $T^{\mu\nu}, T = T_{\mu\nu}g^{\mu\nu}$ or $T = 4V_0 + (T)_{\text{matter}}$. We examine Eq. (1.5) for large λ giving for $\lambda \gg 1$

$$R_{\mu\nu} = -kT_{\mu\nu} + \frac{k}{4}Tg_{\mu\nu}$$

or

$$R_{\mu\nu} = -k(T_{\mu\nu})_{\text{matter}} + \frac{k}{4}T_{\text{matter}}\, g_{\mu\nu} - kV_0 g_{\mu\nu} + kV_0 g_{\mu\nu},$$

$$R_{\mu\nu} = -k(T_{\mu\nu})_{\text{matter}} + \frac{k}{4}T_{\text{matter}}\, g_{\mu\nu}. \tag{1.6}$$

We see here that the false vacuum energy at the metastable maximum of the Weinberg–Coleman potential cancels out of the calculation and we are left with an equation relating to the generation of $g_{\mu\nu}$ by only matter sources. Such a result suggests that a pre-inflationary period might stall the onset of inflation and lead to a homogenizing effect to generate the homogeneous $V(\varphi)$ enjoyed during inflation. It also gives us further reason to pursue creation in early universe studies.

Acknowledgements

I would like to thank the Physics Departments at Williams College and Harvard University for the use of their facilities. I would also like to thank Dave Park for helpful conversations.

References

1. P. Rastall, Phys. Rev. D. *6*, 3357, 1972.
2. L. Smalley, Phys. Rev. D. *12*, 376, 1975.
3. G.A. Barber, Gen. Rel. and Gravitation, *14*, 117, 1982.
4. W. Dittrich (personal communication).
5. C. Wolf, Physica Scripta (in print).

Acta Physica Hungarica 65 (1), pp. 125–134 (1989)

BOOK REVIEWS

Atomic and Molecular Physics of Controlled Thermonuclear Fusion

Proceedings of the NATO Advanced Study Institute held at Santa Flavia, 19-30 July 1982 NATO ASI Series, Series B: Physics, Vol. 101,

Edited by: Charles J. Joachain and Douglass E. Post, Plenum Press, New York – London, 1983

The struggle to conquer controlled thermonuclear fusion as a long-term energy source seems as if it will approach technical realization in a couple of decades to come. The actual problems are wandering from the understanding of confinement (either magnetic or inertial) towards that of the behaviour of the confined plasma and its interaction with the walls of the confinement, in other words with the materials at and inside the vessel and last but not least the means of effective heating mechanisms. Since the production of high temperature and high density plasma seems to be more or less solved the major clues remain to be related to the understanding of elementary and transport properties under the extraordinary conditions and this understanding influences the observational, i.e. diagnostic, processes as well — not only the achievement of the ultimate goal.

The papers in this volume are arranged in three groups: the first offers an overview of fusion energy in general and its magnetic and inertial way; the second treats the calculation and measurement of atomic and molecular processes relevant to fusion (collision theory, e-i-scattering, impact ionization, Rydberg states); the third covers the atomic and molecular physics (kinetic theory), the transport processes (diffusion, ionization, recombination, impurities, instabilities) in high temperature, low density and high density plasmas, the role of atomic and molecular processes in the plasma boundary region. A paper is devoted to neutral particle beam production and injection. Diagnostics is treated in two papers: one on spectroscopic, the other on particle diagnostics. The volume is an excellent guide to the contemporary situation in the multidisciplinary phase of affairs.

I. Abonyi

Quantum Metrology and Fundamental Physical Constants

Proceedings of the NATO Advanced Study Institute, Erice (Sicily) Italy, 16-28 November 1981, NATO ASI Series, Series B: Physics, Vol. 98

Edited by: Paul H. Cutler and A.A. Lucas, Plenum Press, New York – London, 1983

The papers presented in the volume (34 contributions) review the present status of metrology, the science of measurement. The reader develops a broad horizon in this wide reading field where we perhaps may say without exaggeration, a renaissance of interest and a revolutionary development can be witnessed. After the historical review given by P. Giacomo, the papers are arranged in six sections and a shorter summary of seminars. The sections are the following: Basic physics of time, frequency and length measurements and standards — Classical and quantum physics of electrical measurements and standards — Fundamental constants of physics — Metrological applications — Status of the fundamental constants. The papers show the experimental determination of the fundamental constants embedded in their historical technological context, in their role in physical science, in the ongoing possibilities for increasingly accurate measuring effort; in an effort which solves old problems and creates new ones, in an activity which respondsto the needs of science and industry. E.R.Cohen,

in reviewing the status of fundamental constants, introduces the reader to the procedure of fitting the fundamental constants by the least squares analysis which resulted in the newest version of suggested values of fundamental constants (1981).

This magnificent collection of papers will convince those physicists who are not engaged in metrological aspects of the importance in physics, even in fundamental physics, of this — at first sight applied — branch.

I. Abonyi

Fracture Mechanics of Ceramics, Volumes 5 and 6

Proceedings of an International Symposium on the Fracture Mechanics of Ceramic Materials held at The Pennsylvania State University, University Park, PA, 15-17 July, 1981.

Edited by: R.C. Bradt, A.G. Evans, D.P.H. Hasselman, F.F. Lane, Plenum Press, New York – London, 1983.

The theme of the Conference focussed on the mechanical behaviour of ceramic materials in terms of the characteristics of cracks, particularly the roles which they assume in the fracture process. The 78 contributed papers by over 100 authors and co-authors represent the current state of the field.

Volume 5 deals with surface flaws, statistics, and microcracking. This volume contains 39 papers. The most important fields of this volume are as follows: surface flaw models, shear flow and fracture, impact damage resistance, indentation fracture toughness, the stress corrosion limit, fracture of piezoelectric materials, fracture statistics of multiple flaw distributions, microcracking mechanism in ceramics, grain boundary cracking in ceramics and rocks, microcracking models.

Volume 6 deals with measurements, transformations and high-temperature fracture. This volume also contains 39 papers. The most important fields of this volume are as follows: dynamic fracture toughness of glass, fast crack propagation across interfaces, fracture mechanics model for glass, thermodynamics of phase transformation toughening, high temperature fracture toughness measurements, thermal stress fracture of ceramic coatings, crack healing in brittle materials.

J. Giber

Dynamical Processes and Ordering on Solid Surface

Proceedings of the VII. Taniguchi Symposium, Kashikojima, Japan, 10-14 September, 1984

Edited by: Y. Yoshimori and M. Tsukada Springer Series in Solid-State Sciences, Vol. 59 Springer-Verlag, Berlin, Heidelberg, New York, Tokyo, 1985

The 24 papers of the theoretical physical workshop covered two fields of surface physics: dynamical and surface ordering processes.

Most of the papers consider the microphysical approach about the collision trajectories of atoms at the surface, energy transfer between external and internal degrees of freedom. Four papers study the optical phenomena and the dynamics of polaritons following the above processes. The final part deals with the ordering and electronic structure of adsorbed layers.

The fields are only dealt with at macrophysical level, which can be of interest, as a new viewpoint for theoretical physicists, physicochemists and especially, for experts in the theory of adsorption and surface reactions.

J. Giber

H.J. KREUZER and *Z.W. GORTEL: Physisorption Kinetics*

Springer Series in Surface Sciences, Vol. 1, Springer-Verlag, Berlin, Heidelberg, New York, Tokyo, 1986

The purpose of this book is to offer the reader an up-to-date coverage of some of the most important areas of physisorption. It studies the kinetics of the adsorption and desorption of molecules physisorbed on solid surfaces. Altough frequent and detailed reference is made

to experiment, the book is mainly concerned with the theory of the subject, based on the master equation. Experimental data on desorption times, sticking and accommodation coefficients, and time-of-flight spectra are also surveyed.

Contents: Gas-Solid Interaction, The Master Equation, Transition Probabilities in the Master Equation, Desorption Times, Time-of-Flight Spectra, Sticking and Accommodation, Kramers Equation, Summary and Outlook, and a number of excellent review articles, listed in the bibliography (22 pages).

As physisorption kinetics is not a closed and mature subject, the authors' purpose is to give a reasonable basis from which further developments can start.

The Volume will be of interest for researchers in solid state physics and materials science.

J. Giber

KONRAD KREHER: Elektronen und Photonen in Halbleitern und Isolatoren

Wissenschaftliche Taschenbücher, Reihe Mathematik und Physik

Akademie-Verlag, Berlin, 1986

This little book follows the tradition of this series: based on a high level of the theoretical background, it gives a practical and actual talk about the subject. It can be considered as the compendium of some chapters of the book "The Physics of Solids" (published in Hungarian by Tankönyvkiadó, Budapest, 1978) from the same well-known author. These chapters are in more detail strictly for researchers.

The electronic structure, lattice vibrations and optical properties of semiconductor and insulator solid state materials are considered. The main purpose of the book is to describe the electronic states of the perfect crystal and crystal defects in semiconductors and insulators.

The authors follows with attention the crystals of compounds III–V and II–VI in separate chapters. Researchers in semiconductor physics and compouds III–V, II–VI will find this book very useful.

J. Giber

L. O'RAIFEARTAIGH: Group Structure of Gauge Theories

Cambridge Monographs on Mathematical Physics, Cambridge University Press, Cambridge, 1986

This book is written by the Irish physicist Lochlainn O'Raifeartaigh, who is one of the greatest experts in the applications of group theory in theoretical physics. The aim of the monograph is to provide a review of the applications of group theory in gauge theories and their spontaneous breaking.

The simple and elegant presentation is pitched at about the graduate student level but it does not overlap with the existing treatments of gauge theories. Mainly two aspects are treated. These are, the group theoretical background, particularly the global group theory /Part I/ and the algebraic structure of the gauge interactions and of their symmetry breakdown patterns /Part II/. The book does not give a selfcontained introduction into gauge theories, it supposes the knowledge of some of the existing reviews and books on the subject, especially considering such questions as renormalization, confinement, phenomenology, etc. It seems that this work will be a unique source for those theorists who are interested in understanding the spontaneous symmetry breaking patterns. As a very useful last appendix, suggestions for further reading are given also in the monograph.

This book will be of interest to graduate students and to researchers in theoretical physics and applied mathematics, especially those interested in the application of differential geometry and group theory in physics.

Z. Horváth

RICHARD C. FERNOW: Introduction to Experimental Particle Physics

Cambridge University Press, Cambridge, 1986. pp. 421

Particle physics is in the front line of modern science of our age and so both the theoretical and the experimental as well as the technical achievements of this branch of science are undergoing extremely rapid development. In view of this it needs courage for someone — bearing

in mind the time lapse between the writing and the reading of a book — to decide to write a general work on the topic since many concepts and devices begin to become outdated and new ones come into being which cannot yet be mentioned. In spite of this, it is still necessary from time to time to publish general treatises in this field of science in order to facilitate the work of those who would like to deal with particle physics or who have just begun their studies on this subject. Fernow took the risk of partial obsolescence and has solved his task excellently.

His book is meant primarily for advanced level undergraduates and postgraduate students, but it may also be read with benefit by theoretical physicists who would like to gain a deeper insight into the process of obtaining the experimental fact. The book is a useful piece of reading also for those dealing with other branches of physical sciences and even for beginners who are inexperienced in certain experimental fields of particle physics. To write such a book is difficult also from that aspect that it needs hard work, attention, and critical talent to make out the essence from the vast and detailed literature and to collect and work it up in a clear and concise way — as the author has excellently done in this book. He makes known the basic processes and devices necessary for dealing with experimental physics, as well as the newer results. He makes it easier to become acquainted with and to understand the very complicated measuring techniques nowadays used in particle physics. Reading the book or certain parts of it enables one to get thoroughly acquainted with, and learn about what is being dealt with in the literature.

Experimental questions and not theoretical ones are dealt with. Nevertheless, in addition to qualitative descriptions, the physical processes and formulae necessary for experimental work are elaborated thereby saving the reader the trouble of getting the necessary results by long, precise deductions.

The book is divided into 15 Chapters, an Appendix of 7 parts, an Author Index and a Subject Index; there are many illustrations and tables. Chapter 1 is an introduction, making known some basic processes of particle physics; Chapters 2 deals with the electromagnetic, Chapter 3 with nuclear interactions. Chapter 4 is of particular value dealing, as it does, with particle beams and introducing the basic principles of accelerators, the creation of secondary beams and the art of handling the beams. This chapter may well be of great use to Hungarian readers in that having no particle accelerator of their own their knowledge in this field is generally incomplete. In view of the fact that physicists in Hungary have no wish to be specialists in accelerators, they tend to neglect those detailed items of information on the operation of accelerators which are not basic principles but even so are important and may influence the efficiency of their experimental work. This chapter is meant to fill this gap by giving additional information and reference compared with general basic principles but without going into unnecessary detail.

Chapter 5 briefly deals with targets, both standard and special purpose targets. Chapter 6 covers fast electronics. Obviously it is not intended that readers should consider this Chapter as if they wished to take over the job of electronic engineers and try to solve electronics problems as well as being able to construct such installations; it is, however, eminently suitable as a means of getting acquainted with the basic units and the basic electronic solutions, and learning the common language in which they can express their claims and specifications for the engineering experts.

For obvious reasons much of the book deals with detection techniques and with individual detectors. Detectors from that part of the techniques of experimental particle physics which is the nearest to experimental physicists and a knowledge of which is the most necessary for performing certain experiments.

Accordingly Chapters 7–14 deal with the various detectors including: scintillation counters, Cerenkov counters, proportional chambers, drift chambers, calorimeters and special detectors (bubble chamber, emulsions, spark chambers, streamer chamber, transition radiation detector). Of the Chapters dealing with detectors there is a separate one on triggers whose selection is of decisive importance in relation to the reliability of an experiment, and the planning of which needs a high level knowledge of one's profession. Another Chapter discusses detector systems and not only spectrometers used at accelerators with fixed target but also detectors which can be and are to be built near the collision beam accelerators which are to some extent of a different technique. Detectors necessary for experiments other than those connected with accelerators (e.g. the pro-

ton decay experiment) and the processing of measured data are discussed as well.

In the last Chapter some basic experiments are described — including illustrating how different types of accelerators and detectors can be built together to provide a unified setup for a concrete experiment.

The most important physical constants, the periodic table of the elements, a brief and perhaps not too detailed and too exacting chapter on probability and statistics which are necessary for the evaluation of measurements in particle physics can be found in the Appendix. The last of these may be a bit surprising especially in Hungary where the students of the late Academician L. Jánossy still remember the much greater exhaustiveness and accuracy with which the problems of statistical evaluation of measuring data were elaborated and solved. The following topics are also included in the Appendix: cross sections, two-body scattering, motion of ions in a combined electric and magnetic field, and the properties of structural materials from the standpoint of particle physics.

The book can be recommended with good conscience to all those who — beyond basic principles but not in full detail — would like to get acquainted with the techniques of experimental particle physics, and to university students who would like to study particle physics.

D. Kiss

A. LASOTA and *M.C. MACKEY: Probabilistic Properties of Deterministic Systems*

Cambridge University Press, Cambridge, 1985, pp.358

In the last decade there has been a very intensive growth in the analysis of physical, chemical, biological and economic systems that can be profitably studied using densities. To present how densities arise in deterministic systems, the authors give a unified treatment of a variety of systems generating densities, ranging from one-dimensional discrete time transformations through continuous time systems treated by integro-partial-differential equations. Examples have been drawn from many fields to illustrate the utility of the concepts and mathematical tools presented.

The book is divided into eleven Chapters, in which the following important problems are treated: Markov and Frobenius–Perron operators, chaos with densities and asymptotic properties of densities, continuous and discrete time processes, entropy, stochastic perturbations of discrete and continuous time systems. Evidently, the ideas and mathematical methods in this book should thus prove useful in the study of a number of applied sciences. Otherwise, because of the general inaccessibility of the mathematical literature to the nonspecialist, little diffusion of the applicable mathematics into the study of chaotic systems has taken place. This book will help to bridge that gap.

Of course, from the very beginning the authors assume that the reader has an adequate knowledge of advanced calculus and differential equations. Fundamental concepts from measure theory, ergodic theory, theory of manifolds and partial differential equations, probability theory and Markov processes, finally stochastic integrals and differential equations are introduced at least as needed.

The book is very useful to physicists, chemists, economists and biomathematicians studying the chaotic behaviour of different phenomena. It will also be a useful reference or text for mathemathicians and graduate students working in ergodic theory and dynamical systems.

I. Gyarmati

Dimensions and Entropies in Chaotic Systems, Quantification of Complex Behavior

Springer Series of Synergetics,

Edited by: G. Mayer-Kress, Springer-Verlag, Berlin, Heidelberg, New York, Tokyo, 1986, pp. 257, 139 figures

This volume contains the papers contributed to the International Workshop on "Dimensions and Entropies in Chaotic Systems" at the Pecos River Ranch in September 1985. The workshop was held by the Center for Nonlinear Studies of the Los Alamos National Laboratory.

The investigation of chaotic dynamics and especially the quantification of complex behavior has a long tradition. However, in spite of remarkable successes, there are fundamental as

well as numerical problems which led to a series of publications, in which modifications, reformulations and improvements of the original problems and methods have been proposed. Thus, at least at present, there exists an increasing number of competing dimension algorithms but no comprehensive review explaining how they are related. On the other hand, it has become more evident that there is a growing need in different disciplines for methods with which aperiodic and irregular data strings can be characterized. Thus, it seemed to be natural to have a workshop where the problems of these methods for the qualification of complex behavior could be discussed and expanded. The participants hoped that this workshop would help to systematize and unify the various aspects of these problems, since they tried to bring together an interdisciplinary group of scientists with either theoretical or experimental expertise who worked one week on the Pecos River Ranch.

The lectures of the workshop concentrate more on latest results rather than on expository introductions. According to the nature of these lectures, this volume is divided into seven main parts, in which the authors dealt with the mathematical aspects of dimensions, numerical and experimental problems of dimensions and entropies, computation of Lyapunov exponents, accuracy of different algorithms, experimental results and applications and so on. We hope that researchers will find in this book a useful and comprehensive collection of papers for their own research into describing chaotic systems.

I. Gyarmati

Selforganization by Nonlinear Irreversible Processes

Springer Series in Synergetics Vol. 33

Edited by: W. Ebeling and H. Ulbricht Springer-Verlag, Berlin, Heidelberg, New York, 1986

This book contains invited lectures presented at the third International Conference on "Irreversibile Processes and Dissipative Structures" held in Kühlungsborn (GDR) March 1985. The conference was devoted to the study of processes far from thermal equilibrium and to the phenomena of selforganization. This meeting brought together some 160 mathematicians, physicists, chemists and biologists from 10 countries.

The main topics of the conference were basic concepts of selforganization and evolution, such as entropy, instabilities, nucleation, dissipative structures, chaos and turbulence. The contributions cover methods from thermodynamics, the theory of dynamical systems, the theory of stochastic processes, the method of Green's functions, the fluctuation-dissipation theorem etc. Several problems are studied in more detail, e.g., the kinetics of nucleation especially in finite systems, the dynamics of interfaces, reaction–diffusion systems, chemical and biological pattern formation and information processing. Furthermore, several contributions deal with the problem of chaos in temporal and spatio-temporal systems.

The material is arranged in five main chapters: Basic Concepts, Stochastic and Statistic Theory, Dissipative Structures, Evolution Processes, and Chaotic Processes.

The book is recommended for graduate students and research workers being interested in the interdisciplinary field of synergetics.

T. Tél

Picosecond Electronics and Optoelectronics

Proceedings of the Topical Meeting Lake Tahoe, Nevada, March 13-15, 1985, Springer Series in Electrophysics, Vol. 21

Edited by: G.A. Mourou, D.M. Bloom and C.–H. Lee, Springer-Verlag, Berlin, Heidelberg, New York, Tokyo, 1985

This volume contains 51 papers presented in 6 sessions of the Lake Tahoe meeting in 1985.

Over the past decade a number of spectacular advances in the fabrication of crystalline semiconducting devices due mainly to the progress of the different techniques of heteroepitaxy have been experienced. The discovery of two-dimensional behaviour of electrons led to the development of a new breed of ultrafast electronic and optical devices, such as modulation doped FETs, permeable base transistors, and double heterojunction transistors. Comparable progress has been made in the domain of cryo-

electronics, ultrashort pulse generation, and ultrafast diagnostics. Dye lasers can generate 8 fs signals after compression, diode lasers can be modulated at speeds close to 20 GHz and electrical signals are characterized with subpicosecond accuracy via the electro-optic effect. Presently an important interplay between the field of ultrafast optics and electronics is experienced; one of the purposes of the meeting was to foster and enhance the interaction between the two disciplines.

The papers of the Volume are distributed into six parts:

In Part I the state-of-the-art of the respective fields of optics and electronics is presented. The importance of the optical techniques in the analysis of physical processes and device performances is emphasised.

Parts II and III deal with the special aspects of ultrafast carrier transport phenomena in semiconductors. Because of its role in communications, a remarkable part of the meeting was devoted to laser diodes and transducers operating in the picosecond range. The reports on these subjects are in Parts IV and V.

Part VI covers the field of cryoelectronics where impressive results in high speed signal processing and sampling have been obtained.

Cs. Kuti

RABINDRA N. MOHAPATRA: Unification and Supersymmetry, The Frontiers of Quark-Lepton Physics

Contemporary Physics Series

Springer-Verlag, Berlin, Heidelberg, New York, Tokyo 1986, pp. 309

Any truly fundamental advance in understanding the workings of Nature rebuilds the mathematical scaffoldings by emphasizing new descriptions. To what extent would one expect such a new theory to be mathematically revolutionary? Well, this appears to be a matter of taste — and to be sure no one can beat Nature's taste.

This monograph summarizes the state-of-art of supersymmetry at a moment when the convergence of the theory to Nature's taste becomes apparent. Thus the moment is right for a self-contained account of supersymmetry after a hectic period of development. Mohapatra's book is based on a series of graduate courses at the City College of New York and in Maryland.

The Volume begins with a short summary of important basic concepts in particle physics, spontaneous symmetry breaking and the Higgs mechanism. These chapters are hardly more than quick reminders of the key ideas. Unified models of interactions are discussed in greater details, and supersymmetric models occupy about half of the volume. What the reviewer really thinks to be missing is a little more elaboration of string theories. The final chapters are devoted to the applications of supergravity to particle physics and to $N > 1$ supersymmetry groups. The fact still is that these applications still do not abound in successful predictions. However, it is not without pride for the reviewer to discover a chapter in the volume dealing with a model of supersymmetry breaking due to the fellow-countryman János Polonyi.

The volume bears the imprints of unusual care that went into a coherent presentation of the material. The reader seldom encounters a trace of the supersymmetric haste, such as an incomplete reference on p. 64. On the whole, this volume is likely to become a friend of particle theorists for many years to come.

Z. Perjés

I.T. TODOROV: Conformal Description of Spinning Particles

Trieste Notes in Physics

Springer-Verlag, Berlin, Heidelberg, New York, Tokyo, 1986, pp. 74

These notes are based on lectures given by the author in ICTP (Trieste) and elsewhere. The twistor description of conformal space-time transformations and the classical phase spaces of conformal particles are studied.

The material is divided into four parts. The first is concerned with the conformal group of a flat space-time and with the twistor representations of the group. In the second part, various concepts of space-time geometry such as a point or a light ray are shown to arise from subspaces of the twistor space called flag manifolds. The classical phase spaces of spinning free particles are studied in the third part. A canonical symplectic structure on the twistor space in shown to exist, and massless and massive

particles with their respective phase spaces are discussed in separate chapters. The fourth part contains a twistor description of classical massless fields. The Appendices present a Clifford-algebraic approach to twistors and the relation of twistors to Dirac spinors.

The discussion is lucid and readable, the ratio of mathematics to physics in the contents is high, and the influence of P. Budinich's ideas on the subject is felt.

Z. Perjés

Topological Properties and Global Structures of Space-Time

NATO ASI Series, Series B: Physics Vol. 138

Edited by: Peter G. Bergman and Venzo de Sabbata, Plenum Press, New York and London 1986, pp. 289

The Volume contains the written versions of the lectures given at the Ninth Course of the International School of Cosmology and Gravitation held at Erice. The subject of the twenty contributions is diversified to the extent that the Editors of the volume have chosen not to classify the material into sections. It appears that the lectures on space-like infinity, black holes and on singularities pertain most directly to the original goal of the school.

The recent years, the structure of spatial infinity ("spi") has been vigorously studied. Such important matters as the exact formulation of the Einstein quadrupole radiation equation depend critically on the behaviour of the fields at spi. Peter Bergman lectured, in particular, on conserved quantities, solutions and possible quantization of a scalar and a tensor field at spi. The topic was developed further by Piotr Chruściel who described the boundary conditions at spi from a Hamiltonian point of view.

The shock of the collapse of formal definitions of space–time singularities appears now to be over, and a slight progress has already been made towards a sound description of singular points. Some aspects of this are reviewed in C.J.S. Clarke's enlightening lecture to which a list of unsolved problems is appended. R.P.A.C. Newman introduces the reader to the notion of the strength of a singularity, based on the limiting behaviour of non-spacelike geodesics. One may then conjecture that naked singularities are, in some sense, weak. Quite lately it turned out that the spherically symmetric collapse and, in particular, the Tolman–Bondi dust and Vaidya null dust solutions may lead to naked singularities. A strong cosmic censorship conjecture, however, can still be formulated.

Roberto Sussman examines the causal structure and some global properties of Schwarzschild space–time joined to a Friedmann Universe. Such "Swiss cheese" models provide the simplest pictures of a non-asymptotically flat black hole. (Their beautiful Penrose diagrams would have been perhaps esteemed highly at Christies.)

Supermanifolds and strings occupy a sizable proportion of the volume. The introductory talk is written by Gary Horowitz. He points out, among others, certain parallels between strings and twistor theory, especially in the way the space–time manifold is constructed from underlying entities. The supermanifold aspect is further developed by U. Bruzza, J.M. Rabin and A. Rogers, while the Penrose approach to the asymptotic structure of fields is taken up by C.N. Kozameh and E.T. Newman.

It is difficult to do justice to all the contributors within the space allotted here. The book is undoubtedly a valuable source of recent results in global studies of the space-time.

Z. Perjés

R. PENROSE and *W. RINDLER: Spinors and Space-Time*

Vol. 1. Two-spinor calculus and relativistic fields

Cambridge Monographs on Mathematical Physics, Cambridge University Press, Cambridge, 1986, pp. 455

This highly acclaimed encyclopedia of two-spinors is now available in paperback edition. In the past decades, two-spinor techniques have been gaining prominence among theorists. (This has been pioneered, to a considerable extent, by one of the authors, Roger Penrose, whose insights have helped to see the spinorial nature of many physical phenomena in a new light).

Two-spinors occupy a distinguished status among spinor structures. Algebraically, the absence of complicated γ-matrix identities is their obvious advantage over Dirac- or higher-dimensional spinors. Geometrically, two-spinors appear to be woven deep into the causal phenomena in relativity, providing, via this correspondence, an 'explanation' of the four-dimensional nature of space-time. Such notions have promoted the recognition of the utility of two-spinors for the curved space-time manifolds of general relativity. Several difficult chapters of relativity, to mention only the Petrov classification of curvature, or indeed the most general forms of Einstein's gravitational equations, emerge in a spinoral guise as enjoyable exercises.

As one would righteously expect, a monograph dealing with formalisms pays much attention to the *form* of the formalism. The spin coefficient equations of Newman and Penrose adequately illustrate this point. The first and most widely accepted version of these equations contains twelve complex functions called spin coefficients. Later developments, in particular the application of Geroch–Held–Penrose formalism to the quasi-local mass, favour a new notation in which spin coefficients appear in pairs related by a geometric involution. The volume presents the Newman–Penrose equations in this latter form, which choice is likely to be welcome by many workers while slightly disappoint some others.

A number of notational inventions are conveyed here, which may prove to be as significant as is the summation convention of Einstein. The *abstract index notation*, for example, which has become known also as the Battelle convention, re-instates the good old tensor index formalism (and thus is sure to be cheered by many who were educated with no regard to the index-free notation), by re-interpreting components as abstract symbols of the tensor and its structure. (The abstract index notation saves much stammer when translating expressions to a spinor form by making soldering quantities unnecessary). The *blob notation*, on the other hand, is an alternative to the index notation, which represents indices diagrammatically as "legs" joining the kernel blob symbol of a tensorial quantity. It has the advantage that the recognition of index structures becomes a visual task, thereby releaving the mind.

Several useful chapters of space-time lore appear in a coherent presentation in this volume for the first time. This is abundantly true of the last section, in which the reader finds a seducing discussion of vector bundles and Yang–Mills fields, an enlightening account of exact sequences of fields and an easy introduction to initial data on null hypersurfaces — to mention only a few highlights.

This is an encyclopedia on the subject which does not venture to be encyclopedic. The omissions appear to be purposeful, with the aim of discerning the basic concepts in a clear setting. Some minor corrections have been included in the new edition. It takes only a casual glance at any of the illustrations or excerpt from the text (whose style is elegant yet readable without any prior knowledge of spinors) for the reader to ascertain of what is felt throughout the volume: the classy touch of genius.

Z. Perjés

Industrial Application of Radioisotopes

Edited by: G. Földiák, Akadémiai Kiadó, Budapest, 1986 pp. 564

The thick and considerable-sized book is a very correctly edited compendium of all application areas of the radioisotopes in the up-to-date industry. With the Editor as author of one chapter, 16 other experts from different institutions took part as contributors and after all, there are no repetitions, or overlapped parts in the book.

The 8 main topics are: 1. Basic data and definitions, 2. Nuclear instruments and measurements, 3. Radiotracer techniques — study of material-flow in industrial processes, in physical and chemical research and in biologically active chemicals. 4. Radioanalytical methods — based on physical interaction with radiation, activation analysis and analytical application of tracer methods, 5. Nuclear borehole geophysics, 6. Radiation technologies, 7. Industrial radiography — autoradiography, 8. Radiation protection. Each part gives not only a survey of the topic with a few examples, but endeavours to demonstrate — with many block schemes, schematic outlines, measurement configurations, chemical reaction schemes and other figures all methods existing at present.

Particularly valuable are the numerous different tables with many thousand up-to-date

and many, theoretically explained explicit formulas. So the book is very profitable for everyone theoretically or practically interested in the application of radioisotopes in industry.

L. Bozóky

HÉLÈNE LEFEBVRE-BRION and *ROBERT W. FIELD: Perturbations in the Spectra of Diatomic Molecules*

Academic Press, Inc., Publishers, Orlando, 1986, pp. 420

Spectroscopic perturbation in the narrower sense is the phenomenon when, in the branches of a band, the wave numbers and intensities of spectral lines as functions of the rotational quantum number show gradual deviations from the laws observed previously, and then, passing through a maximum, the deviations cease to exist and the original law is restored.

Perturbation in the wider sense is every phenomenon that cannot be described by the model of the separable wave equation. Formulating it in this way, we may say that practically all the theory of molecular spectra belongs here, including the various cases of multiplet structures, spin interactions, Λ-type doublets, intensity anomalies, predissociations, intercombination transitions, etc. Taking all this into account, the authors really take into consideration almost all relevant problems of the structure of diatomic molecules. More precisely, the book deals with the revisualizing of the theory of rotating-vibrating diatomic molecules with nonzero spin and orbital angular momenta, of the calculation of matrix elements of all of the important terms in the molecular Hamiltonian, with the relationships among molecular constants and perturbation parameters and with specific examples.

Whereas, however, the reviewer's monograph on similar problems is primarily concerned with the rotational structure of the spectra of diatomic molecules, the authors of the book reviewed here lay the main emphasis on the electronic structure of molecules. In this regard, the book fills a gap and supplements very well the literature available at present.

At the end of each Chapter the authors list the literature cited by them for that Chapter. Unfortunately, however, the greater part (85%) of the cited literature dates from the period after 1963 (the year when one of the authors (H.L.B.) took up the study of the subject), although the majority of fundamental and pioneering works originate from the 30-35 year period preceding that date. However, the authors fail to pay proper attention to this fact and generally do not quote the original works themselves, but their reformulated, re-written, supplemented and improved versions, sometimes their compilations published after 1963, clad in more up-to-date forms. Thus, the reader who relies on the information contained in the book, is misled under the impression that the fundamental study of perturbations and the development of their theory were the products of the past 25 years.

Apart from this deficiency, the book, in addition to other monographs so far published and used in this field of research, may be regarded as a further useful contribution.

I. Kovács
Department of Atomic Physics
Technical University
Budapest

Manuscript received by Akadémiai Kiadó: 22 July 1987
Received for TEX typesetting by the Computer Automation Institute
of the Hungarian Academy of Sciences: 18 March 1988
Date of publication: 24 February 1989

PRINTED IN HUNGARY

Akadémiai Kiadó és Nyomda Vállalat, Budapest

NOTES TO CONTRIBUTORS

I. PAPERS will be considered for publication in Acta Physica Hungarica only if they have not previously been published or submitted for publication elsewhere. They may be written in English, French, German or Russian.

Papers should be submitted to

Prof. I. Kovács, Editor
Department of Atomic Physics, Technical University
1521 Budapest, Budafoki út 8, Hungary

Papers may be either articles with abstracts or short communications. Both should be as concise as possible, articles in general not exceeding 25 typed pages, short communications 8 typed pages.

II. MANUSCRIPTS

1. Papers should be submitted in three copies.
2. The text of papers must be of high stylistic standard, requiring minor corrections only.
3. Manuscripts should be typed in double spacing on good quality paper, with generous margins.
4. The name of the author(s) and of the institutes where the work was carried out should appear on the first page of the manuscript.
5. Particular care should be taken with mathematical expressions. The following should be clearly distinguished, e.g. by underlining in different colours: special founts (italics, script, bold type, Greek, Gothic, etc.); capital and small letters; subscripts and superscripts, e.g. x^2, x_3; small *l* and l; zero and capital O; in expressions written by hand: *e* and *l*, *n* and *u*, *v* and v, etc.

A List of Symbols on a separate sheet should be attached to each paper.

6. References should be numbered serially and listed at the end of the paper in the following form: J. Ise and W. D. Fretter, Phys. Rev., *76*, 933, 1949.

For books, please give the initials and family name of the author(s), title, name of publisher, place and year of publication, e.g.: J. C. Slater, Quantum Theory of Atomic Structures, I. McGraw-Hill Book Company, Inc., New York, 1960.

References should be given in the text in the following forms: Heisenberg [5] or [5].

7. Captions to illustrations should be listed on a separate sheet, not inserted in the text.
8. In papers submitted to Acta Physica all measures should be expressed in SI units.

III. ILLUSTRATIONS AND TABLES

1. Each paper should be accompanied by three sets of illustrations, one of which must be ready for the blockmaker. The other sets attached to the copies of the manuscript may be rough drawings in pencil or photocopies.
2. Illustrations must not be inserted in the text.
3. All illustrations should be identified in blue pencil by the author's name, abbreviated title of the paper and figure number.
4. Tables should be typed on separate pages and have captions describing their content. Clear wording of column heads is advisable. Tables should be numbered in Roman numerals (I, II, III, etc.).

IV. RETURN OF MATERIAL

Owing to high postage costs, the Editorial Office cannot undertake to return *all* material not accepted for any reason for publication. Of papers to be revised (for not being in conformity with the above Notes or other reasons) only *one* copy will be returned. Material rejected for lack of space or on account of the Referees' opinion will not be returned to authors outside Europe.

Periodicals of the Hungarian Academy of Sciences are obtainable at the following addresses:

AUSTRALIA
C.B.D. LIBRARY AND SUBSCRIPTION SERVICE
Box 4886, G.P.O., *Sydney N.S.W. 2001*
COSMOS BOOKSHOP, 145 Ackland Street
St. Kilda (Melbourne), Victoria 3182

AUSTRIA
GLOBUS, Höchstädtplatz 3, *1206 Wien XX*

BELGIUM
OFFICE INTERNATIONAL DES PERIODIQUES
Avenue Louise, 485, *1050 Bruxelles*
E. STORY-SCIENTIA P.V.B.A.
P. van Duyseplein 8, *9000 Gent*

BULGARIA
HEMUS, Bulvar Ruszki 6, *Sofia*

CANADA
PANNONIA BOOKS, P.O. Box 1017
Postal Station "B", *Toronto, Ont. M5T 2T8*

CHINA
CNPICOR, Periodical Department, P.O. Box 50
Peking

CZECHOSLOVAKIA
MAD'ARSKA KULTURA, Národni třida 22
115 66 Praha
PNS DOVOZ TISKU, Vinohradská 46, *Praha 2*
PNS DOVOZ TLAČE, *Bratislava 2*

DENMARK
EJNAR MUNKSGAARD, 35, Nørre Søgade
1370 Copenhagen K

FEDERAL REPUBLIC OF GERMANY
KUNST UND WISSEN ERICH BIEBER
Postfach 46, *7000 Stuttgart 1*

FINLAND
AKATEEMINEN KIRJAKAUPPA, P.O. Box 128
00101 Helsinki 10

FRANCE
DAWSON-FRANCE S.A., B.P. 40, *91121 Palaiseau*
OFFICE INTERNATIONAL DE DOCUMENTATION ET LIBRAIRIE, 48 rue Gay-Lussac
75240 Paris, Cedex 05

GERMAN DEMOCRATIC REPUBLIC
HAUS DER UNGARISCHEN KULTUR
Karl Liebknecht-Straße 9, *DDR-102 Berlin*

GREAT BRITAIN
BLACKWELL'S PERIODICALS DIVISION
Hythe Bridge Street, *Oxford OX1 2ET*
BUMPUS, HALDANE AND MAXWELL LTD.
Cowper Works, *Olney, Bucks MK46 4BN*
COLLET'S HOLDINGS LTD., Denington Estate,
Wellingborough, Northants NN8 2QT
WM DAWSON AND SONS LTD., Cannon House
Folkstone, Kent CT19 5EE
H. K. LEWIS AND CO., 136 Gower Street
London WC1E 6BS

GREECE
KOSTARAKIS BROTHERS INTERNATIONAL BOOKSELLERS, 2 Hippokratous Street, *Athens-143*

HOLLAND
FAXON EUROPE, P.O. Box 167
1000 AD Amsterdam
MARTINUS NIJHOFF B. V.
Lange Voorhout 9–11, *Den Haag*
SWETS SUBSCRIPTION SERVICE
P.O. Box 830, 2160 Sz Lisse

INDIA
ALLIED PUBLISHING PVT. LTD.
750 Mount Road, *Madras 600002*
CENTRAL NEWS AGENCY PVT. LTD.
Connaught Circus, *New Delhi 110001*
INTERNATIONAL BOOK HOUSE PVT. LTD.
Madame Cama Road, *Bombay 400039*

ITALY
D. E. A., Via Lima 28, *00198 Roma*
INTERSCIENTIA, Via Mazzé 28, *10149 Torino*
LIBRERIA COMMISSIONARIA SANSONI
Via Lamarmora 45, *50121 Firenze*
SANTO VANASIA, Via M. Macchi 58
20124 Milano

JAPAN
KINOKUNIYA COMPANY LTD.
Journal Department, P.O. Box 55
Chitose, *Tokyo 156*
MARUZEN COMPANY LTD., Book Department
P.O. Box 5050 Tokyo International, *Tokyo 100-31*
NAUKA LTD., Import Department
2-30-19 Minami Ikebukuro, Toshima-ku, *Tokyo 171*

KOREA
CHULPANMUL, *Phenjan*

NORWAY
TANUM-TIDSKRIFT-SENTRALEN A.S.
Karl Johansgata 43, *1000 Oslo*

POLAND
WĘGIERSKI INSTYTUT KULTURY
Marszalkowska 80, *00-517 Warszawa*
CKP I W, ul. Towarowa 28, *00-958 Warszawa*

ROUMANIA
D. E. P., *Bucuresti*
ILEXIM, Calea Grivitei 64–66, *Bucuresti*

SOVIET UNION
SOYUZPECHAT — IMPORT, *Moscow*
and the post offices in each town
MEZHDUNARODNAYA KNIGA, *Moscow G-200*

SPAIN
DIAZ DE SANTOS Lagasca 95, *Madrid 6*

SWEDEN
ESSELTE TIDSKRIFTSCENTRALEN
Box 62, *101 20 Stockholm*

SWITZERLAND
KARGER LIBRI AG, Petersgraben 31, *4011 Basel*

USA
EBSCO SUBSCRIPTION SERVICES
P.O. Box 1943, *Birmingham, Alabama 35201*
F. W. FAXON COMPANY, INC.
15 Southwest Park, *Westwood Mass. 02090*
MAJOR SCIENTIFIC SUBSCRIPTIONS
1851 Diplomat, P.O. Box 819074,
Pallas, Tx. 75381-9074
READ-MORE PUBLICATIONS, INC.
140 Cedar Street, *New York, N. Y. 10006*

YUGOSLAVIA
JUGOSLOVENSKA KNJIGA, Terazije 27, *Beograd*
FORUM, Vojvode Mišića 1, *21000 Novi Sad*

Index: 26.022

Acta Physica Hungarica

VOLUME 65 · NUMBERS 2–3, 1989

EDITOR–IN–CHIEF

I. KOVÁCS

EDITORIAL BOARD

Z. BAY, R. GÁSPÁR, I. GYARMATI, N. KÜRTI,
K. NAGY, L. PÁL, P. SZÉPFALUSY, I. TARJÁN,
B. TELEGDI, L. TISZA, E. WIGNER



Akadémiai Kiadó, Budapest

ACTA PHYS. HUNG. APAHAQ 65 (2–3) 135–366 (1989) HU ISSN 0231–4428

ACTA PHYSICA HUNGARICA

A JOURNAL OF THE HUNGARIAN ACADEMY OF SCIENCES

EDITED BY
I. KOVÁCS

Acta Physica publishes original papers on subjects in physics. Papers are accepted in English, French, German and Russian.

Acta Physica is published in two yearly volumes (4 issues each) by

AKADÉMIAI KIADÓ
Publishing House of the Hungarian Academy of Sciences
H-1054 Budapest, Alkotmány u. 21

Subscription information

Orders should be addressed to

KULTURA Foreign Trading Company
1389 Budapest P.O. Box 149

or to its representatives abroad.

Acta Physica Hungarica is abstracted/indexed in Chemical Abstracts, Mathematical Reviews, Science Abstracts, Physics Briefs, Risk Abstracts

© Akadémiai Kiadó, Budapest

CONTENTS

ATOMIC AND MOLECULAR PHYSICS

Study of the convoy electron production from solids with hydrogenic Ni-ions. *J. Kemmler, O. Heil, H. Rothard, K. Kroneberger, S. Lencinas, K. O. Groeneveld, C. Biedermann* and *I. A. Sellin* 135

On the cross sections for electron transfer, ejection, and excitation in coincidence with a hole in a specific shell. *Richard L. Becker* 141

Depth profiling by ion-beam analysis. *K. Ishii* and *S. Morita* 151

Electronegativities and hardnesses of several atoms and ions calculated with the Xα method having self-consistent parameter α. *R. Gáspár* and *Á. Nagy* 159

Wave function effects in K-shell ionization. *T.Mukoyama* 165

Relativistic phenomena in atomic and chemical physics: opportunites for studies with synchrotron radiation. *B. Crasemann* 171

High-resolution electron spectroscopy of radioactive samples using the ESA12 electrostatic spectrometer. *V. Brabec, O. Dragoun, N. Dragounová, J. Novák, M. Fišer, A. Kovalik* and *M. Ryšavý* 183

Ejected electrons at backward angles from He and Ne by He^{2+} impact. *Gy. Szabó, Á. Kövér* and *L. Gulyás* 195

L-shell ionization and L X-ray emission induced by antiprotons. *L. Sarkadi* 201

Resolution and detection of weak X-ray lines using a Si (Li) detector combined with absorbers. *T. Papp* and *J. Pálinkás* 209

An experimental method for resolution calibration of electron spectrometers. *L. Kövér, J. Tóth* and *A. Itoh* 217

Study of the chemical shift of K X-ray lines with a home-built X-ray crystal spectrometer. *I. Török* 225

The reduction of the systematic error caused by the nuclear background in high resolution electron spectroscopy of high-energy ion–atom collisions. *I. Kádár, S. Ricz, B. Sulik, D. Varga* and *J. Végh* 229

An apparatus for low energy atomphysical experiments and the first results. *L. Szótér, J. Macsuga, B. Palásthy* and *G. Vitéz* 239

On the energy dependence of the electron shake processes. *E. Vatai* 257

Ab initio theoretical study of the structures and stabilities of the $LiBeH_3$, Li_2BeH_4 and $LiBe_2H_5$ molecules. *I. Tamássy-Lentei* and *J. Szaniszló* 265

NUCLEAR AND HIGH ENERGY PHYSICS

Measurement of the fission cross-section ratio for $^{237}Np/^{235}U$ around 14 MeV neutron energies. *L. Desdín, S. Szegedi* and *J. Csikai* 271

New data for $^{12}C(p,\gamma)^{13}N$ radiative capture process: note on an anomaly in thick target measurements. *Á.Z. Kiss, E. Koltay* and *E. Somorjai* 277
Low energy alpha scattering on ^{62}Ni. *Z. Máté, S. Szilágyi, L. Zolnai, A. Bredbacka, M. Brenner, K.M. Källman* and *P. Manngard* 287
Nuclear structure of ^{116}In. *T. Fényes* and *Zs. Dombrádi* 295
On the role of anti-bound states in the RPA description of the giant monopole resonance. *T. Vertse, P. Curutchet, R.J. Liotta* and *J. Bang* 305
What happened to the iron in the Sun? *G. Marx* and *D.S.P. Dearborn* 315
Searching for monopoles in Lake Baikal. *G.V. Domogatsky, P. Kakas, S. Fehér* and *D. Kiss* . 323
Dirac particle in a periodic field. *I. Lovas* and *Livia Molnár* 331

INTERDISCIPLINARY

The problem of anomalous near surface diffusion. *J. Giber, S. Kristyán* and *P. Deák* 335
Gaia hypothesis and atmospheric aerosol. *E. Mészáros* 343
Are lymphocytes excitable cells? *S. Damjanovich, M. Balázs* and *J. Szöllősi* 349
Measurement of oxide-layer thickness of internal granules in high-purity aluminium. *S. Takács, F. Ditrói* and *I. Mahunka* 355
A study of third harmonic mode acceleration for the MGC. *Z. Kormány, I. Szücs, A. Valek* and *J. Vámosi* 359

The final manuscript was received by the Editorial Office on 1st February 1988

Manuscript received by Akadémiai Kiadó:
13 May 1988
Manuscript received by TYPOTEX GT
for TEX typesetting on 10 March 1989

Date of publication: 20 October 1989

PRINTED IN HUNGARY

Akadémiai Kiadó és Nyomda Vállalat, Budapest

Acta Physica Hungarica 65 (2–3), pp. 135–139 (1989)

STUDY OF THE CONVOY ELECTRON PRODUCTION FROM SOLIDS WITH HYDROGENIC Ni-IONS*

J. KEMMLER, O. HEIL, H. ROTHARD, K. KRONEBERGER, S. LENCINAS and K.O. GROENEVELD

Institut für Kernphysik der J.W. Goethe Universität
D-6000, Frankfurt/M, Germany

C. BIEDERMANN

Institut für Kernphysik der J.W. Goethe Universität
D-6000, Frankfurt/M, Germany and
University of Tennessee and Oak Ridge National Laboratory
Oak Ridge, Tennessee, USA

and

I.A. SELLIN

University of Tennessee and Oak Ridge National Laboratory
Oak Ridge, Tennessee, USA

We have measured the target thickness dependent convoy electron yields Y_e from hydrogenic Ni^{27+}, Ni^{28+} (15.6 MeV/u) which is discussed in the framework of an extended model for ELC and ECC in solids considering also contributions from excited states. To understand the target thickness dependent evolution in the case of incident Ni^{27+} it must be assumed that convoy electrons produced by ELC arise mainly from excited states. The mean transport length λ_c for convoy electrons for light projectile ions is equal to the attenuation length of isotachic free electrons λ_e, whereas for the heavy ions an enhanced transport length $\lambda_c >> \lambda_e$ must be introduced.

The understanding of electron production in ion–atom and ion–solid collisions in general is based on the same conceptions. Differences arise from the high collision rate for ions penetrating a thin solid, whereas in an ion–atom interaction normally single collision conditions are assumed. As a consequence of this high collision rate the population of excited states for ions penetrating solids is shifted towards higher n and ℓ states in [1]. This atomic charge cloud around a fast highly charged ion inside the solid can be a source for the formation of electrons in low-energy continuum states, i.e. "convoy" electrons accompanying the projectile just above the ionization threshold with direction and velocity close to those of the ion [1].

To understand the mechanism for the production of convoy electrons induced by heavy projectile ions penetrating solid targets we measured the target thickness

*Dedicated to Academician D. Berényi on his 60th birthday.

dependence of the convoy electron production $Y_e(\rho x)$ and the evolution of the outgoing charge states $F(q_f)$ for hydrogen like Ni^{27+} and Ni^{28+} ions. The resulting equilibrium charge fractions are given in Table I.

Table I

Equilibrium charge state fraction $F_\infty(q_f)$ for Ni^{27+} and Ni^{28+} (15.6 MeV/u) on carbon foil

Outgoing charge q_f	Fraction $F_\infty(q_f)$[%]
28	40
27	44
26	12
25	≤ 3

It was attempted to describe the yield $Y_e(\rho x)$ for these heavy hydrogen like ions in the framework of model for ELC (*e*lectron *l*oss to the *c*ontinuum) and ECC (*e*lectron *c*apture to the *c*ontinuum) in solids introduced earlier for the case of light hydrogen projectiles [2] which has later been extended to the case of heavy projectile ions [3].

The essential concept of this model is based on the assumption that convoy electron production is closely related to the charge exchange processes. The number of convoy electrons $Y_{ECC}(q_f)$ produced by the ECC mechanism and detected in correlation with the outgoing charge state q_f is supposed to be proportional to the number of projectiles $N(q_f)$ with charge q_f (see Eq. (1)). In the same way the number of convoy electrons $Y_{ELC}(q_f)$ produced by an ELC event is proportional to the number of projectiles $N(q_{f-1})$ with charge q_{f-1}. To account for the different probabilities for electron loss from excited and ground states the number of projectiles with one electron has to be divided into the ground state fraction and the number of ions in excited states $N^*(q_{f-1})$. For a complete understanding of the relations between charge exchange and convoy electron production therefore a knowledge of the charge and excited state distribution is necessary.

Beside the terms which describe the production of convoy electrons an additional term accounts for the transport of these electrons through the bulk of the solid. In Eq. (1) this has been included by the exponential factor with the characteristic leghth λ_c which describes the inelastic and elastic scattering of convoy electrons by the atoms and electrons of the solid.

$$Y_e(q_f) = \int dx' \exp[(x - x')/\lambda_c] \{ F(q, x') \alpha_c \sigma_{q,q-1} + \\ + F(q-1, x') \alpha_L \sigma_{q-1,q} \}. \quad (1)$$

To evaluate the charge exchange cross sections we apply here the model of charge exchange introduced by Allison [4] for gas-targets. When in a first approach the excited state contribution (otherwise associated with λ_{ce} [3, 6]) is neglected we can determine values for the single electron loss and capture cross section for the studied collision system (Table II).

Table II

Charge changing cross sections for Ni (15.6 MeV/u) incident on solid carbon according to the model of Allison [4]. Also shown are cross sections from [5] for Ni (17.2 MeV/u)

Cross section [5] (10^{-19}cm^2/C-atom)	Ni (15.6 MeV/u)	Ni (17.2 MeV/u)
$\sigma_{28,27}$	0.31	
$\sigma_{27,28}$	0.28	0.082
$\sigma_{27,26}$	0.8	
$\sigma_{26,27}$	2.9	0.074

A comparison to the cross section from [5] shows large differences which could have their origin in the different methods of evaluation of the data. The loss cross sections of [5] shown in Table II can only be compared with some care to our results, because there it was intended to determine single electron loss cross sections from ground states under single collision conditions whereas in the present paper the charge evolution model from Allison was used.

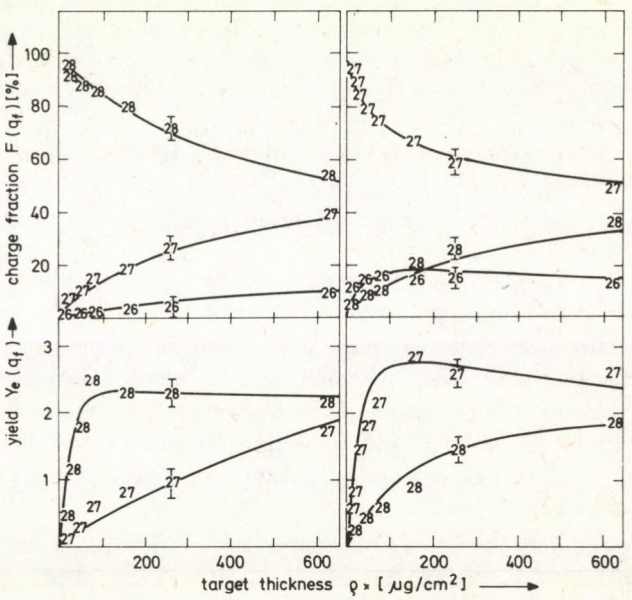

Fig. 1. In the top of the target thickness (ρx) dependence of the charge fraction $F(q_f)$ for incoming projectile ions Ni^{28+} (left side) and Ni^{27+} (right side) with energy $E_p = 15.6$ MeV/u is shown. The bottom displays the according convoy electron yield $Y_e(q_f)$, normalized to the sum of projectiles of all charge states, in coincidence with the outgoing projectile ion with charge q_f for incoming charges Ni^{28+} (left side) and Ni^{27+} (right side). The numbers in the figure denote the outgoing charge q_f

The fitted charge state evolution $F(q_f)$ was introduced into Eq. (1) and the resulting convoy elctron yield $Y_e(q_i, q_f)$ for different combinations of incident q_i and outgoing charge q_f was determined by fitting α_L and α_c and λ_c (see Fig. 1). The result of this procedure is shown in Table III.

Table III

Results of the fitting procedure according to Eq. (1).
The so-called ECC contribution includes both
direct ECC and two step processes as described in the text

Outgoing charge	Equilibrium contribution		λ_c	λ_{ce}
q_f	ECC [%]	ELC [%]	$[\mu g/cm^2]$	
28	49±8	51±8	24±5	200±20
27	67±14	33±14	24±5	—

The corresponding contribution of ECC and ELC events was determined roughly 50% for each case in the equilibrium of the convoy electron production (Table III). Electrons which are captured into highly excited states and immediately lost into the continuum are also accounted as ECC events. From our measurement this contribution cannot be distinguished from direct ECC events [6].

To give a consistent description of the evolution of the convoy electron yield these parameters must also fit the case of Y_e ($q_i = 27$, $q_f = 28$), because in the equilibrium region the origin of the convoy electrons should be the same. But straightfoward usage of these parameters fails in describing the data. A detailed analysis of the yield $Y_e(\rho x)$ according to this model leads to a consistent description of the ρx dependence of the yield Y_e when the influence of the excited states is considered [6]. Also the mean transport length λ_c for these electrons through the bulk of the solid was found to be enhanced, compared with the value for the isotachic free electrons λ_e. In a recent paper Burgdörfer [7] showed that the close correlation between an electron and a highly charged ion can persist for path length much longer than a typical mean free path for free electrons. From our measurements we interpreted the specific increase in the convoy electron yield Y_e ($q_i = 28$, $q_f = 28$) as a hint for the existence of the Coulomb focussing effect. One important argument is that in the present work also the evolution of the charge- and excited states were considered to describe the evolution of the convoy electron yield. From the derived cross sections given in Tables II and III no information can be obtained that only these processes can give a satisfactory explanation for the observed evolution of the convoy electron yield.

This work has been funded by the German Federal Minister for Reseach and Technology (BMFT) under the contract number 060F173/2 Ti476, GSI/Darmstadt, DFG/Bonn, NSF/Washington and NATO/Brussels.

References

1. H. D. Betz, D. Rönschenthaler and J. Rothermel, Phys. Rev. Lett., *50*, 34, 1983.
2. P. Koschar, A. Clouvas, O. Heil, M. Burkhard, J. Kemmler and K. O. Groeneveld, Nucl. Instr. Meth., *B24/25*, 153, 1987.
3. J. Kemmler, O. Heil, C. Biedermann, P. Koschar, H. Rothard, K. Kroneberger, K. O. Groeneveld, A. Köver, L. Gulyas, D. Berényi, P. Focke and W. Meckbach, in: "High-Energy Ion-Atom Collisions" D. Berényi, G. Hock, Eds. Springer, Heidelberg, Lecture Notes in Physics, 294.
4. S. K. Allison, Rev. Mod. Phys., *30*, 1137, 1958.
5. C. J. Sofield, L. S. Bridwell, C. D. Moak, P. D. Miller, D. C. Gregory, C. M. Jones, G. D. Alton and P. L. Pepmiller, Preprint, 1987.
6. J. Kemmler, P. Koschar, O. Heil, C. Biedermann, H. Rothard, H. Kroneberger, S. Lencinas, K. O. Groeneveld and I. A. Sellin, Nucl. Instr. Meth., *B33*, 281, 1988.
7. J. Burgdörfer, ref. 3, ibidem.

Acta Physica Hungarica 65 (2-3), pp. 141-149 (1989)

ON THE CROSS SECTIONS FOR ELECTRON TRANSFER, EJECTION AND EXCITATION IN COINCIDENCE WITH A HOLE IN A SPECIFIC SHELL* **

RICHARD L. BECKER

Physics Division, Oak Ridge National Laboratory
Oak Ridge, TN 37831-6373, USA

A singles (or doubles) measurement of, say, direct ionization has contributions from all events in which one (or two) electrons are ejected, including events in which additional electrons are excited, ejected, or captured. In such inclusive measurements the contributions from events in which more than the minimum required number of electrons are active can become quite significant for reactions induced by multiply charged ions. The sum of the projectile-ion induced "singles" cross sections for direct ionization, electron transfer, and excitation equals that for vacancy production in the target. We show, however, that the analogous sum of "doubles" cross sections for these processes in coincidence with a hole in a particular shell of the target (i.e. with an Auger electron or X-ray) is greater than the "singles" cross section for production of a vacancy in that shell, except in the limit of very weak interactions (exclusively single-electron transitions). The derivation is given in the independent Fermi particle representation, but the result appears to be general. Singles cross sections can be expressed entirely by terms in which only single electron transitions explicitly appear. Doubles (2-fold coincidence) cross sections require also "DET" terms in which double electron transitions appear. The DET terms are responsible for the excess in the coincidence sum mentioned above. Illustrative calculations for He^{2+} and C^{6+} on Ne show the quantitative importance of the DET terms for direct ionization as well as electron transfer. No direct ionization–hole coincidence experiment has been done yet, to our knowledge; it would provide a valuable test of the theory.

1. Introduction

Much of the work in atomic collision theory has gone into methods for calculating amplitudes for single-electron transitions. The simple expressions involving these single particle amplitudes which theorists have used for calculating cross sections usually are thought to describe exclusively single electron transition processes. Actually, these sums of absolute squares of single-electron amplitudes, Eq. (8), describe inclusive single-electron processes, defined precisely as the sum of all processes (involving arbitrarily many electrons) which satisfy the final-state conditions of the experiment. (See the general equations (1) and (3).) This is just what is measured in a "singles" experiment. For example, inclusive single direct ionization includes exclusively double direct ionization, exclusively single direct ionization together with

*Dedicated to Academician D. Berényi on his 60th birthday

**This reserach has been sponsored by the U.S. Department of Energy, Office of Basic Energy Sciences, Division of Chemical Sciences, under contract No. DE-AC05-840R21400 with Martin Marietta Energy Systems, Inc.

single electron transfer, etc. For projectile ions of low nuclear charge, even exclusively double electron processes often may be neglected. But as the capabilities to use strongly interacting, multiply charged ions have improved, it has become important to recognize that the simple theoretical expressions automatically include the contributions of multiple electron processes to "singles" measurements.

A familiar result of the independent particle model is that the cross section for the sum of all the processes which produce at least one "particle" in the final state (i.e. the occupancy of a spin-orbital which was unoccupied initially), namely the sum of the "singles" cross sections for electron transfer, direct ionization, and excitation, is equal to the "singles" cross section for vacancy production. This is clearly true for exclusively single electron processes, but is less obvious for the multiple electron transitions which contribute to the "singles" measurements. In Section 2 we show "why" this equality occurs.

The case of these "particle" production processes in coincidence with a final hole in a specific shell is more complicated. In Section 3 the expression for each of these processes in the independent Fermi particle model [1,2,3] is separated into a term which refers explicitly only to single electron transitions (SETs) and a term which refers explicitly only to double electron transitions (DETs). Each term represents an inclusive process in which a summation is made over all possible transitions of the remaining electrons, which are not explicitly mentioned. The smaller the number of electrons explicitly appearing in a term, the greater is its inclusiveness, as defined in Eqs (1) and (3). We show that the "singles" cross section for the production of a vacancy in a given shell is equal to the "explicitly SET" contribution to the sum of "doubles" cross sections for inclusive single electron transfer, direct ionization, and excitation from that shell. However, the "explicitly DET" terms are non-negligible and can be even larger than the "explicitly SET" terms. Thus, the sum of the total "doubles" cross sections for single "particle" production in coincidence with a specified hole is greater than the "singles" cross section for production of that hole. The reason has to do with differences in the multiple countings of terms in the inclusive cross sections which involve transitions of two or more electrons.

In Section 4 we provide numerical values of cross sections calculated for He^{2+} + Ne at 0.3 MeV/amu and for C^{6+} + Ne at 0.2 MeV/amu by a coupled channels method. These results illustrate the quantitative importance of the "explicitly DET" terms. This is the first calculation which has evaluated the enhancement of the usual "explicitly SET" cross section for direct ionization from a given shell by the "explicitly DET" term. Coincidence experiments to test the prediction of this enhancement would be of interest.

2. Independent Fermi particles

In the independent Fermi particle model (IFPM) the initial state of a target plus projectile system with F electrons is defined by the set of occupied spin-orbitals, h_i $(i = 1, 2, \ldots, F)$, which are eigenfunctions of the mean field (usually Hartree–

Fock) Hamiltonian. The projectile ion will be assumed initially bare or with closed shells which remain inert during the collision. For simplicity we restrict our attention to initial states of the target with at most one valence electron or hole, so that the m-scheme may be used. For a collision with a given value of the impact parameter, b, the semiclassical transition amplitude for the exclusive reaction connecting the normalized and antisymmetrized states $|h_1, \ldots, h_F>$ and $|k_1, \ldots, k_F>$ is

$$< k_1, \ldots, k_F|\mathrm{A}(b)|h_1, \ldots, h_F >= \det[a_{k,h}(b)], \quad k = k_1, \ldots, k_F; \quad h = h_1, \ldots, h_F,$$

where the $a_{k,h}$'s are the single-electron transition amplitudes. The transition probability $\rho^{k_1,\ldots,k_F}(b)$, is the absolute square of the amplitude. The probability for the inclusive reaction in which only $m < F$ of the final spin-orbitals are explicitly specified is defined by

$$\rho^{k_1,\ldots,k_m} \equiv \sum_{\substack{k_{m+1}<\cdots<k_F \\ (\neq k_1,\ldots,k_m)}}{}' \rho^{k_1,\ldots,k_F} = \det\left[a^{(2)}_{k,k'}\right], \quad k, k' = k_1, \ldots, k_m, \tag{1}$$

where the impact parameter has been suppressed and the single-particle transition density matrix elements are given by

$$a^{(2)}_{k,k'} \equiv \sum_{h}^{\mathrm{occ}} a^*_{k,h}\, a_{k',h} = a^{(2)*}_{k',k}. \tag{2}$$

Non-occupancies will be indicated by subscripts. The inclusive probability for m specified distinct vacancies is defined by

$$\rho_{v_1,\ldots,v_m} \equiv \sum_{\substack{k_1<\cdots<k_F \\ (k_i\neq v_1,\ldots,v_m)}}{}' \rho^{k_1,\ldots,k_F} = \det[\delta_{ij} - a^{(2)}_{v_i,v_j}], \quad i, j = 1, 2, \ldots, m. \tag{3}$$

The inclusive probabilities for some specified occupancies and some specified vacancies do not, in general, have such simple forms, but may be obtained from the complementarity relation for occupancy and vacancy [1,2,3],

$$\rho^{k_1,\ldots,k_m}_{v_1,\ldots,v_n} \equiv \rho^{k_1,\ldots,k_m}_{v_1,\ldots,v_n,k} + \rho^{k_1,\ldots,k_m,k}_{v_1,\ldots,v_n}, \quad m < F, \tag{4}$$

where no two of the indices are the same.

The orthonormality and completeness of the single-electron transition amplitudes, i.e. the unitarity of the transition matrix, is represented by

$$\sum_{h}^{\mathrm{occ}} a^*_{h,k}\, a_{h,k'} + \sum_{p}^{\mathrm{unoc}} a^*_{p,k}\, a_{p,k'} = \delta_{k,k'}, \tag{5}$$

where the sums are over initially occupied and unoccupied spin-orbitals, respectively. Reversibility implies

$$|a_{k,k'}| = |a_{k',k}|. \tag{6}$$

An integrated cross section corresponding to a transition probability function ρ or P, or to a sum of probabilities, Q, is calculated from

$$\sigma = 2\pi \int_0^\infty db \cdot b[\rho(b),\ P(b),\quad \text{or}\quad Q(b)]. \tag{7}$$

3. Inclusive single electron processes

The inclusive probability for the final non-occupancy of the spin-orbital k is, from (3), (5), and (6)

$$\rho_k = 1 - \rho^k = 1 - a^{(2)}_{k,k} = 1 - \sum_h^{\text{occ}} |a_{k,h}|^2 = \sum_p^{\text{unoc}} |a_{p,k}|^2. \tag{8}$$

Because (8) contains only terms which refer explicitly to a SET (from h to k or from k to p) it is a common error to think that ρ_h refers to exclusively single vacancy production (in which the hole is in the single electron state h). In fact the inclusive probability ρ_h includes all multiple vacancy production in which one of the holes is in h. From (4)

$$\rho_h = \rho_{h,h'} + \rho_h^{h'}, \quad \text{any} \quad h' \neq h \tag{8a}$$

and, for any $h'' \neq h$ or h',

$$\rho_{h,h'} = \rho_{h,h',h''} + \rho_{h,h'}^{h''} \quad , \quad \rho_h^{h'} = \rho_{h,h''}^{h'} + \rho_h^{h',h''}, \tag{8b}$$

etc. The probability for exclusively single vacancy production (in which the hole is in h_1) is $\rho_{h_1}^{h_2,\ldots,h_F}$. In the case of reactions produced by highly charged projectiles, this exclusive probability may be a small part of ρ_{h_1}. It may be helpful to mentally reword the phrase "inclusive n-fold vacancy probability" as "at least n-fold vacancy probability". For example, $\rho_{h,h'}$ means the probability for at least a vacancy in h together with a vacancy in h'. It is the sum (3) of all probabilities of exclusive reactions having at least these two holes.

Let us subdivide the set $P = \{p,$ initially unoccupied $\}$ of "particle" states p according to $P = E + \overline{E} + I$ where $E = \{e\}$, the excited states of the target, $\overline{E} = \{\bar{e}\}$, the excited states of the projectile, and $I = \{i\}$, the continuum states, which correspond to direct ionization. From (8) the inclusive probabilities for single-electron excitation, transfer, and ejection from the target to specific final states are, respectively,

$$\rho^e = \sum_h^{\text{occ}} |a_{e,h}|^2, \qquad \rho^{\bar{e}} = \sum_h^{\text{occ}} |a_{\bar{e},h}|^2,$$

and

$$\rho^i = \sum_h^{\text{occ}} |a_{i,h}|^2. \tag{9}$$

Let us denote total inclusive single-electron excitation, transfer, and direct ionization expected values by Q^E, $Q^{\bar{E}}$, and Q^I, respectively. Then

$$Q^E = \sum_e^{\text{exc}} \rho^e = \sum_e^{\text{exc}} \sum_h^{\text{occ}} |a_{e,h}|^2,$$

$$Q^{\bar{E}} = \sum_{\bar{e}}^{\text{exc}} \rho^{\bar{e}} = \sum_{\bar{e}}^{\text{exc}} \sum_h^{\text{occ}} |a_{\bar{e},h}|^2, \tag{10}$$

and

$$Q^I = \sum_i^{\text{cont}} \rho^i = \sum_i^{\text{cont}} \sum_h^{\text{occ}} |a_{i,h}|^2.$$

By summing these and using (8) we see that

$$Q^P \equiv Q^E + Q^{\bar{E}} + Q^I \equiv \sum_p^{\text{unoc}} \rho^p = Q_V \tag{11}$$

where

$$Q_V \equiv \sum_h^{\text{occ}} \rho_h = \sum_h^{\text{occ}} \sum_p^{\text{unoc}} |a_{ph}|^2 \tag{12}$$

is the expected value (a sum of probabilities, which can be greater than one) for total inclusive single vacancy production in the target.

Recall that each of these explicitly SET terms is inclusive and includes processes with up to F-electron transitions. For example,

$$\rho^i + \rho^{\bar{e}} = 2\rho^{\bar{e},i} + \rho_i^{\bar{e}} + \rho_{\bar{e}}^i$$

on the left hand side of (11) and

$$\rho_h + \rho_{h'} = 2\rho_{h,h'} + \rho_h^{h'} + \rho_{h'}^h, \qquad h \neq h'$$

on the right. The factor 2 occurs in the same way on both sides because both sides contain quantities of the same, "explicitly SET", form. Larger multiples occur in terms (see (8b)) in which more spin-orbitals are specified explicitly. These multiples are the same on both sides of (11).

We have shown in [2] that an inclusive single vacancy or single occupancy probability can be expanded in terms of number-exclusive probabilities, i.e. probabilities for producing a fixed number of occupancies, P^n, or vacancies, P_n, in a certain set of states. The probability P^n occurs with the coefficient n. (See also [4].) This is appropriate to a (singles) measurement of Q^P because for those terms with n occupancies, each of the n electrons could be detected.

4. Inclusive single-particle, single-hole coincidences

Suppose one attempts to break (11) down into contributions from electrons in the various initially occupied spin-orbitals, h. If we define

$$^{\mathrm{SET}}Q_h^I = \sum_i |a_{i,h}|^2, \qquad ^{\mathrm{SET}}Q_h^{\overline{E}} = \sum_{\overline{e}} |a_{\overline{e},h}|^2$$

and

$$^{\mathrm{SET}}Q_h^E = \sum_e |a_{e,h}|^2, \tag{13}$$

then from (8)

$$^{\mathrm{SET}}Q_h^P \equiv {}^{\mathrm{SET}}Q_h^I + {}^{\mathrm{SET}}Q_h^{\overline{E}} + {}^{\mathrm{SET}}Q_h^E = \rho_h. \tag{14}$$

However, $^{\mathrm{SET}}Q_h^P$ is not the complete IFPM expression for

$$Q_h^P \equiv Q_h^I + Q_h^{\overline{E}} + Q_h^E = \sum_p^{\mathrm{unoc}} \rho_h^p. \tag{15}$$

From (8), (4), and (1) or (3) one has (see also [5])

$$\rho_h^p = \rho^p \rho_h + |a_{p,h}^{(2)}|^2 \equiv {}^{\mathrm{dir}}\rho_h^p + {}^{\mathrm{exch}}\rho_h^p, \tag{16a}$$

where the two contributions are the direct and Pauli exchange terms, respectively. We can rewrite this [6] as

$$\rho_h^p = {}^{\mathrm{SET}}\rho_h^p + {}^{\mathrm{DET}}\rho_h^p, \tag{16b}$$

where the quadratic term, which refers explicitly only to a direct transition from h to p, is

$$^{\mathrm{SET}}\rho^p = |a_{p,h}|^2. \tag{16c}$$

It may be regarded as coming from the exchange term because the latter contains a term $|a_{ph}|^2|a_{hh}|^2$. Once again we remind the reader not to regard $^{\mathrm{SET}}\rho_h^p$ as the probability of the exclusive process $h \to p$ with all other initially occupied spin-orbital states remaining filled. Rather, $^{\mathrm{SET}}\rho_h^p$ contains a sum over all the possible processes involving the $F-1$ electrons other than the one which makes the specified transition.

The DET term in (16b) consists of its direct part

$$^{d\mathrm{DET}}\rho_h^p = {}^{\mathrm{dir}}\rho_h^p = \rho^p \rho_h \tag{16d}$$

plus its exchange part

$$^{e\mathrm{DET}}\rho_h^p = |a_{p,h}^{(2)}|^2 - |a_{p,h}|^2 = -(1 - |a_{h,h}|^2)|a_{p,h}|^2 + \\ + {\sum_{h_1(\neq h)}}' |a_{p,h_1}|^2 |a_{h,h_1}|^2 + C(p,h), \tag{16e}$$

where

$$C(p,h) = 2\,\mathrm{Re} {\sum_{h_1,h_2(h_1<h_2)}}' a_{p,h_1}^* a_{p,h_2} a_{h,h_1} a_{h,h_2}^*. \tag{17}$$

Since

$$1 - |a_{h,h}|^2 = {\sum_{k(\neq h)}}' |a_{k,h}|^2,$$

we may regard all the terms in $^{\mathrm{DET}}\rho_h^p$ as being quartic and explicitly specifying double electron transitions. All the processes involving the remaining $F-2$ electrons are included implicitly. We now have from (16d) and (11)

$$^{d\mathrm{DET}}Q_h^P = Q_V \rho_h = \sum_{h'}^{\mathrm{occ}} \rho_{h'} \rho_h. \tag{18a}$$

By using unitarity we can write $^{e\mathrm{DET}}Q_h^P$ entirely in terms of the initially occupied states, for which the transition amplitudes are sometimes more readily available. We have

$$0 < \sum_{p}^{\mathrm{unoc}} |a_{p,h}^{(2)}|^2 = \rho^h - \sum_{h'}^{\mathrm{occ}} |a_{h',h}^{(2)}|^2 = \rho^h \rho_h - {\sum_{h'(\neq h)}}' |a_{h',h}^{(2)}|^2, \tag{19}$$

so that

$$^{e\mathrm{DET}}Q_h^P = -(\rho_h)^2 - {\sum_{h'(\neq h)}}' |a_{h',h}^{(2)}|^2 < 0 \tag{18b}$$

and

$$^{\mathrm{DET}}Q_h^P = {\sum_{h'(\neq h)}}' [\rho_{h'} \rho_h - |a_{h',h}^{(2)}|^2] = {\sum_{h'(\neq h)}}' \rho_{h',h} > 0, \tag{18c}$$

an elegant form for the DET correction to the leading (SET) contribution, ρ_h (Eq. (14)).

It is usually easier to calculate excitation and direct ionization than to compute electron transfer. Conversely, it is frequently easier to measure electron transfer and excitation than to detect directly ejected electrons. For weakly interacting

collisions one can obtain from (14) an inferred experimental quantity for ionization from state h, namely

$$^{\inf}Q_h^I \equiv \rho_h - Q_h^{\overline{E}} - Q_h^E, \tag{20}$$

where the quantities on the right are assumed measured, with which to compare the theoretical SET value calculated from (13). (If the target initially has only closed shells, the Hartree–Fock field supports no bound excited states, so that Q_h^E is usually negligible. Also, the experimental measurements of inclusive vacancy production, ρ_h, and of $Q_h^{\overline{E}}$ are not often made as a function of the impact parameter, so that only the cross sections integrated over b, Eq. (7) may be available.) However, this procedure fails when the explicitly DET contributions become appreciable. Then we have

$$Q_h^I - \sum_{h'(\neq h)}{}' \rho_{h',h} = \rho_h - Q_h^{\overline{E}} - Q_h^E, \tag{21a}$$

where the right hand side may be obtained experimentally, and where the theoretial ionization-hole coincidence quantity is

$$Q_h^I = \sum_i^{\text{cont}} |a_{i,h}|^2 + \sum_i^{\text{cont}} {}^{\text{DET}}\rho_h^i. \tag{21b}$$

5. Coupled channels calculations

In [7], [8], and [6] we have calculated $\sigma_K^{\overline{E}}$, the inclusive cross section for electron transfer in coincidence with a hole in the K-shell of the target. The importance of the negative exchange term ${}^{e\text{DET}}Q_K^{\overline{E}}$ in reducing the total DET contribution was demonstrated. The calculated $\sigma_K^{\overline{E}}$ was in good agreement with the experiments [9, 10]. To our knowledge no measurements at intermediate impact energy of direct electron ejection in coincidence with a specific vacancy have been made. Here we use (21a) to evaluate Q_h^I and then (21b) to obtain ${}^{\text{DET}}Q_h^I$. The right hand side of (21a) as well as ${}^{\text{DET}}Q_h^P$, Eq. (18c), are calculated by using the unitary version of the one-and-a-half center expansion (OHCE) method in coupled channels theory[11].

One sees from Table I that for each cross section the ratio of the DET to the SET contribution increases with the nuclear charge of the bare projectile, as expected. For the direct ionization, and hence for the total "particle" production, the DET/SET ratio decreases in going from a hole in the K-shell to one in the L-shell. But even for the L-shell a traditional SET calculation of σ_h^I would seriously underestimate the IFPM value. For the cases considered, Table I implies that ${}^{\text{SET}}\sigma_L^I/\sigma_L^I = 56\%$ (He^{2+}) and 34% (C^{6+}). The dependence of these ratios on the impact energy will be reported later. For the electron transfer we found in [6] a very strong energy dependence of DET/SET over part of the energy range. For direct ionization, unlike electron transfer, the exchange part of the DET term is much less than the direct part in our illustrative calculation. A considerable simplification of the calculation of σ_h^I ensues if one includes only the direct part of the DET term.

Table I

Calculated cross sections for inclusive single "particle" (P) production, electron transfer ($\overline{E}$) and direct ionization (I) in coincidence with a hole in the K or L shell, in square meters, and ratios, R, of the DET to the SET contribution to these cross sections.
Cases: (1) He^{2+}+ Ne at 0.3 MeV/amu, (2) C^{6+}+Ne at 0.2 MeV/amu

Case	σ_K^P	$\sigma_K^{\overline{E}}$	σ_K^I	R_K^P	$R_K^{\overline{E}}$	R_K^I
1	2.3×10^{-23}	0.13×10^{-23}	2.2×10^{-23}	2.8	0.69	3.1
2	10.3×10^{-22}	1.6×10^{-22}	8.6×10^{-22}	5.8	1.2	10.2
Case	σ_L^P	$\sigma_L^{\overline{E}}$	σ_L^I	R_L^P	$R_L^{\overline{E}}$	R_L^I
1	7.6×10^{-20}	1.1×10^{-20}	6.5×10^{-20}	0.76	0.73	0.76
2	7.3×10^{-19}	0.5×10^{-19}	6.8×10^{-19}	2.0	3.3	1.9

Acknowledgement

The author extends to Prof. Dénes Berényi his warmest congratulations on his sixtieth birthday. He wishes also to thank him for his hospitality at the ATOMKI workshops and for the stimulation received from him and his colleagues on those memorable occasions.

References

1. R. L. Becker, A. L. Ford and J. F. Reading, IEEE Transactions on Nucl. Sci., *NS-28*, 1092, 1981.
2. R. L. Becker, A. L. Ford and J. F. Reading, Phys. Rev., *A 29*, 3111, 1984.
3. R. L. Becker, A. L. Ford and J. F. Reading, Nucl. Instr. and Meth., *B10/11*, 1, 1985.
4. R. L. Becker, A. L. Ford and J. F. Reading, Nucl. Instr. and Meth., *214*, 49, 1983.
5. J. F. Reading and A. L. Ford, Phys. Rev., *A21*, 124, 1980.
6. R. L. Becker, Several Manifestations of Pauli Correlations in Energetic Ion-Atom Collisions, in Proc. 3^d Workshop on High Energy Ion-Atom Collision Processes, Debrecen, 1987, Springer, Berlin, 1988, p. 447.
7. R. L. Becker, A. L. Ford and J. F. Reading, J. Phys. B: At. Molec. Phys., *13*, 4059, 1980.
8. A. L. Ford, J. F. Reading and R. L. Becker, Phys. Rev., *A23*, 510, 1981.
9. J. R. Macdonald, C. L. Cocke and W. W. Eidson, Phys. Rev. Lett., *32*, 648, 1974.
10. M. Rodbro, E. Horsdal Pedersen, C. L. Cocke and J. R. Macdonald, Phys. Rev. *A19*, 1936, 1979.
11. J. F. Reading, A. L. Ford and R. L. Becker, J. Phys. B: At. Molec. Phys., *14*, 1995, 1981.

Acta Physica Hungarica 65 (2–3), pp. 151–157 (1989)

DEPTH PROFILING BY ION-BEAM ANALYSIS*

K. ISHII

Cyclotron and Radioisotope Center, Tohoku University
980 Sendai, Japan

and

S. MORITA

Research Center of Ion Beam Technology, Hosei University
184 Koganei, Tokyo, Japan

In an ion-beam analysis, a sample is bombarded with charged-particle beams and characteristic X–rays (PIXE), nuclear γ-rays (PIGE) or charged particles produced in the target material are measured. A method for deducing a concentration depth profile of an element in the sample from a yield curve of these reaction products as a function of the projectile energy is derived on the basis of the least-squares method. Validity of this method is demonstrated taking an example of PIXE.

1. Introduction

Elemental analyses with ion beams, such as activation analyses and particle-induced X-ray emission (PIXE), have greatly been developed and recently have come into wide use. In most cases, the analysis can be applied to homogeneous samples, where the concentration is uniform and the result of high accuracy is desired [1].

Methods of depth profiling can be classified into two categories: destructive and non–destructive. In the destructive case, the concentration depth profile of an element in a sample can be directly determined; for example, in secondary-ion mass spectroscopy (SIMS), the surface of a sample is successively etched with Ar-ion beams and secondary ions emitted from the surface are mass-analysed. A method of charged-particle activation analysis combined with uniform irradiation and chemical etching, developed by Itoh and Nozaki [2], is very effective and useful for trace-element analyses. However, a non-destructive method for concentration depth profiling would be much more desirable. The Rutherford backscattering method (RBS) has widely been used, but this is not so effective for trace-element analyses, especially for light trace-element in heavier matrix elements. Recently, several studies have been reported [3–8] on the concentration depth profiling by means of PIXE, where the simultaneous multi-element analysis can be carried out. In many of these methods, approximate functional forms of concentration profile are to be known in advance and a few parameters are determined by fitting experimental

*Dedicated to Academician D. Berényi on his 60th birthday

data with calculations. Brissaud and his coworkers [9] have examined the method of Végh [3] which is based on an iterative procedure associated with data smoothing for depth profiling with PIXE. We introduce here a deconvolution method based on the least-squares method, and demonstrate the validity of this method taking an example of PIXE, though this method can be applied in principle not only to PIXE, but also to particle-induced γ-ray emission (PIGE).

2. Theory

Yields of X-rays, γ-rays or charged particles from a thick target bombarded with ion beams is expressed by

$$Y(R) = C \times \int_0^R dx\, \rho(x)\sigma(R-x), \tag{1}$$

where R is the range of incident beam in the sample and is a function of the incident-beam energy $R(E)$, $\rho(x)$ is the concentration of an impurity element at the depth x from the sample surface, $\sigma(R)$ is the production cross section of the radiation for ion beam with range R, the factor C contains a solid angle, a detection efficiency and beam currents. We assume that the beam direction is perpendicular to the sample surface, the concentration in a plane parallel to the sample surface is uniform, and the beam divergence can be neglected.

For convenience sake in later discussions, we rewrite Eq. (1) as expressed by

$$g(R) = \int_0^R \rho(x)h(R-x)dx, \tag{2}$$

where

$$g(R) \equiv Y(R)$$

and

$$h(R-x) \equiv C \times \sigma(R-x).$$

We develop the concentration $\rho(x)$ into a functional set $[f_1(x), f_2(x), \ldots]$ as expressed by

$$\rho(x) = \sum_{k=1}^{m} C_k f_k(x). \tag{3}$$

Substituting Eq. (3) into Eq. (2), we obtain the following equation,

$$g(R) = \sum_{k=1}^{m} C_k \int_0^R f_k(x)\; h(R-x)dx. \tag{4}$$

A set of $g(R)$ $[g(R_1), g(R_2), \ldots, g(R_n)]$, corresponding to a set of particle range $[R_1 \equiv R(E_1), R_2 \equiv R(E_2), \ldots, R_n \equiv R(E_n)$ with $R_1 < R_2 < \cdots < R_n]$, can be given by experimental measurements. If we know a functional form of the cross section $\sigma(R)$, equations for the coefficients $[C_k]$ can be expressed by

$$B_j = \sum_{k=1}^{m} A_{j,k} C_k, \quad j = 1, 2, \ldots, n, \tag{5}$$

where

$$B_j \equiv g(R_j)$$

and

$$A_{j,k} \equiv \int_0^{R_j} f_k(x)\, h(R_j - x) dx.$$

Now, we apply the least-squares method to Eq. (5). When the sum S of residual squares, which is defined by

$$S \equiv \sum_{j=1} \left(B_j - \sum_{k=1}^{m} A_{j,k} C_k \right)^2 / (\sigma_j)^2, \tag{6}$$

takes a minimum value, a linear equation for $[C_k]$ is required as expressed by

$$F_i = \sum_{k=1}^{m} D_{i,k} C_k, \quad i = 1, 2, \ldots, m, \tag{7}$$

where

$$F_i \equiv \sum_{j=1}^{n} B_j A_{j,i} / (\sigma_j)^2$$

and

$$D_{i,k} \equiv \sum_{j=1}^{n} A_{j,k} A_{j,i} / (\sigma_j)^2.$$

In the above equations, σ_j means the standard deviation of $g(R_j)$. The coefficients $[C_k]$ can be obtained by solving Eq. (7). However, the number m of the coefficients should be determined from other procedures. Akaike has developed the information theory of Kullback–Leibler [10] and has introduced the information criterion [11], so called Akaike's information criterion (AIC), which represents a degree of optimum in the choice of model function and of the number of parameters and is defined by

$$AIC \equiv -2\, \ell\, n(\text{maximum likelihood}) + 2m.$$

In the case where the error is of the normal distribution and absolute values of the experimental error are unknown, AIC can be approximated by

$$AIC = n\,\ell\, nS + 2m. \tag{8}$$

Choosing the value of m and the functional set $[f_k]$, which gives the minimum of AIC, we can obtain the most significant estimation for the concentration $\rho(r)$. Since the non-destructive method is indirect in general, it is very complicated to estimate the accuracy of the reproduced profile $\rho(x)$. In the present method, the error of profile $\delta\rho(x)$ induced by the experimental errors σ_j for $g(x_j)$ can be given by

$$(\delta\rho(x))^2 = \sum_{j=1}^{n} \left(\frac{\partial\rho(x)}{\partial g(x_j)}\right)^2 \sigma_j^2. \tag{9}$$

The coefficient $\partial\rho(x)/\partial g(x_j)$ is calculated from Eqs (3) and (7);

$$\frac{\partial\rho(x)}{\partial g(x_j)} = \sigma_j^{-2} \sum_{k=1}^{m}\sum_{\ell=1}^{m} D_{k,\ell}^{-1}\, A_{j,\ell}\, f_k(x), \tag{10}$$

where the matrix $[D_{k,\ell}^{-1}]$ means the inverse matrix of $[D_{k,\ell}]$.

3. Discussion

By using the present method based on the least-squares method, concentration of an element can be obtained as a function of depth from the surface. We discuss here the validity of this method by taking an example of PIXE, where the reaction cross section is well-known, whereas a nuclear reaction cross section is generally complicated.

The X-ray production cross section by heavy-charged-particle bombardments in low-energy region, usually used in PIXE, is approximately expressed by

$$\sigma(E_i) = \text{const} \cdot E_i^4, \tag{11}$$

where E_i is the incident energy. The range of incident particle is also approximated by

$$R(E_i) = \text{const} \cdot {E_i}^2. \tag{12}$$

As seen from Eq. (11), the X-ray production cross section rapidly decreases with decrease in the incident energy. Thus the contribution of X-rays produced in deep region can be neglected comparing with that at the surface region. This fact makes difficult the profiling in deep region. Therefore, it would be reasonable

to examine our method using the concentration profile which decreases toward the inside of sample. We assume the following function as a model function

$$\rho(x) = e^{-0.1x}. \tag{13}$$

Here, the depth x is in μm. Taking the const. in Eq. (12) as 10.5, the range $R(E_i)$, where E_i is in MeV units, is normalized to that of 2-MeV protons in Al: 42 μm. In accordance with Eqs (1), (11), (12) and (13), we calculate the X-ray yields $Y(R)$ corresponding to the proton range $R_1 = 3$ μm ($E_1 = 0.5345$ MeV), $R_2 = 6\mu$m ($E_2 = 0.7559$ MeV), $R_3 = 9$ μm ($E_3 = 0.9258$ MeV),..., $R_{14} = 42$ μm ($E_{14} = 2.000$ MeV), and take the calculated values with four significant figures as the experimental data.

We assume also the errors for the hypothetical experimental data as

$$\sigma_1/Y(R_1) = 5\%, \ldots, \sigma_{14}/Y(R_{14}) = 1\%, \tag{14}$$

where $\sigma_i/Y(R_i)$ decreases linearly with increase in the data number. Larger errors for lower incident energy take into consideration of the smaller X-ray production cross section for lower incident energy.

We consider two functional sets; one is the Fourier functional set

$$\begin{aligned} f_1(x) &= 1, \\ f_2(x) &= \sin(\frac{2\pi}{L}x), \\ f_3(x) &= \cos(\frac{2\pi}{L}x), \\ f_4(x) &= \sin(\frac{4\pi}{L}x), \\ f_5(x) &= \cos(\frac{4\pi}{L}x), \\ &\vdots \end{aligned}$$

where L takes twice of the beam range for the maximum incident energy, and the other is the polynomial functional set

$$\begin{aligned} f_1(x) &= 1, \\ f_2(x) &= x, \\ f_3(x) &= x^2, \\ &\vdots \end{aligned}$$

The results of depth profiling obtained by our method described in §2 for the hypothetical experimental data are shown in Fig. 1 and Fig. 2. Figure 1 shows

values of AIC for the number of parameters m together with those of S defined by Eq. (6). In the case of the Fourier functional set, the minimum value of AIC is -61.9 and the number of parameters m is determined to be 6. For the polynomial functional set, AIC takes the minimum value of -62.6 for $m = 5$. As seen in the behaviour of AIC and S, the dependence of S on m is also available to determine the number of parameters. The depth profiles reproduced by the present method are shown in Fig. 2, where the dotted lines are the reproduced ones with error bars and the solid lines are the model function of $e^{-0.1x}$. The reproduced profiles agree

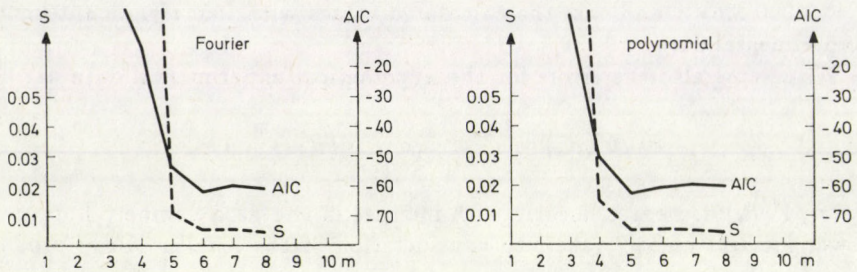

Fig. 1. Akaike's information criterion (AIC) for the Fourier functional set and the polynomial functional set. The solid line shows the AIC of Eq. (8) and the dotted line S represents the sum of residual squares (Eq. 6)

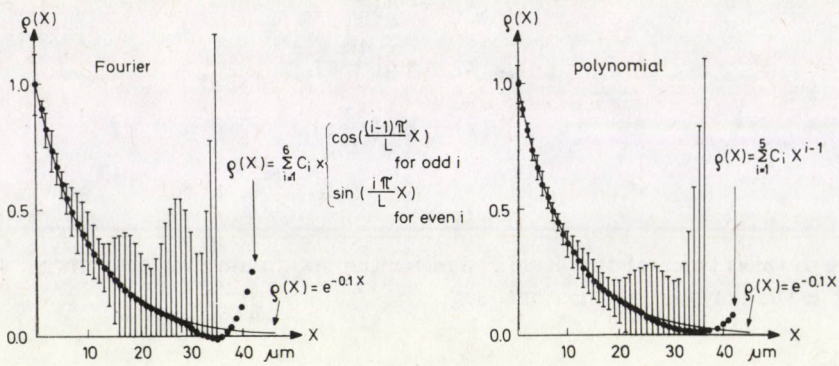

Fig. 2. Depth profiles reproduced by using the Fourier functional set and the polynomial functional set. The solid line represents the model function of the depth profile. The dotted line is the reproduced depth profile and the bars show the accuracy of reproducibility

well with the model function. These agreements are due to good accuracy of the adopted values of hypothetical data with four significant figures. By using the data

obtained with the accuracy of Eq. (14), the depth profile can be reproduced within the error bars. The polynomial functional set gives 20 μm for the reproducible depth range and that of the Fourier functional set gives 15 μm. Therefore, in the present example, it is said that the polynomial set is superior to the Fourier set in the depth profiling.

4. Summary

In order to obtain a concentration depth profile from yield curves of X–rays, γ–rays or charged particles produced by ion-beam bombardments, a method based on the least-squares technique has been derived. In conformity with this method, the depth profile can be derived from experimental radiation yields as a function of the incident-particle energy. Validity of the present method has been shown for the determination of concentration distribution by using PIXE.

Acknowledgement

This work was supported by the Special Project Research on Ion Beam Interaction with Solids from the Ministry of Education, Science and Culture.

References

1. K. Ishii, M. Valladon and J. L. Debrun, Nucl. Instr. and Meth., *150*, 212, 1978.
2. Y. Itoh and Nozaki, J. Radiochemi., 70, 329, 1982.
3. J. Végh, D. Berényi, E. Koltay, I. Kiss, S. Seif Ernasr and L.Sarkadi, Nucl. Instr. and Meth., *153*, 553, 1978.
4. V. Rössinger, Nucl. Instr. and Meth., *196*, 483, 1982.
5. O. Benka, M. Geretschläger and A. Kropf, Nucl. Instr. and Meth., *149*, 441, 1978.
6. G. Brunner, Nucl. Instr and Meth.,*166*, 503, 1979.
7. F. W. Reuter and H. P. Smith, J. Appl. Phys., *43*, 4228, 1972.
8. W.Pafst, Nucl. Instr. and Meth., *124*, 143, 1975.
9. I. Brissaud, J. P. Frontier and P. Regnier, Nucl. Instr. and Meth., *B12*, 235, 1985.
10. S. Kullback, Information Theory and Statistics, Wiley, New York, 1959.
11. H. Akaike, Mathematical Sciences (in Japanese), *153*, 3, 1976.
12. E. Merzbacher and H. W. Lewis, Handbuch der Physik, ed. by S. Flügge, Springer, Berlin, *34*, 166, 1958.

Acta Physica Hungarica 65 (2-3), pp. 159–168 (1989)

ELECTRONEGATIVITIES AND HARDNESSES OF SEVERAL ATOMS AND IONS CALCULATED WITH THE Xα METHOD HAVING SELF-CONSISTENT PARAMETER α *

R. GÁSPÁR and Á. NAGY

Institute of Theoretical Physics, Kossuth Lajos University
4010 Debrecen, Hungary

The Xα method with self-consistent parameter α_{SCF} has been used to calculate electronegativities and hardnesses of several atoms and ions. Slater's transition state method has been applied, too. The Xα results are in agreement with the experimental data and other theoretical values.

1. Introduction

Recently, several chemical concepts have been rigorously established within the density functional theory [1–4]. The electronegativity is defined as the negative of the chemical potential of the density functional theory. The absolute hardness has been recently defined by Parr and Pearson [5] as the derivative of the chemical potential with respect to the number of electrons.

Atomic electronegativities have been calculated using several approximate energy functionals, especially the Xα method with the transition state concept [6] has been widely applied in the calculations [7–11]. Hardnesses of elements have also been determined with the Xα method [10, 11].

Here, electronegativities and hardnesses of several atoms and ions determined with the Xα method having a self-consistent parameter α are presented. (Recently, the ionization energies, electron affinities and chemical potentials of several elements have been calculated with this method [12].) Electronegativities and hardnesses of several singly, doubly and triply ionized positive ions have been calculated. The results are in good agreement with the experimental data.

2. Ab initio self-consistent parameter α in the Xα method

The way of calculating the self-consistent parameter α in the Xα method has been discussed in several earlier papers [13, 14]. Here, only an outline is presented. The starting point of the method is the free-electron gas model. The exchange potential acting on an electron with spin up is given by

*Dedicated to Academician D. Berényi on his 60th birthday

$$V_{X\uparrow}(\vec{r}) = -8F(\varsigma)\left(\frac{3}{4\pi}\rho_{\uparrow}(\vec{r})\right)^{1/3}, \tag{1}$$

where

$$F(\varsigma) = \frac{1}{2} + \frac{1-\varsigma^2}{4\varsigma}\ln\left|\frac{1+\varsigma}{1-\varsigma}\right| \tag{2}$$

and

$$\varsigma = \frac{p}{p_F} \tag{3}$$

is the reduced momentum of the electron considered, p_F is the Fermi momentum and $\rho_{\uparrow}(\vec{r})$ is the total electron density of the electrons having spin up. The usual way of obtaining the Xα exchange potential is to introduce an averaging procedure in the Fermi sphere. If the average is done for the whole Fermi sphere the value proposed by Slater [15], $\alpha = 1$, is given. On the other hand, an average near the Fermi surface for a layer thickness of which goes to zero leads to $\alpha = 2/3$, the value suggested by Gáspár [16] and later Kohn and Sham [17]. A physically more plausible case between these extreme ones can be defined by an average for a layer with $\nu_{i\uparrow} = u_i^* u_i$ electrons in the unit volume near the Fermi surface. It leads to the exchange potential

$$V^i_{x\alpha\uparrow}\left(\vec{r}\right) = -6\alpha^i_{\uparrow}\left(\vec{r}\right)\left|\frac{3}{4\pi}\rho_{\uparrow}\left(\vec{r}\right)\right|^{1/3}, \tag{4}$$

where

$$\alpha^i_{\uparrow}\left(\vec{r}\right) = \frac{\rho_{\uparrow}}{\nu_{i\uparrow}}\left[1 - \frac{1}{2}\varsigma_i^3 - \frac{1}{2}\varsigma_i + \frac{1}{4}(\varsigma_i^2-1)^2\ln\left|\frac{1+\varsigma_i}{1-\varsigma_i}\right|\right] \tag{5}$$

and

$$\varsigma_i = \left(1 - \frac{\nu_{i\uparrow}}{\rho_{\uparrow}}\right)^{1/3}. \tag{6}$$

The expression (6) gives different functions $\alpha^i_{\uparrow}\left(\vec{r}\right)$ for the different spin orbitals u_i. Recently, the r-dependence of the function $\alpha^i_{\uparrow}\left(\vec{r}\right)$ has been studied [18]. It is possible to introduce an average over the shells:

$$\alpha_{\uparrow}\left(\vec{r}\right) = \frac{\sum\limits_{i\uparrow} n_i \alpha^i_{\uparrow}\left(\vec{r}\right)}{\sum\limits_{i\uparrow} n_i}, \tag{7}$$

where n_i is the occupation number of the shell i. It has been shown that $\alpha_{\uparrow}\left(\vec{r}\right)$ has only a slight r-dependence, it can be considered a constant value [14]. This constant value can be determined self-consistently and is generally referred to α_{SCF}. This way of calculating the exchange potential contains no fitting or adjustment, this method can be regarded an ab initio one.

3. Calculation of electronegativity and hardness in the Xα method

The electronegativity χ has been defined [1, 19] as the negative of the chemical potential μ

$$\chi = -\mu = -\frac{\partial E}{\partial N}. \tag{8}$$

It has been shown [1, 7, 12] that the electronegativity can be approximated by the Mulliken formula [20]

$$\chi_M = \frac{1}{2}(I + A), \tag{9}$$

where I and A are the first ionization energy and the electron affinity, respectively. In the Xα method, the electronegativity can be given by the highest occupied orbital energy in open shell systems [7, 12, 21] and with the transition-state method [6] in closed shell systems [7, 12].

The absolute hardness of an atom or a molecule has been defined by Parr and Pearson [5] as

$$\eta = \frac{1}{2}\left(\frac{\partial^2 E}{\partial^2 N}\right)_v = \frac{1}{2}\left(\frac{\partial \mu}{\partial N}\right)_v, \tag{10}$$

where v is the external potential. It has been shown that the hardness can be approximated [5, 10, 11] as

$$\eta = \frac{1}{2}(I - A). \tag{11}$$

Table I
Hardnesses of several atoms (in eV)

Atom	η ($X\alpha_{SCF}$ method)	$\frac{1}{4} < r^{-1} >_i$	$\frac{1}{4} < r^{-1} >_i$ (α_{HF})	Other estimates for η A[10]	B[23]	C[5]
Li	2.08	2.33	2.42	4.03	3.06	2.38
B	2.82	4.17	4.14	4.33	4.39	6.01
C	5.57	5.37	5.32	5.50	5.49	5.00
O	7.39	7.65	7.61	6.14	6.42	6.08
F	8.25	8.77	8.73	7.37	7.52	7.01
Na	2.37	2,13	2.16	3.58	2.91	2.30
Al	2.96	2.62	2.64	2.83	2.94	2.77
Si	3.58	3.30	3.31	3.55	3.61	3.38
P	5.20	3.92	3.93	5.93	5.42	4.86
S	4.68	4.52	4.53	4.08	4.28	4.12
Ci	5.20	5.10	5.11	4.79	4.91	4.70
K	1.96	1.71	1.74	2.84	2.35	1.92
Br	4.60	4.27	4.28	4.28	4.40	4.24

Electronegativities of several atoms calculated with the Xα method having self-consistent parameter α have already been presented [12]. Table I shows the hardnesses of several atoms determined with parameters α_{SCF}. The values in column

A have been obtained from a spin polarized Xα calculation [10] with parameter α_{HF} [22]. The column B presents the results of a local-spin-density calculation [23]. The experimental data obtained from experimental ionization energies and electron affinities using the expression (11) [5] can be seen in the column C. The results of the Xα method with parameter α_{SCF} are in agreement with the other estimates for the hardness. Gazquez and Ortiz [11] have shown that the hardness of an open shell atom can be approximated as the one-quarter of the expectation value r^{-1} of the highest occupied atomic orbital:

$$\eta = \frac{1}{4} < r^{-1} >_i . \tag{12}$$

Table I contains these expectation values determined with parameters α_{SCF} and α_{HF} [11]. They are really close to the other estimates for the hardness.

Parr and Pearson [5] have presented experimental hardnesses for several ions. Calculated values on hardness have not been published. Table II shows the results of the Xα calculations with parameter α_{SCF}. We have obtained the Hartree–Fock results from [25] using Koopmans' theorem. Electronegativities of several positive ions have been calculated in the density functional theory [26]. Table II contains

Table II
Electronegativities, electron affinities and hardnesses of a few ions (in eV)

Ion	χ	A	η	χ	A	η	χ	A	η
	Calculated with ($X\alpha_{SCF}$ method)			Experimental values [5, 24]			Hartree–Fock results [25]		
Al^+	11.85	5.14	6.71	12.4	6.0	6.4	11.75	5.7	6.05
Al^{2+}	23.18	18.56	4.62	23.6	18.8	4.8	22.95	17.8	5.15
Al^{3+}	75.26	27.80	47.46	74.2	28.4	45.8	75.05	28.1	46.95
Ca^+	8.45	5.81	2.71	9.0	6.1	2.9	8.3	5.3	3.0
Ca^{2+}	30.96	11.23	19.73	31.55	11.9	19.65	31.15	11.3	19.85
Ca^{3+}	59.34	50.69	8.65	59.25	51.2	8.05	59.5	51.0	8.5
Fe^+	11.71	8.00	3.72	12.05	7.9	4.15	13.04	7.0	6.04
Fe^{2+}	24.64	15.43	9.21	23.45	16.2	7.25	27.44	19.07	8.36
Fe^{3+}	43.37	33.85	9.52	42.75	30.7	12.05	46.1	35.8	10.3
Br^+	16.78	11.69	5.09	16.7	11.8	4.9	17.6	12.4	5.2
Br^{2+}	27.49	21.87	5.62	28.75	21.6	7.15	28.95	22.8	6.15
Br^{3+}	39.15	33.11	6.04	41.6	35.9	5.7	40.75	35.1	5.65

electronegativities and electron affinities of a few ions calculated with the Xα method using the parameter α_{SCF} and Slater's transition state method [6, 12]. There is good agreement between the calculated and experimental data.

In conclusion, it can be stated that this ab initio way of calculating the exchange potential within the Xα method is useful to determine the electronegativities and hardnesses of atoms and molecules. It is a parameter-free method, there is no fitting or adjustment in it.

References

1. R. G. Parr, R. A. Donelly, M. Levy and W. E. Palke, J. Chem. Phys., *68*, 3801, 1978.
2. N. H. March, J. Chem. Phys., *71*, 1004, 1979.
3. J. A. Alonso and L. A. Girifalco, J. Chem. Phys., *73*, 1313, 1980.
4. N. H. March and R. F. Bader, Phys. Lett., *78A*, 242, 1980.
5. R. G. Parr and R. G. Pearson, J. Am. Chem. Soc., *105*, 7512, 1983.
6. J. C. Slater, The Self-Consistent Field for Molecules and Solids, McGraw-Hill, New York, 1974.
7. L. J. Bartolotti, S. R. Gadre and R. G. Parr, J. Am. Chem. Soc., *102*, 2945, 1980.
8. L. C. Balbás, J. A. Alonso and M. P. Iñiguez, Z. Phys. A., *302*, 307, 1981.
9. S. Manoli and M. A. Whitehead, J. Chem. Phys., *81*, 841, 1984.
10. J. Robles and L. Bartolotti, J. Am. Chem. Soc., *106*, 3723, 1984.
11. J. L. Gázquez and E. Ortiz, J. Chem. Phys., *81*, 2741, 1984.
12. R. Gáspár and Á. Nagy, Acta Phys. Hung., *64*, 405, 1988.
13. R. Gáspár, Acta Phys. Hung., *35*, 213, 1974; Acta Phys. Chim. Szeged, *20*, 321, 1974; Acta Phys. Chim. Debrecen., *19*, 7, 1974.
14. Á. Nagy, Int. J. Quant. Chem., *31*, 269, 1987.
15. J. C. Slater, Phys. Rev., *81*, 385, 1951.
16. R. Gáspár, Acta Phys. Hung., *3*, 263, 1954.
17. W. Kohn and L. J. Sham, Phys. Rev., *140A*, 1133, 1965.
18. Á. Nagy, Phys. Rev., *B34*, 8903, 1986.
19. R. P. Iczkowski and J. L. Margrave, J. Am. Chem. Soc., *83*, 3547, 1961.
20. R. S. Mulliken, J. Chem. Phys., *2*, 782, 1934; *3*, 573, 1934.
21. R. Gáspár and Á. Nagy, Int. J. Quant. Chem., *31*, 639, 1987.
22. K. Schwarz, Phys. Rev., *B5*, 2466, 1972.
23. O. Gunnarson, M. Jonson, B. I. Lundquist, Phys. Rev., *B20*, 3136, 1979.
24. C. E. Moore, Atomic Energy Levels, Vol. III, NBS Circular 467, U.S. Govt. Printing Office, Washington, D. C., 1958.
25. E. Clementi, IBM J. Res. Devel., *9*, 2, 1965.
26. L. C. Balbas, E. Las Heras and J. A. Alonso, J. Phys., *A305* , 31, 1982.

Acta Physica Hungarica 65 (2-3), pp. 165-169 (1989)

WAVE FUNCTION EFFECTS IN K-SHELL IONIZATION*

TAKESHI MUKOYAMA

Institute for Chemical Research, Kyoto University
Kyoto, 606 Japan

The effect of the choice of electronic wave functions in K-shell ionization cross sections in ion–atom collisions has been studied in the plane-wave Born approximation. The ionization cross sections for various target elements by proton impact have been calculated using the relativistic screened hydrogenic wave functions and comparison has been made with those calculated from the Dirac–Fock–Slater wave functions. The results indicate that the wave function effects in K-shell ionization are in general less than a few percent, except for low-energy protons on heavy elements.

1. Introduction

In recent year, K-shell ionization induced by heavy charged-particle impact has been an interesting subject in atomic physics. A large number of accurate experimental data have been accumulated and various theoretical models to explain these experimental results have been developed. The plane-wave Born approximation (PWBA) [1] or the semi-classical approximation (SCA) [2] is most frequently used to compare with the experimental data. For low-energy projectiles it is well-known that modifications of the theories for increased binding energy of the target electron due to presence of the projectile, the Coulomb deflection of the projectile in the nuclear field of the target atom, and the electronic relativistic effects of the target electron are necessary [3]. When the corrections for these effects are incorporated, the theoretical predictions for the K-shell ionization cross sections by light ions are in good agreement with the measured values [4].

However, most of the theoretical calculations have been performed using screened hydrogenic wave functions and there remains an open question about the effect of the choice of electron wave functions on the ionization cross sections, i.e. the wave function effects. In the nonrelativistic case, two conflicting results on the wave function effects for K-shell ionization cross sections have been reported in the PWBA. Basbas et al [5] showed that for low-energy projectiles the Hartree–Slater wave functions give larger values than the hydrogenic wave functions, while in the high-energy region the difference between the values obtained from these two wave functions is negligibly small. On the other hand, Ford et al [6] pointed out that at relatively high proton energy the Hartree–Fock wave functions yield lower K-shell ionization cross sections than the hydrogenic ones.

In the SCA, the impact-parameter dependence of the K-shell ionization probabilities by protons has been calculated with realistic wave functions [7, 8] and

*Dedicated to Academician D. Berényi on his 60th birthday.

compared with that with the hydrogenic wave functions. Their results indicate that except for some energy range the wave function effects are important and become larger for higher projectile energy and for larger impact parameter. Aashamar and Kocbach [7] also showed that the total K-shell ionization cross sections with the Hartree–Fock–Slater (HFS) wave functions are in agreement with the PWBA values [9] with the hydrogenic wave functions, but smaller than the SCA values at high energies. It should be noted that this discrepancy between the PWBA and SCA values comes from the different treatment of the final continuum state [7].

A similar SCA study on the wave function effects has been made by Jakob et al [10] by the use of relativistic Hartree–Fock–Slater or Dirac–Fock–Slater (DFS) and screened hydrogenic (SH) wave functions. For 70-keV protons on Ti, the total K-shell ionization cross section with the DFS wave functions is about 25% less than that with the SH wave functions, while the former is about 10% less than the latter for 190-keV protons.

Until now, no systematic studies on the wave function effects on K-shell ionization cross sections have been reported. In addition, except for the work of Jakob et al [10], all calculations have been done using the non-relativistic wave functions. Especially in the case of the PWBA theory, the screening effect in the hydrogenic wave functions is taken into account through inner and outer screening [1]. Considering these facts, it is worthwhile to test the wave function effect in the PWBA by the use of the relativistic wave functions.

Recently Chen and Crasemann [11] have published an extensive table of the K- and L-shell ionization by protons using the DFS wave functions. It is the aim of the present work to compare their results on K-shell ionization with the SH cross sections and study the wave function effects in K-shell ionization. For this purpose, the relativistic PWBA (RPWBA) calculations with the SH wave functions have been performed following the method of Jamnik and Zupančič [12]. Comparison is made graphically in the form of a ratio of the SH cross section to the DFS cross section as a function of projectile energy for various target elements.

2. Theory

In the PWBA, the K-shell ionization cross section is given by [1]

$$\sigma = 8\pi\,\alpha^2 Z_1^2 \frac{M_1}{E_1} \int_{W_{\min}}^{W_{\max}} \mathrm{d}W \int_{q_{\min}}^{q_{\max}} |F_{ij}(q)|^2 \frac{\mathrm{d}q}{q^3}, \tag{1}$$

where W is the energy transfer, q is the momentum transfer, α is the fine structure constant, and Z_1, M_1, and E_1 are the atomic number, mass, and kinetic energy of the projectile, respectively. The rationalized relativistic units are used throughout the present work, i.e. $\hbar = m_e = c = 1$, where $\hbar$ is the Planck constant divided by 2π, m_e is the rest mass of the electron, and c is the velocity of light in vacuum.

The maximum value of the energy transfer, W_{max}, is taken to be equal to E_1, while the minimum value, W_{min} is set to be the K-shell ionization potential of the target atom. The lower and the upper limits of the momentum transfer are expressed as

$$q^2_{min} = 2M_1E_1\left[1-(1-W/E_1)^{1/2}\right]^2, \tag{2}$$

$$q^2_{max} = 2M_1E_1\left[1+(1-W/E_1)^{1/2}\right]^2. \tag{3}$$

The method to derive the form factor $F_{ij}(q)$ is given in detail elsewhere [13] and the final expressions are written in terms of Gauss-type hypergeometric functions. These results are equivalent to those of Jamnik and Zupančič [12].

The screening effects are taken into account through the inner- and outer-screening method as usual in the PWBA [1]. First, to take into consideration the presence of another K-shell electron the atomic number of the target, Z_2, is replaced by its effective nuclear charge, which is given by $Z_{eff} = Z_2 - 0.3$ using the Slater screening constant. Then the outer screening due to the presence of other electrons is introduced by adding a constant term to the screened Coulomb potential. The constant term is obtained as the difference between the measured K-shell ionization potential and the calculated one from the SH model with Z_{eff}.

3. Results and discussion

The K-shell ionization cross sections for protons on 10 target elements between $Z_2 = 22$ and 92 have been calculated by the method described above in the RPWBA. The energies of the projectile are chosen to be same as those in the table of Chen and Crasemann [11]. The K-shell ionization potential is taken from the table of the binding energies [14]. All the numerical computations of the present work have been made on the FACOM M-780 computer in the Data Processing Center of Kyoto University. The computational accuracy is better than 1%.

In order to compare the present SH results, σ_{SH}, with the DFS cross sections of Chen and Crasemann [11], σ_{DFS}, the ratio σ_{SH}/σ_{DFS} is calculated and plotted against the scaled projectile velocity parameter, $(E_1/\lambda U_K)^{1/2}$, where λ is the ratio of the mass of the projectile to that of the electron and U_K is the K-shell ionization potential.

Figure 1 shows the ratio σ_{SH}/σ_{DFS} as a function of the scaled velocity parameter for five target elements, Ti, Cu, Ba, Au, and U. For other target elements, the obtained points lie between two nearest Z_2 data. It can be seen from the figure that for target elements with low atomic number the SH results are in good agreement with the DFS cross sections in the low-energy region. However, with increasing energy the SH cross sections become larger than the DFS ones.

This fact can be explained as follows. In the present SH model, the atomic potential is produced as a sum of the Coulomb potential with Z_{eff} and a constant term corresponding to the difference between the observed and the calculated K-shell binding energies. Hock pointed out [15] that the atomic potential thus obtained

is a good approximation to the DFS potential of Carlson et al [16] in the vicinity

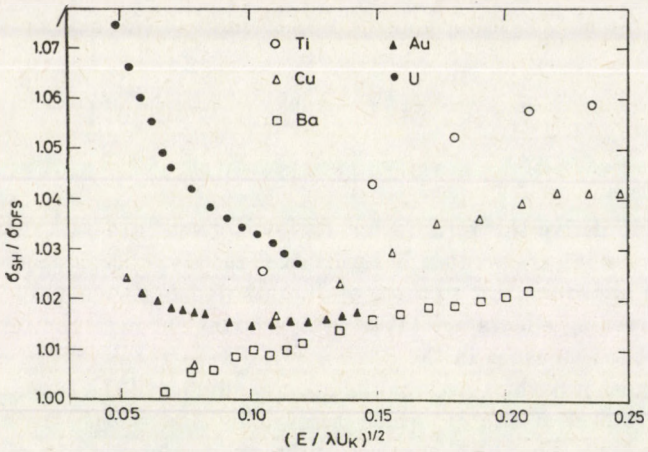

Fig. 1. Ratio of the SH cross section to the DFS cross section for protons on Ti, Cu, Ba, Au and U as a function of the scaled velocity parameter

of the K-shell radius. In the nonrelativistic case, a similar comparsion of the SH and HFS potentials has been made for Ne by Kocbach et al [17].

When the projectile energy is low, the dominant contribution to the atomic form factor $F_{ij}(q)$ comes from the region near to the K-shell radius and agreement between the SH and DFS cross sections is good. On the other hand, for high-energy projectiles the contributions from collisions with large impact parameters become larger and the atomic region with large radial distance becomes important. The present atomic potential is not so good to reproduce the DFS potential at such atomic region and the agreement in the cross section becomes poor. This result is equivalent to the wave function effects in impact-parameter dependence of ionization probabilities studied by the SCA [7,8].

It is interesting to note that for 100-keV protons on Ti the DFS cross section is about 2.5% smaller than the SH value in the present case and about 4% smaller at 200 keV. This discrepancy is very small compared to the case of the SCA calculations of Jakob et al [10]. The reason for this fact can be ascribed to the different treatment of the final state. In the SCA only the inner screening is considered, but the outer-screening effect is also taken into consideration in the PWBA.

For heavy target elements, the SH cross section is considerably larger than the DFS value and rapidly approaches to the latter. In the case of heavy elements, the present atomic potential due to the inner- and outer-screening method may be not so good as for light elements because of the large number of electrons in the atom. However, to exclude the very low-energy region, agreement between the SH and DFS cross sections is within a few per cent.

In conclusion, the screening method used in the PWBA can reduce the discrepancy between the K-shell ionization cross section with the DFS wave function

and those with the hydrogenic wave functions and the wave function effects in K-shell ionization are small except for the case of low-energy projectiles on heavy target elements. The SH model based on the RPWBA can reproduce the DFS cross section within a few per cent for light and medium target elements and for heavy elements in the high-energy region.

References

1. E. Merzbacher and H. Lewis, in: Handbuch der Physik, Vol. 34, ed. by S. Flügge, Springer, 1958, p.166.
2. J. Bang and J. M. Hansteen, Kgl. Dan. Vidensk. Selsk., Mat.-Fys. Medd., *31*, No. 13, 1959.
3. W. Brandt and G. Lapicki, Phys. Rev., *A20*, 465, 1979.
4. H. Paul, At. Data Nucl. Data Tables, *24*, 243, 1979.
5. G. Basbas, W. Brandt and R. Laubert, Phys. Rev., *A7*, 983, 1973.
6. A. L. Ford, E. Fitchard and J. F. Reading, Phys. Rev., *A16*, 133, 1977.
7. O. Aashamar and L. Kocbach, J. Phys. B: At. Mol. Phys., *10*, 869, 1977.
8. K. Aashamar and P. A. Amundsen, J. Phys. B: At. Mol. Phys., *14*, 483, 1981.
9. G. S. Khandelwal, B. H. Choi and E. Merzbacher, Atomic Data, *1*, 103, 1969.
10. A. Jakob, D. Trautmann, F. Rösel and G. Bauer, Nucl. Instr. and Meth., *B4*, 218, 1984.
11. M. H. Chen and B. Crasemann, At. Data Nucl. Data Tables, *33*, 217, 1985.
12. D. Jamnik and Č. Zupančič, Kgl. Dan. Vidensk. Selsk., Mat.-Fys. Medd., *31*, No. 2, 1957.
13. T. Mukoyama and L. Sarkadi, Bull. Inst. Chem. Res., Kyoto Univ., *57*, 33, 1979.
14. C. M. Lederer, J. M. Hollander and I. Perlman, Table of Isotopes, 6th ed., John Wiley & Sons, New York, 1967.
15. G. Hock, private communication, 1977.
16. T. A. Carlson, C.C. Lu, T. C. Tucker, C. W. Nestor and F. B. Malik, ORNL-4614, 1970, unpublished.
17. L. Kocbach, J. M. Hansteen and R. Gundersen, Nucl. Instr. and Meth., *169*, 281, 1980.

Acta Physica Hungarica 65 (2–3), pp. 171–181 (1989)

RELATIVISTIC PHENOMENA IN ATOMIC AND CHEMICAL PHYSICS: OPPORTUNITIES FOR STUDIES WITH SYNCHROTRON RADIATION*

B. CRASEMANN

Department of Physics and Chemical Physics Institute, University of Oregon
Eugene, Oregon 97403, U.S.A.

Opportunities for investigations in atomic and chemical physics are summarized that may arise as next-generation synchrotron-radiation sources become operational. Recent progress in the study of relativistic effects in atoms is reviewed and some applications to chemistry are discussed. It is pointed out that measurements with highly monochromatic, tunable hard X-rays will make it possible to perform important tests of relativistic phenomena in atoms and molecules.

1. Introduction

The study of atoms and molecules with synchrotron radiation has become an active field [1, 2]. The advent of high-intensity, high-resolution tunable monochromatic beams of vuv and soft X-ray photons with a sharp time structure has made it possible to explore dynamical processes in atomic and molecular photoionization over a wide energy range. Progress is being made in gaining insight into the processes that occur during photoexcitation and escape of the photoelectron through the anisotropic molecular field, in terms of such physical observables as photoionization cross sections and branching ratios, photoelectron angular distributions, and spin polarization of photoelectrons [3]. As pointed out by Dehmer et al [2], particularly important probes in this context are resonant photoionization mechanisms, such as shape resonances and autoionization, in which the excited complex is temporarily trapped in a quasibound state, so that the excited electron traverses the molecular core many times before it escapes by tunneling or by exchange of energy with the core. Resonances thus amplify the subtle dynamics of the electron–core interaction.

Work on *shape resonances* is being extended to other and very different systems than the well-studied N_2 and CO [4, 5] and will include new facets such as vibrational effects in polyatomic molecules, continuum–continuum coupling, and interaction with autoionizing states.

Autoionization in atomic and molecular photoionization still offers much room for productive study [6]. This is well-known to be a multichannel process in which a resonantly excited discrete state from one channel couples to the underlying electronic continua of one or more channels leading to ionization. The requisite high

*Dedicated to Academician D. Berényi on his 60th birthday.

resolution for synchrotron-radiation studies of autoionization processes is being attained [6] and has led, for example, to triply differential studies of complex autoionization structures in O_2 [7], CO [8] and CO_2 [9], in which the competition between overlapping and autoionizing resonances can be resolved. Sophisticated insight into autoionization phenomena has been achieved for H_2 in terms of multichannel quantum defect theory [2], and extension to other diatomics and more complicated systems can be anticipated.

X-ray emission spectra measured with high resolution can be very useful to elucidate the properties of excited and ionized atoms and molecules [10, 11]. Particulary interesting recent results include electron-beam excited fluorescence of water vapor [12] and CO [13]. Qualitative interpretation of these spectra can be based on CI wave functions built from separately optimized molecular orbitals [12]. What makes the subject particularly interesting and timely is the success, for example by Larkins' group [14], of *ab initio* molecular orbital self-consistent-field calculations of the energy and intensity of X-ray transitions in simple molecules. This work has shown that a realistic basis for comparsion with experiment can be achieved through multi-center relaxed Hartree–Fock calculations. More generally, the analysis and interpretation of *ab initio* molecular wave functions in comparison with measured observables provides a unique and sound basis for determining the importance of various mechanisms.

We can consequently expect growing interest especially in molecular X-ray emission spectra, and clearly the high monochromaticity and tunability of synchrotron radiation makes it an ideal means to excite flourescence. These properties are particularly important because chemical applications of X-ray spectra excited by traditional means have been inhibited by the general occurrence of multivacancy processes. The presence of spectator holes manifests itself in emission spectra by satellite lines, and opening of channels to these initial configurations leads to additional features in absorption spectra [16]. With synchrotron radiation, high-resolution emission spectroscopy can be carried out as a function of exciting photon energy in regions containing both single- and multiple-vacancy thresholds. This technique, already successfully applied in Auger spectroscopy [17, 18], has been demonstrated by Deslattes and coworkers [16] to be eminently suited for the analysis of multi-vacancy effects in X-ray emission spectra and is likely to lead to exceedingly interesting studies, not only of pure single-vacancy molecular X-ray spectra but also of correlation mechanisms that lead to multiple excitation processes.

Polarization of molecular X-ray fluorescence may become an important new technique for the study of molecular systems [19, 20]. Recent experiments on the National Bureau of Standards beam line in the National Synchrotron Light Source have shown high polarization of the X-ray fluorescence following K-shell excitation of several Cl-containing molecules. The Cl 1s electrons were resonantly excited, and the subsequent Cl Kβ fluorescence was found to be strongly linearly polarized, with the direction of polarization determined by the symmetry of the valence orbital involved in the fluorescence decay that fills the Cl 1s vacancy. For example, in CH_3Cl, valence orbitals of σ symmetry produce fluorescent X rays polarized parallel to the synchrotron-radiation polarization, while fluorescence from π orbitals is po-

larized perpendicularly to the synchrotron-radiation polarization [19]. In sulfur 1*s* threshold excitation of SF_6, broadened emission features were detected that depend strongly on polarization [21]. These discoveries may lead to the development of a sensitive probe for the study of orbital symmetry in more complicated molecular systems, condensed matter, and adsorbates [19].

A further class of new applications of the next-generation synchrotron-radiation sources, not yet realized, will be based on the possibility of generating light with *continuously variable polarization*, from linear through elliptical to circular [22]. This can become an extremely powerful aid in spectroscopy, particularly for chiral molecules [23].

Synchrotron radiation has opened vast possibilities for the study of *dissociation processes*, occurring either in competition with or subsequent to molecular photoionization. Tunability of the radiation permits preparation of molecular ions with well-defined internal energy, and the sharp time structure of the light permits measurements of threshold photoelectron–photoion coincidences by time-of-flight spectrometry [24]. Astonishingly site-specific fragmentation of small molecules following soft X-ray excitation was demonstrated by Eberhardt and coworkers at NSLS [25]. The same group recently performed coincidence experiments between energy-selected Auger electrons and the ions produced in events following the absorption of a soft X-ray photon by a CO molecule [26]; the results lead to new insight into the potential energy curves of the doubly charged molecular ion and the involvement of individual valence electrons in the molecular bond.

An approach to molecular photoionization and photodissociation dynamics that can be expected to benefit greatly from the next-generation synchrotron-radiation sources, such as Super-ACO in Orsay and the Berkeley ALS, is *multiphoton ionization* photoelectron spectroscopy. In particular, the combination of resonantly enhanced multiphoton ionization with photoelectron spectroscopy is likely to become a very versatile and powerful technique [27]. New kinds of related "two-color" experiments will become possible, in which a laser is used in conjunction with radiation from insertion devices in the new sources [23].

Among the many facets of atomic and molecular physics that are becoming accessible for study with synchrotron radiation, we devote the remainder of this paper to the role of relativistic effects, which have been quite extensively investigated in atomic physics and very likely may offer opportunities for fruitful further insights into molecular structure and dynamics.

2. Relativistic effects

2.1. Nature of relativistic effects in atomic structure and transitions

For the sake of perspective, it is useful to look briefly at the more readily calculable relativistic effects in *atomic structure* and transitions [28]. Relativity notably redistributes the electronic charge in an atom. The relativistic mass increase

of fast-moving s and p electrons close to the nucleus reduces the mean radial distance of these electrons from the origin. A simple hydrogenic calculation [29] shows that the electron-mass increase, and hence, the change in orbital radius, reaches 0.5% for $Z/n = 14$ and 5% for $Z/n = 43$, where Z is the atomic number and n, the principal quantum number of the orbital. The $1s$ binding energy is affected by 0.5% for $Z = 19$ and by 5% for $Z = 61$.

The increased electronic charge density near the nucleus produced by the relativistic contraction of s and p orbitals causes increased screening of the nuclear charge, whence outer electrons move further away from the origin. Thus even the wave functions of *per se* nonrelativistic outer electrons, e.g. in the d and f orbitals, can be noticeably affected by relativity (Fig. 1).

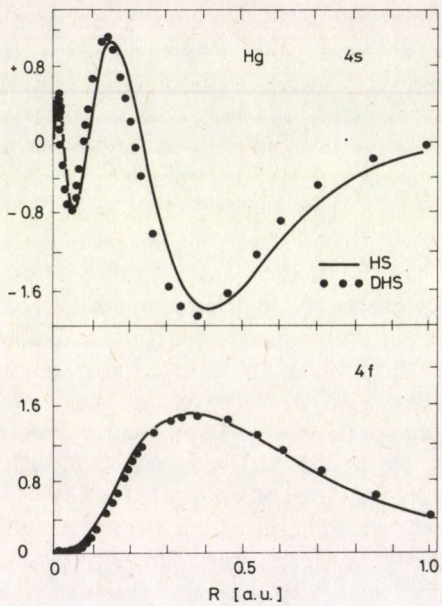

Fig. 1. Nonrelativistic Hartree–Slater and relativistic Dirac–Hartree–Slater $4s$ and $4f$ wave functions in mercury. From Ref. [28]

In addition to relativistic contraction of inner and expansion of outer orbitals, spin–orbit splitting is the second major relativistic effect in atomic structure. Neither electron orbital nor spin angular momentum alone are good relativistic quantum numbers, but the vector sum $\mathbf{j} = \mathbf{l} + \mathbf{s}$ is; the energy splitting between the two j values $l \pm s$ is a relativistic effect that can amount to several electronvolts for the valence electrons and two or three kiloelectronvolts for the $2p$ electrons of heavy atoms.

The third major relativistic factor in atomic structure is the Breit interaction, composed of current–current and retardation contributions [28]. This first dynamic

correction to the electrostatic Coulomb interaction in the relativistic Hamiltonian takes account of the exchange of a single transverse photon. While it affects binding energies relatively little (even 1*s* in heavy atoms only by a fraction of one percent), it has a major impact on the separation of levels of different total angular momentum J, such as spin–orbit splittings: here the Coulomb energy cancels out, being insensitive to angular momentum, and leaves a major role to be played by the Breit interaction.

The radiative corrections of quantum electrodynamics can be of comparable magnitude as the Breit energy and must also be taken into consideration if one wishes to determine level energies to high precision. The radiative corrections comprise the self energy and vacuum polarization (of opposite signs), which together cause the Lamb shift [30]. In Fig. 2 we plot the relative contributions of Breit energy and radiative corrections to the atomic 1*s* level energy, as a function of atomic number.

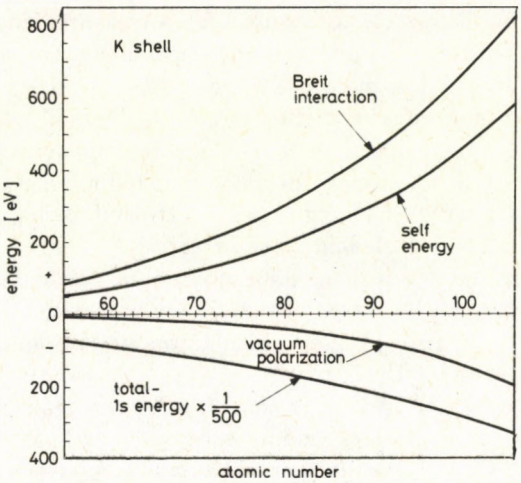

Fig. 2. Shifts produced in the K binding energies of heavy atoms by the Breit interaction, self energy, and vacuum polarization. From Ref. [30]

Transition rates are influenced by relativity due to several factors [30]. These include (i) changes in transition energies, (ii) differences between relativistic and nonrelativistic wave functions: orbital effects caused by the inclusion of the mass-velocity correction, the Darwin term, and the spin–orbit interaction in the Dirac equations, (iii) contributions from the current–current (magnetic) interaction, and (iv) retardation of the Coulomb and magnetic interactions. By artificially including these factors one at a time in numerical calculations, each effect can be studied separately [31–33]. The total effect on, for example, radiationless transitions seems at first sight to be perplexingly uneven; it can be understood, however, by considering how the orbital, current–current interaction, and retardation effects add up in magnitude and phase for both direct and exchange transitions [28].

From an extensive and systematic study of relativistic radiationless transitions, we can deduce some general trends [34]: (i) The orbital (wave function) effect tends to predominate when outer shells are involved; (ii) retardation and magnetic interaction are important for inner shells; (iii) cancellations can greatly reduce the effects of relativity, and (iv) weak transitions can be much more strongly affected by relativity than intense transitions.

2.2. Level energies

Atomic and molecular level energies (hole-state energies or electron binding energies) can in general be significantly affected by relativity, relaxation, finite nuclear size, the quantum electrodynamic corrections discussed above, coupling, correlations, and interaction with radiationless continua [36–38]. Considerable information on these complex factors can be derived from measurements with synchrotron radiation ranging from straightforward photoelectron spectrometry to some of the more sophisticated approaches mentioned in Section 1.

The relativistic independent-particle model can be used to compute the zeroth-order wave functions and energies [39, 40]. Relaxation is accounted for, in the absence of shake processes, by taking the electron binding energy as the difference between the total energies of the excited ionic state and of the ground state, calculated by separate self-consistent-field procedures [38].

Magnetic and retardation contributions can be calculated by means of the Mann—Johnson transverse operator, which includes the effect of the frequency of the exchanged virtual photon [41, 28]. The limits of this approach have not yet been established experimentally.

The nucleus can be treated as a point charge, but this leads to an error of tens of electronvolts in the K-shell binding energy of the heaviest elements. While it is thus necessary to take the finite size of the nucleus into account, it is only the root-mean-square charge radius that affects the result of energy-level calculations, irrespective of the details of the assumed nuclear charge distribution [42].

The importance of the coupling scheme is worth noting. While $j-j$ coupling is natural in relativistic calculations, this is ill-suited for most open outer shells, in which the electrostatic interaction between electrons dominates over the spin–orbit interaction. The suitble scheme for coupling electrons in these open shells thus is LS, which can be implemented by means of the relativistic LS-average scheme [39].

The effects of electron–electron Coulomb correlation on energy levels can be crudely divided into those of ground-state correlation and of dynamic relaxation. The former is essentially the result of broken pairs: there are more pairs in the ground state than in the excited state, whence the binding energy is increased. This effect can be evaluated as a sum of pair energies that survive after cancellation between ground and hole states [43].

A leading type of dynamic relaxation is the interaction with the Auger continuum that affects hole-state levels subject to Coster–Kronig decay. For these levels, fluctuations to virtual Coster–Kronig states will reduce the binding energies. This

type of interaction is the radiationless many-body analog of the electron self energy. It can be treated on the basis of an approach devised by Fano already in 1961 [44] and more recently applied to the problem of Coster–Kronig fluctuations [45].

The theory of correlations is difficult and as yet in a somewhat primitive state. There is no suitable unified relativistic theory of correlations; one is forced to rely on an additive approach in which each effect is calculated separately; moreover, the prevalent nonrelativistic treatment is primarily suited for light atoms only.

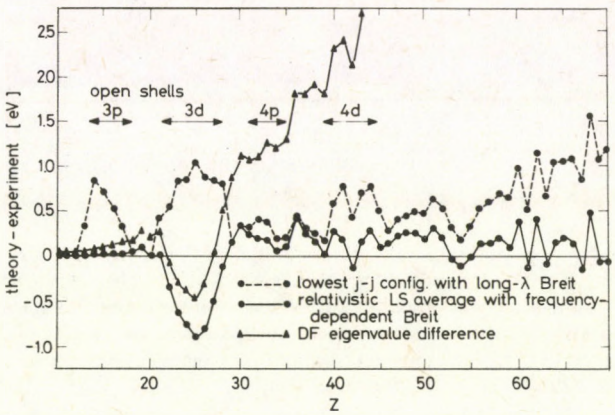

Fig. 3. Differences between calculated and measured spin-orbit splittings between $2p_{1/2}$ and $2p_{3/2}$ hole-state energies, in eV, as functions of atomic number Z. Theoretical energies were calculated in terms of the lowest $j - j$ configuration with the long-wavelength approximation for the Breit interaction (solid circles linked by dashed curve) and from the relativistic LS average with the frequency-dependent form of the Breit interaction (Mann–Johnson operator) (solid circles linked by solid curve). For comparison, the splittings from Dirac–Fock eigenvalues are also shown (triangles linked by solid curve). From Ref. [37]

The magnitude of some of the effects discussed here can be appreciated by comparing calculations with selected results from electron spectrometry [37]. In Fig. 3, we plot the differences between calculated and measured $2p$ spin–orbit splittings as a function of atomic number. The Dirac–Fock eigenvalue differences quickly go off scale, primarily because the Breit energy is not included which plays a major role in the splittings, in which the static Coulomb interaction cancels out. When the frequency-dependent Breit interaction is included and coupling is expressed in terms of the relativistic LS average, calculated splittings agree to within 0.5 eV with measurements up to $Z = 70$. (The discrepancy in the $3d$ open-shell region is well-understood as due to the exchange splitting [46], which is not included in these calculations).

A further comparison between present measurements and state-of-the-art calculations is shown in Fig. 4 for $1s$ and $2s$ binding energies [37]. For the $2s$ level,

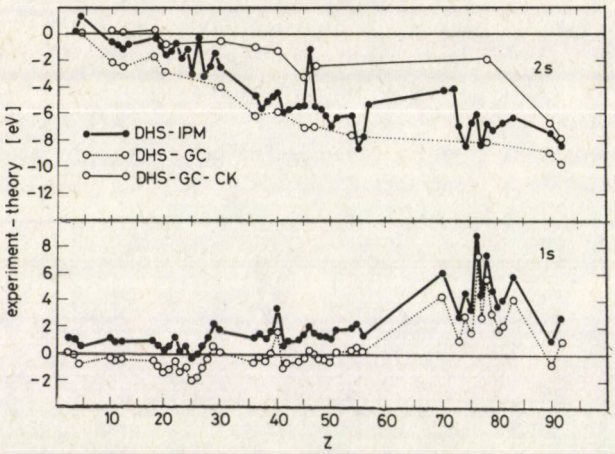

Fig. 4. Differences between measured and calculated K ($1s$) and L_1 ($2s$) electron binding energies (in eV), as functions of atomic number Z. Theoretical energies were calculated from the relativistic independent-particle model alone (DHS–IPM), with inclusion of ground-state correlation (DHS–GC), and with inclusion of ground-state correlation as well as (super-) Coster–Kronig fluctuations (DHS–GC–CK). Energies are plotted as functions of atomic number Z. Curves are drawn as guides for the eye only. From Ref. [37]

inclusion of ground-state correlation and Coster–Kronig fluctuations is seen to reduce the difference between experiment and theory to approximately 2 eV up to $Z = 78$ (where the $2s$ energy is 13.9 keV); above this atomic number, uncertainties in the screening of the self energy becomes the dominant cause of the discrepancy. Valuable insights can be expected from future work on these high-Z level energies, with measurements primarily based on electron spectrometry with synchrotron radiation.

3. Relativistic chemistry

Relativity makes gold yellow and noble, and different from silver; it makes mercury liquid at room temperature and the mercurous ion extra-stable [47, 48]; yet, Pyykkö and Desclaux in a well-known paper noting these facts [47] comment: "most of the existing theoretical chemistry refers to an imaginary world where c would be infinite." Although this statement was made some eight years ago and considerable progress has been made since then [49], it probably still is true to a considerable extent. The main reason is the difficulty inherent in fully relativistic calculations of atoms and, even more so, of molecules.

In fact, no completely correct Hamiltonian exists to describe the interaction between two relativistic electrons [50]. Often it is therefore preferable to use the

nonrelativistic Schrödinger equation and add on relativistic correction terms, using perturbation theory to use the "Pauli limit" operators for the mass correction, the Darwin term, and the spin–orbit and spin–other–orbit interactions. For heavy elements, however, or when highly precise results are needed, there is little choice but to turn to fully relativistic theory based on the Dirac equation.

Fundamental unresolved problems remain in the relativistic theory of many-electron systems [51, 52]. Nevertheless, from a practical point of view for atomic structure calculations, the multiconfiguration Dirac–Fock (MCDF) method offers an effective way of including relativistic effects [38]; quantitative predictions based on this method have become enormously much easier to make in recent years, owing to the ready availability of codes like those of Desclaux [53] and Grant et al [54, 55] and of suitable large-scale computing facilities.

Relativistic effects on atomic orbitals clearly can play an important role in determining molecular and chemical properties by affecting such quantities as bond length, molecular binding energies, bonding characteristics and ionization potentials. Among the best known examples are the chemical properties of gold and mercury. The chemical difference between gold and silver is now understood to be largely a relativistic effects [56–59]. The Hg_2^{2+} ion, isoelectronic with Au_2, would not exist as a stable aqueous ion in nature without the relativistic stabilization by about 1.0 eV of the bond [49]. The contraction of the filled $6s$ orbital makes Hg a more noble element than the preceding group $2B$ elements Zn and Cd [59], and relativistic effects decrease the van der Waals interatomic potential between two mercury atoms by an estimated 45% [48]. An interesting item related to the putatively stable superheavy elements is the prediction by Pitzer [60] on grounds of relativistic arguments that element 112 is likely to be extremely volatile and chemically inert, and that elements 114 and 118 may also be relatively inert gases.

In summary it appears that the importance of relativistic effects, long appreciated in atomic physics, is increasingly being realized in molecular and chemical physics. Despite the difficulties in treating much more complex systems relativistically, obstacles are being overcome with the aid of advanced theoretical approaches and greatly enhanced computing facilities. Synchrotron radiation povides unprecedented opportunities to perform the highly sophisticated measurements that are required to test theoretical advances in this fertile area of investigations.

Acknowledgments

This article is based in part on a lecture given by the author at the Conference "New Opportunities in Chemistry: An International Symposium on the Uses of Synchrotron Radiation in Chemistry", Brookhaven National Laboratory, New York, 4-6 November 1987. The author thanks D. A. Shirley for illuminating comments and for directing his attention to Ref. [60]; he expresses appreciation to S. J. Schaphorst for assistance with the search of the literature. This work was supported in part by the National Science Foundation through Grant PHY-85 16788 and by the Air Force Office of Scientific Research through Grant AFOSR-87-0026.

References

1. B. Crasemann and F. Wuilleumier, in Atomic Inner-Shell Physics, ed. by B. Crasemann, Plenum, New York, 1985, Chapter 7.
2. J. L. Dehmer, A. C. Parr and S. H. Southworth, in Handbook on Synchrotron Radiation, Vol. II, ed. by G. V. Marr, North-Holland, Amsterdam, 1986.
3. J. L. Dehmer, D. Dill and A. C. Parr, in Photophysics and Photochemistry in the Vacuum Ultraviolet, ed. by S. McGlynn, G. Findley and R. Huebner, Reidel, Dordrecht, 1983.
4. S. Krummacher, V. Schmidt, and F. Wuilleumier, J. Phys. *B13*, 3993, 1980.
5. K. Krummacher, V. Schmidt, F. Wuilleumier, J. M. Bizau and D. Ederer, J. Phys., B *16*, 1733, 1983.
6. A. C. Parr, in New Directions in Chemical Analysis, ed. by B. L. Shapiro, Texas A & M University Press, College Station, 1985, p. 162.
7. P. Morin, I. Nenner, M. Y. Adam, M. J. Hubin-Franskin, J. Delwiche, H. Lefebvre-Brion and A. Giusti-Suzor, Chem. Phys. Lett., *92*, 609, 1982.
8. D. L. Ederer, A. C. Parr, B. E. Cole, R. Stockbauer, J. L. Dehmer, J. B. West and K. Codling, Proc. R. Soc. London Ser. A, *378*, 423, 1981.
9. A. C. Parr, D. L. Ederer, J. L. Dehmer and D. M. P. Holland, J. Chem. Phys., *77*, 111, 1982.
10. C. Nordling, in X-Ray and Atomic Inner-Shell Physics-1982, ed. by B. Crasemann, American Institute of Physics, New York, 1982, p.415.
11. L. N. Mazalov, in X-Ray and Inner-Shell Processes in Atoms, Molecules, and Solids, ed. by A. Meisel and J. Finster, Karl-Marx-Universität Leipzig, 1984, p. 327.
12. J. -E. Rubensson, L. Pettersson, N. Wassdahl, M. Backstrom, J. Nordgren, O. M. Kvalheim and R. Manne, J. Chem. Phys., *82*, 4486, 1985.
13. L. Pettersson, N. Wassdahl, M. Backstrom, J. E. Rubensson and J. Nordgren, J. Phys. B, *18*, L125, 1985.
14. R. A. Phillips and F. P. Larkins, Aust. J. Phys., *39*, 717, 1986.
15. P. S. Bagus, C. J. Nelin, and K. Hermann, Aust. J. Phys., *39*, 731, 1986.
16. R. D. Deslattes, Aust. J. Phys., *39*, 845, 1986.
17. G. B. Armen, T. Åberg, K. R. Karim, J. C. Levin, B. Crasemann, G. S. Brown, M. H. Chen and G. E. Ice, Phys. Rev. Lett., *54*, 182, 1985.
18. P. A. Heimann, U. Becker, H. G. Kerkhoff, B. Langer, D. Szostak, R. Wehlitz, D. W. Lindle, T. A. Ferrett and D. A. Shirley, Phys. Rev., A *34*, 3782, 1986.
19. D. W. Lindle, P. L. Cowan, R. E. LaVilla, T. Jach, R. D. Deslattes and R. C. C. Perera, Abstract B-c 22, 14th International Conference on X-Ray and Inner-Shell Processes, Paris, 14-18 September 1987 (unpublished).
20. R. D. Deslattes, private communication.
21. P. L. Cowan, D. W. Lindle, T. Jach, R. E. LaVilla and R. D. Deslattes, Abstract B-c 15, 14th International Conference on X-Ray and Inner-Shell Processes, Paris, 14-18 September 1987 (unpublished).
22. Report of the Workshop on an Advanced Soft X-Ray and Ultraviolet Synchrotron Source: Applications to Science and Technology. Lawrence Berkeley Laboratory Report No. PUB-5451, December 1985 (unpublished).
23. T. Baer, Summary of Workshop "Chemical Applications of Undulator Radiation", Berkeley, May 4-5, 1987 (unpublished).
24. I. Nenner, P. M. Guyon, T. Baer and T. Govers, J. Chem. Phys., *72*, 6587, 1980.
25. W. Eberhardt, T. K. Sham, R. Carr, S. Krummacher, M. Strongin, S. L. Weng and D. Wesner, Phys. Rev. Lett., *50*, 1038, 1983.
26. W. Eberhardt, E. W. Plummer, I. W. Lyo, R. Reininger, R. Carr, W. K. Ford and D. Sondericker, Aust. J. Phys., *39*, 633, 1986.
27. P. M. Dehmer, J. L. Dehmer and S. T. Pratt, Comments At. Mol. Phys., *19*, 205, 1987.
28. B. Crasemann, M. H. Chen and H. Mark, J. Opt. Soc. Am. B *1*, 224, 1984.
29. K. G. Dyall, Aust. J. Phys., *39*, 667, 1986.

30. M. H. Chen, B. Crasemann, M. Aoyagi, K. -N. Huang and H. Mark, At. Data Nucl. Data Tables, *26*, 561, 1981.
31. M. H. Chen and B. Crasemann, Phys. Rev., A *28*, 2829, 1983.
32. M. H. Chen, E. Laiman, B. Crasemann, M. Aoyagi and H. Mark, Phys. Rev., A *19*, 2253, 1979.
33. M. H. Chen, B. Crasemann and H. Mark, Phys. Rev. A, *21*, 436, 1980.
34. M. H. Chen, B. Crasemann and H. Mark, Phys. Rev. A, *21*, 449, 1980.
35. M. H. Chen, in X-Ray and Atomic Inner-Shell Physics-1982, ed. by B. Crasemann, American Institute of Physics, New York, 1982, p.331.
36. B. Crasemann, in Proceedings of the X-84 International Conference on X-Ray and Inner-Shell Processes in Atoms, Molecules and Solids, Leipzig, 1984, ed. by A. Meisel and J. Finster, Karl-Marx-Universität Leipzig, 1984, p. 51.
37. M. H. Chen, B. Crasemann, N. Mårtensson and B. Johansson, Phys. Rev. A, *31*, 556, 1985.
38. B. Crasemann, K. R. Karim and M. H. Chen, At Data Nucl. Data Tables, *36*, 355, 1987.
39. I. Lindgren and A. Rosén, Case Stud. At. Phys., *4*, 93, 1974.
40. I. P. Grant, Adv. Phys., *19*, 747, 1970.
41. J. B. Mann and W. R. Johnson, Phys. Rev., A *4*, 41, 1971.
42. G. Soff, private communication, 1984.
43. D. R. Beck and C. A. Nicolaides, in Excited States in Quantum Chemistry, ed. by C. A. Nicolaides and D. R. Beck, Reidel, Dordrecht, 1978.
44. U. Fano, Phys. Rev., *124*, 1866, 1961.
45. M. H. Chen, B. Crasemann and H. Mark, Phys. Rev. A, *24*, 1158, 1981.
46. S. P. Kowalczyk, L. Ley, F. R. McFeely and D. A. Shirley, Phys. Rev., B *11*, 1721, 1975.
47. P. Pyykkö and J.-P. Desclaux, Acc. Chem. Res., *12*, 276, 1979.
48. K. S. Pitzer, Acc. Chem. Res., *12*, 271, 1979.
49. P. A. Christiansen, W. C. Ermler and K. S. Pitzer, Ann. Rev. Phys. Chem., *36*, 407, 1985.
50. See, e.g., L. Armstrong, Jr., in Structure and Collisions of Ions and Atoms, ed. by I. A. Sellin, Springer, Berlin, 1978, Chap. 3.
51. J. Sucher, in Relativistic Effects in Atoms, Molecules and Solids, ed. by G. L. Malli, Plenum, New York, 1983, p. 1.
52. I. P. Grant, Aust. J. Phys., *39*, 649, 1986.
53. J. -P. Desclaux, Comput. Phys. Commun., *9*, 31, 1975.
54. I. P. Grant, B. J. McKenzie, P. H. Norrington, D. F. Mayers and N. C. Pyper, Comput. Phys. Commun., *21*, 207, 1980.
55. B. J. McKenzie, I. P. Grant and P. H. Norrington, Comput. Phys. Commun., *21*, 233, 1980
56. P. S. Bagus, Y. S. Lee and K. S. Pitzer, Chem. Phys. Lett., *33*, 408, 1975.
57. H. Hotop, R. A. Bennet and J. Lineberger, J. Chem. Phys., *58*, 2373, 1973.
58. J. Kordis, K. A. Gingerich and R. J. Seyse, J. Chem. Phys., *61*, 5114, 1974.
59. N. C. Pyper, I. P. Grant and R. B. Gerber, Chem. Phys. Lett., *49*, 479, 1977.
60. K. S. Pitzer, J. Chem. Phys., *63*, 1032, 1975.

Acta Physica Hungarica 65 (2–3), pp. 183–194 (1989)

HIGH-RESOLUTION ELECTRON SPECTROSCOPY OF RADIOACTIVE SAMPLES USING THE ESA 12 ELECTROSTATIC SPECTROMETER*

V. BRABEC, O. DRAGOUN, N. DRAGOUNOVÁ, J. NOVÁK, M. FIŠER, A. KOVALÍK and M. RYŠAVÝ

Nuclear Physics Institute of the Czechoslovak Academy of Sciences
250 68 Řež near Prague, Czechoslovakia

The ESA 12 cylindrical mirror spectrometer was equipped with the Al X-ray tube, electron transport system and retarding lens to measure both conversion electron and photoelectron spectra of solid radioactive samples. The instrumental resolution better than 1 eV was conserved but there is still a possibility to increase luminosity of the hole set up. Various photoelectron spectra are presented to demonstrate the instrumental quality. Temperature characteristics of the high-voltage power supplies were improved. The background of the channeltron increased from 1.5 to 6.5 counts/min during ten years of work with the radioactive samples. Long time experience in the operation of the spectrometer is described.

1. Introduction

More than ten years ago, in September 1977, we recorded the first electron spectra on the new ESA 12 electrostatic spectrometer which was developed for us in the Institute of Nuclear Research of the Hungarian Academy of Sciences (ATOMKI). The spectrometer, which is a double pass cylindrical mirror analyser, was intended to measure low-energy internal conversion and Auger electrons emitted in a radioactive decay. The spectrometer parameters together with the first results can be found in joint paper [1] of Hungarian and Czechoslovak physicists.

Reliable performance and further improvements of the ESA 12 spectrometer enabled us to solve various tasks of high-resolution spectroscopy of the electrons emitted during nuclear transformations. The attention was paid mainly to the energy region of tenths and units of keV which is of difficult access to more common magnetic spectrometers.

In the field of nuclear physics, we could prove the existence and determined quantum characteristics of the 4.025 ± 0.020 keV pure E2 transition in ^{208}Po [2] and of the 1.565 ± 0.006 keV M1 + $(1.1 \pm 0.3) \times 10^{-4}$ E2 transition in ^{201}Hg [3]. For nuclear chemistry, we developed a new method [4] of the valent state determination of the trace amounts of several radionuclides in solid deposits, which is based on measurements of the chemical changes of the conversion electron energies. Using this method, we investigated simple inorganic ^{99m}Tc oxocompounds [5], chelates [6]

*Dedicated to Academician D. Berényi on his 60th birthday

and halides [7]. In the field of atomic physics, we studied the KLL Auger electrons of manganese [8] and determined lifetime of vacancies in several N-subshells of mercury [3]. As for technology applications, we examined the efficiency of various chromizing procedures by measuring the relative intensity of the low-energy Auger electrons in the ^{51}Cr decay [9].

Recently, the spectrometer was equipped with an Al X-ray tube, electron transport system and retarding lens (see Fig. 1) so that our experimental possibilities were extended to the X-ray photoelectron spectroscopy (XPS) studies of the radioactive samples. To our knowledge, such investigations were so far carried out only in very few laboratories, since the commercial XPS spectrometers are not equipped for the work with radioactive materials.

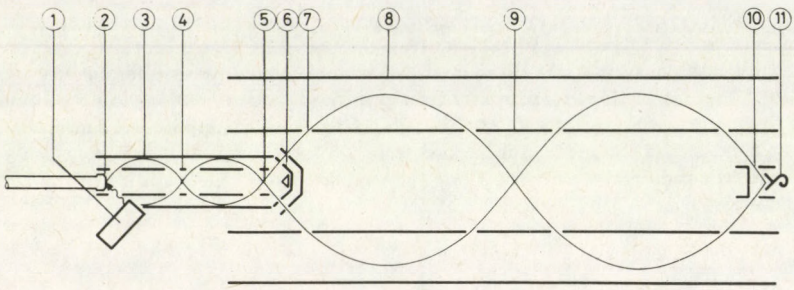

Fig. 1. Scheme of the extended ESA 12 spectrometer: 1 - X-ray tube, 2 and 5 - source at the X and AN positions, respectively, 3, 4 - outer and inner cylinder of the transport system, 6 - middle electrode of the retarding lens, 7, 10 - variable slits, 8, 9 - outer and inner cylider of the analyser, 11 - detector

The details of the ESA 12 reconstruction will be described elsewhere. Here, we summarize the results of adjusting measurements as well as the experience gained in the long-time operation of the spectrometer.

2. Modes of the spectrometer operation

Two modes of the ESA 12 operation - without any retardation and with proportional retardation - were recommended for the energy regions of 0.1 to 20 keV and 0.1 to 15 keV, respectively. The relative analyser resolution, $(\Delta E/E)_{\mathrm{instr}}$, is adjustable from 0.1 to 1.0 % [1].

In our attempts to increase the absolute resolution, $\Delta E_{\mathrm{instr}}$, and still keep the reasonable luminosity we examined systematically various modes of the measurement. The best results were obtained when the radioactive source was put to a variable positive voltage while the analyser (with its inner cylinder grounded) was set for the fixed pass energy. Although there was no retarding lens between

the source and the analyser, narrow and rather intensive zero-energy-loss peaks of the conversion electron lines were recorded. This is probably due to the fact that the dimensions of both the radioactive source and analyser entrance slit are much smaller than their distance. Since then, we measured hundreds of spectra in this way, mainly with the pass energy of 60 eV.

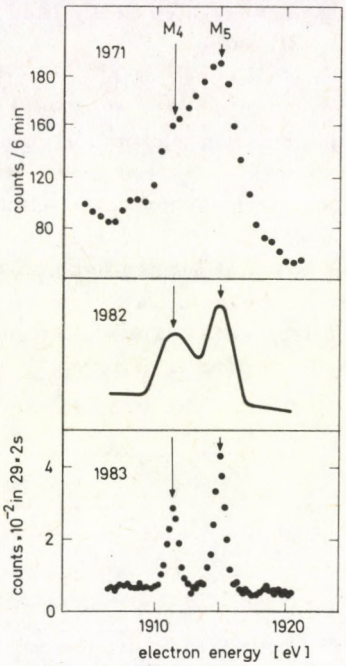

Fig. 2. The M_4 and M_5 conversion lines of the 2.17 keV transition in ^{99}Tc recorded: in 1971 - with a Vanderbilt iron free double focusing spectrometer [10], in 1982 - with a HP 5950 A electrostatic spectrometer of Hewlett Packard in Moscow [11] and in 1983 - with the ESA 12 electrostatic spectrometer in Řež [4]

Using this mode with the 40 eV pass energy and maximum slits of 4 mm we obtained the FWHM of 1.0 eV for the M_4 and M_5 conversion lines of the 2.17 keV E3 transition in ^{99}Tc (Fig. 2), which are the narrowest lines ever recorded in the internal conversion electron spectroscopy. The theoretical estimate for the natural width of these lines in a free technetium atom is $\sim$ 0.3 eV [12]. Further decreasing of the electron pass energy to 20 eV did not result in any improvement in FWHM of the lines. No influence of disperse magnetic fields of the electrical transformers and motors in the spectrometer neighbourhood on the investigated conversion lines in ^{99}Tc was recognized.

The measuring mode without retardation is utilized in the experiments requiring the largest attainable luminosity at the expense of a moderate resolution.

3. Extension of the spectrometer

We expect that the combination of the high-resolution conversion electron spectroscopy with the well developed X-ray photoelectron spectroscopy will render us new possibilities for investigating the solid radioactive samples. Promising are:

(1) the precise energy calibration of the zero-energy-loss peaks of the conversion electron lines based on the well-known photoelectron lines, e.g. the C1s line of the hydrocarbon contamination layer on the source surface,

(2) the precise determination of the nuclear transition energies from the energy differences of the conversion and photoelectron lines corresponding to the same valent state of the same element. This approach eliminates both the uncertainties in electron binding energy of the investigated decay products and the spectrometer work function (see e.g. [13]) and

(3) the examination of the elemental or even valent composition of the surface layer of the sample from which the conversion electrons and the photoelectrons can be emitted without energy losses. This information is of importance for the interpretation of the measured spectra as well as for the development of the sample preparation methods required for precision conversion electron spectroscopy.

To keep the good parameters of the spectrometer it was decided to prepare all additional parts separately in Debrecen and to assemble them in Řež to avoid a possible damage during transportation of the whole instrument. Naturally, extensive adjusting and calibration measurements were needed after the assembling.

The scheme of the modified spectrometer is shown in Fig. 1.

3.1. X-ray source

Our present X-ray tube with the high purity Al anode has the following working parameters: the anode voltage of +9 kV and the emission current not exceeding 13 mA. For some tasks, the emission current should increase to ~ 40 mA. The anode is directly cooled by distilled deionized water flowing through the closed circuit at the speed 1.5 l/min, while the cathode holder is cooled with tap water. Conductivity of the distilled water is periodically tested not to exceed 70 μS/cm. The X-ray tube stability is regularly checked by the C1s photoelectron line of the standard sample. After some small improvement the stability seems to be acceptable. The photographic spot of X-rays at the sample surface shows the asymmetrically distributed photon beam; the region of the maximum intensity does not coincide with the centre of the sample.

3.2. Transport system

The transport system is in fact a small double pass cylindrical mirror analyser with the theoretical resolution of 8% transferring electrons from the X to AN position (see Fig. 1 and Section 3.4). Its transmission is mainly limited by the X-ray tube housing which penetrates into the cylinders of the transport system.

The design of the transport system relied on calculations of the electron trajectories in the electrostatic field of an ideal cylindrical condenser. Recently, we

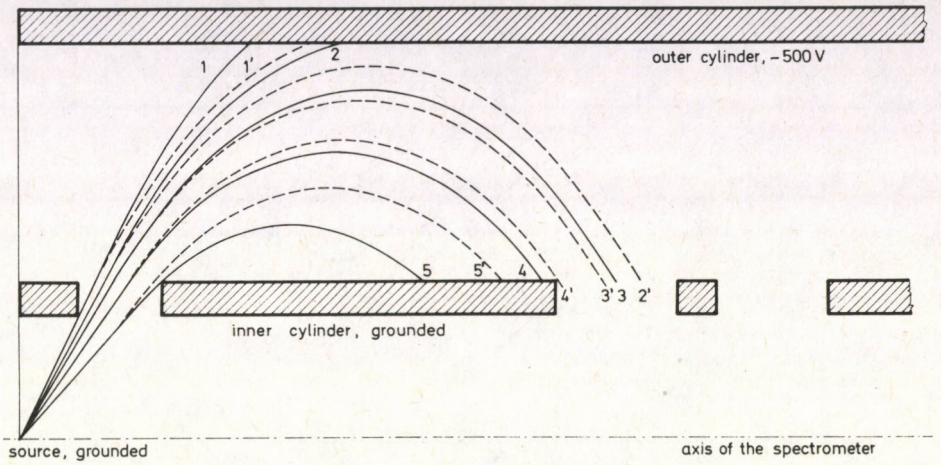

Fig. 3. Comparison of electron trajectories in an idealized electric field of cylindrical condenser (dashed lines, primed) with those in actual field of true geometrical arrangement of the ESA 12 transport system (full lines, unprimed). Initial kinetic energy of electrons is 1 keV. The emission angles of electrons emitted from a point source are: $1 - 46^o$, $2 - 43^o$, $3 - 40^o$, $4 - 36^o$, and $5 - 30^o$

calculated the electrostatic field in the actual transport system of the ESA 12 spectrometer using the computer program [14]. As can be seen from Fig. 3, there is a great difference between the electron trajectories in ideal and real fields. Therefore, we intend to perform extensive calculations to understand better the focusing properties of ESA 12 spectrometer and attempt to improve its luminosity while keeping the highest resolution.

3.3. Retarding lens

The retardation of electrons is performed by the retarding lens which is composed of three conical electrodes between the analyser and the transport system (Fig. 1). The first and the third electrode is connected to the inner cylinder of the transport system and the analyser, respectively. The optimum potential of the middle electrode, U_m, was found experimentally to be 40% of the total retarding voltage, U_r, for the analyser pass energies between 50 and 150 eV (Fig. 4).

We did not find any substantial changes in shape and intensity of the conversion lines measured before and after the spectrometer reconstruction, i. e. with and without the retarding lens, respectively.

3.4. Sample introduction system

The new sample introduction system enables us to put the sample into one of the following positions (see Fig. 1):

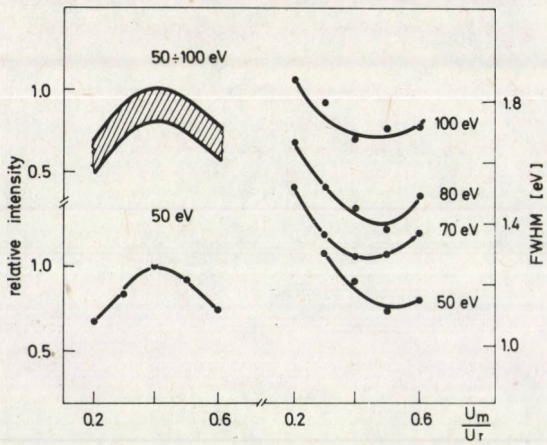

Fig. 4. Adjustment of the middle electrode potential, U_m, of the retarding lens by measuring the intensity and resolution of the conversion line. U_r is total retardation voltage between the first and third electrode of the retarding lens. The measurements were carried out for five values of the pass energy, E_p, between 50 and 100 eV

- AN - position in the analyser (as before extension, used for conversion measurements only),
- X - position for both photoelectron and conversion measurements. The same radioactive sample can be measured in both positions, the change is realized without taking it out of the spectrometer. The best position of both measuring points on the spectrometer axis was optimized experimentally.

4. Calibration measurements

The M_4 and M_5 conversion lines of the 2.17 keV transition in ^{99}Tc were utilized in calibration measurements after the spectrometer reconstruction. First, the ratio of the line intensities measured with the same source at the AN and X positions, I_{AN}/I_X, was examined as a function of the electron pass energy, E_p. This ratio was found to be ~ 4 for $E_p = 1850$ eV, but it varies between 10 and 15 for pass energies in the region of about 60 to 200 eV.

Secondly, the dependence of the spectrometer resolution and luminosity on the pass energy, E_p, ranging from 1850 to 60 eV was investigated with the source in both AN and X positions (for example, see Fig. 5). The results indicate that the components of the electron optical system are not yet perfectly fitted together

which underlines the importance of the calculations outlined in Section 3.2.

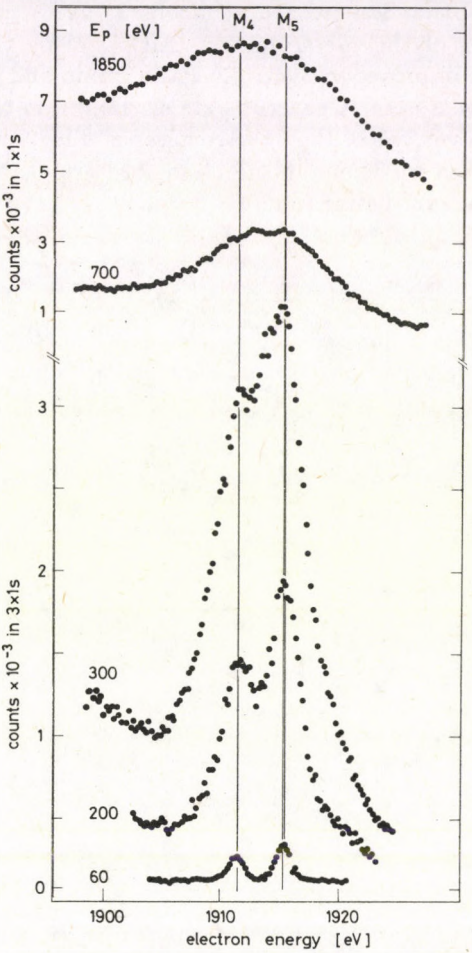

Fig. 5. The M_4 and M_5 conversion lines of the 2.17 keV transition in ^{99}Tc taken at various pass energies ranging from E_p = 60 eV to 1850 eV with the source in AN position

To verify the quality of our XPS measurements we examined samples with well-known spectra. We found our spectra, some of which are shown in Fig. 6, to be comparable with those from the literature. In addition, we recorded the XPS lines of the radioactive ^{99}Tc, too (right bottom of Fig. 6).

5. Some experiences

5.1. Vacuum system

Since 1977, the ESA 12 spectrometer has been operating many thousand hours without any serious failure. Although its vacuum chamber is pumped almost

continuously, the two orbitron ion getter pumps, also made in the ATOMKI, needed cleaning only three times. During measurements, the vacuum is usually 2×10^{-5} Pa even with the X-ray tube switched on and decreased to about 2×10^{-3} Pa when the sample is put in or taken out of the spectrometer. After closing the sample introduction system, the vacuum improves to 3×10^{-4} Pa in 1 min and to 7×10^{-5} Pa in 10 min. In some experiments even 10 sources were exchanged in the spectrometer within several hours. However, when the spectrometer is filled with nitrogen to atmospheric pressure, e.g. when we demount and clean the X-ray tube, it takes several days time to recover a vacuum better than 10^{-4} Pa.

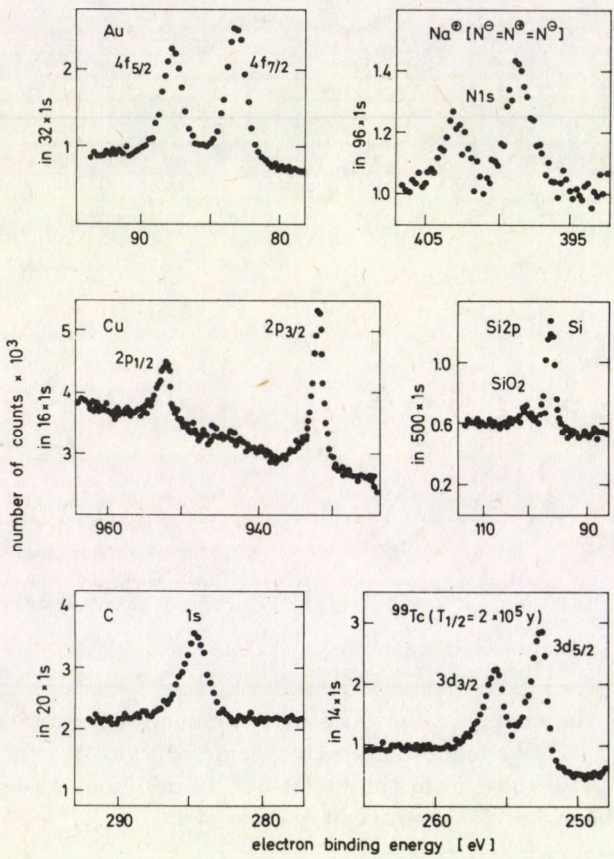

Fig. 6. Examples of photoelectron spectra excited by Al K_α radiation and recorded with the ESA 12 electrostatic spectrometer. Four of them are spectra of standard samples as Au, sodium azide, Cu and Si. The last two are photoelectron spectra taken from radioactive samples: ^{99m}Tc with the hydrocarbon contamination layer (left bottom), the C1s line is suitable for energy calibration of the conversion electron lines, and the 10^{-5}g amount of the ^{99}Tc (right bottom)

As for the mechanical parts of the spectrometer, only two metal sealed valves has to be repaired, one of them being extensively utilized in the sample introduction system and the second one closing the orbitron pump.

Since the mean free path of keV electrons in solids is in the order of nm it is important to avoid a contamination of the sample surface by titanium vapours from the ion getter pump. To examine this effect we placed the source holder with a clean Pt foil of 50 mm^2 area into the ESA 12 spectrometer and pumped it continuously for 14 days. Then, the Ti deposit on the foil surface was searched for by neutron activation analysis and X-ray photoelectron spectroscopy; the number of Ti atoms was estimated to be $\leq 10^{15}$ and $\leq 10^{13}$, respectively. Therefore, we do not expect any deterioration of our electron spectra caused by the Ti contamination layer.

5.2. High-voltage power supplies

The quality of the electron spectra taken at high instrumental resolution depends critically on the stability of precision high-voltage power supplies. Since 1977, we have been utilizing the same 8 kV floating and 3 kV programmable power supplies made at ATOMKI. In their long operation, only a few repairs were necessary, e.g. a change of the mechanical switches. The producer guaranteed the $\pm 5 \times 10^{-5}$ change of the full scale voltage per one degree of the temperature change or 10% change of the mains voltage. In connection with the high resolution measurements, we examined the power supplies with the aim to improve their stability.

The power supplies without covers were tested first in a conditioning chamber. We found that the mechanical switches were responsible for the most output voltage instabilities we observed. After putting the switches out of operation by soldering circuits in the 3 kV power supply, the voltage random instabilities disappeared and the relative temperature coefficient improved about 30 times. All the following tests were done with the 3 kV and 8 kV power supplies connected in series with switches off and output voltage set to 100 V and 1000 V, respectively.

The influence of the relative humidity up to 60% is negligible since the relative humidity coefficient was found to be less than $5 \times 10^{-7}/\%$. The effect is expected to rise with higher voltage and humidity.

In comparison with the conditioning chamber, the tests in the original ESA 12 rack showed that the temperature coefficient of power supplies changed its sign from + to − and in absolute value it was 2 to 4 times higher (Fig. 7). This behaviour of power supplies corresponds to a settled temperature. During sudden temperature changes the voltage overshoots were observed (see Fig. 8), i.e. the short term temperature coefficient was even worse.

We suggested the separate frame with an intensive cooling. The frame and power supply units are now without covers and the cooling is arranged by 9 fans located under the supplies. The temperature characteristics are about the same as those measured in the conditioning chamber (Fig. 7). No voltage overshoots were observed during sudden temperature changes in this arrangement.

The results are summarized in Table I.

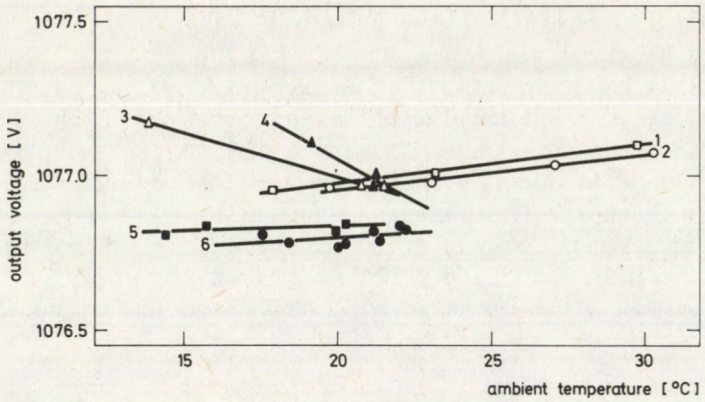

Fig. 7. Temperature characteristics of power supplies with switches off taken at settled temperature. Ambient temperature was measured with an uncertainty of ±0.1 °C. Output voltage of 1077 V measured by a Keithly 191 voltmeter was determined on 1σ level with the short term absolute accuracy of ±0.025 V at 21°C and ±0.068 V at 13°C and 31°C. The characteristics were recorded with the power supplies: 1,2 - in a conditioning chamber, 3,4 - in the original rack of the ESA 12 spectrometer, 5,6 - in a separate frame with intensive cooling

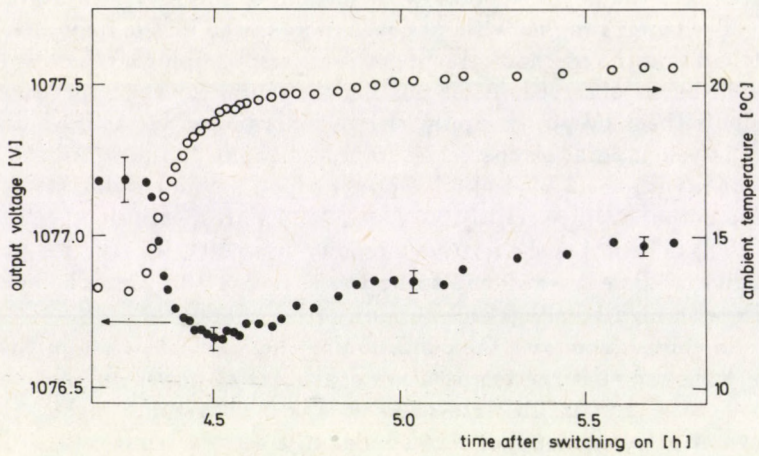

Fig. 8. Output voltage response to a sudden temperature change for power supplies in the original ESA rack with switches off. Temperature and output voltage were measured with the same accuracy as in the case of Fig. 7

Table I
The characteristics of power supplies

Location	Type	Output voltage [kV]	Switches	Relative temperature coefficient[a]
	−3 kV	−1.0		
			on	$+2.5\times10^{-4}/°C$
Conditioning chamber (4 fans)	+3 kV	+1.1		
	+3 kV	+1.1		$+8.7\times10^{-6}/°C$
			off	
	+3 kV and −8 kV in series[b]	+0.1 +1.0		$+1.2\times10^{-5}/°C$
Original rack	+3 kV and −8 kV in series[b]	+0.1 + 1.0	off	$-5\times10^{-5}/°C$[c]
				$-3\times10^{-4}/°C$[d]
Frame with intensive cooling (6 fans)	+3 kV and −8 kV in series[b]	+0.1 + 1.0	off	$+5.4\times10^{-6}/°C$[e]

[a] Maximum measured value
[b] The negative output terminal of the −8 kV floatable power supply was connected to the positive output terminal of the +3 kV power supply (total output voltage is positive)
[c] After temperature settlement
[d] During the sudden temperature change (Fig. 8)
[e] Voltage stability is $< 1.8\times10^{-5}$ for ± 10% mains change

5.3. Detector

In the ESA 12 spectrometer, the same piece of the channeltron (type B419 BL/01, Mullard, England) detecting the focused electrons has been utilized for 10 years. Usually, the counting rate does not exceed some hundreds/s and the safety system guarantees switching off the high-voltage power supply at a vacuum worse than 1×10^{-2} Pa.

At the beginning, the channeltron background was about 1.5 counts/min [1]. During the years, the radionuclides with half-lives ranging from 1.6 h to 2.6 y were investigated and the background was followed systematically to reveal possible contamination of the instrument. When $^{207-210}$At ($1.6h \leq T_{1/2} \leq 8.3h$) and volatile compounds of ^{99m}Tc ($T_{1/2} = 6h$) were studied the background increased sometimes to 10^2 counts/min. In other cases, the background increased to 10–40 counts/min. Recently, no radioactive source was put into the spectrometer for two months owing to the calibration XPS measurements and the background decreased to 6.5 counts/min with fully opened slits and to 1.5 counts/min when the slits were closed. Thus the long time contamination of the ESA spectrometer is not serious and it is probably not concentrated near the channeltron.

6. Conclusion

During ten years of the ESA 12 operation, we have taken more than 2000 spectra of the conversion electrons, Auger electrons and, recently, also photoelectrons emitted from radioactive sources. Most of them were taken in the energy region of the order of keV. The information we gained [1–9] is of interest to nuclear physics, nuclear chemistry and to some extent also to atomic physics.

We also demonstrated how an instrument, made in laboratory conditions, for research, should be continuously improved to meet the requirements of the new tasks. In the case of the ESA 12 spectrometer, this could be achieved only in close cooperation with the physicists of the ATOMKI, Debrecen.

Acknowledgement

We are indebted to Academician D. Berényi for his informal interest and continuous support in all stages of developing the ESA 12 spectrometer. Our sincere thanks are also due to his collaborators Drs. D. Varga, I. Cserny, I. Kádár, Á. Kövér, L. Kövér, Gy. Mórik and J. Tóth for their willing help and advice. We acknowledge Dr. N. G. Shakun's assistance, who kindly provided the program for the calculations of the charged particle trajectories.

References

1. D. Varga, I. Kádár, Á. Kövér, I. Cserny, Gy. Mórik, V. Brabec, O. Dragoun, A. Kovalík and J. Adam, Nucl. Instrum. Meth., *192*, 277, 1982.
2. O. Dragoun, V. Brabec, A. Maštalka, A. Kovalík, M. Ryšavý, M. Ya. Kuznetsova and Yu. V. Norseev, Nucl. Phys., *A391*, 29, 1982.
3. O. Dragoun, V. Brabec, M. Ryšavý, A. Špalek and K. Freitag, Z. Phys. A – Atomic Nuclei, *326*, 279, 1987.
4. O. Dragoun, M. Fišer, V. Brabec, A. Kovalík, A. Kuklík and P. Mikušík, Phys. Lett., *99*, 187, 1983.
5. M. Fišer, V. Brabec, O. Dragoun, A. Kovalík, J. Frána and M. Ryšavý, Int. J. Appl. Radiat. Isot., *36*, 219, 1985.
6. M. Fišer, V. Brabec, O. Dragoun, A. Lázničková, A. Kovalík and M. Ryšavý, Appl. Radiat. Isot., *37*, 1213, 1986.
7. M. Fišer, V. Brabec, O. Dragoun, A. Kovalík, M. Ryšavý and N. Dragounová, Appl. Radiat. Isot., *39*, 943, 1988.
8. V. Brabec, O. Dragoun, M. Ryšavý, M. Fišer, A. Kovalík, I. Cserny and I. Kádár, Z. Phys. A - Atoms and Nuclei, *311*, 37, 1983.
9. V. Rössiger, A. Freyer, E. Hartmann, C. Treutler, V. Brabec, O. Dragoun, A. Kovalík, Isotopenpraxis, *22*, 87, 1986.
10. W. M. Lacasse, J. H. Hamilton, Nucl. Phys., *A171*, 641, 1971.
11. V. N. Gerasimov, A. G. Zelenkov, V. M. Kulakov, V. A. Pchelin, M. V. Sokolovskaya, A. A. Soldatov and L. V. Chistyakov, Zh. Eksp. Teor. Fiz., *82*, 362, 1982.
12. O. Keski-Rahkonen and M. O. Krause, At. Data Nucl. Data Tables, *14*, 139, 1974.
13. V. N. Gerasimov, A. G. Zelenkov, V. M. Kulakov, V. A. Pchelin, A. A. Soldatov and L. V. Chistyakov, Yader. Fiz., *34*, 3, 1981.
14. S. B. Vorozhcov, N. G. Shakun, Meeting on Programming and Mathematical Methods for Solving the Physical Problems, JINR D10-7707, Dubna, 159, 1974 (in Russian).

Acta Physica Hungarica 65 (2–3), pp. 195–200 (1989)

EJECTED ELECTRONS AT BACKWARD ANGLES FROM He AND Ne BY He^{2+} IMPACT*

GY. SZABÓ, Á. KÖVÉR and L. GULYÁS

Institute of Nuclear Research of the Hungarian Academy of Sciences (ATOMKI)
4001 Debrecen, Hungary

The theoretical and experimental double differential cross sections for ejected electrons are compared for the 0.5 MeV/u He^{2+}–He, Ne collision systems at backward observation angles. The theoretical values are calculated within the framework of first Born approximation. The agreement between the theoretical and experimental values is rather good for the He, but not for the Ne target.

Introduction

The ejection of electrons from atoms by ion impact is one of the most important mechanisms in atomic collision physics. The double differential cross section (DDCS) for ejected electrons (differential in energy and emission angle) provides direct information on the ionization process. The knowledge of this distribution is important not only for the comprehensive understanding of the fundamental interaction mechanism but also for a number of practical fields. The results may be directly applied in the field of radiological, plasma and solid–state physics, astronomy etc.

It was shown early that the first Born approximation using H-like wave functions describes well the total ionization cross sections. However, a discrepancy between theory and experiment was found at small and large ejection angles in the DDCS values of ejected electrons [1, 2]. A similar disagreement was observed when the semiclassical binary-encounter approximation [1] was used for calculations.

The discrepancy at small ejection angles was qualitatively explained by taking into account the electron capture to continuum process (ECC) [1, 2].

For large angle discrepancies Madison [3] suggested that the deviation was not due to inadequacies in the Born approximation but rather to the inaccurate wave functions employed. The systematic studies [3–6] over a wide range of targets (He, Ar, Kr), incident projectile energies and ejection angles, showed that the calculations which employ Hartree–Slater wave functions gave reliable results for proton and electron impact. The existing experimental data have been summarized by Toburen[7].

Recently, the heavy projectiles (C^{6+}, O^{8+}, Ne^{10+}, Mo^{40+}) impact has been investigated. The calculation of Fainstein et al [8] using the continuum distorted wave eikonal initial state model (CDW-EIS) [9], for these heavy projectiles gave a

*Dedicated to Academician D. Berényi on his 60th birthday

better agreement with the experimental data than the Born calculations mentioned above.

Although a lot of theoretical and experimental effort has been done there is still a need for investigating the process of electron ejection at backward observation angles for projectiles heavier than proton and targets heavier than He.

He and Ne targets and 0.5 MeV/u He^{2+} projectile were chosen for investigations. The data measured and calculated for He target were used to test the calculations for these relatively simple target and projectile species. The Ne target is a good candidate for testing the calculations for a relatively heavy target which has electrons only on the K and L shells. The data measured for Ar target were used for calibrating the experimental set up.

Experimental procedure

The experimental apparatus has been described elsewhere [10] so only a brief description is given here.

The He^{2+} projectiles were prepared from He^{+} ones by using a gas stripper. The He^{+} ions were produced by the 5 MV Van de Graaff accelerator of ATOMKI. Electrons ejected from the collision into backward angles (95°– 170°) in the laboratory frame were measured by a distorted field cylindrical mirror electron spectrometer (designated as ESA-13) made in ATOMKI. Three channel electron detectors have been used to measure the electron spectrum at three different angles simultaneously [11]. The acceptance angle of the spectrometer at each measured angle was ±4°. The relative energy resolution was $dE/E = 0.5\ \%_0$.

The absolute double differential cross sections were determined (see in details in our earlier publication [10]) by comparing the existing experimental absolute DDCS values [12] for Ar target with the intensity of measured electrons. For Ne and He targets the target density relative to Ar was determined by remeasuring the known absolute cross sections of Rutherford scattering of protons and of elastic scattering of electrons on He, Ne and Ar.

The estimated experimental error originated from the statistical error of the measured data and from the error of the absolute DDCS data used for normalization.

PWBA calculations

Let us assume that a particle of charge z, mass M, and initial momentum $\mathbf{k}_0$ (all in atomic units) ionizes an atom of atomic number Z. The triple differential cross section (TDCS) is given in Born approximation [2, 3] by

$$\frac{d^3\sigma_{if}}{dE\, d\Omega_e d\Omega} = \frac{4\,M^2}{k_0^2 K^4} \left| < \Psi_f | \sum_j \exp\left(i\mathbf{k}\mathbf{r}_j\right) | \Psi_i > \right|^2 , \qquad (1)$$

where Ψ_i and Ψ_f are the initial and final antisymmetric atomic wave functions, respectively, with the continuum part normalized per unit energy. $d\Omega_e$ and $d\Omega$ are the solid angle of the ejected electrons and of the scattered particles, respectively. E is the energy of ejected electrons. $\mathbf{K}=\mathbf{k}_0-\mathbf{k}_f$ is the momentum transfer ($\mathbf{k}_f$ is the momentum of the scattered particle). Eq. (1) can be reduced if Ψ_i and Ψ_f are expressed as antisymmetric products of single particle functions with the assumption that there is no core relaxation

$$\frac{d^3\sigma_{n\ell_0 m_0 E_k}}{dE\, d\Omega_e d\Omega} = \frac{4M^2}{k_0^2 K^4} |< \Psi_{E_k} | \exp(i\mathbf{kr}) | \Psi_{n\ell_0 m_0} >|^2 , \qquad (2)$$

where $n\ell_0 m_0$ are the quantum numbers of the ionized electron. The summation over the quantum numbers gives the TDCS of ejected electrons.

In order to determine the numeric values of DDCS Ψ_{E_k} and $\exp(i\mathbf{kr})$ should be expanded according to the spherical harmonics and then the equation can be integrated over the solid angle of scattered projectile. The detailed expression for DDCS can be found in the papers of Madison [3] and of Manson et al [2, 4].

In our numerical calculations similarly to that of [3–6] the initial state $(n\ell_0 m_0)$ was described by one-electron orbitals calculated according to Hartree–Slater [13]. The final continuum orbitals of ejected electrons are taken to be solutions to the radial Schrödinger equation with the same central potential as the initial state.

Madison and Manson [5] employed Hartree–Fock wave functions in their calculation for the determination of the ionization cross sections of the Ar $3p$ subshell. They found that the results did not differ too much from that obtained with Hartree–Slater wave functions. The agreement between theory and experiment was not improved by their calculations.

Results and discussion

Figure 1 shows the comparison of the experimental data with the theoretical DDCS values calculated in the frame of the first Born approximation described above for the He^{2+} He collision system as the function of the emission angle. As it is shown the values agree fairly well inside the limits of the experimental error ($\approx 40\%$).

Madison and Manson [5] compared their calculated DDCS values with the experimental ones for the H^+–He collision system at different impact energies (0.1, 0.2, 0.3 and 2 MeV) in a wide (0° –170°) angular region. Manson et al [4] published a comparison for the collision system similar to mentioned above in the 0.3 MeV and 5 MeV impact energy range. They found that the agreement between the theory and the experiment is rather good, even at large angles.

For Ne target we are the first to make such a comparison. Our results can be found in Fig. 2. Here the agreement is not so good as it was for He target. As it is seen in Fig. 2 the discrepancy is rather large around 55 eV electron energy but at higher energies the agreement is better inside the limit of error.

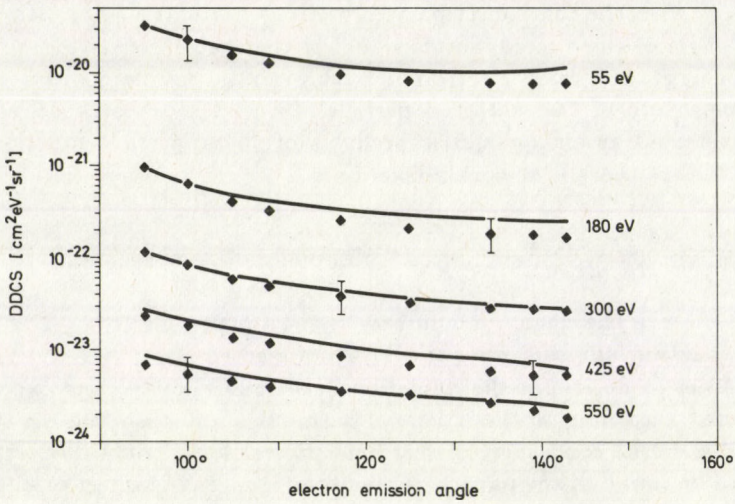

Fig. 1. Comparison of experimental and theoretical DDCS values as function of the observation angle at five energies of ejected electrons for 0.5 MeV/u He^{2+}–He collision. • experimental data; —— first Born approximation

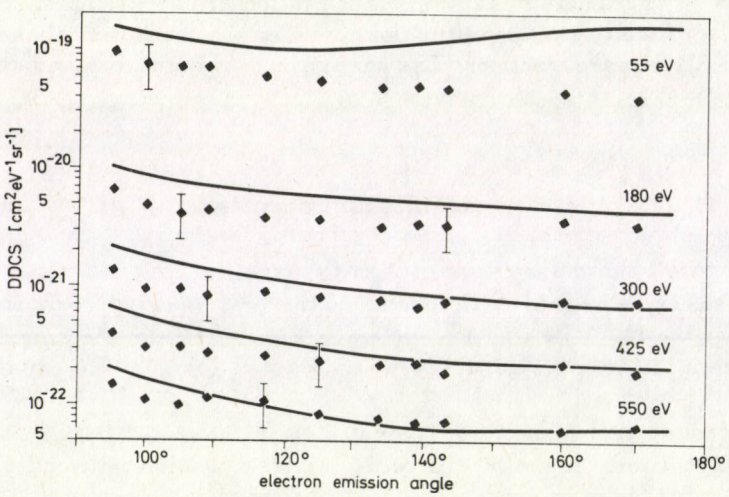

Fig. 2. Comparison of experimental and theoretical DDCS values as function of the observation angle at five energies of ejected electrons for 0.5 MeV/u He^{2+}–Ne collision. • experimental data; —— first Born approximation

A similar result has been published by Madison and Manson [5], who have

calculated the DDCS of ejected electrons for H^+–Ar collision system. Their calculations covered a wide range of impact energy from 0.05 MeV to 5 MeV and a wide angular region. Here the agreement between the experiment and the theory is significantly worse than that for the He target. It is surprising that the agreement is better at low impact energies (0.05 MeV and 0.1 MeV) than at higher ones because it is expected that the first Born approximation gives better results at higher impact energies. Their results are similar to ours, namely the discrepancy between the experiment and the theory is larger at low ejected electron energy than at higher electron energy values. When using Hartree–Fock wave functions their results were the same, too.

Conclusions

The intensity and angular distribution of ejected electrons originating from the 0.5 MeV/u He^{2+}–He, Ne collisions were investigated at backward ejection angles. The DDCS calculations were done in the frame of first Born approximation.

For He target the agreement between the experimental and threoretical DDCS values is rather good inside the limits of experimental errors. A similar agreement was found for H^+–He collision system, too [3, 4].

For Ne target the difference between the experimental and theoretical DDCS values is larger than it was for He target. The tendency of this discrepancy is similar to that which was found for H^+–Ar collision system [5].

We hoped that if the discrepancy found for Ar target is caused by the frozen (spectator) electrons which do not take part in the collision, the agreement would be better for Ne target. However, the discrepancy found for Ne target indicates that further theoretical and experimental investigations are needed.

The recently published CDW-EIS approximation [8] seems to be a good candidate for those calculations where the target is heavier than He. In this model the interaction between the ejected electron and the scattered projectile is taken into consideration, which is not included in the Born approximation.

Acknowledgement

The authors wish to express their thanks to Professor S. T. Manson for providing his computer program to calculate the DDCS with the HS wave functions for target ionization.

References

1. M. E. Rudd and J. K. Macek, Case Studies in Atomic Physics, *3*, 47, 1972.
2. S. T. Manson, Proc. of 2nd Workshop on High-Energy Ion–Atom Collision Processes, Debrecen, 27-28 Aug., 1984, ed. D. Berényi and G. Hock, Akadémiai Kiadó, Budapest, 1985, p. 15.
3. D. H. Madison, Phys. Rev., *A8*, 2449, 1973.

4. S. T. Manson, L. H. Toburen, D. H. Madison and N. Stolterfoht, Phys. Rev., *A12*, 60, 1975.
5. D. H. Madison and S. T. Manson, Phys. Rev., *A20*, 825, 1979.
6. L. H. Toburen and S. T. Manson, Abstract of Papers of XIth ICPEAC (The Society for Atomic Collision Research, Japan, 1979), p. 628.
7. L. H. Toburen, Proc. of Int. Sem. on High–Energy Ion–Atom Collision Processes, Debrecen, 17–19 March, 1981, ed. D. Berényi and G. Hock, Akadémiai Kiadó, Budapest, 1982, p. 53.
8. P. H. Fainstein, V. H. Ponce and R. D. Rivarola, J. Phys. B.: At. Mol. Phys., *21*, 287, 1988.
9. D. S. F. Crothers and I. F. McCann, J. Phys. B.: At. Mol. Phys., *16*, 3229, 1983.
10. Á. Kövér, Gy. Szabó, L. Gulyás, K. Tőkési, D. Berényi, O. Heil and K. O. Groeneveld, J. Phys. B: At. Mol. Phys. *21*, 3231, 1988.
11. Á. Kövér, D. Varga, E. Szmola, Gy. Mórik, L. Gulyás, K. Tőkési, to be published in Nucl. Instrum. Meth.
12. M. E. Rudd, L. H. Toburen and N. Stolterfoht, At. Data Nucl. Data Tables, *23*, 405, 1979.
13. F. Herman and S. Skillman, Atomic Structure Calculations, Prentice–Hall, Englewood, Clipps, N. I., 1963.

Acta Physica Hungarica 65 (2–3), pp. 201–207 (1989)

L-SHELL IONIZATION AND L X-RAY EMISSION INDUCED BY ANTIPROTONS*

L. SARKADI

Institute of Nuclear Research of the Hungarian Academy of Sciences (ATOMKI)
4001 Debrecen, Hungary

The ionization of the L shell of atoms by energetic antiprotons has been studied theoretically for the first time. In addition to the effects discussed by Brandt and Basbas for the K shell, for the L shell a further effect has been shown to contribute to the particle–antiparticle differences in the cross sections. The effect is a result of coupling processes between the different L substates. As a demonstration, model calculations based on the second-order Born approximation have been performed for gold in the energy range 0.2 – 1 MeV.

1. Introduction

The *l*ow-energy *a*ntiproton *r*ing (LEAR) constructed recently at the CERN has opened up a new field of the physics of atomic collisions. The experimental possibility to change the sign of the electric charge of the projectile (i.e. the sign of the interaction) provides a sensitive test of the theoretical descriptions. Studies of collisions involving antiprotons contribute to a better understanding of the interaction of the antimatter with the "ordinary" matter surrounding us.

As an example, I mention the first experiment made by Andersen et al [1] in this new field. The group measured the ratio of double to single ionization for p^- – He collisions in the energy range from 0.5 to 5 MeV. Their results show a considerable difference from the ratios obtained for p^+ – He collisions. The difference is manifestation of the electron correlation according both to realistic and model-like calculations [2, 3]. Since electron correlation is among the hot topics of collision physics, the atomic data obtained at the CERN are of special importance.

Inner-shell excitation (ionization) of heavier atoms represents also an area, where particle–antiparticle differences may be observed. For very asymmetric collisions the gross features of the ionization phenomena can be well described by first-order (direct) theories. These theories predict the dependence of the cross section on the projectile atomic number (Z_1) proportional to Z_1^2. However, the cross section behaves in the predicted way only at high impact velocities. With decreasing velocity several effects may cause deviation from the "Z_1^2 law": for positively charged projectiles the deflection and retardation of the ionizing particle in the Coulomb field of the target nucleus, the increase of the binding energy of the target electrons due to the adiabaticity of the collisions, and the polarization of the

*Dedicated to Academician D. Berényi on his 60th birthday

electron cloud. The first two effects may reduce the cross section by several orders of magnitude, while the polarization (which occurs at relatively large velocity) increases it only by a few per cent. The first-order perturbation theories corrected for these effects show a remarkable agreement with the experimental cross sections in a broad range of the collision velocity and the target atomic number, particularly for K-shell ionization [4], where a large number of experimental data are available.

For antiparticles the direct theories predict the same cross sections as for particles because of the Z_1^2 dependence. The effects described above, however, are sensitive to the sign of the interaction [5, 6]. Firstly, the trajectory of the antiparticle is different from that of the particle: instead of deflection away it is bent towards the target nucleus. The deeper penetration into the electron cloud and also the acceleration of the projectile give rise to a drastic increase of the ionization probability. Secondly, the electronic binding energy is reduced in this case and causes a further increase in the ionization cross section. The resulting particle–antiparticle difference could be pointed out by the detection of the X-rays or Auger electrons following the inner-shell ionization. To the knowledge of the author no such experiment has been done so far, probably because the intensity of the antiproton beam at the CERN is still too low for this purpose.

Another kind of deviations from the first-order theories occur for shells consisting of degenerate or nearly degenerate subshells, e.g. for the L shell. The main difficulty arising here is that the ionization of the subshells cannot be regarded as independent processes, especially for strong perturbations represented by heavier ions. As we have shown experimentally and theoretically [7–12], the dynamical couplings among the L subshells of heavy elements may lead to deviations of order of magnitude for collisions with ions as heavy as oxygen. Though for a long time this effect has been considered to be negligible for proton impact, recent accurate measurements [19] and calculations [20] proved the existence of the subshell couplings also for the case of such less violent collisions.

The contribution from the intrashell couplings to the cross section can be expressed as higher-order terms of the Born series of the ionization amplitude. For example, in the second-order approximation — in addition to the leading Z_1^2 term — terms proportional to Z_1^3 and Z_1^4 also contribute to the cross section. The source of the particle–antiparticle difference is the Z_1^3 term. Our previous second-order model calculations [10] showed that this "interference" term may take large values. Consequently, significant differences are excepted between proton- and antiproton excitation of the L subshells. The detailed theoretical investigation of this effect was the primary aim of the present work.

2. The theoretical model

The computational difficulties arising for second- or even higher-order calculations are well known. To overcome the difficulties we have tried to give quantitative descriptions on the basis of simple physical consideration and applying several approximations. In the last years these attempts resulted in the more or less classical

"two-step model" [8], and two more exact quantum mechanical treatments referred to as "second-order SCA (*S*emi-*C*lassical *A*pproximation) calculations" [10, 13] and "coupled-states theory" [14]. The coupled states theory — regarded as the most complete description — is based on the solution of a set of coupled differential equations governing the time-evolution of the L-substate amplitudes. While this theory is suitable also for the treatment of strong perturbations represented by heavy ions [15], the second-order SCA is limited only for the case of small perturbations, where in turn it gives identical results with the coupled-states model.

The quantity determined by the above models is an estimate of the higher-order contribution to cross sections calculated in a first-order ionization theory. One of the best first-order theories is the ECPSSR model [16]. It gives an excellent description of the ionization of inner shells by light-ion impact in a large range of the collision velocity. The model is widely used to calculate cross sections, mainly for the reason that its computational simplicity makes it easily available also for experimentalists. The ECPSSR description has been developed from the *p*lane-*w*ave *B*orn *a*pproximation (PWBA) including corrections for the effects mentioned in the introduction: the Coulomb-deflection, the binding, and the polarization effect. Two further corrections are also applied in this model. One accounts for the relativistic effects in the target atomic states which are neglected in the original formulation of the PWBA. The other correction takes into consideration the energy loss of the projectile during the ionization process.

The first step done in the present work was the modification of the ECPSSR for negatively charged projectile. In an exact theory this would mean the following automatic replacement in the ionization cross section

$$\sigma(\bar{p}\,; Z_1) = \sigma(p\,; -Z_1), \tag{1}$$

where Z_1 is always positive and p and $\bar{p}$ denote particle and antiparticle. However, one must be cautious when approximations are applied. The procedure of automatic replacement Z_1 by $-Z_1$ works for the binding and polarization effect, buth it fails for the Coulomb-deflection effect [5]. In the latter case the following approximation is used for the so-called Coulomb-deflection factor

$$C(x) = (n-1) \int_1^{T_M} \frac{e^{-xt}}{t^n}\, dt \approx (n-1)\, E_n(x), \tag{2}$$

with

$$x = \pi\, d\, q_0 \zeta .$$

Here d denotes the half distance of closest approach in a head-on collision, $\hbar q_0$ is the minimum momentum transfer and ζ is a parameter connected with the binding and polarization effects. T_M corresponds to the maximum energy transfer to the electron to be ionized. $E_n(x)$ is the exponential integral of order n, where $n = 10$ for

s state (K and L_1 shell) and $n = 12$ for p state (L_2 and L_3 shell). For antiparticles the replacement Z_1 by $-Z_1$ leads to

$$C(x) = (n-1) \int_1^{T_M} \frac{e^{+xt}}{t^n}\, dt. \tag{3}$$

This integral is divergent. However, the integrand has a broad minimum which makes relatively easy to cut the "unphysical" contribution from large values of the argument t. This procedure is justified by the vanishingly small probability for large energy transfers.

For inclusion of the subshell coupling effects the results of the second-order calculations of Sarkadi and Mukoyama [10] were used. Since the second-order model has been described in details in previous works [10, 12, 13], here I only cite its basic equations. Including only L substates as intermediate (virtual) states, in the framework of the semi-classical approximation the time-dependent perturbation theory leads to the following second-order amplitude for a transition from an initial bound state $| i >$ to a final ionized state $| f >$ (in atomic units)

$$a_f^{(2)} = -i \int_{-\infty}^{\infty} dt \left[U_{fi} \exp\left(-i \int_{-\infty}^{t} dt'\, U_{ii} \right) + \sum_{n_L (\neq i)} U_{f n_L} (-i) \int_{-\infty}^{t} dt'\, U_{n_L i} \exp\left(-i \int_{-\infty}^{t'} dt''\, U_{ii} \right) \right], \tag{4}$$

with the notations

$$U_{mk}(t) = V_{mk}(t) \exp(i\omega_{mk} t),$$
$$V_{mk}(t) = \int d\bar{r}\, \Psi_m^* V(t) \Psi_k, \tag{5}$$
$$\omega_{mk} = E_m - E_k.$$

Here n_L is the short notation of the quantum numbers (l, j, m_j) of the eight L substates (including also the degenerate states), $V(t)$ is the perturbing potential due to the Coulomb interaction between the projectile and the target electron. Ψ_m and Ψ_k are one-electron energy eigenstates, and E_m and E_k are the corresponding energy eigenvalues of the unperturbed atom. In Eq. (4) the first term describes the direct ionization, the second term gives contribution from two-step processes.

After using several approximations the second-order effects for an L subshell labelled by i are expressed in the form of a correction factor

$$\sigma_i \text{ (2nd order)} \approx R_i\, \sigma_i \text{ (1st order)}. \tag{6}$$

R_i is a second-order polynomial of the projectile atomic number

$$R_i = 1 + F_{1i} Z_1 + F_{2i} Z_1^2. \tag{7}$$

Here the coefficients F_{1i} and F_{2i} depend only on the collision velocity and on the properties of the target atom.

3. Results and discussion

An ECPSSR code with proper inclusion of the Coulomb effect for antiparticle (see Eq. (3)) was run for the cases of proton and antiproton collisions on gold in the energy range $0.2 - 1$ MeV, and the resulting cross section values were corrected for the subshell coupling effects according to Eq. (6). In the correction factors R_i the coefficients F_{1i} and F_{2i} were taken from the previous calculations [10] performed also for gold.

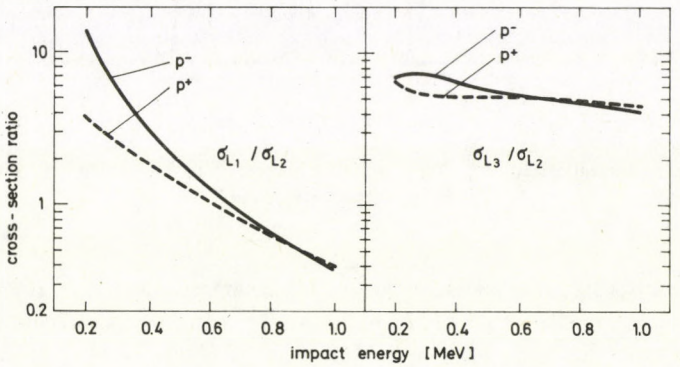

Fig. 1. Ratios of L-subshell ionization cross sections for proton- and antiproton bombardment of gold as a function of the impact energy

Of course, considerable enhancement of the L-subshell ionization cross sections can be observed for antiprotons due to the opposite Coulomb- and binding effect. Since this phenomenon has been discussed in detail for the K shell by other authors [5, 6], the *absolute* cross sections are not analyzed here. For the L shell more gentle effects of another kind can be studied through the *ratios* of the subshell cross sections. The L_1 to L_2 and L_3 to L_2 ratios obtained in the present work are plotted in Fig. 1. Increasing proton–antiproton difference can be observed with decreasing bombarding energy, particularly for the L_1 to L_2 ratio. Since the Coulomb- and binding effects modify the cross section of each subshell to a similar extent, they almost cancel for ratios, and thereby a significant part of the difference in Fig. 1 comes from the second-order correction. In Eq. (7) the term proportional to Z_1 — the interference term — is sensitive to the sign of the projectile charge, therefore in principle the coefficients F_{1i} could be deduced from a measurement including protons and antiprotons.

The simplest way to prove the above ideas experimentally is the detection of L X-rays following the proton- and antiproton excitation. The spectra expected to be recorded by a Si(Li) detector have been simulated by computer calculations and plotted in Fig. 2.

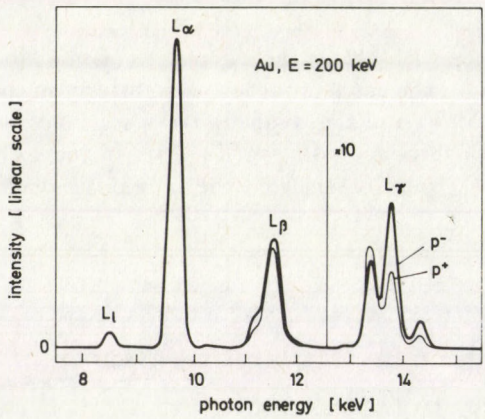

Fig. 2. Computer simulation of L X-ray spectra expected to be excited by 200 keV protons and antiprotons from gold

The bombarding energy is 200 keV. A constant resolution of 200 eV (FWHM) over the whole photon energy range was assumed. In the calculations the fluorescence and Coster–Kronig yields were taken from Chen et al [17], for the X-ray transition probabilities the values calculated by Scofield [18] were used. The spectra are normalized in intensity to the L_α peak. The most striking difference can be observed in the structure of the L_γ group. Smaller changes are seen for the L_β group, as well. We note that the particle–antiparticle difference appearing in the L X-ray spectrum of heavy elements can be used in principle to distinguish matter from antimatter. The APIXE (*a*ntiparticle-*i*nduced *X*-ray *e*mission) method for construction of a self-calibrating particle–antiparticle detector first has been proposed by Brandt and Basbas [5]. For example, such a detector could be used to study the antiparticle flux present in the interplanetary particle background. The proposal of Brandt and Basbas is based on the following principle. Two targets are exposed and the excited K X-rays are detected. One of the targets is relatively light (e. g. aluminium) and responds equally to particles and antiparticles in a bombarding energy range in which the other, heavier target (e. g. tin) gives a distinctive X-ray yield.

The detector based on L-shell excitation would have the advantage that one needs only one target to be exposed. Such a target may be present naturally in the Universe, and its radiation could directly give information about the density of the antiparticles.

4. Conclusion

The present work has shown that for L-shell ionization in addition to the Coulomb-, binding-, and polarization effects the subshell coupling processes signif-

icantly contribute to the particle–antiparticle difference, particularly in ratios of the subshell cross sections. However, it should be stressed that the calculations have been made with numerous approximations. For example, while the Coulomb effect has been taken into account for the first-order (ECPSSR) cross sections, the second-order correction factors have been established applying only straight line for the path of the projectile. For proton impact the more accurate calculations made recently [20] have proved that such an approximation is justified. Extension of the accurate calculations for antiprotons is planned in the near future, and then it is hoped to draw more reliable conclusions.

References

1. L. H. Andersen, P. Hvelplund, H. Knudsen, S. P. Møller, K. Elsener, K. -G. Rensfelt and E. Uggerhøj, Phys. Rev. Lett., *57*, 2147, 1986.
2. J. F. Reading and A. L. Ford, Phys. Rev. Lett., *58*, 543, 1987.
3. L. Végh, Phys. Rev., *A37*, 992, 1988.
4. H. Paul and W. Obermann, Nucl. Instr. and Meth., *214*, 15, 1983.
5. W. Brandt and G. Basbas, Phys. Rev., *A27*, 578, 1983.
6. G. Mehler, B. Müller, W. Greiner and G. Soff, Phys. Rev., *A36*, 1454, 1987.
7. L. Sarkadi and T. Mukoyama, J. Phys. B: Atom. Molec. Phys., *13*, 2255, 1980.
8. L. Sarkadi and T. Mukoyama, J. Phys. B: Atom. Molec. Phys., *14*, L255, 1981.
9. J. Pálinkás, L. Sarkadi, B. Schlenk, I. Török, Gy. Kálmán, C. Bauer, K. Brankoff, D. Grambole, C. Heiser, W. Rudolph and H. J. Thomas, J. Phys. B: Atom. Molec. Phys., *17*, 131, 1983.
10. L. Sarkadi and T. Mukoyama, Nucl. Instr. and Meth., B *4*, 296, 1984.
11. T. Papp, J. Pálinkás, L. Sarkadi, B. Schlenk, I. Török and K. Kiss, Nucl. Instr. and Meth., B *4*, 311, 1984.
12. L. Sarkadi and T. Papp, Acta Phys. Hung., *58*, 75, 1985.
13. L. Sarkadi, J. Phys. B: Atom. Molec. Phys., *19*, 2519, 1986.
14. L. Sarkadi, J. Phys. B: Atom. Molec. Phys., *19*, L755, 1986.
15. L. Sarkadi and T. Mukoyama, J. Phys. B: Atom. Molec. Phys., *20*, L559, 1987.
16. W. Brandt and G. Lapicki, Phys. Rev., *A 23*, 1717, 1981.
17. M. H. Chen, B. Crasemann and H. Mark, Phys. Rev., *A 24*, 177, 1981.
18. J. H. Scofield, At. Data Nucl. Data Tables, *14*, 121, 1974.
19. W. Jitschin, G. Materlik, U. Werner and P. Funke, J. Phys. B: Atom. Molec. Phys., *18*, 1139, 1985.
20. L. Sarkadi and T. Mukoyama, Phys. Rev., *A37*, 4540, 1988.

Acta Physica Hungarica 65 (2–3), pp. 209–215 (1989)

RESOLUTION AND DETECTION OF WEAK X-RAY LINES USING A Si(Li) DETECTOR COMBINED WITH ABSORBERS* **

T. PAPP and J. PÁLINKÁS

Institute of Nuclear Research of the Hungarian Academy of Sciences (ATOMKI)
4001 Debrecen, Hungary

A method to obtain high resolution and at the same time maintain high detection efficiency using absorbers in front of a Si(Li) detector is described. The method is analysed and its potentials are demonstrated by using it to resolve the $L_{\alpha 2}$ and $L_{\alpha 1}$ lines of Au and to measure the L_s and L_t lines of Pt excited by charged particle impact. The possible use of the method in other cases is discussed.

1. Introduction

In ion–atom collision studies the detection of X-rays offers an important and efficient method to obtain information on collision events. Therefore the details of the X-ray spectra, fluorescence yields, transition rates and branching ratios have to be known in high precision e.g. to deduce the ionization cross sections from the measured X-ray intensities. In general, the structure of the X-ray spectra, the transition rates, branching ratios, etc. constitute a data base vital in all branches of atomic and applied physics research.

The prominent X-ray lines of the K, L, M,... spectra are allowed electric dipole ($E1$) transitions. The higher order multipole terms ($M1, E2, M2, \ldots$) can modify the transition rates or produce some weaker lines in the spectrum. To test the theoretical description of the higher order multipole terms is important since these terms sensitively depend on the outer part of the wavefunction, which is complicated to test with other methods. In the case of multiply ionized ions a large number of satellite lines appears close to the diagram lines. To verify the reliability of ion–atom collision theories and the theoretical descriptions of the X-ray spectra, efficient and high resolution detection of usually weak X-ray lines is required. The clear detection of these weak lines by good resolution (but low efficiency) crystal spectrometers is hindered by the low intensity [1]. The resolution of high efficiency Si(Li) detectors is usually not enough to resolve these lines. The problem is especially pronounced in the ten keV energy region, where the resolution of simple crystal spectrometers and Si(Li) detectors is nearly comparable.

In this paper we describe a method to obtain high resolution and at the same time high efficiency for certain X-ray lines using a Si(Li) detector combined with appropriate absorbers. These lines were previously unresolved and undetected with Si(Li) detectors.

*Dedicated to Academician D. Berényi on his 60th birthday

**Work supported by MTA-OTKA grant No. 1184-1185

2. The background of the method

In the X-ray region absorbtion edges can provide very good resolution if one finds a material with its K-absorbtion edge falling between the two X-ray lines to be resolved. This material can be used as an absorber in front of a Si(Li) detector and the intensity of the line above the absorbtion edge will be much (e.g. a factor of 300) more reduced than the intensity of the line below the absorbtion edge. If this method is used for lines of comparable intensity, the higher energy line will be so strongly attenuated, that the Si(Li) detector behind the absorber detects only the X-ray line below the absorbtion edge. Weak dipole forbidden X-ray lines usually fall in the close vicinity of a strong electric dipole line in the spectrum, so even if the resolution of a Si(Li) detector would allow the separation by means of a fitting procedure, the weak lines are buried in the tail of the strong peak. If the strong electric dipole line falls above the absorbtion edge of an appropriate absorber, it will be reduced so that the much less reduced weak lines just below the absorbtion edge will be detectable.

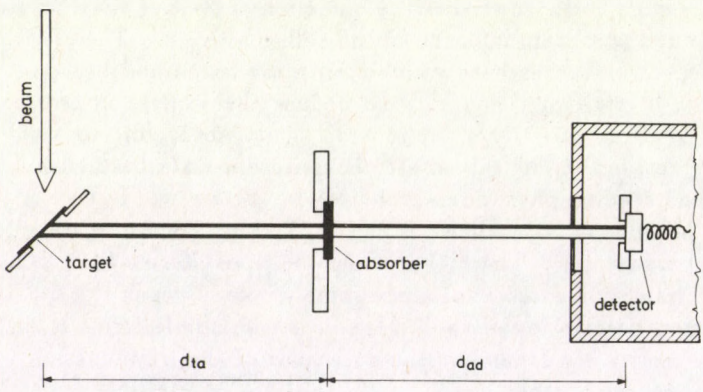

Fig. 1. Experimental arrangement

With this experimental arrangement (see Fig. 1), however, we face the problem that the strongly absorbed X-ray lines ionize the K-shell of the absorber, and the K X-ray emitted in the decay of these vacancies reaches the Si(Li) detector and produces unwanted lines usually in the region of the studied X-ray lines.

To obtain an estimate of the intensity of the fluorescent K X-ray intensity and to optimize the experimental arrangement, we have calculated the number of K_α X-ray photons ($N_\alpha(\varsigma)$) observed by the Si(Li) detector, if the detector detected N_ς photons in the ς X-ray line emitted from the target bombarded by a narrow beam of charged particles:

$$N_\alpha(\varsigma) = N_\varsigma(\omega/4\pi)(\sigma_K/\mu)\left[e^{\mu t} - 1\right] s_a \left[(1/d_{ta})^2 + (2/d_{ta}d_{ad}) + (1/d_{ad})^2\right], \quad (1)$$

where $\mu = \mu(\zeta) - \mu(K_\alpha)$ is the difference of the total attenuation cross sections for the exciting ζ and the fluorescent K_α (self absorbtion) lines, σ_K is the K-shell photoionization cross section of the absorber material for the ζ X-ray line, ω is the K_α fluorescence yield, t is the absorber thickness, s_a is the exposed surface area of the absorber, d_{ta} is the distance between the target and the absorber, d_{ad} is the distance between the absorber and the detector.

This result immediately tells that to minimize the K X-ray intensity the absorber surface area has to be minimized and for a fixed detector–target distance the $d_{ta} = d_{ad}$ condition has to be satisfied.

3. Experiments and discussion

This experimental arrangement has been used to measure the L X-ray spectra of Au ionized by the 6–20 MeV He^+ beam of the MGC cyclotron, the 500 KeV proton beam of the Cockroft–Walton accelerator of the ATOMKI and the 2.5 MeV proton beam of the tandem accelerator of the Zentralinstitut für Kernforschung (Rossendorf, DDR).

In the He^+ impact measurements the 6–20 MeV He^+ beam from the MGC cyclotron of the ATOMKI enters an evacuated scattering chamber and impinges on a thin vacuum evaporated target mounted in the centre of the chamber. The X-ray spectra form the target detected with three Si(Li) detectors. The absorbers on an Al holder can be mounted in front of the Si(Li) detectors.

In this experiment the absorber was used primarily to attenuate the $L_{\alpha 1}$ line of Au, and measure the angular distribution of the $L_{\alpha 2}$ line [2], which otherwise cannot be resolved. A 22 mg/cm^2 Zn absorber has 41% transmission for the $L_{\alpha 2}$ line of Au and 0.15% for the $L_{\alpha 1}$ line. Consequently the L_α line of the spectrum measured by a Si(Li) detector behind the absorber is mainly (97%) the $L_{\alpha 2}$ line. Fig. 2 shows the spectra obtained with and without absorber. The spectra were analysed with a computer code fitting Gaussian peaks on quadratic background to the measured spectra.

The effect of the absorbtion edge appears also in the shape of the background and the background was fitted with a linear function plus a step-function convolved with a Gaussian. The width of this Gaussian corresponded to the detector resolution.

In the 500 keV proton measurement the experimental setup was basically the same as applied and described in previous angular distribution measurements [3]. The collimated beam of projectiles enters a small (3 cm in diameter) scattering chamber and impinges on a thin vacuum evaporated target mounted in the centre of the scattering chamber and tilted at 45° with respect to the beam direction. The X-rays passing through a thin PET and Al window of the chamber, the absorber and altogether 5 cm air reach the active area of the detector. The absorber mounted on a 2 mm thick Al frame can be installed at variable distance between the target and the detector. The 22 mg/cm^2 zinc absorber of 20 mm^2 surface area were installed at $d_{ta} = 32$ mm from the target and $d_{ad} = 23$ mm from the detector. X-rays from the

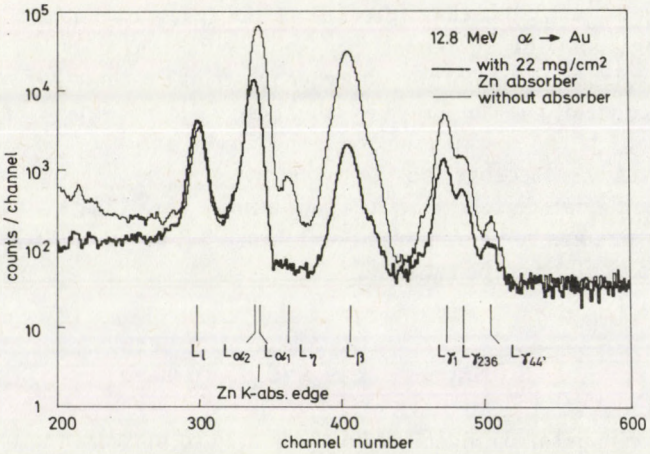

Fig. 2. L X-ray spectra of gold induced by 12.8 MeV He^{2+} ion impact recorded by a Si(Li) detector with and without a 22 mg/cm^2 Zn absorber

1.5 mm diameter beamspot on the target were detected with a Kevex Si(Li) detector of 10 mm^2 active area. In the spectrum the K_α line of the zinc absorber appears as a "shoulder" at the high energy side of the L_ℓ peak. The intensity can be determined by fitting the K_α, L_ℓ complex with two Gaussian functions. The intensity from the fit is found to be in excellent agreement with the intensity calculated according to Eq. (1), using the mass absorbtion coefficients given in [4]. The K_α intensity is found to be 10% of the intensity of the L_ℓ peak. From the well-known K_α/K_β ratio it can be calculated that the K_β line gives negligible (0.4%) contribution to the L_α intensity.

The method of using absorbers in front of a Si(Li) detector can dramatically improve the detection sensitivity for weak X-ray lines in the vicinity of strong electric dipole transitions if the strong line falls above the absorbtion edge of the absorber. This condition is well satisfied for Pt using Cu absorber. The weak L_s and L_t lines fall below the K absorbtion edge of Cu while the intense L_α line falls behind. The detection of these weak lines on the low energy side of the intense L_α peak is impossible without absorber because of the tail of the L_α peak. Using 22 mg/cm^2 Cu absorber in front of a Si(Li) detector the efficiency for the L_α is reduced by a factor of 400 while the efficiency for the L_s and L_t lines reduced by only a factor of 2, so that these lines are easily detectable.

The L X-ray spectra of thick Pt target excited by 500 keV p, 2.5 MeV p and 6 MeV alpha particles were recorded using 22 mg/cm^2 Cu absorber. The spectrum taken with 2.5 MeV p using 22 mg/cm^2 Cu absorber is displayed in Fig. 3. The spectrum was fitted with an appropriate number of Gaussian peaks on linear + step function background. The K_α line of Cu was also fitted in the spectra, while the K_β line was constructed from the known K_α/K_β ratio and $K_\alpha - K_\beta$ energy difference.

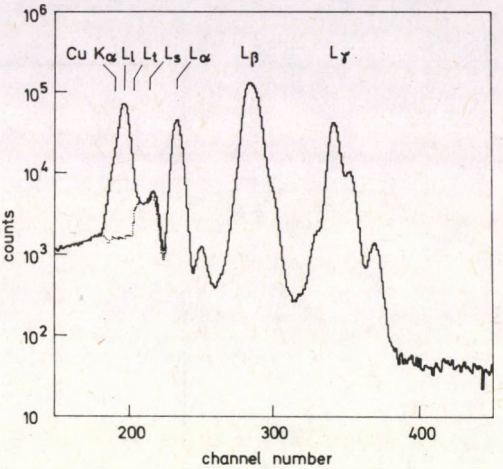

Fig. 3. L X-ray spectrum of platinum excited by 2.5 MeV p and recorded by a Si(Li) detector with 22 mg/cm^2 Cu absorber (solid curve) and the spectrum after subtracting the L_ℓ line of platinum and the K_α and K_β lines of copper (points)

Table I

Target and absorber combination for the detection of the L_s line

Target	Absorber	$E_{abs.edge}-E_{Ls}$ (eV)	$E_{Ls}-E_{K\beta 1}$ (eV)
Sm	V	167.5	−130.9
Gd	Cr	290.0	−247.9
Ho	Mn	142.1	−94.9
Tm	Fe	347.2	−294.0
Yb	Fe	117.4	−64.2
Hf	Co	256.3	−196.2
Re	Ni	163.3	−96.4
Ir	Cu	321.3	−243.9
Pt	Cu	57.3	+20.1
Hg	Zn	205.7	−117.0
Pb	Ga	400.7	−296.7
Bi	Ga	126.2	−22.2
Th	Se	393.5	−235.0

The spectrum obtained subtracting the L_ℓ line of Pt and the K_α and K_β lines of Cu is also displayed (points) in the Figure. This spectrum clearly shows the appearance of the L_s and L_t lines. The intensity of these lines is found a factor of four higher than the theoretical values of Scofield [5].

A further possibility is to use this principle to separate the multiple ionization satellites of L X-rays from the diagram lines. In Fig. 4 the principle of separation is shown, where the calculated satellite structure of the L_α line of Au and that of the L_ℓ line of Tl is given, when these targets are ionized with 1 MeV/amu F ions.

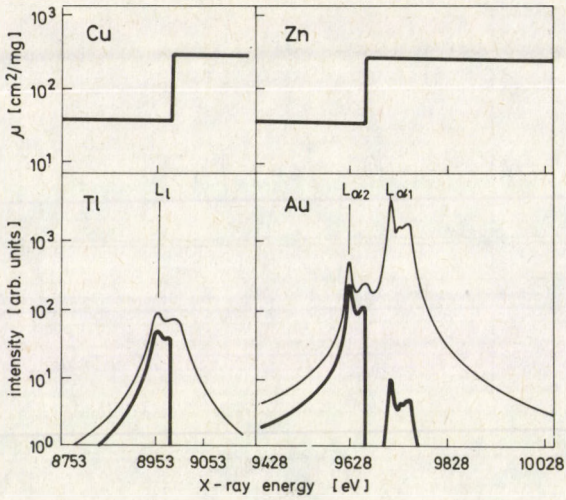

Fig. 4. The calculated satellite structure of Tl and Au L X-rays induced by 1 MeV/amu F projectiles (weak line) and the spectra after Cu and Zn absorbers, respectively (strong line). The mass absorbtion coefficients are also shown

Table II
Target and absorber combination for the detection of the $K_{\alpha 3}$ line

Target	Absorber	$E_{abs.edge}-E_{K\alpha 3}$ (eV)	$E_{K\alpha 3}-E_{K\beta 1}$ (eV)
As	Ga	28.0	76.0
Se	Ge	99.6	21.9
Br	As	173.3	−34.5
Ru	Nb	93.7	270.7
Rh	Mo	196.8	199.1
Xe	Sn	85.3	623.0
Cs	Sb	216.3	544.1
Ba	Te	360.2	455.5
Gd	Pr	138.5	1115.5
Tb	Nd	286.3	1016.7
Dy	Pm	455.0	917.0
W	Er	61.8	1744.0
Os	Yb	397.2	1532.8

The mass absorbtion coefficients of Zn and Cu absorbers and the spectra modified by the absorbers are also given. In this case the absorbtion edge falls between the satellites and the diagram line, consequently the Si(Li) detector detects mainly the diagram line.

Table III
Target and absorber combination for the resolution of the L_α and $L_{\alpha 2}$ lines

Target	Absorber	$E_{abs.edge}-E_{L\alpha 2}$ (eV)	$E_{L\alpha 2}-E_{K\beta 1}$ (eV)
Au	Zn	32.7	56.0
Po	Ge	87.8	33.7
U	Br	31.2	147.4

In Tables I, II and III a summary of target and absorber combinations is given for the different possible uses of this method. In all these cases with the appropriate choice of the absorber thickness a transmission ratio of about 400 can be obtained so that the transmission for the lines to be detected below the absorbtion edge is about 0.5.

References

1. G. B. Deodhar and B. D. Padalia, Naturwiss., Dtsch., *49*, 373, 1962.
2. T. Papp and J. Pálinkás, XVth International Conference on the Physics of Electronic and Atomic Collisions, Brighton, United Kingdom, 22 – 28 July, 1987.
3. J. Pálinkás, L. Sarkadi, B. Schlenk, I. Török, Gy. Kálmán, C. Bauer, K. Brankoff, D. Grambole, C. Heiser, W. Rudolph and J. H. Thomas, J. Phys. B. : At. Mol. Phys., *17*, 131, 1983.
4. W. H. McMaster, N. Kerr Del Grande, J. H. Malett, J. H. Hubbel, University of California, Lawrence Radiation Laboratory, UCRL-50171.
5. J. H. Scofield, Phys. Rev., *179*, 9, 1969.

Acta Physica Hungarica 65 (2–3), pp. 217-223 (1989)

AN EXPERIMENTAL METHOD FOR RESOLUTION CALIBRATION OF ELECTRON SPECTROMETERS* **

L. KÖVÉR, J. TÓTH

Institute of Nuclear Research of the Hungarian Academy of Sciences (ATOMKI)
4001 Debrecen, Hungary

and

A. ITOH

Rigaku Industrial Corporation, 14-8 Akaoji-cho, Takatsuki-shi
Osaka 569, Japan

A series of X-ray photoelectron spectroscopic (XPS) measurements for testing the performance and determining the spectrometer function of electron spectrometers is described. The method is based on the determination of the natural line width Rh $3d_{5/2}$ in Rh metal by the help of the Coster–Kronig broadening and Auger intensity ratio evaluated from the Rh $3d_{3/2}$ and $M_{45}N_{45}N_{45}$ Auger spectra, respectively. Applicability of the method is demonstrated in the case of different electron spectrometers, comparing the data obtained in this way to the results of an alternative procedure based on the analysis of conduction band photoelectron spectra of Rh metal samples.

1. Introduction

The observed single core lineshape $S(E)$ in an X-ray photoelectron spectrum is a convolution of the inherent energy distribution $P(E)$, determined by the finite lifetime of the core hole created, and the instrumental function, $R(E)$:

$$S(E) = \int_{-\infty}^{\infty} P(E')R(E - E')dE', \tag{1}$$

whre $R(E)$ is a convolution of the function describing the energy distribution of the exciting X-rays $X(E)$, and the spectrometer function, $W(E)$:

$$R(E) = \int_{-\infty}^{\infty} X(E')W(E - E')dE'. \tag{2}$$

*Dedicated to Academician D. Berényi on his 60th birthday

**Partly supported by Japan Society for Promotion of Science

In this approximation, the broadening effects coming from other sources (inelastic scattering of photoelectrons in solids, charging, electronic noise e.g.) are not taken into account. Attainable accuracy in quantitative applications of XPS is significantly dependent on the knowledge of the spectrometer function. Precise determination of $W(E)$ can make possible a considerable resolution enhancement by deconvolution to the level of discerning the natural level widths. On the other hand, reliable methods for obtaining spectrometer functions experimentally, are important from the point of view of resolution calibration and characterization of electron spectrometers. Although the spectrometer function can sometimes be predicted by calculations, experimental methods for determination of $W(E)$ are obviously indispensable.

There are various methods for the experimental determination of spectrometer functions, we mention here only those used most commonly. Measurement of the linewidth of an elastically scattered electron beam, keeping the beam current constant is described e.g. by Van Eenbergen and Bruninx [1]. $W(E)$ can also be determined (usually more precisely) from the shape of the Fermi edge of the valence band photoelectron spectrum of a metal having a featureless conduction band considering its cut–off to be a step function, the derivative of the spectrum at the Fermi edge provides then the spectrometer function [2]. One could also fit the spectrum of a core level whose inherent contribution to the measured line shape is well known, by convoluting this known function with the known function of the exciting radiation and treating the parameters of a mathematical spectrometer function as variables. In the practical use of the latter method the observed Ag $3d_{5/2}$ core line shape is analyzed [3].

2. Method for resolution calibration and performance test of electron spectrometers by using Rh metal samples

Resolution calibration of electron spectrometers, applying the method based on the measurement of the line width of an elastically scattered electron beam can be difficult in the low pass energy mode of the analyzer, because of the relatively high thermal broadening due to the emissive thermocathodes and because of possible solid state effects on the elastic line shape. Application of the Fermi-edge method often suffers from large error except in the case of a very good statistics. In this paper a procedure is proposed for resolution calibration similar to the last one mentioned in the previous section except that the line involved in the analysis is the Rh $3d_{5/2}$ instead of the Ag $3d_{5/2}$. While in the case of Ag $3d_{5/2}$ line the natural linewidth can be determined only by assuming a known spectrometer function, the Rh $3d_{5/2}$ inherent linewidth Γ_A can be derived from the results of two independent experiments on the basis of the following formula [4]:

$$\Gamma_A = \frac{5\Gamma_{CK}}{2I_A - 3}, \tag{3}$$

where Γ_{CK} and I_A denote the Coster–Kronig broadening of the Rh $3d_{3/2}$ photoelectron line and the $M_5N_{45}N_{45}/M_4N_{45}N_{45}$ Auger intensity ratios, respectively. Γ_{CK}

and I_A are experimentally obtainable from the measured Rh $3d$ and $M_{45}N_{45}N_{45}$ Auger spectra. The procedure for evaluation of Γ_{CK} and I_A from the experimental data is based on the similarity of the shape of the component lines of the doublet spectra, except (in the case of the $3d_{3/2}$ line) a Lorentzian broadening due to the $M_4M_5N_{45}$ Coster–Kronig process allowed in Rh metal. Decomposition of such doublets can be attained by subtracting an energy shifted (and broadened in the case of the $3d_{3/2}$ line) replica of the first line, multiplied by a factor corresponding to the ratios of the respective relative photoionization or Auger transition rates. A detailed description of the mathematical procedure can be found in earlier papers of Mårtensson et al [4, 5]. For the evaluation of our results we used a modified and improved version of this method [9].

In the resolution calibration method proposed here the first step is the experimental determination of Γ_A(Rh $3d_{5/2}$). Comparing the result obtained with a reference one, a stringent test is performed on the quality of the measurement (including the high and low kinetic energy regions of the whole observed photoelectron spectrum) as well as on the reliability of the evaluation software applied. By adjusting the instrument in a proper way a close agreement should be attained between the Γ_A obtained experimentally and the reference value. As a second step, $W(E)$ can be determined by the deconvolution of a Lorentzian having a width corresponding to $\Delta X + \Delta P\ (= \Gamma_A)$ (for the contributions from the exciting radiation and the core level, independently, Lorentzian shape can be assumed) from the experimental Rh $3d_{5/2}$ XPS spectrum having a single line profile created in the first step of the calibration procedure.

The width of the spectrometer function determined in this way can be compared to that obtainable from the Rh valence band edge. There are several reasons to prefer Rh metal for the procedures described above: the relatively high Γ_{CK} and low Γ_A [4] as well as the similarity of the valence band photoelectron spectra of the Rh and Pd metals [6].

3. Experimental

Pure (99.9 grade) Rh metal plates were used as samples in three different kinds of XPS instruments N° 1, 2, 3). For in situ cleaning of the sample surfaces extensive Ar^+ ion etching was applied. In order to test how sensitive is the resolution calibration method described to the level of surface contamination, the measurements were performed at a relatively low vacuum level (10^{-5} Pa in the case of spectrometers N° 1, 2 and 10^{-6} Pa in the case of spectrometer N° 3). Except the spectrometer N° 3, where Al K_α was used, photoelectron spectra were excited by Mg K_α radiation. All measurements were performed in fixed analyzer transmission (FAT) working mode using pass energies $E_p = 75, 25$ and 50 eV, in the case of spectrometers N° 1, 2 and 3, respectively. Energy calibration of the spectrometers was made by the help of Cu $2p$ and Ag $3d$ lines of pure metal samples [7, 8]. Determination of Γ_{CK} and I_A as well as the creation of the single line $3d_{5/2}$ profile were made following the method described in [4, 5]. For details of the iterative

deconvolution procedure used for obtaining $W(E)$, see [9].

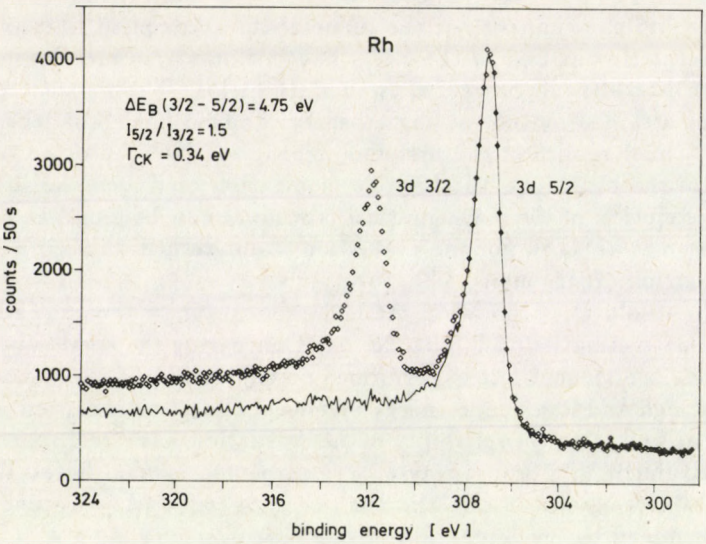

Fig. 1. Al K_α excited Rh 3*d* photoelectron spectrum (dotted) measured by spectrometer N° 3, and Rh $3d_{5/2}$ single line profile (continuous line) after deconvolution of the line $3d_{3/2}$ using the "broadened replica" method [4, 5, 9]

Table I

Experimentally determined energy widths (eV) and Auger intensity ratios

Spectrometer	Γ_A	I_A	Γ_{CK}	$\Delta S(3d_{5/2})$	ΔW	ΔW_F
	+0.17	+4.44				
1	0.20	6.67	0.40±0.05	1.6±0.1	1.1±0.1	0.9±0.3
	−0.09	−2.22				
2	0.17±0.08	6.67±2.22	0.36±0.05	1.3±0.1	0.9±0.1	0.7±0.3
3	0.16±0.09	6.67±2.22	0.34±0.05	1.3±0.1	0.8±0.1	1.1±0.3

Γ_A : Rh $3d_{5/2}$ level width; I_A: $I_{M5N45N45}/I_{M4N45N45}$ Rh Auger intensity ratio;
Γ_{CK} : $M_4M_5M_{45}$ Coster–Kronig broadening of the Rh $3d_{3/2}$ level;
$\Delta S(3d_{5/2})$: the measure $3d_{5/2}$ line width (obtained by fit of a Voigt shape);
ΔW : experimentally determined width of the spectrometer function from the $3d_{5/2}$ line (obtained by fit of a Gaussian)
ΔW_F : experimentally determined width of the spectrometer function from the derivative of the valence band Fermi edge (obtained by fit of a Gaussian)

4. Results and discussion

The experimental results obtained by application of the described method for resolution calibration in the case of three different XPS instruments are summarized in Table I. Figs 1 – 3 illustrate the data evaluation procedure followed.

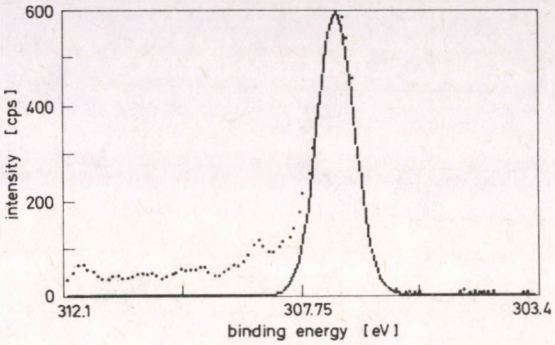

Fig. 2. The Rh $3d_{5/2}$ single line profile after deconvoluting the contribution from the Al $K_{\alpha\ 1,2}$ excitation and the life time of core hole $3d_{5/2}$ (dots), fitted by a Gaussian (bars)

The Rh $3d_{3/2}$ profile derived from the "broadened replica method" deconvolution [4, 5, 9] of the $3d_{3/2}$ peak (Fig. 1) shows a physically reasonable single lineshape proving the consistency of the procedure attaining a proper parameterization. In all other cases oscillations occur in the low kinetic energy side of the created $3d_{5/2}$ line shape [4, 5, 9]. An expressed asymmetry of the line shape can be observed, however, on the one hand due to the interaction between the core hole and the electrons in the conduction band and on the other hand due to inelastic electron scattering processes [3]. In the present approximation we assumed that this asymmetry did not influence considerably the value evaluated for ΔW. Similar single lineshapes were obtained for the Rh $3d_{5/2}$ line in the case of each spectrometer. Deconvoluting the contributions due to the exciting radiation and the finite lifetime of the core hole, the result gives the spectrometer function (Fig. 2) except the asymmetric part discussed. ΔW then can be determined, as shown in the Figure, by a Gaussian fit.

Fig. 3 shows an example for the evaluation of the spectrometer function from an alternative procedure using the derivative of the Rh valence band spectrum near the Fermi edge.

In Table I, the scattering values for Γ_A and Γ_{CK} reflect (in agreement with the values determined for ΔS) the differences in the level of accuracy of the independent measurements. Weighting the respective mean values of Γ_A with the square of the inverse of the estimated errors, and including the value of (0.20+0.10) eV measured by Mårtensson and Nyholm, a weighted average of Γ_A (0.18 eV) is derived for the Rh $3d_{5/2}$ core level width. Comparing the values of ΔW and ΔW_F in Table I, the results obtained for the width of the spectrometer functions agree within the error of the determination, although the accuracy of our resolution calibration method is considerably better. To attain a similar accuracy (not mentioning problems with systematic deviations) in the case of the Fermi edge derivation method requires

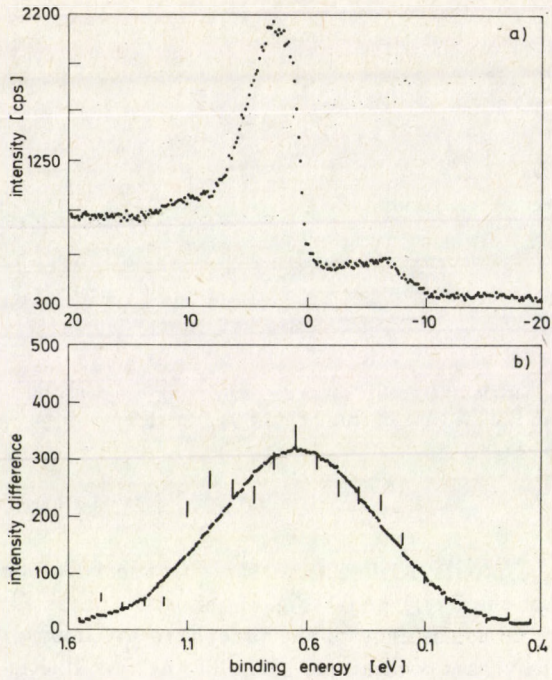

Fig. 3

a. Rh valence band photoelectron spectrum (measured by spectrometer N° 1)
b. Derivative of the spectrum shown in Fig. 3a (error bars), fitted by a Gaussian (dots)

much longer measuring time and more careful and sophisticated analysis.

The reliability of the results can be estimated by using an approximating formula. If $P(E)$, $X(E)$, $W(E)$ are all Gaussians, the full width of half maximum (FWHM) of the measured line ΔS is given by

$$\Delta S = \left((\Delta P)^2 + (\Delta X)^2 + (\Delta W)^2\right)^{1/2}, \tag{4}$$

where ΔP, ΔX and ΔW correspond to the FWHM values of the functions $P(E)$, $X(E)$ and $W(E)$, respectively. Substituting the corresponding values of ΔW, ΔX and Γ_A, the relative deviations of the computed ΔS from the measured ones are in the case of the spectrometers N° 1, 2, 3: 20, 10 and 6%, respectively (computed values are systematically lower).

In summary, the practical applicability of the resolution calibration method based on the absolute Rh $3d_{5/2}$ level width has been demonstrated in the case of three different electron spectrometers.

Acknowledgement

The authors are indebted to Professor K. Taniguchi and Dr. I. Cserny for their valuable contribution to this work.

References

1. A. Van Eenbergen and E. Bruninx, J. Electron Spectrosc. and Rel. Phenom., *37*, 265, 1985.
2. P. M. Th. M. Van Attekum and J. M. Trooster, J. Electron Spectrosc., *18*., 135, 1980.
3. G. K. Wertheim and S. B. Dicenzo, J. Electron Spectrosc., *37*, 57, 1985.
4. N. Mårtensson and R. Nyholm, Phys. Rev. B, *24*, 7121, 1981.
5. R. Nyholm and N. Mårtensson, Chem. Phys. Letters, *74*, 337, 1980.
6. N. V. Smith, G. K. Wertheim, S. Hüfner and M. T. Traum, Phys. Rev. B, *10*, 3197, 1974.
7. K. Asami, J. Electron Spectrosc. and Rel. Phenom., *9*, 469, 1976.
8. G. Johansson, J. Hedman, A. Berndtsson, M. Klasson and R. Nilsson, J. Electron Spectrosc. and Rel. Phenom., *2*, 295, 1973.
9. I. Cserny, L. Kövér, J. Tóth and M. Fiser, J. de Physique, *48*, C9–1017, 1987.

Acta Physica Hungarica 65 (2–3), pp. 225–228 (1989)

STUDY OF THE CHEMICAL SHIFT OF K X-RAY LINES WITH A HOME-BUILT X-RAY CRYSTAL SPECTROMETER*

I. TÖRÖK

Institute of Nuclear Research of the Hungarian Academy of Sciences (ATOMKI)
4001 Debrecen, Hungary

A home-built X-ray crystal spectrometer was used to study the chemical shifts of K X-ray lines. Thick samples of elementary silicon and SiO_2 (quartz glass) were used as targets, and they were bombarded by 3.2 MeV He^+ ions. The observed shifts of order of 1 eV are in agreement with those found in the literature.

1. Introduction

For extending the X-ray measurements at ion–atom collisions in our Institute towards higher resolution, a plane crystal Soller-type spectrometer was built in our workshop and was tested in our laboratories [1, 2, 3, 4]. The aim in constructing the spectrometer was to build an instrument of average characteristics, at moderate price, which is easily moveable from one accelerator to the other.

The spectrometer uses a rhombic goniometer, its principle is seen in Fig. 1.

The Soller slits have a nominal angular divergence of 0.3 degrees. The detector is a flow proportional counter working with P-10 gas. The detector signals are acquired by a single board computer based multichannel analyzer. This microcomputer also controls the measurement: a) sets the initial position of the 2-theta angle range to be scanned, b) gates the detector signals into subsequent channels of the analyzer memory for the dwell-time of multichannel scaling, determined by counting the target current integrator pulses for a preset number, c) gives stepping pulses to the driving motor of the goniometer to increment the 2-theta value with a preset value, d) displays the spectra (also during the acquisition time), e) stores the spectra on 5.25" floppy disks, f) permits simple evaluation of the obtained spectra. A more detailed description of the instrument is in preparation.

The instrument was tested for energy resolution and for mechanical stability – reproducibility. The resolution values were somewhat better than those estimated from the nominal angular divergence of the Soller slits. Probably the sheets are not plane enough, so they are tightening the free way of the X-rays. The reproducibility is about 0.03 degrees. We found that a good test for the overall performance of the crystal spectrometer is to use it in detecting chemical shifts of order of 1 eV. This part of the tests will be shown in the following.

*Dedicated to Academician D. Berényi on his 60th birthday

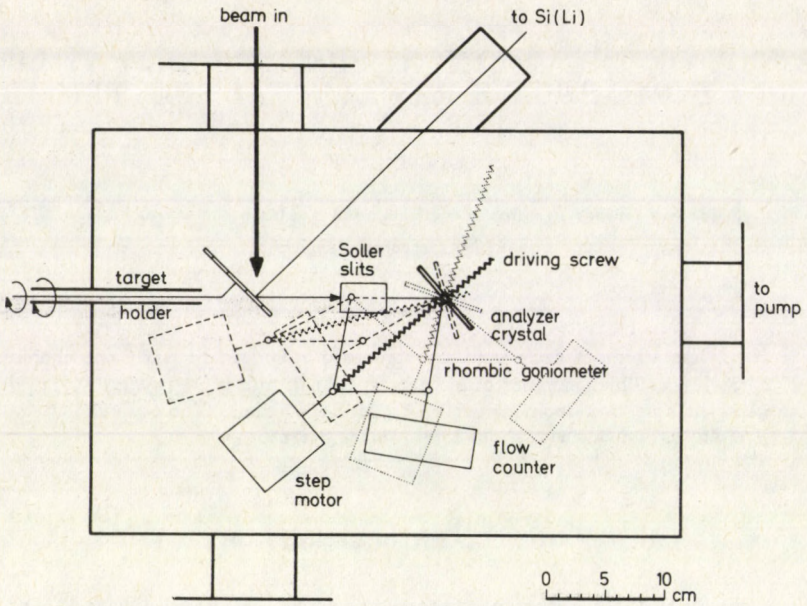

Fig. 1. The working principle of the rhombic goniometer. The rhombus is shown in three different positions (dotted line, full line, dashed line)

2. Experimental procedure

We chose elementary silicon and SiO_2 (quartz glass) as sample materials, for which chemical shift data are already available in the literature [e.g. 5, 6]. Disks were made from a piece of silicon and from quartz glass: their diameters are about 10 mm, their thicknesses are 2 – 2.5 mm. The samples were bombarded by 3.2 MeV He^+ ions from the 5 MV Van de Graaff generator of the ATOMKI. About 1 microamper target currents were used. The spectra were taken in several scans for each target material. The individual spectra for each sample were summed up to get acceptable statistics. We used an ADP analyzing crystal ($2d = 1.064$nm), and the angular increment was 0.05 degrees. The measured spectra were normalized at the $K_{\alpha_{1,2}}$ line. The obtained spectra are shown in Fig. 2. As only the shifts were measured no instrumental or other corrections have been made.

3. Results and discussion

The helium excited silicon and silicon dioxide spectra show intense satellite structure. The K_α and K_β diagram lines as well as their satellite display different shifts. The obtained chemical shifts are listed in Table I, together with the corresponding values from [5, 6]. The plus sign means that the line of SiO_2 spectrum

is at higher energy than the corresponding line in the Si spectrum. Graeffe et al [5] measured the shifts with a double crystal spectrometer in X-ray fluorescence. McWherter et al [6] measured the shifts also by ion excitation, using 3.2 MeV He ions. Both mentioned measurements were made with better resolution than ours (5.6 eV versus 2.4 eV by McWherter et al and 1.1 eV by Graeffe et al). We could not resolve the $K_{\alpha 1}$ and $K_{\alpha 2}$ lines and also the individual component peaks in the multiplet KL^i peaks were not resolved. So we determined only an average shift for $K_\alpha L^{1,2,3}$ lines. Because of the poor statistics we could not get shift value for the $K_\alpha L^4$ and $K_\beta L^{2,3}$ peaks. For the $K_\beta L^1$ line the difference in the low energy edge of the composite peaks is given. Comparing the spectra in the cited references and from our measurements it is seen that the chemical shifts are in agreement, considering the estimated errors which were about 0.2 –0.4 eV for McWherter et al, about 0.1 eV for Graeffe et al, and about 0.35 eV in our case. Graeffe et al measured only the K_α and $K_\alpha L^1$ satellites.

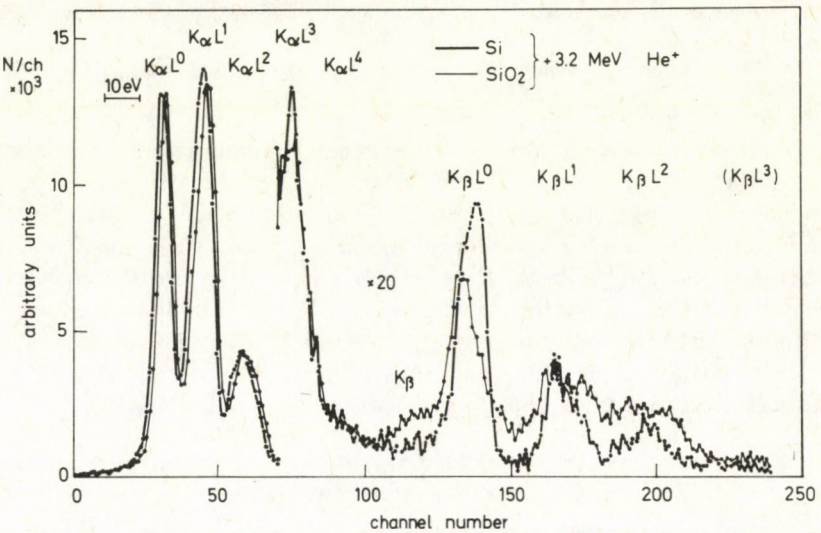

Fig. 2. The silicon K X-ray spectra from elementary silicon and from SiO_2 (quartz glass) bombarded by He ions

We also obtained the $K_{\beta'}$ peak in the low energy tail of the K_β line, which can be seen in the SiO_2 spectrum of McWherter et al. This transition can be obtained only from compounds. McWherter et al mention an interpretation of it as a "crossover transition", when a 2*s* electron of oxygen fills an 1*s* vacancy of silicon. Using this simple picture a transition energy of only 5 eV less than the measured value can be predicted. Molecular-orbital calculations predict a $K_{\beta'}/K_\beta$ ratio of one third to one fourth, but this ratio is closer to one fifth both in McWherter et al and in our spectrum. The positive shifts of the K_α diagram and satellite lines can be interpreted as the result of transferring silicon M-shell electrons to oxygen during compound formation. The negative shifts of K_β diagram and satellite lines are due to negative shift in the valence band of SiO_2, which is a solid state effect.

Table I
The measured chemical shifts of silicon K X-ray lines

X-ray line	Initial vacancies	Energy shift [eV]		
		Ref. [5]	Ref. [6]	Present work
$K_{\alpha 1,2}$	KL^0	+0.58	+0.6	+0.8
$K_{\alpha'}$	KL^1	+1.29	+0.9	+1.1
$K_{\alpha 3}$	KL^1	+1.16	+1.3	+1.1
$K_{\alpha 4}$	KL^1	+1.13		+1.1
$K_{\alpha 5}$	KL^2		+1.0	+1.1
$K_{\alpha 6}$	KL^2		+0.5	+1.1
K_{α}	KL^3		0.0	0.0
K_{α}	KL^4		−0.1	
$K_{\beta'}$	KL^0			
K_{β}	KL^0		−2.8	−2.5
$K_{\beta''}$	KL^1		−2.4	−2.1
$K_{\beta'''}$	KL^1		−1.6	
K_{β}	KL^1			
K_{β}	KL^2		−1.6	
K_{β}	KL^2		−0.2	

The peak shapes and the relative intensities of diagram and satellite lines are similar in the spectra of McWherter et al and in our spectra. E.g. the top of $K_\alpha L^2$ peak is more flat in the SiO_2 spectrum, and this is true for $K_\beta L^1$ and $K_\beta L^2$ peaks too; for the K_β diagram line the low-energy edge is steeper in SiO_2 spectrum, and the high-energy edge is steeper in the Si spectrum; the relative intensity of K_β diagram line is greater in the Si spectrum, while the $K_\beta L^1$ and $K_\beta L^2$ lines are more intense in the SiO_2 spectrum.

It is seen that despite the moderate specifications of our spectrometer, chemical shifts of about 1 eV can be detected with it.

Acknowledgements

Thanks are due to the crew of the Van de Graaff generator for providing stable ion beams. This work was supported partly by MTA-OTKA grant No. 1184-1185.

References

1. I. Török and B. Tóth, ATOMKI Ann. Rep. 1986, p. 60.
2. I. Török and B. Tóth, ATOMKI Ann. Rep. 1987, p. 66.
3. I. Török and B. Tóth, Materials of NATO Advanced Study Institute "X-ray Spectroscopy in Atomic and Solid State Physics", Vimeiro, Portugal, Aug. 30.– Sept. 12., 1987, to be published.
4. I. Török and B. Tóth, in Proceedings of the X-87 14th International Conference on X-ray and Inner-shell Processes, Paris, September 14–18, 1987, J. de Physique, C9 suppl. au no. **12**, *48*, C9–79, 1987.
5. G. Graeffe, H. Juslén and M. Karras, J. Phys. B: At. Mol. Phys., *10*, 3219, 1977.
6. J. McWherter, D. K. Olsen, H. H. Wolter and C. F. Moore, Phys. Rev., *A10*, 200, 1974.

Acta Physica Hungarica 65 (2–3), pp. 229–238 (1989)

THE REDUCTION OF THE SYSTEMATIC ERROR CAUSED BY THE NUCLEAR BACKGROUND IN HIGH RESOLUTION ELECTRON SPECTROSCOPY OF HIGH-ENERGY ION–ATOM COLLISIONS*

I. KÁDÁR, S. RICZ, B. SULIK, D. VARGA and J. VÉGH

Institute of Nuclear Research of the Hungarian Academy of Sciences (ATOMKI)
4001 Debrecen, Hungary

The presence of background radiation emitted by the products of nuclear reactions is a source of systematic error in high resolution electron spectroscopy of high-energy ion–atom collisions. A detailed discussion of the role of the different background sources contributing to this systematic error is given. A method for decreasing this systematic error and its effect to the decomposition of electron spectra is presented.

Introduction

The high resolution Auger electron spectrum obtained in the high-energy heavy-ion – atom collisions is a copious source of spectroscopical and collision information. In the collision of highly charged heavy projectile ions with the target atoms usually more than one electron is expelled from the target, therefore many different and often really exotic atomic levels can be investigated, and one can get an insight into the mechanism of the collision, too.

Looking at the first high resolution Ne K-Auger electron spectra measured at the 5.5 MeV X^{q+}–Ne collisions in Dubna at the U-300 cyclotron [1–6] and at the MGC cyclotron in Debrecen we found rather poor reproducibility, worse than that expected on the basis of the number of detected events and Poisson statistics. Indeed, the detailed evaluation revealed experimental errors exceeding the statistical expectation. The higher was the collision energy above the Coulomb barrier, the larger was this distortion in the electron spectra. We suspected the reason of this increased error in the variation of the nuclear background. The radiation emitted in nuclear reactions produced by the heavy-ion beam in the target and in the mechanical parts of the beam collimating system as well as in the Faraday cup represent a nuclear background in these measurements. Although the cross section for the atomic phenomena is usually much larger than that for the nuclear reactions, the small density of the gas target often used in the measurement of ion–atom collisions decreases the relative weight of the atomic events comparable to the nuclear ones.

For obtaining reasonably exact spectra first of all we tried to detect independently the actual intensity of this background. For this purpose two detectors have

*Dedicated to Academician D. Berényi on his 60th birthday

been used. One of them — placed inside the spectrometer chamber, in the neighbourhood of the detectors measuring the electrons from the collision — detected the scattered electrons. This detector was a channeltron not seeing the electrons coming from the target area. A second one — a scintillation gamma detector located outside the spectrometer chamber — has been used for the detection of the gamma photons. Unfortunately we could not compensate properly the background contribution in the intensity values according to the count rates obtained by using these detectors.

The Ne K-Auger spectra are rather complicated at this projectile energy because of the presence of many satellite lines due to multiple ionization (200 - 300 lines depending on the actual collision). For the decomposition, or at least partial decomposition of the spectra accurate knowledge of the line shape and precise knowledge of the intensities and their errors is required. In order to be able to measure spectra precise enough for the purpose of decomposition we have developed a combined electronic and mathematical method to decrease the detected intensity of the nuclear background and to take into account the remaining systematic error in the spectra.

Experimental arrangement

The experimental arrangement used in these measurements consists of the beam transport and collimating system, the stripper foil, the target, the spectrometer and the Faraday cup. It is schematically depicted in [1].

The spectrometer is an electrostatic electron spectrometer designed for simultaneous energy and angular distribution measurements [7]. The energy analyzer unit itself consists of a spherical and a double pass, double focussing cylindrical mirror. The spherical mirror ensures the transport of electrons from the collision plane to the vertically directed cylindrical energy analyzer unit. For high resolution measurements the analyzer is completed with a spherical decelerating lens located before the entrance slit of the cylindrical mirror. The spectrometer works in the constant pass energy mode.

The target is a neon gas beam. This very thin target allows only single collision events to take place, i.e. the projectile charge state is the same in all the collision events.

The measurement of angular distribution implies a small sensitive volume seen by the spectrometer, i.e. the need for good collimation or good focussing of the beam. In our case the emittance of the ion beam and the required small acceptance of the spectrometer – target combination has necessitated the use of collimating apertures. Unfortunately, the good collimation means in case of a beam of big emittance that a significant part of the beam is lost on the collimating parts, producing nuclear reactions there.

Systematic errors in the measured electron energy distribution

There are at least two possible reasons for the systematic error found in the spectra. The first one could be an ion beam cross section which is larger than the corresponding cross section of the sensitive volume of the spectrometer. In this case the beam current measured by the Faraday cup (which is used to normalize the intensities measured at the different energy points) is differing from that able to ionize the atoms inside the sensitive volume. If, for any reason — changing extraction conditions in the cyclotron, slightly different beam control — the density distribution of projectile ions is changing inside the cross section of the collimated beam, the conditions of normalization are also changed point by point. The weight of this kind of systematic error is also increasing at better energy resolution, since the larger deceleration ratio makes the sensitive volume of the spectrometer smaller. This kind of systematic error could have been eliminated by appropriate collimation of the ion beam. In the following this source of systematic error will be neglected.

The second reason which is not as easy to eliminate as the previous one is the presence of the nuclear background mostly due to the nuclear reactions.

There are several places in the experimental arrangement where unwanted background events can take place, both nuclear and atomic. The background intensity seen by the electron detectors (channel electron multipliers in our spectrometer) comes from the following sources:

1. Cosmic rays — this component of the background produces an intensity which is statistically constant in time (and generally negligible compared to all the other effects present).

2. Electrons ejected from the target and scattered on the spectrometer electrodes. Their intensity is proportional to the intensity of the ion beam traversing the target material in the sensitive volume of the spectrometer. They are generally adequately shielded by the different parts of the double pass cylindrical mirror construction of the analyzer, therefore they are detected with a very low efficiency.

3. Prompt low energy gamma rays coming from the target and from the Faraday cup as well as the secondary electrons ejected by them from the walls and parts of the spectrometer in the proximity of the detectors. The efficiency of the whole spectrometer is much less to the scattered electrons than to those coming directly from the target. The intensity of these gamma photons and secondary electrons is proportional to the beam intensity traversing the target material in the sensitive volume of the spectrometer. The intensity of the low energy gamma photons emitted from the target is negligibly small compared to the intensity of the electrons coming from the atomic processes because of the large atomic to nuclear cross section ratio.

4. Low energy prompt gamma rays originating from the different parts of the beam collimating system, and also from the surroundings due to the interactions with neutrons as well as the secondary electrons ejected by them in the neighbourhood of the detectors. This component of the background is changing according to the changes in the cyclotron and beam handling. Thus it is not proportional to the intensity of the ion beam crossing the target.

5. Low energy gamma photons from long-lived radioactive isotopes produced in nuclear reactions in the different parts of the beam transport and collimating system as well as in the Faraday cup.

The above background contributions originating from different sources can be divided in two distinct groups:

a.) background intensity proportional to the projectile current traversing the target material in the sensitive volume of the spectrometer (contributions 2 and 3) and

b.) background intensity not proportional to that projectile current (contributions 4 and 5). A special group of this latter is the intensity statistically constant in time (1).

The measurement of the electron energy distribution is performed serially, i.e. point by point, by changing the focussing potential applied to the electrodes of the spectrometer. The measurement is continued at each energy point until we collect a predetermined amount of charge — the same at each point — in the Faraday cup connected to the spectrometer. This mode of measurement reproduces the real, undistorted electron energy distribution in the ideal, background free case with an ideal, well focused ion beam with no collimating elements. In a real environment the reproduction of the undistorted energy distribution requires the ratio of the intensity of the measured phenomenon to that of the background to be statistically constant during the measurement in each energy point. For this the background intensity itself should be proportional to the ionizing projectile ion current usually changing in time.

Generally, proportionality is not ensured, since the activity of the long-lived radioactivity produced by nuclear reactions in the environment or in the collimating parts of the beam guiding system is not depending on the actual value of the beam current ionizing the target, but on the average value of the total ion current, or more exactly, on the value of the total beam charge accumulated on the different sites of the beam transport and collimating system. Taking into account this non-proportionality of the background intensity to the active beam current one should reformulate the necessary conditions for the reproduction of the original electron energy distribution by a serial measurement.

Now supposing the background to be constant in time, one can measure an undistorted energy distribution if the beam current is also constant during the measurements at each energy point, since in this case the ratio effect/background is also constant. Actually the activity of long-lived isotopes produced by the irradiation is continuously increasing during the measurement, i.e. its intensity is not constant. A quasi-constancy of this background intensity is a requirement easier to fulfil, namely, if the measurement is performed in repeated cycles the constancy of the background intensity should hold only inside one single cycle. In case of linearly increasing background intensity the deviation from the constancy is decreased in proportion of the ratio of the time necessary to measure one single cycle to the total measurement time. Still remains the problem of constancy of the beam current. At a real (not ideal) accelerator it is difficult to ensure a constant beam current. That is why one uses integrators to normalize the intensity of the measured spectra to

the same amount of accumulated charge. As a consequence the measurement time spent at different electron energy values is generally different.

The background contribution due to low energy prompt gamma rays and prompt neutrons is a source of systematic background variation exceeding the statistical expectation, since the strong collimation involves the loss of a substantial part of the original beam at the collimator parts, and minor changes in the beam guiding can strongly affect the distribution of this kind of beam losses at the different collimator parts. These changes in the distribution of the radiation sources are reflected in a change in the gamma ray production cross sections and in a change of the efficiency of their detection. The variation of this background contribution causes systematic error in the electron spectrum. This contribution cannot be systematically decreased by measuring in repeated cycles, one can only hope that there will be some suitable averaging of this effect by adding the independently measured cycles. The weight of this error is larger at better spectrometer resolution, the detection efficiency being smaller.

A further effect giving rise to the same type of systematic error is the variation of beam intensity. The changing beam intensity in the presence of a background component not proportional to the beam intensity crossing the sensitive volume of the spectrometer causes a variation of the effect to background ratio.

Reduction and testing of the systematic error

The real solution to eliminate the systematic error caused by the nuclear background in the electron spectra is the complete elimination of the background radiation. This is usually not possible if one is working with high emittance cyclotron beams and needs a well collimated beam inside the measuring apparatus. The best we can do is to decrease the background as much as it is possible, reject those spectra where our efforts were not successful (the remaining systematic error is too large) and to take into account in the evaluation procedure the remaining systematic error.

Our efforts to reduce the effects of the background on the measured spectra were the following.

1. First of all one should have a quantitative method to evaluate the reproducibility of the measured spectra. For this purpose a mathematical method has been developed to test the successive measurement cycles for statistical reliability of the spectra. (And attributing a realistic error to those which are not acceptable, or simply to reject them.)

2. The most straightforward way to decrease the effect of the prompt and delayed background radiation is to place at least the first collimating stage (where the largest loss of beam intensity occurs) at the largest possible distance from the spectrometer and so from the detectors. The proper choice of the material of the collimating apertures also helps, one should avoid light elements, like carbon, for example.

3. The intensity of the background components still remaining there was further decreased by an appropriate fast coincidence gating by the microstructure of the beam.

The mathematical method for testing the similarity of independent measurement cycles

The spectra measured under identical circumstances should be similar, but — due to the uncertainty of the measurement caused by the statistical nature of the phenomenon to be measured — not identical. Our aim was to define the similarity a in quantitative way and to make more exact the decision, whether the two spectra measured in two different measuring cycles can be considered to be two statistically identical samples taken from the same distribution, or not.

Supposing that all the measuring conditions are identical, the experienced deviation in two intensity values measured at the same energy point in two different measurement cycles are caused only by statistical fluctuations. Since the measure of the statistical fluctuation is known, the expected and empirical variation can be compared. We introduced a statistical quantity characterizing the complete spectrum and not only one point of it. Let us compare the k-th and j-th measurement cycles, both of them containing n comparable data. Let $Y_{k,i}$ and $Y_{j,i}$ be the electron intensities measured in the i-th point at an energy E_i, $d_{k,i}$ and $d_{j,i}$ their actual deviation from their "real" value. Let the expected or "real" value of the intensity be Y_i at the energy E_i and σ_i its variance. Thus the measured intensities can be expressed as

$$Y_{k,i} = Y_i + d_{k,i}, \quad \text{and} \quad Y_{j,i} = Y_i + d_{j,i}. \tag{1}$$

By expressing the normalized difference of these two intensities measured in different spectra one obtains the probability variable r_i with unity variance and zero mean.

$$r_i = r_i^{k,j} = \frac{(d_{k,i} - d_{j,i})}{\left(\sigma_{k,i}^2 + \sigma_{j,i}^2\right)^{1/2}}. \tag{2}$$

Here the variance of the expected value of the intensity is approximated by the quantities $\sigma_{k,i}$ and $\sigma_{j,i}$, the estimated uncertainties of the measured intensity values. This variable is independent of the structure of the spectrum. Further on the parameters of this distribution will be taken to be the quantitative measure of the similarity of the j-th and k-th spectra and these parameters will be analyzed by the methods of the mathematical statistics.

Calculating the empirical values for the expected value and for the variance of the distribution one gets

$$< r >= \frac{1}{n}\sum_{i=1}^{n} r_i \quad \text{and} \quad s^2 = \frac{1}{n}\sum_{i=1}^{n} r_i^2 - < r >^2. \tag{3}$$

The expected values of $< r >$ and s^2 are zero and unity, respectively. The statistical criteria for the value of these parameters [9] determine whether the data obtained in i-th and k-th runs are compatible. The average $< r >$ is an $N(0, n^{-1/2})$ variable, hence a confidence interval can be given to the average at a predefined probability level. For example, if this level is 99.73%, the confidence interval is $(-3\sigma, +3\sigma)$, and $\sigma = n^{-1/2}$. This allows for example for $+/-0.1$ deviation for $< r >$ in case of $n = 900$ points.

The variance s^2 has a χ^2 distribution. Its actual values can be evaluated by using a χ^2 test table.

When comparing spectra with systematic errors the calculated $< r >$ and s^2 values deviate from their expected values. One can then decide (usually on an empirical basis) whether one should accept or reject the given measurement cycles.

When adding the accepted measurement cycles the error of intensity data has been substituted by their empirical scatter found in the given cycles when it was significantly higher than their error. This produces a more realistic error which is already acceptable by the decomposition procedure.

Synchronizing the detected events by the microstructure of the cyclotron beam

The pulsed nature of the cyclotron beam offers a possibility to synchronize the detection process and the presence of the beam. Since the cyclotron beam arrives in small packets having a few nanosecond width followed by several tens of nanosecond break, the useful events are produced only when the ion packet is present at the target, the pause contributing only to the background intensity. By gating the detecting circuitry with a signal derived from the beam itself one can select the useful time periods for the detection, neglecting the rest of the time. This method gives a possibility of reducing the background not only because the detection of the long-lived activity is reduced according to the beam to pause ratio, but also because the prompt gamma detection efficiency is also greatly reduced due to the different time of flight of the gamma photons from the collimator to the detectors and that of the focused electrons along their path inside the spectrometer. Since the longest part of the flight path of the electrons lies inside the analyzing cylindrical mirror, the constant pass-energy mode of the electron energy analyzer has been used throughout the measurements, ensuring approximately constant flight time for the detected electrons in their path from the target to the detector.

The block scheme of the gating electronics and the schematic view of the spectrometer and the different background sources are shown in Fig. 1. An example of the time spectrum obtained at the output of the time to amplitude converter is shown in Fig. 2. The ratio of the width of the selected window to the total time difference between two consecutive beam pulses (amounting to about 90 nanoseconds in the actual case) makes it possible to decrease the background due to the long-lived radioactivity by a factor of three.

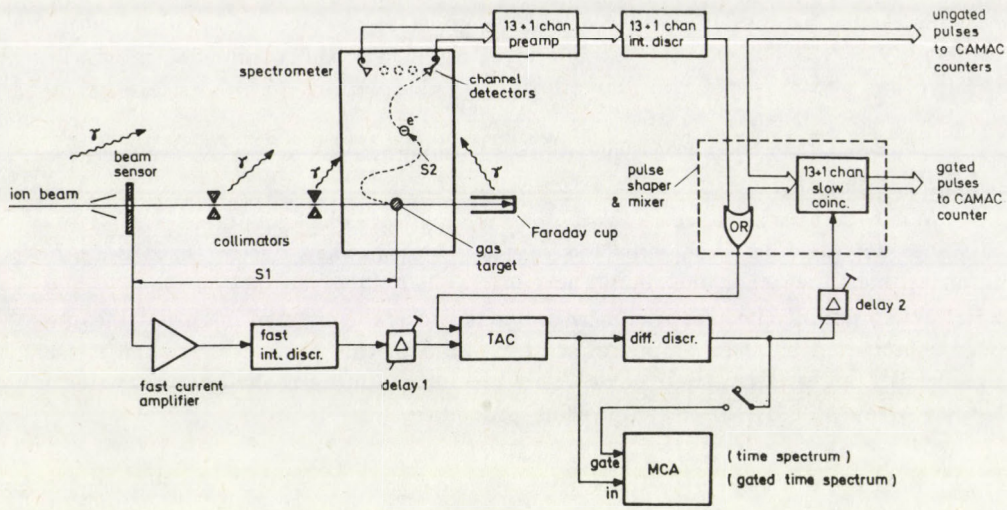

Fig. 1. Schematic view of the geometry of the spectrometer and collimators as well as the block scheme of the electronic circuits gating the detection of electron in coincidence with the time arrival of the beam

In Fig. 3 two cycles of a measurement well above the Coulomb barrier (72.8 MeV C^{2+}–Ne collision) are shown with and without gating. One can see the improvement not only in the decrease of the level of the background, but also in the decreased scattering of the measured intensity values at the individual energy points. A quantitative evaluation of the improvement is also shown in the Figure. The spectra recorded without gating should be rejected at 3σ level, while those with gating are acceptable at nearly 1σ level.

Conclusions

When investigating ion–atom collisions one is facing the problem that the presence of the nuclear background causes systematic error in the electron spectra measured serially as is the case of electrostatic or magnetic electron spectrometers without a possibility of simultaneously detecting the total energy range to be measured. This systematic error can be reduced both by decreasing the level of background radiation either by placing the sources of this radiation to a significant distance from the detectors and by applying a suitable electronic gating which synchronizes the beam microstructure and the detection of events to be measured.

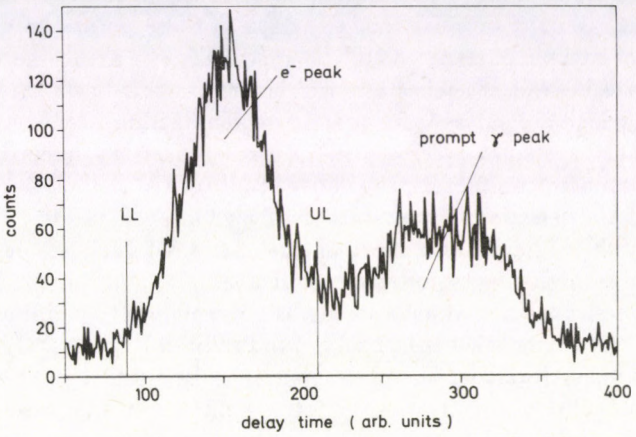

Fig. 2. A typical time spectrum showing the separation of the peaks due to the prompt gamma rays and electrons, respectively. UL and LL are the upper and the lower edges of the selected time window. Hundred channels on the horizontal scale correspond to on approximately 23 nanoseconds

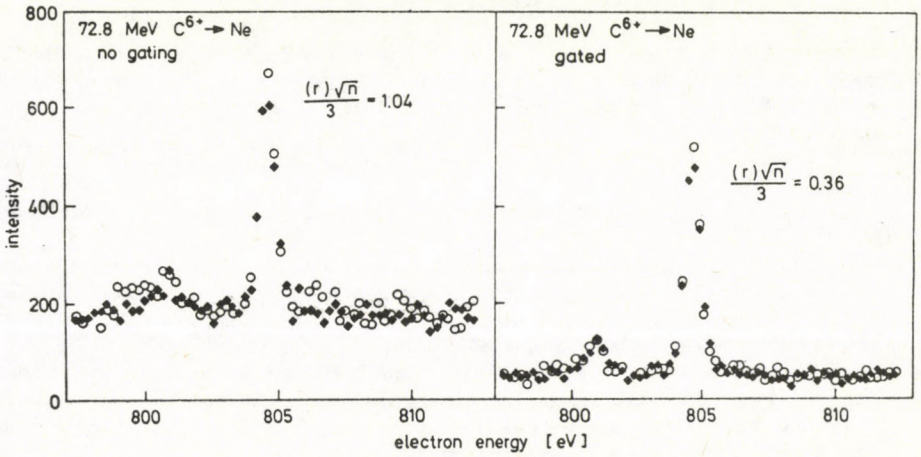

Fig. 3. A demonstration of the effect of the gating on the electron spectra: Comparison of two identical cycles from the same measurement without and with gating

A suitable mathematical procedure has been developed to test the statistical reliability of the measured data. The procedure is based on the comparison of the individual measurement cycles in pair. On the basis of the quantitative results of this statistical procedure one can decide whether to accept the given cycles as statistically reliable, or to reject them because their systematical error is too large.

If one retains a spectrum for evaluation in spite of the systematic error found in certain points, one should suppose that the data in these points do not follow the Poisson statistics and their error should be increased by taking the experimental scatter of the data instead of their statistical error. On this basis one can compose a set of spectra which are suitable for precise decomposition procedures.

Although the systematic error due the presence of the nuclear background could not be eliminated completely, the above steps for the reduction of the nuclear background and the selection of the statistically good spectra for evaluation gave satisfactory results in the case of most of the measured high resolution electron spectra obtained in high-energy ion–atom collisions.

The facts described above have a general consequence to serial measurements performed in an environment where a background radiation not exactly proportional to the active intensity (exciting the phenomenon to be studied in the volume seen by the spectrometer) of the excitation source is emitted. In this case the precision of the measured spectra is limited rather by the systematic error caused by this background than by the time spent with the measurement. In our case the best precision was obtained when using a statistically compatible subset selected from the complete set of measured cycles.

References

1. I. Kádár, S. Ricz, V. A. Shchegolev, B. Sulik, D. Varga, J. Végh, D. Berényi and G. Hock, J. Phys. B: At. Mol. Phys., *18*, 275, 1985.
2. I. Kádár, S. Ricz, V. A. Shchegolev, D. Varga, J. Végh, D. Berényi, G. Hock and B. Sulik, Phys. Lett., *A115*, 439, 1986.
3. S. Ricz, I. Kádár, V. A. Shchegolev, D. Varga, J. Végh, D. Berényi, G. Hock and B. Sulik, J. Phys. B: At. Mol. Phys., *19*, L411, 1986.
4. B. Sulik, I. Kádár, S. Ricz, D. Varga, J. Végh, G. Hock and D. Berényi, Nucl. Instr. Meth., *B28*, 509, 1987.
5. I. Kádár, S. Ricz, B. Sulik, D. Varga, J. Végh and D. Berényi, in "High-energy Ion–Atom Collisions" (Proc. 3rd Workshop on High Energy Ion–Atom Collision Processes, August 3 – 5, 1987, Debrecen, Hungary) Lecture Notes in Physics, Vol. 294, Eds. D. Berényi and G. Hock, Springer–Verlag, Heidelberg, 1988, p. 479.
6. S. Ricz, J. Végh, I. Kádár, B. Sulik, D. Varga and D. Berényi, in "High-energy Ion–Atom Collisions" (Proc. 3rd Workshop on High Energy Ion–Atom Collision Processes, August 3 – 5, 1987, Debrecen, Hungary) Lecture Notes in Physics, Vol. 294, Eds. D. Berényi and G. Hock, Springer–Verlag, Heidelberg, 1988, p. 197.
7. A. Kövér, D. Varga, Gy. Szabó, D. Berényi, I. Kádár, S. Ricz, J. Végh and G. Hock, J. Phys. B: At. Mol. Phys., *16*, 1017, 1983.
8. J. Végh and I. Kádár, in Proceedings of the 2nd Workshop on High Energy Ion–Atom Collision Processes, Debrecen, Hungary, August 27 – 28, 1984. Eds. D. Berényi and G. Hock, Akadémiai Kiadó, Budapest, 1985, p. 179.
9. M. G. Kendall and A. Stuart, The Advanced Theory of Statistics, Griffin and Co., London, 1963.

Acta Physica Hungarica 65 (2–3), pp. 239–256 (1989)

AN APPARATUS FOR LOW ENERGY ATOMPHYSICAL EXPERIMENTS AND THE FIRST RESULTS*

L. SZÓTÉR, J. MACSUGA, B. PALÁSTHY and G. VITÉZ

Department of Physics of Technical University for Heavy Industry
3515 Miskolc-Egyetemváros, Hungary

An experimental apparatus for the investigation of the energy dependence of the excitation cross-section of atomic states by electron impact is described. The exciting electron beam is produced by a trochoidal electron monochromator. The best energy homogeneity of the beam is characterized by 40 meV (FWHM) even below 1 eV mean energy. The cross-section is studied by setting up the optical excitation function. The possibilities of the apparatus and method are compared with other experimental possibilities. New experimental information about the excitation of Cd is discussed in case of negative resonance, and the effect of post-collision interaction on the optical excitation function of Cd has been observed for the first time.

1. Introduction

The apparatus and the first experiments done with it, which are the subject of this paper, are the beginning of our long-term research project for the investigation of the excitation processes in the electron–atom and electron–ion collisions using improved energy resolution in the low (1 – 20 eV) energy range.

The great activity in this field is motivated from several points of view. First of all, the information about these collision processes is needed for different parts of physics and technology as plasma physics, laser physics, physics of planetary and stellar atmospheres, etc. On the other hand, the earlier ideas about both elastic and inelastic scattering processes of the low energy electron–atom impacts were changed qualitatively as the result of the investigations in the last two decades. This change is mostly due to the discovery of "resonance" and "post-collision interaction". The improvement of the experimental methods and the development of the theory were simultaneously the cause and result of this discovery. This progress led to the evolution and continuous development – which is carried on even today – of two new atomphysical research branches.

The result obtained from the investigation of the intermediate compound state of the electron–target system shows that the atomic shell "resonance" plays a very important role in the electron atom collisions. The great importance of the "resonance" was absolutely clear at the moment when Schulz announced observing it [1], as it appears from Massey's keynote at the third ICPEAC in 1963, in which he called the observation of "resonance" "the most exciting development in atomic

*Dedicated to Academician D. Berényi on his 60th birthday

physics in twenty years" [2]. Although, the immediate aim of our research is only the investigation of electron–atom collisions but the range of importance of "resonance" exceeds it and overlaps the fields of electron–ion [3 – 5], electron–molecule [6, 7], ion–ion [8] impacts, etc. as well. In spite of the fact that twenty five years have passed since the discovery of "resonance" there is only little information on this process even now. Additionally, — beside its successes — there are serious limits of the theory of "resonance" concerned, so, to a certain extent, the results of the experiments exceed the theory.

The "post-collision interaction", which was discovered after "resonance", provides a further fundamental mechanism for some scattering processes in atomic physics. Though this phenomenon was observed previously in ion–atom collisions in 1966 [9], the discovery of "post-collision interaction" in case of electron–atom collisions was observed only in 1974 [10]. This late discovery can be partly the cause that there is even less knowledge about the effects of this second process than about those of "resonance". However, even the existing theoretical and experimental results show that "post-collision interaction" is a common phenomenon. That is, its role is very important not only in low energy collisions but in case of inner shell ionization of target atoms by electrons [11, 12] or photons [13, 14] as well.

We think, with our new experimental device, it is possible to gain new and important information about the possible excitation processes of electron–atom collisions at low energy, especially in the not fully searched fields mentioned above.

2. Excitation processes and experimental possibilities

In this chapter we first give a short description of the most important and general knowledge about "temporary negative ions" and "post-collision interactions". We outline the role of these two types of processes in the field of electron impact on atoms at low energy. Next, on this basis, we will outline the possibilities of our new experimental device in the field mentioned.

2.1. Negative ion resonances

In all cases when an electron spends longer time in the neighbourhood of an atom than the normal transit time through the atom, the object can be considered as a "temporary negative ion", also called "resonance" [15]. In most cases the average lifetime of these temporarily bounded states of atom– electron systems are in the order of $10^{-13} - 10^{-14}$ s. (So we will not deal with stable negative ions.)

In case of low energy electron–atom collisions every chemical element can form a short-lived negative ion when the incident electron attaches temporarily itself either to the excited state of the atom or to the ground state of the atom.

In genealogy, the configuration of the target, from which the negative ion state is derived, is called "parent". One can distinguish between two distinct types of resonances, namely those that lie energetically below the parent state and those that

lie above it. Resonances which appear just below the various excitation thresholds of atoms are called "*Type I* resonances" or "Feshbach resonances". Resonances which lie energetically above their parents are called "*Type II* resonances" or "shape resonances" [15].

Mechanistically, *Type I* resonance is imagined as a process in which the incoming electron virtually excites one or more target electrons to an excited orbital, thereby creating a hole in the core. This means that the electron will see the slight positive charge of the less screened nucleus and binds itself to the target atom for a short time. This type of resonance usually lies approximately $0 - 0.5$ eV below the parents.

In case of *Type II* resonance the incoming electron is trapped by a penetrable centrifugal barrier which is set up as the sum of the angular momentum of the incoming electron and the potential well of the excited and polarised target atom. Energetically *Type II* resonance usually lies only a few tenths of an electronvolt above the parents.

Resonances spontaneously decay into atom and free electron in the individual characteristic time $\tau \propto 1/\Gamma$, where Γ is the energy width of the resonance. Their decays are most probable into those atomic energy levels which lie energetically close below the resonance (instead of the processes which are forbidden by the selection rule). Thus shape resonance is usually wider than Feshbach resonance because the decay of *Type II* resonance is more likely to the parent state because this lies close below.

One can find a surprising analogy between resonances in atomic shell and those in compound nuclei. Though similar models were developed in nuclear physics earlier but the model of the phenomenon mentioned was set up almost independently three decades later [2].

Because of their short lifetime, most resonances cannot be studied directly (for example with a mass spectrometer). But there is another good opportunity to investigate resonance, because generally it has a very strong effect on the elastic electron–atom scattering [16] and the excitation of the atomic levels by electron impact [17]. The recognition of the resonance and the experimental identification of its characteristics can be carried out by the precise measurement of the energy dependence of the (elastic or inelastic, total or differential) cross-sections which are typical of the different processes. The basis of this method is that the cross-section of the direct excitation or elastic scattering varies slowly with energy while the effects of the temporary negative ions on the collision processes appear only in narrow energy ranges which are in the order of $0.1 - 0.01$ eV.

Because of the very sharp structures on the slowly varying "background" of the direct processes, the investigation of the cross-section must be carried out by an instrument whose resolution is better than the energy range of the resonances. As the result of the instrumental developments since the early sixties there have been a great many kinds of electron monochromators and analysers (capable of measuring angular and energy distribution as well [16, 17]), in spite of this, the implementation of a good energy resolution, especially in the range of some eV-s, is not everyday practice yet. This can be one of the most fundamental causes of the

fact that nowadays there are only about a dozen atoms [16 – 18] whose resonances were experimentally investigated in details. On the other hand, the theoretical methods worked out up till now give adequate results only in the low energy region. (Because in this case the number of the possible reaction channels is not too large [17].) One of the most important limits of the theory is that the role of the electron correlation is not sufficiently cleared. On the other hand, in case of heavy atoms, the relativistical methods are hardly developed.

2.2. Post-collision interaction

"Post-collision interaction" (PCI) is the phenomenon when a short-lived autoionizing state of an atom is excited by an electron whose energy is slightly higher than the threshold and, immediately after the excitation, the scattered electron has a small excess energy and remains very close to the atom at the instant of autoionization. This slow inelastically scattered electron serves to screen the ejected electron from the nucleus. The end-result of this dynamic screening effect is that the ejected electron loses little of its initial kinetic energy in overcoming the attractive Coulomb potential, and emerges from the system with a net gain in energy. The increment of the kinetic energy of the ejected electron must be counter-balanced by a corresponding loss of the energy of the scattered electron. If the energy exchanged exceeds the residual kinetic energy of the scattered electron, the latter will be effectively captured by the ion and they together form one of the singly excited states of the neutral atom [19]. In this case the energy gained by the ejected electron will be more than the available kinetic energy of the scattered electron with the binding energy of the singly excited bound state. Thus PCI can lead to the indirect excitation of Rydberg states of the atoms and can also appear in the energy spectra of the ejected electrons.

Although the correlation between the results of the calculation based on the qualitative model above and the issues of the available experiments is good [20, 21], the satisfactory quantitative theory of this process has not been worked out yet. However, there seem to exist fruitful theoretical efforts that describe the excitation and decay of the autoionization state as a whole and do not deal with them separately [22].

Both the theoretical and experimental results show that the widths of the PCI structures on the excitation functions [19, 23] or on the ejected electron spectra [24] are in the order of 0.1 – 0.01 eV. So, generally, the experimental resolution needed for the investigation of the resonance is also satisfactory for the observation of the PCI phenomenon.

2.3. Possibilities of the optical method

The excitation of the atomic level by electron impact at low energy can be investigated by a monoenergetic electron beam using the experimental apparatus

described in the next section. The method is called "optical" because the photons emitted spontaneously by the excited atoms are detected. The result of this procedure is the "optical excitation function" (OEF). The OEF shows the relative intensity of a chosen spectral line of a free atom as the function of the energy of the incident electron beam. This curve shows the influence of all the elementary processes having an effect on the population of the upper level of the spectral line.

According to our knowledge the fine structure of an OEF is determined fundamentally by the following four processes: direct excitation; cascade (in this case the population of the level observed can increase if the excited atom can reach the investigated level by photon emission); resonance and PCI as we noticed above. Naturally these processes are not independent of each other because, in general, the most prominent fine structure on the OEF-s is exactly the result of the interference between the direct excitation on the one hand and resonances or PCI-s on the other hand. (In the excitation of atomic levels the phenomenon expressed by the well known Wigner Threshold Law [16] usually manifests itself within an extremely narrow energy range, immediately above the excitation onset, so generally it remains undetectable even with the best apparatus available.) The influence of any other possible excitation or deexcitation process on the OEF [25] can be practically eliminated by giving an appropriate upper limit both to the concentration of the target atoms and the current density of the exciting beam.

Another possibility for the investigation of the excitation of atoms is the electron-spectroscopical method. The most popular one is the "energy loss spectroscopy", which is suitable for the direct observation of the excitation of an individual atomic level. In this case, the measurement of energy dependence of the cross-section necessarily implies the variation of the energy of the electrons in primary beam as well as the detection of the electrons. In the special case of the inelastic differential cross-section measurements the electrons which lost an amount of energy equal to the excitation energy of the level being studied are detected, at a fixed scattering angle [26].

As the third method we can mention the experiments where the yield of the atoms in the lowest-lying metastable state is measured as the function of the energy of the exciting electron beam [27 – 29].

One of the most significant advantages of the optical method is that it makes the separate excitation of many more atomic levels possible than the other two methods do. The main reason for this fact is that today the resolution of the light monochromators is better — by one or two orders — than the best electron-spectroscopical resolution. Therefore, only the optical method is suitable to distinguish the atomic levels lying very close to each other (1 meV) under the ionization threshold. So the appearance of resonance and PCI and their effect on the excitation cross-section can be investigated by the optical method at a great number of levels of the same atom. Because the PCI appears only in the excitation of the upper levels [19], the optical method is essential for its observation. A disadvantage of the optical method is that only the total cross-section is measured, which gives of course less detailed information than the differential cross-section which can be measured in an electron scattering experiment.

This latter is the main advantage of the second method, because the differential electronic excitation function allows the symmetry of the resonant state to be determined, what's more, the cascade effect has not any influence on it. Its importance is that the identification of the resonance states can generally be carried out by comparing the electronic excitation functions set up at appropriately chosen scattering angles [26].

The energy dependences of the excitations of the high lying levels are summarized and stored by means of cascades on the excitation functions of the metastable states. Hence the third method is suitable for getting comprehensive information about the most significant resonances. But at the same time the limit of this method is that it can provide only summarized information about the excitation of several levels. This is the reason why it cannot be used for the investigation of PCI.

To summarize, the methods mentioned above supplement each other and none of them can be considered as a universal one. Therefore beside the apparatus described in the following Section, in the future we intend to determine the angle and energy distribution of scattered electrons with an electron-spectroscopical method.

3. Experimental apparatus and method

The optical method, noticed above, and the trochoidal electron monochromator were not used for electron–atom collisions at low energy in our country. This is the reason why we discuss both the technique and the apparatus in greater detail than usual.

The optical excitation function is the intensity of light at a chosen wavelength as the function of the energy of electrons which bombard the emitting atoms. The quality of obtainable information is determined by the energy homogeneity of the exciting electron beam. Therefore we could not hope for finer structures than the full width of energy distribution of the exciting electron beam at half maximum (FWHM). The electron beam gained from some source can be made homogeneous by separating, hence the intensity of energy homogenized beam is low at low energy. In the collision chamber the density of free atoms cannot be increased arbitrarily to avoid secondary effects [25]. The low electron intensity and low density of particles result in a relatively low rate of photon emission. Additionally, there can be a difference of three orders of magnitude between the excitation cross-sections of different spectral lines. Under these conditions, the measurement of light intensity can be realised by photon counting.

For the solution of the tasks outlined above experimental equipment had to be set up. According to our bibliographical information from 1968 to late 1987, there are six research laboratories where there are or used to be similar devices. (See the list at the end of the article.) The device established in our Department is an improved version of the apparatus working in the Institute for Nuclear Research Uzhgorod, USSR. The block diagram of our apparatus is shown in Fig. 1.

The vacuum system is composed of a vacuum chamber, made of non-ferromagnetic stainless steel, with a volume of 50 dm^3, approximately; an adsorption low

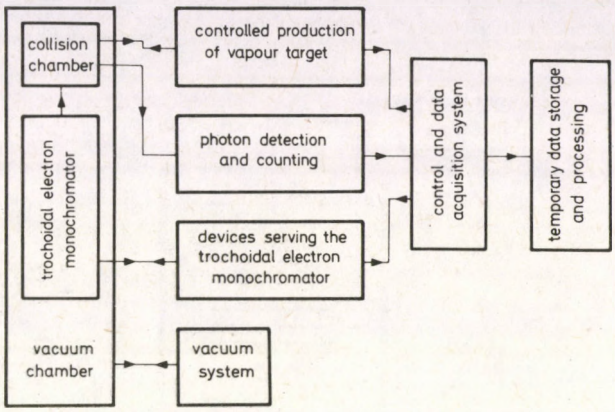

Fig. 1. Block diagram of the main units of the experimental apparatus

vacuum pump; a titanium sublimation high vacuum pump used for pumping during the baking of the electron monochromator; and a sputter-ion pump with a pumping speed of 250 dm^3/s producing 10^{-8} mbar final pressure. At the choice of pumps the aim was to perform oilless pumping because charging of thin isolator films created on surfaces can be disturbing as low energy measurements. For the same reason the whole system can be baked at 350°C. In our experiments it was kept at about 320 ±1 °C. The background pressure of the residual gases in the vacuum chamber did not exceed 1×10^{-7} mbar (uncorrected ionization gauge reading and the pressure of the target vapour was about 10^{-3} mbar in the collision chamber. The target was Cd (natural isotope composition) evaporized from a heated capsule. In the collision chamber the concentration of metal atoms was stabilized by keeping the temperature of the whole system stable within 1°C. Previously the Cd was purified by evaporation and recondensation into the capsule and it was sealed up under vacuum in another low vacuum system. The capsule was cracked up in the high vacuum system after baking the whole system at 350 °C for tens of hours.

The sketch of the collision chamber and the trochoidal electron monochromator (TEM) is shown in Fig. 2. The TEM consists of an electron gun, an energy selector and an accelerator electrode whose potential determines the mean electron beam energy. In the electron gun an undirectly heated oxide-coated cathode was used whose electron current is about 1 mA with an energy spread of the order of 1 eV. The TEM, developed by Stamatovic and Schulz [30, 31], has been applied to a variety of low energy electron scattering studies because it produces relatively high energy resolution especially at low energy. This is an advantage principally over the electrostatic monochromators which usually cannot be operated at an energy lower than 1 eV [32]. The energy selector used in the TEM is really a velocity selector whose sketch is shown in Fig. 3.

The electrons enter the velocity selector along the x-axis through the entrance

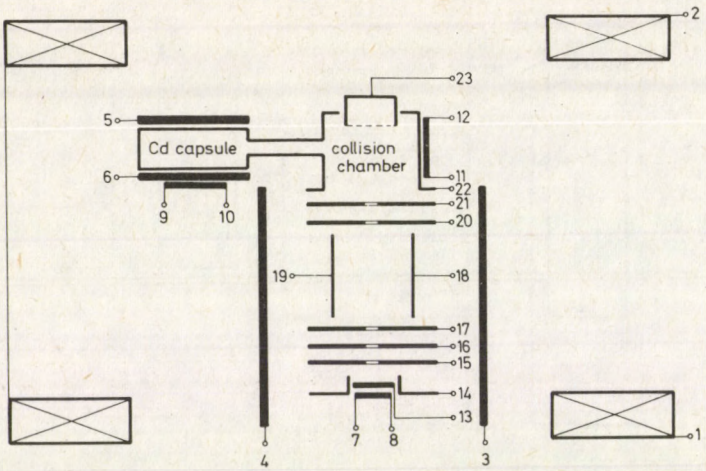

Fig. 2. (1–2) Helmholtz coils, (3–4) stove of the TEM, (5–6) stove of the Cd capsule, (7–8) heater of cathode, (9–10) thermoresistor Pt-100 for the Cd capsule, (11–12) thermoresistor Pt-100 for the collision chamber, (13) cathode surface, (14–15–16) electron optics, (17–18–19–20) energy selector, (21) accelerator electrode, (22) collision chamber, (23) Faraday cage

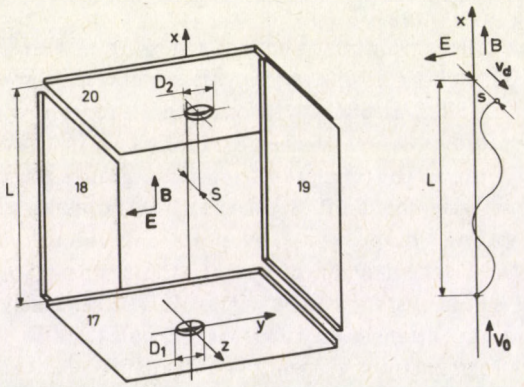

Fig. 3. The sketch of the velocity selector and an individual electron trajectory (scales are distorted). The numbering of the electrodes is the same as in Fig. 2

aperture D_1, where they move in static, homogeneous and mutually perpendicular electric and magnetic field. The velocity of the incident electrons is approximately parallel to the direction of the magnetic field. The equation of motion of an electron, in the crossed electrostatic and magnetic field, is given by

$$\frac{d\mathbf{v}}{dt} = \frac{e}{m}(\mathbf{E} + [\mathbf{v} \times \mathbf{B}]),$$

where $\mathbf{v}$ is the instantaneous velocity of the electron, t is the time, e and m are the

charge and the mass of the electron, respectively, while **E** is the electric field and **B** is the magnetic induction. If **E** is directed to $-y$ and **B** is directed to $+x$, then; taking into account the initial conditions:

$$\begin{aligned} x(0) &= 0, & v_x(0) &= V_{x0}; \\ y(0) &= Y_0, & v_y(0) &= V_{y0}; \\ z(0) &= Z_0, & v_z(0) &= V_{z0}; \end{aligned}$$

the solution is

$$x = V_{x0}t,$$

$$y = 1/\omega[(V_{z0} - E/B)\cos\omega t + V_{y0}\sin\omega t - V_{z0} + E/B] + Y_0,$$

$$z = 1/\omega[(V_{z0} - E/B)\sin\omega t - V_{y0}\cos\omega t + V_{y0}] + (E/B)t + Z_0,$$

where

$$\omega = \frac{eB}{m}$$

is the cyclotron frequency. So, under the action of the crossed fields, the electrons describe different types of trochoidal (cycloidal) trajectories in the yz plane combined with a uniform motion in x direction (given by V_{x0}). From the equation of path it can be seen that the electrons experience a deflection in the z direction with a drift speed

$$V_d = \frac{E}{B},$$

if V_{z0} and V_{y0} are negligible in comparison with V_{x0}. Under these conditions at a given length L of the selector field the electrons are deflected with

$$S = V_d \frac{L}{V_{x0}}$$

in the direction perpendicular to both **E** and **B**. Therefore, the deflection of the electrons with various energy – and velocity as well – is inversely proportional to the x component of their velocity. From the deflected beam it is possible to cut out a part beam whose energy homogeneneity is better than that of the incident one. If the spread beam is bordered by an exit electrode whose aperture D_2 is displaced by S along the z-axis with respect to the axis of the incident aperture, the full width at the base of the energy distribution at the exit of the separator is

$$\Delta W = \frac{(EL)^2 m(D_1 + D_2)}{B^2 S^3} + eD_1 E,$$

and the mean energy is

$$W = \frac{(EL)^2 m}{2e(BS)^2},$$

where D_1 and D_2 are the diameters of the apertures, respectively [33]. In our case the specification of the parameters of the velocity selector was preceded by Monte-Carlo simulation [34].

Because even the weakest ferromagnetism of the parts of the TEM can disturb its operation, all the elements exposed to the electron beam are constructed from bronze which can be baked in high vacuum. Ceramic rings are used as spacers and insulators between electrodes. In the TEM built the diameters of the entrance and exit apertures are $D_1 = 0.5$ mm and $D_2 = 0.8$ mm, respectively. The centre of the exit aperture is displaced by $S = 4$ mm from the axis. The length of the selector field is $L = 16$ mm. The electrostatic field is produced by deflector plates (18, 19 in Fig 3). The deflector plates are made by machining a cylinder of the same diameter as the electrode disks and by cutting it in half along its axis. The spacing between the two parallel surfaces of the deflector is approximately 4 mm, while the potential difference between them is some volts. This potential difference is divided asymmetrically with respect to the entrance electrode. The homogeneous magnetic field is produced by Helmholtz coils, placed around the vacuum chamber. In the selector field the available maximum value of the magnetic induction is approximately 1.5×10^{-2} T. The selector is followed by an accelerator electrode (21 in Fig. 2). Its aperture has the same diameter and lies on the same axis as the exit of the selector. The accelerator electrode not only sets the required mean energy of the monoenergetic electron beam but serves as the entrance wall of the collision chamber as well. The opposite parallel wall is a metal grid closing the Faraday cage insulated from the collision chamber. The third side of the collision chamber is a cylinder with a polished inner surface, 15 mm in diameter. The axis of the cylinder coincides with the axis of the electron beam. There are two holes in the wall of the cylinder; one of them, 3 mm in diameter, provides the target vapour and the other one, 12 mm in diameter, closed by a fused silica window for the emitted photons. The polished cylinder, like a mirror, increases the intensity of light leaving the collision chamber.

The electrons of the beam are collected by the Faraday cage. The current measurement is performed by frequency counting of a current-frequency converter. The intensity of light can be normalized to unit current of the exciting electron beam by means of this frequency. The energy distribution of the electron beam is determined by derivation of retarding curves. The best FWHM obtained by this TEM was 40 meV at a beam intensity of about 2 nA on the Faraday cage. (see Fig. 4)

In front of the window on the collision chamber there is also a fused silica window on the vacuum chamber. In the collision chamber the trajectories of the electrons are nearly straight lines, so the collisions also take place along these lines, therefore the emitting atoms form a linear light source. The image of this light source on the inlet slit of the grating monochromator is formed by a lens combination consisting of two fused silica lenses. The resolution of the grating monochromator is 20 nm/mm and operates from 200 nm to 750 nm using the available grates.

The exit slit of the light monochromator is followed by a photon counting system. The front element of this system is a fused silica lens forming the exit

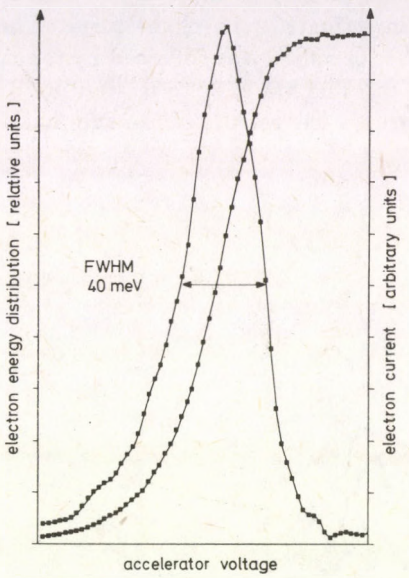

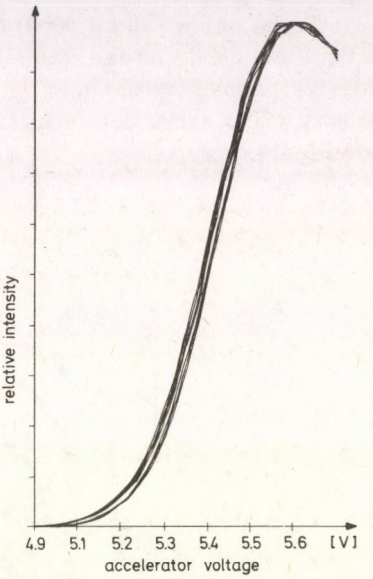

Fig. 4. Retarding curve and electron energy distribution

Fig. 5. The near-threshold leading edge of Cd line, wavelength of 326.1 nm ($5^1S_0 \longleftarrow 5^3P_1$). The curves are normalized to unity and projected on the same coordinate system

slit on the cathode of a photomultiplier tube. To minimize the dark counts, a photomultiplier tube with a cathode of a small diameter was used. To reduce the thermal emission of the cathode and dynodes as well as to reduce the fluctuation of gain, the photomultiplier tube was cooled and kept at -40 ± 1 °C. For cooling vapour flow of liquid nitrogen was used. Using this procedure the mist over the optical and electronical elements can be avoided. After impedance matching the photomultiplier tube is connected to a voltage comparator. To get the best signal-to-noise ratio there are related values of the applied high voltage and the discrimination threshold determined by the intensity of light. For a given tube, the related values were determined by calibrating measurements. On the output of the electronics after the comparator the detected photons appear as TTL pulses. The light intensity of a given spectral line is supposed to be proportional to the mean frequency of TTL pulses.

One point of the excitation function can be obtained by counting the emitted photons at a given voltage of the accelerator electrode in a given time, then subtracting the pulses counted without the electron beam during the same time. The error caused by the fluctuation of the beam current can be eliminated by measuring the current and normalizing the light intensity. In our case the normalized light intensities of different spectral lines covered three orders of magnitude. Therefore, to get the excitation function – relating to the different spectral lines – with similar

statistical characteristics, the counting time was as long as necessary to gather the same number of pulses (about 6000) on the investigated part of the curve. The exposure time was fixed and the required number of pulses was collected by repeating the counting period several times. (It made checking the long term stability of the system easy.) The excitation functions shown are the results of the summation of the individual exposures.

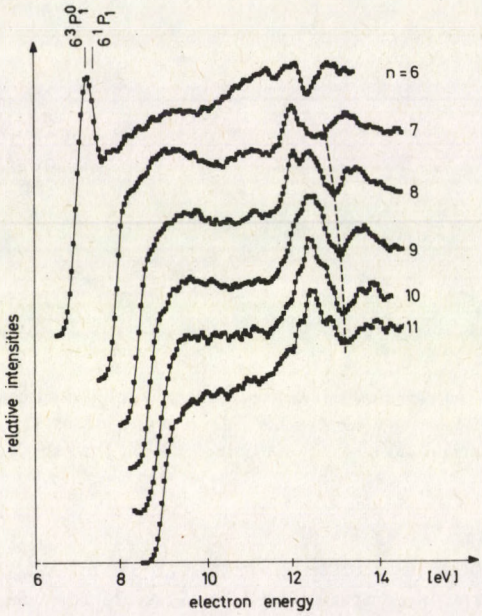

Fig. 6. Optical excitation functions of the Cd for the $5^3P_1 \longleftarrow 6^1S_0$ and $5^1P_1 \longleftarrow n^1S_0$ transitions (n=7 – 11)

It is possible to obtain information on the physical processes of the electron–atom collisions by comparing the different optical excitation functions of a spectral series. It involves comparing the structures of different excitation functions. The aim was to measure excitation functions of a spectral series, as many as possible by using the best obtainable resolution. It is a charateristic of the TEM that a chosen resolution can be set at various electron currents [33]. Therefore, at first the TEM must be adjusted to a state of operation where the current is maximum at the required resolution. Since the time for measurement of one excitation function sometimes amounted to twenty hours, this required special control of the stability of the experimental conditions. For this purpose the FWHM and the mean energy of the beam had to be checked and corrected to the same value as far as possible. The supervision of the FWHM was performed by the retarding method, as it was noticed above, while checking the mean beam energy was performed using a characteristic

structure of an intensive spectral line. It is suitable to use the interval of the excitation function where the steepness is constant in a wider energy range than the FWHM of the exciting beam. Hence, in this case the steepness of the measured excitation function remains unchanged independently of the FWHM. In our case the near-threshold rising part of the excitation function of Cd line wavelength of 326.1 nm ($5^1S_0 \leftarrow 5^3P_1$) was used. This part of the curve was repeatedly taken every four hours. As it is shown in Figure 5, the shift of the curves, therefore the variation of the mean beam energy as well, was less than ± 15 mV, or ± 15 meV, respectively, during the whole measurement period.

The mean electron beam energy is not identical with the accelerator voltage, but the good correlation of the curves shown proves that the difference between them is nearly constant in time. In the present measurements the average value of the intersection of the axis of abscissas and the tangent lines to the curves at the rising part of constant gradient was taken to be the known threshold energy (3.80 eV) of the 5^3P_1 Cd level. Taking the difference between this abscissa and the threshold potential (3.80 V), it is the potential difference with which, shifting the accelerator voltage, the real average energy of the beam, therefore the real energy scale can be obtained. On the basis of this method, in accordance with our calibrating measurements, the energy scale of the curves, taken at different times, is calibrated to an accuracy of approximately ± 15 meV without any other modification. Because the present experiments have been carried out with a resolution of 120 to 200 meV, which is one order greater than the inaccuracy of the energy scale, its further correction is unreasonable.

Because of the great number of the simultaneously measured parameters the experiment was carried out with the aid of an intelligent CAMAC system, where the signal sources were individually adjusted. The CAMAC system performed the regulation of the parameters, collected the data and transmitted them to a personal computer for temporary storage and processing.

4. Results and discussion

The first test of our apparatus was performed by taking up OEF-s of Cd which had been known from previous experiments [35, 36]. Our results show a very good correlation with the results of other papers in spite of the fact that those results were obtained by using different kinds of apparatus. The reliability check was carried out in case of an element which is difficult to manage from an experimental point of view, so the successful experiments show that the arrangement can be used not only in case of gases but in case of metal vapours as well.

Figures 6–8 contain curves which hold new information about the excitation of Cd by electron impact. We have not calibrated the spectral detection sensitivity of our apparatus, so the light intensities in different OEF-s are not comparable. But — apart from the energy resolution — the curves were set up under the same experimental conditions.

Let us consider first the energy range below the first ionization potential

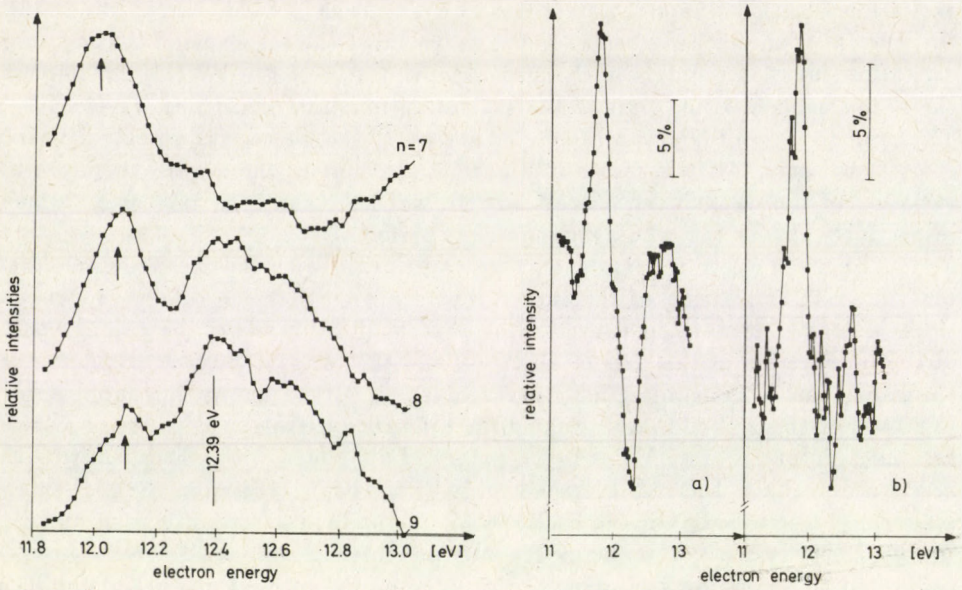

Fig. 7. Optical excitation functions of the Cd for the $5^1P_1 \longleftarrow n^1S_0$ transitions with a FWHM of about 120 meV

Fig. 8. Optical excitation functions of the Cd for the (a) $5^3P_2 \leftarrow 5^3D_{123}$ and (b) $5^3P_2 \leftarrow 6^3D_{123}$ transitions with a FWHM of about 120 meV

(8.99 V). The curves in Fig. 6 belonging to the same spectral series were measured with an energy spread of 200 meV (FWHM). (As we know, such a great number of OEF-s of a spectral series with such a good resolution have not been determined yet.)

Let us focus our attention on the characteristic maximum of the first curve at 7.25 eV. First of all, this maximum cannot be originated from a cascade because the lowest 6^3p_1 and 6^1P_1 levels from which the transition to the 6^1S_0 level is possible, lie much higher in energy than the rising part of this maximum. On the other hand, above the energy of the 6^3P_1 level the OEF is decreasing. Since this maximum lies below the first ionization potential, the maximum can be the result of direct excitation or indirect excitation via an intermediate resonance or both of them.

It can be seen from Table I that the correlation between the spectroscopical threshold and the measured excitation threshold is very good in case of the five curves of the n^1S series. (This means an additional justification of the energy calibration.) Again the first curve is the one for which the difference between the measured and spectroscopical threshold is greater — by one order — than that for the others. The significant shift of the observed excitation onset suggests that the effect of the direct excitation of the 6^1S_0 Cd level on the excitation cross-section

is very small just above the threshold. There are electron energy loss experiments indirectly related to this fact [37, 38]. In their cases the peaks coinciding with the energy of the 6^1S_0 level could be detected at relatively higher excitation energy (some ten volts) in the inelastic scattering. But even at this higher energy, the excitation probability of n^1S Cd level can be found less than that of the n^1P level by one order.

On this basis we suppose that the characteristic maximum on the first curve at about 7.25 eV is not mainly caused by direct excitation but is due to a resonance. We would like to notice that there have been determined some special values of energy, where the fine structures of the OEF-s show the influence of the typically multichannel effect of the different resonances [35]. For that very reason our above supposition is supported by the fact that the energy in question coincides with the previously revealed position of the resonance structures on the OEF-s of the 5^1P_1 and 6^3S_1 levels [35, 36].

Table I

Comparison between measured* and spectroscopic thresholds for OEF-s shown in Fig. 6

Radiating level	6^1S	7^1S	8^1S	9^1S	10^1S	11^1S
Wavelength [nm]	441.3	515.5	430.7	398.2	381.8	372.4
Measured threshold [eV]	6.82	7.81	8.28	8.52	8.68	8.78
Spectr. threshold [eV]	6.61	7.82	8.3	8.53	8.66	8.75
Difference [eV]	0.21	−0.01	−0.02	−0.01	0.02	0.03

* The measured thresholds were determined by extrapolating the linear portion of the excitation onsets down to the energy axis.

From the sphere of the possible resonances the ones are out of the question whose electron configurations are $5s^2nl$ type. As it has been proved [39, 40] the influence of these shape resonances on the decay to the ground state – as parent state – is limited to the energy range of the elastic scattering. We can disregard the next $5s5p^2$ resonances on the basis of the next comparison: the resonances corresponding to the $nsnp^2$ electron configuration are in the vicinity of the lowest lying $^{1,3}P$ levels both in case of the Mg^- [17] and in the case of Hg^- [41, 42] which are lighter and heavier than Cd, respectively. So, we hope for the same in case of Cd as well. The fact that the $5s6s^2\ ^2S$ resonance is Feshbach resonance lying close below the 6^1S_0 level in question helps the selection among the $5s6lnl$ configurations. In the end the resonances corresponding to the $5s6s6p$ or $5s6p^2$ electron configurations next in turn are the most probable candidates to cause the characteristic maximum on the OEF of the 6^1S_0 Cd level with their decay.

However, we cannot determine the concrete resonance corresponding to these configurations which causes this characteristic maximum. The cause of this – which is a rule rather than an exception – is that there is no direct information at all about the energy of the concrete resonance states associated with excited states of cadmium. But there are no indirect data because the energy positions of the doubly excited states of In, Sn^+, Sb^{++} etc., which form the isoelectronic sequence of the Cd^-, are not known sufficiently.

However, we can notice the analogy with the 2^2P and 2^2D resonances of helium corresponding to the similar $1s2s2p$ and $1s2p^2$ electron configuration which cause wide maxima on the excitation functions of the ^1S and ^3S states [6, 16]. In case of the mentioned electron configuration of the Cd, due to the departure from the LS-coupling we have to take into account not only the spectral doublets but the possible spectral quartets as well. After all the above interpretation can be regarded a working hypothesis.

Now let us consider the energy range above the ionization potential, where the PCI can appear as well. In the analysis of Figs 6–8 we will use the following typical characteristics to distinguish between the origin of the different structures. The most important and previously verified regularities are the following:

(i) In case of a certain resonance, due to its multichannel decay, the structures produced on different OEF-s appear at the same energy [15, 17, 35].

(ii) Observing the excitation of states lying closer to the ionization threshold, the PCI structures move to higher electron energy [19, 20, 23].

Our measurement seems to be the first occasion when PCI structures have been observed on the OEF-s of Cd. The n^1S curves in Fig. 6 show a pronounced structure just above the dashed curve which clearly shifts towards higher energies with increasing principal quantum numbers, so they must be caused by PCI. Let us now consider the structures below the dashed curve. To investigate these structures in detail, more accurate measurements were performed, as shown in Fig. 7. We can suppose PCI origin of the maxima marked by arrows according to the qualitative condition of (ii). (Although the shift of the maxima is not too large, it is out of the question that the shift is much greater than our experimental inaccuracy.) The PCI origin of the maxima in the energy range 12.01–12.1 eV is supported by electron-spectroscopical measurements [24]. In that paper the ejected electron spectra resulting from electron excitation of autoionizing levels in Cd vapour is studied. There a clear PCI shift is observed in the same energy range where we did.

The indirect PCI excitation mechanism producing the above maxima can be summarized as follows

$$e + \mathrm{Cd}(5^1S_0) \rightarrow \mathrm{Cd}^{\alpha i} + e_s \rightarrow \mathrm{Cd}^+ + e_s + e_f \xrightarrow{PCI} \mathrm{Cd}^*(n^1S_0) + e_f,$$

where $\mathrm{Cd}^{\alpha i}$ denotes the autoionizing state and the subscripts s and f refer to the slow scattered and the fast ejected electrons, respectively.

Let us consider the structures appearing at the same energy on the different OEF-s. They are most probably caused by an indirect excitation process via intermediate compound states associated with autoionizing states of the natural Cd atom. In Fig. 7 there are three fine structure elements lying at 12.39 eV.

The abscissas of the main maxima on the curves in Fig. 8 are also close to each other. Though the intensities of the maxima are relatively small with respect to the "background" and their dispersion is relatively high so the positions of the maxima are not too well defined, in spite of this we do not expect a shift which is characteristic of PCI. Thus we think the two maxima originate from resonance.

There are electron scattering experiments which predict at least 20 autoionizing states between 11.5 eV and 14.5 eV and in some cases they are separated only

by some hundredths eV [24, 43]. Because their effects overlap each other and there can be interferences, it is impossible to find the autoionizing states corresponding to the different structures till there are available results with an improved resolution. But we can declare the indirect excitation corresponding to resonance or PCI is caused by the $4d^{10}5pnl$ and $4d^{9}5s^{2}nl$ type autoionizing states. Although the above mentioned two structures in Fig. 8 had already been observed but then the energy calibration was less accurate and the experiment was not repeated at different concentrations of the target vapour [35]. In case of the last two OEF-s the concentration was less than half of the concentration of the above mentioned measurement. Because the intensities of the structures with respect to the excitation "background" are the same as they were in the previous measurements (see the line segments in Fig. 8), we can eliminate the influence of some secondary effects and can predict that the structures are the results of the clear excitation process.

Acknowledgement

The authors are greatly indebted to Prof. D. Berényi for his distinguished interest in their work.

Appendix

List of the laboratories using TEM

1. Yale Univ., New Haven, USA (A. Stamatovich et al)
2. Univ. of Leyden, Leyden, The Netherlands (G. I. Verhart et al)
3. Univ. Laval, Quebec, Canada (D. Roy et al)
4. Argonne Nat. Lab., Argonne, USA (J. Eichler et al)
5. Univ. of Maryland, College Park, USA (M. R. McMillan et al)
6. Inst. For Nuclear Res., Uzhgorod, USSR (O. B. Shpenik et al)

References

1. G. J. Schulz, Phys. Rev. Lett., *10*, 104, 1963.
2. M. A. Biondi, H. Herzenberg and C. E. Kuyatt, Phys. Today, *32*, No. 10, 44, 1979.
3. V. A. Bazilev and M. I. Tsebesov, Uspekhi Phys. Nauk., *133*, 617, 1981 (in Russian).
4. V. P. Zhdanov, J. Phys. B: At. Mol. Phys., *15*, L 297, 1982.
5. A. I. Zapesochny, A. I. Imre, I. S. Aleksakhin, I. P. Zapesochny and O. I. Zatsarinny, Zh. Eksp. Teor. Fiz., *90*, 1972, 1986 (in Russian).
6. H. S. W. Massey, Negative Ions, Cambridge University Press, Cambridge, 1976.
7. B. M. Smirnov, Otritzatylny iony (Negative Ions) Atomizdat, Moscow, 1978 (in Russian).
8. F. Brouillard and J. W. Mc Gowan (editors), Physics of Ion–Ion and Electron–Ion Collisions, Plenum Press, New York, 1983.
9. R. B. Barker and H. W. Berry, Phys. Rev., *151*, 14, 1966.

10. P. J. Hicks, S. Cvejanovič, J. Comer, F. H. Read and J. M. Sharp, Vacuum, *24*, 573, 1974.
11. W. Sandner, J. Phys. B: At. Mol. Phys., *19*, L 863, 1986.
12. R. Huster, W. Sander and W. Mehlhorn, J. Phys. B: At. Mol. Phys., *20*, L 287, 1987.
13. M. Borst and V. Schmidt, Phys. Rev. A., *33*, 4456, 1986.
14. A. Russek and W. Mehlhorn, J. Phys. B: At. Mol. Phys., *19*, 911, 1986.
15. G. J. Schulz, Rev. Mod. Phys., *45*, 378, 1973.
16. F. H. Read, Phys. Scripta, *27*, 103, 1983.
17. V. I. Lengyel, V. T. Navrotsky and E. P. Sabad, Uspekhi Phys. Nauk., *151*, 425, 1987 (in Russian).
18. L. Szótér, Fiz. Szemle, *7*, 257, 1985 (in Hungarian).
19. T. van Ittersum, H. G. M. Heideman, G. Nienhuis and J. Prins, J. Phys. B: At. Mol. Phys., *9*, 1713, 1976.
20. G. Nienhuis and H. G. M. Heideman, J. Phys. B: At. Mol. Phys., *8*, 2225, 1975.
21. S. Hedman, K. Helenelund, L. Asplund, U. Gelius and K. Siegbahn, J. Phys. B: At. Mol. Phys., *15*, 799, 1982.
22. M. Ya Amusia, M. Yu. Kuchiev and S. A. Sheinerman, Zh. Eksp. Teor. Fiz., *76*, 470, 1979 (in Russian).
23. O. P. Shpenik, I. P. Zapesochny, E. E. Kontrosh, E. I. Nepijpov, N. I. Romanyuk and L. Szótér, Zh. Eksp. Teor. Fiz., *76*, 846, 1979 (in Russian).
24. S. M. Kazakov, A. I. Korotkov and O. B. Shpenik, Pisma Zh. Techn. Phys., *6*, 421, 1980 (in Russian).
25. S. E. Frish, Opt. Spektry Atomov (Optical Spectra of Atoms), Izd. Fiz.-Math. Lit., Moscow-Leningrad, 1963 (in Russian).
26. D. J. Andrick, J. Phys. B: At. Mol. Phys., *12*, L 175, 1979.
27. S. J. Buckman, P. Hammond, F. H. Read and G. C. King, J. Phys. B: At. Mol. Phys., *16*, 4039, 1983.
28. S. J. Buckman, P. Hammond, G. C. King and F. H. Read, J. Phys. B: At. Mol. Phys., *16*, 4219, 1983.
29. O. B. Shpenik, A. N. Zavilopulo, A. V. Snegursky and I. I. Fabrikant, J. Phys. B: At. Mol. Phys., *17*, 887, 1984.
30. A. Stamatovich and G. J. Schultz, Rev. Sci. Instr., *39*, 1752, 1968.
31. A. Stamatovich and G. J. Schultz, Rev. Sci. Instr., *41*, 423, 1970.
32. W. Steckelmacher, J. Phys. E., Sci. Instr., *6*, 1061, 1973.
33. D. Roy, Rev. Sci. Instr., *43*, 535, 1972.
34. B. Palásthy, Doctoral Thesis, NME-Miskolc (Tech. Univ. for Heavy Industry, Miskolc), 1985 (in Hungarian).
35. O. B. Shpenik, I. P. Zapesochny, L. Szótér, E. E. Kontrosh and A. N. Zavilopulo, Zh. Eksp. Teor. Fiz., *65*, 1797, 1973 (in Russian).
36. I. P. Zapesochny, L. Szótér, O. B. Shpenik and A. N. Zavilopulo, Dokl. Akad. Nauk SSSR, *214*, 1288, 1974 (in Russian).
37. W. R. Newell, K. J. Ross and J. B. P. Wickes, J. Phys. B: At. Mol. Phys., *4*, 684, 1971.
38. B. Marinkovič, V. Pejčev, D. Filipovič and L. Vuškovič, Abstr. XV. ICPEAC (Brighton), 186, 1987.
39. P. D. Burrow, J, A. Michejda and J. Comer, J. Phys. B: At. Mol. Phys., *9*, 3225, 1976.
40. S. M. Kazakov, Pisma Zh. Techn. Phys., *7*, 900, 1981.
41. N. S. Scott, P. G. Burke and K. Barschat, J. Phys. B: At. Mol. Phys., *16*, L 361, 1983.
42. L. Koch, T. Heindorff and E. Reichert, Z. Phys. A, *316*, 127, 1984.
43. V. Pejčev, D. Rassi and K. J. Ross, J. Phys. B: At. Mol. Phys., *10*, L 629, 1977.

Acta Physica Hungarica 65 (2-3), pp. 257-264 (1989)

ON THE ENERGY DEPENDENCE OF THE ELECTRON SHAKE PROCESSES*

E. VATAI

Institute of Nuclear Research of the Hungarian Academy of Sciences (ATOMKI)
4001 Debrecen, Hungary

Time-dependent corrections were calculated for shake-up and shake-off probabilities and compared with the neon valence shell shake-up probabilities. Electron shake-up is shown to be time-independent in contrast with collision processes, supplying an additional evidence that distinct levels of non-separability exist and the electron–proton connection is capable of preventing the time development of the electron system.

1. Introduction

It was proved more then fifty years ago by von Neumann [1] that quantum systems developing according to the time–dependent Schrödinger equation remain in pure state independently of the interaction or the distance between the subsystems. The state vector of a subsystem, (that is its energy, momentum, spin, etc.), cannot be given separately. This conflicts with the result of the measurement, in which the subsystem is always found in a well determined state. The problem was solved by von Neumann in the following way: The measurement is a sudden irreversible process, which is not described by the Schrödinger equation, therefore it is capable of separating the subsystem, on which the measurement is made, from the remaining part of the system.

The above non-separable (indivisible) character and the related non-locality of quantum processes, as well as the problem of the measurement, are well known and debated questions of quantum theory [2,3]. Recently, important developments were achieved concerning non-separability. The spin-polarization experiment of Aspect et al [4] and the investigation of the energy transfer in β decay by the author [5] have proved that non-separability exists independently of the actual form of the theory and it cannot be eliminated by the introduction of hidden variables into the theory. This indicates that a physical entity underlaying non-local connection exists.

An indication that the above entity not only exists, but may have different properties for differing systems, is being published by the author [6]. This conclusion is based on the different behaviour of the atom depending on the origin of the ionizing electron. The interaction of the atom with an electron or any other charged particle in a collision process is well described by the time-dependent Schrödinger equation. The situation changes radically when the ionizing electron is originally bound in the atom or created in the nucleus: The ionization is described in this

*Dedicated to Academician D. Berényi on his 60th birthday

case by the projection approach, which corresponds to the sudden change of the potential. This time development does not follow the Schrödinger equation, because the Coulomb potential in many cases changes slowly due to the slow speed of the electron. The above time-independence can be explained by the effect of non-separability or non-local connection. This implies that a straightforward explanation of the different behaviour is that non-local connection has different properties in these two cases. The electron–nucleus connection is strong enough to prevent the time-dependent development of the atom, while the electron–electron connection is not.

This result plays an important role in proving that non-separability is established by connective strings (c-strings) [7], therefore a detailed description of the calculations and their comparison with additional experimental results is given in the following.

2. Time-dependent calculations of shake probabilities

The general expression valid for both electron impact ionization and excitation and for shake-processes can be obtained by the method of variations of constants [8] from the time-dependent Schrödinger equation.

$$(H^0 + \mathcal{V}(t))\psi_n = i\hbar\frac{\partial\psi_n}{\partial t}. \tag{1}$$

Writing $\psi_n = \mathbf{S}_s\ a_{ns}(t)\phi_s\ \exp(-i\varepsilon_n\ t/h)$, where ϕ_s is the solution of the unperturbed equation. The following equation is obtained for the $n \to m$ one electron transition amplitude

$$i\hbar\frac{\partial a_{mn}}{\partial t} = \mathbf{S}_s\ a_{ns}\ V_{ms}\ \exp\left(\frac{i}{\hbar}\varepsilon_{ms}t\right), \tag{2}$$

with $V_{ms} = \int \phi_m^*\,\mathcal{V}(t)\phi_s dt$ and $\varepsilon_{ms} = \varepsilon_m - \varepsilon_s$. Approximate solutions for collisions are given by the first and second Born, the distortion approximations, etc. The dependence of the excitation probability on the velocity $\mathbf{v}$ of the relative motion [8] is $\mathbf{v}^{-2}$ in first Born approximation (i.e. at high velocities) and it is proportional to $\mathbf{v}$ in the adiabatic approximation ($\mathbf{v} \to 0$). The experimental results are reproduced by these approximations fairly well (see for example [9]). Existing small differences are regarded as eliminable by increasing the accuracy of the approximations.

Shake processes are characterized by a persistent change of the Coulomb potential. For example in β decay both the initial and final atoms are stable. We discuss this case in the following in some detail.

The solution of Eq. (1) yields the following transition amplitude for persistent perturbations [5]

$$d_{ai} = \int \frac{\partial}{\partial t}\left(\frac{V_{ai}}{\gamma_{ai}}\right)\ \exp\left(\frac{i}{\hbar}\int_0^\infty \gamma_{ai}\,dt\right)\,dt, \tag{3}$$

where V_{ai} is the same as in Eq. (2) and $\gamma_{ai} = (\varepsilon_a + V_{aa}) - (\varepsilon_i + V_{ii})$. The time dependence of γ_{ai} can be neglected, because $(V_{aa} - V_{ii}) \ll (\varepsilon_a - \varepsilon_i)$.

Existing time dependent calculations were made with exponential dependence of the potential change on the inter-electron distance (see Thomas [10] and references quoted there). Thomas used the following potential $V(t) = -V_0 f(t)$ and $\partial f(t)/\partial t = \exp(-t^2/2t_0^2)$. Exponential change is, however, much quicker than the change of the Coulomb potential, which depends on the inter-electron distance as $1/r_{12} \sim 1/vt$. Here v is the relative speed of the β particle or photoelectron. The use of the exponential change of potential simplifies the calculations.

The monopol nature of the shake transitions investigated experimentally allows one to limit the multipol expansion of $1/r_{12}$ to the first term ($\ell = 0$). The average change of the potential in this approximation is given as

$$\begin{aligned} V(t) &= \frac{Z}{R_{\max}} = \frac{Z}{vt_0} \quad \text{and} \quad \frac{\partial f}{\partial t} = 0 \quad \text{if} \quad t < t_0 \\ &= \frac{Z}{r} = \frac{Z}{vt} \quad \text{and} \quad \frac{\partial f}{\partial t} = \frac{t_0}{t^2} \quad \text{if} \quad t < t_0, \end{aligned} \tag{4}$$

where $R_{\max} = \max(R_i, R_n)$ and $t_0 = R_{\max}/v$; n and i are the orbitals in which photoionization and shakeup occurs respectively; Z is the nuclear charge. One may put $R_n = 0$ for β decay.

Substitution of Eq. (4) into (3) gives

$$d_{ai} = -\frac{V_{ai}}{\gamma_{ai}} t_0 \int_{t_0}^{\infty} \exp(i\gamma_{ai} t) \frac{dt}{t^2}. \tag{5}$$

The factor V_{ai}/γ_{ai} is the transition amplitude calculated in the projection approach by using the first order perturbation theory. The second part of Eq. (5) is the time-dependent correction, which was calculated by numerical integration. Details of the calculations are given in the Appendix.

Requirements on the accuracy of the approximations are decreased because of the large difference between the experimental and the time corrected theoretical results (see Figs 1 and 2).

The transition amplitude in the projection approach V_{ai}/γ_{ai} was replaced by the experimental high energy limit, which is an upper limit of the true amplitude. The corrections, which are not discussed here, are all coming from second and higher order terms of the perturbation expansion, which is decreasing as powers of $\Delta Z_{\text{eff}}/Z_{\text{eff}} \sim 0.05$–$0.1$. These corrections are the contributions of the off diagonal terms in Eq. (2); the effect of electron correlation, etc. The error of the numerical integration as determined from the comparison with the approximation of Hastings [11] is smaller than 0.1% and therefore can be neglected. We consider that the possible relative error caused by the neglect of the higher order corrections is not larger than $\pm 15,; \pm 10$ and $\pm 5\%$ for shake processes accompanying $1s$ photoeffect in N_2, Ne and Ar respectively [6]. The dependence of the time corrected curves on

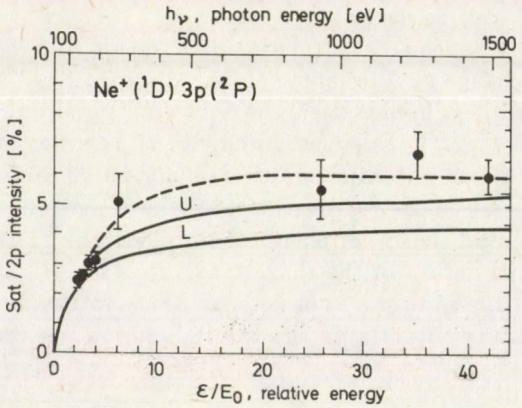

Fig. 1. Comparison of the experimental energy-dependence of the $(^1D)3p(^2P)$ excitation of neon at photon energies from 100 to 1500 eV [12] with the time-dependent theoretical results. Curves U and L are calculated for an upper and a lower bound of the shake energy (see text for details)

the changes of the shakeup energies is demonstrated in Figs 1 and 2, where upper and lower limiting curves calculated for energies $\gamma_{ai} = 40$ and 20 eV are displayed. These values of γ_{ai} differ from the shakeup energies ($\sim$ 30 eV) as much as 30%.

The substantial difference between the time corrected theory calculated by us and the experimental results imply that the conclusion is not expected to change if one increases the accuracy of the calculations.

3. Comparison with the experimental results

The experimental results for the 1*s* shakeoff in β decay, nitrogen shakeup, neon shakeoff and argon shakeup and shakeoff were compared with the time corrected theoretical results in [6]. This comparison has revealed that shake processes are time independent even at low speed of the β or photoelectron, i.e. these processes are not described by the time-dependent Schrödinger equation. Additional experimental results, the energy dependence of neon's shakeup, is examined below. Shakeup of neon's valence electrons was investigated by Wuilleumier and Krause [12] in photoeffect induced by photons with energy between 100 and 2000 eV, and Becker et al [13] between 49 and 150 eV. The experimental time (or energy) dependence is published for lines with energies $\gamma_{ai} = 34.31$, 31.45 and 30.47 eV, therefore we calculated a common upper and lower limiting curve with $\langle R\rangle = 0.87$ a.u., $\gamma_{ai}=$ 43 eV and $\langle R\rangle = 0.93$ a.u. and $\gamma_{ai} = 20$ eV, respectively.

Comparison of the experimental results with the time-dependent correction multiplied by the asymptotic experimental value is given in Figs 1 and 2. The observation of Armen et al [14] indicating that shakeup becomes constant above 60 eV was used to determine the asymptotic values of $(^3P)3p(^2P^0)$ and $(^1D)3s(^2D)$

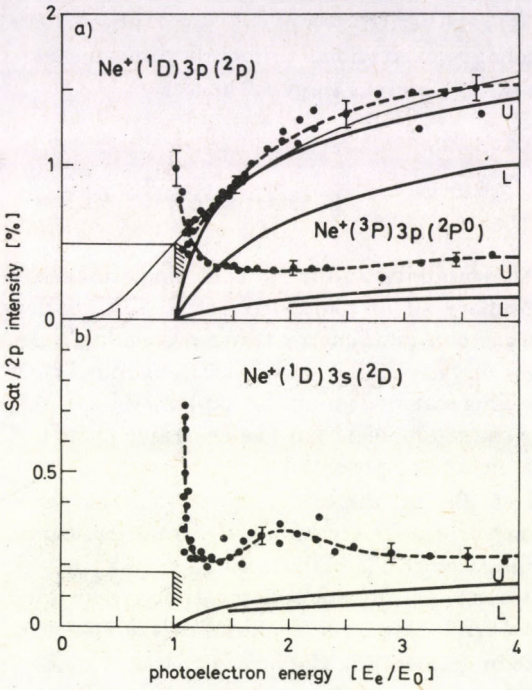

Fig. 2. Comparison of the experimental energy-dependence of the shakeup probabilities for neon photoexcitation at photon energies from 49 to 150 eV [13] with the time-dependent theoretical result

shakeup intensities. Low energy resonances are independent of shake processes and their origin is not discussed here. The above two shake transitions corroborate with the conclusion of paper [6] that shake processes are not described by the time-dependent calculations.

The $(^1D)3p(^2P)$ excitation seems to be of different nature, as suggested already by Wuilleumier and Krause [12]. One may observe that at low energies (see Fig. 2) the experimental points might be described by the time correction, if we increase the asymptotic limit from 2.4% to $\sim$ 3.2%. This is possible because this limit was not measured in [13]. The change of the total angular momentum of the atom in this excitation process $\Delta L = 1$ is another evidence against the shake origin of this transition. There is further indication that the $(^1D)3p(^2P)$ excitation is not of inner-atomic origin. One may notice that the asymptotic limit measured by Wuilleumier and Krause [12] is 6% while the one given by Becker et al [13] is from 2.4 to 3.7%, i.e. they differ far beyond the experimental errors. Such difference is expected when the probability of the process depends on the experimental setup, for example on the density of the target. The above features are expected if

this transition is induced e.g. by secondary interaction of photoelectrons with the neon atoms in the target. Verification of this assumption is possible for example by calculating the secondary excitation's probability and measurement of the relative intensity of this peak for different target densities.

4. Discussion

It has been shown above and in [6] that shake processes are independent of the speed of the primary (β or photo-) electron. This independence might have been deduced from the non-local energy transfer found in β decay [5]. It was shown that large values of energy, ~20 keV in the case examined there, can be transferred in a non-local way. This transfer cannot be explained by the change of the Coulomb field, therefore one cannot expect that the rearrangement of the atom follows the time-dependent change of the potential.

It is clear from [6] and the foregoing as well that atomic electrons behave differently depending on the origin of the electron perturbing the atom: (1) The effect of a bombarding electron is well described by the time-dependent Schrödinger equation. (2) The electron–atom interaction is time-independent even at low relative speed if the electron originates from the atom or the nucleus.

The Ne shakeup discussed in the present paper provides an example in which both kinds of transitions may occur at the same time: These are the time-independent shakeup and the energy-dependent secondary excitation.

We may conclude that the neon $2p$ satellite spectrum provides an additional evidence about the existence of two distinct levels of non-separability (or connection). One of them is effective when the electron, which causes the excitation or ionization, has been originally bounded in the same atom or created in the nucleus. This connection between the electron and the nucleus is strong enough to prevent time-dependent interaction between the electrons of the atom. A different kind of connection exists between the electrons. The time-dependent character of the interaction of the atomic electrons during the collision with an outer electron shows that non-separability is possible on a weaker level as well. The validity of non-separability cannot be questioned, because the electrons are undistinguishable and antisymmetrisation of the wave function is required in both cases.

The theory–independent existence of non-separability proved in [5] requires the existence of some physical entity underlying non-separability. We name this entity connective string (c-string) for definiteness. The different properties of $e^- - e^-$ processes discussed in [6] and above imply that c-strings have different capabilities in electron–proton and electron–electron relations (i.e. they are different). String structure of the connection cannot be deduced from the experimental results discussed in the present paper: Experimental results on neutral particle production [13] are used to make this conclusion in a separate paper [7].

The summary of the achievements of the present paper is the following. Details of the calculations of the time-dependent corrections have been given. New

experimental evidence is analysed, which supports the previous conclusion on the existence of different levels of non-separability.

The present paper is dedicated to the sixtieth birthday of Professor D. Berényi, Director of the Institute. The author is grateful for the helpful attention with which he followed his scientific work from its beginning.

Appendix

The integral in Eq (5) can be transformed to

$$d_{ai} = -V_{ai} t_0 \exp(i x_0) \left\{ \frac{1}{x_0} + i \int_{x_0}^{\infty} \frac{\cos(x - x_0)}{x} dx - \frac{\sin(x - x_0)}{x} dx \right\},$$

with $x = \gamma_{ai} t$. This can be integrated by using the approximation of Hastings [10] in the interval $1 < x_0 < \infty$, equivalent to $0 < v < \gamma_{ai} R_a$, which is only a small range of speed. Integration can be performed in a broad range of speed using numerical integration. The square of the amplitude can be written as

$$|d_{ai}|^2 = \left| \frac{V_{ai}}{\gamma_{ai}} \right|^2 \left\{ 1 + 2\, x_0 [\cos x_0 si(x_0) - \sin x_0 ci(x_0)] + x_0 \left\{ [si(x_0)]^2 + [ci(x_0)]^2 \right\} \right\},$$

where $si(x) = -\int_x^{\infty} \frac{\sin t}{t} dt$ and $ci(x) = -\int_x^{\infty} \frac{\cos t}{t} dt$. Making use of the transformations (Ryzhik and Gradstein [16])

$$\cos x_0 si(x_0) - \sin x_0 ci(x_0) = -\frac{1}{x_0} \int_0^{\infty} e^{-y} \frac{1}{1 + (y/x_0)^2} dy,$$

$$[si(x_0)]^2 + [ci(x_0)]^2 = \int_0^{\infty} e^{-y} \frac{ln[1 + (y/x_0)^2]}{y} dy.$$

The integrals on the right-hand side can be calculated by numerical integration with weight $\exp(-y)$. The fifteen point integration (see Krylov [17]) was used for the general calculations, while the approximation of Hastings [11] enables us to control the numerical integration.

References

1. J. von Neumann, Mathematische Grundlagen der Quantenmechanik, Springer, Berlin, 1932; English translation: Mathematical Foundations of Quantum Mechanics, Princeton Univ. Press, Princeton, N. Y., 1955.

2. B. d'Espagnat, Conceptual Foundations of Quantum Mechanics, Benjamin, Reading, Massachusetts, 1976; Phys. Rep., *110*, 201, 1984.
3. M. Jammer, The Philosophy of Quantum Mechanics, Wiley-Interscience, New York, 1974.
4. A. Aspect, P. Grangier and G. Roger, Phys. Rev. Lett., *47*, 460, 1981; A. Aspect, J. Delibard and G. Roger, Phys. Rev. Lett., *49*, 1804, 1982.
5. E. Vatai, J. Phys., B*20*, L731, 1987.
6. E. Vatai, Phys. Rev., A*38*, 3777, 1988.
7. E. Vatai, to be published.
8. D. R. Bates, Quantum Theory, vol. 1, Academic Press, New York, 1961.
9. H. Jakubowicz and D. L. Moores, J. Phys., B*14*, 3733, 1981. J. Lower, I. E. McCarthy and E. Weigold, J. Phys., B*20*, 4571, 1987.
10. T. D. Thomas, Phys. Rev. Lett., *52*, 417, 1984.
11. C. Hastings, Approximation for Digital Computers, Princeton Univ. Press, Princeton, 1955.
12. F. Wuilleumier and M. O. Krause, Phys. Rev., A*10*, 242, 1974.
13. U. Becker, R. Holzel, H. G. Kerkhoff, B. Langer, D. Szostak and R. Wehlitz, Phys. Rev. Lett., *56*, 1120, 1986.
14. G. B. Armen, T. Åberg, Kh. Karim et al., Phys. Rev. Lett., *54*, 182, 1985.
15. W. Koenig, F. Bosch, P. Kienle, C. Kozhuharov, H. Tsertos, E. Berderman, S. Huchler and W. Wagner, Z. Phys., A*238*, 129, 1987.
16. I. M. Rizhik and I. S. Gradstein, Tables of Series, Products and Integrals, Verlag d. Wissenschaften, Berlin, 1957.
17. V. I. Krylov, Approximate Integral Calculus, Nauka, Moscow, 1967 (in Russian).

Acta Physica Hungarica 65 (2-3), pp. 265-270 (1989)

AB INITIO THEORETICAL STUDY OF THE STRUCTURES AND STABILITIES OF THE $LiBeH_3$, Li_2BeH_4 AND $LiBe_2H_5$ MOLECULES*

I. TAMÁSSY-LENTEI and J. SZANISZLÓ

Institute of Theoretical Physics, Kossuth Lajos University
4010 Debrecen, Hungary

Investigations were carried out to study the geometrical data and stability of some small molecules containing the elements Li and Be. Among others, properties of the $LiBeH_3$, Li_2BeH_4 and $LiBe_2H_5$ were determined using the FSGO method. The structure and the stability of the above mentioned systems are discussed and the dissociation energies for some possible chemical processes are determined. The results are in agreement with other calculated theoretical values available.

Introduction

Nowadays both the experimental and the theoretical studies of lithium compounds are very significant and lithium chemistry is getting more and more important. One of the most important questions is the stability, moreover the reactivity of these compounds. From this point of view the interaction of the Li cation with other systems (atoms, ions, molecules, etc.) is essential.

Earlier [1] we investigated the interaction of lithium with the water-type (O^{--}, OH^-, OH_2, OH_3^+), further the ammonia-type (N^{---}, NH^{--}, NH_2^-, NH_3, NH_4^+) molecules and molecular ions; the stability and the geometrical data of these isoelectronic systems were determined.

Besides this we have studied several physical properties of some simple systems containing the elements Li and Be [2].

Similarly, at present we intend to examine some complex hydrides of the mentioned light elements: the $LiBeH_3$, Li_2BeH_4 and $LiBe_2H_5$ and some related anions and cations as well. The existence of these molecules in the gas phase, their structures and stabilities are interesting. The equilibrium geometries, the most stable configurations, some possible reactions and dissociations are also investigated.

Method

The calculations were carried out using the FSGO (Floating Spherical Gaussian Orbital) model [3]. This method is a very simple ab initio one. The total electronic wave function of the system is composed from floating-type (off-centre)

*Dedicated to Academician D. Berényi on his 60th birthday

spherical Gaussian functions. The different Gaussians are double occupied in the singlet ground state. The orbital radii and the coordinates of the orbital-centre vectors are considered to be variational parameters. The total energy of the system, E, is minimized to all electronic and geometrical parameters.

The $LiBeH_3$

A complete geometry optimization for the $LiBeH_3$ gives as the most stable structure a configuration having C_{2v} symmetry (I), containing two equivalent bridging hydrogens (see Fig. 1).

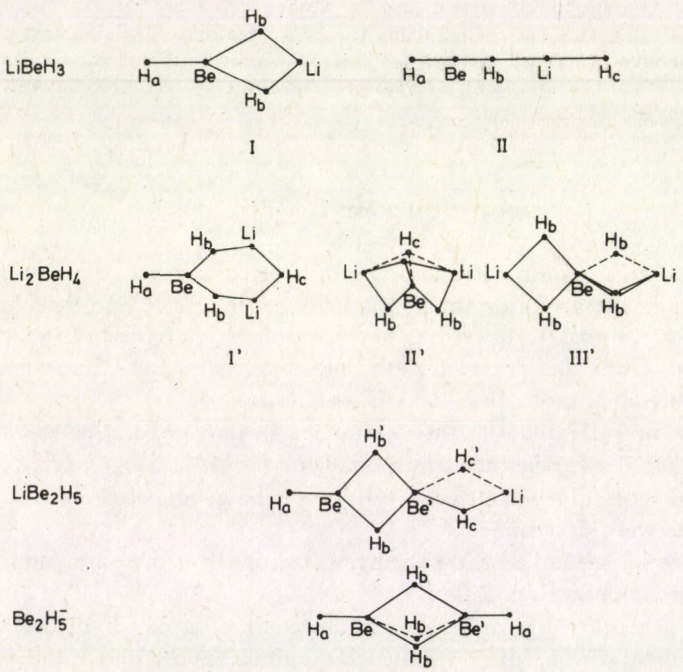

Fig. 1. Alternative configurations of $LiBeH_3$, Li_2BeH_4, $LiBe_2H_5$ and $Be_2H_5^-$

The system is a planar one; there were 13 variational parameters optimized.

Considering the $LiBeH_3$ as a linear system having $C_{\infty v}$ symmetry (II), it was necessary to optimize 14 variational parameters.

The results for the equilibrium geometry are summarized in Table I (distances in atomic units, angle in degrees), together with other theoretical values.

Dill, Schleyer, Binkley and Pople [4] performed MO-type examination with STO-3G, further 6-31G basis set.

Boldyrev et al [5] treated the investigated systems by ab initio Hartree–Fock–Roothaan type calculations.

The examination of Würthwein, Krogh-Jespersen and Schleyer [6] was carried out at various levels of ab initio MO theory, MP2(6-31G)/(4-31G).

Table I

Optimized geometrical parameters for the $LiBeH_3$ at the alternative configurations I and II (Fig. 1); nuclear distances, R (in atomic units); angle (in degrees)

	I				II	
	FSGO	[4], [6]	[5]	[7]	FSGO	[4]
$R(BeLi)$	4.096	4.078	4.300		6.017	6.013
$R(BeH_a)$	2.718	2.430	2.580	2.56	2.645	2.438
$R(BeH_b)$	2.907	2.721	2.800	2.79	2.621	2.489
$R(LiH_b)$	3.323	3.201	3.389	3.40	3.396	3.524
$R(LiH_c)$					3.257	2.853
$\angle(H_bBeH_b)$	106.9°	103.2°	104°			

Cimiraglia, Persico, Tomasi and Charkin [7] employed the third-order Möller–Plesset perturbation theory.

The calculated FSGO total energies, E, in the alternative configurations I and II for the $LiBeH_3$ are (in atomic units):

$$E(I) = -19.8615, \qquad E(II) = -19.7985.$$

The Li_2BeH_4

We have examined various structural possibilities for the Li_2BeH_4. The most stable structure (I', lowest in energy) and two others (II', III', next-best energetically) are presented (see Fig. 1).

The configuration I' has a cyclic planar structure with C_{2v} symmetry (with 17 variational parameters).

The configuration II' has the Li atoms on two faces of a BeH_4 tetrahedron, the structural type has C_{2v} symmetry (with 16 variational parameters).

The configuration III' has oppposite edge arrangement with D_{2d} symmetry (with 9 variational parameters).

The results for the geometry are summarized in Table II (distances in atomic units, angles in degrees), together with other theoretical values [6], [7].

Among others Boldyrev, Sukhanov, Zakhzevski and Charkin [8] performed calculations for the Li_2BeH_4 within the Hartree–Fock–Roothaan method using double-zeta basis sets.

The calculated FGSO total energies, E, in the alternative configurations I', II' and III' for the Li_2BeH_4 are (in atomic units):

$$E(I') = -26.5064, \quad E(II') = -26.5019, \quad E(III') = -26.4995.$$

Table II

Optimized geometrical parameters for the Li_2BeH_4 at the alternative configurations I', II', and III' (Fig. 1); nuclear distances, R (in atomic units); angle (in degrees)

	I'			II'		III'		
	FSGO	[6]	[7],[8]	FSGO	[6]	FSGO	[6]	[7],[8]
$R(BeLi)$				3.7667	3.7133	4.1369	4.0346	
$R(BeH_a)$	2.7266	2.4358	2.60					
$R(BeH_b)$	2.8639	2.6853	2.75	2.8334	2.6078	2.9901	2.7382	2.85
$R(BeH_c)$	7.0	6.5951		3.1764	2.8553			
$R(LiH_b)$	3.2452	3.1521	3.26	3.5309	3.3674	3.3105	3.1577	3.30
$R(LiH_c)$	3.3582	3.1729	3.42	3.5785	3.4714			
$\angle(H_bBeH_b)$	118.5°	116.1°	115.5°	139.0°	139.4°	104.8°	102.6°	102.0°
$\angle(LiH_bBe)$	121.8°	124.9°		71.6°	76.6°	75.2°	77.4°	
$\angle(LiH_cLi)$	94.0°	100.7°		102.8°	107.2°			

Table III

Optimized geometrical parameters for the $LiBe_2H_5$ and $Be_2H_5^-$; nuclear distances, R (in atomic units); angle (in degrees)

	$LiBe_2H_5$			$Be_2H_5^-$		
	FSGO	[9]	[7]	FSGO	[9]	[7]
$R(BeH_a)$	2.69	2.54	2.53	2.78	2.60	2.60
$R(Be'H_b)$	3.00	2.75	2.75	3.02	2.91	2.91
$R(BeH_b)$	2.90	2.86	2.85	3.02	2.91	2.91
$R(Be'H_c)$	2.94	2.72	2.72			
$R(LiH_c)$	3.45	3.43	3.43			
$R(BeBe')$	3.99	3.83		3.54	3.53	
$R(Be'Li)$	4.34	4.27				
$\angle(H_aBeH_b)$	131.5°	132.0°		125.8°	127.3°	127.3°
$\angle(H_bBeH_b')$	97.1°	95.9°	95.9°	89.3°	87.2°	
$\angle(H_bBe'H_b')$	92.7°	100.2°			87.2°	
$\angle(H_cBe'H_c)$	104.8°	107.1°	107.0°			
$\angle(H_cLiH_c)$	84.7°					

The $LiBe_2H_5$ and the $Be_2H_5^-$

We have examined the complex hydride analogously: the $LiBe_2H_5$, further the $Be_2H_5^-$ ion to regard the stability of the system and the possible decays. As a results of the optimization a configuration of the $LiBe_2H_5$ with bridged H_b and H_c atoms is a stable one; the $Be_2H_5^-$ anion has three bridged H_b atoms between the Be atoms (see Fig. 1).

The results for the geometry are listed in Table III (distances in atomic units,

angles in degrees), together with other theoretical values [7].

For the mentioned systems Kirillov, Boldyrev, Klimenko and Charkin [9] performed ab initio calculations within the framework of the Hartree–Fock–Roothaan method using different basis sets.

The calculated FSGO total energies, E, for the $LiBe_2H_5$ and $Be_2H_5^-$ are (in atomic units):

$$E(LiBe_2H_5) = -33.1245, \qquad E(Be_2H_5^-) = -26.9368.$$

Results for the energetic stability

One can examine the stability of the above mentioned systems from the point of view of certain chemical reactions.

The predicted dissociation energies for some possible gas phase processes connected with two or three different parts are presented in Table IV (in atomic units), together with other theoretical values.

To determine the above mentioned quantities one part of the necessary FSGO total energies for the products (molecules, ions) are taken from earlier calculations [3], [2]:
$E(Li^+) = -5.9449$, $E(Be) = -12.2502$, $E(H_2) = -0.9559$,
$E(LiH) = -6.5727$, $E(BeH_2) = -13.214$, $E(BeH_3^-) = -13.655$,
$E(Li_2) = -12.2817$, $E(Be_2) = -24.2173$, $E(Be_2H_4) = -26.4742$;
further from [10]:
$E(LiH_2^+) = -6.920$, $E(Li_2H^+) = -12.618$;
moreover our results are:
$E(LiBeH) = -18.8500$, $E(LiBeH_4^-) = -20.2784$. All of the last mentioned total energies are given in atomic units.

One can see that the $LiBeH_3$, Li_2BeH_4 and $LiBe_2H_5$ systems are stable regarding all of the processes considered here. The dissociations to LiH (or BeH_2) and other parts are energetically favourable. The greatest energies belong to the reactions which result in the separation of a Li^+ cation and a remaining system. This is in agreement with the expectation.

Conclusion

One can determine the stability of some small molecules containing elements Li and Be, the $LiBeH_3$, Li_2BeH_4, $LiBe_2H_5$, using the very simple ab initio FSGO method. The systems investigated at present are stable and one can produce the equilibrium geometry (nuclear distances, valence angles), and the structures of the mentioned systems. The existence of these molecules in the gas phase is also predictable, the direction of some possible chemical reactions and the energies for dissociation processes are reasonable.

Table IV

Dissociation energies (in atomic units) for different reactions connected with the $LiBeH_3$, Li_2BeH_4 and $LiBe_2H_5$

$LiBeH_3$

Type of reaction	FSGO	[4]	[5]	[6]	[7]
$LiBeH_3 \rightarrow Li^+ + BeH_3^-$ I	0.261		0.239	0.2456 0.2341	0.237
$LiH + BeH_2$	0.074	0.057 0.064	0.0599 0.0581	0.0592 0.0641	0.0592
$LiH + Be + H_2$	0.083		0.101		
$LiBeH + H_2$	0.056	0.069	0.068		
$LiBeH_3 \rightarrow LiH + BeH_2$ II	0.012	0.015 0.013			

Li_2BeH_4

Type of reaction	FSGO(I')	[6]	[8]	[7]
$Li_2BeH_4 \rightarrow (LiH)_2 + BeH_2$	0.0517		0.0526	
$Li_2 + H_2 + BeH_2$	0.0548		0.0925	
$LiH + LiBeH_3$	0.0722	0.0692	0.0670	0.0670
$2(LiH) + BeH_2$	0.1170			
$Li_2H^+ + BeH_3^-$	0.2328			
$Li^+ + LiBeH_4^-$	0.2831		0.2854	

$LiBe_2H_5$

Type of reaction	FSGO	[7]	[9]
$LiBe_2H_5 \rightarrow LiBeH_3 + BeH_2$	0.0490	0.046 0.058	0.0854
$LiH + Be_2H_4$	0.0776	0.0759 0.0828	0.108
$Li^+ + Be_2H_5^-$	0.2428	0.219 0.2167	0.219

References

1. I. Tamássy-Lentei and J. Szaniszló, Acta Phys. Hung., *51*, 101, 1981.
2. I. Tamássy-Lentei and J. Szaniszló, Acta Phys. Chem. Szeged., *20*, 351, 1974; Acta Phys. Chim. Debr., *21*, 7, 1978.
3. A.A. Frost, J. Chem. Phys., *47*, 3707, 3714, 1967; J. Phys. Chem., *72*, 1289, 1968; S.Y. Chu and A.A. Frost, J. Chem Phys., *54*, 764, 1971.
4. J.D. Dill, P.v.R. Schleyer, J.S. Binkley and J.A. Pople, J. Am. Chem. Soc., *99*, 6159, 1977.
5. A.I. Boldyrev and O.P. Charkin, J. Struct. Chem., *18*, 783, 1977 (in Russian); A.I. Boldyrev, L.P. Sukhanov and O.P. Charkin, Chem. Phys., *51*, 205, 1980.
6. E.-U. Würthwein, M.-B. Krogh-Jespersen and P.v.R. Schleyer, Inorg. Chem., *20*, 3663, 1981.
7. R. Cimiraglia, M. Persico, J. Tomasi and O.P. Charkin, J. Comp. Chem., *5*, 263, 1984.
8. A.I. Boldyrev, L.P. Sukhanov, V.G. Zakhzevski and O.P. Charkin, Chem. Phys. Lett., *79*, 421, 1981.
9. Yu.B. Kirillov, A.I. Boldyrev, N.M. Klimenko and O.P. Charkin, Koord. Him., *7* , 1832, 1981 (in Russian); Chem. Phys. Lett., *84*, 604, 1981.
10. N.K. Ray, J. Chem. Phys., *52*, 463, 1970.

Acta Physica Hungarica 65 (2–3), pp. 271–275 (1989)

MEASUREMENT OF THE FISSION CROSS-SECTION RATIO FOR $^{237}Np/^{235}U$ AROUND 14 MEV NEUTRON ENERGIES* **

L. DESDIN***, S. SZEGEDI and J. CSIKAI

Institute of Experimental Physics, Kossuth Lajos University
4001 Debrecen, Hungary

Fission cross-section ratio was determined for $^{237}Np/\ ^{235}U$ around 14 MeV neutron energies with a back-to-back ionization chamber. Neutrons were produced by a 180 kV accelerator using the T(d, n)^{4}He reaction. No significant energy dependence was found in the cross section ratio.

Introduction

The ^{237}Np fission cross-section is often used in dosimetry. For such a purpose, an accurate knowledge of the ^{237}Np to ^{235}U fission cross-section ratio is necessary. These data are also required for a systematic study of fission cross-sections.

A number of ratio measurements have been reported in this range of 13.5–15 MeV. Behrens et al [1] have measured the fission cross section ratio of ^{237}Np to ^{235}U as a function of neutron energy using fission chamber, threshold cross-section method and time-of-flight technique.

Fission cross-section ratio for $^{237}Np/\ ^{235}U$ has been determined by Várnagy et al [2] using solid state nuclear track detectors in combination with the jumping spark counting evaluation technique. Carlson et al [3] have reported a relative measurement of $^{237}Np/\ ^{235}U$.

Fast neutron fission cross-section measurements for ^{237}Np have been reviewed by Cross et al [4] and Lapenas [5]. Alkhazov et al [6] measured the σ value for the ^{237}Np(n, f) at 14.8 MeV by time correlated associated particle method. The σ (^{237}Np(n, f)) was measured with the absolute method by White et al [7] and by Moat [8]. These absolute data can be converted to the $^{237}Np/^{235}U$ ratios using evaluated ^{235}U(n, f) cross-sections from ENDF/B-V [9].

The analysis of the $^{237}Np/^{235}U$ fission cross-section ratios around 14 MeV shows discrepancies in the magnitude of the reported data.

At 14.1 MeV the value of White et al [7] is about 8% higher than that of Behrens et al [1]. The trend in the data observed by Carlson et al [3] agrees with that of Behrens et al [1] around 14 MeV. The Adamov et al [10] value at 14.7 MeV is about 10% higher than that of Behrens et al [1]. The Várnagy's [2] data within

* Dedicated to Academician D. Berényi on his 60th birthday.

**This work was supported by the Hungarian Research Foundation (Contract No. 259).

***On leave from the Institute of Nuclear Science and Technology, Havana, Cuba

the limits of the errors are in good agreement with the Lapenas' [5] data, but they are systematically higher than the data of Behrens et al [1]. The Alkhazov et al [6] value at 14.8 MeV is about 3% higher than the Várnagy's [2] value at the same energy.

The aim of this work was to measure the $^{237}Np/^{235}U$ fission cross-section ratio with a back-to-back chamber to clear up the discrepancies in the previous data.

Experimental procedure

A schematic drawing of the experimental arrangement is shown in Fig. 1.

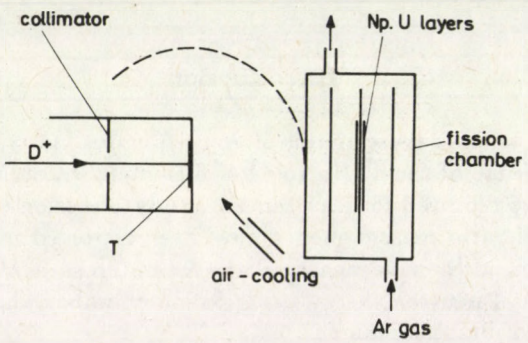

Fig. 1. Scattering-free irradiation arrangement used in the present work

The fission detector was a low-mass, double ionization chamber filled with argon gas of about 10^5 Pa. The cylindrical fission chamber was made of 0.5 mm aluminium. Both parts of the chamber were operated at 500 V with a plate separation of 6 mm. This chamber was placed at a distance of 7 cm from the beam spot on the tritium target.

The irradiation of fissile samples was performed by fast neutrons produced in the $^3H(d, n)^4He$ reaction using a 180 kV accelerator. The intensity of the analysed D^+ beam was about 70 μA. The energy of neutrons was changed by the emission angle, i.e. the chamber was placed at different directions to the deuteron beam of about 10 mm diam. The neutron energies and their spreads are given in Table III for the geometrical arrangement shown in Fig. 1.

The fissile samples were prepared at the Hlopin Institute in Leningrad (USSR) where their isotopic compositions and thicknesses (summarized in Table I) have been determined. The ^{235}U and ^{237}Np, as tetrafluorides, were deposited onto Al holders (0.2 mm thick and 40 mm diameter).

Table I

Isotopic composition and masses of the fissile samples

Sample	Isotopic composition (%)			Mass (μg)
	^{234}U	^{235}U	^{236}U	
U				481
	0.0010	99.9955	0.0035	
	^{237}Np	^{239}Pu	^{241}Am	
Np				418
	99.9917	0.0078	0.0005	

Table II

Range of correction factors and errors

Effect	Range of correction (%)	Range of error (%)
statistical	–	0.6–0.8
extrapolation of fission spectrum to zero bias	2–4	0.4–0.8
fission fragment loss in sample deposits	1.8	0.18
mass ratio	–	4.24
forward–backward anisotropy	negligible	–
thermal and epithermal neutrons	1	–
fission due to other isotopes	negligible	–
total	4.0–5.4	4.3–4.4

Table III

Cross-section ratio $^{237}N/^{235}U$

Angle	Neutron energy (MeV)	$\sigma_{nf}(^{237}Np/^{235}U)$
0°	14.80 ± 0.17	0.999 ± 0.043
30°	14.70 ± 0.15	1.054 ± 0.046
60°	14.45 ± 0.12	1.042 ± 0.045
90°	14.12 ± 0.08	1.021 ± 0.044
120°	13.75 ± 0.10	1.006 ± 0.043

A rather good separation of the alpha particles and the fission fragments can be observed in the experimental spectrum (Fig. 2).

In order to obtain the total number of fission events in the deposits, a correction was performed for the loss of the pulses under the base line by extrapolation of the fragment pulse-height spectrum to zero energy.

To determine the channel number corresponding to zero pulse height, the linearity of the system was measured by a pulse generator.

A correction for the fission fragments absorbed in the layer of fissionable nuclides was introduced.

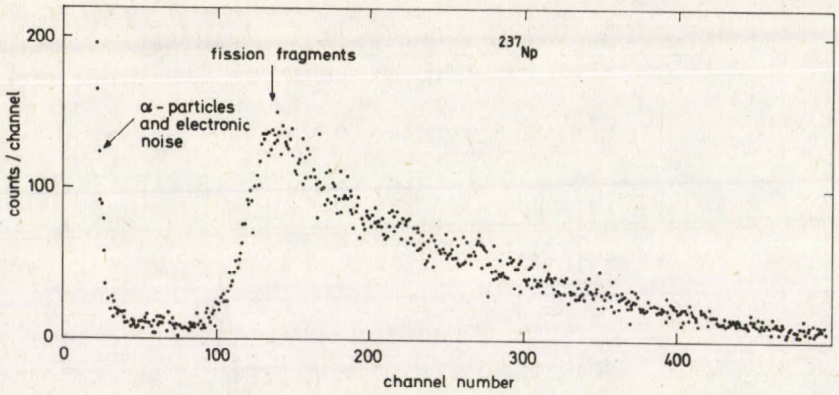

Fig. 2. A pulse-height distribution of the fission fragments

Pairs of ^{237}Np and ^{235}U samples were placed back to back in the chamber. Two orientations were possible: first, when the ^{237}Np sample was placed near the neutron source, and second, when the ^{235}U sample was placed in the same position.

At each neutron energy, measurements of the relative fission rates were made with both of these orientations.

When the results from the above two orientations were averaged, the effects of geometry, neutron scattering in the support plates between the deposits and the momentum transfer were eliminated.

The contribution of the thermal and epithermal neutron background to the fission events in the case of ^{235}U has been determined by experiment using the $^{164}Dy(n, \gamma)^{165}Dy$ reaction and the cadmium difference method. It was found that the background neutrons increased the cross-section of $^{235}U(n,f)$ by about 1%. This effect is caused mainly by the epithermal neutrons in our experimental arrangement.

Results and discussion

The results obtained in this experiment are given in Table III. Table II lists the corrections to the data and the magnitudes of the errors. Root-mean-square errors were used in every case. The error of the fission cross-section ratios is mainly due to the uncertainty in the determination of the total amounts of ^{237}Np and ^{235}U isotopes. Our results in comparison with some previous data are shown in Fig. 3.

As it can be seen in the Figure no significant energy dependence has been found in the fission cross-section ratio for $^{237}Np/^{235}U$ around 14 MeV. The cross-section ratio obtained in this experiment is in good agreement with the result of Behrens and is in average about 8% and 15% lower than those given by Várnagy

et al and Lapenas, respectively.

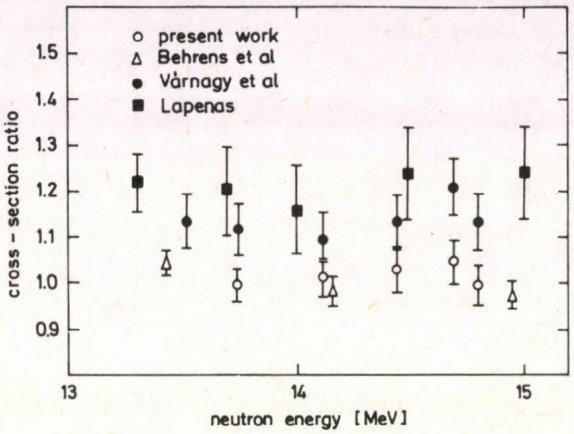

Fig. 3. Cross-section ratio for $^{237}Np/^{235}U$ around 14 MeV

Acknowledgement

The authors are grateful to Mr. J. Szegedi for his assistance during the measurements.

References

1. J.W. Behrens et al, Nucl. Sci. Eng., *80*, 393, 1982.
2. M. Várnagy et al, NIM, *196*, 465, 1982.
3. G.W. Carlson et al, Proc. Int. Conf. Nucl. cross-section for Science and Technology, Knoxville, Tennessee, October 22-26, 1979, NBS Special Publication, 1980.
4. W.G. Cross et al, Nucl. Sci. Eng., *58* , 377, 1975.
5. A.A. Lapenas, Izmerenye spectrov neytronov aktivationnym metodom izdatelstvo znatne, Riga, 1975.
6. I.D. Alkhazov, Kiev Conference, Neytronnayia fizika, *T3* , 155, 1977.
7. P.H. White et al, J. Nucl. Energy., *21* , 671, 1967.
8. A. Moat (ref. from W. Hart, AHSB(S) R169. Risley Warrington Lancashire (1969)).
9. Handbook of nuclear activation data. TRS No. 273, page 73, IAEA, Vienna, 1987.
10. V.M. Adamov et al, ref. 3, page 995.

Acta Physica Hungarica 65 (2–3), pp. 277–286 (1989)

NEW DATA FOR $^{12}C(p,\gamma)^{13}N$ RADIATIVE CAPTURE PROCESS: NOTE ON AN ANOMALY IN THICK TARGET MEASUREMENTS*

Á.Z. KISS, E. KOLTAY and E. SOMORJAI

Institute of Nuclear Research, Hungarian Academy of Sciences, (ATOMKI)
4001 Debrecen, Hungary

In an earlier publication of Poyarkov and Sizov [1] an anomaly has been found in the position of some gamma lines from the decay of selected (p, γ) resonances, when observed in thick target experiments. No explanation was found for the effect. The reliability of their observation has been checked in the present work based on a repeated experiment for the case of the $E_p^{res} = 1699$ keV resonance [4] in the $^{12}C(p, \gamma)\ ^{13}N$ reaction. Under the improved experimental conditions in this measurement the appearance of the anomaly has not been confirmed; with a more accurate energy position $E_p^{res} = 1688.7 \pm 0.7$ keV the discrepancy between thin and thick target observations of the resonance has been resolved.

Introduction

The observation of an anomaly in thick target experiments on radiative capture reaction by Poyarkov and Sizov [1] is related to the application of thick target gamma spectroscopy determination of resonance energies and widths through γ-energy measurements, as introduced by Blatt et al [2] and Kurtz et al [4].

Based on the fact that best Ge(Li) detectors today offer the energy resolution in gamma ray spectroscopy nearly equal to the beam energy definition of an average Van de Graaff accelerator, when beam quality and definition are less than optimum, the classical scanning over separate resonances excited in thin target case can be replaced by exciting a number of resonances simultaneously in a thick target. Energy and width of the resonance directly available on the bombarding energy scale in the former case will be deduced from the γ-energy scale of the gamma spectrum in the latter one. The transformation between emitted E_γ and exciting E_p energies, obtained in γ- spectrum and p excitation curve, respectively, is given from reaction kinematics for (p, γ) case as

$$E_\gamma = E_p \frac{A}{A+1} + E_B - E_{\mathrm{exc}}, \tag{1}$$

where A denotes target mass number, E_B denotes the binding energy of the compound system, E_{exc} is the excitation energy of the final state. The intensity relation expressed by the gamma spectrum $F\ (E_\gamma)$ writes

$$F(E_\gamma) = N_p \cdot \frac{d\sigma}{d\Omega}\ (E_p, \theta)\ \frac{A+1}{A}\ \frac{dx}{dE}\ n\ d\ \Omega, \tag{2}$$

*Dedicated to Academician D. Berényi on his 60th birthday

where N_p stands for the flux of bombarding protons entering the target with energy E_{p_o}, $d\sigma/d\Omega$ is the differential cross section of (p, γ) reaction for proton energy E_p, and observation angle θ, n is the density of target nuclei in the sample, dE/dx is the stopping power and $d\Omega$ denotes the detection solid angle. From Eq. (1) it follows that from a peak in the gamma spectrum with position E_γ^{res} and width Γ_γ^{res} thin target values E_p^{res} and $\Gamma = \Gamma_\gamma^{res} \frac{A+1}{A}$ can be obtained. Due to the fact that step-by-step scanning in thin target case is replaced by a simultaneous determination of corresponding points of gamma spectrum in the thick target measurements, the influence of target conditions and instabilities in bombardment and detection will disappear in the latter case.

The reliability of the thick target E_γ method has been proved in papers [2] and [3] through a comparison with thin target results in ^{12}C(p, γ)^{13}N and ^{27}Al (p, γ)^{28}Si reactions, respectively. In the former case clean gamma spectra were obtained with an elaborate three crystal pair spectrometer, while the application of a single low efficiency Ge(Li) detector in the latter case resulted in spectra with considerable Compton contribution.

A further test performed on targets ^{12}C, ^{16}O, ^{24}Mg and ^{28}Si with protons in the energy range 400–2500 keV was described in paper [1]. Authors found in their experiment that when the proton is captured near the 1699 keV resonance [4] in the reaction ^{12}C(p, γ)^{13}N, decaying to ground state and first excited state in ^{13}N end nucleus, the γ- spectrum from the thick target is not equal to the sum of the spectra from thin targets of equal total length. With other words, the gamma energy E_γ^{res}, obtained from the transformation of E_p^{res} through Eq. (1), differs from the observed position E_γ of the corresponding gamma line by the values $\triangle E$ = 12 keV and 23 keV, respectively. A good agreement between E_γ^{res} and E_γ was observed at 457 keV resonance. A less pronounced anomaly is probably present in the ^{16}O(p, γ)^{17}F reaction around 2663 keV resonance and in ^{28}Si (p, γ)^{29}P reaction.

The aim of the present work was to repeat some of the measurements in work [1] under experimental conditions different from those used by Poyarkov and Sizov. Independent energy calibration and better energy definition of the beam together with an increased efficiency of the Ge(Li) detector in the present case helped us in decreasing experimental errors and locating E_p^{res} and E_γ^{res} more accurately. The existence of the anomaly has not been confirmed by the present experiment and consistent values were found for the data E_p^{res}, E_γ^{res} and E_γ with $\triangle E = 0$.

Experimental conditions and results

Bombarding proton beam with energies 1500 keV$\leq E_p \leq$ 1900 keV was obtained from the 5 MV Van de Graaff accelerator of the Institute of Nuclear Research in Debrecen. For energy calibration use was made of the E_p=991.9 keV and 1747.6 keV resonances in ^{27}Al(p, γ)^{28}Si and ^{13}C (p, γ)^{14}N reactions, respectively. The accurate beam energy calibration has been facilitated in the present case by the fact that both the reaction under investigation and that used in the calibration are excited on the same target simultaneously, the respective resonances are

near to each other within the energy interval 50 keV. The corresponding data are evaluated from the same spectrum, taken with NaI(Tl) detector, on the basis of gamma counts in the 3.5 MeV and 9.17 MeV (+SE+DE) lines for the $^{12}C(p, \gamma)^{13}N$ and $^{13}C(p, \gamma)^{14}N$ reactions, respectively. The uncertainty of the absolute energy scale and the energy spread of the bombarding proton beam was estimated to be less than 2 keV. In measuring the thin target excitation curve a carbon layer of 20 $\mu g/cm^2$ thickness was used while in thick target experiments a graphite plate of 2 mm was bombarded. The excitation curves were measured through the detection of the ground state transition in ^{13}N by a 10 cm×10 cm dia NaI(Tl) scintillation detector. The gamma spectra in thick target measurements were detected by a coaxial 105 cm^3 Ge(Li) detector with an overall energy resolution of 4.9 keV for the 3.254 MeV line of ^{56}Co. In some cases, thin target excitation curves were deduced also through the evaluation of Ge(Li) spectra taken with fine bombarding energy steps. Target to detector distances 10 cm and 5.5 cm were used in NaI and Ge(Li) measurements, respectively.

The statement of Poyarkov and Sizov [1] on the existence of an anomaly in thick target measurements is related to the energy levels and transitions as well as the location of ^{12}C resonances shown schematically in Fig. 1 with level data taken from the compilation [4]. The data found in their work are summarized in Table I. The energy position of the second and first resonances found in earlier measurements [4] has been confirmed in their work, the appearence of the anomalies in second to first and second to ground state gamma transition energies does not fit in the scheme.

Measurements with thick target method

The quality of gamma spectra, when remeasured in the present work for locating the second (p, γ) resonance by thick target method, was improved upon those in work [1] by increased Ge(Li) efficiency in two respects. Increased photopeak to Compton ratio made background contribution smaller, consequently, the reliability of the extracted spectroscopic information was enhanced. On the other hand, increased relative weight of full energy photopeak makes the structure of the spectrum simpler through decreased contribution in single escape and double escape peaks. The influence of the above effects on the quality of the spectrum is clearly demonstrated in Fig. 2 where gamma spectra taken at a bombarding energy E_{p_0}=1800 keV and detection angle $\theta = 90°$ on thick carbon target, in work [1] and in the present experiment are shown in upper and lower curves, respectively.

The gamma lines belonging to the decays of second and first excited states in ^{13}N are clearly demonstrated. There is an overall decrease of Compton contribution in the latter case while double escape peak for the first case is present with a strong difference in the intensity appearing in the separate experiments.

The broad Gaussian gamma peaks in Fig. 3 correspond to the second $^{12}C(p, \gamma)^{13}N$ resonance in thick target gamma spectrum measurements with E_{p_0}= 1800 and 1900 keV.

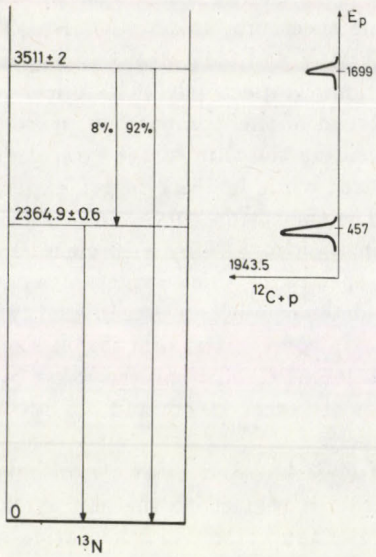

Fig. 1. Resonances in $^{12}C+p$ reaction and excited states in ^{13}N nucleus as shown in the compilation [4]

The centres of the peaks were determined by χ^2 fitting of experimental data to calculated resonance curves as

$$F(N_k) = a + b(N_k - N_0) + \frac{d}{(N_k - N_r)^2 + (\Gamma/2)^2} \tag{3}$$

or

$$F(N_k) = a + b(N_k - N_0) + c(N_k - N_0)^2 + \frac{d}{(N_k - N_r)^2 + (\Gamma/2)^2} \tag{4}$$

Table I

Observed E_p^{res} resonance energies, transformed E_γ^{res} energies, observed positions E_γ of the corresponding gamma lines, Γ level width and anomalies in energy positions $\Delta E = E_\gamma^{res} - E_\gamma$, observed in work [1] for $^{12}C(p, \gamma)^{13}N$ reaction

E_p^{res} (keV)	E_γ^{res} (keV)	E_γ (keV)	Γ (keV)	ΔE (keV)
457	2366	2366	39	0 ± 2
1699	3512	3500	65	12 ± 2
1699	1146	1123	65	23 ± 3

types, where N_0 is the channel where fitting procedure is started, N_f is the channel where fitting procedure is ended, N_k is a channel in the above interval, N_r is the

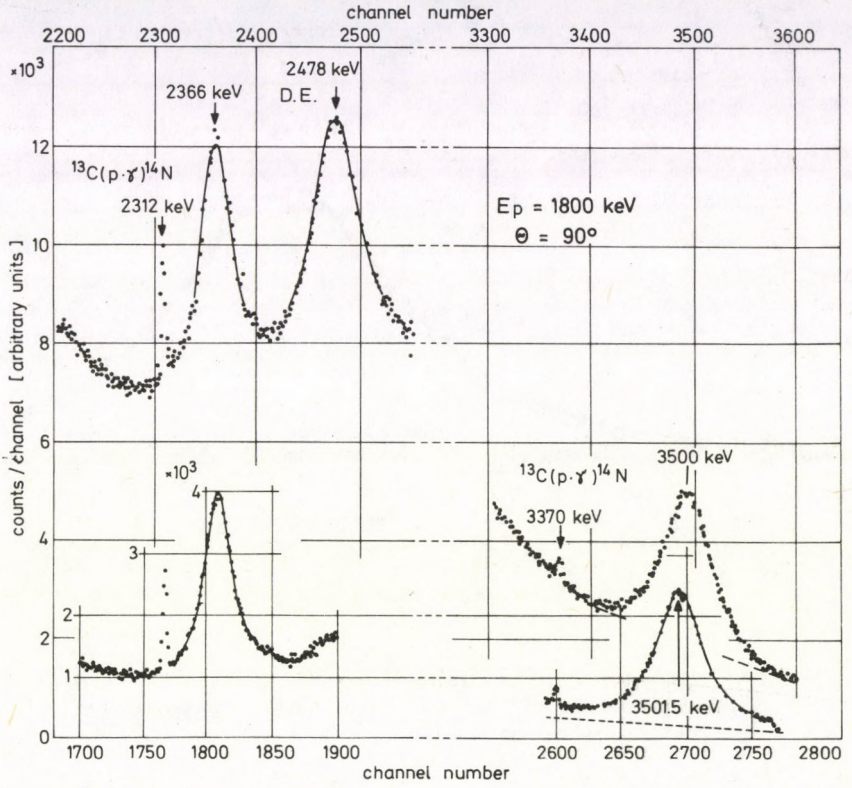

Fig. 2. The comparison of thick target gamma spectra from $^{12}C(p,\gamma)^{13}N$ radiative capture process; upper curve: paper [1]; lower curve: present work

position of the resonance maximum, Γ_γ^{res} is the width of the peak, a, b, c and d are fitting parameters further to N_γ and Γ_γ^{res}. Results for E_γ^{res} and Γ_γ^{res} from fitting procedures with different entrance proton energies, values of N_0 and N_f as well as for different background shapes are gathered in Table II. Mean values for E_γ^{res} and Γ_γ^{res} are given from averaging over cases 1–6 and 1–9 at the last line of the Table.

Two additional tests were performed on the above treated resonance.

On the one hand we wanted to clear up whether or not the maximum of the peak in the gamma spectrum will be displaced when the energy E_{p_0} of the incoming proton beam is varied from the resonance energy to higher values. One could suppose namely that the anomaly observed in thick target case will appear only at higher bombarding energies, because the thick target represents only a thin target layer at bombarding energies near to the resonance. As shown in Fig. 4 the shape of the peak gives an evidence for the same peak position in all bombarding energies. Arrows indicate excitation energies corresponding to the energy E_{p_0}.

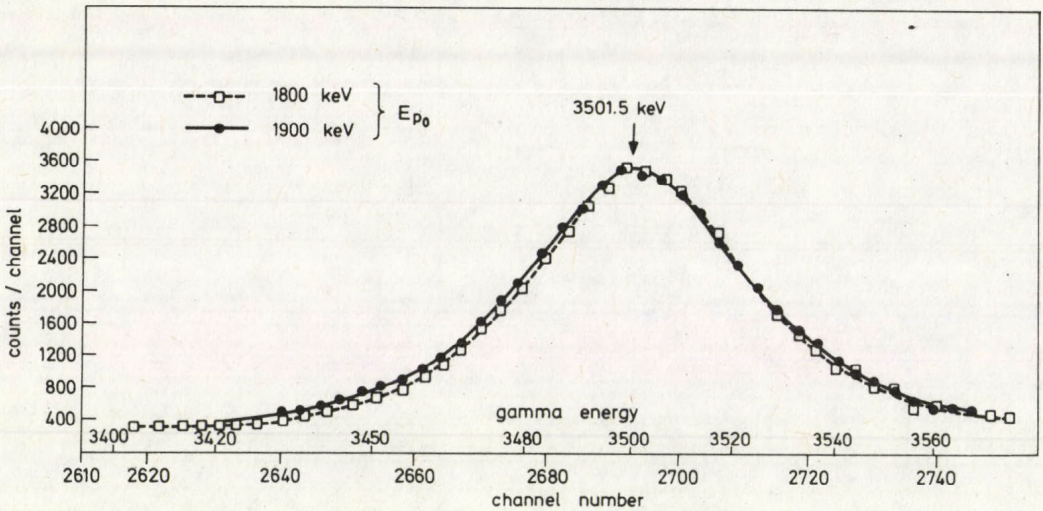

Fig. 3. Resonance observed in thick target gamma spectra with bombarding proton energies 1800 and 1900 keV

Table II

Energy E_γ^{res} and width Γ_γ^{res} of peak observed in thick target gamma spectroscopy method. For other notations see main text

Case	E_{p0}	N_0	N_f	Spectrum shape	N_γ^{res}	E_γ^{res}	Γ_γ^{res}	χ^2
	keV	channel		Equation	channel	keV	keV	
1	1800	2620	2750	3	2693.8	3501.5	57.5	1.019
2	1800	2670	2730	3	2693.4	3501.4	59.5	0.705
3	1800	2620	2750	4	2693.7	3501.3	61.7	0.837
4	1900	2630	2750	3	2693.6	3501.2	60.3	1.045
5	1900	2660	2730	3	2694.5	3502.9	63.1	1.006
6	1900	2630	2750	4	2693.6	3501.2	61.4	1.039
7	2100	2660	2730	3	2695.2	3503.8	63.6	1.020
8	2100	2640	2770	3	2695.1	3503.6	60.6	1.089
9	2100	2640	2770	4	2695.2	3503.8	64.2	0.912
	Mean values					3501.5	60.6	
			(1-6)			±0.6	+ 1.8	
						3502.3	61.3	
			(1-9)			± 1.1	± 2.0	

On the other hand, the Doppler effect will cause a gamma energy shift

$$\triangle E_\gamma^{\text{Doppler}} = E_{\gamma_0} \frac{v}{c} \cos\theta \qquad (5)$$

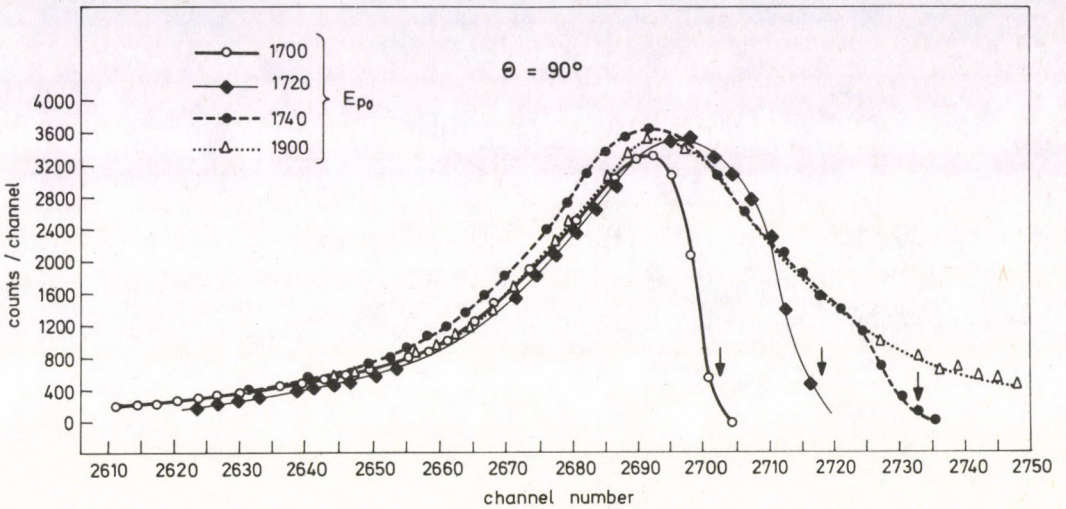

Fig. 4. Resonance shape observed in thick target gamma spectra with bombarding energies near to the resonance

observed in the direction θ, where v denotes the speed of the recoil nucleus. In order to distinguish between the claimed anomaly and Doppler shift we completed our earlier measurements performed at $\theta = 90°$ with similar measurements at angles 0°, 30°, 45° and 60°.

The results shown in Fig. 5 indicate that angular dependence of $\triangle E_\gamma^{\text{Doppler}}$ described by Eq. (5) is obtained for our thick target measurements, and for $\theta = 90°$ we regained the gamma energy in Table II with an accuracy slightly influenced by the finite solid angle of the Ge(Li) detector.

The results indicate at the same time that background correction has been performed properly during spectrum evaluation, i.e. the claimed anomaly cannot be ascribed to the influence of a process other than compound reaction.

A strong anomaly has been found in work [1] on the decay of the same resonance through the transition to the first excited state for ^{13}N; the observed difference amounted to $\triangle E = E_\gamma^{\text{res}} - E_\gamma = 1146\text{–}1123\text{=}23$ keV in this case. Unfortunately, the experimental conditions in the present case did not permit us to contribute with new observations on the question of existence of an anomaly in this transition. A gamma line with energy 1120 keV present in the labor background represents a high source of error in the detection of the weak (branching ratio: 8%) transition, even in the case when the detector is shielded with a lead absorber of 5 cm thickness.

Direct measurement of excitation curves

Thin and thick target excitation curves measured through step by step energy variation of the bombarding proton beam are shown in Fig. 6.

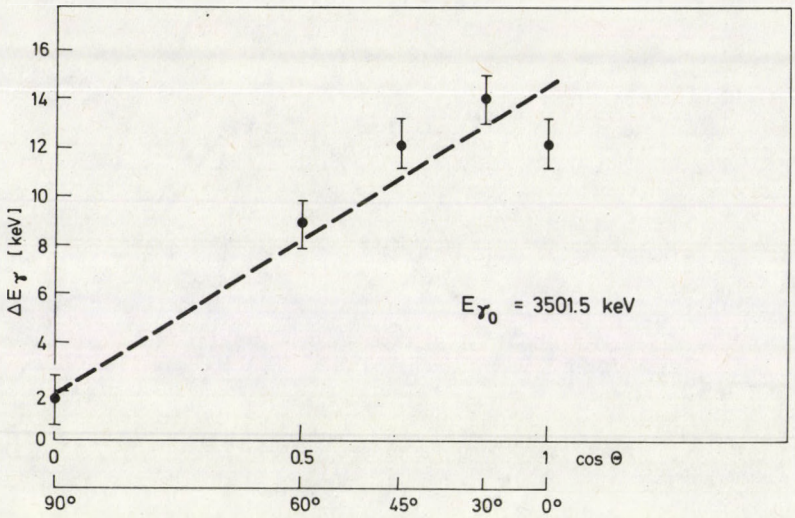

Fig. 5. Energy shift of $E_{\gamma 0}$ as the function of detection angle

The curves through full triangles represent thick target excitation, where gamma yields were determined as gross areas of the peak E_γ=3501.5 keV in a NaI spectrum. Full and open circles represent similar data taken on thin target in two separate runs. Background corrected peak areas from NaI and Ge(Li) spectra are shown by full squares and open triangles, respectively. The position of the resonance appears clearly in all cases, the careful evaluation of the experimental data results in the energy $E_p = 1689 \pm 2$ keV.

Conclusion

Our new data for the second resonance in $^{12}C(p, \gamma)^{13}N$ radiative capture process are presented in Table III. For E_p^{res} and E_γ^{res} two different pairs of data are given as obtained from the conventional energy scanning and thick target gamma spectroscopy methods. In the first case, E_γ^{res} is deduced from E_p^{res}, here the accuracies are determined by the energy definition of the bombarding beam including energy straggling in the thin target. In the second case E_p^{res} is deduced from E_γ^{res} with a higher accuracy given by the energy calibration in the gamma spectrum. (The error value given contains also the inaccuracy resulting from the subtraction of different shapes of background.) In the calculation use was made of the Q-value Q_0=1943.5 keV taken from the compilation [4].

As clearly indicated by the consistency of the data, the existence of an anomaly published earlier is not confirmed. The positive message of paper [1] is in its calling the attention to the fact that earlier measurements by Blatt et al [2] dealing with the technical aspects of the thick target technique, on the one hand,

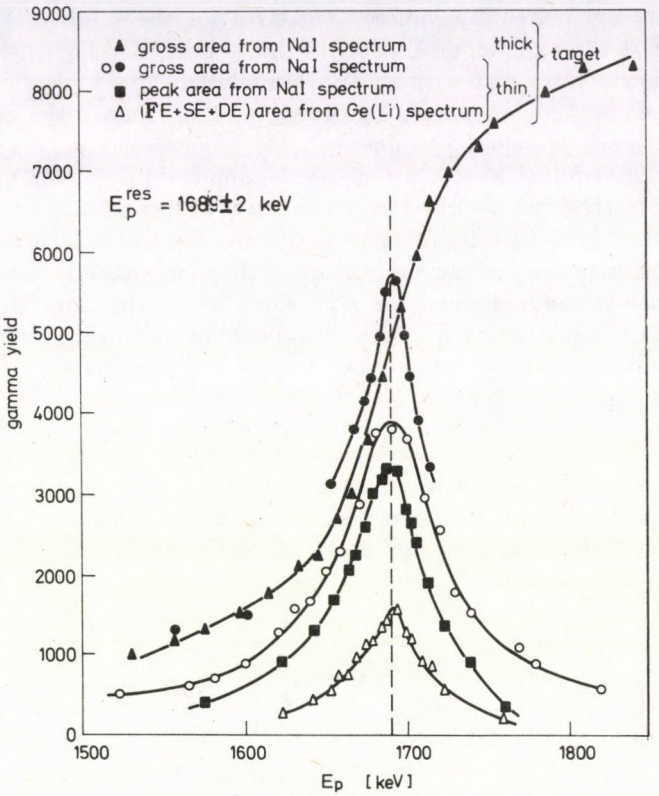

Fig. 6. Excitation curves measured on thin and thick targets. For notations see the main text

Table III

New consistent set of data for the second resonance in $^{12}C(p, \gamma)^{13}N$ and its ground state decay

E_p^{res} (keV)	E_γ^{res} (keV)	E_γ (keV*)	Γ (keV)	ΔE (keV)
1689 ± 2	3502 ±2			
conventional method				
		3501.5 ± 0.7	65.6 ± 1.8	0 ± 2
1688.7 ± 0.7	3501.5 ± 0.7			
thick target method				

* deduced through averaging over cases 1 to 6 in Table II

and those of Rolfs and Azuma [5] aiming at a search for direct capture process, on the other, lead to an inconsistency of the data E_p^{res} and E_γ related to the second resonance in $^{12}C(p, \gamma)^{13}N$ radiative capture process. Recent measurements by Brown et al [6] refer to the named resonance as that at 1.7 MeV only. Our data

in Table III represent a consistent set, the need for the supposition of an anomaly is not present any more. An indirect argument for the validity of our new E_p^{res} value is given in the paper of de Esch and van der Leun [7]. The authors report the appearance of the resonance with an apparent shift to lower energies compared to the position E_p=1.7 MeV reported by Brown et al [6]. Part of the discrepancy will disappear with our present E_p^{res} value.

Some methodological conclusions on the applicability of thick target gamma spectroscopy method can be drawn from the above experiments, as well. E_p^{res} values are equal within the accuracies in both cases, however, better accuracy in the latter case calls one's attention to the application of the new method. A slight difference in the absolute values and errors for E_γ^{res} and Γ shown in Table II for cases with different averaging interval in E_{p_0} indicates the influence of complex energy spectra increasing with the width of this interval. In practical applications the width should be taken as small as possible, i.e. $E_{p_0} \gtrsim E_p^{res}$ should be selected.

Note added in proof. In a recent manuscript Poyarkov forwarded new arguments by the observation of the transition to the first excited state which in his view may support the original statement on the existence of the anomaly. Thanks are due for his contribution in a period of the measurements.

References

1. V.A. Poyarkov, I.V. Sizov, Yadernaya Fizika, *45*, 1515, 1987.
2. S.L. Blatt, D.B. Nichols, R.G. Arns, J.D. Goss and H.J. Hausman, Nucl. Instr. Meth., *61*, 232, 1968.
3. E. Kurtz, K. Battleson, D.K. McDaniels and D.J. Horen, Nucl. Instr. Meth., *69*, 56, 1969.
4. F. Ajzenberg-Selove, Nucl. Phys., *A449*, 1, 1986.
5. C. Rolfs, R.E. Azuma, Nucl. Phys., *A227*, 291, 1974.
6. J.C. Brown, R.G. Seyler, T.L. Tsin, S.L. Blatt, Phys. Rev., *C 31*, 1607, 1985.
7. H.P.L. de Esch, C. van der Leun, Nucl. Phys., *A476*, 316, 1988.

Acta Physica Hungarica 65 (2–3), pp. 287–294 (1989)

LOW ENERGY ALPHA SCATTERING ON ^{62}Ni*

Z. MÁTÉ, S. SZILÁGYI, L. ZOLNAI

Institute of Nuclear Research of the Hungarian Academy of Sciences (ATOMKI)
4001 Debrecen, Hungary

Å. BREDBACKA, M. BRENNER, K.-M. KÄLLMAN and P. MANNGÅRD

Department of Physics, Åbo Akademi
Turku, Finland

Elastic α-particle differential cross sections have been measured at 12.8, 14.5, 16.3 and 18.1 MeV on ^{62}Ni in the angular range from 20 to 166 degrees. The angular distributions were analysed in terms of the optical model. The energy dependence of the volume integrals was compared with the prediction of a model based on the dispersion relation between the real and imaginary parts.

1. Introduction

Elastic scattering data are generally analysed in terms of the optical model. Since most of the reaction theories utilize distorted waves to describe the scattering of the projectile from the target, the extraction of optical model potentials from elastic scattering data is the necessary starting point for gaining information on nuclear structure from reaction processes.

With the development of the realistic two-nucleon and three-nucleon transfer codes, interest has developed again in the establishment of good optical parameters for the elastic scattering of α-particles to use them in the analyses of (α,p), (p, α), (α, d), and (d, α) reactions [1–5].

In order to extract information it is necessary to measure experimental data with high precision over a wide angular range mainly at large angles, where the refraction properties of the optical potential are manifest and the α-particle penetrates deeper into the nucleus. Unfortunately, the extraction of optical potential parameters for composite particles suffers at lower incident energies from the well known ambiguities.

Recently the low energy behaviour of the optical model potential was investigated in several theoretical works [6–10]. According to these investigations an anomaly can be observed in the energy dependence of the optical model potential parameters and volume integrals when these quantities are compared with the ones obtained at higher bombarding energies.

*Dedicated to Academician D. Berényi on his 60th birthday

In this work we decided to study experimentally the α elastic scattering process on ^{62}Ni target at low bombarding energies. Only a few α elastic scattering experiments have been reported so far on this target nucleus at incident energies near the Coulomb barrier. The α-scattering data on ^{62}Ni can be found in references [11–19] in the energy interval of 18–104 MeV.

This paper presents experimental angular distributions of elastically scattered α-particles on ^{62}Ni at incident energies near the Coulomb barrier and their optical model analysis. The aim of the investigation was to extend the available experimental information for low energies, and in this way to provide optical model parameters and to study their energy dependence.

2. Experimental procedure and results

The experiments were performed at the sector-focused MGC type cyclotron of the Åbo Akademi (Turku, Finland) by using an energy analysed beam. Beam monitoring was accomplished by means of a Faraday cup located 30 cm behind the scattering chamber and, additionally by a monitor detector. The beam was focussed on the target to a spot of less than 2 mm diameter. The target used in the experiment was a self-supporting foil of highly enriched ^{62}Ni (97.94 per cent) of 180 μg/cm^2 thickness.

The target and the four surface barrier silicon detectors were placed inside a general purpose scattering chamber of 60 cm diameter. One of the detectors was fixed at 90 degrees with respect to the beam direction as monitor detector. Three other detectors were used as an array fixed on a rotatable plate of the scattering chamber to measure angular distribution data. Detector angular acceptance varied from 0.5 degrees to 1.0 degrees with corresponding solid angles between 0.5 and 1 msr. The energy resolution in the particle spectra was about 100 keV for the energy of the elastic peak.

All the detectors, including the monitor detector, had essentially identical electronic chains consisting of charge sensitive pre-amplifier and main amplifier. The analogue signals from these detector systems were fed to a routing unit. The signals from the routing unit were fed to an ADC. The data of the ADC were mixed to a computer controlled ND-66 analyser. Comparison of the singles analogue rate accepted by the ADC with the total analogue rate obtained from the detector systems allowed dead-time corrections to be made. This correction was limited to 0.5 per cent by limiting the counting rate via a reduction of the incident beam current.

Spectra were obtained at 12.8, 14.5, 16.3 and 18.1 MeV incident α-energies from 20 to 166 degrees in the laboratory system. A few spectra were taken at forward angles at 4.5 MeV bombarding energy as well. The normalisation of the differential cross section data was done by using the assumption that the cross section at 4.5 MeV is identical with the Rutherford scattering cross section.

At angles of the forward hemisphere the target normal was set to 135 degrees with respect to the beam while for angles of the backward hemisphere the target

normal was set to 45 degrees with respect to the beam direction. Overlap points for both target positions were taken each time the target was rotated.

The spectra were analysed by a PDP-11/23 computer. The experimental angular distributions are shown in Fig. 1 (dots).

The main uncertainties in the evaluation of the cross sections were those due to the beam current integration and the counting statistics. The error in absolute differential cross section is estimated to be less than 15 per cent. The relative error is smaller than 10 per cent.

3. Optical model analysis

In a phenomenological optical model analysis of the α elastic scattering, the effect of the target nucleus on the α-particle is characterized by a spherically symmetric local complex potential. In the present analysis the optical potential is of the usual form

$$V(r) = V_C(r) - V f(r,\ r_v,\ a_v) - iW f(r,\ r_w,\ a_w), \tag{1}$$

where $f(r,\ r_x,\ a_x)$ is a Saxon-Woods form factor given by

$$f(r,\ r_x,\ a_x) = \{1 + \exp[(r - R_x)/a_x]\}^{-1} \tag{2}$$

for both the real and imaginary potentials with $R_x = r_x A_T^{1/3}$, r_x being the radius parameter, a_x being the diffuseness parameter and A_T being the mass number of the target nucleus. The finite size of the incident α-particle has not been taken into account explicitly in making the parametrization. The $V_C(r)$ Coulomb potential has been taken as that due to a uniformly charged sphere of radius R_C:

$$\begin{aligned} V_C(r) &= Z_i Z_T (3 - r^2\ /R_C^2)/2R_C \qquad && r \le R_C \\ &= Z_i Z_T / r && r > R_C, \end{aligned} \tag{3}$$

where $R_C = r_c A_T^{1/3}$, r_c being the Coulomb radius parameter and A_T again being the mass number of the target nucleus with atomic number Z_T bombarded by a projectile with atomic number Z_i. Throughout this work r_c has been taken to be 1.4 fm.

The search routine in the programme ECIS [20] used in this work minimized the usual χ^2 parameter given by

$$\chi^2 = \frac{1}{N} \sum_{i=1}^{N} \left\{ \frac{\sigma_{\text{theo}}(\theta_i) - \sigma_{\text{exp}}(\theta_i)}{\triangle\sigma_{\text{exp}}(\theta_i)} \right\}^2, \tag{4}$$

where $\sigma_{\text{theo}}(\theta_i)$, $\sigma_{\text{exp}}(\theta_i)$ and $\triangle\sigma_{\text{exp}}(\theta_i)$ are, as usual, the predicted cross section from the optical model, the experimental cross section and the uncertainty in the experimental cross section, respectively, at the angle θ_i.

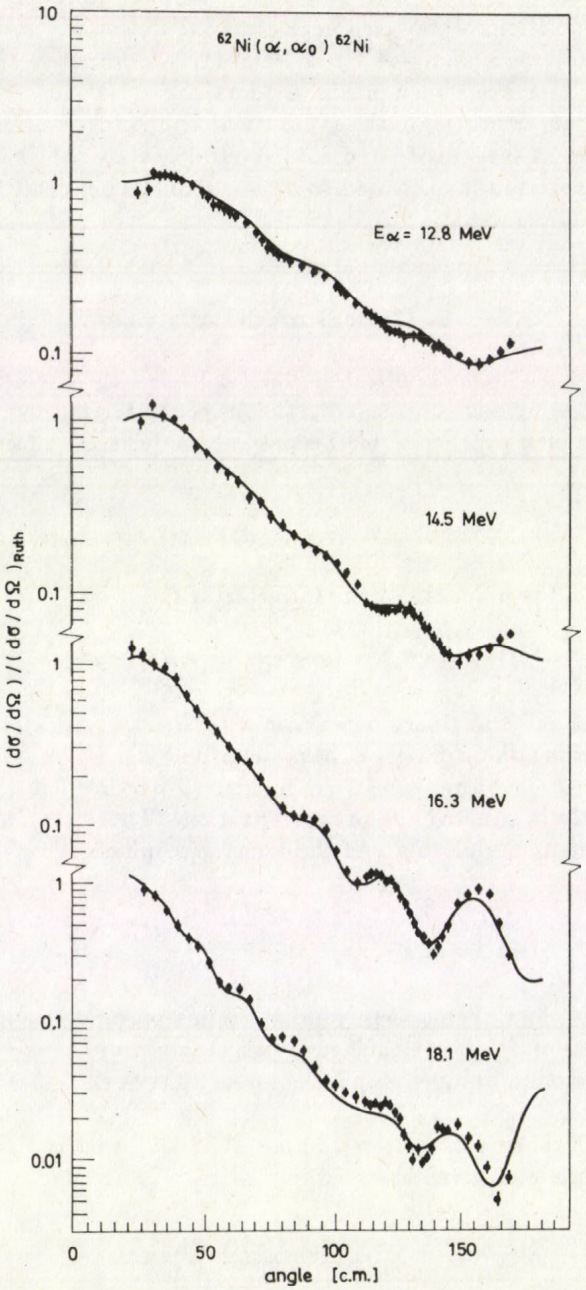

Fig. 1. The experimental angular distributions for the elastic scattering of alpha particles from ^{62}Ni compared with the optical model fits using the $J_V \approx 460$ MeV.fm^3 parameter set of Table I

Table I
Optical model parameters for the elastic scattering of α-particles from ^{62}Ni

E_α [MeV]	V [MeV]	r_v [fm]	a_v [fm]	W [MeV]	r_w [fm]	a_w [fm]	J_V [MeV fm^3]	J_W [MeV fm^3]	χ^2
12.8	210.8	1.40	0.56	12.4	1.80	0.14	667	76	0.5
14.5	207.0		0.51	32.7	1.00	0.62	646	42	0.4
16.3	211.2		0.52	14.1	1.70	0.20	659	73	1.0
18.1	198.1		0.58	16.1	1.69	0.39	631	84	1.6
12.8	137.2	1.45	0.58	11.9	1.79	0.21	481	72	0.6
14.5	133.6		0.54	12.5	1.63	0.38	463	59	0.5
16.3	133.0		0.54	16.5	1.48	0.14	462	57	1.9
18.1	126.3		0.59	13.1	1.71	0.41	445	71	1.8
12.8	104.6	1.50	0.56	10.5	1.81	0.52	402	65	0.5
14.5	101.8		0.52	10.8	1.66	0.34	387	53	0.5
16.3	105.0		0.50	10.3	1.72	0.15	397	55	1.2
18.1	94.6		0.58	11.7	1.72	0.39	366	64	2.0
12.8	60.5	1.55	0.54	9.86	1.58	0.50	254	43	0.8
14.5	57.0		0.53	7.67	1.67	0.36	239	39	0.6
16.3	58.0		0.52	14.4	1.67	0.24	242	80	6.1
18.1	31.5		0.72	5.61	1.86	0.47	139	39	2.6

The results of the searches are listed in Table I. One can observe the usual discrete optical potential families with volume integrals per interacting nucleon pair, J_V, differing by approximately 100 MeV.fm^3. Four optical potential families have been found at each energy. They are shown in Table I together with the corresponding volume integrals J_V, J_W and χ^2-values.

There is very little evidence from the χ^2 values for these families to allow a clear choice to be made as to the most appropriate family. It has been shown that at sufficiently high incident energies there is only one optical model family present [21–29]. This happens when the incident α-particle has sufficient energy for its individual nucleons to undergo collisions within the nucleus that lead to recoil and scattered particles emerging which are on average above the nucleon binding energy, so that the Pauli principle no longer operates. At lower energies, since it is not probable that the α-particle penetrates into the nuclear interior and "sees" the nuclear potential there, the reactions contributing most to the reaction cross section take place mainly in the region of the strong absorption radius and thus they do not determine uniquely the details of the wave functions in the nuclear interior.

To choose the most appropriate parameter set we used the results of an experimental analysis given in [14]. In this work England et al have found six equivalent optical model families for $\alpha + {}^{62}$Ni at 25 MeV bombarding energy. Comparing their real volume integral values with the ones obtained at higher energies [25–29]

they could identify which family corresponds to the unique one at the high energies. Their choice was extrapolated to our case by comparison of the data shown in Fig. 2.

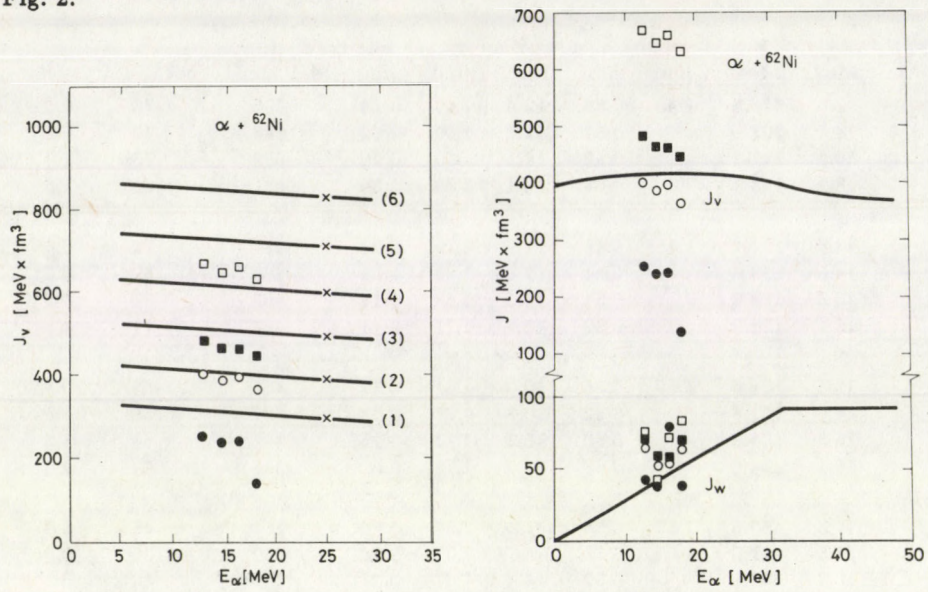

Fig. 2. Comparison of the volume integrals per interacting nucleon pair for the real part of different optical model families obtained in the alpha+^{62}Ni experiments. The symbols x and the straight lines represent quantities taken from [14]. The other symbols correspond to data obtained in the present work

Fig. 3. Comparison of the experimental volume integrals per interacting nucleon pair obtained in the present work (symbols) with the results of a dispersion relation analysis given in [9] (solid lines)

The crosses correspond to the J_V values obtained in [14] (family number 3 was found to be the most appropriate one). The straight lines have the same slope (−1.78 fm^3) also taken from [14] (Fig. 8). The comparison shows that the $J_V \approx$ 460 MeV/fm^3 family should be considered as the most appropriate one in our case. Further confirmation that this family is the most meaningful one comes from its use in the DWBA analysis of (α, p), (α, d) and (α, t) reactions on nickel isotopes at 25 MeV [30]. In that work, only the family defined above reproduces the slopes and details of the oscillations in the experimental angular distributions in these reactions.

4. Energy dependence of the alpha optical potential

An anomaly in the energy dependence of the real depth of the proton optical potential at the Coulomb barrier has been observed at heavy [31] and medium mass

nuclei [32]. It was shown that a large part of this anomaly could be attributed to channel coupling effects [33]. Recent papers [6–8] report on rapid variations and anomalous behaviour of the nucleus–nucleus potential for energies E in the vicinity of the top of the Coulomb barrier. It was shown that there are general theoretical arguments [9–10] for expecting such an energy dependence of the potential parameters at low energies, based on the dispersion relation which connects the real and imaginary parts of the complex optical potential. This relation is based on the causality principle and it has the following form for the volume integrals:

$$J_V(E) = J_0(E) + \frac{P}{\pi} \int \frac{J_W(E')}{(E' - E)} \, dE' \, . \tag{5}$$

Here P means the "principal value" of the integral, J_0 is a slowly and smoothly E depending term. It is expected that $J_W(E')$ decreases rapidly for energies below the Coulomb barrier. Because of the above mentioned formula the real part is expected to be bell shaped near the top of the Coulomb barrier. Mahaux et al proposed a simple schematic model with linear E dependence for the imaginary potential in [9] and applied this model for describing available experimental data on α+Ni processes. One of the representative linear fits to the volume integrals J_W taken from [9] is shown in the lower part of Fig. 3 as a solid line. For such a simple $J_W(E)$ function the dispersion relation (5) reduces to a simple analytical formula and provides the $J_V(E)$ function shown by a solid line in the upper part of Fig. 3.

The volume integrals obtained in the present work are compared with these model functions also in Fig. 3. The $J_V \approx 460$ MeV/fm^3 family which was found to be the most appropriate one on the basis of the empirical analysis has J_V values close to the model curve. This means that the results of the present experiment are in accordance with those fitted in [9]. However, the finer details of the prediction (the bell shaped form of J_V) cannot be tested because of the limited energy range and the experimental uncertainties.

5. Conclusion

In this investigation the elastic differential cross-sections of 12–18 MeV α-particles scattered from ^{62}Ni have been measured. The analysis of the elastic scattering data has given satisfactory fits in terms of the optical potential with a Saxon-Woods form. Four potential families were found in this energy interval. The volume integrals decrease roughly linearly with increasing energy. On the basis of the behaviour of the volume integrals one of the families was found to be joined to the optical parameter set found at higher bombarding energy. This choice is consistent with the model description of the volume integrals based on the dispersion relation between the real and imaginary parts of the potential.

Acknowledgement

The authors are grateful to Prof. B. Gyarmati and to T. Vertse for helpful discussions.

References

1. M.J. Schneider and W.W. Daehnick, Phys. Rev., *C4*, 1649, 1971.
2. H. Nann, W.S. Chien, A. Saha and B.H. Wildental, Nucl. Phys., *A292*, 195, 1977.
3. H. Nann, W.S. Chien and A. Saha, Nucl. Phys., *A292*, 205, 1977.
4. P.A. Smith, R.A. Emigh, N.J. DiGiacomo, G.R. Smith and R.J. Peterson, Phys. Rev., *C19*, 1767, 1979.
5. Y. Tagishi, K. Katori, M. Sasagase, M. Sato and T. Mikumo, Nucl. Phys., *A339* 262, 1980.
6. J.S. Lilley, B.R. Fulton, M.A. Nagarajan, I.J. Thompson and D.W. Banes, Phys. Lett., *151B*, 181, 1985.
7. B.R. Fulton, D.W. Banes, J.S. Lilley, M.A. Nagarajan and I.J. Thompson, Phys. Lett., *162B*, 55, 1985.
8. A. Baeza, R. Bilwes, J. Diaz and J.L. Ferrero, Nucl. Phys., *A419*, 412, 1984.
9. C. Mahaux, H. Ngô and G.R. Satchler, Nucl. Phys., *A449*, 354, 1986.
10. C. Mahaux, H. Ngô and G.R. Satchler, Nucl. Phys., *A456*, 134, 1986.
11. W. Trombik, K.A. Ebelhard, G. Hinderer, H.H. Rossner, A. Widinger and J.S. Eck, Phys. Rev., *C9*, 1813, 1974.
12. C.B. Fulmer, J. Benveniste and A.C. Mitchell, Phys. Rev., *165*, 1218, 1968.
13. A.A. Cowley, P.M. Cronje, G. Heymann, S.J. Mills and J.C. van Staden, Nucl. Phys., *A229*, 256, 1974.
14. J.B.A. England, S. Baird, D.H. Newton, T. Picazo, E.C. Polacco, G.J. Pyle, P.M. Rolph, A. Alabau, E. Casal and A. Garcia, Nucl. Phys., *A388*, 573, 1982.
15. V.V. Alekseev, O.F. Nemec, J.S. Strok, K.O. Tereneckij and V.V. Tokarevskij, Izv. AN. SSSR Ser. Fiz., *39*, 123, 1975.
16. C. Pirart, M. Bosman, P. Leleux, P. Macq and J.P. Meulders, Phys. Rev., *C17*, 810, 1978.
17. M. Bosman, P. Leleux, P.C. Macq, J.P. Meulders and C. Pirart, Phys. Rev., *C11*, 628, 1975.
18. D.G. Madland, P. Schwandt, W.T. Sloan, P. Shapiro and P.P. Singh, Phys. Rev., *C9*, 1002, 1974.
19. H. Rebel, R. Löhken, G.W. Schweimer, G. Schatz and G. Hauser, Z. Physik, *256*, 258, 1972.
20. J. Raynal, Notes on ECIS (Service de Physique Theorétique, CERN-Sacley, 91101, GIF-sur-Yvette CEDEX)
21. D.A. Goldberg and S.M. Smith, Phys. Rev. Lett., *29*, 500, 1972.
22. S.M. Smith, G. Tibell, A.A. Cowley, D.A. Goldberg, H.G. Push, W. Reichart and N.S. Wall, Nucl. Phys., *A207*, 273, 1973.
23. D.A. Goldberg, S.M. Smith, H.G. Pugh, P.G. Roos and N.S. Wall, Phys. Rev., *C7*, 1938, 1973.
24. D.A. Goldberg, S.M. Smith and G.F. Burdzik, Phys. Rev., *C10*, 1362, 1974.
25. L.W. Put and A.M.J. Paans, Nucl. Phys., *A291*, 93, 1977.
26. E. Friedmann and C.J. Batty, Phys. Rev., *C17*, 34, 1978.
27. N.S. Wall, A.A. Cowley, R.C. Johnson and A.M. Kobos, Phys. Rev., *C17*, 1315, 1978.
28. A.A. Cowley and N.S. Wall, Phys. Rev., *C17*, 1322, 1978.
29. Th. Dalbra, G.H. Gregoire, G. Paic, R. Ceulneer, F. Michel, R. Vanderporten, A. Budzanowski, H. Dabrowski, L. Freindl, K. Grotowski, S. Micek, R. Planeta, A. Strzalkowski and K. Eberhard, Phys. Rev., *C18*, 1237, 1978.
30. D.H. Newton, Ph.D. thesis, Univ. of Birmingham, 1981.
31. J.S. Eck and W.J. Thompson, Nucl. Phys., *A237*, 83, 1975.
32. B. Gyarmati, T. Vertse, L. Zolnai, A.I. Barishnikov, A.F. Gurbich, N.N. Titarenko and E.L. Yadrovsky, J. Phys. G: Nucl. Phys., *5*, 1225, 1979.
33. B. Gyarmati, R.G. Lovas, T. Vertse and P.E. Hodgson, J. Phys. G: Nucl. Phys., *7*, L209, 1981.

Acta Physica Hungarica 65 (2-3), pp. 295-304 (1989)

NUCLEAR STRUCTURE OF ^{116}In*

T. FÉNYES and ZS. DOMBRÁDI

Institute of Nuclear Research of the Hungarian Academy of Sciences (ATOMKI)
4001 Debrecen, Hungary

The low-lying positive parity states of ^{116}In have been described within the framework of the interacting boson– fermion–fermion / odd–odd truncated quadrupole phonon model (IBFFM/OTQM). The calculations reproduce the energy levels and known electromagnetic moments. γ-branching ratios have also been calculated and compared with the existing experimental data.

1. Introduction

The level scheme of ^{116}In nucleus was studied from (d, p) reaction by Moorhead et al [1] and Alexeev et al [2], as well as from (n, γ) reaction by Rabenstein et al [3], Schreckenbach et al [4], Corvi and Stefanon [5], Alexeev et al [2], and Kondurov et al [6]. The results obtained till 1980 were compiled by Blachot et al [7].

The magnetic dipole and electric quadrupole moments of the 1_1^+ ground and 5_1^+ isomeric states of ^{116}In were measured by several groups (Lederer et al [8], Winnacker et al [9], Grupp et al [10] and Eberz et al [11]).

As a result of the experimental studies the level scheme of ^{116}In is rather well known below $\approx$ 1300 keV excitation energy, presenting a good basis for theoretical investigations.

The level properties of ^{116}In have been interpreted using different models. Rabenstein et al applied a proton hole coupled to neutron quasiparticle [3], Van Gunsteren a proton hole coupled to number projected neutron quasiparticle model [12]. The energy splittings of p–n configurations by residual short range Wigner and singlet interactions were calculated by Alexeev et al [2]. The negative parity levels of ^{116}In have been described by Van Maldeghem et al [13] within the framework of neutron-quasiparticle proton–hole multiplets coupled to quadrupole phonon excitations of the core. The splittings of the energies of several p–n multiplets as a function of $J(J+1)$ was calculated on the basis of the parabolic rule by Paar [14] and Fényes et al [15]. (Here J means the spin of the nuclear state.)

Nevertheless from the specified theoretical investigations only Gunsteren has given such description, in which many positive parity states, and not only energetics, but also wave functions, electromagnetic moments and transition rates have been treated. His results are in a reasonable agreement with the experiment, with the exception that the staggering in energies is too strong and the quadrupole strengths

*Dedicated to Academician D. Berényi on his 60th birthday

are too weak. In some cases the theoretical γ branching ratios strongly differ from the experimental ones.

In order to see whether the explicit treatment of the collective quadrupole degree of freedom can help the above shortcomings, we have calculated the energy levels and electromagnetic properties of the positive parity states of ^{116}In using IBFFM/OTQM. This model has proved formerly to be effective for the description of ^{112}In [16] and ^{114}In [15, 17] nuclei.

2. IBFFM/OTQM description

2.1. Hamiltonian

The calculations were performed on the basis of the truncated quadrupole phonon model for odd–odd nuclei (OTQM) [18, 19]. This model is equivalent to the interacting boson–fermion–fermion model (IBFFM) at a phenomenological level [18].

The Hamiltonian of the model is given by

$$H_{\mathrm{OTQM}} = H_{\mathrm{TQM}} + \sum_{i=p,\,n} H^i + \sum_{i=p,\,n} H^i_{\mathrm{PVI}} + H_{\mathrm{RES}}, \tag{1}$$

where H_{TQM} is the SU(6) quadrupole phonon Hamiltonian of the even–even core.

H^i denotes the quasiparticle Hamiltonian of the odd proton ($i = p$) and odd neutron ($i = n$) in a spherical potential.

H^i_{PVI} is the Hamiltonian of the particle-vibration interaction for proton and neutron, which consists of three terms [18]:

$$H^i_{\mathrm{PVI}} = H^i_{\mathrm{MON}} + H^i_{\mathrm{DYN}} + H^i_{\mathrm{EXC}}, \tag{2}$$

where H^i_{MON} is the Hamiltonian of the monopole interaction. This is proportional to the A^i_0 monopole interaction strength. H^i_{DYN} characterizes the dynamical interaction (proportional to the Γ^i_0 strength). H^i_{EXC} denotes the Hamiltonian of the exchange interaction (with Λ^i_0 strength).

H_{RES} is the residual interaction between the odd proton and neutron. We have considered only a central delta force of the form

$$H_{\mathrm{RES}} = 4\pi\delta\,(\mathbf{r}_p - \mathbf{r}_n)\,[v_D + v_S \boldsymbol{\sigma}_p \cdot \boldsymbol{\sigma}_n]\,. \tag{3}$$

where v_D and v_S are the parameters of the Wigner and Bartlett forces, δ is the Dirac δ symbol, $\mathbf{r}_p$ and $\mathbf{r}_n$ are the position vectors of the proton and neutron, respectively and the $\boldsymbol{\sigma}$-s are the Pauli spin matrices.

The Hamiltonian (1) was diagonalized in the quasiproton–quasineutron weak coupling basis

$$|(j_p\, j_n)\; j_{pn},\ \mathrm{NI}\ ;\ \mathrm{J}\rangle \tag{4}$$

where j_{pn} is the resulting angular momentum of the j_p and j_n states, I is the angular momentum of the N-phonon state, and J is the total angular momentum.

The computer code IBFFM/OTQM used in the calculations was written by Brant, Paar and Vretenar [20].

2.2 Parameters

The core excitations were approximated with harmonic vibration. This is an acceptable approach, if we want to describe only low energy states, where the contribution of two (and higher) phonon components is small. We used $\hbar\omega_2 = 1.293$ MeV effective phonon energy, which agrees with the experimental energy of the 2_1^+ state of ^{116}Sn.

Since we are considering the low-lying states in a nearly spherical nucleus, we can use reduced boson/phonon number $N_{\max} = 2$ [21]. This strongly reduces the scope of computations, without sizeable effect on the properties of the low-lying states which are being investigated.

The shell-model space consisted of the $1g_{9/2}$ subshell for the proton quasiparticle and the $2d_{5/2}$, $1g_{7/2}$, $3s_{1/2}$, $2d_{3/2}$ subshells for neutron quasiparticles.

The strengths of the residual force were adjusted to the energy spectrum of ^{116}In: $v_D = -0.4$ MeV and $v_S = -0.1$ MeV (including radial integrals).

The V^2 occupation probabilities, the quasineutron energies, the strength parameters of the proton–core and neutron–core interactions, the effective charges and gyromagnetic ratios are listed in Table I. They were different for Set I and Set II calculations.

The V^2 occupation probabilities were taken from the systematics of experimental data [22 – 28] (Set I) and from the Nilsson plus BCS model calculations of Maldeghem et al [13] (Set II).

The quasineutron energies were fitted to the experimental level energies of ^{116}In, but they are not far from the energies of the corresponding ^{117}Sn states [29]: $E(\nu d_{3/2}) - E(\nu s_{1/2}) = 0.159$ MeV, $E(\nu d_{5/2}) - E(\nu s_{1/2}) \approx 1.020$ MeV (not pure state, $\nu s_{1/2} \otimes 2_1^+$ admixture is present), $E(\nu g_{7/2}) - E(\nu s_{1/2}) = 0.712$ MeV.

The strength parameters of the proton–core interaction have been determined from the splitting of the $\pi\tilde{g}_{9/2} \otimes 2_1^+$ multiplet of ^{115}In [30] by PTQM (*p*article *t*runcated *q*uadrupole phonon *m*odel [31]) calculations. $\Lambda_0^P \approx 0$ is a reasonable value, taking into account that the phonon consists mainly of neutron excitations.

Similarly, the strength parameters of the neutron–core interaction have been obtained from the splitting of the $\nu\tilde{h}_{11/2} \otimes 2_1^+$ multiplet of ^{117}Sn [32] by PTQM calculations and from former parabolic rule calculations [15] (Set I parameters). In Set II parametrization the Γ_0^n, Λ_0^n, and A_0^n values were fitted to the energies of positive parity states of ^{117}Sn by PTQM calculations.

Employing the wave function from diagonalization, we have calculated the electromagnetic properties. The effective charges and gyromagnetic ratios used were close to the standard values in both parametrizations.

Table I
Parameters of the IBFFM/OTQM calculations

Parameters		Set I	Set II
Occupation probabilities	$V^2(\pi g_{9/2})$	0.87	0.87
	$V^2(\nu s_{1/2})$	0.45	0.399
	$V^2(\nu d_{3/2})$	0.27	0.253
	$V^2(\nu d_{5/2})$	0.91	0.944
	$V^2(\nu g_{7/2})$	0.80	0.869
Quasineutron energies, MeV	$E(d_{3/2}) - E(s_{1/2})$	0.15	0.22
	$E(d_{5/2}) - E(s_{1/2})$	1.25	1.33
	$E(g_{7/2}) - E(s_{1/2})$	0.866	0.99
Strength parameters of the nucleon-core interaction, MeV	Γ_0^p	1.1	1.0
	Λ_0^p	0.0	0.0
	A_0^p	0.1	0.0
	Γ_0^n	0.7	0.5
	Λ_0^n	0.2	1.1
	A_0^n	0.0	0.15
Effective charges	$e_{e.\,p}^p$	1.5 e	1.5 e
	$e_{e.\,p}^n$	0.5 e	0.5 e
	e^{VIBR}	1.8 e	2.65 e
Effective gyromagnetic factors	g_s^p	0.45 $g_s^{p,\,\mathrm{free}}$	0.5 $g_s^{p,\,\mathrm{free}}$
	g_l^p	1.0	1.0
	g_s^n	0.5 $g_s^{n,\,\mathrm{free}}$	0.6 $g_s^{n,\,\mathrm{free}}$
	g_l^p	0	0
	g_R	Z/A=0.4224	0.4224

3. Results and discussion

3.1. Level energies and wave functions

The experimental and theoretical energy spectra of the positive parity states of ^{116}In are shown in Fig. 1. The main features of the experimental scheme have been well reproduced in both parametrizations.

The wave-functions of some low-lying states are shown in Table II. According to the Set II calculations the total strength of the $\pi\tilde{g}_{9/2}\,\nu\tilde{g}_{7/2}$ configuration in the wave function is more than 82 % for the 1_1^+, 2_1^+, 3_2^+, 4_3^+, 5_3^+, 6_2^+, 7_2^+ and 8_1^+ states. The 3_1^+, 4_2^+, 5_2^+, 6_1^+ $\pi\tilde{g}_{9/2}\nu\tilde{d}_{3/2}$, 4_1^+ and 5_1^+ $\pi\tilde{g}_{9/2}\nu\tilde{s}_{1/2}$ and 2_2^+ and 7_1^+ $\pi\tilde{g}_{9/2}\nu\tilde{d}_{5/2}$ states are also rather pure (the total strength of the given configuration in the wave function is $\geq$ 79 %). This can explain, why the simple parabolic rule calculations could well reproduce the energy splittings of these multiplets as a function of the level spin [14, 15].

It is an interesting feature of the energy spectrum that the $^{116}_{49}\mathrm{In}_{67}$ 1^+ ground state has $\pi\tilde{g}_{9/2}\nu\tilde{g}_{7/2}$ configuration, although the $\nu\tilde{g}_{7/2}$ state is an excited one in the

neighbouring $N = 67$ ^{117}Sn nucleus. In the lowest-spin $\pi\tilde{g}_{9/2}\nu\tilde{g}_{7/2}$ state the overlap of the proton and neutron wave functions is large, consequently the interaction between them is very strong. A similar phenomenon was observed in ^{114}In and ^{112}In nuclei [33, 17, 16], too.

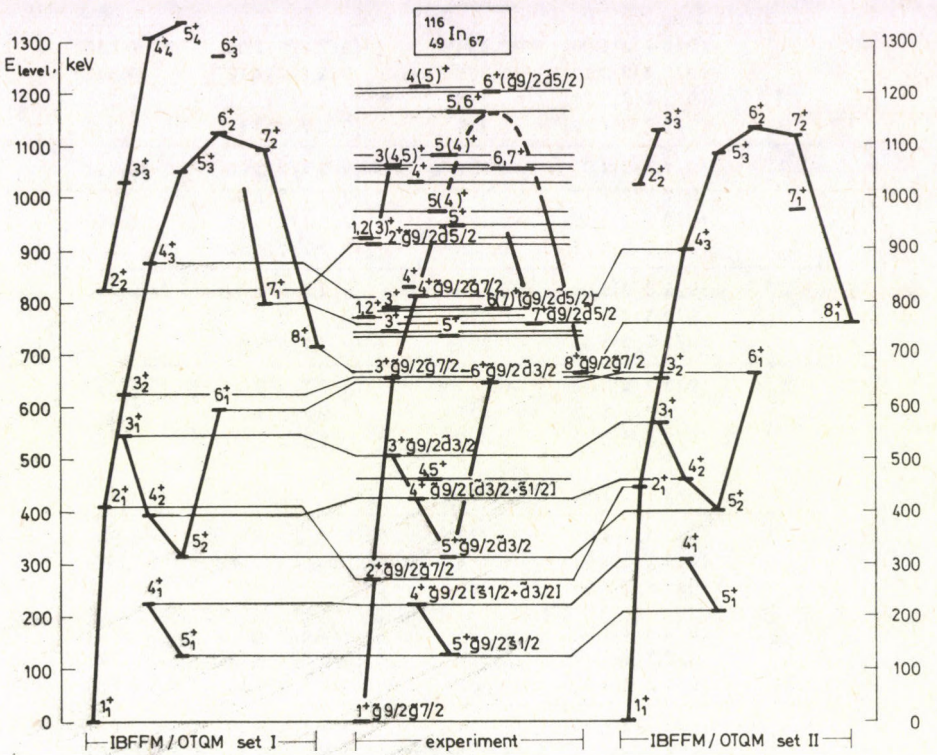

Fig. 1. Positive parity states of ^{116}In below $\approx$ 1300 keV. The theoretical level schemes are the results of the present IBFFM/OTQM calculations. The experimental data were taken from Alexeev et al [2]

3.2. Electromagnetic moments

The magnetic dipole (μ) and electric quadrupole (Q) moments of the 1_1^+ and 5_1^+ ^{116}In states are summarized in Table III. The empirical values have been obtained from the corresponding moments of the neighbouring odd In and odd Sn nuclei on the basis of simple additivity relations [34].

The sign of the moments was properly reproduced both in the IBFFM/OTQM and additivity relation calculations.

Table II

Wave functions of some low-lying positive parity states of ^{116}In calculated in IBFFM/OTQM. The basis states $|(j_p\, j_n)\, j_{pn}, \mathrm{NI}\, ; \mathrm{J}\rangle$ are denoted by $(j_p\, j_n)\, j_{pn}$, NI for given J. Only amplitudes larger than 5 % are listed

State, J^π	Set I		Set II	
1_1^+	(9/2,7/2)1,00	−0.834	(9/2,7/2)1,00	0.855
	(9/2,7/2)2,12	0.363	(9/2,7/2)2,12	−0.347
	(9/2,7/2)3,12	−0.273	(9/2,7/2)1,12	0.252
	(9/2,7/2)1,12	−0.255	(9/2,7/2)3,12	0.240
2_1^+	(9/2,7/2)2,00	−0.731	(9/2,7/2)2,00	−0.721
	(9/2,7/2)1,12	−0.512	(9/2,7/2)1,12	−0.533
	(9/2,7/2)4,12	−0.272	(9/2,7/2)3,12	0.265
	(9/2,7/2)3,12	0.250	(9/2,7/2)4,12	−0.235
3_1^+	(9/2,3/2)3,00	−0.769	(9/2,3/2)3,00	−0.792
	(9/2,3/2)3,12	−0.375	(9/2,3/2)3,12	−0.352
	(9/2,7/2)3,00	−0.297	(9/2,7/2)3,00	−0.313
3_2^+	(9/2,7/2)3,00	−0.669	(9/2,7/2)3,00	−0.632
	(9/2,7/2)1,12	−0.427	(9/2,7/2)1,12	−0.497
	(9/2,3/2)3,00	0.337	(9/2,3/2)3,00	0.354
	(9/2,7/2)5,12	−0.238		
	(9/2,7/2)2,12	−0.233		
4_1^+	(9/2,1/2)4,00	0.722	(9/2,(9/2,1/2)4,00	-0.848
	(9/2,1/2)4,12	0.434	(9/2,(9/2,1/2)4,12	-0.391
	(9/2,3/2)4,00	0.339		
4_2^+	(9/2,3/2)4,00	0.737	(9/2,3/2)4,00	0.832
	(9/2,3/2)4,12	0.395	(9/2,3/2)4,12	0.375
	(9/2,1/2)4,00	−0.387	(9/2,3/2)5,12	−0.275
5_1^+	(9/2,1/2)4,00	−0.715	(9/2,1/2)5,00	0.837
	(9/2,1/2)5,12	−0.437	(9/2,1/2)5,12	0.389
	(9/2,3/2)5,00	0.387	(9/2,(9/2,3/2)5,00	-0.235
	(9/2,3/2)5,12	0.250		
5_2^+	(9/2,3/2)5,00	0.713	(9/2,3/2)5,00	0.815
	(9/2,1/2)5,00	0.412	(9/2,3/2)5,12	0.335
	(9/2,3/2)5,12	0.338	(9/2,(9/2,1/2)5,00	0.257
	(9/2,3/2)4,12	0.241		

The experimental and IBFFM magnetic dipole moments agree within 7 %. The IBFFM calculations show that the contribution of the collective electromagnetic operator to the magnetic moments is small. This can explain, why the simple additivity relation predicts the magnetic moments correctly, and why the [12] quasiparticle calculations gave reasonable results.

The experimental and IBFFM theoretical electric quadrupole moments agree within 32 %. The dominant components of the electric quadrupole moments are

the collective ones. This effect can be simulated in the quasiparticle calculations with relatively large effective charges.

Table III
Magnetic dipole (μ in μ_N)and electric quadrupole (Q in eb) moments of the 1_1^+ and 5_1^+ ^{116}In states

Electromagnetic moments		State			
		1_1^+ ground (14.10 s)		5_1^+ (54.15 min)	
μ_{exp}		2.7863 (10)	[7, 9]	4.235 (15)	[11]
μ_{emp}		3.04		4.53	
μ_{IBFFM}	SET I	2.75		4.51	
	SET II	2.79		4.44	
μ_{theor}	[13]	2.842		4.92	
μ_{theor}	[12]	2.93		4.55	
Q_{exp}		0.09 (2)	[7, 9]	0.802 (12)	[11]
		0.11 (1)	[10]		
Q_{emp}		0.17		0.82	[11]
Q_{IBFFM}	SET I	0.136		0.66	
	SET II	0.145		0.62	
Q_{theor}	[35]	0.104			
Q_{theor}	[12]	0.056			

3.3. Transitions between low-lying states

The experimental and theoretical transitions between the well-established low-lying states are shown in Fig. 2.

As expected, strong $M1$ transitions appear between the neighbouring J and $J+1$ members of the same $p-n$ multiplet. The electromagnetic character and multipolarity of transitions are correctly described in all cases.

The $E2$ strength of the $3_2^+ \to 1_1^+$ $\pi\tilde{g}_{9/2}\nu\tilde{g}_{7/2}$ intramultiplet transition is ≈ 8 Weisskopf units, i.e. the transition is moderately enhanced (according to both parametrizations).

The experimental relative transition intensities were reproduced by the calculations generally within a factor of ≈ 7. Greater discrepancies were observed for the $5_2^+ \to 4_1^+$ (in both Sets), and partly for the $3_1^+ \to 4_1^+$ (in Set II) and $4_2^+ \to 5_2^+$ (in Set I) transitions. According to the (d , p) studies, the 4_1^+ and 4_2^+ states are not pure, they contain strong $\pi\tilde{g}_{9/2}\nu\tilde{s}_{1/2} + \pi\tilde{g}_{9/2}\nu\tilde{d}_{3/2}$ components [2]. The relative intensity of the $5_2^+ \to 4_1^+$ transition was reproduced in no one of the existing calculations (Rabenstein et al [3], Gunsteren [12]). It seems that the decay of the 3_1^+, 4_2^+ and 5_2^+ states cannot be described simultaneously. In Set I calculations the

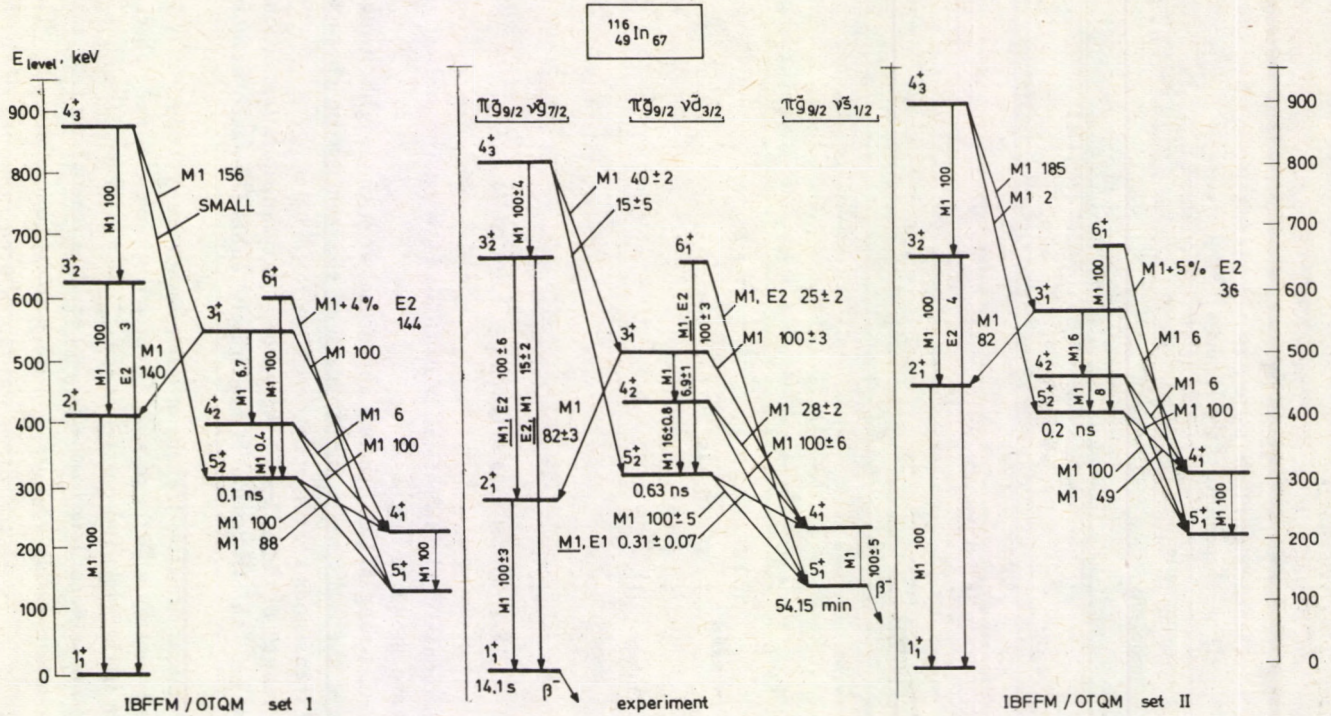

Fig. 2. Transitions between the low-lying states of ^{116}In. After the type and multipolarity of transition the relative transition intensity can be found. The theoretical data are the results of the present IBFFM/OTQM calculations. M1 at the theoretical transitions means that the intensity of the E2 component is less than 1 %. The experimental data (including main configurations) show the results of (n, γ) and (d, p) studies of Alexeev et al [2]

decay of 3_1^+ is relatively well reproduced and there are problems with the other two states. In Set II the decay of the 4_2^+ state is described relatively well, and if we decrease significantly Γ_0^n, one can describe the decay of 5_2^+ at the price of destroying the quality of the description of the other two states. The main difference between the three approximations is that they give different purity for 4_1 (and other) states. This internal inconsistency can be solved by enlargement of the quasiparticle configuration space. Neither the inclusion of πp, πf and many neutron states by Gunsteren, nor adding of collective degree of freedom could help. May be the inclusion of the $\pi d_{5/2}$ intruder state would result in a better theoretical description.

Acknowledgement

The authors are grateful to Prof. V. Paar, Dr. D. Vretenar and Dr. S. Brant for making available to us the computer codes PTQM and OTQM.

This work was supported partly by the National Scientific Research Foundation (OTKA).

References

1. J. B. Moorhead, B. L. Cohen and R. A. Moyer, Phys. Rev., *165*, 1287, 1968.
2. V. L. Alexeev, B. A. Emelianov, D. M. Kaminker, Yu. L. Khazov, I. A. Kondurov, Yu. E. Loginov, V. L. Rumiantsev, S. L. Sakharov and A. I. Szmirnov, Nucl. Phys., *A262*, 19, 1976.
3. D. Rabenstein, D. Harrach, H. Vonach, G. G. Dussel and R. P. I. Perazzo, Nucl. Phys., *A197*, 129, 1972.
4. K. Schreckenbach, A. A. Suarez and T. von Egidy, Z. Naturforsch., *28a*, 1308, 1973.
5. F. Corvi and M. Stefanon, Nucl. Phys., *A233*, 185, 1974.
6. I. A. Kondurov, Yu. E. Loginov and V. V. Martinov, Abstracts of the XXXVI. Conf. on nuclear spectroscopy and structure of atomic nuclei, Harkov, 1986, Nauka, Leningrad, 1986, p. 82.
7. J. Blachot, J. P. Husson, J. Oms, G. Marguier and F. Haas, Nucl. Data Sheets, *32*, 287, 1981.
8. C. M. Lederer, V. S. Shirley, E. Browne, J. M. Dairiki, R. E. Doebler, A. A. Shihab–Eldin, L. J. Jardine, J. K. Tuli and A. B. Buyrn, Table of Isotopes, J. Wiley, New York, 1978.
9. A. Winnacker, H. Ackermann, D. Dubbers, J. Mertens, P. von Blanckenhagen, Z. Phys., *244*, 289, 1971.
10. H. Grupp, H. Ackermann, W. Buttler, K. Dörr, P. Heitjans and H.–J. Stöckmann, Nucl. Phys., *A386*, 56, 1982.
11. J. Eberz, U. Dinger, G. Huber, H. Lochmann, R. Menges, R. Neugart, R. Kirchner, O. Klepper, T. Kühl, D. Marx, G. Ulm, K. Wendt and ISOLDE collaboration, Nucl. Phys., *A464*, 9, 1987.
12. W. F. Van Gunsteren, Nucl. Phys., *A265*, 263, 1976.
13. J. Van Maldeghem, K. Heyde and J. Sau, Phys. Rev. C, *32*, 1067, 1985.
14. V. Paar, Nucl. Phys., *A331*, 16, 1979.
15. T. Fényes, Zs. Dombrádi, A. Krasznahorkay, J. Gulyás J. Timár, T. Kibédi and V. Paar, to be published in Fizika (Zagreb); Zs. Dombrádi and T. Fényes, ATOMKI Ann. Rep. 1988, p. 22, Debrecen.
16. T. Kibédi, Zs. Dombrádi, T. Fényes, A. Krasznahorkay, J. Timár, Z. Gácsi, A. Passoja, V. Paar and D. Vretenar, Phys. Rev. C, *37*, 2391, 1988.
17. J. Timár, T. Fényes, T. Kibédi, A. Passoja, M. Luontama, W. Trzaska and V. Paar, Nucl. Phys., *A455*, 477, 1986.

18. V. Paar, in In-Beam Nuclear Spectroscopy, ed. Zs. Dombrádi and T. Fényes, Akad. Kiadó, Budapest, 1984, Vol. 2, p. 675.
19. S. Brant, V. Paar and D. Vretenar, Z. Phys. *A319*, 355, 1984; T. Hübsch, V. Paar and D. Vretenar, Phys. Lett., *B151*, 320, 1985; V. Lopac, S. Brant, V. Paar, O. W. B. Schult, H. Seyfarth and A. B. Balantekin, Z. Phys., *A323*, 491, 1986; S. Brant, V. Paar, D. Vretenar, G. Alaga, H. Seyfarth, O. Schult and M. Bogdanovic, Phys. Lett., *B195*, 111, 1987.
20. S. Brant, V. Paar and D. Vretenar, IKP Jülich, 1985 (unpublished).
21. A. B. Balantekin and V. Paar, Phys. Lett., *B169*, 9, 1986.
22. D. G. Fleming, Can. J. Phys., *60*, 428, 1982.
23. B. Rosner, Phys. Rev., *B136*, 664, 1964.
24. A. Calboreanu and S. Mancas, Nucl. Phys., *A266*, 72, 1976.
25. R. A. Emigh, C. A. Fields, M. L. Gartner, L. E. Samuelson and P. A. Smith, Z. Phys., *A308*, 165, 1982.
26. S. A. Hjorth, Ark. Fys., *33*, 183, 1967.
27. R. G. Markham and H. W. Fulbright, Phys. Rev. C, *9*, 1633, 1974.
28. S. Harar and R. N. Horoshko, Nucl. Phys., *A183*, 161, 1972.
29. J. Blachot and G. Marguier, Nucl. Data Sheets, *50*, 63, 1987.
30. W. K. Tuttle, III, P. H. Stelson, R. L. Robinson, W. T. Milner, F. K. McGowan, S. Raman and W. K. Dagenhart, Phys. Rev. C, *13*, 1036, 1976.
31. V. Paar, S. Brant, L. F. Canto, G. Leander and M. Vouk, Nucl. Phys., *A378*, 41, 1982.
32. M. Sekiguchi, O. Hashimoto, Y. Shida and T. Soga, J. Phys. Soc. Japan, *52*, 1134, 1983.
33. W. B. Walters, in Nuclear Structure, Reactions and Symmetries, ed. R. A. Meyer and V. Paar, World Scientific, Singapore, 1986, p. 742.
34. R. J. Blin-Stoyle, Rev. Mod. Phys., *28*, 75, 1956; P. J. Brussaard and P. W. M. Glaudemans, Shell-Model Applications in Nuclear Spectroscopy, North-Holland, Amsterdam, 1977, p. 256.
35. A. Winnacker, unpublished results (1978), see in [10].

Acta Physica Hungarica 65 (2–3), pp. 305–313 (1989)

ON THE ROLE OF ANTI-BOUND STATES IN THE RPA DESCRIPTION OF THE GIANT MONOPOLE RESONANCE*

T. VERTSE

Institute of Nuclear Research of the Hungarian Academy of Sciences (ATOMKI)
4001 Debrecen, Hungary

P. CURUTCHET, R. J. LIOTTA

Research Institute of Physics, S-104 05 Stockholm, Sweden

and

J. BANG

The Niels Bohr Institute, University of Copenhagen, DK-2100 Copenhagen Ø, Denmark

The limit of the applicability of the resonant random phase approximation method is tested by calculating escape widths in the giant monopole resonance of ^{16}O and comparing them to the results of a time dependent Hartree–Fock calculation. Though the widths of the narrow s-wave component agree reasonably well, the broad p-wave component shows large disagreement, which cannot be cured by complementing the basis with anti-bound states in the RPA calculation.

Introduction

Considerable interest has focused recently on the decay properties of giant multipole resonances. This is induced mainly by the modern experimental techniques which opened a possibility for measuring the decay widths of the giant resonance into selected final states. The accumulation of experimental data has initiated a search for more convenient theoretical methods for calculating the parameters of the giant resonance. Since giant resonances are located at high excitation energies, they often decay by particle emission. Their width is composed of two important parts: the "escape width" $\Gamma^{\uparrow}$, which represents the coupling to the continuum, and the spreading width $\Gamma^{\downarrow}$ measuring the coupling to two-particle–two-hole and more complex configurations. In light nuclei the escape width exhausts a major part of the total width Γ therefore the proper treatment of the coupling of the giant resonance to the continuum is very important. The effect of the continuum is treated exactly in the coupled-channels calculations [1], in the continuum shell model [2] or in the time dependent Hartree–Fock calculations (TDHF) [3] all of them being tedious and offering little insight into the decay process. Since the giant multipole

*Dedicated to Academician D. Berényi on his 60th birthday.

resonance is described generally by using random phase approximation (RPA), different versions of the continuum RPA [4–7] can also be used but they share at least one of the disadvantages mentioned for the exact methods. In order to overcome these difficulties, a fast approximate method called "resonant RPA" (RRPA) has been proposed recently [8]. It has turned out to be especially very powerful for heavy nuclei, where the application of the other methods is extremely difficult. In the RRPA the single particle basis is composed of bound single particle states and single particle resonant (Gamow) states, and the completeness relation of Berggren [9] is used together with regularization methods for calculating the divergent integrals. The use of Gamow states takes care automatically of the possibility of the particle emission from the unbound particle states. Another advantage of the RRPA method is that after neglecting the effect of a complex continuum we deal only with discrete eigenstates of the single particle Hamiltonian therefore methods well known from nuclear structure calculations can be used. The price we pay for this convenience is that our method is an approximate one. The continuum itself has some sort of structure since it contains a background and several single particle resonances. Through the resonant basis states the RRPA includes the effect of the narrow resonances in the region of the giant resonance but not the slowly varying background. In this way the RRPA is able to describe a major part of the escape width and the fragmentation of the multipole strength i.e. the Landau damping and at the same time it opens certain insight into the building up and the decay of the giant resonance. The RRPA assumes that the giant resonance is based mainly on $1p$-$1h$ states where the particle is either bound or quasi-bound; i.e. the width of the single particle resonance is not very large. In most cases this assumption is satisfied due to the effect of the Coulomb or/and centrifugal barriers, and the results of the exact methods are well approximated by those of the RRPA calculations [8]. Therefore the RRPA proved to be a very powerful approximation which gives reliable estimate of the escape width, the structure and the fragmentation of the resonance if the assumptions of its applicability are fulfilled. An exception is the case of the giant monopole resonance (GMR) in ^{16}O calculated recently [10] using the TDHF method with very unrealistic assumptions, namely: by neglecting the spin–orbit and Coulomb interactions in order to speed up the calculation. In the ^{16}O a 0^+ state is composed of $1p$-$1h$ states of low orbital angular momenta (s and p) only. It is well known that low l resonances are very broad in the abscence of Coulomb barrier (see e.g. Table II). The condition of the applicability of the RRPA is clearly not fulfilled in this case, therefore a comparison of the results of the TDHF and RRPA methods offers a chance to check the limit of the applicability of the RRPA method. Another attractive feature of the calculation in [10] is that it offers a unique example for testing the importance of anti-bound states, since we can try to improve the RPA description by using anti-bound states if the RRPA fails.

We will generalize the RRPA by complementing the single particle basis with anti-bound states as well and call this approximation pole RPA (PRPA). Anti-bound states are the worst behaving pole solutions of a finite potential since they grow exponentially without oscillations as the distance from the origin increases. Therefore the regularization method of Zel'dovich [11] and the completeness relation

given by Berggren [9] cannot be used. Anti-bound states have been used earlier in the Mittag–Leffler expansion of the unit operator, the scattering amplitude and the Green's function for the case of simple model potentials [12]. But this is the first attempt to use anti-bound states in a somewhat realistic nuclear calculation and we hope to get valuable information about the importance of their contribution.

Table I

Comparison of the bound single particle energies of the static SCHF calculation for ^{16}O with those calculated by using the code GAMOW [18] in the SCHF potential. All energies are in MeV

n	l	E_{nl}(SCHF)	E_{nl}(GAMOW)
0	0	−32.160	−32.167
0	1	−18.034	−18.048
0	2	−2.170	−2.182
1	0	−0.357	−0.382

Table II

Energies of the single particle resonances and antibound states in the SCHF potential of [10]

n	l	Re(E_{nl})	Im(E_{nl})	n	l	Re(E_{nl})	Im(E_{nl})
2	0	8.32	−51.95	1	1	11.76	−29.81
3	0	32.97	−64.66	2	1	13.14	−52.63
6	0	56.07	−71.15	3	1	37.93	−70.27
7	0	78.91	−87.01	6	1	67.49	−83.98
9	0	−30.47	0.00	9	1	−2.62	0.00
4	0	−19.52	−16.16	5	1	−21.89	−14.49
5	0	−9.83	−35.08	4	1	−8.63	−33.01

In the next part we discuss the pole expansions of the unit operator and introduce another form of the completeness relation. We describe some details of the RRPA and PRPA calculations and present their results for the GMR in ^{16}O in the third part. Finally a summary and some concluding remarks are given in the last part.

Pole expansion of the unit operator

In the RPA calculation, where continuum effects are taken into account, one deals with 1p-1h configurations with continuous energies because the particle is in a scattering state. In an exact treatment of the problem we have to use the well-known completeness relation of Newton [13] where both the unit operator and the Green's function are expanded on a basis formed from all the bound and scattering states. The contribution of the scattering states is an integral for the wave number

k on the whole real axis and the most inconvenient feature of this method is that we have to discretize somehow the infinite k domain in order to be able to calculate this integral. There are methods for decreasing the importance of the continuum contribution by changing to a complex contour of integration on the complex k-plane (see e.g. in [14]). The goal is to get rid of the integral and keep a finite sum of pole terms. This can be achieved if we use a Mittag–Leffler expansion [12] where we have to restrict ourselves for a finite region of space centred at the origin, and the unit operator, or more precisely an operator that projects onto this space, is expanded on a discrete (infinite) set of solutions of a given Hamiltonian containing all pole solutions of the partial wave Green's function $G_l(k;r,r')$: bound states, anti-bound states, decaying and capturing resonances. In practice the basis should be truncated therefore the exactness is lost. The method is only valid for a finite region of the radial distance r and the basis is not an orthogonal one. Nevertheless it has the advantage that all integrals are finite therefore no regularization is needed.

Another form of the completeness relation, which is valid on an unlimited spherical region, was introduced by Berggren [9] who generalized the definition of the scalar product. An essential part of this generalization is that in bra position the complex conjugate of the radial wave function is to be used while there is no change in the spin-angular part. We will denote this operation with a tilde. He formed a biorthogonal set from bound states and two types of resonances (decaying and capturing ones) by using a regularization method [11] with Gaussian convergence factor. The resonances included in his set were selected by defining a curve $L = L^+ + L^-$ of the complex k–plane like the one shown in Fig. 1. The L contour is symmetric with respect to the origin i.e. if $k \in L^+$ then $-k \in L^-$ and its slope is limited by the condition: $\arg(k) > -\frac{\pi}{4}$. The completeness relation of Berggren states that

$$P_L = \sum_{lmn} |lmn\rangle\langle\tilde{lmn}| + \int_{L^+} |k\rangle d\overrightarrow{k}\langle\tilde{k}| \qquad (1)$$

acts as a unit operator in the space of all states $|\Phi\rangle$ in such a way that the radial component $h(r) = r < r, Y_{lm}|\Phi >$ goes asymptotically to zero faster than any exponential or behaves as e^{ikr} with k values lying above the contour L. The summation in Eq. (1) refers to all bound states and the selected set of decaying resonances with k_{ln} between L^+ and the real axis. The purpose of introducing the L contour is that we want to neglect the integral in Eq. (1) and use only the finite sum of the first term. We have a great flexibility in choosing the contour L, i.e. in deciding which are the resonances we include into the basis. On the other hand, we have only a limited amount of experience in deciding this. We know only that if there are narrow resonances in the region of our interest then they play an important role while the rest should have little effect on the results.

The peculiarity of the GMR studied in this work is the lack of narrow resonances due to the lack of potential barrier. (See Table II and Fig. 1) Therefore we have no chance to approximate the result of the TDHF calculation if we are not able to enlarge the basis considerably by including "unphysical" resonances with $-\frac{\pi}{2} < \arg(k_{ln}) \leq -\frac{\pi}{4}$. We can indeed include these resonances without any dif-

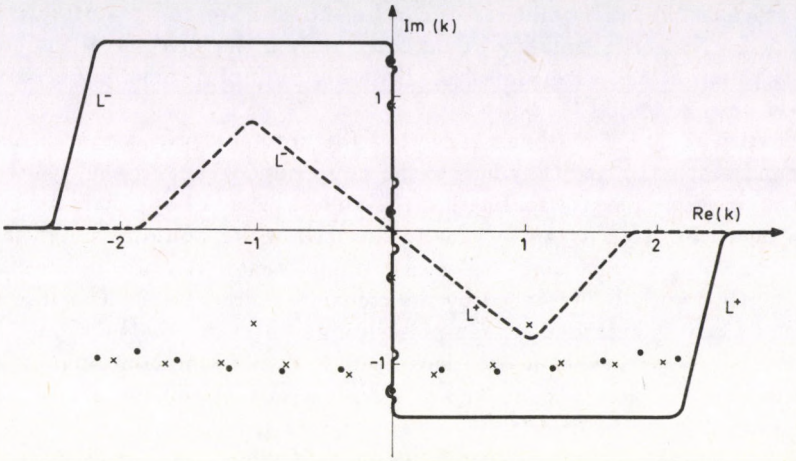

Fig. 1. Poles of the single particle Green's function on the complex k-plane for $l = 0$ (dots) and $l = 1$ (crosses) in the SCHF potential of [10]. Full and dashed lines are contours of integration for the completeness relations discussed in the text

ficulty since the restriction of $\arg(k) > -\frac{\pi}{4}$ was a consequence of the use of the Gaussian convergence factor in [9]. It was shown in [15] that any form of $\exp(-\epsilon r^p)$ can serve as convergence factor if $1 < p$ and all of them lead to the same result. Therefore the slope of L^+ can be increased so that $\arg(k) > -\frac{\pi}{2}$, and poles arbitrarily close to the negative imarinary k–axis can be included into the basis.

A natural next step would to be include anti-bound states into the basis as well but this cannot be done with using a convergence factor of any form. Nevertheless we can try to use another regularization method which was proposed first in [15] and became known later as "exterior complex scaling" [16]. In its simplest form the radial distance from the origin: r is rotated to the complex r–plane beyond some distance R_0:

$$r = \begin{cases} r & \text{for } r \leq R_0, \\ R_0 + |r - R_0| \exp(i\phi) & \text{for } r > R_0. \end{cases} \tag{2}$$

Let us restrict ourselves to nuclear potentials of finite range and assume that only point Coulomb potential is active at $r = R_0$. Then we should not bother about the dilation analyticity of the potential in the internal region: $r < R_0$. We can adjust the region in which the pole solutions are square integrable simply by changing the rotation angle ϕ. For example with $\phi \leq \frac{\pi}{2}$, $\phi \to \frac{\pi}{2}$ we achieve that all bound states and decaying resonances are square integrable and one can form a biorthogonal set from them. If we increase the rotation angle further, with $\phi > \frac{\pi}{2}$ all the anti-bound states and decaying resonances become square integrable and one can form a biorthogonal set from them. The question is if the anti-bound states are orthogonal or not to the bound states. One can show easily that an anti-bound state is orthogonal to all the deeper lying bound states. The orthogonality of an anti-

bound state to the less bound states can be shown if we apply a complex rotation with $\phi > \frac{\pi}{2}$. Non-orthogonality would occur only if the energies of the bound and the anti-bound states were identical. But this kind of degeneracy occurs only in infinitely deep potential.

Several recipes have been suggested for normalizing resonances [9, 15] and anti-bound states [12] and they lead to the same value whenever they can be applied [17]. The exterior complex scaling has the widest range of applicability but in this work a closed form [15] was used due to the lack of the Coulomb potential.

In the PRPA calculation we used a completeness relation of the form given in Eq. (1) but with L^+ replaced by the contour $\mathcal{L}^+$ of Fig. 1. The summation in the first term was extended to the poles lying above and to the right of $\mathcal{L}^+$. As we discussed above these pole solutions $|lmn>$ form a biorthonormal basis. In the RRPA calculation the $\mathcal{L}^+$ contour was modified so that the two anti-bound states were excluded from the basis.

RRPA and PRPA calculations

Since we wanted to compare the results of our RPA approaches to that of the TDHF calculation [10] we tried to use the same parameters as far as it was possible. The potential in which the single particle basis states were calculated was the one produced in the SCHF calculation at $t = 0$. It was done by using the $t_0 - t_3$ density dependent Skyrme interaction [3] of the form:

$$V(\vec{r}_1, \vec{r}_2) = \left[t_0 + \frac{1}{6} t_3 \rho \left(\frac{\vec{r}_1 + \vec{r}_2}{2}\right)\right] \delta\left(\vec{r}_1 - \vec{r}_2\right), \tag{3}$$

where $t_0 = -1000$ MeV fm^3 and $t_3 = 15000$ MeV fm^6 are the parameters of the force and ρ is the self-consistent density. The normalized basis functions were calculated by using the external potential option of the code GAMOW [18]. By adjusting the reduced mass, good agreement has been achieved between the bound state energies calculated with the code GAMOW and those produced by the SCHF calculations as one can see in Table I. The complex energies of the anti-bound states and resonances are listed in Table II, where n is not the number of nodes any more but a sequence number of the pole used only for identification purpose. Due to the lack of spin-orbit and Coulomb potentials, $l = 0$ states are twice, $l > 0$ states are four times degenerate. In order to describe a GMR, the particle wave functions were expanded on the $l < 2$ unoccupied single particle states and by combining them with the $(0s)^{-1}$ and $(0p)^{-1}$ hole states $1p$-$1h$ configurations were formed. In the RRPA 38 unperturbed $1p$-$1h$ states were formed from the states whose energies are listed in Table I and Table II (except the two $n = 9$ anti-bound states) while in the PRPA all states with energies shown in Table II were used and 44 unperturbed $1p$-$1h$ states were formed. The RPA calculations were carried out by using the density dependent interaction of Eq. (3), in which the density was the self-consistent density of the SCHF calculation at $t = 0$.

Table III
Position and full width of the s and p component of the GMR in ^{16}O produced by different theories. All energies are in MeV

Theory	E_s	Γ_s	E_p	Γ_p
TDHF	33.00	2.50	24.5	12.0
RRPA	33.57	2.22	25.8	115.0
PRPA	33.54	2.40	26.2	115.0

The form of our RPA equations is similar to the one obtained within a bound representation

$$\begin{pmatrix} A & B \\ -B & -A \end{pmatrix} \begin{pmatrix} X_n \\ Y_n \end{pmatrix} = \omega_n \begin{pmatrix} X_n \\ Y_n \end{pmatrix}, \tag{4}$$

where ω_n is the energy, the X_n and Y_n are the forward and backward amplitudes in the n-th eigenstate. The matrix elements of the matrices A and B are calculated with the $1p$-$1h$ states mentioned above. Details of the calculations are given elsewhere [8], here we only note that the interaction of Eq. (3) leads to the radial integrals to be calculated:

$$I_{pqrs} = \mathrm{Reg} \int_0^\infty r^2 \, dr \; R_p(r) R_q(r) v(r) R_r(r) R_s(r) \tag{5}$$

with

$$v(r) = \begin{cases} 1 \\ \rho(r) \end{cases}, \tag{6}$$

where $R_i(r)$ and Reg denote the radial part of the single particle wave function and an appropriate procedure for regularizing the divergent integral, respectively. Though it is always possible to regularize this integral by rotating r with an appropriate ϕ angle, one cannot define a common ϕ value in the case of PRPA which would be suitable for all possible combination of ph states. In order to avoid the inconvenience of selecting different ϕ angles for each combination of ph states, we simply cut off $v(r)$ beyond R_0 while calculating the radial integrals.

Since the ph energies and the radial integrals are generally complex, the ω_n eigenenergies and the X_n and Y_n amplitudes in the corresponding eigenfunction will also be complex. In the spirit of the Berggren theory we consider the imaginary part of the results as a measure of the uncertainty of the quantity characterized by the real part. For example in the case of the energy of the correlated state:

$$\omega_n = E_n - i \frac{\Gamma_n}{2} \tag{7}$$

E_n gives the position and Γ_n the width of the n-th state. Since in this level the RPA cannot account for decaying into $2p$-$2h$ or more complicated configurations, Γ_n should be compared to the sum of the escape width and the Landau damping calculated by the TDHF calculation.

In Table III we compare the results of the TDHF, the RRPA and PRPA calculations. The main features of the TDHF results are reproduced qualitatively, namely that the GMR is composed of two parts: a narrow peak by around 33 MeV based mainly on the $(0s)^{-1}1s$ configuration (97 % according to the RPA) and a broad bump separated from the s peak about 9 MeV, built up mainly from $l = 1$ configurations. Though the positions of the peaks and the width of the narrow s component are reasonably well reproduced by both RRPA and PRPA, the width of the p component is seriously overestimated (by almost one order of magnitude). This huge disagreement clearly shows the deficiences of our RPA approaches even if we have no information about the uncertainty of the TDHF result, which could also be considerably large for a resonance of short lifetime, where even the validity of the exponential decay law could be questioned.

On the other hand the fact that the features of the $l = 0$ peak are well reproduced shows that both RRPA and PRPA have some predicting power. The inclusion of anti-bound states brought the results somewhat closer to those of the TDHF calculation but their contributions were small.

The identification of the main components of the GMR was done by studying the values of the isoscalar energy weighted sumrule (EWSR): S_c for the operator $r\frac{\partial V}{\partial r}$ with the V of Eq. (3). The EWSR selected three of the correlated states in the energy range 15–40 MeV for which the S_c is considerably enhanced. These were the two states listed in the Table III and a third one at $\omega_n = (23 - i35)$ MeV having $l = 0$ character. Nevertheless this structure could not be resolved in the TDHF description because of the large overlapping with the p component.

Conclusion

A limit of the applicability of the RRPA was reached when its result was compared to that of the TDHF description of the GMR in ^{16}O, where Coulomb and spin–orbit interactions were not taken into account. We thought that the inclusion of the effect of anti-bound states could perhaps decrease the discrepancies between the two descriptions. Therefore we have generalized the completeness relation of Berggren and by using this formed a new RPA approach that we called PRPA in which the single particle basis was complemented with anti-bound states. Repeating the calculations with the PRPA we observed some improvement, which showed that the anti-bound states have a non-negligible contribution in the RPA description of the GMR but their importance is small altogether. It was interesting to observe that the known property of the RPA EWSR namely: that the total values of the uncorrelated and correlated EWSR coincide, is satisfied even in the case of the PRPA.

Acknowledgement

The authors are greatly indebted to Drs T. Berggren, J. M. Pacheco, B. Gyarmati and R. G. Lovas for valuable discussions. One of the authors (T. V.) whishes to thank the NORDITA for the financial support and The Niels Bohr Institute for the hospitality and good working conditions he enjoyed in Copenhagen.

References

1. B. Buck and A. D. Hill, Nucl. Phys., *A95*, 271, 1967.
2. C. Mahaux and H. A. Weidenmüller, Shell model approach to nuclear reactions, North Holland, Publ. Comp., Amsterdam, 1969.
3. S. Stringari and D. Vautherin, Phys. Lett., *88B*, 1, 1979.
4. S. Shlomo and G. Bertsch, Nucl. Phys., *A243*, 507, 1975.
5. G. Co and S. Krewald, Nucl. Phys., *A433*, 392, 1985.
6. R. De Haro, S. Krewald and J. Speth, , Nucl. Phys., *A388*, 265, 1982.
7. Nguyen Van Giai, P. F. Bortignon, F. Zardi and R. Broglia, Phys. Lett., *199B*, 155, 1987.
8. T. Vertse, P. Curutchet, O. Civitarese, L. S. Ferreira and R. J. Liotta, Phys. Rev., *C37*, 876, 1988.
9. T. Berggren, Nucl. Phys., *A109*, 265, 1968.
10. J. M. Pacheco, E. Maglione and R. A. Broglia, Phys. Rev., *C37*, 2257, 1988.
11. Ya. B. Zel'dovich, ZhETF(USSR) 39, 766, 1960, JETP(Sov. Phys.), *12*, 542, 1961.
12. J. Bang, F. A. Gareev, M. H. Gizzatkulov and S. A. Goncharov, Nucl. Phys., *A309*, 381, 1978.
13. R. G. Newton, J. Math. Phys., *1*, 319, 1960.
14. W. J. Romo, Nucl. Phys., *A398*, 525, 1983.
15. B. Gyarmati and T. Vertse, Nucl. Phys., *A160*, 523, 1971.
16. B. Simon, Phys. Lett., *71A*, 211, 1979.
17. T. Vertse, P. Curutchet and R. J. Liotta, Proceedings of the Symposium on "Resonances — the unifying route towards the formulation of dynamical processes", Wärmland, Sweden, Aug. 19–26, 1987, Springer Verlag, to be published.
18. T. Vertse, K. F. Pál and Z. Balogh, Comput. Phys. Commun., *27*, 309, 1982.

Acta Physica Hungarica 65 (2–3), pp. 315–322 (1989)

WHAT HAPPENED TO THE IRON IN THE SUN?*

GEORGE MARX

Department of Atomic Physics, Roland Eötvös University
1088 Budapest, Hungary

and

DAVID S.P. DEARBORN

Lawrence Livermore National Laboratory, University of California
Livermore, USA

> For me, the solar neutrino experiment was thrilling. It's inspiring that nature is doing something mysterious, that is to say, something we don't understand. We all feel that the Sun is telling us something important. And this experiment was the means of communicating with the Sun's center. There is always a sense of gratitude when a new truth is being revealed. It's almost spiritual. It's as if the performer of the experiment were a prophet, going to the mountain wilderness in search of a message from God. And the message came from this god, the Sun, and said: "You do not understand me."
> (Donald D. Clayton: The Joshua Factor, 1986)

If the mixture of hydrogen and iron is hot enough for an almost complete ionization of iron, and at the same time it is cool and dense enough to produce polarization of the electron sea around the iron ions, the Debye–Hückel approximation predicts separation of an iron-rich phase from the hydrogen-rich phase. The necessary conditions of this separation are fulfilled for most of the solar interior. The precipitation of iron towards the solar center may result in the formation of an inactive core (rich in heavy elements) at the center of the Sun, as it has been postulated to explain some observed anomalies in the non-radial g-mode oscillations. The depletion of the heavy elements from the highly ionized regions of the Sun reduces the opacity by 15–30 percent, decreases the central temperature by half a million K, and thus suppresses the most energetic component of the solar neutrino flux, coming from the Boron decay. For a chlorine detector, the estimated neutrino signal is decreased considerably with respect to the Standard Solar Model prediction, for a gallium detector it remains practically unchanged.

Nuclear fusion of the solar hydrogen goes via the reaction chain:

$$p + p \rightarrow D + e^+ + \nu\,, \qquad (p + e^- + p \rightarrow D + \nu < 1\%\,),$$
$$p + D \rightarrow {}^3\mathrm{He} + \gamma,$$
$${}^3\mathrm{He} + {}^3\mathrm{He} \rightarrow {}^4\mathrm{He} + p + p\,.$$

*Dedicated to Academician D. Berényi on his 60th birthday

In the case of considerable He admixture the last reaction competes with the reaction

$$^3\mathrm{He} + {}^4\mathrm{He} \rightarrow {}^7\mathrm{Be} + \gamma \ .$$

^{7}Be may capture an electron (slow weak process):

$$e^- + {}^7\mathrm{Be} \rightarrow {}^7\mathrm{Li} + \nu, \qquad p + {}^7\mathrm{Li} \rightarrow {}^8\mathrm{Be} \rightarrow {}^4\mathrm{He} + {}^4\mathrm{He} \ ,$$

or it may capture proton (by tunnelling through high Coulomb barrier):

$$p^+ + {}^7\mathrm{Be} \rightarrow {}^8\mathrm{B} \rightarrow {}^8\mathrm{Be} + e^+ + \nu, \qquad {}^8\mathrm{Be} \rightarrow {}^4\mathrm{He} + {}^4\mathrm{He} \ .$$

The total outcome is anyway

$$2e^- + 4p^+ \rightarrow \mathrm{He}^{++} + 2\nu + 24.6 \text{ MeV} \ .$$

Dividing the observed solar luminosity $L_\odot = 3.86 * 10^{26}$ watt by 12 MeV one gets the neutrino current originating at the Sun. The current density at the Earth turns out to be $8 * 10^{14} \nu \mathrm{m}^{-2} \mathrm{s}^1$. To catch the solar neutrinos, Ray Davies has used a chlorine target:

$$\nu + {}^{37}\mathrm{Cl} \rightarrow {}^{37}\mathrm{A} + e^-, \qquad {}^{37}\mathrm{A} \rightarrow {}^{37}\mathrm{Cl} + e^+ + \nu \ .$$

The Standard Solar Model [1, 2] predicts a rate of about 6+1.5 SNU. (1 SNU=1 Solar Neutrino Unit=10^{-36} capture/atom/s.) The observed capture rate, 2.07±0.25 SNU [2] is incompatible with the Standard Model.

This disagreement was the starting point of many investigations [3]. New neutrino interactions were postulated; this, however, introduced arbitrary parameters into the calculations. The observed neutrino flux of the SN1987A has nevertheless indicated a high degree of neutrino stability. Making the Sun dramatically time dependent could offer a chance to suppress the neutrino flux temporarily, but the variation in time would prevent any unique theoretical prediction. The aim of this paper is to call the attention to the possibility, that simply by making the Solar Model more accurate, one can get neutrino capture rates more compatible to the observed value *without* introducing any new arbitrary parameter.

The energy threshold for neutrino capture by chlorine is high (0.81 MeV), the cross section increases steeply by energy, consequently the main contribution (4.7 SNU) to the expected capture rate (~6 SNU) comes from the decay of ^{8}B (max E_ν=14 MeV) [4]. The formation of ^{8}B is possible only by the tunnelling of the proton through the high Coulomb barrier of ^{7}Be. Under solar conditions ($T \sim 10^{10}$K, $kT \sim 1$ keV) this reaction is strongly suppressed (below 0.02%). Due to the extreme energy sensitivity of the Gamow tunnelling ($\sim T^{20}$) a decrease of the central solar temperature just by 5% would suppress the formation of ^{8}B by 65% (below 1.7 SNU), which could give an acceptable overall capture rate.

The temperature profile within the Sun is given essentially by

$$-dI/dr = \kappa\rho(r) \ P(r) \ /4\pi r^2 \ ,$$

where $I \sim T^4$ is the density of the energy current of the radiation, and $P(r)$ is the nuclear power liberated in a sphere of radius r. This means that the temperature gradient is proportional to the opacity κ. Starting from the solar surface of known temperature, a reduced opacity would result in lower central temperature.

At solar temperatures H and He are fully ionized. Free–free transitions absorb photons less intensively than bound–bound or bound–free transitions, therefore an important contribution to the opacity comes from the incompletely ionized heavier atoms like Fe. Elimination of Fe from the solar interior may decrease the opacity by 15–30% which can explain the reduction of the central temperature. This leads us to the question: How soluble is the iron in the Sun?

For the majority of the solar material Fe is ionized to Fe^{16+} and Fe^{24+}. These highly charged ions exert a polarizing effect in the sea of free electrons. To treat the Sun as an *almost* ideal gas we shall take this effect into account in first order of the Debye–Huckel approximation. The electric potential U can be described by

$$\nabla^2 U(r) = -\rho/\varepsilon_0 = -\sum_z (Ze/\varepsilon_0)\, n_z(r) \ ,$$

with

$$n_z(r) \sim \exp[-ZeU(r)/kT] \ ,$$

therefore in linear approximation

$$\nabla^2 U(r) = -(e/\varepsilon_0) \underline{\sum Z n_z(\infty)} \, [1 - (Ze/kT)\, U(r) + \ldots] \ .$$

Due to the macroscopic neutrality of the plasma, the underlined sum vanishes. The remaining linear equation has a Yukawa-type solution around the Fe ion:

$$U(r) = (Ze/4\pi\varepsilon_0)\ \exp(-r/r_0)/r = (Ze/4\pi\varepsilon_0)(r^{-1} - r_0^{-1}) + \ldots$$

(in linear approximation). The average potential of the screening charges ($U_0 = -Ze/4\pi\varepsilon_0 r_0$) leads to a Coulomb energy density in the plasma:

$$E_C/V = 0.5 \sum_z Z e n_z(\infty) U_0 \ .$$

When the energy, the pressure and the Gibbs free energy are calculated for the *almost ideal gas* , this term has to be taken into account as well beside the kinetic terms of the ideal gas approximation. If one plots the Gibbs free energy in terms of Fe concentration, the ideal gas mixing terms is concave from below, the Coulomb correction is, however, convex. The resulting curve (Fig. 1) has a double tangent for a wide range of temperature and density. The Gibbs free energy curve running

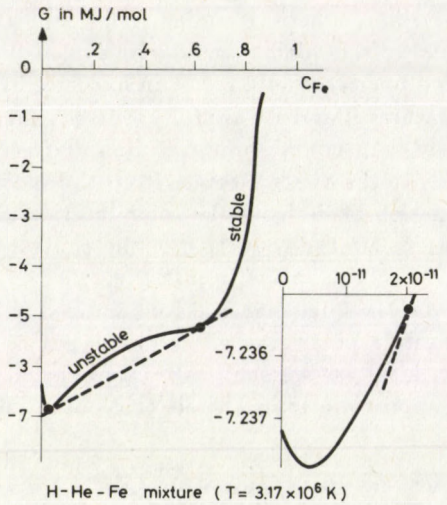

Fig. 1. Gibbs free energy versus iron concentration

above the double tangent indicates an instable region in which phase separation occurs.

This separation has been described by Pollock and Adler [5,6], and their conclusion has turned out to be rather model independent, as shown by Ruff and co-workers in a series of papers [7,8]. The approximations got critical remarks from Pitzer (concerning the negativity of the pair correlation functions [9]), from Iyetomi and Ichimaru (stressing the polarization of the ionic background in the binary ionic mixture [10]). A more detailed calculation has shown, however, that negative pair correlation function can be avoided, the polarization effect on the ions is small compared to that on the electrons, thus the original statement has been confirmed [11]: highly charged ions (like Fe) are practically insoluble in the solar plasma.

What happens to the separated iron droplets? They are in temperature and pressure equilibrium with their H–He rich environment, but their specific weight is much higher, their opacity is much larger. Detailed calculations indicate [11] that the downward weight ($\sim10^8$N/m) exceeds the upward directed radiation push ($\sim10^3$N/m) by orders of magnitude. This means that the heavier elements precipitate from the internal solar plasma and form an "iron core" at the center of the Sun, of the size of a few per cent of the solar radius.

The existence of an iron core with $r\sim0.05r_\odot$ has been postulated by C. A. Rouse, based upon the consistency of the stellar structure solutions [12]. Such a dense core may explain the discrepancies found in the frequencies of the g-mode oscillations. (The non-radial vibrations are quite sensitive to the internal structure [13,14].)

In the upper layers Fe is not so heavily ionized, it remains soluble, therefore the solar surface shows the cosmic Fe abundance ($7.3*10^{-4}$). The solubility drops

Table I
Hydrogen distribution (%) inside the Sun

Mass fraction	Model 1 Standard	Model 2 15% reduction	Model 3 15% reduction, core	Model 4 30% reduction
0	37.8	41.0	0	43.8
0.001	38.7	41.9	0	44.6
0.002	39.7	42.8	41.9	45.0
0.003	40.5	43.6	42.7	46.3
0.004	41.1	44.1	43.4	46.9
0.005	41.6	44.7	44.0	47.4
0.01	43.8	46.8	46.3	49.6
0.05	53.5	54.6	56.2	59.2
0.10	59.7	62.6	62.7	65.6
0.15	63.9	66.7	66.9	69.8
0.20	66.8	69.6	69.7	72.6
0.25	68.6	71.4	71.6	74.5
0.3	70.0	72.8	73.0	76.0
0.4	71.7	74.5	74.7	77.6
0.5	72.4	75.3	75.5	78.4
0.6	72.8	75.7	75.9	78.0
0.7	73.0	75.9	76.1	70.0
0.8	73.1	76.0	76.2	79.1
0.9	73.1	76.0	76.2	79.1
1	73.1	76.0	76.2	79.1

practically to zero for $r < 0.85 r_\odot$. (It is calculated to be $5*10^{-6}$ for $r = 0.8 r_\odot$ where Fe^{16+} is present. It is 10^{-14} at $r = 0.2 r_\odot$ because of Fe^{24+}.) By making the modest assumption that iron is practically eliminated for $T > 3$ million K, the Livermore code indicates a drop of 15–30% in the opacity. In this way, solar models can be obtained which give the observed luminosity ($L_\odot$) and age ($t_\odot = 4.55 * 10^9$y). We have started with the standard model of Rodger Ulrich (Model 1). Then we have reduced the opacity by 15% for $T > 3$ million K (with lesser reduction between 1 and 3 million K, Model 2). One can calculate the case of the inert iron core as well, which has been formed by the phase separation of the heavy elements in the regions being hotter than 3 million K keeping the 15% reduction of opacity. (As a matter of fact, to simplify the computation in the Model 3, the innermost 0.15% of the solar material — corresponding to 1.8% of the solar radius — was postulated to be He, which excludes fusion reactions at the core, thus it imitates the iron core.) Finally, we repeated the calculation of Model 2 with 30% reduction of the opacity for $T > 3$ million K (with a transient region of smaller reduction, Model 4). The main conclusions of the four models are summarized in the Table I (hydrogen distributions) and in the Table II (temperature distributions). We see that the outcomes of the Models 2 and 3 are similar, the inert core does not have a large influence.

Fig 2 shows the temperatures and hydrogen concentrations in the central region. (In outer regions the differences between the models are smaller.) To get the luminosity $L_\odot$ at the time $t_\odot$, the almost ideal gas model — with its lower central temperature — needs more hydrogen.

Table II
Temperature distribution inside the Sun (million K)

Mass fraction	Model 1 Standard	Model 2 15% reduction	Model 3 15% reduction, core	Model 4 30% reduction
0	15.417	15.031	14.825	14.689
0.001	15.346	14.962	14.825	14.622
0.002	15.205	14.859	14.825	14.521
0.003	15.136	14.757	14.757	14.421
0.004	15.066	14.689	14.723	14.388
0.005	14.997	14.655	14.655	14.322
0.01	14.757	14.387	14.421	14.093
0.05	13.489	13.183	13.213	12.912
0.10	12.473	12.218	12.218	11.940
0.15	11.641	11.402	11.402	11.119
0.20	10.914	10.690	10.690	10.520
0.25	10.328	10.116	10.139	9.931
0.3	9.772	9.572	9.572	9.376
0.4	8.750	8.551	8.551	8.414
0.5	7.816	7.656	7.656	7.534
0.6	6.871	6.778	6.778	6.668
0.7	5.984	5.878	5.878	5.794
0.8	5.012	4.920	4.920	4.853
0.9	3.828	3.749	3.741	3.698
1	0.006	0.006	0.006	0.006

Instead of the standard $x(0) = 73\%$ the Sun has to start with larger initial hydrogen concentration $x(0) = 76 - 79\%$ (which is still compatible with the spectroscopic evidence). The temperature distributions in the central region are shown for the different models on Fig. 2.

The predicted neutrino capture rates for Cl and Ga targets are summarized in Table II. For the chlorine target the decreased opacity model gives a value at about 3 SNU which does not differ significantly from the measured neutrino signal (Fig. 3, [15,16]).

In case of a Ga target the threshold is so low (0.236 MeV) that almost 70% of the expected neutrino capture rate is due to the *pp* and *pep* neutrinos which are unaffected by the decreased temperature. The model — presented here – confirms the expectation of a high capture rate (at about 100 SNU) in the Ga experiment. (This is in contrast with other theories, where for a wide range of the new parameters both the Cl and the Ga signals are suppressed.)

Table III
Expected capture rates (in SNU=10 capture/atom/s units)

Target	Model 1 Standard	Model 2 15% reduction	Model 3 15% reduction, core	Model 4 30% reduction
Chlorine	5.44	3.55	3.44	2.54
Gallium	121	107	106	

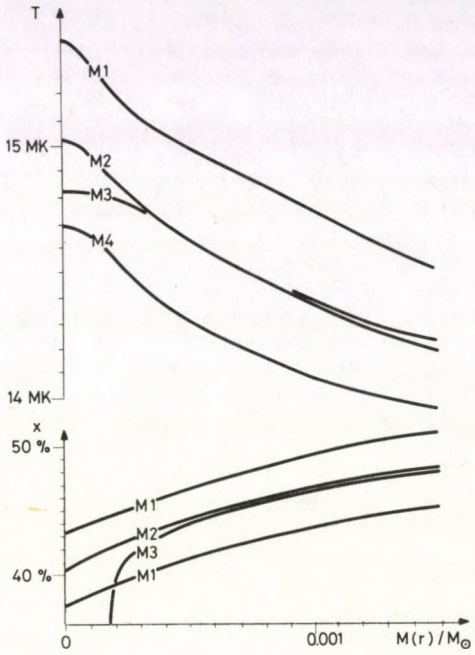

Fig. 2. Temperature and hydrogen distribution in the central region

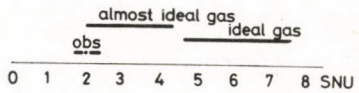

Fig. 3. Observed and expected neutrino signal in chlorine target

Acknowledgement

The authors are indebted to Prof. R. Mössbauer for his enlightening critical remarks.

References

1. See e.g. J.N. Bahcall, Rev. Mod. Phys., *50*, 881, 1978.
2. R. Davies, Proc. Underground Physics, Baksan, USSR , 1987. ed. by Y. Zatsepin, Moscow, 1988.

3. See the review of G. Marx, in "Sun and Planetary Systems", ed. by W. Fricke and G. Teleki, D. Reidel, New York, 1982.
4. G. Marx and N. Menyhárd, Mitteilungen der Sternwarte Budapest, 44, 1960.
5. E.L. Pollock and B.J. Adler, Nature, *275*, 41, 1978.
6. B.J. Adler, E.L. Pollock and J.P. Hansen, Proc. Nat. Acad. Sci., *77*, 6272, 1980.
7. I. Ruff, J. Liszi and K. Gombos, Astrophys. J. *289*, 409, 1985.
8. I. Ruff and J. Liszi, Chem Phys. Letters, *116*, 335, 1985.
9. K.S. Pitzer, Proc. Nat. Acad. Sci., *77*, 3103, 1980.
10. H. Iyetomi and S. Ichimaru, Phys. Rev., *A34*, 3203, 1986.
11. I. Ruff, G. Marx and D. Dearborn, Astronomy and Space Science, 1988.
12. C.A. Rouse, Astron. Astrophys., *126*, 102, 1983.
13. C.A. Rouse, Astron. Astrophys., *149*, 65, 1985.
14. C.A. Rouse, Solar Physics, *106*, 217, 1986.
15. G. David, G. Marx and I. Ruff, Proc. Neutrino '84, ed. by K. Kleinknecht, 1984.
16. D.S.P. Dearborn, G. Marx and I. Ruff, Progr. Theor. Phys., *77*, 12, 1987.
17. G. Marx, Proc. Underground Physics, Baksan, USSR, 1987, ed. by Y. Zatsepin, Moscow, 1988.

Acta Physica Hungarica 65 (2–3), pp. 323–329 (1989)

SEARCHING FOR MONOPOLES IN LAKE BAIKAL*

G.V. DOMOGATSKY, P. KAKAS, S. FEHÉR and D. KISS

Central Research Institute for Physics
1525 Budapest, Hungary

This paper reports on the results of the 50-day operation of a stationary monopole search instrument installed in Lake Baikal in April 1986. An upper limit was estimated for the intensity.

Long-term physical experiments started at Lake Baikal [1], with the aim of:

1 – detecting high energy cosmic neutrinos;

2 – searching for relativistic magnetic monopoles [2];

3 – searching for super-heavy slow magnetic monopoles [3,4].

In order to realize the above aims a special technique was elaborated which required that a large number of photomultipliers be sunk in Lake Baikal to a depth of about 1300 m and that the Čerenkov radiation generated by the electrically charged particles be detected. Čerenkov radiation may be generated by relativistic charged particles (muons) originating from the interaction of high energy neutrinos or by the products of proton decay accelerated by monopoles. Thus the water of the lake is used for two tasks: it acts as the target material of the interaction and as the working material of a large Čerenkov detector. The water layer of about 1000 m over the instrument serves to substantially reduce the cosmic background. The most suitable period for installation is March when optical sensors fixed to the carrying cable were lowered into the water of the lake through a hole in the ice of about 1×1 m. The detector system is held in position at the bottom of the lake with an anchor and the upper part of it is kept extended by means of buoys (Fig. 1).

The buoys are located 15 m beneath the surface of the water so as to eliminate the disturbing effect caused by waves. The device is located at the southwest part of Lake Baikal at about 50 km from the Institute for Limnology (Fig. 2).

In spring the thickness of the ice reaches 70–80 cm, thus it is both convenient and safe to drive on it. Ice is needed only at the time of installation; due to the anchor and the buoys the system is able to provide data all the year round for the computer station on the shore (about 5 km away).

It is a fact that the utilization of the water of the lake substantially decreases the costs of the experiment — being available in practically unlimited quantity and cost-free. However, the calculation of the fiducial volume (acceptance) from which the light can still be detected by the detector system with good efficiency is rather complicated.

*Dedicated to Academician D. Berényi on his 60th birthday

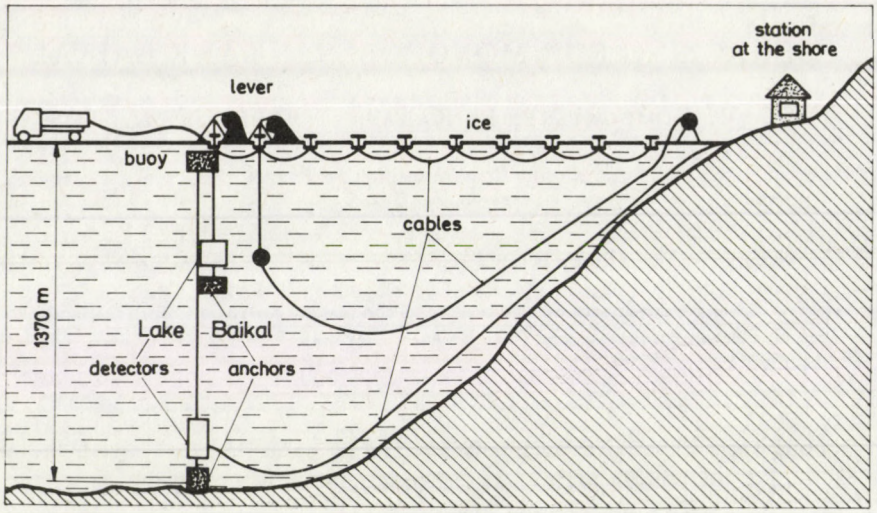

Fig. 1. Installation of the SMSS in Lake Baikal and electronic connection with the shore

The water of the lake is well-known for its cleanliness and pellucidity for one is able to see as far down as 30–40 m some places. At the same time one has to add that pellucidity is better near the shores of the Hawaiian Islands where American scientists have installed a similar system.

We installed — as a preliminary experiment — a short stationary string (SSS) in 1984 that operated for 50 days [5]. The experience gained has demonstrated that our plans relating to long term measurements carried out with a detector of much greater volume are realistic.

In April 1986 a stationary monopole search string (SMSS) of greater size was located in Lake Baikal (Fig. 3). This SMSS contained 36 FEU-49 type Soviet photomultipliers of 15 cm diameter.

The SMSS consists of seven independent detectors; 6 of these contain 24 photomultipliers and the 7th detector contains the other 12. This latter detector represents the telescope by which muons of atmospheric origin, cosmic showers, and muons originating from neutrino interactions and coming upwards, can be detected. Relativistic monopoles are also sought by this detector. The basic task of the other six detectors is to search for super-heavy slow monopoles.

The signals of the SMSS are due to be processed as follows. Each detector contains a trigger system that enables data to be stored in an electronic module (Fig. 3). Any detector can be connected to the data transfer cable through a commutator under the water by means of instructions from the computer centre on the shore. The information stored in the chosen detector, the pulse-frequency of certain multipliers, and the results of various tests can be transferred to the shore on the request of the shore-based computer. After interrogation, the electronic system

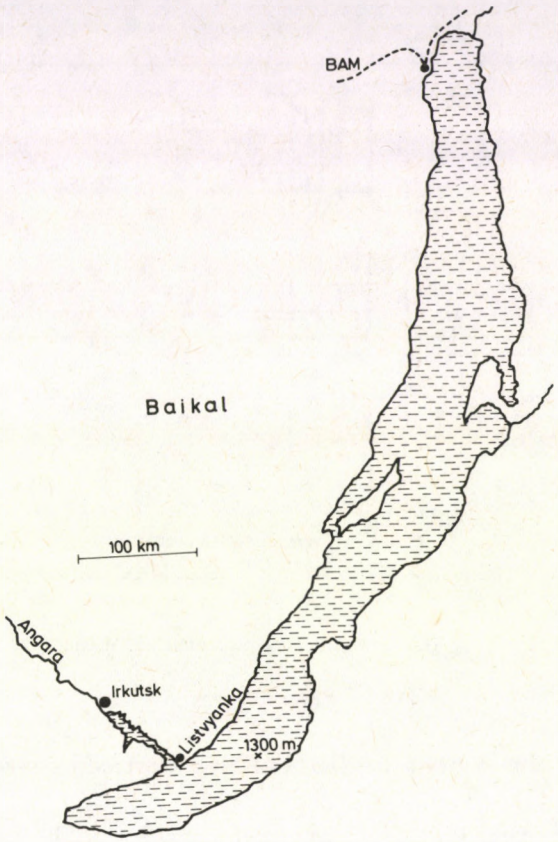

Fig. 2. Sketch map of Lake Baikal showing the location of the experiment

of the detector is reset to the normal position.

The telescope mentioned earlier contains 6 photomultiplier modules and a common electronic module (Fig. 4).

Each optical module has two photomultipliers looking in opposite directions. The power supply of the telescope, the discriminators, the trigger-system, the time and amplitude analysers, the memory, and the circuits for the data transfer are all to be found in the electronic module. There are three different trigger-conditions for the telescope that can be set by a command from the shore. These are:

1 – if two optional photomultipliers respond at the same time within $0.5\mu s$;
2 – if two of the three photomultiplier-pairs looking downwards give signals at the same time within $0.5\mu s$;
3 – if all the three pairs looking downwards give signals at the same time within $0.5\mu s$.

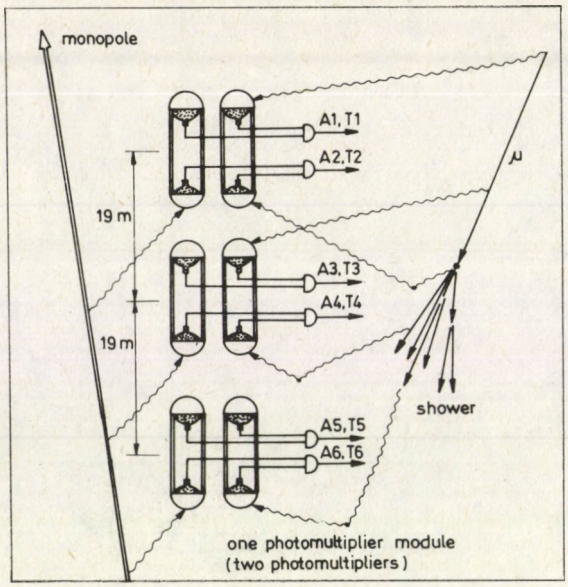

Fig. 3. Telescope with six photomultiplier modules

The most essential measurements that can be performed by means of the telescope are as follows:

1 – Relativistic particles — such as muons ($\beta = \frac{v}{c} > 0.75$) originating from neutrino interaction or from relativistic magnetic monopoles — moving upwards can be recorded. These monopoles — if they exist at all — have a mass smaller than 6×10^{10} GeV and the galactic magnetic fields can accelerate them to an energy higher than 10^{20} eV [6]. Their energy loss is smaller than 10 GeV·cm^2 · g^{-1} [7]. The most problematic background for the muons and monopoles going upwards are showers that are generated below the telescope by muons going downwards.

2 – The pulse rate generated by radiation muons can be measured and, based on the results, the space- and time-dependence of the optical characteristics of Baikal's water can be studied.

3 – The variation of the luminescence of water can be measured. For this purpose the pulse rate of the photomultipliers is measured periodically.

The other six monopole detectors on the string each have two multiplier modules and independent electronic units, including the power supplies of the detectors, the discriminators, the event selector logic necessary for the selecting of super heavy monopoles as well as the memory and the necessary communication circuits.

The most important possible reaction for detecting super heavy slow mono-

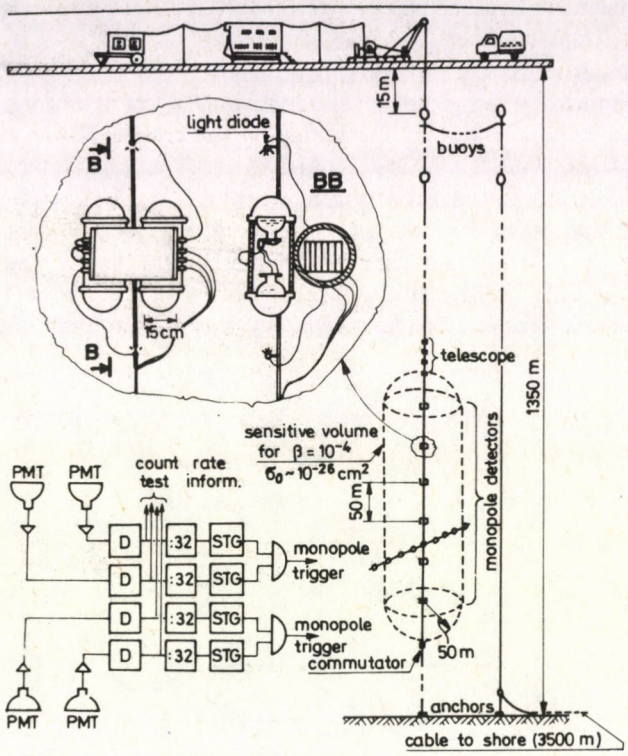

Fig. 4. Arrangement of the electronics
D — low level discriminator
STG — slidable time gate
:32 frequency distributor
PMT — photomultiplier tube

poles can be the following:

$$\text{Mon} + p = \text{Mon} + e^+ + \text{pions}.$$

If such a monopole passes alongside the device, then the pulse rate of the photomultipliers must be higher. The duration of the higher pulse rate depends on the velocity of the monopole. The maximum sensitivity of the present detector falls into the $\beta = 10^{-5}$–10^{-3} velocity range. It constitutes a trigger event if the pulse rate of any two multipliers looking in the same direction increases simultaneously during 0.5 ms. The trigger condition is fulfilled by the electronic system (Fig. 3.). The threshold level of the discriminator is set for 0.3 photoelectron. Simultaneously, further information on the velocity and direction of the movement of the monopole is recorded. The monopole detectors are calibrated by a special flash tube placed

50 m from them, and the electronics is checked by light-emitting diodes that can be controlled from the shore.

In contrast to similar measurements carried out underground, where acceptance is determined by the geometrical dimensions of the detectors, the SMSS acceptance for slow monopole flux is determined by the cross-section of the proton decay catalysed by them. The SMSS is equipped to give the most interesting information on the monopole flux in the velocity range $\beta = 10^{-5} \ldots 10^{-3}$. Then $\sigma_c = 0.17 \cdot \beta^{-2}$ [8], assuming that $\sigma_0 \approx 10^{-28}\text{cm}^2$, this being otherwise an acceptable estimation.

During the 50-day operation of the instrument not a single monopole was detected by the SMSS. From this an upper limit with a confidence level of 90% can be given for the isotropic flux of super heavy slow monopoles (Fig. 5):

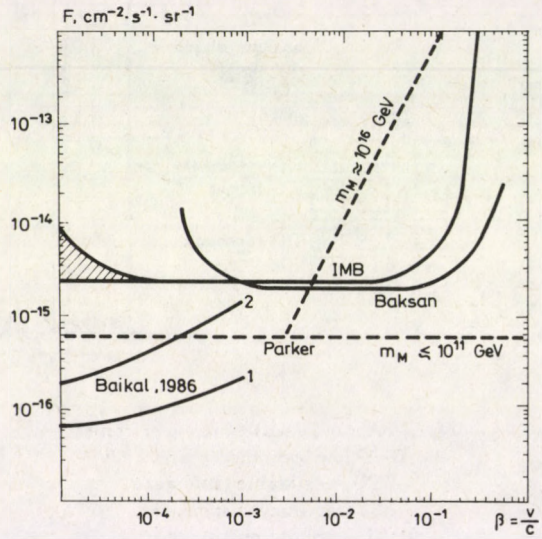

Fig. 5. Upper limits of the magnetic monopole fluxes having a confidence level of 90%, versus the $\beta = v/c$ velocity. Astrophysical limits are marked with dotted lines. The two curves obtained for the Baikal experiment differ from each other in the value relating to the efficiency cross section of the catalysation process of the proton decay ($\sigma = 0.17\sigma_0/\beta^2$):
1. $\sigma_0 = 10^{-26}\text{cm}^2$ 2. $\sigma_0 = 10^{-25}\text{cm}^2$

$$F_{sm} \lesssim 6.5 \cdot 10^{-17}\text{cm}^2 \cdot \text{s}^{-1} \cdot \text{sr}^{-1}, \qquad \text{if} \qquad \sigma_0 \gtrsim 10^{-26}\text{cm}^2,$$

and

$$F_{sm} \lesssim 2.0 \cdot 10^{-16}\text{cm}^2 \cdot \text{s}^{-1} \cdot \text{sr}^{-1}, \qquad \text{if} \qquad \sigma_0 \geq 10^{-28}\text{cm}^2.$$

It is clear that a Čerenkov signal can only be obtained if the following three conditions are simultaneously fulfilled:

- there are monopoles;
- there is a proton decay;
- the decay of protons is catalysed by the monopoles.

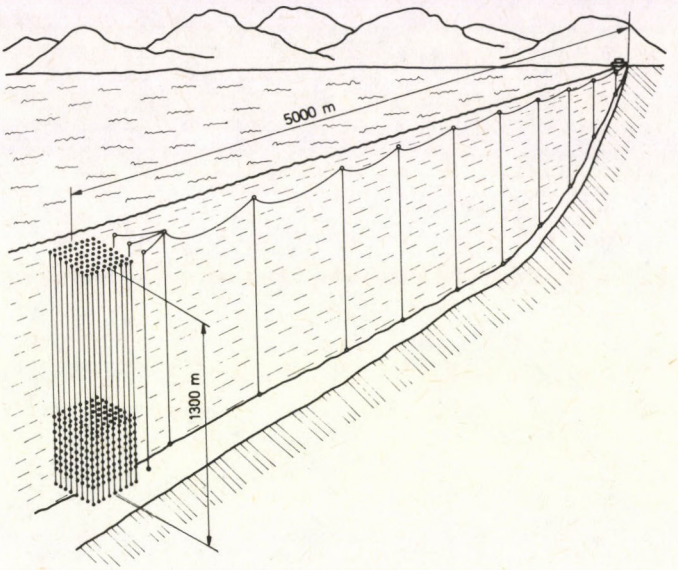

Fig. 6. Planned strings in the lake

In the future our aim is to enlarge the effective light sensing the surface of the multipliers by elaborating new types, and to have some thousands of multipliers (Fig. 6).

References

1. G.V. Domogatsky, Rep. at Int. Conf., "Neutrino-82" Balatonfüred.
2. I.M. Frank, JINR Preprint P4-11777, 1978.
3. V.A. Rubakov, JETPh Lett., *33*, 644, 1981.
4. V.A. Rubakov, M.S. Serebryakov, Nucl. Phys., *B218*, 240, 1983.
5. G.V. Domogatsky, Rep. at Int. Conf. "Neutrino-84" Dortmund.
6. E. Goto, Prog.Theor.Phys., *30*, 700, 1963.
7. S.P. Ahlen, Phys.Rev., *D17*, 229, 1978.
8. J. Arafune, M. Fukugita, Phys. Rev. Lett., *50*, 1901, 1983.

Acta Physica Hungarica 65 (2–3), pp. 331–334 (1989)

DIRAC PARTICLE IN A PERIODIC FIELD*

I. LOVAS and LIVIA MOLNÁR

Kossuth Lajos University, Institute of Physics
4010 Debrecen, Hungary

An exact solution of the Dirac equation is given in a vector meson field which is periodic only in space and constant in time. This solution is in some sense analogous to the one of the well-known Volkov type.

The exact solution of the Dirac equation has been found by Volkov [1] in 1935 for an electron moving in a periodic electromagnetic field. The transversal electromagnetic field is given by

$$A_\mu(x) = a_\mu \cos k_\nu x^\nu, \tag{1}$$

where

$$a_\mu k^\mu = 0, \tag{2}$$

consequently the Lorentz condition

$$\partial_\mu A^\mu = 0 \tag{3}$$

is fulfilled.

Searching for the antiferromagnetic state of the nuclear matter [2] a similar problem has been encountered. An exact solution of the Dirac equation is needed in a periodic vector meson field. This field, however, is periodic only in space and constant in time. The components of the vector field are given as follows:

$$\begin{aligned} \omega^0(x) &= \overline{\omega}^0, \\ \omega^1(x) &= \overline{\omega}^1 \cos k_3 x^3, \\ \omega^2(x) &= \omega^3(x) = 0, \end{aligned} \tag{4}$$

where $\overline{\omega}^0$ and $\overline{\omega}^1$ are constant amplitudes and

$$\partial_\mu \omega^\mu = 0 \tag{5}$$

is obviously satisfied.

*Dedicated to Academician D. Berényi on his 60th birthday

Our aim is to find the exact solution of the Dirac equation given as

$$[\gamma_\mu(i\partial^\mu - g\omega^\mu(x)) - m^*]\psi(x) = 0. \tag{6}$$

Here m^* is the effective mass of the nucleon moving in a constant scalar field $\bar{\sigma}$

$$m^* = m - g_\sigma \bar{\sigma}. \tag{7}$$

The "magnetic" field determined by the vector meson field given above has also a periodic behaviour in space. Using the standard expression for the field strength

$$F_{\mu\nu} = \partial_\nu \omega_\mu - \partial_\mu \omega_\nu, \tag{8}$$

it is easy to see that only one component of the "magnetic" field is different from zero,

$$H^2(x) = F^{31}(x) = k^3 \bar{\omega}^1 \sin k^3 x_3. \tag{9}$$

The wave number $k^\mu(0,\ 0,\ 0,\ k^3)$, the polarization of the vector field $\bar{\omega}^\mu(\bar{\omega}^0,\ \bar{\omega}^1,\ 0,\ 0)$ and the "magnetic" field $H^\mu\ (0,\ 0,\ H^2,\ 0)$ are mutually orthogonal.

For the exact solution of (6) we assume the following form:

$$\psi(x) = (a(\xi) + b(\xi)\sigma)\ \exp[-i(p_\mu x^\mu + S(\xi))]u, \tag{10}$$

where

$$\sigma = \frac{i}{2}(\gamma_1\gamma_3 - \gamma_3\gamma_1) \tag{11}$$

and

$$S(\xi) = \int_{\xi_0}^{\xi} I(\xi')d\xi'. \tag{12}$$

The real functions $a(\xi)$, $b(\xi)$, $S(\xi)$ and $I(\xi)$ are assumed to depend on the variable $\xi = k_\mu x^\mu$.

Substituting (10)–(12) into the Dirac equation (6) the following equation is obtained:

$$\begin{aligned}&\{i\not{k}\, a'(\xi) + (\not{p} + \not{k}I - g\not{\omega} - m^*)a + \\ &+[i\not{k}\, b'(\xi) + (\not{p} + \not{k}I - g\not{\omega} - m^*)b]\sigma\}u = 0.\end{aligned} \tag{13}$$

The spinor amplitude u is defined as the solution of the following equation:

$$(\not{p} - g\gamma_0\overline{\omega}^0 - m^*)u = 0. \tag{14}$$

Using this relation, (13) can be reduced to the following form:

$$(A\sigma + B)\, u = 0, \tag{15}$$

where

$$\begin{aligned} A &= -k^3 a'(\xi) + ik^3 I(\xi)a(\xi) - g\omega^1(\xi)b(\xi) + 2p^1 b(\xi); \\ B &= -k^3 b'(\xi) + ik^3 I(\xi)b(\xi) - g\omega^1(\xi)a(\xi) + 2ip^3 b(\xi). \end{aligned} \tag{16}$$

Eq. (15) is fulfilled if

$$A^2 = B^2. \tag{17}$$

The real and imaginary part of this equation can be written as follows:

$$\begin{aligned} &(-k^3 a' - g\omega^1 b + 2p^1 b)^2 - (k^3 Ia)^2 = \\ &\quad = (g\omega^1 a + k^3 b')^2 - (k^3 Ib + 2p^3 b)^2, \end{aligned} \tag{18}$$

$$\begin{aligned} &(-k^3 a' - g\omega^1 b + 2p^1 b)k^3 Ia = \\ &\quad = -(k^3 b' + g\omega^1 a)(k^3 Ib + 2p^3 b). \end{aligned} \tag{19}$$

Let us assume that $a(\xi) = 1$, then explicit expressions can be obtained for the function $b(\xi)$ and for its derivative:

$$b = \pm \frac{k^3 I}{k^3 I + 2p^3}, \tag{20}$$

$$b' = -\frac{2(p^1 k^3 I + p^3 g\omega^1)}{k^3(k^3 I + 2p^3)}. \tag{21}$$

By eliminating the function $I(\xi)$, a first order differential equation can be derived for $b(\xi)$:

$$b' = \pm b\left(\frac{g\omega^1}{k^3} - \frac{2p^1}{k^3}\right) - \frac{g\omega^1}{k^3}. \tag{22}$$

The exact solution of this equation can be found in the following form:

$$b(\xi) = -\frac{2p^1}{k^3} \exp[\pm d(\xi)] \int \exp[\mp d(\xi)] d\xi \pm 1 \tag{23}$$

where

$$d(\xi) = \frac{g\bar{\omega}^1}{k^3} \sin \xi - \frac{2p^1}{k^3} \xi. \tag{24}$$

It is easy to see that in the absence of the periodic vector meson field the function $b(\xi)$ vanishes:

$$b(\xi) \to 0 \text{ if } \bar{\omega}^1 \to 0. \tag{25}$$

Using the exact solution given by the equation (23), an explicit expression can be derived for $I(\xi)$:

$$I(\xi) = -\frac{2p^3}{k^3} \left(1 \mp \frac{\exp[\mp d(\xi)]}{\frac{2p^1}{k^3} \int \exp[\mp d(\xi)] d\xi} \right). \tag{26}$$

It is to be noted that there is a freedom of choosing one of the three introduced functions $a(\xi)$, $b(\xi)$, $I(\xi)$. Here the assumption $a(\xi) = 1$ was taken. Investigations are going on concerning the existence and applicability of other solutions of the same type.

Note added in proof. P. Hraskó kindly called our attention to the fact that this solution of the Dirac equation only exists on very special conditions.

References

1. D.M. Volkov, Z. Phys., *94*, 250, 1935.
2. B.L. Friman, P.A. Henning, preprint, GSI 8806, 1988; Yu.B. Ivanov, Nucl. Phys., *A 474*, 693, 1987.

Acta Physica Hungarica 65 (2–3), pp. 335–342 (1989)

THE PROBLEM OF ANOMALOUS NEAR SURFACE DIFFUSION*

J. GIBER, S. KRISTYÁN and P. DEÁK

Physical Institute of the Technical University
1521 Budapest, Hungary

Anomalously fast and slow diffusion *perpendicular* to the surface in the near surface region of solids have been reported in the literature. The possible reasons of the anomalies are discussed. A simple model is solved to show the effect of the driving force due to surface-free enthalpy excess.

1. Introduction

Diffusion, though being a basically atomic process, is usually described on a continuum theoretical basis. If the only driving force of the diffusion is a concentration gradient, the time evolution of the concentration in a plane perpendicular to the direction of the diffusion is given by Fick's second law:

$$\frac{\partial c}{\partial t} = \frac{\partial}{\partial z}\left[D\frac{\partial c}{\partial z}\right], \tag{1}$$

where the diffusion coefficient, D is usually taken to be independent of z and c;

$$D = D_0 \exp(-Q/RT), \tag{2}$$

where Q is the virtual activation energy of diffusion. Typical values of D_0 are between 10^{-2}–1 cm^2/s and those of Q are between 50–300 kJ/mol for solid state bulk diffusion.

In the past few years, diffusion experiments have been reported indicating that the diffusion coefficient in the near surface region may be different from that in the bulk. Anomalously enhanced [1–3] as well as slow [4–8] diffusion has been found close to the surface by different authors. The diffusion coefficient in the fast diffusion case may be 3–6 orders of magnitude higher than for bulk diffusion. It is difficult to compare and explain results obtained by different experimental techniques due to their different sensitivities. Among the usual methods chemical sectioning, Auger electron spectroscopy (AES) and secondary ion mass spectroscopy (SIMS) have depth resolutions of 10^{-5}, $5\cdot10^{-9}$ and 10^{-9} m, resp. and the minimum diffusions which can be measured are $5\cdot10^{-16}$, 10^{-22} and $5\cdot10^{-24}$ m^2/s, resp. [9]. There can be a variety of factors contributing to the observed anomalies in near

*Dedicated to Academician D. Berényi on his 60th birthday

surface diffusion including "shadow" effects originating from unclear experimental situations.

In this paper we attempt to summarize some of the ramifying and often confusing experimental literature, isolating different possible causes for the anomalous diffusion at the surface. In Section 2 we will consider the extra driving force introduced by the presence of the surface together with the reaction induced surface segregation. In Section 3 the effect of the near surface vacancy concentration will be estimated together with the influence of ion bombardment during measurements. Finally, in Section 4, the prospects of further theoretical and experimental research will be outlined.

2. The driving force of diffusion at the surface

Investigating room temperature outdiffusion of Pb from a 2.10^{-7} m thick Ag overlayer deposited on a (111) oriented Pb substrate Chen and Sansalone [10,11] could fit their data to a curve of the type

$$\frac{c_1(t) - c_b}{c_1(\infty) - c_b} = 1 - \exp[-t/\tau], \tag{3}$$

where c_b is the bulk concentration, c_1 is the concentration in the surface layer. The time constant τ was found to be 60 s, corresponding to a diffusion coefficient of about $D = 5 \cdot 10^{-13}$ cm^2/s. Although the authors claim this value to be characteristic at room temperature, the application of ion bombardment makes the actual temperature of the sample questionable. Anyhow, the bulk diffusion coefficient of Pb in Ag is in the order of 10^{-16}–10^{-18} cm^2/s between 400 and 600 °C [12], so the results of Chen and Sansalone indicate a higher diffusion rate. Sparnaay [13,14] reported a time constant of about 300 s for the outdiffusion of Au from Cu single crystals at 386 K.

In contrast, De Rugy and Viefhaus [15] using the equation

$$c_s = \frac{2c_b}{a}\sqrt{\frac{Dt}{\pi}}, \tag{4}$$

(where c_b is the equilibrium bulk concentration and a is the lattice parameter) for describing the initial stage of surface segregation of Si in Fe single crystals have found a diffusion coefficient with $Q = 289$ kJ/mol and $D_0 = 4 \cdot 10^2$ cm^2/s in good agreement with bulk data. The problem in this result is that Eq. (4) assumes the surface to be an ideal sink and so the values obtained by it bear a quite limited validity.

To describe the enhanced diffusion coefficient in a surface segregation we have to take into account the driving force due to the presence of the surface. We consider the evolution of the surface composition from an equilibrium bulk composition upon the creation of a surface. In first approximation, we assume that the only driving

force is due to the differences in the excess of the surface free enthalpies of the components. Sparnaay and Thomas have reported [14] a thermodynamic analysis of a similar model of segregation in an A_xB_{1-x} alloy. For the concentration of the solute in the i-th layer after the time t they obtained

$$c_i(t) - c_b = \frac{[c_b^2/c_1(\infty) - c_b]a}{\sqrt{\pi Dt}} \exp\{-\frac{c_b^2}{4Dt}\}. \tag{5}$$

It is evident that (5) is not valid if t goes to infinity. However, as will be shown, a solution to this problem can be found which behaves appropriately in each limit. We consider a single crystal of the alloy A_xB_{1-x}, where x is the equilibrium composition variable in the bulk. We assume an ideal behaviour of the alloy, i.e. that the interactions between A and B atoms are the same as A–A and B–B interactions. The validity of this assumption is discussed in [14]. Let us start with a freshly cleaved surface at $t = 0$. The A atoms will move along the z axis toward the surface at $z = 0$ (the i-th bulk layer being at $z = ia$, where a is the distance of the lattice planes along z). We assume a vacancy assisted diffusion. The diffusing atom moves in a periodic potential the peak heights of which are determined by the free enthalpies of vacancy formation and of activation of motion, $G = G_f + G_m$. The potential near the surface is modified by the free enthalpy excess, γ^*, of the diffusing atom in J/mol units. Since usually in case of an excess-free enthalpy-induced segregation only the composition of the topmost layer differs significantly from that of the bulk [14, 16–18], we assume that the driving force acts mainly between the first two layers. The resulting potential [16, 17] is shown in Fig. 1.

We will neglect evaporation assuming a relatively high heat of atomization [16]. We will describe the time evolution of the surface concentration by one-dimensional atomic fluxes based on reaction rate theory. The presence of the potential gradient at the surface makes the probability of jumping to a neighbour plane asymmetric. The "reactions" are

$$L_1 \underset{f_+}{\overset{f_-}{\rightleftharpoons}} L_2 \underset{f_0}{\overset{f_0}{\rightleftharpoons}} L_3 \underset{f_0}{\overset{f_0}{\rightleftharpoons}} \dots \underset{f_-}{\overset{f_+}{\rightleftharpoons}} L_N, \tag{6}$$

where L_i is the i-th plane from the surface (which is L_1), f_0 is the jumping frequency in the bulk and $f_+ > f_0 > f_-$. The jumping frequencies at the surface can be related to that of the bulk [19] (see Fig. 1) by

$$f_\pm = f_0 \exp[\pm\frac{\gamma^*}{2RT}]. \tag{7}$$

The concentration of solute atoms in mole fraction can be described as

$$\dot{x}_1 = -(f_-)x_1 + (f_+)x_2, \tag{8a}$$

$$\dot{x}_2 = +(f_-)x_1 - (f_+ + f_0)x_2 + (f_0)x_3, \tag{8b}$$

$$\dot{x}_i = +(f_0)x_{i-1} - 2(f_0)x_i + (f_0)x_{i+1}; \qquad i = 3, \dots, N-2, \tag{8c}$$

$$\dot{x}_{N-1} = +(f_0)x_{N-2} - (f_+ + f_0)x_{N-1} + (f_-)x_N, \tag{8d}$$

$$\dot{x}_N = +(f_+)x_{N-1} - (f_-)x_N, \tag{8e}$$

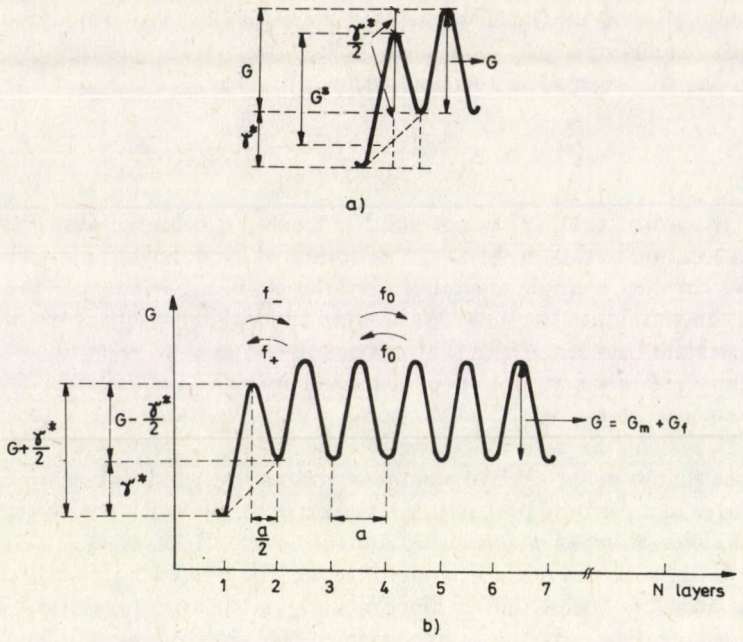

Fig. 1. Potential diagram for the diffusing atom near to the surface (Assumptions: $G^{(s)} \approx G$, weak segregation).Notations:

a = lattice parameter
γ^* = free enthalphy excess of the surface ("surface tension") in J/mol
G = free enthalpy ($\approx$ energy) of the segregating particle
G^s = free enthalpy ($\approx$ energy) of the segregating particle at the surface
G_m = free enthalpy of motion
G_f = free enthalpy of formation of vacancies
f = jumping frequency ($f_+ > f_0 > f_-$)

where x_i is the mole-fraction concentration of the solute atom in L_i. Eq. (8c) is compatible with Fick's second law $\left(\dot{x} = \frac{\partial}{\partial z}\left[D\frac{\partial x}{\partial z}\right]\right)$ in the bulk for the approximation of the second derivative, d^2x_i/dz^2 by finite differences gives $(x_{i+1} - 2x_i + x_{i-1})/2a^2$, and $f_0a^2/2$ is just the bulk diffusion coefficient D. With the initial conditions $x_i(0) = x_0$ for all i, and keeping in mind that $\sum x_i(t) = Nx_0$ for every t, it follows that in equilibrium $(\dot{x}_i(t = \infty) = 0, i = 1, 2, \ldots, N)$:

$$x_i(t = \infty) = \frac{Nx_0}{(N-2) + 2f_+/f_-}, \quad i = 2, \ldots, N-1, \tag{9a}$$

$$\overline{x}^s(t = \infty) \equiv x_1(t = \infty) = x_N(t = \infty) =$$
$$= \frac{f_+}{f_-}x_2(t = \infty) = \exp\left[\frac{\gamma^*}{RT}\right] \cdot x_2(t = \infty). \tag{9b}$$

Equation (9b) describes the equilibrium segregation in this model.

In [16] similar equations have been used for a computer simulation. Using a Laplace transformation to the system of equations in (8) we arrive at the matrix equation

$$\mathcal{A}\,\mathbf{X} = \mathbf{x}_0, \tag{10}$$

where $\mathbf{X}^+ = [X_1, X_2, \ldots, X_N]$, $\mathbf{x}_0 = [x_0, x_0, \ldots, x_0]$, and $\mathcal{A}$ has a tridiagonal form and its elements contain only the f_0, f_+, f_- frequencies and the Laplace parameter p. Using a time unit of $1/f_0$, the eigenvalues are negative. The lowest two eigenvalues are approximately the same and are in the order of $-(1+\exp[\gamma^*/2RT])$. The highest eigenvalue is always zero for every N. After inverse Laplace transformation, the concentration in the top layer is:

$$x^s(t) \equiv x_1(t) = \alpha_1 + \sum_{i=2}^{N-1} \alpha_i \cdot \exp[e_i t] + \alpha_N \cdot t \cdot \exp[e_N t], \tag{11}$$

where e_N is the lowest eigenvalue ($e_1 = 0$). The α_1 coefficient gives the $x_1(t = \infty)$. Fig. 2 shows the plot of Eq. (11) for $\exp(\gamma^*/2RT) \geq 10$ values ($N = 20$).

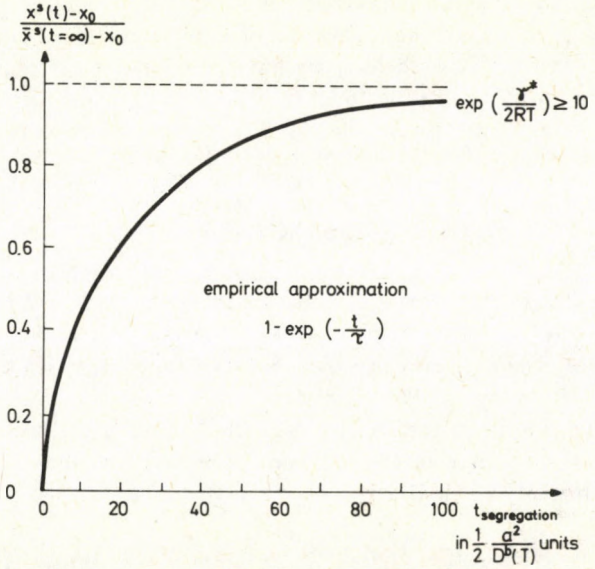

Fig. 2. Time dependence of the relative increase in the concentration of the segregating component

The horizontal axis is the time in $1/f_0 = a_0/2D^b(+)$ units, while the perpendicular axis shows the relative increase in the concentration of the segregating component. The γ^* values can be found in [18].

The solution (11) differs basically from that of Fick's second law in the bulk and cannot be obtained by simply modifying the latter, i.e. with a "mirror plane" [19]. Eq. (11) is valid for $t = \infty$, too.

A curve of the form of (3) can be fitted to (11). The bulk diffusion coefficient of Au in Cu at 386 K is about $3 \cdot 10^{-17}\text{cm}^2/\text{s}$ [13]. With a lattice parameter of $a = 3.6 \cdot 10^{-10}$ m this gives $1/f_0 = \frac{a^2}{2D} = 21.6$ s. Using this time unit the fit τ (11) with γ^*Au=74 kJ/mol, i.e. $\exp(\gamma^*/2RT) \sim 10^5$, results in a time constant, $\tau = 361$ s which compares to the measured value of 300 s [13,14].

Since the outdiffusion coefficient at the surface is $D^s = a^2 f_+/2$, its ratio to the bulk diffusion coefficient $D \equiv D^b = a^2 f_0/2$ is

$$\frac{D^s}{D^b} = \frac{f_+}{f_0} = \exp\left[\frac{\gamma^*}{2RT}\right], \quad D^s > D^b. \tag{12}$$

For T=300 °C using the γ^* values of [18] this is between $5 \cdot 10^2$ and $5 \cdot 10^5$.

Our model was based on the assumption that no chemical reactions involving the solute occur at the surface. In several papers, observed time constants of the evolution of surface concentrations have been reported to indicate anomalously slow near surface diffusion [6–8,20]. In most of these cases, however, the process is reaction limited [4,5] and the measured time constant is characteristic not of the diffusion process (but e.g. of the formation of a precipitate [7,20] or of the dissociation of an oxide [4,5]). Nevertheless, we have to consider the case when a surface reaction provides an extra driving force for the diffusion, i.e. the reaction induced segregation. In a simple approach, the Eq. (12) has to be extended by a factor [21] proportional to

$$\sim \exp(\triangle G/RT), \tag{13}$$

where $\triangle G$ is the free enthalpy of the surface reaction (e.g. A or B). If $\triangle G_A$ is more exothermic than $\triangle G_B$, the diffusion rate is increased. If it is the other way round, the outdiffusion of A can be slowed down, or even the process can be reversed. For example in a Cu–Fe alloy the Cu atoms are segregating to a free surface, while in case of a surface oxide layer the Fe atoms do the same. If the surface reaction acts to amplify the driving force of the diffusion, the order of magnitude of the ratio (12) can approximately be doubled.

3. The near surface vacancy concentration and the effect of ion bombardment

In the case of vacancy assisted diffusion, the activation energy of the diffusion consists of two terms

$$Q_v = Q_f + Q_m, \tag{14}$$

where Q_f is the heat of formation of a vacancy, Q_m is the heat of activation for the exchange of an atom with a neighbouring vacancy. Substituting (14) into (2)

$$D = D_0 \cdot \exp[-Q_v/RT] \cdot \exp[-Q_m/RT], \tag{15}$$

the second term is proportional to the equilibrium concentration of vacancies. In a first approximation, we may substitute it by the actual vacancy concentration (even if produced under non-equilibrium circumstances).

At some surfaces and interfaces the vacancies used to accumulate. For example, it has been shown [22] that the vacancy concentration of silicon near to an Si/SiO_2 interface is 10–100 times that of the bulk. Accordingly the diffusion coefficient for a vacancy assisted diffusion can be expected to be 10 to 100 times higher than in the bulk.

Many of the diffusion experiments have been carried out by applying ion bombardment in course of the experiment. The increasing vacancy concentration due to radiation damage led to an increase of the diffusion coefficient [2,3]. The enhancement of diffusion rate due to ion bombardment cannot be attributed, however, solely to the radiation damage. Li and Koshikawa have found [1] an increase of the diffusion coefficient in the order of 10^6. The most probable explanation appears to be the "knock-on" effect, i.e. the kinetic energy exchange between the primary ions and the diffusing species. Since the profile of energy loss of primary ions are known from Siegmund's theory, this factor could be taken into account in a computer simulation.

4. Prospects of further research

The considerations summarized in this paper serve as the basis of our theoretical and experimental research. Our aim is to provide a series of well controlled experiments on near-surface diffusion free from "shadow" effects and provide an interpretation for them generalizing the above considerations. We believe that this work will result in important consequences. For example, we see a possibility for interpreting preferential sputtering as a segregation effect accelerated by the energy transfer between the bombarding and diffusing particles. This assumption seems to be supported by the fact that the preferred component in sputtering is almost always the one which in a pure state has the lower surface free enthalpy excess, i.e. the one which is likely to segregate [18].

References

1. R.S. Li and T. Koshikawa, Surf. Sci., *151*, 459, 1985.
2. P.S. Ho, Surf. Sci., *72*, 253, 1978.
3. J. Roth, W. Moller, D.B. Poker and K. Wittmaack, Nuclear Instruments and Methods in Physics Research, *B13*, 409, 1986.

4. J.P.Stark, Solid State Diffusion, John Wiley and Sons, New York - London - Toronto, pp. 212-217, 1976.
5. D.K. Reiman and J.P. Stark, Acta Met., *18*, 63, 1970.
6. D.L. Styris and C.T. Tomizyka, J. Appl. Phys., *34*, 1001, 1963.
7. O.L.J. Gijzeman, F.C. Shonten and G.A. Bootsma, Surf. Sci., *71*, 174, 1978.
8. A.J. Mortlockt, The Journal of the Australian Institute of Metals, *14*,/2/, 98, 1969.
9. R.W. Cahn and P. Haasen, Physical Metallurgy I-II., North-Holland Physics Publishing, New York, 1983.
10. C.H. Chen and F.J. Sansalone, Appl. Phys. Lett., *48*, 1072, 1986.
11. C.H. Chen and F.J. Sansalone, Surf. Sci., *163*, L688, 1985.
12. D. Heitkamp, W. Biermann and T.S. Lundy, Acta Metallurgica, *14*, 1201, 1966.
13. M.J. Sparnaay, Thermodynamics /with an emphasis on surface problems/, Surface Science Reports, *4*, 3/4, 1984.
14. M.J. Sparnaay and G.E. Thomas, Surf. Sci., *135*, 184, 1983.
15. H. De Rugy and H. Viefhaus, Surf. Sci., *173*, 418, 1986.
16. C.D. Stinespring and W.F. Lawson, Surf. Sci., *150*, 209, 1985.
17. S. Hofman and J. Erlewein, Surf. Sci., *77*, 591, 1978.
18. L.Z. Mezey and J. Giber, Japanese Journal of Applied Physics, *21*, 1569, 1982.
19. J.R. Manning, Diffusion Kinetics for Atoms in Crystals, Van Nostrand, Princeton, 1968.
20. F. Bezuidenhout, J. Du Plessis and P.E. Viljoen, Surf. Sci., *171*, 392, 1986.
21. J. Giber, L.Z. Mezey and D. Marton, Proc. of the Int.Conf.SIMS VI. Paris, 1987, Ed.: Beninghoven et al, John Wiley and Sons, New York, 1988.
22. J. Giber, P. Deák and D. Marton, Phys. Stat. Sol. /b/*79*, K 89, 1977.
23. J.M. Blakely, Surface Physics of Materials, Academic Press, New York, Vol. I-II., 1975.
24. W. Jost and K. Hauffe, Diffusion Methoden der Messung und Auswertung, Dietrich Steinkopff Verlag, Darmstadt, 1972.
25. T.S. Lundy and R.A. Padgett, Trans., AIME, *242*, 1897, 1968.
26. S. Hofmann and J. Erkewein, Scripta Met., *10*, 857, 1976.
27. K. Moller and L. Holmlid, Surf. Sci., *173*, 264, 1986.
28. T. Koshikawa, K. Goto, N. Saeki, R. Shimizu and E. Sugata, Surf. Sci., *79*, 461, 1979.
29. J.C. Hamilton and J.M. Blakely, Surf. Sci., *91*, 199, 1980.
30. M.A. Gesley and L.W. Swanson, Surf. Sci., *159*, 496, 1985.
31. M. Pierantoni, B. Aufray and F. Cabane, Acta Metall., *33*, 9, 1625, 1985.
32. C. Ocal, S. Ferrer and N. Garcia, Surf. Sci., *162*, 558, 1985.
33. H. Yamamoto, T. Kikuchy and K. Furuya, Surf. Sci., *177*, 229, 1986.
34. K. Nishi, K. Sakamoto and J. Ueda, J. Appl. Phys., *59*, 4177, 1986.
35. G.L.P. Berning and W.J. Coleman, Surf. Sci., *173*, 411, 1986.
36. L. Holmid, K. Moller and E. Sanchez, Surf. Sci., *173*, L627, 1986.
37. L.Z. Mezey, F. Reti and J. Giber, to be submitted to Surf. Sci., Technical University of Budapest.
38. G. Carter and J.S. Colligon, Ion Bombardment of Solids, Heinemann Educational Books, London, 1968.

Acta Physica Hungarica 65 (2–3), pp. 343-347 (1989)

GAIA HYPOTHESIS AND ATMOSPHERIC AEROSOL*

E. MÉSZÁROS

Institute for Atmospheric Physics
1675 Budapest, Hungary

According to Lovelock's Gaia hypothesis atmospheric gases are under biospheric control. In recent years this theory was extended to atmospheric aerosol by postulating that aerosol particles in the air as well as physical processes regulated by them (e.g. atmospheric solar radiation transfer, cloud and precipitation formation) are controlled more or less by the biosphere. The aim of this paper is to discuss this possibility in some detail.

1. Introduction: the Gaia hypothesis

The Earth's atmosphere is a strange gas mixture. First, as Sillén [1] pointed out, under our conditions the stable state of nitrogen and oxygen would be in nitrate compounds dissolved in ocean water. In other words, this means that the state of the atmosphere is far from the physicochemical equilibrium. Second, as the results of spacecraft observations show, the composition of the air cannot be considered "normal" in the solar system. It is believed that the biosphere–atmosphere interactions have played an important part in the formation and evolution of the atmosphere of our planet. Lovelock and Margulis [2] even proposed that the atmosphere is regulated directly by the biosphere, and the atmosphere can be considered as a contrivance in which each gas has its own function. These authors concluded that the atmosphere is part of the biosphere.

This theory, called the Gaia hypothesis, was further developed by Lovelock [3] who explained the biospheric function of several atmospheric gases. Among other things, Lovelock mentioned in his book that the atmospheric transport of sulfur, the main component of the tropospheric aerosol (see later), is controlled in some measure by the marine biota. Nevertheless, he did not consider the fact that the air is a dispersed system containing, beside gases, solid and liquid aerosol particles as well. However, if we accept the concept that atmospheric gases are under biospheric control, it is very improbable that the aerosol particles in the air and the phenomena regulated by them are independent of the biosphere.

The aim of this paper is to discuss this problem in some detail. However, before doing this, the relationship between the atmospheric aerosol and sulfur cycle should briefly be presented.

*Dedicated to Academician D. Berényi on his 60th birthday

Acta Physica Hungarica 65, 1989
Akadémiai Kiadó, Budapest

2. Aerosol and sulfur cycle

About twenty years ago the physical and chemical properties of tropospheric aerosols were practically unknown. An important step in understanding the tropospheric particles was made by Junge [4] who pointed out that the major part of the troposphere (80% of its volume), except air layers above continents, is filled with an aerosol of similar concentration (100–200 cm^{-3}) called the tropospheric background aerosol. It was evident that the majority of these particles is in the size range of fine particles with a radius smaller than about 0.5 μm. However, the chemical composition of the particles was an open question.

The composition of tropospheric background aerosol in the fine size range was first determined by Mészáros and Vissy [5] who sampled the particles in the air areas above the oceans of the Southern Hemisphere. Their studies demonstrated that this aerosol consists of particles of two types: fine sulfur containing (ammonium sulfate* and sulfuric acid) particles and coarse particles composed of sea salt. However, the number concentration of these latter was found to be very small as compared to the number of sulfate particles. This result was later confirmed by several observational programs [6,7]. While sea salt contains a sulfate fraction, it was believed that fine particles form by condensation from some gaseous sulfur species. Further studies [8] demonstrated that photochemical processes play an important role in the formation of these particles.

On the other hand, it was found that, due to the excretion of phytoplankton, oceanic water emits a rather large amount of dimethyl sulfide (DMS) especially in the warmest, most saline areas of the ocean [3]. DMS reacts in the air with free radicals (mostly OH) to form sulfur dioxide and consequently particulate sulfur (see e.g. [9]).

While the emission of DMS by the ocean surface is well demonstrated, we have very uncertain ideas concerning the release of aerosol forming sulfur gases by the land biota. It is more or less accepted that hydrogen sulfide, produced under anaerobic conditions by microorganisms [10], is the more probable candidate. The estimates of several authors [11, 12, 13] indicate that the total continental emission of H_2S varies between about 1 and 10 $TgSyr^{-1}$, which is less than the oceanic DMS emission estimated to be 40 $TgSyr^{-1}$ [14]. It should be noted in this respect that according to Mészáros [15] the emission of biogenic sulfur gases determined on the basis of global sulfur budget calculations is 43 $TgSyr^{-1}$ which just exceeds the DMS release proposed by Andreae and his associates [14]. Thus, to our present knowledge we can conclude that sulfate particles found in the remote troposphere (under conditions undisturbed by human activities) must form from biogenic DMS released by the world ocean.

Finally, we note that non-biogenic continental sulfur sources also emit sulfur gases into the atmosphere. An obvious natural source is provided by volcanic eruptions during which sulfur dioxide is released. While the emission rate of volcanic SO_2 is not well established, one may assume that it can be neglected for a longer

*Note that ammonia is of biospheric origin

time period [15]. Another well-known non-biospheric type of sulfur source is due to human activities which disturb considerably the natural sulfur cycle at present. Owing mostly to the burning of fossil fuels, a large amount of SO_2 is released over industrialized regions. This amount is at least as much as the DMS quantity emitted by the biosphere. The determination of the possible effect of this source on the properties of the tropospheric background aerosol is one of the most important tasks of present research. It must be taken into account, however, that this source has operated practically only during the last two centuries.

3. Sulfate particles as climate regulators

Shaw [16] was the first to propose that the Gaia hypothesis can be extended to the atmospheric aerosol. He speculated that fine sulfate particles are exactly appropriate to opalize the atmosphere. This is due to the fact that the size of the particles is comparable to the wavelength of solar radiation of maximum intensity. Shaw postulated that the practically constant average temperature at the Earth surface since the emergence of life has been regulated by the biosphere through the sulfur cycle. More exactly, more DMS was emitted during warmer periods leading to the formation of sulfur containing particles which resulted in cooling. That is, in warmer periods the area (and the temperature) of the oceans increased owing to the melting of sea ice. In contrast, in warmer periods the inverse phenomenon occurred.

In a recent paper, Charlson et al [13] highly improved this speculation by arguing that sulfate particles of biospheric origin not only opalize the atmosphere but also serve as condensation nuclei for cloud formation. Since the optical properties of the clouds depend on the number of droplets (condensation nuclei) sulfate particles control significantly the albedo of the clouds: in the case of more droplets the albedo increases which causes cooling in the subcloud air layers. By using a relatively simple model, Charlson and his co-workers calculated a decrease of 1.3 K in the mean surface temperature for an increase of 30% in the number of condensation nuclei.

4. Gaia and water cycle

It can be demonstrated by thermodynamic and kinetic calculations that the condensation of water vapour in the atmosphere would be impossible without condensation nuclei. Without nuclei condensation begins at a saturation ratio of about 4 (relative humidity of 400%) on negative gaseous ions, but in the atmosphere the saturation ratio very rarely exceeds the value of 1.01 [17]. Thus, if there were no aerosol particles in the atmosphere the cloud and precipitation formation (or, in other words the water cycle crucial for terrestrial life) would be absolutely impossible.

In Section 2 we have discussed that the troposphere is filled with sulfate particles of biologic origin. These particles are soluble in water and constitute the class of condensation nuclei under remote conditions [18]. This means that the very existence of the water cycle would be questionable if there were no DMS emissions by the oceans. Thus we can postulate that the gases emitted by the biosphere (oceanic ecosystems) produce nuclei which make water available to another part of living systems (terrestrial biota). Briefly, it cannot be excluded that the biosphere regulates the water cycle [19].

However, there are some problems which should not be disregarded. If the above hypothesis is true there should be a net sulfur (nuclei) transport from the oceanic air to the atmosphere above the continents. Without going into details we note that some authors [3, 11, 13] propose such a transport, while according to others (e.g. [9]) an inverse flux is more probable. However, this latter opinion is based on the results of present measurements influenced by anthropogenic perturbations.

On the other hand, in continental air generally more condensation nuclei (and sulfate particles*) are detected than over the oceans, at least in air layers near the surface [20]. However, above an altitude of a few kilometers there are practically no differences between continental and oceanic observations in agreement with the concept of a homogeneous tropospheric background aerosol discussed previously. Condensation nuclei in the surface air over North America and Europa are mostly of anthropogenic origin. It is estimated that presently only about 20% of sulfate particles over Europe comes from natural sources [21]. However, except the last two centuries, the effects of human activities were obviously non-existent. Secondly, while fossil fuel burning modifies the sulfur cycle in the industrial area, this fact does not deny the concept that during the Earth's history the water cycle has basically been controlled by the biosphere through gaseous sulfur emission. Nevertheless, the possible effects of human activities on the natural distribution of precipitation should be carefully investigated. Our studies in this field [21] show that no anthropogenic effects can be detected in European precipitation during the last century. This means that we have not been able (fortunately) to modify the natural water cycle in spite of the fact that man has produced a considerable amount of sulfate particles and consequently condensation nuclei.

5. Conclusion: need for further research

According to our present knowledge the biosphere influences considerably the quantity and quality of atmospheric aerosol particles through sulfur gas emissions. In other words this means that the climate and water cycle, regulated by sulfate particles predominant in the tropospheric background, are probably also under biospheric control. Further research is needed, however, to clarify some important issues.

*Even under continental conditions sulfates constitute the majority of water soluble materials. Other particle types in the fine (e.g. carbonaceous particles) and coarse (e.g. soil particles) size ranges are insoluble in water and are very ineffective condensation nuclei.

A more detailed study of the emission of sulfur gases by the land biota and a more reliable estimation of the preindustrial sulfur exchange between oceanic and continental air are obviously needed. The understanding of climatic factors affecting DMS emission and the determination of the relationship between DMS emission and condensation nuclei properties also seem to be necessary.

References

1. L.G. Sillén, Tellus, *18*, 198, 1966.
2. J.E. Lovelock and L. Margulis, Tellus, *26*, 2, 1974.
3. J.E. Lovelock, Gaia. A new look at life on Earth, Oxford University Press, Oxford, 1979.
4. C.E. Junge, Atmospheric Chemistry and Radioactivity, Academic Press, New York and London, 1963.
5. A. Mészáros and K. Vissy, J. Aerosol Sci., *5*, 101, 1974.
6. P. Winkler, Geophys. Res. Lett., *2*, 45, 1975.
7. E.K. Bigg, J. Appl. Meteorol., *19*, 521, 1980.
8. E.K. Bigg, J.L. Grass and C. Evans, J. Atmosph. Chem., *1*, 203, 1984.
9. O.B. Toon, J.F. Kasting, R.P. Turco and M.S. Liu, J. Geophys. Res., *92*, 943, 1987.
10. W. Jaeschke, H.-W. Georgii, H. Claude and H. Malewski, Pure and Appl. Geophys., *116*, 465, 1978.
11. L. Granat, H. Rodhe and R.O. Hallberg, Ecological Bulletin, *22*, 89, 1976.
12. G. Várhelyi and G. Gravenhorst, Időjárás, *85*, 126, 1981.
13. R.J. Charlson, J.E. Lovelock, M.O. Andreae and S.G. Warren, Nature, *326*, 655, 1987.
14. M.O. Andreae, R.J. Ferek, F. Bermond, K.P. Byrd, R.T. Engstrom, S. Hardin, P.D. Houmira, F. Le Marrec, H. Raemdonck and R.B. Chatfield, J. Geophys. Res., *90*, 12891, 1985.
15. E. Mészáros, Atmospheric Chemistry, Elsevier, Amsterdam, 1981.
16. G.E. Shaw, Climatic Change, *5*, 297, 1983.
17. J.B. Mason, The Physics of Clouds, Clarendon Press, Oxford, 1971.
18. E. Mészáros, A. Mészáros and K. Vissy, Proc. 8th. Intern. Conf. Nucleation, Leningrad, 431, 1975.
19. E. Mészáros, Atmosph. Env., *22*, 423, 1988.
20. S. Twomey and T.A. Wojcjechowski, J. Atmosph. Sci., *26*, 684, 1969.
21. E. Mészáros and G. Várhelyi, Időjárás, *86*, 76, 1982.

Acta Physica Hungarica 65 (2–3), pp. 349–353 (1989)

ARE LYMPHOCYTES EXCITABLE CELLS?*

S. DAMJANOVICH, MARGIT BALÁZS and J. SZÖLLŐSI

Department of Biophysics, University Medical School of Debrecen
4012 Debrecen, Hungary

Nerve and muscle cells are defined traditionally as excitable cells, due to their capacity to react to external stimuli with subsequent electric and/or mechanical responses.

Another category of cells, eminently among them the round-shaped blood cells, in particular the best studied lymphocytes, are classified as non-excitable cells.

We try to present evidence that lymphocytes may also be accepted as excitable cells. A bit far-reaching, further generalization could be formulated claiming that every cell can be considered as an excitable one.

Introduction

Nerve and muscle cells are large enough to offer a better target for electrophysiological investigations like voltage clamp and patch clamp, than any of the round-shaped cells.

Thus the former provided the experimental objects to deal with electric properties and stimuli–response correlations in the more than two-hundred year history of electrophysiology (and electric phenomena as well). This history started with the discovery of Luigi Galvani that the muscle of frogs suspended on copper hooks from a steel wire twitched when chance contact completed the circuit.

The refinement of techniques and theoretical background as well in recent years enables us to understand more closely the electric properties of the so-called non excitable cells.

As a general approximation for the description of resting membrane potential the Nernst equation based Goldmann–Hodgkin–Huxley equation is widely accepted. Any change in the equilibrium initiates diffusion potential as well and the resulting hyper- or depolarization involves a number of compensating or cooperative mechanisms, known as channel activities.

The lymphocytes, like nerve or muscle cells have voltage gated, ligand gated and G-protein gated channels. These channels are integral (transmembrane) proteins having a virtual channel, specific for certain types of hydrophylic ions, like Na^+, K^+, Ca^{2+}, Cl^-, etc. Voltage gating means the opening (or closing) a channel upon the changing transmembrane potential. Ligand gating is a regulatory possibility through the binding of a specific ligand to the channel or its immediate vicinity, thereby influencing the passage of ions through steric hindrance or evoked comformational changes. G-protein gating means a complex regulatory circle where the

*Dedicated to Academician D. Berényi on his 60th birthday

channel opening or closing depends upon protein–protein interactions. The origin of the name is that guanin nucleotides bind proteins to trigger a transmembrane signaling process [1]. The best elaborated examples are those of the molecular changes after a photon absorption in the retina, i.e. in the cones and rods of the eye.

Lymphocytes are known to have many physiologic and pathophysiologic functions like antibody production or the elimination of foreign grafts through cellular immune reactions. The former function belongs to the so-called B and the latter one to the T lymphocytes. When any of these actions are initiated by external stimuli we consider the lymphocyte as an activated one. The activation of lymphocytes involves for all practical purposes the obligatory depolarization of the resting potential. This step of the transmembrane signal processing is ubiquitous and has rather ill-defined relationship to the complex chain of other early activation steps. In order to understand the complexity of the processes taking place parallel to or sequentially with the membrane potential change we need a short survey on transmembrane signaling.

Transmembrane signaling

Membrane depolarization, i.e. changing the transmembrane potential difference is interwoven with numerous biochemical events. In order to understand the functional meaning of depolarization we need some basic knowledge of the complexity of the transmembrane signaling process as a whole. Briefly we can claim that membrane bound receptors have key roles in communicating information from the extracellular milieu to the intracellular world. These receptors are integral membrane proteins which participate in the initiation of essential biological processes such as the transport of ions or of macromolecules and the generation of intracellular messengers [2,3]. These processes are usually initiated through ligand–receptor interactions, often resulting in dimerization and aggregation, and are generally termed transmembrane signaling [4-9]. Recent advances in the field, particularly the knowledge of how a hormone–receptor complex, once formed, conveys information to other molecules and initiates biological responses within the cell, provide us with a framework for posing specific questions related to receptor function and the transduction of biological signals [9, 10].

Some elements of signal transduction between ligand–receptor interaction at the plasma membrane and effector response within the cell are known in considerable detail. Synthesis and liberation of cyclic mononucleotides (cAMP and cGMP), diacylglycerols (DG-s), inositol polyphosphates and eicosanoids, and their relation to changes in $[Ca^{2+}]_i$ and pH_i, and the regulation of the Ca^{2+}/phospholipid-dependent kinase, PKC, cyclic nucleotide- and Ca^{2+}/calmodulin-dependent protein kinases are the prime targets of widespread biochemical investigation [2, 8, 9]. The possible mechanisms of membrane receptor transduction also include a variety of biophysical events. Changes in membrane voltage; activation of ion fluxes through voltage-sensitive and insensitive Ca^{2+}, K^+ and other small-ion channels; comformational changes in integral membrane proteins as a result of the changes in V_{pm}; pH

regulation via ion transporters such as the amiloride-sensitive Na^+/H^+ exchanger, all provide biophysical platforms for signal transduction [2, 4, 9, 11, 12]. Ligand–receptor interaction may initiate structural modifications such as aggregation, capping and endocytosis through vesicle formation from coated pits [13]. Liberation of Ca^{2+} into the cytosol as a result of the activation process permits control of target proteins such as enzymes and contractile elements either directly or via Ca^{2+} dependent regulatory proteins, such as calmodulin and myosin light-chain kinase [14]. Intramembrane processes resulting ligand–receptor interactions may induce changes in the cytoskeletal structures, thereby participating in cellular activation [2]. And this list of potentialities is far from complete.

The final effectors of transmembrane biochemical and biophysical signal processing involve phosphorylation/dephosphorylation reactions and the generation of phospho/dephosphoproteins ultimately responsible for the control of the cell function [2, 8, 9], including energy metabolism and activation of nucleic acid and protein synthesis. Phosphorylation may also change the equilibrium between the recyclings of membrane bound receptors, or may lead to the liberation of peptides having specific (messenger) functions within the cytosol [2].

The generation of immune responses requires changes in membrane constituents which promote the interaction of a number of cell types including antigen-presenting cells, *T* cells and *B* cells. The activation, clonal expansion and differentiation of *T* and *B* lymphocytes is triggered by the immunizing antigen and by non-antigen products of the interacting cells. The Major Histocompatibility Complex (MHC) restricted interaction of the antigen (that is the MHC/antigen complex) with antigen-recognizing receptors on *T* cells, the cross-linking of antigen receptor molecules on *B* cells by antigen (or in model experiments by anti-Ig antibodies) as well as the binding of macrophage and/or lymphocyte derived factors to the corresponding receptors generate signals by which quiescent cells are driven into a poised state. Although the biochemical basis of signal transduction by antigen receptors and *T* cell receptors is not yet clarified, there is evidence for a fundamental role of the phosphatydil inositol (PI) signal transduction pathway in *T* and *B* cell activation [15].

One of the best models for studying the control of mammalian cell growth and proliferation is the response of lymphocytes to mitogenic agents which stimulate growth, DNA synthesis and division [16]. Results from several studies imply that early increases in intracellular ionized Ca^{2+} ($[Ca^{2+}]_i$) play an important role in the stimulation of lymphocytes by mitogens [17] and that these changes in $[Ca^{2+}]_i$ are related to the activation of the PI signal transduction pathway in which the action of phospholipase C on PI results in the formation inositoldiphosphate ($InsP_2$) which is further hydrolyzed to form DGs and inositol polyphosphates which are actively involved in signal-transduction [18]. These compounds function as dual second messengers controlling two major ionic events implicated in cell proliferation. The DGs are potent physiological activators of PKC which act in the plane of the membrane. Consequent stimulation of the Na^+/H^+ antiporter, a substrate for PKC, causes alkalinization of the cytosol which is thought to be a primary signal in cell proliferation. The inositol polyphosphates, in particular $InsP_3$ and its metabolite,

$InsP_4$, mediate the release of Ca^{2+} into the cytosol from the endoplasmic reticulum storage depot [18] and from the extracellular milieu via the plasma membrane, respectively [19]. Alkalinization of the cytosol appears to be a prerequisite for the $InsP_3$-dependent gating of Ca^{2+} release from the endoplasmic reticulum [20], so that increased pH_i and $[Ca^{2+}]_i$ are thought to be crucial synergistic signals in cell growth and proliferation. These cellular events are supposed consequences of the action of growth factors [15, 16].

Membrane depolarization appears to be an important intermediate event in the antigen receptor mediated signal transfer pathway in *B* lymphocytes, occurring proximal to the branching of the PI signal transduction cascade [21]. The cross-linking of antigen receptors by an antigen or by anti-Ig antibodies is the first step in the cascade of biophysical and biochemical events which ultimately drive inositolpolyphosphate and diacylglycerol messenger systems [21], presumably with subsequent increased pH_i via PKC activation, and increased $[Ca^{2+}]_i$ via the generation of $InsP_3$ and possibly $InsP_4$. However, the precise way in which these transduction events are integrated to influence *B* cell activation, despite their importance in signal transfer, remains unclear. One objective of current research is to elucidate the functional relationship between agonist-induced changes in membrane polarity and activation of the PI pathway by monitoring changes in $[Ca^{2+}]_i$ and amiloride-sensitive changes in pH_i. From this point of view the possible role of the PI pathway in the function of Fc- receptors, complement-receptors, and IL-2 receptors (FcR, CR, IL-2R) might be important.

Arguments suggesting that lymphocytes are excitable cells

The depolarization of the cytoplasmic membrane involves a number of dynamic structural changes in the molecular elements of the membrane. Although propagated potentials spreading alongside the cytoplasmic membrane have not been detected yet, this fact might be attributed to the size of the cells (5–15 μm in diameter assuming a spherical shape) and the relatively imperfect instrumentation.

Besides the microscopic aggregations in the cell membrane elements upon activation a submicroscopic rearrangement has become also attainable for studies [1, 13, 22–27].

Lymphocytes definitely change their surface structure like the nerve or muscle cells upon stimuli causing depolarization [4]. They respond to stimuli by changing their electrical properties, as well as metabolic pattern. Some messengers are sequestred into the cytoplasm among them even big molecules like the phosphokinase C.

Thus, our conclusion is that those parameters, attributed to the classic excitable cells like nerve and muscle cells can also be found to accompany *T* and *B* lymphocytes, thereby supporting our suggestion that these cells are excitable ones. The lack of direct evidence so far for every cell to fulfil the above criteria may not allow us to generalize this statement, however, there is a fair chance that evidence will be accumulated soon.

References

1. J. Szöllősi, S. Damjanocich, S.A. Mulhern and L. Trón, L, Progr. Biophys. molec. Biol., *49*, 65, 1987.
2. P. Cuatrecasas, The Harvey Lectures, Series *80*, 89, 1986.
3. B. Alberts, D. Bray, J. Lewis, M. Raff, K. Roberts and D.D. Watson, Molecular Biology of the Cell, Garland Inc., New York and London, 1983.
4. M. Balázs, J. Matkó, J. Szöllősi, L. Mátyus, M.J. Fulwyler and S. Damjanovich, Biochem. Biophys. Res. Commun., *140*, 999, 1986.
5. P. Cuatrecasas, Ann. Rev. Biochem., *43*, 169, 1974.
6. D.R. Sibley, J.L. Benovic, M.G. Caron and R.J. Lefkowitz, Cell, *48*, 913, 1987.
7. I.H. Pastan and M.C. Willingham, Ann. Rev. Physiol., *43*, 239, 1981.
8. M.J. Berridge and R.F. Irvine, Nature, *312*, 315, 1984.
9. J. Cambier, J.G. Monroe, K.M. Coggeshall and J. Ranson, Immunology Today, *6*, 218, 1985.
10. M.C. Sakar and L.E. Hokin, J. Membr. Biol., *89*, 193, 1986.
11. J.G. Monroe and M.C. Cambier, J. Exp. Med., *157*, 2073, 1983.
12. G.L. L'Allemain, A. Granchi, E. Cragoe, Jr. and J. Pouyssegur, J. Biol. Chem., *259*, 4313, 1984.
13. R. Zidovetzki, Y. Yarden, J. Schlessinger and T.M. Jovin, Proc. Natl. Acad. Sci., *78*, 6981, 1981.
14. T.Y. Tsien, T. Pozzan and T.J. Rink, Nature, *295*, 68, 1982.
15. M.J. Berridge and R.F. Irvine, Nature, *312*, 315, 1984.
16. U. Nishizuka, Nature, *308*, 693, 1984.
17. T.R. Hesketh, J.P. Moore, J.D.H. Morris, M.V. Taylor, J. Rogers, G.A. Smith and J.C. Metcalfe, Nature (Lond.), *313*, 481, 1985.
18. P. Downes and R.H. Michell, Mol. Aspects Cell. Regul., *4*, 2, 1985.
19. M.D. Housley, Trends Biochem. Sci., *12*, 1, 1987.
20. W. Siffert and J.W.N. Akkerman, Nature, *325*, 456, 1987.
21. J.C. Cambier, J.G. Monroe, K.M. Coggeshall and J.T. Ransom, Immunol. Today, *6*, 218, 1985.
22. L. Trón, J. Szöllősi, S. Damjanovich, S.H. Helliwell, D.J. Arndt-Jovin and T.M. Jovin, Biophys. J., *45*, 939, 1984.
23. J. Szöllősi, L. Trón, S. Damjanovich, S.H. Helliwell, D.J. Arndt-Jovin and T.M. Jovin, Cytometry, *5*, 210, 1984.
24. S. Damjanovich, L. Trón, J. Szöllősi, R. Zidovetzki, W.L.C. Vaz, F. Regateiro, D.J. Arndt-Jovin and T.M. Jovin, Proc. Natl. Acad. Sci. USA, *80*, 5985, 1983.
25. J. Szöllősi, L. Mátyus, M. Balázs, I. Ember, M.J. Fulwyler and S. Damjanovich, Cytometry, *8*, 120, 1987.
26. J. Szöllősi, S. Damjanovich, C.K. Goldman, M.J. Fulwyler, A. Aszalós, G. Goldstein, P. Rao, M.A. Talle, and T.A. Waldmann, Proc. Natl. Acad. Sci. USA, *84*, 7246, 1987.
27. L. Trón, J. Szöllősi and S. Damjanovich, Immunol. Letter, *16*, 1, 1987.

Acta Physica Hungarica 65 (2-3), pp. 355–358 (1989)

MEASUREMENT OF OXIDE-LAYER THICKNESS OF INTERNAL GRANULES IN HIGH-PURITY ALUMINIUM*

S. TAKÁCS, F. DITRÓI and I. MAHUNKA

Institute of Nuclear Research of the Hungarian Academy of Sciences (ATOMKI)
4001 Debrecen, Hungary

High-purity aluminium samples and mixtures containing different amounts of alumina were irradiated by 13 MeV ^{3}He particles. The aim of the investigation was to determine the oxide-layer thickness on the surface of internal aluminium granules. Measurement was carried out by determining the bulk oxygen concentration in the samples, and calculating the oxide-layer thickness, by using model conditions about the microstructure of the aluminium samples.

Introduction

The extended use of aluminium in its high-purity form and in different types of alloys made in the conventional way and/or by powder metallurgy technology makes it necessary to investigate the purity and the microstructure of these materials. Oxygen is a very important element in connection with metals both on the surface and in the volume, too. A limited number of methods is known for the determination of bulk oxygen concentration in aluminium. Now we only deal with nuclear methods, especially Charged Particle Activation Analysis (CPAA).

This method is very useful when the half-life of the radio isotope produced from the element in question is different from the half-lives of the other confusing isotopes. The detection limit and accuracy of CPAA is quite good, compared with other methods [1]. The ^{3}He and triton particles are the best choices for bombardment [2, 3] because of the good irradiation and detection parameters. Our cyclotron can accelerate protons, deuterons, ^{3}He and ^{4}He particles, so we applied ^{3}He for irradiation.

For oxygen determination the $^{16}O(^3He,p)^{18}F$ and $^{16}O(^3He,n)^{18}Ne \rightarrow ^{18}F$ reactions were used [4]. Their cross-sections and yields data are published in [5]. The half-life of the produced ^{18}F isotope (110 min) is long enough for comfortable measurement.

The purpose of our recent investigation was to determine the surface layer thickness of an aluminium-oxide layer on the surface of internal granules of an aluminium sample pressed from high-purity (4N) aluminium powder. The main oxygen content in this type of aluminium metal is supposed to be on the surface of the internal granules.

*Dedicated to Academician D. Berényi on his 60th birthday

Experimental

The aluminium samples were positioned in an evacuated analytical chamber and were irradiated by ^{3}He particles. The beam energy was chosen to be 13 MeV and the current was 1–4 microampers. The irradiation time was 5–20 min depending on the sample type. The gamma-spectra of the irradiated targets were measured by Ge(Li) detector and the data were collected by a Canberra multichannel analyser type S35-plus in order to investigate the gamma-lines of all activated elements. For the determination of the oxygen concentration the $E_\gamma = 511$ keV the annihilation peak of ^{18}F was used after separating it from other radiation by half-life measurement. The time between the end of irradiation and the beginning of the measurement (cooling time) was approximately an hour.

Two types of samples were irradiated, both of them were disk-shaped and pressed from powder. The first type of samples was pressed from high-purity (4N) aluminium powder, the other was made from a mixture of high-purity aluminium and aluminium-oxide powder about 50 μm in particle diameter.

Determination of the oxide-layer thickness on the surface of granules

To avoid the inaccuracy in beam-current determination we used standard samples with known oxygen content. These samples were made from a homogeneous mixture of aluminium and alumina powder. By means of the standard samples we could use the relative method for the determination of oxygen concentration.
Model conditions and the initial data and formulae were:

r: radius of the Al granules supposed to be spheres
d: thickness of oxide layer on the surface of the granule
$V_1 = (4/3)\pi r^3$: aluminium volume in a single granule measured in cm^3
$V_2 = 4\pi d r^2$: oxide volume in a single granule measured in cm^3
$m = m_1 + m_2 = V_1\varrho_1 + V_2\varrho_2$: mass of a granule measured in g
n=1/m : number of granules in 1 g material
O=m$_2$N : number of oxygen atoms in a granule disregarding the bulk oxygen content in the granule
C=On : number of oxygen atoms in 1 g aluminium powder
N=1.7705 10^{22} : number of oxygen atoms in 1 g of alumina
$M = M_1 + M_2$: mass of the mixture of M_1 g aluminium powder and M_2 g alumina powder
N(O) : number of oxygen atoms in 1 g mixture
ϱ_1 ϱ_2 : density of aluminium and alumina respectively
$a = \varrho_2/\varrho_1$: ratio of densities
Using the above definitions we get for N(O)

$$N(O) = \frac{M_1 C + M_2 N}{M} = \frac{N}{M}\left[\frac{M_1 da}{da + r/3} + M_2\right] . \qquad (1)$$

After substituting of $M_2 = 0$ in (1) the number of oxygen atoms in 1 g aluminium powder is given as

$$N'(O) = N\frac{da}{da + r/3} . \tag{2}$$

The ratio of (1) and (2) gives a simple formula which contains among other parameters the thickness of alumina on the surface of a single granule.

$$R = \frac{N(O)}{N'(O)} = 1 + \frac{M_2 r}{3Mda} . \tag{3}$$

From (3) we get

$$d = fr , \tag{4}$$

where

$$f = \frac{1}{3a(R-1)\left[\frac{M_1}{M_2} + 1\right]} . \tag{5}$$

The f involves only such parameters which can be measured easily by using standards and the relative method.

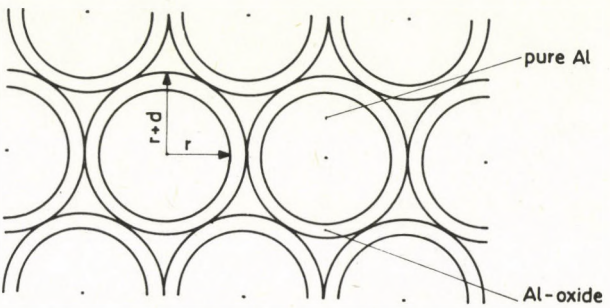

Fig. 1. Model conditions and parameters for the microstructure of aluminium samples pressed from powder

Results and discussion

The average granule size of the investigated aluminium powder was about 50 μ in particle diameter. Knowing the average granule diameter we could determine the thickness of the alumina layer on the surface of a single granule, which in this case was: $d = (8.5 + 3)$ nm.

The inaccuracy in thickness determination is due to the approximated value of granule diameter, and to the interfering radiation of other isotopes. To avoid these errors longer irradiation time, and chemical separation of the ^{18}F isotope should be used.

Applying the above described method, the quality of the products of powder metallurgy can be improved. It is also possible to determine the surface-oxide layer thickness not only in the case of aluminium but of other metals, too.

References

1. J. Pauwels, BCR Information series No. 25, EUR6240 EN.
2. C. Vandecasteele, P. Goethals, R. Kieffer and J. Hoste, Bull. Soc. Chim. Belg., *84*, 673, 1975.
3. H. Petri and C.S. Sastri, Z. Anal. Chem., *227*, 25, 1975.
4. S. Takács, F. Ditrói, F. Tárkányi, F. Szelecsényi, The Åbo Akademi Biennial Report, 1983/84, p. 95.
5. J. Fitschen, R. Beckmann, U. Holm and H. Neuert, Int. Journal of Appl. Rad. and Isotopes, *28*, 781, 1977.

Acta Physica Hungarica 65 (2–3), pp. 359–366 (1989)

A STUDY OF THIRD HARMONIC MODE ACCELERATION FOR THE MGC*

Z. KORMÁNY, I. SZÜCS, A. VALEK and J. VÁMOSI

Institute for Nuclear Research of the Hungarian Academy of Sciences (ATOMKI)
4001 Debrecen, Hungary

The investigation of the acceleration process in the third harmonic mode of operation is presented for a compact isochronous cyclotron. Beam dynamical studies were carried out by numerical calculation of ion motion in the centre and the main region of acceleration, applying the measured magnetic and calculated electric field data. The required conditions for accelerating particles with charge to mass ratio of 1/3 and 1/4 were determined. A new central geometry was designed to improve the focusing characteristics in the third harmonic mode of operation. The results of the calculations were experimentally confirmed by test runs with $^3He^+$ and $^4He^+$ beams, showing the possibility of accelerating heavier ions with charge to mass ratio down to 1/4.

1. Introduction

The MGC-20 cyclotron of the Institute was manufactured and installed by the Efremov Scientific Research Institute of Electrophysical Apparatus, Leningrad. This machine was designed to accelerate ions of hydrogen and helium isotopes with a charge to mass ratio in the range of $e/m = 1 - 0.5$. Mainly the first harmonic mode of operation is used, but low energy alpha particle and deuteron beams are accelerated on the third harmonics of the revolution frequency.

Because of the increasing interest in heavier ion beams (up to neon), which should accelerate with a lower charge to mass ratio in the third harmonic mode of operation, an extensive study of this mode has been carried out. Not only the possibility of acceleration was investigated, but the reason of beam intensity loss, observed in this mode of operation. The results of beam dynamical calculations, completed for particles of $e/m = 1/3$ and $1/4$, were experimentally confirmed by the acceleration of $^3He^+$ and $^4He^+$ ions.

*Dedicated to Academician D. Berényi on his 60th birthday

2. Investigation of the acceleration process

2.1. Isochronous field formation

The cyclotron has 4 pairs of low-power concentric coils to form the radial profile of the magnetic field [1]. To determine the necessary coil currents the Garren method [2] was used. The calculations were based on magnetic field data measured on site in the installation period. After calculating an approximate field value, the equilibrium orbit was determined in this field by numerical integration and the field value was corrected to obtain the proper revolution time. The optimum coil currents were determined minimizing the phase error caused by the deviation of the real field from the isochronous value.

The results of calculation at the maximum induction of the magnet for ions of $e/m = 1/3$ is shown in Fig. 1.

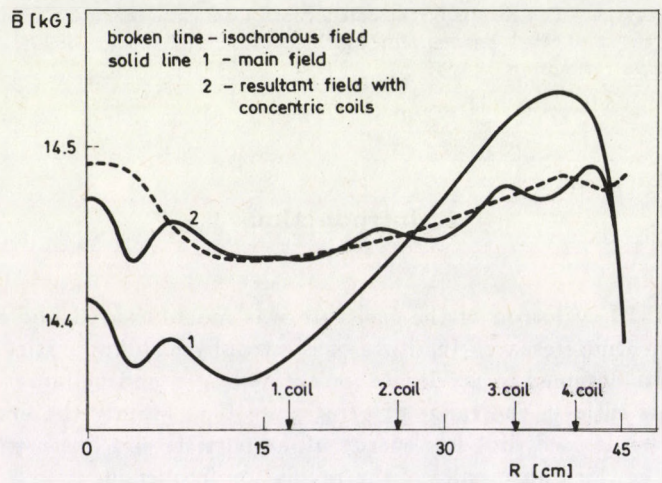

Fig. 1. The resultant field with optimum coil setting

The resultant field is isochronous to the radius $R = 43.5$ cm, the difference between the real and the isochronous values is less then 10 G outside the central region. This gives rise to the small phase error shown in Fig. 2, where its sine is plotted versus the radius.

2.2. Radial stability

The stability of the radial motion was examined in the resultant magnetic field. The existence of stability in both planes can be seen in Fig. 3, which shows the radial and axial betatron frequencies as the function of beam energy.

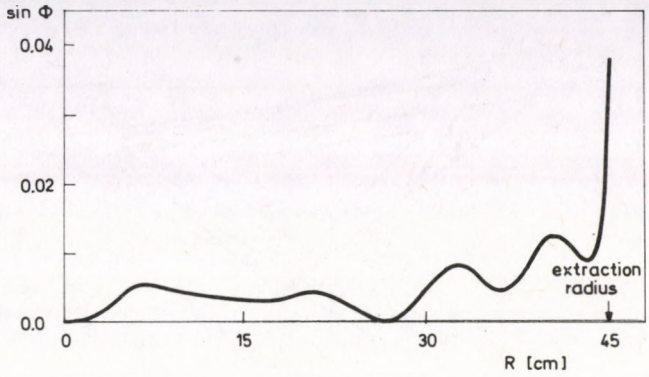

Fig. 2. The phase error in the resultant field

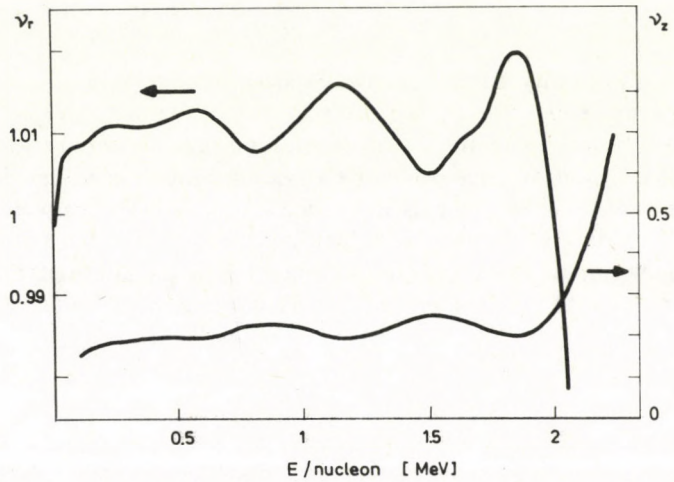

Fig. 3. The radial and axial betatron frequencies

The $\nu_r = 1$ resonance occurs only in the central region and near to the extraction radius. The latter is used in the precessional extraction: with the appropriate tuning of the outer valley coils it increases the orbit separation at the deflector. The MGC cyclotron has another set of valley coils, the inner ones, which serve to provide orbit centering in the central region.

The radial stability of particle motion was investigated in the region where it is not affected by the valley coils. The stability limits in the radial phase-space are plotted in Fig. 4 at several particle energies corresponding to radii within this region.

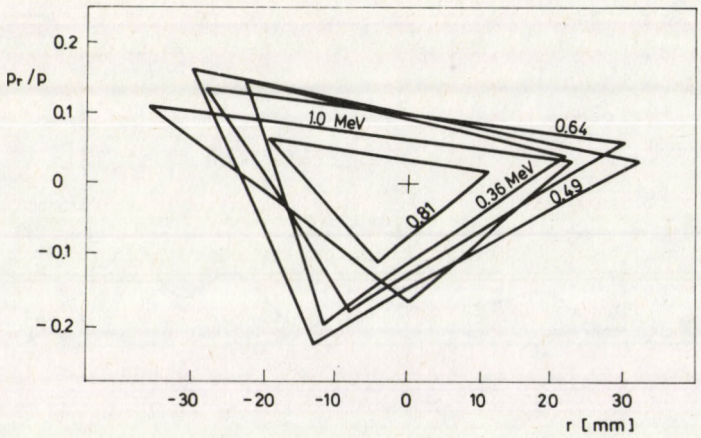

Fig. 4. Stability regions in the radial phase space

The area of stability triangle increases with energy, it has a maximum at $E = 0.49$ MeV/nucleon, then it decreases to the minimum value at $E = 0.81$ MeV/nucleon and increases again. The minimum is due to the small-scale oscillation of the resultant field and it corresponds to a local minimum of the radial betatron frequency observable in Fig. 3. It is not serious because the beam makes only a few turns in this region, so it goes through this energy quickly. On the other hand, even this minimum area of the stability region is large enough and Fig. 5 shows that outside the central region there is quite a large area for orbit centres to be placed in.

2.3. Orbit centering

The inner orbits in the centre of a cyclotron can be calculated with appropriate accuracy if only a detailed and accurate electric field map is given. In our case this map was determined by a FORTRAN code written in the JINR [3], which solves the Laplace equation in three dimensions by the relaxation method.

As the calculations show the motion of orbit centres in the third harmonic mode is strongly affected by the dee voltage amplitude: the lower the dee voltage the better the beam centered. The dee voltage cannot be lowered without limit because it determines not only the orbit centering but the starting phase interval of the ions. As a result of these calculations the dee voltage of 25 kV was chosen as a compromise which provides simultaneously a reasonable range of starting phase and minimum departure of orbit centres from the magnet centre.

Acceleration of particles into stable orbits can be achieved if the inner valley coils can centre the beam well, i.e. they place the orbit centres within the stability

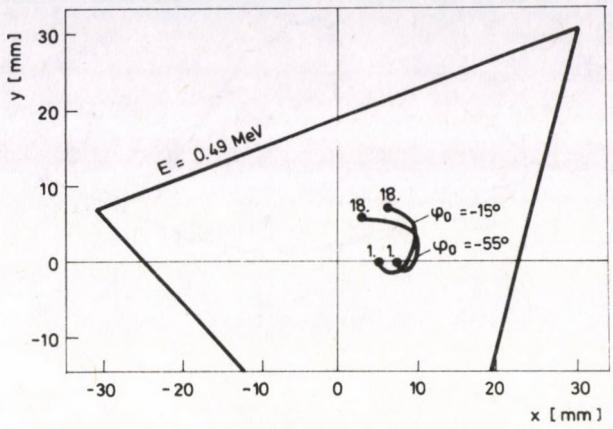

Fig. 5. Orbit centre motion with the optimum setting of the inner valley coils

region. Since the effect of the inner valley coils extends to the radius of about 20 cm, the calculations of orbit centering were carried out to the energy corresponding to this radius. The result of the optimum coil setting for two different values of starting phase is shown in Fig. 5. It indicates that the orbit centres lie within the stability limits, so the inner valley coils are capable of providing centered orbits for heavier ions, too.

The results of the calculations and the conclusions for particles of $e/m = 1/4$ were very similar to the ones presented for $e/m = 1/3$.

3. Investigation of the central region

3.1. Intensity loss

The beam intensity in the third harmonic mode of operation is about four times lower than it is in the first harmonic mode. The observed intensity loss cannot be tolerated regarding the difficulties of producing multiply charged heavy ions. The beam loss was supposed to occur near the centre, because there was no significant change in the intensity measured at larger radii by internal probe.

Simulation of particle motion in the central region was carried out by applying the measured magnetic and calculated three dimensional electric field data. The major conclusions of this study are: firstly, the accelerating gaps are too wide and, as a result, the gap crossing time is long and the energy gain is smaller than that in the first harmonic mode; secondly, the present central geometry in the third harmonic mode provides insufficient axial electric focusing. The smaller energy gain, especially during the second gap crossing, causes not well centered orbits and

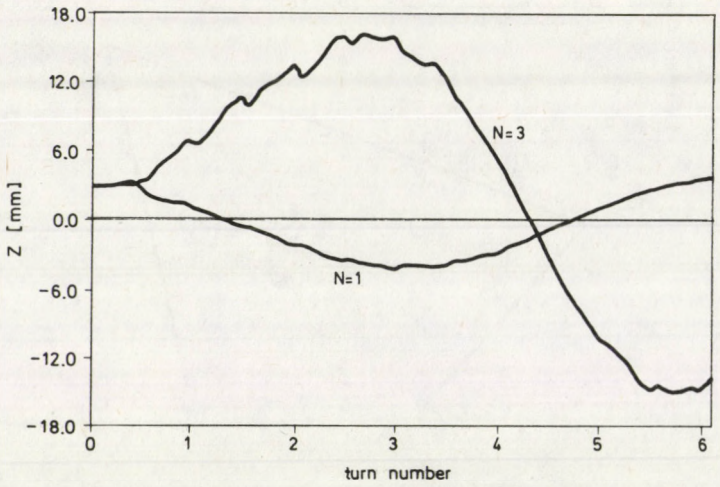

Fig. 6. Axial oscillation of the $\varphi_0 = -20^0$ particle in first and third harmonic modes of operation

low beam quality, the absence of axial focusing force gives rise to relatively large betatron amplitudes, as it is shown in Fig. 6.

3.2. Modification of the central geometry

To remove the defects mentioned above a new central geometry was designed. First the effect of gap size reduction in the central region was examined: the moderate dee voltage in the MGC cyclotron makes it possible to apply an accelerating gap as small as 10 mm. Orbit calculations in this geometry showed observable but insufficient improvement both in beam centering and in axial focusing. The required accelerating properties were achieved by a new ion source – puller location. The method of Smith [4] was applied to increase the azimuthal length of the first half turn, pushing the phase of the successive gap crossings into positive direction.

The construction of the MGC cyclotron allows a simple way to lengthen the first half turn by rotating the ion source with its adjusting mechanism around the geometric centre. The optimum angle of rotation was determined by numerical calculation of particle motion in the modelled geometry. 10° of rotation was found where the required axial electric focusing is accompanied by the maximum energy gain in this case. Numerical orbit calculations show good beam behaviour in this modified central geometry. Well-centered orbits can be achieved by proper setting of the valley coils. The orbit centre of the central particle is displaced from the geometric centre less than 1 mm at $R = 20$ cm. Moreover, the modification leads to significantly smaller axial oscillations and the beam size is in accordance with the acceptance of the central geometry.

On the basis of this study the mechanical design of the new fillers of the dees has been completed as well.

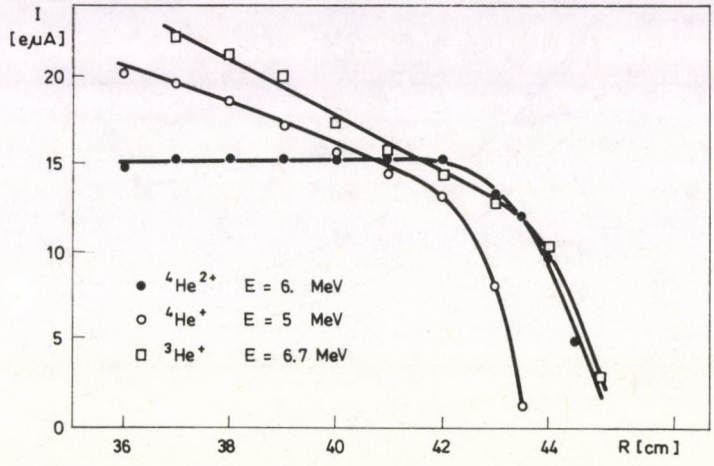

Fig. 7. Intensity of internal beam for various He ions. The arc power of the ion source was 500 W for producing $^4He^{2+}$ ions and about 70 W for others

4. Experimental results

Presently the MGC cyclotron has a low arc power Livingstone-type ion source. Since this source is not expected to produce the necessary heavy ions, $^3He^+$ and $^4He^+$ ions were chosen to model heavy ion beams with charge mass ratios 1/3 and 1/4.

Test runs with $^3He^+$ and $^4He^+$ ions confirmed the results of the above calculation. With the calculated currents in the concentric and the inner valley coils sharp resonances were found on the internal beam probe, showing the existence of third harmonic mode acceleration. By the proper setting of the outer valley coils and the deflector voltage the beams were extracted and transported to the first external probe in the beam transport system. The extraction efficiencies were about the same as for particles with higher charge to mass ratio.

Fig. 7 shows the radial dependence of the beam intensities measured by the internal probe at radii near to the extraction.

The steady fall of the intensity for $^3He^+$ and $^4He^+$ ions is due to charge exchange processes, occurring with residual gas atoms. The importance of this effect in the acceleration of not fully stripped ions is demonstrated in Fig. 8, where the intensities measured at various radii are shown as a function of the pressure in the cyclotron vacuum chamber.

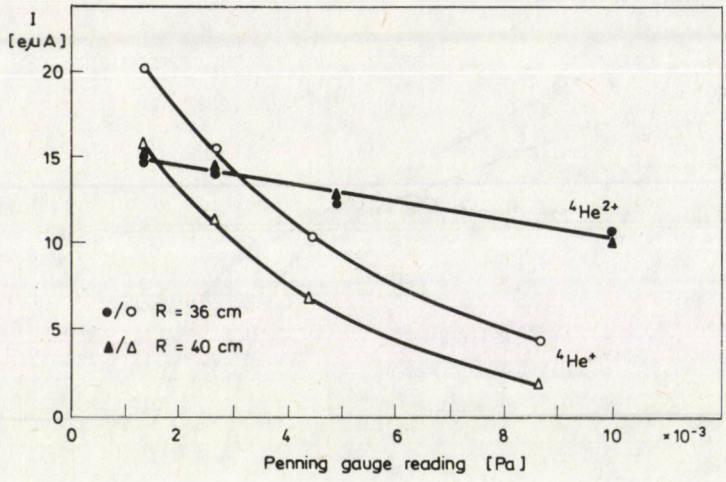

Fig. 8. Intensity of 6 MeV $^4He^{2+}$ and 5 MeV $^4He^+$ ions versus the vacuum chamber pressure

Our calculations and the test runs show that the MGC-20 cyclotron is capable of accelerating heavier ions with a charge to mass ratio down to 1/4.

References

1. A.N. Galaev et al, NIIEFA preprint B-0347, 1978.
2. A.A. Garren, Nucl. Instr. Meth., *18, 19*, 309, 1962.
3. S.B. Vorostzov et al, JINR preprint D 10-707, 1974.
4. W.I.B. Smith, Nucl. Instr. Meth., *9*, 49, 1960.

NOTES TO CONTRIBUTORS

I. PAPERS will be considered for publication in Acta Physica Hungarica only if they have not previously been published or submitted for publication elsewhere. They may be written in English, French, German or Russian.

Papers should be submitted to

Prof. I. Kovács, Editor
Department of Atomic Physics, Technical University
1521 Budapest, Budafoki út 8, Hungary

Papers may be either articles with abstracts or short communications. Both should be as concise as possible, articles in general not exceeding 25 typed pages, short communications 8 typed pages.

II. MANUSCRIPTS

1. Papers should be submitted in three copies.
2. The text of papers must be of high stylistic standard, requiring minor corrections only.
3. Manuscripts should be typed in double spacing on good quality paper, with generous margins.
4. The name of the author(s) and of the institutes where the work was carried out should appear on the first page of the manuscript.
5. Particular care should be taken with mathematical expressions. The following should be clearly distinguished, e.g. by underlining in different colours: special founts (italics, script, bold type, Greek, Gothic, etc.); capital and small letters; subscripts and superscripts, e.g. x^2, x_3; small *l* and l; zero and capital O; in expressions written by hand: *e* and *l*, *n* and *u*, *v* and v, etc.

A List of Symbols on a separate sheet should be attached to each paper.

6. References should be numbered serially and listed at the end of the paper in the following form: J. Ise and W. D. Fretter, Phys. Rev., *76,* 933, 1949.

For books, please give the initials and family name of the author(s), title, name of publisher, place and year of publication, e.g.: J. C. Slater, Quantum Theory of Atomic Structures, I. McGraw-Hill Book Company, Inc., New York, 1960.

References should be given in the text in the following forms: Heisenberg [5] or [5].

7. Captions to illustrations should be listed on a separate sheet, not inserted in the text.
8. In papers submitted to Acta Physica all measures should be expressed in SI units.

III. ILLUSTRATIONS AND TABLES

1. Each paper should be accompanied by three sets of illustrations, one of which must be ready for the blockmaker. The other sets attached to the copies of the manuscript may be rough drawings in pencil or photocopies.
2. Illustrations must not be inserted in the text.
3. All illustrations should be identified in blue pencil by the author's name, abbreviated title of the paper and figure number.
4. Tables should be typed on separate pages and have captions describing their content. Clear wording of column heads is advisable. Tables should be numbered in Roman numerals (I, II, III, etc.).

IV. RETURN OF MATERIAL

Owing to high postage costs, the Editorial Office cannot undertake to return *all* material not accepted for any reason for publication. Of papers to be revised (for not being in conformity with the above Notes or other reasons) only *one* copy will be returned. Material rejected for lack of space or on account of the Referees' opinion will not be returned to authors outside Europe.

Periodicals of the Hungarian Academy of Sciences are obtainable at the following addresses:

AUSTRALIA
C.B.D. LIBRARY AND SUBSCRIPTION SERVICE
Box 4886, G.P.O., *Sydney N.S.W. 2001*
COSMOS BOOKSHOP, 145 Ackland Street
St. Kilda (Melbourne), Victoria 3182

AUSTRIA
GLOBUS, Höchstädtplatz 3, *1206 Wien XX*

BELGIUM
OFFICE INTERNATIONAL DES PERIODIQUES
Avenue Louise, 485, *1050 Bruxelles*
E. STORY-SCIENTIA P.V.B.A.
P. van Duyseplein 8, *9000 Gent*

BULGARIA
HEMUS, Bulvar Ruszki 6, *Sofia*

CANADA
PANNONIA BOOKS, P.O. Box 1017
Postal Station "B", *Toronto, Ont. M5T 2T8*

CHINA
CNPICOR, Periodical Department, P.O. Box 50
Peking

CZECHOSLOVAKIA
MAD'ARSKA KULTURA, Národni třida 22
115 66 Praha
PNS DOVOZ TISKU, Vinohradská 46, *Praha 2*
PNS DOVOZ TLAČE, *Bratislava 2*

DENMARK
EJNAR MUNKSGAARD, 35, Nørre Søgade
1370 Copenhagen K

FEDERAL REPUBLIC OF GERMANY
KUNST UND WISSEN ERICH BIEBER
Postfach 46, *7000 Stuttgart 1*

FINLAND
AKATEEMINEN KIRJAKAUPPA, P.O. Box 128
00101 Helsinki 10

FRANCE
DAWSON-FRANCE S.A., B.P. 40, *91121 Palaiseau*
OFFICE INTERNATIONAL DE DOCUMENTATION ET LIBRAIRIE, 48 rue Gay-Lussac
75240 Paris, Cedex 05

GERMAN DEMOCRATIC REPUBLIC
HAUS DER UNGARISCHEN KULTUR
Karl Liebknecht-Straße 9, *DDR-102 Berlin*

GREAT BRITAIN
BLACKWELL'S PERIODICALS DIVISION
Hythe Bridge Street, *Oxford OX1 2ET*
BUMPUS, HALDANE AND MAXWELL LTD.
Cowper Works, *Olney, Bucks MK46 4BN*
COLLET'S HOLDINGS LTD., Denington Estate,
Wellingborough, Northants NN8 2QT
WM DAWSON AND SONS LTD., Cannon House
Folkstone, Kent CT19 5EE
H. K. LEWIS AND CO., 136 Gower Street
London WC1E 6BS

GREECE
KOSTARAKIS BROTHERS INTERNATIONAL BOOKSELLERS, 2 Hippokratous Street, *Athens-143*

HOLLAND
FAXON EUROPE, P.O. Box 167
1000 AD Amsterdam
MARTINUS NIJHOFF B. V.
Lange Voorhout 9–11, *Den Haag*
SWETS SUBSCRIPTION SERVICE
P.O. Box 830, 2160 Sz Lisse

INDIA
ALLIED PUBLISHING PVT. LTD.
750 Mount Road, *Madras 600002*
CENTRAL NEWS AGENCY PVT. LTD.
Connaught Circus, *New Delhi 110001*
INTERNATIONAL BOOK HOUSE PVT. LTD.
Madame Cama Road, *Bombay 400039*

ITALY
D. E. A., Via Lima 28, *00198 Roma*
INTERSCIENTIA, Via Mazzé 28, *10149 Torino*
LIBRERIA COMMISSIONARIA SANSONI
Via Lamarmora 45, *50121 Firenze*
SANTO VANASIA, Via M. Macchi 58
20124 Milano

JAPAN
KINOKUNIYA COMPANY LTD.
Journal Department, P.O. Box 55
Chitose, *Tokyo 156*
MARUZEN COMPANY LTD., Book Department
P.O. Box 5050 Tokyo International, *Tokyo 100-31*
NAUKA LTD., Import Department
2-30-19 Minami Ikebukuro, Toshima-ku, *Tokyo 171*

KOREA
CHULPANMUL, *Phenjan*

NORWAY
TANUM-TIDSKRIFT-SENTRALEN A.S.
Karl Johansgata 43, *1000 Oslo*

POLAND
WĘGIERSKI INSTYTUT KULTURY
Marszalkowska 80, *00-517 Warszawa*
CKP I W, ul. Towarowa 28, *00-958 Warszawa*

ROUMANIA
D. E. P., *Bucuresti*
ILEXIM, Calea Grivitei 64–66, *Bucuresti*

SOVIET UNION
SOYUZPECHAT — IMPORT, *Moscow*
and the post offices in each town
MEZHDUNARODNAYA KNIGA, *Moscow G-200*

SPAIN
DIAZ DE SANTOS Lagasca 95, *Madrid 6*

SWEDEN
ESSELTE TIDSKRIFTSCENTRALEN
Box 62, *101 20 Stockholm*

SWITZERLAND
KARGER LIBRI AG, Petersgraben 31, *4011 Basel*

USA
EBSCO SUBSCRIPTION SERVICES
P.O. Box 1943, *Birmingham, Alabama 35201*
F. W. FAXON COMPANY, INC.
15 Southwest Park, *Westwood Mass. 02090*
MAJOR SCIENTIFIC SUBSCRIPTIONS
1851 Diplomat, P.O. Box 819074,
Pallas, Tx. 75381-9074
READ-MORE PUBLICATIONS, INC.
140 Cedar Street, *New York, N. Y. 10006*

YUGOSLAVIA
JUGOSLOVENSKA KNJIGA, Terazije 27, *Beograd*
FORUM, Vojvode Mišića 1, *21000 Novi Sad*

Index: 26.022

Acta Physica Hungarica

VOLUME 65, NUMBER 4, 1989

EDITOR–IN–CHIEF

I. KOVÁCS

EDITORIAL BOARD

Z. BAY, R. GÁSPÁR, I. GYARMATI, N. KÜRTI,
K. NAGY, L. PÁL, P. SZÉPFALUSY, I. TARJÁN,
B. TELEGDI, L. TISZA, E. WIGNER



Akadémiai Kiadó, Budapest

ACTA PHYS. HUNG. APAHAQ 65 (4) 367–449 (1989) HU ISSN 0231–4428

ACTA PHYSICA HUNGARICA

A JOURNAL OF THE HUNGARIAN ACADEMY OF SCIENCES

EDITED BY
I. KOVÁCS

Acta Physica publishes original papers on subjects in physics. Papers are accepted in English, French, German and Russian.

Acta Physica is published in two yearly volumes (4 issues each) by

AKADÉMIAI KIADÓ
Publishing House of the Hungarian Academy of Sciences
H-1054 Budapest, Alkotmány u. 21

Subscription information

Orders should be addressed to

KULTURA Foreign Trading Company
1389 Budapest P.O. Box 149

or to its representatives abroad.

Acta Physica Hungarica is abstracted/indexed in Chemical Abstracts, Mathematical Reviews, Science Abstracts, Physics Briefs, Risk Abstracts

© Akadémiai Kiadó, Budapest

CONTENTS

ELEMENTARY PARTICLES AND FIELDS

Painlevé property and Bäcklund transformation of SU(2) Yang–Mills–Higgs system. *B. V. Baby* 435

ATOMIC AND MOLECULAR PHYSICS

Rotational analysis of the $A^6\Sigma$–$X^6\Sigma$ transition of chromium monofluoride. *V. M. Dubov, D. V. Tschechovskoy, E. A. Shenyavskaya* and *I. Kovács* 411

Spectrum of atomic electrons ionised by an intense field. *P. Kálmán* 425

Effect of hydrogen bonding on the polarization of fluorescence of 4-methyl-7-hydroxy coumarin. *R. Giri, S. S. Rathi, M. K. Machwe* and *V. V. S. Murti* 431

OPTICS

Investigation of electric field distribution in Z-cut KDP Q-switch modulator crystals. *R. Sh. Alnayli Cs. Kuti, J. S. Bakos* and *I. Tóth* 395

CONDENSED MATTER

Аппроксимация зонной сртуктуры полупроводников IV группы. В. А. Филиков, В. Н. Гордеев, В. А. Лигачев и О. Е. Акимов 367

On superfluid ^{3}He–^{4}He mixtures in magnetic fields. *R. Gonczarek* 381

Calculation of electron density and surface energy by variation method. *A. Iskander* and *L. Orosz* 391

Characteristics of laser-heated titanium in a nitrogen atmosphere. *L. Nánai, I. Hevesi, B. S. Luk'yanchuk, E. M. Morozova, A. S. Rogachev, A. V. Simakhin, N. M. Sukonkhina* and *G. A. Shafeev* 405

ERRATUM 441

BOOK REVIEWS 443

Acta Physica Hungarica 65 (4), pp. 367–379 (1989)

АППРОКСИМАЦИЯ ЗОННОЙ СТРУКТУРЫ ПОЛУПРОВОДНИКОВ IV ГРУППЫ

В. А. ФИЛИКОВ, В. Н. ГОРДЕЕВ, В. А. ЛИГАЧЕВ и О. Е. АКИМОВ

Московский энергетический институт, Москва, СССР

(Поступило 6-ого января 1987)

Анализируется *kp*–метод расчета зонных структур. Обнаружены: неоднозначность матричных элементов оператора нмпульса и неудовлетворительная картина энергетической диаграммы в Σ-направлении, а также в некоторых других несимметричных направлениях. Предлагается: линеаризовать закон дисперсии, аппроксимировать энергетические состояния зоны проводимости соответсвующими плоскостями, использовать систему линейных уравнений, полученных из инвариантных соотношений, для подгонки параметров.

Предметом исследования является kp–метод как таковой предложенный авторами работ [1]–[4]. На примере зонных структур элементов IV группы выявлены возможности и ограничения этого метода. Показано, что существуют две серьезные трудности: неоднозначность нахождения параметров импульса и нарушение симметрии энергетических состояний даже в непосредственной близости от запрещенной зоны. Устранить недостатки возможно, если воспользоваться аппроксимирующими плоскостями. Они дают помимо наглядной модели уровней, раскрывающих картину "взаимодействия" состояний, еще и дополнительную информацию для однозначной подгонки параметров импульса. Линейная аппроксимация позволяет более точно воссоздать зонную структуру в масштабах всего k-пространства первой зоны Бриллюэна.

Анализ начнем с замечания И. М. Цидильковского: "Согласие зонной структуры с экспериментом вдоль главных направлений симметрии зоны Бриллюэна нельзя считать убедительным доказательством правильности зонной картины — имеется очень много свободных параметров для подгонки теории к эксперименту, вследствие чего однозначность процедуры неочевидна". [5] (с. 251).

Действительно, зонная структура $\alpha-$Sn в Σ направлениии (рис. 1) при параметрах импульса [3] найденных для Δ и Λ напрпавлений, оказывается неудовлетворительной — все состояния Σ_5 должны оканчиваться в точках X_5 или во всяком случае вблизи них.

Аналогичная картина наблюдается для Ge и Si. Особенно плохо выглядят три нижних энергетических уровня с симметрией Σ_1 (если спин-орбитальное взаимодействие не учитывать). Например, для Ge они должны оканчиваться в трех точках $X_1^l = -0.715\text{Ry}$, $X_4 = -0.224\text{Ry}$ и $X_1^u = 0.103\text{Ry}$, а они оканчиваются в точках с энергнями -0.739Ry, -0.075Ry и 0.922Ry,

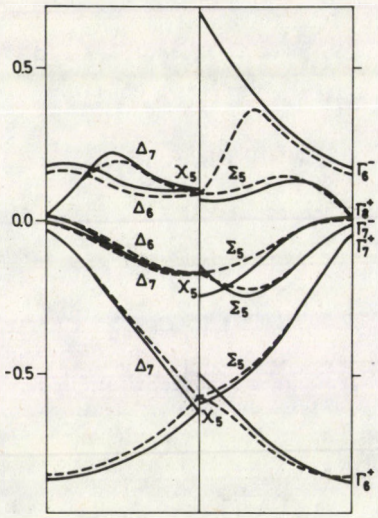

Рис. 1. Зонная структура α–Sn в Δ и Σ направлениях; сплошные линии — kp-метод; пунктирные — ОПВ. Энергия на этой и других диаграммах дается в ридбергах (Ry)

соответственно. Это слишком большие расхождения, свидетельствующие о серьезных изъянах в структуре зон в целом. Между тем подгонка Σ_1 кривых невозможна, так как они зависят от тех же четырех параметров импульса $P_1 - P_4$, от которых зависят и кривые Δ_1 и Δ_5. Любое изменение этих параметров моментально приводит к нарушению общей картины энергетических состояний в Δ направлении, да и в Λ тоже.

Чтобы исправить положение с Σ_1, необходимо казалось бы присоединить к гамильтониану дополнительные верхние уровни. Однако учет состояний от следующего вектора обратной решетки с индексами $\langle 220 \rangle$, приводит резкому росту числа неизвестных параметров, а значит, и к повышению и без того высокого уровня неопределенности задачи в целом. Последняя проблема является наиболее серьезной для этого метода.

Если симметричную 15×15 матрицу kp–гамильтониана записать так, как это сделано в табл. I, то машинное время на подгонку параметров можно существенно сократить путем введения в программу системы линейных уравнений относительно квадратов искомых параметров из инвариантных сумм попарных и тройных произведений собственных значений, выведенных по матрицам симметричных Δ и Λ направлений.

Таблица I

Верхняя часть симметричной 15×15-матрицы kp–гамильтониана. P_1-P_{10} — параметры импульса; k_x, k_y, k_z — координаты волнового вектора ($k=2\pi a_0/a_c$, где a_0 — боровский радиус, a_c — постоянная решетки); $H_i=\Gamma_i+K_x^2+K_y^2+K_z^2$ — диагональный матричный элемент (Γ_i приведены в табл. II); коэффициенты $a=\sqrt{3/2}.\bar{a}=-\sqrt{3}/2.\bar{b}=1/\sqrt{2}.c=\sqrt{2}$

H_1	○	P_4k_x	○	○	○	○	○	○	P_4k_y	○	○	○	P_4k_z	○
	H_2	P_3k_x	○	○	○	○	○	○	P_3k_y	○	○	○	P_3k_z	○
		H_3	P_1k_y	○	○	○	○	○	○	P_2k_y	○	P_1k_z	○	P_2k_x
			H_4	○	P_9k_x	$P_{10}k_x$	○	$\bar{b}P_5k_x$	P_2k_x	○	$\bar{a}P_5k_x$	○	○	○
				H_5	P_7k_x	P_8k_x	○	cP_6k_x	P_2k_x	○	○	○	P_2k_y	○
					H_6	○	P_9k_x	○	○	P_7k_x	○	P_9k_y	○	P_7k_y
						H_7	$P_{10}k_x$	○	○	P_8k_x	○	$P_{10}k_y$	○	P_8k_y
							H_8	cP_5k_x	P_1k_x	○	○	○	P_1k_y	○
								H_9	○	$\bar{b}P_6k_x$	○	$\bar{b}P_5k_y$	○	$\bar{b}P_6k_y$
									H_{10}	P_2k_x	○	○	○	○
										H_{11}	$\bar{a}P_6k_x$	○	○	○
											H_{12}	aP_5k_x	○	aP_6k_y
												H_{13}	P_1k_z	○
													H_{14}	P_2k_z
														H_{15}

Можно было бы привлечь уравнения, составленные из матриц Σ направления, например, для определения параметров P_5 и P_6:

$$\Sigma_2 = \begin{pmatrix} H_8 & -\sqrt{3}P_5K & 0 \\ -\sqrt{3}P_5K & H_9 & -\sqrt{3}P_6K \\ 0 & -\sqrt{3}P_6K & H_{11} \end{pmatrix},$$

но, как отмечалось, ввиду плохой общей картины зон в Σ направлении, эти уравнения лучше не использовать.

Наиболее оптимальной системой линейно независимых уравнений является, по-видимому, следующая

$$K_x^2(H_1P_3^2 + H_2P_4^2) = H_1H_2H_3 - X_1X_2X_3, \tag{1}$$

$$K_x^2(H_5P_1^2 + H_4P_2^2) = H_{13}H_{14}H_{15} - X_{13}X_{14}X_{15}, \tag{2}$$

$$K_x(P_3^2 + P_4^2) = \sum_{j=1}^{2}\sum_{j=i+1}^{3}(H_iH_j - X_iX_j), \tag{3}$$

$$K_x(P_1^2 + P_2^2) = \sum_{j=13}^{14}\sum_{j=i+1}^{15}(H_iH_j - X_iX_j), \tag{4}$$

$$K^2\left(\tfrac{1}{3}P_1^2 + \tfrac{1}{3}P_2^2 + P_5^2 + P_6^2\right) = \sum_{i=8}^{10}\sum_{j=i+1}^{11}(H_i'H_j' - L_iL_j), \tag{5}$$

$$\begin{aligned} K^2\left[\tfrac{1}{3}(H_5' + H_9')P_1^2 + \tfrac{1}{3}(H_4' + H_9')P_2^2 + (H_3' + H_5')P_5^2 + (H_4' + H_3')P_6^2\right] \\ = \sum_{i=8}^{9}\sum_{j=i+1}^{10}\sum_{k=j+1}^{11}(H_i'H_j'H_k' - L_iL_jL_k), \end{aligned} \tag{6}$$

$$\begin{aligned} K^2\left(\tfrac{4}{3}P_1^2 + \tfrac{4}{3}P_2^2 + P_3^2 + P_4^2 + P_7^2 + P_8^2 + P_9^2 + P_{10}^2\right) \\ = \sum_{i=1}^{6}\sum_{j=i+1}^{7}(H_i'H_j' - L_iL_j), \end{aligned} \tag{7}$$

$$\begin{aligned} K_x^2\Big[2(H_6 + H_5 + H_7)P_5^2 + 2(H_4 + H_6 + H_7)P_7^2 \\ + (H_6 + H_4 + H_9)P_8^2 + (H_9 + H_5 + H_7)P_9^2 + (H_6 + H_9 + H_5)P_{10}^2\Big] \\ = \sum_{i=5}^{7}\sum_{j=i+1}^{8}\sum_{k=j+1}^{9}(H_iH_jH_k - X_iX_jX_k). \end{aligned} \tag{8}$$

Число скобок в правой части уравнений равно числу сочетаний по индексам, например, для формулы (8) оно равно C_5^3, т.е. 10, (7)–(21) и.т.д. В зависимости от выбора цели и приоритета в наборе экспериментальных данных,

можно пойти различными путями: малые параметры (P_7, P_{10}) приравнять нулю или, например, числу 0.1; считать взаимодействие между некоторыми состояниямн эквивалентным, т.е. пойти по пути уменьшения числа параметров; воспользоваться результатами эксперимента по циклотронному резонансу [1]; варьировать по одному, двум параметрам или числам из табл. II.

Таблица II

Значения энергии (в ридбергах) для Ge в трех основных точках первой зоны Бриллюэна X, Γ и L. Звездочкой отмечены экспериментальные величины, взятые в основном из [6], остальные числа соответствуют зонной структуре Ge, рассчитанной методом псевдопотенциала [6]

i	Γ_i	Γ	X_i	Δ	L_i	Λ
1	−0.926*	Γ_1^l	−0.654*	Δ_1	−0.779*	Λ_1
2	0.459	Γ_1^u	1.365	Δ_1	0.933*	Λ_1
3	0.239*	Γ_{15}	0.096*	Δ_1	0.062*	Λ_1
4	0.000*	Γ_{25}^l	−0.272*	Δ_5	−0.566*	Λ_1
5	0.909	$\Gamma_{25'}^u$	1.455	$\Delta_{2'}$	1.040	Λ_1
6	0.0735*	$\Gamma_{2'}^l$	0.096*	$\Delta_{2'}$	0.573*	Λ_1
7	0.992	$\Gamma_{2'}^u$	2.642	$\Delta_{2'}$	2.295	Λ_1
8	0.000*	$\Gamma_{25'}^l$	0.829*	$\Delta_{2'}$	−0.110*	Λ_3
9	0.669	$\Gamma_{12'}$	0.829	$\Delta_{2'}$	0.993*	Λ_3
10	0.239*	Γ_{15}	0.829	Δ_5	0.309*	Λ_3
11	0.909	$\Gamma_{25'}^u$	1.626	Δ_5	1.720	Λ_3
12	0.669	$\Gamma_{12'}$	1.014*	$\Delta_{1'}$	0.933*	Λ_3
13	0.000*	$\Gamma_{25'}^l$	−0.272*	Δ_5	−0.110*	Λ_3
14	0.239*	Γ_{15}	0.829	Δ_5	0.309*	Λ_3
15	0.909	$\Gamma_{25'}^u$	1.626	Δ_5	1.720*	Λ_3

Использование здесь табл. II с ориентировочными значениями энергии, взятыми из расчета зоны Ge методом псевдопотенциала [6], не должно показаться странным, так как kp–метод в том варианте, который предложили авторы работ [1]–[4], не мог обойтись без расчетных данных другого, более точного метода. Воспользовавшись табл. II и системой уравнений (1)–(8) находим параметры P_i для Δ направления (табл. III).

Для Λ направления эти параметры дают довольно значительное отклонение от экспериментальных значений. Чтобы найти P_i, которые подходили бы и для Δ, и для Λ направлений, необходима вариационная процедура. Если не признавать функциональной зависимости параметров импульса от волнового вектора, то в результате подгонки произойдет отклонение найденных параметров от фактических. Критерий наименьшего квадратичного отклонения не является гарантией однозначности вариационной процедуры. В десятимерном пространстве параметров импульса существует несколько однопорядковых локальных экстремумов, попадающих в область среднеквадратичных ошибок (δ) не превывающих 0.01 по сумме всех известных эксперментальных точек (табл. II).

Некоторые параметры (табл. III, строка 4) имеют очень близкие по ве-

Acta Physica Hungarica 65, 1989

Таблица III

Параметры импульса. В строке Ge(Δ) приведены параметры Ge удовлетворяющие Δ направлению и найденные с помощью системы уравнений (1)–(8) ; Ge(10) — десять оптимально найденных параметров для Δ и Λ направлений; Ge(9) — девять параметров ($P_6=P_9$), найденных с помощью вариационной процедуры и.т.д.

	δ	P_1	P_2	P_3	P_4	P_5	P_6	P_7	P_8	P_9	P_{10}
α–Sn[3]	—	1.002	–0.3891	0.952	0.356	0.641	1.272	0.557	1.079	1.120	0.038
Si[3]	—	1.050	–0.807	1.080	0.206	0.830	1.210	–0.090	1.320	1.200	0.100
Ge[3]	—	1.070	–0.752	1.200	0.532	0.805	1.436	0.1715	1.623	1.360	0.100
Ge(Δ)	0.0	1.104	–0.878	1.101	0.4486	0.847	1.129	0.1818	1.580	1.190	0.100
Ge(10)	0.00072	1.1319	–0.7566	1.077	0.4050	0.8430	1.1997	0.2658	1.2891	1.276	–0.4417
Ge(9)	0.00073	1.1336	–0.7533	1.077	0.4045	0.8440	1.2068	0.2742	1.2857	1.2068	–0.4509
Ge(8)	0.00126	1.1110	–0.7769	1.1110	0.4045	0.8600	1.1992	0.2407	1.2270	1.992	–0.46691
Ge(7)	0.00272	1.1171	–0.7578	1.1171	0.4190	0.8514	1.2179	1.2269	1.2179	1.2179	–0.4659
Ge(6)	0.007147	1.1634	–0.7284	1.1634	0.4254	0.8560	1.1634	0.2056	1.1634	1.1634	-0.6236
Ge(6)	0.0295	1.1073	–0.8286	1.1073	0.4203	0.8286	1.107	–0.1411	1.3084	1.3084	0.3592
Ge(5)	0.0143	1.1452	–0.8104	1.1452	0.4206	0.8104	1.1452	0.1707	1.1452	1.1452	–0.6968
Ge(5)	0.01156	1.1829	–0.6792	1.1829	0.3666	0.8082	1.1829	0.3666	1.1829	1.1829	–0.5321
Ge(5)	0.007513	0.07513	1.1536	–0.7258	1.1536	0.8657	21.1536	0.18505	1.1536	1.1536	–0.7258

личине значения. Если иметь ввиду только кривые зонной структуры, то можно обойтись меньшим числом параметров. В строке 5 табл. III приведены 10 оптимально найденных параметров, дающих минимальную суммарную ошибку ($\delta = 0.0007$). Затем два наиболее близких параметра принимались за один и вариация уже производилась по 9 параметрам. Таким образом, число параметров удается уменьшить в два раза. Желательно при нахождении нужных матричных элементов в дополнение к экспериментальным данным ориентироваться еще на какой-то общий конфигурационный каркас зон.

Если состояние электрона описывать уравнением $dp/dt = F$, что в изотропном пространстве эквивалентно выражению $dv/dt = m^{-1}F$, то в анизотропном пространстве это выражение запишется в тензорной форме $dv_i/dt = m_{ij}^{-1}F_j$ $(i, j = x, y, z)$. Эффективная масса (m_{ij}) непосредственно связана с квадратичным элементом закона дисперсии и играет важную роль вблизи экстремальных точек $(\nabla E(k) = 0)$. Во всех прочих точках k-пространства именно линейный член разложения закона дисперсии является определяющим.

Аппроксимация энергетического ландшафта формами, индуцированными только линейными элементами дает в руки практиков наглядную схему уровней. Коэффициенты уравнений являются надежными идентификаторами химических элементов и содержат полезную информацию о свойствах реальных материалов.

На рис. 2 пунктирными линиями a и b обозначены два характерных направления. Если немного отступить от симметричного направления Δ, соответствующего энергетическому сечению E_1 и снова рассчитать восемь нижних состояний зоны проводимости в сечении E_2 (рис. 3), то двукратновырожденное состояние Δ_5 расщепится во всех точках кроме одной, которая соответствовала точке пересечения прямых a и b.

Это наводит на мысль о важности последних. Говорить здесь просто как о взаимодействии двух долин Δ_2', значит высказывать довольно поверхностное суждение. Когда мы проследим за ходом изменения зонной структуры при движении вертикальной плоскости энергетического сечения E вдоль оси K_y то заметим, что перемещение этих и других аналогичных прямых подчинено определенному закону, и на квадратной грани зоны Бриллюэна (рис. 3, сечение E_3) энергетические состояния образуют некий симметричный рисунок. При этом исходная прямая a займет горизонтальное положение вблизи уровня 1.0Ry , а прямая b расщепится на прямую b_1, которая практически соответствует положению прямой b, и b_2 — нижнюю горизонтальную прямую, расположенную около нулевого уровня.

На примере кремния произведем анализ симметрии плоскостей, которые лучше всего видны через энергетические сечения $E_4 - E_7$ в гексагональной грани первой зоны Бриллюэна. То, что линейность во многом сохраняется и в глубине зоны Бриллюэна, иллюстрируется сечениями E_6' и E_2'. Будем рассматривать восемь нижних состояний зоны проводимости Si (рис. 4).

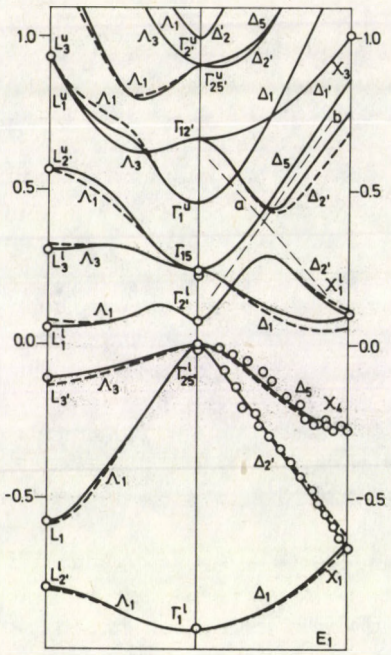

Рис. 2. Зонные структуры Ge, рассчитанные *kp*–методом, в Δ и Λ направлениях; сплошные линии — 10 оптимальных параметров (табл. III, строка 5); штрихпунктирные — 5 оптимальных параметров (табл. III, строка 13); пунктирные прямые *a* и *b* — следы аппроксимирующих плоскостей; белые кружки —экспериментальные значения энергии [6], [7].

Черными кружками показаны точки соответствия. Из сравнения сечений $E_4 - E_7$ следует, что состояние 1 опускается с уровня 1.7Ry (E_5) до 0.4Ry (E_7). Причем изменение величины энергии происходит строго пропорционально движению плоскости сечения E_i по гексагональной грани. Таким образом, состояние 1 как бы скользит вдоль наклонной плоскости, которую мы тоже обозначили цифрой 1 (рис.7). Угол пересечения прямых 2 и 3 в сечениях $E_4 - E_7$ остается постоянным, а точка их пересечение перемещается с уровня 0.75Ry(E_5) до 1.35RyE_7. Следовательно можно говорить о наличии еще двух наклонных плоскостей, 2 и 3. В центральном сечении E_6 прямые 1, 2, 3 пересекаются; значит точка L_1^u (лежащая на плоскости 1) и двукратновырожденная точка L_3^u (плоскости 2 и 3) образуют общую точку пересечения всех трех плоскостей. Введя на гексагональной грани местную координатную систему (E, K_x', K_y'), можно получить три уравнения плоскостей.

Следующий шаг состоит в том, чтобы полученные уравнения плоскостей перевести в четырехмерное пространство E, K_x, K_y и K_z. Как и следовало ожидать при наличии оси симметрии C_3, все три уравнения будут

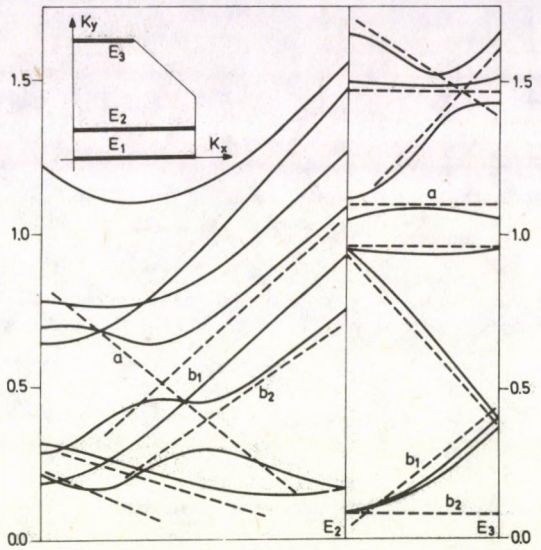

Рис. 3. Зонная структура Ge, рассчитанная kp–методом, параметрами из [1]; сечения E_2, E_3; пунктирные прямые — следы аппроксимирующих плоскостей

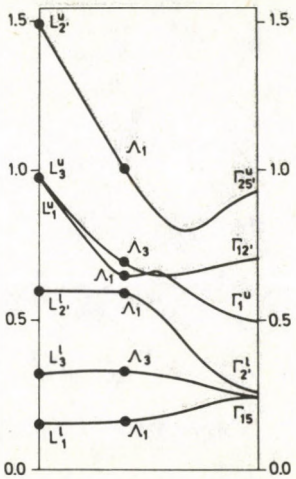

Рис. 4. Восемь энергетических состояний зоны проводимости Si, рассчитанных kp–методом в Λ направлении; черные кружки — точки соответствия с энергетическими состояниями в сечении E_6 и E_6'

переходить одно в другое при циклической перестановке переменных K_x, K_y, K_z. Поэтому достаточно привести лишь одно уравнение

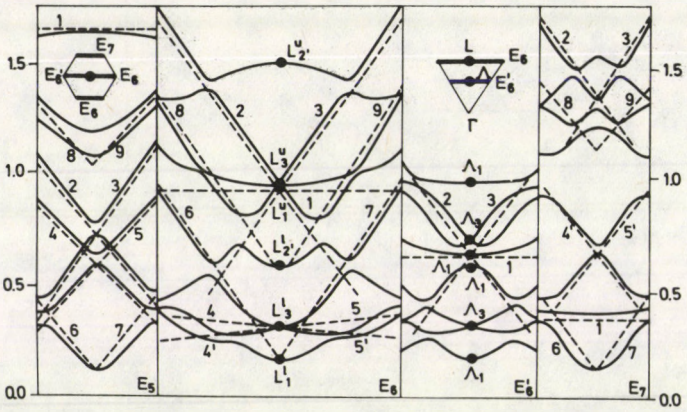

Рис. 5. Зонная структура Si, рассчитанная kp–методом; сечения E_5 — E_7

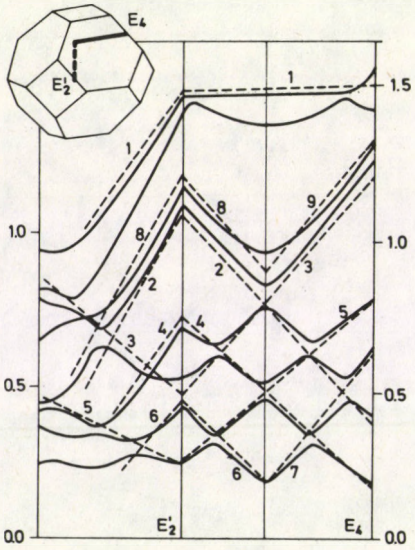

Рис. 6. Зонная структура Si, рассчитанная kp–методом; сечения E_4 — E_2

$$0.270K_x - 0.704K_y + 0.432K_z - 0.495E + 0.477 = 0, \tag{9}$$

которое здесь записано в нормальной форме. Уравнение для аналогичных

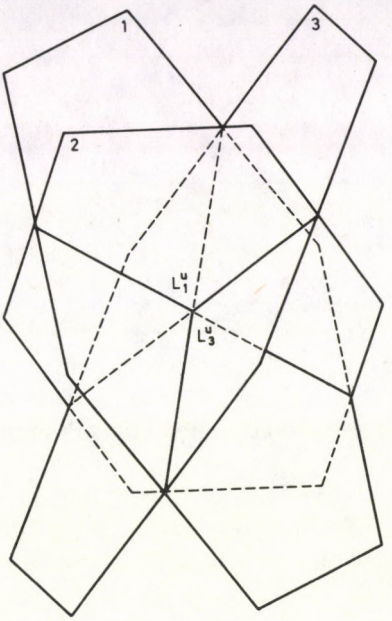

Рис. 7. Пространственное расположение аппроксимирующих плоскостей 1, 2, 3

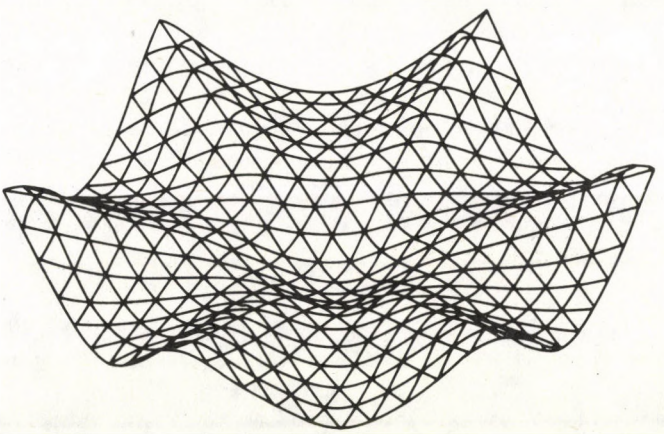

Рис 8. Дно зоны проводимости Ge в гексагональной грани, рассчитанное kp–методом

плоскостей зонной структуры германия выглядит следующим образом:

$$0.106K_x - 0.590K_y + 0.480K_z - 0.638E + 0.320 = 0. \qquad (10)$$

Чтобы получить уравнения плоскостей, следы которых обозначены цифрами 4, 5, 6, 7, 4′ и 5′ достаточно записать по одному выражению, соответственно для Si и Ge:

$$0.164K_x - 0.696K_y + 0.532K_z - 0.452E + 0.053 = 0, \tag{11}$$

$$0.330K_x - 0.723K_y + 0.394K_z - 0.459E + 0.433 = 0, \tag{12}$$

и произвести дважды замену по схеме $K_x \to K_y$, $K_y \to K_z$, $K_z \to K_x$; затем, осуществив операцию $K_x \to K_x$, $K_y \to K_z$, $K_z \to K_y$, снова дважды повторить циклическую перестановку. Таким образом, мы получим 6 уравнений, которые аппроксимируют все нижные состояния зоны проводимости. Шесть плоскостей нетрудно вычертить отдельно, как мы это сделали для трех плоскостей 1, 2, 3. Однако лучшей иллюстрацией их взаимного расположения является графическое изображение результатов точного машинного расчета дна зоны проводимости (рис. 8).

Мы видели, что максимальная гармония плоскостей приходится на границы зоны Бриллюэна. Поэтому построение плоскостей вообще говоря желательно начинать именно с границ. По мере приближения к точке Г линейность исчезает. Кроме того, энергетические состояния непосредственно прилегающие к запрещенной зоне также искривлены гораздо больше, чем вдали от нее. Идеальную и полную систему плоскостей можно легко воссоздать по зонной структуре, рассчитанной, например, методом псевдопотенциала [6], если формфакторы положить равными нулю. При наличии кристаллического потенциала плоскости во многом сохраняют свое относительное положение.

Главным здесь является то, что плоскость, проходящая в одной зоне Бриллюэна должна иметь продолжение в другой, смежной зоне. Например, сечения E_5–E_7 (рис. 5) должны быть абсолютно идентичными, а плоскости 2 и 3 (E_5) одного многогранника должны продолжаться в виде плоскостей 4 и 5 (E_5) другого многогранника. На рис. 5 и 6 не видно по крайней мере еще трех важных уровней, которые бы описывались уравнением (9) через инверсию (для первого октанта это эквивалентно замене $k_x \to k_y$, $k_y \to k_z$, $k_z \to k_y$). Ход кривых 8 и 9 вызывает сомнение.

Зонная структура, рассчитанная методом псевдопотенциала свободна от этих недостатков (рис. 9): сечения E_5 и E_7 тождественны. Не обсуждая того, насколько точно должны совпадать точки A, A' и A'', можно сказать, что они являются надежным ориентиром в подгонке матричных параметров.

Восстановить симметрию зон с помощью приведенной матрицы (табл. I) не удается. В дальнейшем предполагается, использовать несколько иную матрицу, которая получится, если вектор $\langle 200 \rangle$ разложить на Γ_1, Γ_{12} и Γ_{15}. В этом случае имеем следующие матрицы в Σ направлении Σ_1 (7×7), Σ_2 (1×1), Σ_3 (4×4), Σ_4 (3×3), вместо Σ_1 (5×5), Σ_2 (3×3), Σ_3 (6×6), Σ_4 (1×1), соответственно. Аналогично изменятся матрицы для Δ и Λ направлений, а

вместе с ними уравнения (1)–(8). За счет процедуры сокращения числа параметров (табл. III), матрицу kp–гамильтониана можно увеличить до размеров 27×27, подключив к ней вектор $\langle 220 \rangle$.

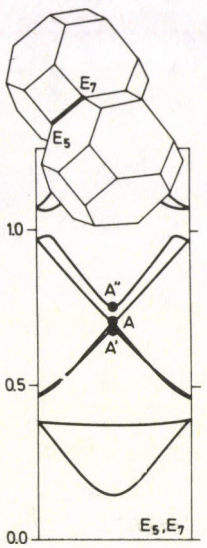

Рис. 9. Зонная структура Si в сечении E_5, E_7, рассчитанная методом псевдопотенциала

Литература

1. M. Cardona, F. H. Pollak, Phys Rev., *142*, 530, 1966.
2. M. Cardona, P. McElroy, F. H. Pollak, K. Shaklee, Solid State Commun., *4*, 319, 1966.
3. F. H. Pollak, C. W. Higginbotham, M. Cardona, J. Phys. Soc. Japan, Suppl., *21*, 20, 1966.
4. F. H. Pollak, M. Cardona, J. Phys. Chem. Sol, *27*, 423, 1966.
5. И. М. Цидильковский, Электроны и дырки в полупроводниках, "Наука", Москва, 1972.
6. W. D. Grobman, D. E. Eastman, L. L. Freeout, Phys. Rev. B., *12*, 4405, 1975.
7. T. C. Hsich, T. Miller, T. C. Chiang, Phys. Rev. B., *30*, 7005, 1984.

Acta Physica Hungarica 65 (4), pp. 381–389 (1989)

ON SUPERFLUID ^{3}He–^{4}He MIXTURES IN MAGNETIC FIELDS

R. GONCZAREK

Institute of Physics, Technical University of Wrocław
50-370 Wrocław, Poland

(Received 23 August 1987)

The problem of superfluid ^{3}He–^{4}He mixtures with S-wave-pairing is considered in a strong magnetic field. It is shown that the order of the phase transition to a normal phase generated by a strong magnetic field depends on the Landau parameter F_0^a. This fact allows us to classify ^{3}He–^{4}He mixtures just as superconductors where type-I is realized if $F_0^a < 1$ and type-II is realized in the opposite case.

1. Introduction

According to the theoretical investigations [1] in ^{3}He–^{4}He mixtures for concentrations $x \leq 5\%$ S-pairing is preferred with a growing tendency to P-pairing for higher concentrations. The estimated value of phase transition temperature $T_c \leq 5 \cdot 10^{-6}$K at concentrations $x = 1.3\%$ and $x = 5\%$.

Moreover, the Landau parameter F_0^a becomes positive (it is negative in ^{3}He although it is small $F_0^a \approx 0.09$. Nevertheless, it should be a function of pressure. Such tendencies of ^{3}He–^{4}He mixtures allow us to consider them as neutral superfluids with the singlet or triplet state Cooper's pairs for small or high concentrations, respectively. In the present paper we only consider neutral BCS systems in a strong magnetic field ($\mu_B H \gtrsim \Delta$), which constitute a qualitatively new problem. The properties of ^{3}He–^{4}He mixtures for high concentrations are analogous as properties of superfluid ^{3}He which were investigated in relation to values of the Landau parameter F_0^a in [2] in detail.

2. The system of basic equations

In order to consider the specified problem we employ the results obtained in [3] when the particle–hole symmetry is assumed. The gap equation and the paramagnetic field in the unit volume have the forms (cf. [4])

$$\Delta = \frac{1}{4}\,\nu_0 g_0 \Delta \int_0^{\xi_p} \frac{d\xi}{E}\left(\operatorname{th}\frac{E+\mu_B H_T}{2T} + \operatorname{th}\frac{E-\mu_B H_T}{2T}\right), \tag{2.1}$$

$$H_p = \frac{1}{2\mu_B} \int_0^\infty d\xi \left(\text{th} \frac{E + \mu_B H_T}{2T} - \text{th} \frac{E - \mu_B H_T}{2T} \right), \tag{2.2}$$

where

$$\Delta \equiv \Delta(T, H) \quad , \quad E = \sqrt{\xi^2 + \Delta^2}.$$

H_T is the total magnetic field, g_0 is the pairing interaction parameter, ν_0 is the density of states on the Fermi surface and μ_B denotes Bohr's magneton. Since all vectorial quantities appearing in the problem are parallel, we neglect their vectorial character and consider their positive values only. In case of the homogeneous BCS system none of the used quantities depends on the direction of the momentum vector, hence the total magnetic field is of the form [3]

$$H_T = H - F_0^a \, H_p. \tag{2.3}$$

We emphasize that F_0^a is the sole parameter of Fermi liquid interaction which modifies the total magnetic field. Equations (2.1)–(2.3) constitute the system of nonlinear integral equations which have to be solved simultaneously. Moreover, the obtained solutions should contain bifurcation points. Let us complete the above equations with the following formula [5]

$$\Delta\Omega = \int_0^\Delta d\Delta'(\Delta')^2 \frac{\partial}{\partial \Delta'} \left(\frac{1}{g_0} \right), \tag{2.4}$$

which defines the thermodynamic potential difference in relation to the normal state. Below we consider the formulated problem in two limit cases: $T = 0$ and $T \to T_c$.

3. The zero-temperature case

In the limit $T = 0$ the expressions (2.1) and (2.2) reduce to the forms

$$\left(\frac{H_p + H_T}{H_1} \right)^{\frac{\Delta}{\Delta(0)}} = 1 \tag{3.1}$$

and

$$H_p = \sqrt{H_T^2 - \left(\frac{\Delta}{\mu_B} \right)^2}, \tag{3.2}$$

where

$$H_1 \equiv \frac{\Delta(0)}{\mu_B} \tag{3.3}$$

and we also apply the relation

$$1 = \frac{1}{2}\,\nu_0\, g_0\, \ln\,\frac{2\,\xi_p}{\Delta(0)}. \tag{3.4}$$

$\Delta(T)$ denotes the value of the energy gap in the absence of a magnetic field. Analysing (3.1) we state that the investigated problem possesses two qualitatively different solutions which have to be considered as two independent cases, i.e.:

i) when Δ is constant ($\Delta = \Delta(0)$) and it rapidly vanishes for $H = H_0 \leq H_1$, and

ii) when Δ is constant ($\Delta = \Delta(0)$) for $H < H_1$ and it varies its value in a continuous way for $H \geq H_1$ down to zero when $H = H_2$.

In the former case we have

$$\Delta = \begin{cases} \Delta(0) & \text{if } H < H_0 \leq H_1, \\ 0 & \text{if } H \geq H_0, \end{cases} \tag{3.5}$$

and

$$H_p = \begin{cases} 0 & \text{if } H < H_0, \\ \frac{H}{1+F_0^a} & \text{if } H \geq H_0. \end{cases} \tag{3.6}$$

Since the parameter H_0 defines the value of a magnetic field when the system approaches a normal state, it can be found by free-energy comparison from the following relation

$$\frac{1}{4}\,\nu_0\,\Delta^2(0) = \frac{1}{2}\,\frac{\nu_0\,\mu_B^2\,H_0^2}{1+F_0^a}. \tag{3.7}$$

Hence we obtain

$$H_0 = H_1\sqrt{\frac{1}{2}(1+F_0^a)} \tag{3.8}$$

and because of $H_0 \leq H_1$ we get

$$F_0^a \leq 1. \tag{3.9}$$

In this way we state that if the system possesses type–I properties, the inequality (3.9) has to be fulfilled.

In the latter case under discussion the gap equation reduces to the form

$$H_1 = H_p + H_T, \tag{3.10}$$

and substituting this into (2.3) we can derive the paramagnetic field for $H \geq H_1$ in the form

$$H_p = \frac{H - H_1}{F_0^a - 1} \tag{3.11}$$

and hence, using (3.2) we find

$$\Delta^2 = \frac{\mu_B^2\,H_1}{F_0^a - 1}\,[(1+F_0^a)\,H_1 - 2H]. \tag{3.12}$$

The demand of positive paramagnetic field implies the following inequality

$$F_0^a > 1, \tag{3.13}$$

which ensures also that the energy gap becomes the decreasing function of the external magnetic field. On the other hand, (3.12) allows us to derive the value of the critical magnetic field H_2 for which the energy gap Δ vanishes. We find it in the form

$$H_2 = \frac{1}{2}(1 + F_0^a)\, H_1, \tag{3.14}$$

where the condition (3.13) ensures that $H_1 < H_2$. In the limit case when $F_0^a = 1$ the critical magnetic fields H_1 and H_2 become equal and the system shows properties attributed to the former discussed case. So, we can introduce the critical magnetic field H_c (i.e. if $H_1 = H_2$, we denote them by H_c) which is equal to H_1. In order to sum up the obtained results we emphasize that the energy gap can tend to zero in the continuous way only if the Landau parameter $F_0^a > 1$; then, the energy gap and the paramagnetic field express themselves in the following forms

$$\Delta = \Delta(0) \begin{cases} 1 & \text{if } H \leq H_1, \\ \left[\dfrac{(1+F_0^a)H_1 - 2H}{(F_0^a - 1)\, H_1}\right]^{1/2} & \text{if } H_1 \leq H \leq H_2, \\ 0 & \text{if } H \geq H_2, \end{cases} \tag{3.15}$$

$$H_p = \begin{cases} 0 & \text{if } H \leq H_1, \\ \frac{H - H_1}{F_0^a - 1} & \text{if } H_1 \leq H \leq H_2, \\ \frac{H}{1+F_0^a} & \text{if } H \geq H_2. \end{cases} \tag{3.16}$$

Let us estimate now the Gibbs free-energy difference for magnetic fields H such as $H_1 \leq H \leq H_2$. Employing (2.4), (2.1), (3.4) and (3.16) we obtain (cf. [6])

$$\Delta G = -\frac{\nu_0}{4q}(\sqrt{p^2 + q\Delta^2} - p)^2 \tag{3.17}$$

where

$$p = \frac{\mu_B H}{1 + F_0^a} \quad , \quad q = \frac{F_0^a - 1}{F_0^a + 1}$$

thus

$$\Delta G = -\frac{\nu_0\, \mu_B^2\, (H_2 - H)^2}{(F_0^a + 1)(F_0^a - 1)} \tag{3.18}$$

and hence we state that ΔG is always negative if $F_0^a > 1$ and $H < H_2$, and $\Delta G = 0$ if $H = H_2$. For $H = H_c$ the Gibbs free-energy difference reduces to the form

$$\Delta G = -\frac{1}{4}\, \nu_0\, \Delta^2(0)\, \frac{F_0^a - 1}{F_0^a + 1}. \tag{3.19}$$

The latest relation demonstrates that the Gibbs free-energy difference is equal to zero if $H = H_c$ and $F_0^a = 1$, i.e. for the type-I systems. In this way we have proved that the neutral BCS systems reveal the paramagnetic duality which is determined by the values of the Landau parameter F_0^a. If $F_0^a \leq 1$, the energy gap vanishes and the appearing paramagnetic magnetization ($M = \nu_0 \mu_B^2 H_p$) attains the same value as for the normal system for the value H_0 ($H_0 \leq H_1$), and if $F_0^a > 1$, then while the external magnetic field changes from H_1 to H_2 the energy gap decreases from the value $\Delta(0)$ to zero and the paramagnetic magnetization increases from zero to a value of the normal state. Since according to (3.18) the latter discussed state is more stable in comparison with the former one, it is always realized if $F_0^a > 1$. Moreover, we can introduce the κ-parameter and assume that

$$\kappa = \frac{1}{2}(1 + F_0^a), \tag{3.20}$$

then $H_2 = H_c \kappa$ and the condition

$$\kappa > 1 \tag{3.21}$$

is equivalent to (3.13).

4. The region nearby T_c

In the temperature region under discussion we have

$$\frac{\Delta}{T_c} \ll 1 \qquad \text{and} \qquad \frac{\mu_B H}{T_c} \ll 1. \tag{4.1}$$

These relations allow us to expand integrands in a power series, then the expressions (2.1) and (2.2) reduce to the forms (cf. refs. [6–8])

$$\Delta = \frac{1}{2} \nu_0 g_0 \Delta \left\{ \ln \frac{2\xi_p}{\Delta(0)} + \ln \frac{T_c}{T} - \frac{7\zeta(3)}{8\pi^2 T_c^2} [\Delta^2 + 2\mu_B^2 H_T^2] + \right.$$

$$\left. + \frac{93\,\zeta(5)}{128\pi^4 T_c^4} [\Delta^4 + 8\Delta^2 \mu_B^2 H_T^2 + \frac{8}{3} \mu_B^4 H_T^4] \right\} \tag{4.2}$$

and

$$H_p = H_T \left[1 - \frac{7\zeta(3)}{4\pi^2 T_c^2} \Delta^2 \right]. \tag{4.3}$$

The expression (2.3) keeps its form. Moreover, (4.2) after applying (3.4) reduces to the form

$$\ln \frac{T_c}{T} = \frac{7\zeta(3)}{8\pi^2 T_c^2} [\Delta^2 + 2\mu_B^2 H_T^2] +$$

$$- \frac{93\,\zeta(5)}{128\pi^4 T_c^4} [\Delta^4 + 8\Delta^2 \mu_B^2 H_T^2 + \frac{8}{3} \mu_B^4 H_T^4]. \tag{4.4}$$

Substituting (4.3) into (2.3) we can derive the total magnetic field in the form

$$H_T = \frac{H}{1+F_0^a} + \frac{7\,\zeta(3)}{4\pi^2}\,\frac{\Delta^2}{T_c}\,\frac{F_0^a}{(1+F_0^a)^2}\,H_2, \tag{4.5}$$

where we put $H = H_2$ in the last (small) term in order not to surpass the accuracy of the theory.

In order to derive the value of the critical magnetic field H_2 we propound two sharply contrasting methods.

1. In analogy to [8] and [9] we can assume that the energy gap Δ has to vanish ($\Delta = 0$) when $H = H_2$, then (4.4) and (4.5) reduce to the forms

$$\ln\frac{T_c}{T} = \frac{7\zeta(3)}{4\pi^2 T_c^2}\,\mu_B^2 H_{T2}^2 - \frac{31\,\zeta(5)}{16\pi^4 T_c^4}\,\mu_B^4 H_{T2}^4 \tag{4.6}$$

and

$$H_{T2} = \frac{H_2}{1+F_0^a}. \tag{4.7}$$

Hence, after neglecting the last term in (4.6) we get

$$H_2(T) = \gamma\, H_1(0)\left(1-\frac{T}{T_c}\right)^{1/2}(1+F_0^a), \tag{4.8}$$

where

$$\gamma = \frac{2\,e^C}{\sqrt{7\zeta(3)}} = 1.23, \qquad \Delta(0) = T_c\,\pi\,e^C$$

and $C = 0.577$ is Euler's constant.

Employing the relation [8]

$$\Delta(T) = \beta\left(1-\frac{T}{T_c}\right)^{1/2}\Delta(0), \tag{4.9}$$

where

$$\beta = \gamma\sqrt{2} = 1.74,$$

which can be also obtained from (4.4) after putting $H = 0$ we can rewrite (4.9) in the form

$$H_2(T) = (1+F_0^a)\frac{\Delta(T)}{\sqrt{2}\mu_B}. \tag{4.10}$$

Although the obtained expressions (4.8) and (4.10) define $H_2(T)$ as a function of the Landau parameter F_0^a we cannot separate a κ-parameter. The obtained critical exponent is equal to 0.5 which is inconsistent with its value derived from thermodynamic potential estimation (see below). Therefore, we also submit the competitive treatment of the problem (cf. [6] and [7]).

2. Employing (2.4) and (4.2) we state that the main term of the thermodynamic potential difference is of the form

$$\Delta\Omega = -\nu_0 \frac{7\,\zeta(3)}{32\,\pi^2 T_c^2}\,\Delta^4(T). \tag{4.11}$$

Now, comparing the thermodynamic potential of the normal and superfluid states we obtain the following relation

$$\frac{7\,\zeta(3)}{16\,\pi^2 T_c^2}\,\Delta^4(T) = \frac{\mu_B^2\,H_0^2(T)}{1+F_0^a} \tag{4.12}$$

from which after applying (4.9) we get

$$H_0(T) = \gamma\,H_1(0)\,\left(1-\frac{T}{T_c}\right)\sqrt{1+F_0^a}. \tag{4.13}$$

According to the above relations and in opposition to (4.8) we state that

$$\frac{\mu_B\,H_c(T)}{T_c} \sim \left[\frac{\Delta(T)}{T_c}\right]^2, \tag{4.14}$$

then

$$\frac{\mu_B\,H}{T_c} < \frac{\mu_B\,H_2(T)}{T_c} \ll \frac{\Delta(T)}{T_c} \ll 1 \tag{4.15}$$

and hence the magnetic field should be treated as a small perturbing effect. In order to solve such a specified problem we can compare terms of the same order in (4.4) then we get (4.9) and the following relation (cf. [6] and [7])

$$\frac{93\,\zeta(5)}{128\,\pi^4 T_c^4}\,\Delta^4(T) = \frac{7\,\zeta(3)\,\mu_B^2\,H_2^2(T)}{4\,\pi^2\,T_c^2(1+F_0^a)^2}, \tag{4.16}$$

where all quantities are taken with a suitable accuracy. Substituting (4.9) into (4.16) after some transformations we obtain

$$H_2(T) = \alpha\,H_1(0)\,(1-\frac{T}{T_c})(1+F_0^a), \tag{4.17}$$

where

$$\alpha = \frac{e^C}{7\,\zeta(3)}\sqrt{\frac{186\,\zeta(5)}{7\,\zeta(3)}} = 1.01.$$

Let us note that now the critical exponent is equal to unity and it is the same as in (4.13). This fact allows us to compare the critical magnetic fields in

general. Hence in analogy to the previous consideration we can assume that type–II superfluidity is realized in a system if the critical magnetic field $H_2(T)$ fulfils the relation

$$H_0(T) < H_2(T). \tag{4.18}$$

Substituting (4.13) and (4.17) into (4.18) after some transformations we obtain the following equivalent condition

$$F_0^a > \varepsilon - 1, \tag{4.19}$$

where $\varepsilon = (\gamma/\alpha)^2$ and in the frame of applied formalism it expresses itself as follows

$$\varepsilon = \frac{98\,\zeta^2(3)}{93\,\zeta(5)} = 1.47. \tag{4.20}$$

Since in the limit case when $F_0^a = \varepsilon - 1 = 0.47$ we have $H_0(T) = H_2(T)$ and also after introducing $H_c(T)$ in the form

$$H_c(T) = \eta\, H_c(0)\,(1 - \frac{T}{T_c}), \tag{4.21}$$

where

$$\eta = \alpha\,\varepsilon = \gamma^2/\alpha$$

and

$$\eta = 4\,e^C\sqrt{\frac{7\,\zeta(3)}{186\,\zeta(5)}} = 1.49 \tag{4.22}$$

we can write

$$H_2(T) = \frac{1 + F_0^a}{\varepsilon}\, H_c(T). \tag{4.23}$$

The relation (4.23) allows us to define the κ-parameter in the form

$$\kappa(T_c) = \frac{1 + F_0^a}{\varepsilon}. \tag{4.24}$$

According to the obtained results (3.13) and (4.19) we state that the magnetic properties of ^{3}He–^{4}He mixtures can undergo change when the temperature tends to T_c and F_0^a is contained in the interval $(\varepsilon - 1, 1)$, then type–I systems become ones of type–II. Moreover, when the Fermi liquid interaction is neglected ($F_0^a = 0$) type–I superfluidity can be realized in the system under consideration only.

5. Concluding remarks

The results obtained here prove that superfluid ^{3}He–^{4}He mixtures located in strong magnetic fields should reveal qualitatively different properties which can be classified into two groups according to the Landau parameter F_0^a (cf. [10]). Let us

note that temperature modifies the introduced classification in a small degree only and the results obtained in $T = 0$ and $T \to T_c$ limits are consistent. Owing to this the approach propounded in the Ginzburg–Landau limit becomes competitive to the typical approach [8–9] making its results implausible. Moreover, in the presented approach the introduced parameter η ($\eta = 1.49$) can be improved according to the experimental data just as in superconducting systems where η is assumed to be equal to 2 (cf. [5–7]). In conclusion, note that the presented temperature approach allows us to consider the problem also for small values of $\Delta \neq 0$. Then the obtained results are parallel with the ones obtained in [6] for redefined κ after assuming the space-homogeneity of a system.

This paper was carried out under the Contract CPBP 02.02.

References

1. M. Pfitzner, J. Low Temp. Phys., *61*, 141, 1985.
2. R. Gonczarek, Acta Phys. Polon., *A70*, 255, 1986.
3. R. Gonczarek, Acta Phys. Polon., *A70*, 231, 1986.
4. R. Gonczarek, Acta Phys. Polon., *A69*, 605, 1986.
5. A. L. Fetter and J. D. Walecka, Quantum Theory of Many-Particle Systems, McGraw-Hill, Inc. New York, 1971.
6. R. Gonczarek, Acta Phys. Polon., *A73*, 683, 1988.
7. R. Gonczarek, Acta Phys. Polon., *A71*, 59, 1987.
8. K. Maki and T. Tsumeto, Prog. Theor. Phys., *31*, 945, 1964.
9. G. Sarma, J. Phys. Chem. Solids, *24*, 1029, 1963.
10. K. S. Bedell and D. E. Meltzer, Phys. Rev., *B33*, 4543, 1986.

Acta Physica Hungarica 65 (4), pp. 391–393 (1989)

CALCULATION OF ELECTRON DENSITY AND SURFACE ENERGY BY VARIATION METHOD

A. ISKANDER and L. OROSZ

Institute of Physics, Technical University of Budapest
1521 Budapest, Hungary

(Received in revised form 10 November 1987)

Using the results of the electron density functional method the minimum of the energy functional was used for the calculation of simple, jellium metal surface electron densities. The results approximate rather closely the densities calculated by Lang [5] using a more exact method.

It is well known that the non-degenerate ground state energy of an interacting electron system (like a metal surface) is a unique functional of the $n(\bar{r})$ local electron density.

Hohenberg–Kohn–Sham (H–K–S) have shown, that the $E[n]$ functional has its minimum value at the true $n(\bar{r})$ electron density [1, 2]. A few authors used this property of $E[n]$ for calculating surface energy or other important physical quantities [3, 4]. Lang and Kohn have calculated the electron density using the H–K–S theorem solving the equivalent one-electron problem self-consistently [5].

Szeifert [6] published a simple analytical form approximating within a few per cent the numerical results of the Lang calculation, where four parameters have been used and these were given as a function of r_s (r_s is the Wigner–Seitz radius characterizing the bulk electron density).

In the present work (partially an abbreviated version of the thesis of A. I.) a similar variation function with three parameters was used for searching for the minimum of the energy functional $E[n]$, where, using the explicit form:

$$E[n] = E_{es}[n] + E_{xc}^{LDA}[n] + E_k[n]. \tag{1}$$

Here $E_{es}[n]$ is the electrostatic energy, $E_{xc}^{LDA}[n]$ is the exchange-correlation energy within the local density approximation and $E_k[n]$ is the kinetic energy contribution using the Thomas–Fermi–Weizsäcker approximation. The metal is assumed to be in the region $x > 0$. In detail

$$E_{es}[n] = \frac{1}{2} \int_{-\infty}^{\infty} \{n(x) + n_+(x)\} V_{es}(x)\, dx, \tag{2}$$

where $V_{es}(x)$ is the electrostatic potential and $n_+(x)$ is the positive background charge density

$$E_{xc}^{LDA}[n] = -\frac{0.458}{r_s}\int_{-\infty}^{\infty} n(x)^{4/3}\,dx + \int_{-\infty}^{\infty}\frac{0.44\,n(x)^{4/3}}{r_s + 7.8\,n(x)^{1/3}}\,dx, \tag{3}$$

$$E_k[n] = \frac{1.105}{r_s}\int_{-\infty}^{\infty} n(x)^{5/3}\,dx + \frac{0.0013}{r_s^2}\int_{-\infty}^{\infty}\frac{1}{n(x)}\left(\frac{dn}{dx}\right)^2\cdot dx. \tag{4}$$

The form of the variational function is

$$n(x) = \frac{1}{2}[1 + \mathrm{th}\{p(x-\varphi)\}] + \theta(x-\varphi)\cdot K\cdot\left[\frac{\sin q(x-\varphi)}{[q(x-\varphi)]^2} + \frac{\cos q(x-\varphi)}{q(x-\varphi)}\right], \tag{5}$$

where $\theta(x-\varphi)$ is a step function, and p, q, K, φ are variational parameters. Because of the electric neutrality, $K = q\cdot\varphi$.

The results are shown in Table I, while Figure 1 gives some information on the extremal nature of the energy functional by the aid of a 3D computer graphics drawn at K = opt, while q and p have been selected at 6 different values around the minimum at $r_s = 5$.

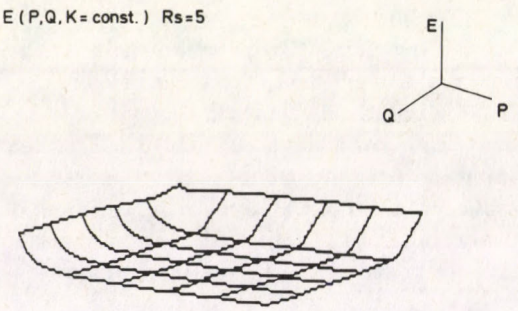

Fig. 1

Table I

Values of parameters according to Szeifert's calculation

r_s	3.0	4.0	5.0	6.0
p	5.662	6.503	7.240	7.904
q	9.336	9.472	9.605	9.715
K	0.226	0.292	0.357	0.421
E	−0.01798	−0.01183	−0.00749	−0.00493

Values of parameters according to our calculation

r_s	3.0	4.0	5.0	6.0
p	7.814119	10.294116	12.556860	14.181372
q	10.109411	10.129215	10.159608	10.199018
K	0.057882	0.107647	0.161765	0.215294
E	−0.01801167	−0.01185116	−0.00750087	−0.00494102

Figure 2 shows the electron density obtained, while Fig. 3 displays the differences between the Lang values and the present calculation (delta 2) and the differences between the Lang values and the Szeifert calculation (delta 1) at $r_s = 5$.

The $n(x)$ obtained approximates the Lang calculation fairly well except in the vicinity of the surface when the potential does change most significantly.

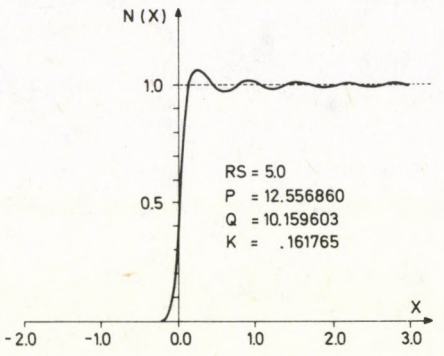

Fig. 2

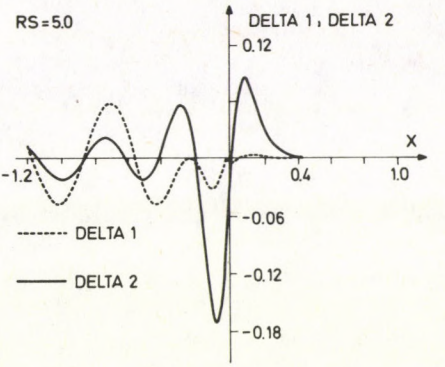

Fig 3

The relatively close approximation is rather remarkable according to the view of the authors because of the approximate nature of the kinetic energy term of (1). On the other hand, one has to realize that the shape of the variational function (5) is rather advantageous showing up an oscillatory character in the metal (where typically Friedel oscillations will be found).

References

1. P. Hohenberg and W. Kohn, Phys. Rev., *136*, B 864, 1964.
2. W. Kohn and L. S. Sham, Phys. Rev., *140*, A 1133, 1965.
3. J. R. Smith, Phys. Rev., *181*, 522, 1969.
4. W. Schmickler and D. Henderson, Phys. Rev., *B30*, 3081, 1984.
5. N. D. Lang and W. Kohn, Phys. Rev., *B1*, 4555, 1970.
6. Z. Szeifert, Acta Phys. Hung., *56*, 419, 1981.

Acta Physica Hungarica 65 (4), pp. 395–404 (1989)

INVESTIGATION OF ELECTRIC FIELD DISTRIBUTION IN Z-CUT KDP Q-SWITCH MODULATOR CRYSTALS

R. SH. ALNAYLI*, CS. KUTI, J. S. BAKOS and I. TÓTH

Institute of Physics, Technical University of Budapest
1521 Budapest, Hungary

(Received in revised form 14 January 1988)

Experimental study on the electric field distribution in longitudinal Z-cut KDP modulator crystals devoted to Q-switching of high power solid-state lasers has been performed. Effect of electrode width to crystal length ratio and that of the ratio of the crystal length to size of aperture edge on voltage and transmission uniformity of rectangular modulator cells with stripe electrodes is reported.

1. Introduction

Pockels cells constructed with longitudinally driven Z-cuts of KDP (potassium dihydrogen phosphate)-type electrooptic crystals are preferred to other light modulators for Q-switching of high power solid-state lasers owing to their high extinction ratio, negligible temperature sensitivity, fast electronically controllable response, and high resistivity against laser damage [1]. In longitudinal Z-cut KDP modulator

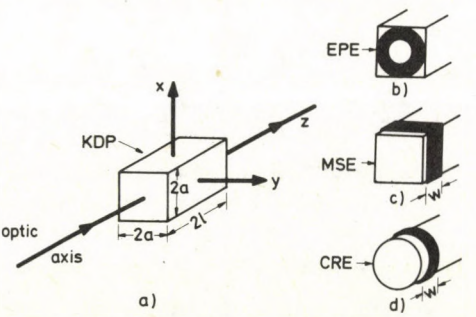

Fig. 1. Longitudinal Z-cut KDP samples and electrode configurations for high power laser applications

crystals the light propagates along the Z-directed driving electric field (Fig. 1), i.e. parallel to the optic axis. The optic axis light propagation – when apart

*On leave from Iraq for Ph. D. scholarship

from negligible contributions caused by crystal imperfections (grown in and induced stresses) and partial walk-off due to beam divergence and slight misalignment of the optic axis only the electrooptically induced birefringence acts on the light – gives the possibility of high extinction over extended apertures and offers operation free of the influence of temperature fluctuations. A compensation of the natural birefringence and temperature stabilization are not required that results in simple construction of the modulators.

On the other hand, the modulation of light propagating along the optic axis of KDP crystals is inherently coupled with the longitudinal driving configuration that involves the well-known problems in electroding of the modulator crystals to meet the requirements of uniform transmission and extinction for high-power Q-switch applications.

2. Electrode configurations for longitudinal Z-cut KDP modulators

A longitudinal Z-cut KDP modulator crystal acts on a polarized light beam propagating along the optic axis as an electrically controlled birefringent retarder-plate of birefringence

$$\Delta n = n_0^3 * r_{63} * E_z, \tag{1}$$

where E_z, r_{63} and n_0 are the Z-component of the electric field strength, the appropriate electrooptic coefficient, and the ordinary index of refraction, respectively [2]. The phase shift (or retardation) between the "slow" and "fast" components of a linearly polarized light beam of wavelength λ is proportional to the optical path difference and is determined as follows:

$$\Gamma = 2\,\pi/\lambda * n_0^3 * r_{63} * \int_{-\ell}^{+\ell} E_z\, dz. \tag{2}$$

Here the integration is taken along the ray path between the faces of the modulator crystal according to Fig. 1. The retardation can be expressed in a practical form of

$$\Gamma = \pi * V/V_{1/2}, \tag{3}$$

where

$$V = \int_{-\ell}^{+\ell} E_z\, dz. \tag{4}$$

and $V_{1/2}$ are the effective driving voltage and the half-wave voltage, respectively.

Intensity modulation takes place using a polarizer placed behind the modulator cell that transmits the amplitude-modulated component of the emergent light of

controlled ellipticity. The ellipticity is determined by the electrically modulated retardation. The actual modulation characteristics depends also on the arrangement of the polarizers. The transmission of a conventional intensity modulator consisting of the electrooptic crystal placed between crossed polarizers, if the incident light is polarized parallel to the bisector between the "slow" and the "fast" axis, is given as follows:

$$T = T_0 * \sin^2 \Gamma/2 = T_0 * \sin^2(\pi/2 * V/V_{1/2}). \tag{5}$$

The transmission distribution is principally determined by the distribution of the effective driving voltage V. The effective driving voltage – as shown by (4) –depends on the electric field distribution inside the modulator crystal.

Two optical arrangements are commonly used for electrooptic Q-switching of solid-state lasers [1]:

In the first one the modulator crystal placed between crossed polarizers is located in front of the rear mirror of the laser resonator. If no voltage is applied the Q-switch is closed. The switch will be opened when an electrical pulse of half-wave voltage is switched on the crystal (pulse-on Q-switch) because of the half-wave retardation that causes a 90° rotation of the polarization of the laser beam.

In the second arrangement the modulator crystal is placed between a polarizer and the rear mirror. In this case the Q-switch is closed when a voltage causing right angle rotation of the polarization of the double passed laser beam is applied on the crystal. Since the light crosses the crystal twice, only about half the half-wave voltage is required to close the laser resonator. The switch can be opened by switching-off the voltage of the modulator crystal (switch-off operation). The switch-off Q-switching is preferred to the pulse-on one owing to its lower driving voltage requirement and the electronically preferable switch-off operation.

Nevertheless, the switch-off Q-switching is restricted in power performance compared with the pulse-on operation. Namely, if the Q-switch is electrically closed, the extinction is limited by the nonuniformity of the effective driving voltage. The nonuniform extinction at high pump energy results in prelasing – i.e. laser oscillation can occur before the instant of Q-switching [1] – and the Q-switched operation can be accomplished only at decreased pump energy.

Investigations on electrode configurations to ensure uniform transmission over large apertures of longitudinal Z-cut KDP modulators were reported earlier [3–9]:

Transparent, conductive metal-oxide coatings deposited directly onto the Z-faces ensure fairly uniform electric field distribution, however, they are not suited for fast, high power Q-switching because of their large electrical resistance, moderated transmission, and low threshold to laser damage [3].

Recently, a very effective system to generate high transmission plasma electrodes ensuring very fast switching of ultrahigh power over extremely large apertures has been developed for laser fusion experiments [4]. Nevertheless, practically they are out of interest for common applications owing to their rather sophisticated way of operation.

High optical power and subnanosecond response can be attained using metal-plate electrodes with circular aperture openings (see Fig. 1b) bonded to the end

faces of the KDP crystals [5]. The main drawback of the end-plate electroded (EPE) electrooptic-cells, commercially also available in the early seventies, is a significant nonuniformity appearing as a gradual decrease of the driving field towards the central part of the aperture because of fringing of the electric field. The wider the clear aperture, the larger the decrease is.

To produce longitudinal controlling electric field in electrooptic modulator crystals an electrode arrangement with metal stripe electrodes (MSE) bonded to lateral sides of the crystal near its ends (see Fig. 1c) was proposed by Vitkov [6]. In spite of an obvious fringing due to the electrode configuration an astonishingly uniform effective driving potential over the full cross-section as a clear aperture was predicted from the analytical solution of the Laplace equation. The preference of the MSE configuration to the EPE was supported by investigations of Demirchan et al [7] and Kamach et al [8] modelling the electric field in an electrolytic tank and solving numerically the Laplace equation, respectively. Comparison of the results of the analytical, the model, and the numerical treatment is given in [8] and good agreement of the last one with experiments is mentioned.

A similar, stripe electrode configuration was developed by Steinmetz et al [9]. The cylindrical symmetry of dielectric properties around the optic axis of KDP-type crystals was exploited for further smoothing of the potential distribution. Numerical solutions of the Laplace equation for the electric field inside cylindrical, Z-cut DKDP (deuterized KDP) samples with cylindrical ring stripe electrodes (CRE) on the barrel of the samples (see Fig. 1d) were calculated. A calculated measure of the voltage nonuniformity was processed into parallel nomograms as a function of normalized electrode width (the width to length ratio) for a series of CRE cells with a discrete sequence of aspects ratios. The experimental data fitted the nomograms well. A comparison with EPE cells proved the superiority of the CRE configuration considering both the voltage uniformity and capacity determining the speed of response. Partically only CRE-cells are commercially available today.

Considering the significant improvement experienced in output energy of our Nd-glass laser [10] when the EPE KDP Q-switch cell was exchanged with a MSE one we decided to perform a detailed experimental study on the electric field distribution in stripe electroded, rectangular KDP Z-cuts. On the one hand, rectangular samples were investigated since we prefer them to cylindrical ones because of easy manufacturing. On the other hand, we have been dealing with the investigation of rectangular Z-cuts as we are interested in the development of longitudinal KDP modulators with reduced piezooptic influences. According to our recent results [11] rectangular Z-cuts with lateral faces cut perpendicular to the bisectors of the XY-crystallographic plane (45° Z-cut) are characterized by moderated generation of acoustic waves giving rise to disturbing piezooptic transients as compared with the 0° Z- and even the cylindrical Z-ones.

3. Experimental procedure

Our standard Z-cut KDP samples – of a length of 25 mm and aperture size of 15 mm × 15 mm or 20 mm × 20 mm – prepared as reported earlier [10] were electroded with 0.1 mm copper stripes of a width varying in a range from 2 to 10 mm in 2 mm steps. The copper strips were cemented onto the lateral faces of the crystal samples near to the optical windows with conductive silver paint to get reliable electrical contact and mechanical bond. The capacitance of every sample was measured on an a.c. capacitance bridge working at an angular frequency of 10^4 s^{-1}. The MSE samples were mounted into a variable holder attached to an adjustable optical mount consisting of an XY-translator and an angular gimbal.

In contrast to common high voltage measurements of voltage nonuniformity of longitudinal KDP modulator cells [9, 10] to avoid electric break-down owing to reduced electrode distances a low voltage method was developed. The distribution of the effective driving voltage across the aperture was measured as follows: An intensity modulator constructed with the modulator crystal of a given electrode configuration (KDP) placed between crossed polarizer (A, P) was optically biased to half-opened state by a quarter-wave plate ($\lambda/4$) inserted between the polarizer and the modulator crystal as shown in Fig. 2. In such a way the linear part of the modulation characteristics given as

$$T = T_0 * \sin^2(\pi/4 + \pi/2 * V/V_{1/2}) \tag{6}$$

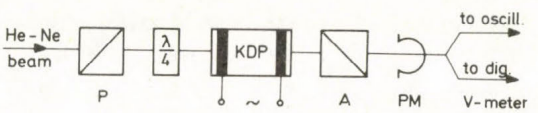

Fig. 2. Experimental set-up for measurement of the effective driving voltage

could be used offering benefits of a low voltage and fast relative method. With an a. c. driving of frequency far under the fundamental acoustic resonance of the piezoelectric modulator crystals the amplitude v of the modulated light measured on the output of the photomultiplier (PM) is proportional to that of the effective driving voltage V introduced in (4) above. The actual distribution of the effective driving voltage was obtained by scanning the aperture with the He–Ne beam of 1 mm diameter. The scanning was actually realized by translation of the modulator crystal with the XY-translator of the optical mount. The scanning was done along straight lines parallel to the X and Y-axes in 1 mm steps. Every translation step was followed by a procedure of careful optical alignment adjusting the isogyre pattern before reading the PM. The intensity of the incoming laser beam was continuously monitored to correct the intensity drift due to the long period instability of the laser. The actual value of the transmission coefficient, T_0, was also measured and every PM reading was corrected.

Linearity with the driving amplitude up to 600 V peak to peak voltage and independence of the driving frequency in the 0.05 – 20 kHz audio-frequency range of the RM output was obtained. The experimental error resulted from the short time instability of the laser intensity and the inaccuracy of the reading of the oscilloscope was estimated to be about 5%. A typical graph of the PM output scanning the laser beam along straight lines parallel to the aperture edges is shown in Fig. 3.

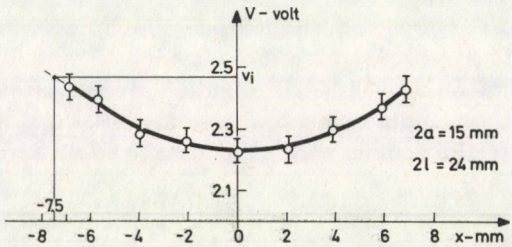

Fig. 3. PM-output along the centre line of the aperture with inter-electrode extrapolation

For a given electrode configuration when a symmetrical d. c. driving of magnitude less than $1/10 * V_{1/2}$ was applied, within the experimental error, the same effective driving field distribution was measured as in the a. c. measurement. Considering the reduced experimental error of the d. c. measurement because of averaging of the short time fluctuations of the laser intensity and higher precision of the d.c. reading by the digital V-meter, in the cases of electrode configurations of higher voltage uniformity the d. c. method was applied. The reduced error was estimated to be less than 3%.

4. Processing of the experimental data

For the sake of comparison with the results of calculations performed earlier on rectangular and cylindrical KDP Z-cut modulator crystals the effective driving voltage distributions were extrapolated into the inter-electrode region ($x = \pm a$, $y = \pm a$) where measurements could not be carried out. A linear extrapolation was applied to get v_i, the inter-electrode driving voltage, shifting the boundaries of the measured distributions outwards on both sides, by half the diameter of the measuring laser beam (Fig. 3). The effective voltage distributions were normalized to the voltage values obtained in the middle point of the aperture. As independent variables normalized coordinates (x/a and y/a) were introduced.

The normalized distributions could be compared only indirectly, by the help of the CRE nomograms of voltage nonuniformity of [9], with the results of calculations for rectangular modulator crystals summarized in [8]. The voltage nonuniformity introduced as

$$\Delta V = |1 - V_z/V_{1/2}| \tag{7}$$

by Steinmetz et al [9] could be determined as follows: considering that V_z was the voltage between the electrodes inducing half-wave retardation ($V_z > V_{1/2}$) along the investigated path, i.e. in a given point of the aperture, the voltage nonuniformity could be calculated from our experimental data by

$$\Delta V = V_z/V_{1/2} - 1 = V_i/V - 1 = v_i/v - 1. \tag{8}$$

Here, by relationship $V_z/V_{1/2} = V_i/V$ and $V_i/V = v_i/v$, linearity of the Laplace equation and that of the modulation were taken into account, respectively.

The voltage nonuniformity obtained in the middle point of the aperture was illustrated as a function of the normalized electrode width, i.e. the ratio of the electrode width (w) to the half length (l) of the crystal (Fig. 4). As a parameter the normalized length, i.e. the ratio of the length ($2l$) to the aperture edge ($2a$) was used. The corresponding capacitance nomograms constructed from the measured capacitance of the modulator cells were illustrated on the same graph.

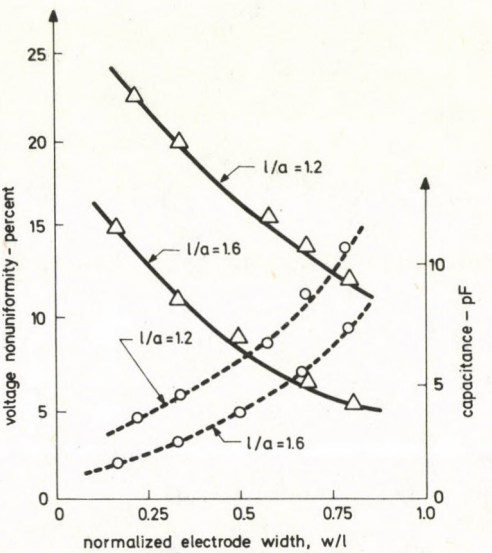

Fig. 4. Voltage nonuniformity and the capacitance of the modulator cells versus normalized width

5. Discussion

A direct comparison of our results with those of Steinmetz's calculations is possible by the help of the parallel nomograms with a sequence of aspects ratios reported in [9]. The comparison is displayed on Fig. 5, where the CRE nomograms of the voltage nonuniformity for normalized length of 1.4 and 2 are shown (broken lines) together with those obtained in this work. A similar dependence

on the normalized electrode width can be observed. For the sake of quantitative comparison the CRE nomogram of the normalized length parameter 1.6 obtained by interpolation is also illustrated (dotted line). A graphical interpolation has been performed taking into account the full system of parallel nomograms reported by Steinmetz. The voltage nonuniformity of our MSE rectangular modulator crystals with normalized length of 1.6 is estimated to be higher by 20 % than that of the CRE cylindrical ones of the same normalized length.

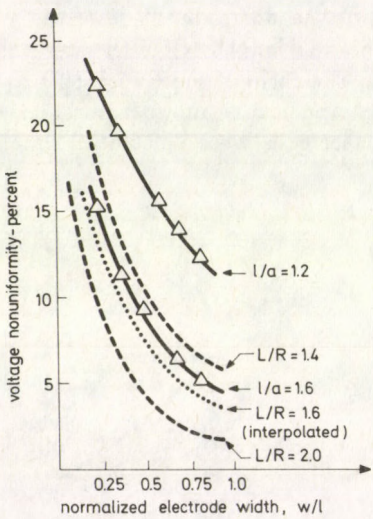

Fig. 5. Comparison of the CRE and the MSE results

On the other hand, as mentioned above, only an indirect comparison of our results is possible with those of the calculations performed on the electric field distribution in rectagular modulator cells because there are numerical results only at the normalized length of 2 and the normalized electrode width of 0.33 reported. As a reference the CRE results by Steinmetz et al should be taken at the same pair of normalized length and normalized width parameters. The corresponding magnitudes of voltage nonuniformity determined from driving field distributions summarized in [8] can be expressed in percentage of the CRE result as listed in Table I. From our experimental result an excess voltage nonuniformity of about 0.2 as compared with the CRE result has been extrapolated.

The high degree of uniformity of voltage distribution reported in [6–8] seems to be overestimated. Probably it is due to the assumptions introduced to reduce the solution of the Laplace equation. The voltage nonuniformity of our rectangular MSE cells slightly higher than that of the CRE ones is thought to be reasonable

and might partially result from the lower symmetry of the electric field generated in rectangular samples. As a reason for the excess voltage nonuniformity an unsatisfactory electric contact between the electrodes and the crystal can be excluded. The extrapolation of the driving field distribution to the inter-electrode region was performed in order to get rid of influences by voltage drop. Moreover, the observed symmetry of the driving voltage distributions measured gives evidence of a reliable, uniform electrical contact. By all means, the emphasized similarity in the voltage nonuniformity dependence on the normalized electrode width can be considered as an experimental verification of Steinmetz's numerical treatment in a wide range of geometrical parameters.

Table I

Voltage nonuniformity by different investigators

Investigation	ref.	percentage
analytical	[6]	0.31
model	[7]	0.60
numerical	[8]	0.45
numerical and experimental	[9]	1.00
experimental	this work	1.20

With regard to the switch-off operation motivating our investigations let us consider some conclusions:

From a rather rough estimation for a voltage closed longitudinal Pockels cell the electrically induced average extinction over a circular aperture of $R = a$ must be less than $(\pi/6) * (\Delta V)^2$. Since a linear variation of the transmission uniformity was assumed this limit is fairly overestimated. For example, the voltage extinction ratio for our modulator cell of lowest (5.6%) voltage nonuniformity is to be less than 1:600 over a clear aperture of 15 mm diameter. This value is fairly promising as compared with the intrinsic extinction ratio of 1:1000 measured in the middle of the aperture of the same modulator crystal placed between crossed polarizers using the laser beam of 1 mm diameter. In order to reduce the voltage extinction below the intrinsic one the increase of the normalized length or the normalized electrode width is offered by the voltage nonuniformity nomograms (Fig. 4.). In the case of our example the latter can be excluded owing to the risk of electrical break-down due to the small electrode distance. Namely, according to our earlier experience [10], the lower limit of the MSE electrode distance was about 5 mm, even if the crystal was embedded in silicon rubber of high quality electrical insulation. On the other hand, it is not practical to decrease the electrode distance because of the increase of the cell capacitance that results in decreasing the switching speed of the Q-switch modulator. According to the dependence of the transmission uniformity on the normalized length, an increase of that, i. e. the elongation of the modulator crystal, can result in a significant decrease of the voltage extinction. However, the elongation of the modulator crystal is restricted by spoiling the intrinsic extinction ratio. The longer the optical path is, the larger the effect of the crystal imperfections and the

ray walk-off on the extinction will be. Elongation of the modulator crystals results in an increased insertion loss also limiting the power performance of the Q-switched lasers. A moderated elongation might be combined with a simultaneous, but breakdown limited, increase of the electrode width to achieve the required improvement. Properly sized 45° Z-cut KDP samples with reduced piezooptic influences are in preparation in order to perform experimental verification and apply them in our repetitively Q-switched Nd-YAG lasers being under development.

Acknowledgements

The research has been sponsored by the National Research Foundation of Hungary under grant number 446/86. The authors wish to express their gratitude to Mr. A. B. Kiss for his valuable technical assistance.

References

1. W. Koechner, Solid-State Laser Engineering, Springer-Verlag, New York, Heidelberg, Berlin, 1976.
2. A. Yariv and P. Yeh, Optical Waves in Crystals, John Wiley and Sons, New York, Chichester Brisbane, Toronto, Singapore, 1984.
3. R. Goldstein, Laser Focus, p. 21, February, 1968.
4. J. Goldhar and M. A. Henesian, IEEE J. Quant. El., *QE-22*, 1137, 1986.
5. W. R. Hook and R. P. Hilberg, Appl. Opt., *10*, 1179, 1971.
6. M. G. Vitkov, Opt. Spectr., *24*, 420, 1968.
7. K. C. Demirchan, R. P. Kiatkin and A. B. Novgorodcev, Electrichestvo, N°7, p. 63, 1972.
8. U. E. Kamach, R. P. Kiatkin and E. N. Kozlovski, Opt. Mech. Prom., N°4, p. 18, 1975.,
9. L. L. Steinmetz, T. W. Pouliot and B. C. Johnson, Appl. Opt., *12*, 1468, 1973.
10. J. Bakos, T. Juhász, Cs. Kuti and L. Vannay, Acta Phys. Hung., *57*, 313, 1985.
11. Cs. Kuti, T. Juhász, J. Bakos and L. Vannay, Acta Phys. Hung., *61*, 247, 1987.

Acta Physica Hungarica 65 (4), pp. 405–409 (1989)

CHARACTERISTICS OF LASER-HEATED TITANIUM IN A NITROGEN ATMOSPHERE

L. NÁNAI and I. HEVESI

Department of Experimental Physics
Attila József University, Szeged, Hungary

B. S. LUK'YANCHUK, E. M. MOROZOVA, A. S. ROGACHEV, A. V. SIMAKHIN, N. M. SUKONKHINA and G. A. SHAFEEV

Institute of General Physics, Academy of Sciences USSR
Moscow, USSR

(Received in revised form 7 March 1988)

Experiments are reported on the laser light induced nitridation of titanium. A strong dependence of the TiN synthesis conditions on the temperature of the sample and the compounds in the gaseous environment is revealed. An existence of an optimum power for achieving a good homogeneity of the layer and improving the self-stabilization effect is proved.

There is considerable interest in the dynamics of laser light heated metals in active gaseous surroundings. Laser-induced heating is especially interesting from a certain scientific aspect (instability, stochastic oscillations, autowaves, etc.) and because of its prospective applications (synthesis of refractory compounds, modification of surface structures and surface properties). The nitridation of titanium (among other metals) has been investigated in [1,2].

The different methods of synthesis of titanium nitride can be divided into two groups:

a. processes carried out under conditions not far from equilibrium (annealing of titanium in a nitrogen atmosphere)

b. processes carried out far from equilibrium (plasma-chemical deposition, laser-induced synthesis, synthesis by explosion, etc.).

In the formation of titanium nitride in a high pressure ($1–60.10^5$ Pa) chamber by plasma-chemical and laser-induced methods an intensive bombardment of the Ti surface by nitrogen ions can be observed as a consequence of the optical discharge. In order to increase the kinetic energy of the bombarding ions, an accelerating electric field is sometimes applied. In this case, a very effective formation of titanium nitride can be observed if the thin surface layer of Ti is melted. It is possible by this means to synthetize a titanium nitride layer with a thickness of 10μm [1, 2]. In the target zone covered by laser light-induced plasma, columnar titanium nitride microcrystals may be seen.

There is also considerable interest in the synthesis of titanium nitride in air under CW laser light, when the melting of the surface layer, the optical discharge

near the surface and the substantial ionization of ambient nitrogen do not occur. In this case the non-equilibrium process of the heterogeneous reaction is connected only with the existence of high spatial gradients of the temperature in the volume of the target.

A CW–YAG laser of average power of 150 W was used to illuminate samples of titanium platelets (VT-1 and VT-2 types) of 1.5×1.5 cm^2 size. In different experiments, the thickness of the samples varied from 0.2 mm to 0.5 mm, and their mass from 300 mg to 700 mg. The targets were mechanically polished and chemically etched in a mixture of sulphuric, hydrofluoric and nitric acids before illumination. After etching, the samples were washed in distilled water. Treatment of the samples was continued in a vacuum chamber at $1.3\ 10^{-4}$ Pa. The samples were annealed under laser light (the total surface was covered by laser light) with a power of 80 W in order to reach a temperature of 770 °C.

Annealing for ~30 min was sufficient for the recrystallization of titanium targets, during which the surface assumed a metallic shine and (because of the increasing absorptivity) the temperature decreased to 500 °C. Further treatment in vacuum did not cause any changes in the structural and optical properties. Samples prepared in this way had a good resistance to different etchants (as compared with mechanically polished ones) and guaranteed the good reproducibility of the results.

After etching, the vacuum chamber was filled with nitrogen at $1–10^5$ Pa. The laser beam was focused on the surface of the target in a spot with a diameter of 1.5 mm. The light power was chosen so that the temperature of the targets (in different experiments) attained 800–1500 °C.

The investigations revealed the strong dependence of the TiN synthesis conditions on the temperature of the sample, the compounds in the gaseous environment, and the duration of the laser pulse.

If the gas used was technical nitrogen containing more than 1% of carbonaceous impurities, a black layer of carbo-nitride grew on the surface of the titanium.

The chemical compounds in the layer were investigated by means of X-ray electron spectroscopy. When even a little carbon and oxygen-containing impurities were present, mainly carbon oxide layers were synthetized. In oxygen-free environment, carbon nitride layers were synthesized. These layers had a rather inhomogeneous structure, and it was therefore interesting to check the local changes in the compounds as a function of the distance from the beam axis in the radial directions. Local X-ray analysis (carried out by Galchenko) on targets which exhibited a melting path in places, associated with the centre of the beam. The microphoto in Fig. 1 shows a relief from this part of the targets. Electron back-scattering analysis was performed on this area of the sample showing that a surface layer with an atomic weight lower than that of Ti grew on the Ti support. At the sites illuminated by the laser light, this surface layer (thickness 3–5 μm) was destroyed. Fig. 2 shows a cross-section of the sample with a TiN layer of a thickness about $\sim 10\mu$m.

The nitrogen and carbon distributions revealed by characteristic X-ray spectral lines show that the average distributions of carbon and nitrogen in the non-destroyed layer of carbo-nitride are uniform, but at the same time there are large local differences in the compounds formed: there are local parts rich in carbon and

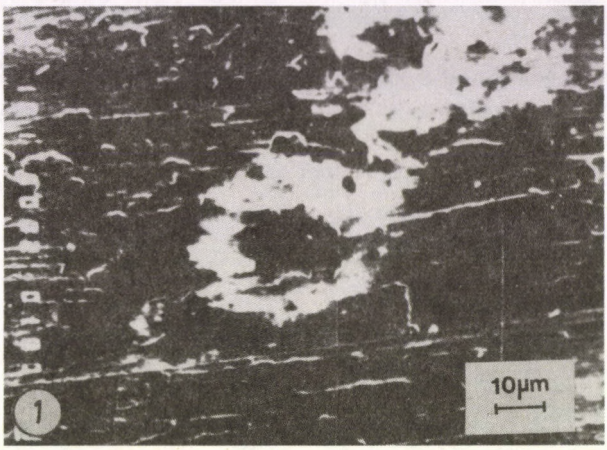

Fig. 1. Microphotogram of the sample in the centre of the illuminated area

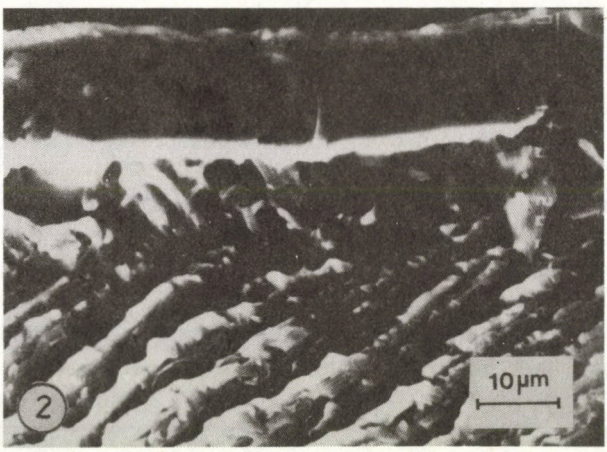

Fig. 2. Cross section of the sample with TiN surface layer

other parts poor in carbon.

It is clear from these experiments that, in order to have a homogeneous nitride layer, very pure nitrogen should be used and the temperature should not exceed

the melting point of titanium.

In further experiments therefore, we used only pure nitrogen and the surface temperature was kept below 1400 °C. Under these conditions, a homogeneous layer of gold-coloured TiN was grown without any sign of damage.

At low pressures ($p \sim 10^4$ Pa) and at $T \sim 1400$°C, the TiN layer had a ring form. At increasing pressure (up to 10^5 Pa) and decreasing temperature (up to 1100 °C) TiN was synthesized as a spot with a diameter of ~ 10 mm and a thickness of 30 μm during an illumination time of 15 min.

The temperature change in the spot centre is presented as a function of the laser power in Fig. 3.

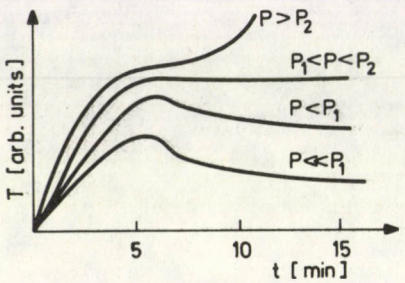

Fig. 3. Temperature in the centre of the illuminated zone vs time at different laser light powers

The reason for the competition of the two mechanisms is that these have different signs of feedback between the temperature and the chemical degrees of freedom of the system. TiN has a high conductivity, and consequently a low absorptivity, as compared with the metallic titanium target. During synthesis, therefore, the absorptivity of the target decreases (process with negative feedback). On the other hand, in the dissolution of N in Ti and in the process of synthesis heat is released (process with positive feedback) which causes an effective burning of the target at certain powers of the laser light. If the power of the laser light is so low that it does not cause burning of the target, there are two different regimes of temperature change: a regime of activation (the temperature passes through a maximum) and a regime without activation (the temperature increases monotonously). In the system with the regime of activation we observed effects of self-stabilization for chemical processes; this self-stabilization improves the inhomogeneity of the growing layer. On the other hand, decrease of the power causes a decrease in the thickness of the layer. Therefore, an optimum power should be found which is high enough to produce a satisfactorily thick layer, and low enough to improve the self-stabilization effect sufficiently to achieve a good homogeneity of the layer.

TiN layers growing at optimum laser power during illumination for 5 min had a thickness of ~ 300μm, small-grain structures 5–10 μm in size and a surface unevenness of less than 5μm. Under given conditions of power and illumination time, the grain size depends on the temperature gradient: as the temperature gradient

increases, the grain size decreases. This result is very similar to those observed at laser light induced vanadium oxidation [3].

The high value of temperature gradient does not make the homogeneous crystallisation possible in laser light covered areas. The grain size decreasing is made easier by nonisothermality of the process and is helped by the two competition processes mentioned above, too.

References

1. A. L. Galiev and L. L. Krapivin, Dokl. AN SSSR, *251* (2), 336, 1980.
2. V. N. Anisimov and R. V. Arutunyan, Preprint Inst. of Atomic Energy No. 3931/9, Moscow, 1984.
3. F. V. Bunkin, N. A. Kirichenko, B. S. Luk'yanchuk, A. V. Simakhin, G. A. Shafeev, L. Nánai and I. Hevesi, Acta Phys. Hung., *54*, 111, 1983.

Acta Physica Hungarica 65 (4), pp. 411–424 (1989)

ROTATIONAL ANALYSIS OF THE $A\ ^6\Sigma - X\ ^6\Sigma$ TRANSITION OF CHROMIUM MONOFLUORIDE

V.M. DUBOV, D.V. TSCHECHOVSKOY and E.A. SHENYAVSKAYA

Department of Chemical Thermodynamics, Institute for High Temperatures of the USSR Academy of Sciences Moscow 127412, USSR

I. KOVÁCS

Department of Atomic Physics, Technical University 1521 Budapest, Hungary

(Received 15 March 1988)

Rotational analysis of the $A\ ^6\Sigma - X\ ^6\Sigma$ (3–0 and 4–0) bands of CrF was carried out. The anomalous spin-splitting in the upper states was interpreted by taking into account the combined effect of the centrifugal distortion and the perturbations by close lying $^6\Pi$ terms.

Introduction

The electronic spectrum of CrF was not known until recently. The CrF spectrum in the 700–1100 nm region was obtained in emission and absorption when different kinds of mixtures containing Cr and F (CaF_2 +Cr, Cr+CrF_3, CrF_3) were heated up to 1300–2500°C. By analogy with the CrH spectrum the bands were assigned to the A $^6\Sigma$ – X $^6\Sigma$ transition. The results of vibrational and preliminary rotational analyses were published in Ref. [1].

This paper deals with the rotational analysis of the 3–0 and 4–0 bands of the A $^6\Sigma$ – X $^6\Sigma$ transition.

Rotational analysis

The 3–0 and 4–0 bands consist of six pairs of R_i and P_i branches. Satellite branches were not detected. The wavenumbers of rotational lines are given in Table I.

The relative numbering has been established by finding agreement between the combination differences $\triangle_2 F_i''(N) = R_i(N-1) - P_i(N+1)$ of the 3–0 and 4–0

bands. The absolute numbering has been found by the requirement that $\triangle_2 F(N) \approx 4B(N+1/2)$ plotted as a function of N should go through zero at $N = -1/2$.

The $\triangle_2 F_i''(N)$ values form six successive sets which differ from each other regularly by about 0.02 cm^{-1}. From the formulas for the rotational terms of the $^6\Sigma$ state given by Rao [2] (see also [3]) it follows that the contribution of spin–spin interaction in combination differences at sufficiently large values of N is negligibly small and $\triangle_2 F_i(N) - \triangle_2 F_{i+1}(N) \approx 2\gamma$. The assignment to different components given here is based on this relation assuming that $\gamma'' > 0$. It should be noted that the upper states combination differences $\triangle_2 F_i'(N) = R_i(N) - P_i(N)$ have close values but do not reveal such regularity as those of the lower state.

Determination of rotational constants

The calculation of rotational constants has been performed in 4 stages.

I. It can be shown from the rotational terms of the $^6\Sigma$ state obtained by Rao [2] (see also [3]) that:

$$\text{a)} \quad \sum_{i=1}^{6} F_i(J) = 17.75B - 35\gamma - 105.875D + (6B - 105D)J(J+1) - 6DJ^2(J+1)^2, \tag{1}$$

$$\text{b)} \quad (1/6)\sum_{i=1}^{6} F_i(J) = (4B - 76D)(J+1/2) - 8D(J+1/2)^3, \tag{2}$$

$$\text{c)} \quad \sum_{i=1}^{6}(R_i(J-1) + P_i(J)) = 12\,T_0 + 35(B' - B'') - 211.755(D' - D'') - 70(\gamma' - \gamma'') + (12(B' - B'') - 222(D' - D''))J^2 - 12DJ^4. \tag{3}$$

Thus spin-splitting constants do not occur in the summation of combination differences $\triangle_2 F_i(J)$. Using the simple relations (2) and (3) the constants B, D and the "effective zero lines" T_v which include all terms independent of J were calculated by least squares technique (see Table IV, column I). Table IV gives also the numbers of combination differences "n" used in a fit and standard deviations of fitting "S". Eq. (2) was used previously for calculating rotational constants of CrH [4,5]. It should be noted that this method permits to use only a small part of experimental data. That is why the D values obtained differ considerably from those estimated by Kratzer's relation.

II. Following Van Vleck [7] we took the Hamiltonian in the form:

$$H = H_{\text{rot}} + H_{SS} + H_{SR}, \tag{4}$$

where

$$H_{\text{rot}} = B(\mathbf{J} - \mathbf{S})^2 - D(\mathbf{J} - \mathbf{S})^4, \tag{4a}$$

$$H_{SS} = (2/3)\lambda\,(3S_z^2 - \mathbf{S}^2), \tag{4b}$$

$$H_{SR} = \gamma\,(\mathbf{J} - \mathbf{S})\mathbf{S}. \tag{4c}$$

Table I

Rotational lines of the 3–0 band

N	R_1	P_1	R_2	P_2	R_3	P_3	R_4	P_4	R_5	P_5	R_6	P_6
4.0												
5.0												
6.0												
7.0												
8.0	11634.57				11635.01		11634.82					
9.0	34.40				34.82		34.57					
10.0	34.11	11620.03	11633.78		34.57		34.22					
11.0	33.78	18.36	33.24		34.22	11618.88	33.78	11618.61				
12.0	33.33	16.60	32.78	11616.29	33.78	17.13	33.24	16.80				
13.0	32.78	14.64	32.28	14.21	33.24	15.27	32.62	14.94	11630.08			
14.0	32.14	12.78	31.69	12.28	32.62	13.31	31.88	12.78	29.67		11631.88	
15.0	31.42	10.76	31.01	10.29	31.88	11.29	31.12	10.76	29.05	11608.14	31.13	
16.0	30.58	08.55	30.20	08.14	31.01	09.10	30.20	08.42	28.38	06.15	30.28	11608.41
17.0	29.67	06.33	29.22	05.93	30.08	06.83	29.22	06.15	27.53	04.08	29.47	06.15
18.0	28.66	03.96	28.28	03.64	29.05	04.47	28.11	03.64	26.50		28.38	03.81
19.0	27.53	01.54	27.22	01.20	27.92	02.00	26.95	01.20	25.34	11599.48	27.23	01.39
20.0	26.30	11599.05	26.02	11598.72	26.68	11599.48	25.66	11598.59	24.06	96.97	26.07	11598.89
21.0	24.96	96.41	24.70	96.08	25.34	96.84	24.31	95.89	22.71	94.32	24.96	96.27
22.0	23.56	93.67	23.31	93.39	23.94	94.10	22.85	93.10	21.29	91.54	23.42	93.56
23.0	22.10	90.82	21.85	90.58	22.42	91.26	21.29	90.26	19.74	88.67	21.99	90.82
24.0	20.48	87.89	20.26	87.69	20.80	88.35	19.67	87.27	18.14	85.70	20.48	87.89

Table I (continued)

Rotational lines of the 3–0 band

N	R_1	P_1	R_2	P_2	R_3	P_3	R_4	P_4	R_5	P_5	R_6	P_6
25.0	18.78	84.94	18.61	84.69	19.09	85.31	17.94	84.20	16.43	82.67	18.88	84.94
26.0	17.02	81.80	16.80	81.60	17.29	82.17	16.13	81.09	14.64	79.56	17.13	81.89
27.0	15.09	78.60	14.94	78.42	15.40	78.96	14.21	77.82	12.78	76.36	15.27	78.77
28.0	13.12	75.28	12.96	75.11	13.37	75.65	12.21	74.49	10.76	73.04	13.37	75.48
29.0	11.03	71.89	10.87	71.74	11.29	72.23	10.09	71.05	08.71	69.64	11.29	72.15
30.0	08.83	68.39	08.71	68.28	09.10	68.74	07.91	67.56	06.58	66.16	09.19	68.74
31.0	06.58	64.81	06.45	64.71	06.83	65.13	05.64	63.96	04.35	62.60	06.99	65.19
32.0	04.19	61.11	04.08	61.01	04.47	61.44	03.26	60.27	02.00	58.94	04.66	61.58
33.0	01.70	57.34	01.60	57.24	02.00	57.65	00.80	56.50	11599.61	55.22	02.26	57.89
34.0	11599.14	53.46	11599.05	53.39	11599.38	53.77	11598.27	52.63	97.10	51.39	11599.75	54.08
35.0	96.48	49.47	96.41	49.41	96.75	49.80	95.63	48.66	94.49	47.46	97.10	50.15
36.0	93.67	45.36	93.67	45.36	93.97	45.71	92.90	44.65	91.82	43.45	94.32	46.10
37.0	90.82	41.24	90.82	41.24	91.13	41.55	90.08	40.49	89.07	39.36	91.44	42.00
38.0	87.89	36.96	87.89	36.96	88.18	37.30	87.18	36.26	86.18	35.18		37.73
39.0	84.83	32.60	84.83	32.60	85.13	32.92	84.20	31.91	83.22	30.91		33.30
40.0	81.65	28.15	81.65	28.15	82.02	28.52	81.09	27.53	80.21	26.57		
41.0	78.42	23.60	78.42	23.60	78.77	23.97	77.90	23.05	77.10	22.13		
42.0	75.11	18.97	75.11	18.97	75.48	19.40	74.67	18.43	73.88	17.61		
43.0	71.65	14.22	71.65	14.22	72.05	11.60	71.31	13.79	70.59	12.97		
44.0	68.12	09.40	68.12	09.40	68.54	09.80	67.86	09.01	67.19			
45.0	64.53	04.46	64.47	04.46	64.94	04.89	64.32		63.71	03.48		
46.0	60.80	11499.50	60.73	11499.50	61.24	11499.90	60.73	11499.24	60.13			
47.0	56.99	94.38	56.90	94.38	57.47	94.84	56.99	94.24	56.50	11493.67		
48.0	53.09		52.95		53.58		53.22		52.76			
49.0	49.07		48.94		49.62		49.31		48.94			
50.0	44.99		44.80		45.55		45.36		44.99			
51.0	40.78		40.57		41.39		41.24		40.98			

Table I (continued)

Rotational lines of the 4–0 band

N	R_1	P_1	R_2	P_2	R_3	P_3	R_4	P_4	R_5	P_5	R_6	P_6
3.0			12198.95									
4.0			99.37									
5.0			99.62	12192.16								
6.0			99.82	91.03								
7.0			99.88	89.80								
8.0			99.82	88.45	12200.81							
9.0	12199.62		99.62	86.97	00.65							
10.0	99.33		99.37	85.33	00.32	12186.36						
11.0	98.86	12183.67	98.95	83.67	199.88	84.66			12198.66			
12.0	98.35	81.78	98.52	81.87	99.37	82.90	12199.33		98.13	12181.78		
13.0	97.75	79.75	97.92	79.99	98.86	80.95	98.66		97.40	79.75		
14.0	97.06	77.84	97.27	77.99	98.13	78.92	97.92		96.69	77.66		
15.0	96.27	75.72	96.43	75.88	97.27	76.83	97.06		95.84	75.43		
16.0	95.37	73.49	95.56	73.69	96.43	74.63	96.10	12174.47	94.89	73.16		
17.0	94.35	71.16	94.57	71.32	95.37	72.22	95.06	72.05	93.86	70.86		
18.0	93.30	68.75	93.54	69.00	94.35	69.80	93.86	69.58	92.70	68.41		
19.0	92.02	66.24	92.29	66.47	93.05	67.29	92.70	66.99	91.47	65.86	12192.16	12166.47
20.0	90.74	63.63	91.03	63.88	91.75	64.69	91.33	64.37	90.16	63.18	90.88	63.88
21.0	89.35	60.90	89.59	61.19	90.36	61.97	89.89	61.66	88.79	60.44	89.59	61.19
22.0	87.82	58.07	88.12	58.39	88.79	59.13	88.35	58.76	87.22	57.65	88.12	58.39
23.0	86.20	55.18	86.57	55.51	87.22	56.25	86.73	55.83	85.64	54.69	86.57	55.51
24.0	84.53	52.18	84.86	52.50	85.49	53.22	84.98	52.75	83.95	51.65	84.98	52.54
25.0	82.71	49.05	83.06	49.39	83.67	50.10	83.18	49.64	82.13	48.54	83.18	49.51

Table I (continued)

Rotational lines of the 4–0 band

N	R_1	P_1	R_2	P_2	R_3	P_3	R_4	P_4	R_5	P_5	R_6	P_6
26.0	80.79	45.82	81.14	46.17	81.78	46.88	81.28	46.38	80.28	45.39	81.38	46.38
27.0	78.83	42.54	79.20	42.90	79.75	43.60	79.20	43.09	78.29	42.07	79.45	43.09
28.0	76.69	39.12	77.10	39.50	77.66	40.16	77.10	39.62	76.20	38.69	77.47	39.83
29.0	74.47	35.59	74.89	36.00	75.43	36.66	74.89	36.15	74.05	35.18	75.43	36.40
30.0	72.22	31.98	72.58	32.38	73.16	33.03	72.58	32.50	71.80	31.60	73.16	32.87
31.0	69.80	28.27	70.20	28.77	70.75	29.31	70.20	28.77	69.44	27.93	70.86	29.31
32.0	67.29	24.47	67.69	24.88	68.22	25.51	67.69	24.95	66.99	24.17	68.48	25.51
33.0	64.69	20.55	65.10	20.96	65.63	21.59	65.10	21.08	64.46	20.30	66.00	21.77
34.0	61.97	16.53	62.39	16.96	62.89	17.56	62.39	17.06	61.83	16.38	63.45	17.86
35.0	59.13	12.42	59.58	12.86	60.09	13.46	59.64	12.97	59.13	12.32	60.80	13.87
36.0	56.25	08.20	56.66	08.65	57.19	09.24	56.80	08.80	56.25	08.20	58.07	09.83
37.0	53.22	03.95	53.67	04.34	54.24	04.92	53.82	04.51	53.39	03.95	55.18	05.70
38.0	50.10	12099.49	50.55	12099.93	51.11	00.53	50.78	00.14	50.37	12099.69	52.24	01.39
39.0	46.88	95.00	47.33	95.47	47.91	12096.03	47.63	12095.64	47.33	95.25	49.22	12097.09
40.0	43.60	90.40	44.07	90.86	44.62	91.44	44.35	91.13	44.07	90.70	46.13	92.62
41.0	40.16	85.67	40.65	86.16	41.24	86.76	41.01	86.44	40.82	86.16		88.13
42.0	36.66		37.15		37.76	81.96	37.60		37.49			
43.0	33.03	75.97	33.55	76.46	34.15		34.03		34.03	76.67		
44.0	29.31	70.90	29.83		30.45		30.45		30.45			
45.0	25.51		26.05		26.70		26.77		26.77			
46.0					22.87							
47.0					18.86							
48.0					14.80							
49.0					10.64							
50.0					06.35							

and the parity case (a) basis functions $|\Omega^{\pm}>$ for $^6\Sigma$ state:

$$|1/2^{\pm}> = 2^{-1/2}\,[|1/2> \pm |-1/2>], \tag{5a}$$

$$|3/2^{\pm}> = 2^{-1/2}\,[|3/2> \pm |-3/2>], \tag{5b}$$

$$|5/2^{\pm}> = 2^{-1/2}\,[|5/2> \pm |-5/2>]. \tag{5c}$$

Using this basis set the 6×6 $^6\Sigma^+$ Hamiltonian matrix reduces to two 3×3 matrices, one for the e (F_1, F_3, F_5) and one for the f (F_2, F_4, F_6) rotational levels. The non-zero matrix elements are given in Table II. The same matrix elements were obtained by Gordon and Merer in the analysis of the $^6\Sigma - X\ ^6\Sigma$ bands of MnO[6]. It should be noted that the formulas (1), (2) and (3) can be easily derived from the sum of the diagonal matrix elements of Table II.

Table II

Non-zero matrix elements of the rotational Hamiltonian (Eq. 4) for a $^6\Sigma$ electronic state in Hund's case (a) basis; $Z = J(J+1)$

$$\langle 5/2^{\pm}|H|5/2^{\pm}\rangle = \frac{20}{3}\lambda - \frac{5}{2}\gamma + \left(Z - \frac{15}{4}\right)\left(B - D\left(Z + \frac{5}{4}\right)\right)$$

$$\langle 5/2^{\pm}|H|3/2^{\pm}\rangle = \sqrt{5\left(Z - \frac{15}{4}\right)}\left(-B + \frac{1}{2}\gamma + D\left(2Z + \frac{1}{2}\right)\right)$$

$$\langle 5/2^{\pm}|H|1/2^{\pm}\rangle = -D\sqrt{40\left(Z - \frac{15}{4}\right)\left(Z - \frac{3}{4}\right)}$$

$$\langle 3/2^{\pm}|H|3/2^{\pm}\rangle = B\left(Z + \frac{9}{4}\right) - \frac{4}{3}\lambda - \frac{13}{2}\gamma - D\left(Z^2 + \frac{43}{2}Z + \frac{107}{16}\right)$$

$$\langle 3/2^{\pm}|H|1/2^{\pm}\rangle = \sqrt{2\left(Z - \frac{3}{4}\right)}\,(\gamma - 2B + 2D\,(2Z + 13 \mp (3J+2)))$$

$$\langle 1/2^{\pm}|H|1/2^{\pm}\rangle = -\frac{16}{3}\lambda - \gamma\left(\frac{17}{2} \pm \frac{3}{2}\left(J + \frac{1}{2}\right)\right) + B\left(\frac{33}{4} + Z \mp 3\left(J + \frac{1}{2}\right)\right) -$$
$$- D\left(Z^2 + \frac{67}{2}Z + \frac{1029}{16} \mp 6\left(Z + \frac{33}{4}\right)\left(J + \frac{1}{2}\right)\right)$$

Note: Upper and lower signs refer to the e and f levels, respectively

The molecular constants B, D, λ and γ were calculated using the program FUMILI [9] to perform a nonlinear least-squares fit of differences of eigenvalues $F_i(J+1)$ and $F_i(J-1)$ of the $^6\Sigma$ (a) matrix to observed combination differences $\Delta_2 F_i(J)$. The eigenvalues of the matrix were obtained by using the program for a numerical diagonalization EIGEN [8].

A total of 219 combination differences for the ground $v = 0$ state were included in the fit. The fit is quite good as can be seen from the value of "S" (see Table IV); the deviations between measured and calculated values $\triangle_2 F_i''(N)$ correspond to errors of measurements. However, the results for upper states are poor. The differences between calculated and observed $\triangle_2 F_i(N)$ are large and systematic for each component.

III. In order to obtain a better fit for the upper $^6\Sigma$ states data we took into account the first centrifugal correction terms of the spin interactions H_{cd}, so that we used the Hamiltonian in the form

$$H = H_{\rm rot} + H_{SS} + H_{SR} + H_{cd}, \tag{6}$$

where (11)

$$H_{cd} = (1/3)\,\lambda_D[(3S_z^2 - \mathbf{S}^2)(\mathbf{J}-\mathbf{S})^2 + (\mathbf{J}-\mathbf{S})^2\,(3S_z^2 - \mathbf{S}^2)] + \\ + \gamma_D(\mathbf{J}-\mathbf{S})\mathbf{S}\,(\mathbf{J}-\mathbf{S})^2. \tag{6a}$$

The non-zero matrix elements of H_{cd} are given in Table III. The results of fitting for the upper states are presented in Table IV, column III. As can be seen the agreement with experimental data is noticeably improved.

Table III

Non-zero matrix elements of H_{cd} (Eq. 6a) for a $^6\Sigma$ state in a Hund's case (a) basis; $Z = J(J+1)$

$$\langle 5/2^{\pm}|H|5/2^{\pm}\rangle = \left(\frac{20}{3}\lambda_D - 5\gamma_D\right)\left(Z - \frac{15}{4}\right)$$

$$\langle 5/2^{\pm}|H|3/2^{\pm}\rangle = \sqrt{5(Z-\frac{15}{4})}\left(\frac{8}{3}\lambda_D + \gamma_D\left(\frac{37}{4} + Z\right)\right)$$

$$\langle 5/2^{\pm}|H|1/2^{\pm}\rangle = -\gamma_D\sqrt{\left(Z - \frac{15}{4}\right)\left(Z - \frac{3}{4}\right)}$$

$$\langle 3/2^{\pm}|H|3/2^{\pm}\rangle = -\frac{4}{3}\lambda_D\left(\frac{17}{4} + Z\right) - \gamma_D\left(13Z + \frac{61}{4}\right)$$

$$\langle 3/2^{\pm}|H|1/2^{\pm}\rangle = \sqrt{2\left(Z - \frac{3}{4}\right)}\left(\frac{20}{3}\lambda_D - \gamma_D\left(3Z \mp \left(Z - \frac{85}{4}\right)\right)\right)$$

$$\langle 1/2^{\pm}|H|1/2^{\pm}\rangle = -\frac{16}{3}\lambda_D\left(\frac{33}{4} + Z \mp 3\left(J + \frac{1}{2}\right)\right) - \\ - \gamma_D\left(17Z + \frac{273}{4} \pm \frac{3}{2}\left(J + \frac{1}{2}\right)\left(\frac{101}{4} + Z\right)\right)$$

Note: Upper and lower signs refer to the e and f levels, respectively

Table IV

Rotational constants of CrF

A. $A\ ^6\Sigma$ state

	$v = 3$				$v = 4$			
	Methods of calculation							
	I	II	III	IV	I	II	III	IV
T_v	11631.38(2)				12197.50(4)			
B_v	0.3327(1)	0.33230(1)	0.33236(4)	0.33203(8)	0.3302(4)	0.33050(1)	0.33040(3)	0.3302(1)
$D_v 10^7$	7.9(9)	5.1(1)	5.22(1)	4.1(3)	3.1(1)	6.0(1)	5.16(1)	4.2(3)
λ		−0.0032(5)	-0.0026(3)			-0.0198(1)	-0.46(1)	
$\lambda_D 10^4$			-1.056(4)				-1.503(1)	
$\gamma 10^3$		4.74.(4)	7.583(6)	14(2)		2.71(5)	8.6908(5)	11(3)
$\gamma_D 10^6$			-0.0542(1)				-1.388(2)	
ε				-1.0(1)				-0.7(1)
$\tau 10^5$				5.3(7)				8.7(7)
$\sigma 10^6$				3.3(4)				3.6(4)
n	22	175	175	175	24	176	176	176
S	0.055	0.480	0.203	0.114	0.034	0.240	0.122	0.087

B. $X\ ^6\Sigma$ state

Method	B_0	$D_0 \times 10^7$	λ	$\gamma \times 10^2$	n	S
I	0.37941(4)	5.8(2)				
II	0.37936(1)	5.54(2)	-0.0079(1)	1.170(3)	219	0.068

The inclusion of the higher order spin-rotation interaction term $H_{SR}^{(3)}$ of [10] and [11] does improve the fit, but the spin-splitting constants turned out to be undeterminable.

IV. One of us proposed to explain the anomalous spin-splitting in the $A\ ^6\Sigma$ state by taking into account the perturbations by the not so far lying $^6\Pi$ states and the first correction terms of centrifugal distortion of the spin–spin and spin-rotation interactions. These effects were considered earlier in Ref. [3] p. 97, [11], p. 330.

Since in most of the multiplet Σ states, in general, the Hund's case (b) form

gives a good approximation we get for the multiplet term values

$$F_N(N) = T_N(N) + H_N^{SS}(N) + H_N^{SR}(N), \tag{7}$$

where

$$T_N(N) = BN(N+1) - DN^2(N+1)^2, \tag{7a}$$

$$H_N^{SS}(N) = [\varepsilon + \tau_1 N(N+1)]\langle JN\,|3\,S_z^2 - \mathbf{S}^2|_b JN\rangle, \tag{7b}$$

$$H_N^{SR}(N) = [\gamma + \sigma_1 N(N+1)]\langle JN \mid \mathbf{RS}\,|_b JN\rangle, \tag{7c}$$

$$\langle JN \mid 3\,S_z^2 - \mathbf{S}^2\,|_b JN\rangle = -\frac{(3/2)C(C+1) - 2N(N+1)S(S+1)}{(2N-1)(2N+3)}, \tag{8}$$

$$\langle JN \mid \mathbf{R}\,\mathbf{S}\,|_b JN\rangle = (1/2)C; \qquad C = J(J+1) - N(N+1) - S(S+1),$$

$$\tau_1 = \frac{4\,B_e^2}{\omega_e^2}\,\tau_e \left(\frac{\partial \varepsilon}{\partial\,\tau}\right)_{\tau=\tau_e}; \qquad \sigma_1 = \frac{4\,B_e^2}{\omega_e^2}\,\tau_e \left(\frac{\partial \gamma}{\partial \tau}\right)_{\tau=\tau_e},$$

$$\varepsilon = (2/3)\lambda \tag{9}$$

and $N = J - S,\ J - S + 1, \ldots J + S$. These formulas are valid for Σ terms of any multiplicity in Hund's case b).

As it was shown earlier [12] the perturbation effect has the same form as Eqs (7b) and (7c) with the only difference that instead of τ_1 and σ_1 τ_2 and σ_2 are the following

$$\tau_2 = a(B_i - B_k)\,\frac{|\xi|^2}{(h\nu)^2}, \qquad \sigma_2 = b(B_i - B_k)\frac{\xi\eta^* + \xi^*\eta}{(h\nu)^2} \tag{10a}$$

where

$$\xi = H^{SO}\,(\Pi, \Sigma), \qquad \eta = (B\,L_\xi)(\Pi\Sigma) \tag{10b}$$

and a and b are numerical constants depending on the multiplicity of the Σ terms. $H^{SO}(\Pi\Sigma)$ is the matrix element of the spin–orbit interaction and $(B\,L_\xi)(\Pi\Sigma)$ arise from the terms neglected at the separation of the wave equations. That means, if we take into consideration for case b) the complete term formulas (the centrifugal correction also included) the constants determined experimentally contain not only the effect of the centrifugal distortions but also the perturbation effect by the neighbouring terms transferred by the spin–orbit interaction, too. So in the complete formulas $\sigma = \sigma_1 + \sigma_2$ is also to be written instead of σ_1 and σ_2 and $\tau = \tau_1 + \tau_2$ instead of τ_1 and τ_2, respectively.

Application of the theory to the $^6\Sigma$ terms

As the sextet term has not been treated completely in the literature the detailed application in this case will be demonstrated. Let us write the term formulas for each component of the $^6\Sigma$ term according to (6) and (7a), (7b), (7c)

$$F_1(N) = \nu_0 + T(N) - 10\varepsilon\frac{N}{2N+3} + \frac{5}{2}\gamma N - 5\,[\sigma(N+1) - \tau]N^2,$$

$$F_2(N) = \nu_0 + T(N) + \varepsilon[1 + \frac{27}{2N+3}] + (1/2)\gamma(3N-5) - [\sigma(3N-5)(N+1) + \\ + \tau(N+15)]N,$$

$$F_3(N) = \nu_0 + T(N) + \varepsilon[4 + \frac{27}{2N+3} - \frac{15}{2N-1}] + (1/2)\gamma(N-8) - \\ - [\sigma N(N+1)(N-8) - 2\tau(2N-3)(N+4)],$$

$$F_4(N) = \nu_0 + T(N) + \varepsilon[4 + \frac{15}{2N+3} - \frac{27}{2N-1}] - (1/2)\gamma(N+9) + \\ + [\sigma N(N+1)(N+9) - 2\tau(2N+5)(N-3)],$$

$$F_5(N) = \nu_0 + T(N) + \varepsilon[1 - \frac{27}{2N-1}] - (1/2)\gamma(3N+8) + [\sigma(3N+8)N - \\ - \tau(N-14)](N+1),$$

$$F_6(N) = \nu_0 + T(N) - 10\varepsilon\frac{N+1}{2N-1} - (5/2)\gamma(N+1) + 5\,[\sigma\,N + \tau](N+1)^2. \quad (11)$$

Forming the appropriate combination differences, we get

$$\Delta_2F_1(N) = \Delta_2T(N) - \frac{60\varepsilon}{(2N+1)(2N+5)} + 5\gamma - 10\sigma(3N^2+2N+1) + \\ + 20\tau N,$$

$$\Delta_2F_2(N) = \Delta_2T(N) - \frac{108\varepsilon}{(2N+1)(2N+5)} + 3\gamma - 2\sigma(9N^2-4N-2) - \\ - 2\tau(2N+15),$$

$$\Delta_2F_3(N) = \Delta_2T(N) - 48\varepsilon\frac{2N-13}{(2N-3)(2N+1)(2N+5)} + \gamma - \\ - 2\sigma(3N^2-14N-7) - 4\tau(4N+5),$$

$$\Delta_2F_4(N) = \Delta_2T(N) + 48\varepsilon\frac{2N+15}{(2N-3)(2N+1)(2N+5)} - \gamma + \\ + 2\sigma(3N^2+20N+10) - 4\tau(4N-1),$$

$$\Delta_2F_5(N) = \Delta_2T(N) + \frac{108\varepsilon}{(2N-3)(2N+1)} - 3\gamma + 2\sigma(9N^2+22N+11) - \\ - 2\tau(2N-13),$$

$$\Delta_2F_6(N) = \Delta_2T(N) + \frac{60\varepsilon}{(2N-3)(2N+1)} - 5\gamma + 10\sigma\,(3N^2+4N+2) + \\ + 20\tau(N+1), \quad (12)$$

where

$$\triangle_2 T(N) = (4B - 6D)(N + 1/2) - 8D(N + 1/2)^3. \tag{13}$$

The expressions on the left-hand side were produced numerically from the observed combination differences and by the computer fitting of the right-hand side theoretical values by the least-squares method the numerical values of the coefficients B, D, ε, γ, σ and τ were determined as shown in Table IV, column IV for the upper states of the $A\,^6\Sigma - X\,^6\Sigma$ transition of the CrF molecule.

Summarising, it can be stated that the recently observed anomalous behaviour of the $A\,^6\Sigma$ term of the CrF molecule — in accordance with the experimental data — is correctly explained by the combined effect of the centrifugal distortion of the spin-spin and spin-rotation interactions and the perturbation by closer lying terms.

Discussion

The values of the constants B, D, λ and γ for the ground $X\,^6\Sigma$ state describe quite correctly the experimental data (see Fig.1).

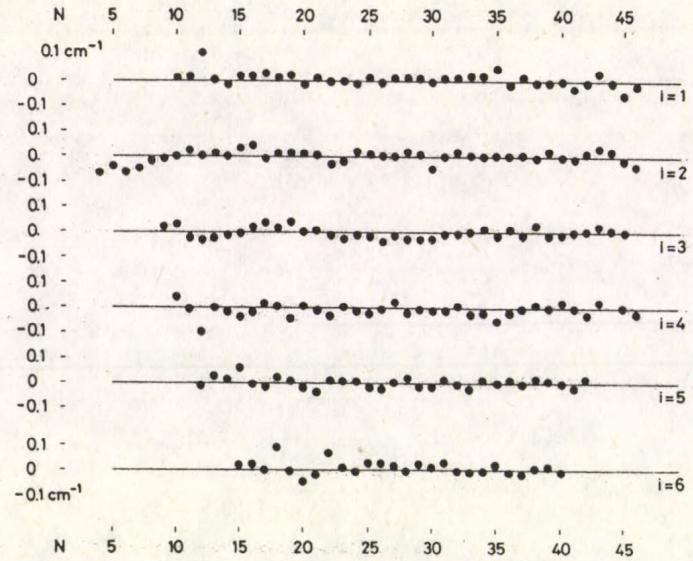

Fig. 1. Deviations $\triangle_2 F_i^{II\,exp}(N) - \triangle_2 F_i^{II\,calc}(N)$ for the $X^6\Sigma(v = 0)$ state

For the $A\,^6\Sigma$ (v=3 and v=4) state two sets of rotational constants were obtained from the III and IV methods of calculations. Both sets give good approximations of the $F(N)$ (see Figs 2 and 3). The less good results for the $A\,^6\Sigma$ (v=3) level as compared with those for the $A\,^6\Sigma$ ($v = 4$) level can be due to homogeneous

perturbation by high levels of the ground state ($v \approx 19$) detected in the vibrational structure of the $A\ ^6\Sigma - X\ ^6\Sigma$ transition [1].

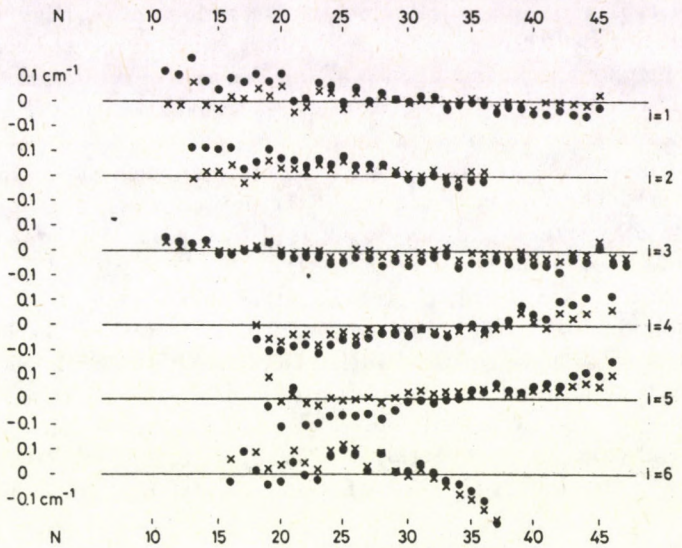

Fig. 2. Deviations $\Delta_2 F_i^{'\,exp}(N) - \Delta_2 F_i^{'\,calc}(N)$ for the 3–0 band, • • • Method III, × × Method IV

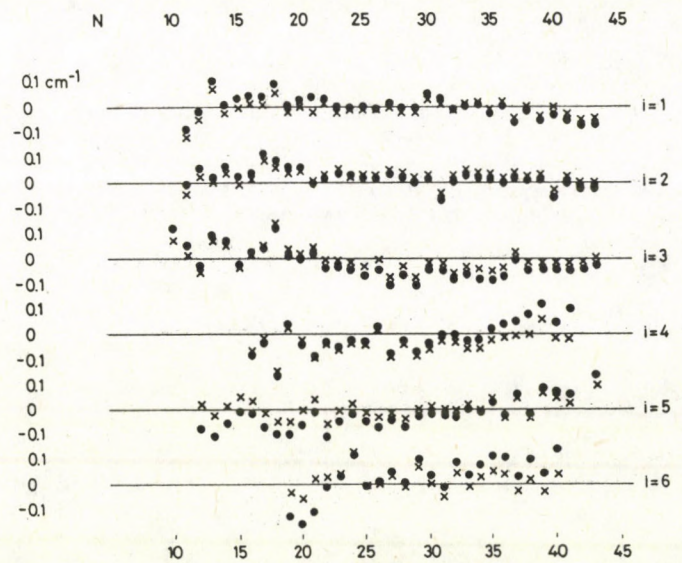

Fig. 3. Deviations $\Delta_2 F_i^{'\,exp}(N) - \Delta_i F^{'\,calc}(N)$ for the 4–0 band • • • Method III, × × Method IV

It should be noted that the constants B, D and γ for the $A\ ^6\Sigma$ state derived from the different treatments have very close values. But the λ or ε values can be considered only as estimations. For the calculation of reliable values of the spin–spin parameters it is necessary to include measurements of $\triangle_2 F$ at low values of N. But assignments of the R_i lines at $N < 10$ are very perplexed because of their strong overlapping near the band heads. From two sets of rotational constants we prefer the constants obtained using Kovács' relations (method IV) because they give a little better fit to experimental data.

The results of the analysis give an indirect evidence about the electronic structure of CrF. The matrix treatment of the ground state data shows that it is unaffected by other states and can be ascribed to the $3d^5$ $(\delta^2\pi^2\sigma)$ configuration which gives rise to only one sextet term $X\ ^6\Sigma$.

In contrast to that, the $A\ ^6\Sigma$ state is bathed in a comparatively dense manifold of electronic states. The vibrational analysis [1] revealed the homogeneous perturbations which can be explained by interactions with high vibrational levels of the ground state. The rotational analysis has required the inclusion of effects due to perturbations by the not so far lying $^6\Pi$ terms. This implies that the $A\ ^6\Sigma$ state belongs to the d^4 $(\delta^2\pi^2)\sigma_{4S}$ configuration. The super-configuration $d^4\sigma_{4S}$ gives rise to the near lying $^6\Pi$ and $^6\triangle$ terms, the first one is probably the perturbing state.

References

1. V.M. Dubov, E.A. Shenyavskaya, Opt. i Spektr., *62*, 326, 1987.
2. K.S. Rao, Ind. J. Phys., *26*, 47, 1952.
3. I. Kovács, Rotational Structure in the Spectra of Diatomic Molecules, Akadémiai Kiadó, Budapest and Adam Hilger Ltd, London, 1969.
4. B. Kleman and U. Uhler, Canad. J. Phys., *58*, 642, 1959.
5. S.O. Connor, Proc. Roy. Ir. Acad., *65A*, 96, 1967.
6. R.M. Gordon and A.J. Merer, Canad, J. Phys., *58*, 642, 1980.
7. J.H. Van Vleck, Phys. Rev., *33*, 467, 1929.
8. Сборник научных программ на фортране, Т.I, Москва, 1974.
9. Сборник прикладных программ "Дубна", Т.4, Д, 520.
10. J.M. Brown and D.J. Milton, Mol. Phys., *31*(2), 4409, 1976.
11. I. Kovács, Acta Phys. Hung., *48*, 323, 1980.
12. I. Kovács, Acta Phys. Hung., *32*, 5, 1972.

Acta Physica Hungarica 65 (4), pp. 425–430 (1989)

SPECTRUM OF ATOMIC ELECTRONS IONISED BY AN INTENSE FIELD

P. KÁLMÁN

Department of Experimental Physics, Institute of Physics
Technical University of Budapest
1521 Budapest, Hungary

(Received 29 March 1988)

Gauge problems arising in recent multiphoton ionisation computations are discussed. The recent results of Reiss [18],[19] based on his earlier formulae [20] are queried.

Nowadays the problem of multiphoton stripping of atoms including the above-threshold ionisation phenomena is intensely investigated both experimentally [1]–[8] and theoretically [9]–[16]. Some of the experiments [7] can be fairly well explained by the theory of Keldysh [17].

In two recent articles [18],[19] the spectrum of emitted atomic electrons originated from multiphoton ionisation of xenon was analysed and qualitative agreement was found with above-threshold ionisation experiments [6], [8]. Both articles [18], [19] are based on an earlier work of Reiss [20], where the effect of intense radiation field on weakly bound systems was discussed in a great detail using Volkov [21] solutions as final states but contrary to Keldysh [17], who used the electric-dipole (Göppert-Mayer, $\mathbf{xE}$) gauge, Reiss [20] worked in the radiation (Coulomb, $\mathbf{pA}$) gauge. It was claimed by Reiss [20] that the approximation used was equivalent to that of Keldysh [17]. However, differences in the formulae for the S matrix elements and transition probabilities per unit time appeared, although these must be invariant under gauge transformation. We think that these differences are the consequence of an incorrect use of the radiation gauge in Reiss's paper [20].

In order to discuss the situation we show that the S matrix element computed by Keldysh [17] in the electric-dipole gauge remains unchanged under transformation into the radiation gauge if one carefully carries out this transformation [22], [23], i.e. the S matrix element is gauge invariant as it is expected. Doing this we point out those steps of [20] which lead to formulae different from that of [17]. As the recent articles [18], [19] are based on the criticised formulae of [20] the results of these papers are also questioned.

The S matrix element, which describes the photodetachment, can be derived from formula (3) of [20]

$$(S-1)_{fi} = -\frac{i}{\hbar}\int dt \int d^3r\ \psi_f^{g*}(\mathbf{r},t)\ P^g(\mathbf{r},t)\ \psi_i^g(\mathbf{r},t), \tag{1}$$

where ψ_f^g is the final state of the free charged particle in the presence of the electromagnetic field and ψ_i^g is the initial, unperturbed bound state, which is well known.

$P^g(\mathbf{r},t)$ stands for that term which will be considered as perturbation in the time-dependent Schrödinger equation. The index g notes that the wave functions and the operator P depend on the choice of gauge.

Expression (1) is evaluated by Keldysh [17] in the electric-dipole gauge and by Reiss [20] in the radiation gauge. Therefore, first we briefly summarize those well known results which we need in order to treat the gauge transformation problem [22], [23].

The Schrödinger equation is written in the following form

$$\{\varepsilon^g(t) + F^g(t)\}\ \psi^g(\mathbf{r},t) = 0, \tag{2}$$

where $\varepsilon^g(t)$ is the time-dependent instantaneous energy operator of the system

$$\varepsilon^g(t) = \frac{1}{2m}\left(\mathbf{p} - \frac{e}{c}\,\mathbf{A}^g(\mathbf{r},t)\right)^2 + V(\mathbf{r}) \tag{3}$$

and $F^g(t)$ is defined as

$$F^g(t) = eU^g(\mathbf{r},t) - i\hbar\frac{\partial}{\partial t}. \tag{4}$$

Here $\mathbf{p}$ is the operator associated with the momentum of the particle, which has a gauge-independent form $\mathbf{p} = -i\hbar\nabla$, U_g and $\mathbf{A}^g$ are the scalar and vector potentials, respectively, describing the electromagnetic radiation and $V(\mathbf{r})$ stands for the atomic potential. If we transform the electromagnetic potentials from a gauge g to another one g' as usual, then the operators (e.g. operator O) and the state vector of a physical system are also transformed by a unitary transformation $T(\mathbf{r},t)$ as

$$O^{g'} = T(\mathbf{r},t)\ O^g\ T^+(\mathbf{r},t), \tag{5a}$$

$$\psi^{g'}(\mathbf{r},t) = T(\mathbf{r},t)\ \psi^g(\mathbf{r},t), \tag{5b}$$

with

$$T(\mathbf{r},t) = \exp\,(ie\,\chi(\mathbf{r},t)/\hbar c). \tag{6}$$

Here $\chi(r,t)$ is an arbitrary function, which governs gauge transformation. The function

$$\chi_{ER}(\mathbf{r},t) = \mathbf{A}(t).r \tag{7}$$

corresponds to that gauge transformation which transforms from the electric-dipole gauge into the radiation gauge. Here and throughout the paper the long wavelength approximation (LWA) is used.

Only those operators can correspond to physical quantities which have gauge invariant eigenvalues. The instantaneous energy operator $\varepsilon^g(t)$, the operator $F^g(t)$ and the mechanical momentum $\pi^g = \mathbf{p} - e/c\ \mathbf{A}^g$ all represent physical quantities. In the LWA the eigenvalues of ε^g are time-independent and in the electric-dipole gauge $\varepsilon^E = H_0$ with $H_0 = \mathbf{p}^2/2m + V(\mathbf{r})$, which is the unperturbed Hamiltonian and represents a nonphysical quantity. Thus the eigenvalues of ε^g in all gauges are equal to the eigenvalues of H_0 which are usually known. Furthermore, the eigenstates of the two operators are also identical in the electric-dipole gauge.

Now in order to reconstruct Keldysh's calculation we consider the Schrödinger equation in the electric dipole gauge. In this case $\mathbf{A}^E = 0$ and $U^E = -\mathbf{r}.\mathbf{E}$ so (2) reads

$$\{H_0 - i\hbar\ \partial/\partial\ t - e\mathbf{r}.\mathbf{E}(t)\}\ \psi^E(\mathbf{r},t) = 0, \tag{8}$$

where we used the $\varepsilon^E = H_0$ and the $F^E = -i\hbar\ \partial/\partial\ t - e\mathbf{r}.\mathbf{E}(t)$ equalities. The index E refers to the electric-dipole gauge. If we start the solution of (8) with the time dependent wavefunction

$$\psi_n^E(\mathbf{r},t) = \exp\ (-iE_nt/\hbar)\ \Phi_n(\mathbf{r}), \tag{9}$$

which satisfies the $[H_0 - i\hbar\ \partial/\partial\ t]\ \psi^E(\mathbf{r},t) = 0$ equation, then the $-e\mathbf{r}.\mathbf{E}(t)$ term can be considered as perturbation in (1), i.e.

$$P^E(\mathbf{r},t) = -e\mathbf{r}.\mathbf{E}(t). \tag{10}$$

The wave function $\Phi_n(\mathbf{r})$ is that eigenstate of H_0 which has an eigenvalue E_n. Thus $\psi_n^E(\mathbf{r},t)$ of the form (9) corresponds to the initial state in (1). Before obtaining the final state we restrict ourself to the linearly polarized case investigated by Keldysh [17]. Then the electric field strength is given as $\mathbf{E}(t) = \mathbf{E}\ \cos(\omega t)$. As final state we use the wavefunction of a free electron in this field ([17], formula (6))

$$\psi_f^E(\mathbf{r},t) = \exp\frac{i}{\hbar}\left\{\left(\mathbf{p} + \frac{e\mathbf{E}}{\omega}\ \sin(\omega t)\right)\cdot\mathbf{r} - \right.$$

$$\left. - \int_0^t \frac{1}{2m}\left(\mathbf{p} + \frac{e\mathbf{E}}{\omega}\ \sin(\omega\tau)\right)^2 d\tau\right\}. \tag{11}$$

If we use in (1) the initial, final states and the perturbation P^E given above (formulas (9), (11) and (10), respectively), then we get

$$(S-1)_{fi} = -\frac{i}{\hbar}\int dt \int d^3r\ \psi_f^{E*}(\mathbf{r},t)\ P^E(\mathbf{r},t)\ \psi_n^E(\mathbf{r},t) \tag{12}$$

and from (12) with the usual procedure the transition probability per unit time of the multiphoton detachment process can be obtained. This is Keldysh's result.

As a next step we show that if one evaluates (1) in the radiation gauge then the result is also (12). Using the rules of the gauge transformation (5a,5b) and formulae (6) and (7) we obtain the initial and final state wave functions and the operator of perturbation in the radiation gauge as

$$\psi^R(\mathbf{r},t) = T_{ER}(\mathbf{r},t)\ \psi^E(\mathbf{r},t) \tag{13a}$$

and

$$P^R(\mathbf{r},t) = T_{ER}(\mathbf{r},t)\ P^E(\mathbf{r},t)\ T^+_{ER}(\mathbf{r},t) \tag{13b}$$

with

$$T_{ER}(\mathbf{r},t) = \exp\ (ie\mathbf{r}.\mathbf{A}(t)/\hbar c), \tag{14}$$

where the index R refers to the radiation gauge. As the operators T_{ER} and P^E are commuting, i.e. $T_{ER}\ P^E = P^E\ T_{ER}$, and T_{ER} is unitary

$$P^R(\mathbf{r},t) = P^E(\mathbf{r},t). \tag{15}$$

Putting (15) into (1), using(13a) and again the unitarity of T_{ER} the equivalence of the result with (12) becomes obvious.

Finally, in order to point out the inconsistencies in the calculation of Reiss [20] we discuss the problem once more in detail.

We start with the problem of what kind of state can be considered as a bound, initial state of definite energy in the radiation gauge. In view of the considerations given at the beginning of this comment it seems obvious that the eigenfunctions of the instantaneous energy operator (3) are appropriate for this. Their eigenvalues are identical with the eigenvalues of H_0 and the wavefunctions in the radiation gauge can be obtained from (9) applying transformation (13a) with (14)

$$\psi^R_n(\mathbf{r},t) = \exp\ (ie\mathbf{r}.\mathbf{A}(t)/\hbar c)\ \psi^E_n(\mathbf{r},t). \tag{16}$$

These wave functions obey the equation

$$\varepsilon^R(t)\ \psi^R_n(\mathbf{r},t) = E_n\ \psi^R_n(\mathbf{r},t). \tag{17}$$

However, in the radiation gauge Reiss [20] uses an incorrect initial state of the form

$$\psi_i(\mathbf{r},t) = \Phi_n(\mathbf{r})\ \exp\ (-iE_nt/\hbar), \tag{18}$$

which is exactly the initial wave function ψ^E_n in the electric-dipole gauge given by (9),

Applying again transformation (13a) with (14) on (11) we obtain the final state in the radiation gauge which is of Volkov type [21]

$$\psi_f^R(\mathbf{r},t) = \exp\frac{i}{\hbar}\left\{\mathbf{p}\cdot\mathbf{r} - \int_0^t \frac{1}{2m}\left(\mathbf{p} + \frac{e\mathbf{E}}{\omega}\sin(\omega\tau)\right)^2 d\tau\right\}. \tag{19}$$

This is used also by Reiss [20] as final state. Thus the initial and final states of Reiss are inconsistent as they are taken at different gauges.

The incorrect use of the initial state wave function by Reiss results in a perturbation term [20]

$$P^R(\mathbf{r},t) = -\frac{e\mathbf{A}(t).(-i\hbar\nabla)}{m\,c} + \frac{e^2\mathbf{A}(t)^2}{2mc^2}, \tag{20}$$

which is also incorrect. This can be shown in the following way. In the radiation gauge $U^R = 0$ and $\mathbf{A}^R = \mathbf{A}(t)$, thus the Schrödinger equation (2) has the form

$$\left\{\varepsilon^R(t) - i\hbar\,\partial/\partial\,t\right\}\,\psi^R(\mathbf{r},t) = 0, \tag{21}$$

with

$$\varepsilon^R(t) = \frac{1}{2m}\left(\mathbf{p} - \frac{e}{c}\mathbf{A}(t)\right)^2 + V(r). \tag{22}$$

We make a formal modification of this equation adding to and subtracting from it the same quantity $e\mathbf{r}.\mathbf{E}(t)$. Then (21) can be written as

$$\left\{[\varepsilon^R(t) - i\hbar\,\partial/\partial\,t + e\mathbf{r}.\mathbf{E}(t)] - e\mathbf{r}.\mathbf{E}(t)\right\}\,\psi^R(\mathbf{r},t) = 0. \tag{23}$$

Substituting (16) into (23) and using (17) and

$$\mathbf{E}(t) = -\frac{\partial}{c\partial t}A(t), \tag{24}$$

we can recognize that the effect of the square bracket on the wave function (16) gives null. Thus, contrary to Reiss [20], the last term in (23) has to be considered as perturbation in the radiation gauge

$$P^R = -e\mathbf{r}.\mathbf{E}(t), \tag{25}$$

which, in accordance with (15), is the same as in the case of electric-dipole gauge (10). This follows from the correct choice of the initial state (16).

Summarizing, our statements are as follows:

Reiss [20] uses improper initial state wave function and improper perturbation term (Eq. (20) in this note) in the radiation gauge.

As a consequence, formulae (11), (12) and (26), (42) for $(S-1)_{fi}$ and the transition probabilities per unit time (31), (32) and (45) of Reiss [20] are not correct. Formula (45), which describes the case of linear polarization, significantly differs from the correct result of Keldysh [17], [18].

Finally the results of recent calculations [18], [19] are also questionable because these are based on the formulae criticized above.

The author is indebted to A. Tóth for valuable discussions.

References

1. P. Agostini, M. Clement, F. Fabre and G. Petite, J. Phys. B; At. Mol. Phys., *14*, L491, 1981.
2. P. Agostini, F. Fabre, G. Mainfray, G. Petite and N. K. Rahman, Phys. Rev. Lett., *42*, 1127, 1979.
3. P. Kruit, J. Kimman and M. J. van der Wiel, J. Phys. B; At. Mol. Phys., *14*, L597, 1981.
4. P. Kruit, J. Kimman, H. G. Muller and M. J. van der Wiel, Phys. Rev., *A28*, 248, 1983.
5. L. A. Lompré, A. L'Huillier, G. Mainfray and C. Manus, J. Opt. Soc. Am., *B2*, 1906, 1985.
6. F. Yergeau, G. Petite and P. Agostini, J. Phys. B; At. Mol. Phys., *19*, L663, 1986.
7. F. Yergeau, S. L. Chin and P. Lavigne, J. Phys. B; At. Mol. Phys., *20*, 723, 1987.
8. P. H. Bucksbaum, M. Bashkansky, R. R. Freeman, T. J. McIlrath and L. F. DiMauro, Phys. Rev. Lett., *56*, 2590, 1986.
9. H. G. Muller and A. Tip, Phys. Rev., *A30*, 3039, 1984.
10. H. G. Muller, A. Tip and M. J. van der Wiel, J. Phys. B: At. Mol Phys., *16*, L679, 1983.
11. K. Rzazewski and R. Grobe, Phys. Rev., *A33*, 1855, 1986.
12. A. Dulcic, Phys. Rev., *A35*, 1673, 1987.
13. K. C. Kulander, Phys. Rev., *A35*, 445, 1987.
14. K. C. Kulander, Phys. Rev., *A36*, 2726, 1987.
15. B. Chen, F. H. M. Faisal, S. Jetzke, H. O. Lutz and P. Scanzano, Phys. Rev., *A36*, 4091, 1987.
16. M. Crance, Phys. Lett. C; Phys. Rep., *144*, 117, 1987.
17. L. V. Keldysh, Sov. Phys.-JETP, *20*, 1307, 1965.
18. H. R. Reiss, J. Phys. B; At. Mol. Phys., *20*, L79, 1987.
19. H. R. Reiss, J. Opt. Soc. Am., *B4*, 726, 1987.
20. H. R. Reiss, Phys. Rev., *A22*, 1786, 1980.
21. D. M. Volkov, Z. Phys., *94*, 250, 1935.
22. R. R. Schlicher, W. Becker, J. Bergou and M. O. Scully, in Quantum Electrodynamics and Quantum Optics, ed. by A. O. Barut, Plenum, New York, 1984, p. 405.
23. W. E. Lamb, Jr. R. R. Schlicher and M. O. Scully, Phys. Rev., *A36*, 2763, 1987.

Acta Physica Hungarica 65 (4), pp. 431–434 (1989)

SHORT COMMUNICATIONS

EFFECT OF HYDROGEN BONDING ON THE POLARIZATION OF FLUORESCENCE OF 4-METHYL-7-HYDROXY COUMARIN

R. GIRI, S. S. RATHI, M. K. MACHWE* and V. V. S. MURTI

Department of Physics and Astrophysics
Department of Chemistry, University of Delhi
Delhi-110007 India

(Received 11 March 1987)

Introduction

The polarization of fluorescence of molecules in solution has been reported to depend upon various factors viz. viscosity of the solvent [1]; migration of the excited state energy from the originally excited state molecule to a neighbouring molecule [2]; shape and size of the fluorescent molecule [3]; temperature, hydrogen bonding [4], etc. Perrin's formula giving a correlation between polarization and viscosity is not able to explain completely the effect of the solvent on polarization, particularly when the viscosity is low.

Hydrogen bonding capability of a fluorescent molecule is generally inferred from the alterations in both the activation and the fluorescence wavelengths on changing the solvents. The shifts in activation and fluorescence wavelengths may indicate that the solvent associates with the solute in the ground state, or the excited state, and there is a good possibility that this could be due to hydrogen bonding. But by merely observing the excitation and emission spectra it is not always possible to infer conclusively that hydrogen bonding is taking place [5]. In present investigation it is suggested that fluorescence polarization measurement can be used for detecting hydrogen bonding.

Experimental

The polarization of fluorescence of 4-methyl-7-hydroxy Coumarin in different solvents (Conc. $\sim 10^{-7}$g/cm^3) is measured at room temperature ($\sim 20° \pm 2°$C) with an Aminco Bowman Spectrophotofluorometer.

The 4-methyl-7-hydroxy Coumarin used in the present study was synthesised according to literature method [6] and was checked for purity by m.p. and T.L.C. Double distilled water and A.R. grade solvents were used for the preparation of the solutions. All the solvents were checked for scattering at the excitation wavelength as well as for any fluorescent contamination. The correction due to scattering, to the

*The author to whom correspondence should be addressed

intensity of fluorescence was found to be less than 0.5%. The concentration of the compound in solution was kept quite low ($\sim 1.0\times 10^{-7}$g/cm^3) so as to minimize the effect of self-absorption in the solution. In each solvent, the excitation and emission peaks were located and the polarization was calculated by the method described by [7] Azumi and McGlynn

$$P = (I_{EE} - GI_{EB}) / (I_{EE} + GI_{EB}), \tag{1}$$

where I is the observed intensity, the first and the second scripts refer to the orientations of polarizer and analyzer and G is the grating correction factor given by $G = I_{BE}/I_{BB}$.

Results and discussion

The average values of polarization at peak excitation and emission wavelengths (λ_{ex} and λ_{em}) are listed in Table I. The values of molecular weight and viscosity of the solvents, taken from the standard tables of constants [8,9] are also included in Table I.

Table I

Percentage polarization (P) of 4-methyl-7-hydroxy coumarin in solvents of molecular wt. M and viscosity η

	Solvent	λ_{ex} [nm]	λ_{em} [nm]	Viscosity[8,9] $10^3\cdot$Rd$\cdot s$ η	Mol.wt. (M) [mol]	% Polarization (P)
1.	Water	323	449	1.00	18.01	1.1
2.	Methanol	324	388	0.54	32.04	2.1
3.	Formamide	334	452	3.76	45.04	3.3
4.	Ethanol	325	386	1.08	46.07	3.7
5.	n-propanol	330	395	2.24	60.10	5.1
6.	Butanone	340	385	0.42	72.11	9.1
7.	n-butanol	325	388	2.00	74.12	6.4
8.	Benzene	321	389	0.60	78.12	7.8

The polarization of fluorescence of a substance in solution as a function of viscosity, molecular volume, temperature, lifetime of the excited state, etc. is given by Perrin's formula

$$(1/P - 1/3) = (1/P_0 - 1/3)\,(1 + RT\tau/\eta\, V). \tag{2}$$

In the present case, the Perrin's plot, $1/P$ vs $1/\eta$ is not linear and hence the observed change in polarization cannot be completely accounted for by change

in viscosity alone. Since a low concentration is used, electromagnetic coupling of neighbouring solute molecules and its depolarizing effect due to energy migration is small. It is, therefore, necessary to look for some other cause to account for this variation in polarization. One such possible cause could be hydrogen bonding.

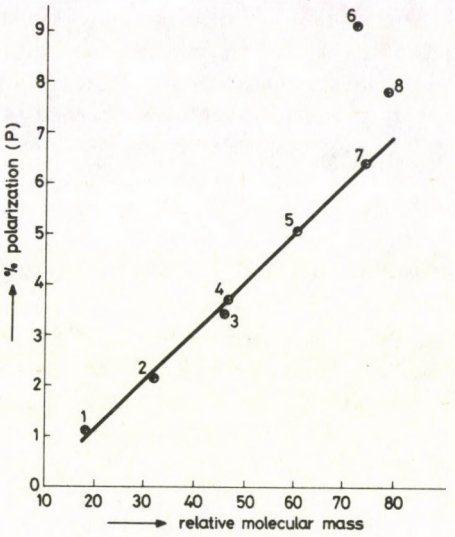

Fig. 1. Percentage polarization (P) vs relative molecular mass (M)

The extent and strength of hydrogen bonding would, of course, be different for different solvents. But in every case, whenever hydrogen bonding takes place, the effective molecular volume of the bonded complex molecule will increase. Due to this increase in molecular volume, a higher value of polarization is expected according to Perrin's formula. It is not possible to calculate exactly the molecular volume of the hydrogen-bonded molecule but a good approximation would be to assume that with higher molecular weight of the solvent, the effective size would be larger. This change in volume is not necessarily linearly dependent on the molecular weight. In Table I, the solvents are arranged in order of increasing molecular weight. From Table I, it is seen that the percentage polarization increases with the increase in molecular weight of the solvent. Figure 1 shows a plot of percentage polarizations vs molecular weight of the solvent. It may be noted that except in the case of benzene and butanone all the points lie on a straight line. This linear variation is a clear indication of hydrogen bonding in all these solvents. However, this variation needs to be examined in greater detail because the viscosity of solvent also changes. The effect of viscosity and hydrogen bonding on polarization can be seen distinctly in those pairs of solvents where they produce opposite effects. For example, consider the pair of solvents water and methanol: water has higher viscosity than methanol and according to Eq. (2) the percentage polarization should

be more in water than in methanol. But this is not borne out by the experimental values (Table I). If we consider hydrogen bonding, a molecule hydrogen-bonded with water will be of smaller size than the one associated with methanol and hence the polarization in water should be less. As the two effects are superimposed, it is possible to get polarization in water less than in methanol, as is actually observed. Same type of argument could be extended to other pairs of solvents, viz. (1) Formamide and Ethanol (2) Formamide and n-propanol (3) Formamide and n-butanol (4) n-propanol and n-butanol, where there is apparent failure of linearity of ($1/P$ vs $1/\eta$) plot (see Eq. (2)). In all these cases, the polarization is lower in a solvent of higher viscosity and is contrary to well established viscosity effect. This lends support to the proposed idea that the molecular weight of the solvent (when hydrogen bonding can take place) has a definite effect on the polarization and it manifests itself through hydrogen bonding. As stated above, in Fig. 1 the points corresponding to benzene and butanone do not lie on the straight line. This indicates the absence of hydrogen bonding in these solvents and this is as expected from their structure. The polarization can get affected by other specific interactions and change in the value of τ, however, it appears that hydrogen bonding has a dominant effect.

Thus the present study indicates that the fluorescence polarization measurements provide a sensitive method for detecting hydrogen bonding taking place in a solvent.

References

1. F. J. Perrin, Phys. Radium, *7*, 370, 1926.
2. G. Weber, Adv. in Protein Chem., *8*, 415, 1953; *75*, 335, 1960.
3. S. S. Rathi and M. K. Machwe, Phys. Letters, *25A*, 41, 1967.
4. M. K. Machwe, Indian J. of Pure and Applied Physics, *20*, 590, 1982.
5. P. P. Feofilov, The Physical Basis of Polarization Emission, Consultant Bureau, New York, 1961.
6. A. I. Vogel, Elementary Practical Organic Chemistry, Part I: Small Scale Production, Second Edition, Longmans, London, 363, 1966.
7. T. Azumi and S. P. McGlynn, J. Chem. Phys., *37*, 2413, 1962.
8. Handbook of Chemistry and Physics, Chemical Rubber Publishing Co., Cleveland, Ohio, 1963.
9. G. W. C. Kaye and T. H. Laby, Tables of Physical and Chemical Constants, Longmans, London, 1966.

Acta Physica Hungarica 65 (4), pp. 435–440 (1989)

PAINLEVÉ PROPERTY AND BÄCKLUND TRANSFORMATION OF SU(2) YANG–MILLS–HIGGS SYSTEM

B.V. BABY

International Center for Theoretical Physics
34100, Trieste, Italy

(Received 30 April 1987)

The Painlevé property (PP) of partial differential equation (PDE) is very extensively used to establish the integrability of various dynamical systems [1,2,3]. Ward [4] has extended the PP, well known in the context of ordinary differential equations, to PDEs. A system of PDEs in n independent variables are considered in the complex domain, the coefficients being analytic on C^n. If S is an analytic noncharacteristic complex hyper surface on C^n, then every solution of the PDE which is analytic on S is meromorphic on C^n. A weaker form of the PP was suggested by Weiss et al [1], while studying the Lorentz series expansion of the solution in the neighbourhood of a movable singularity.

Ward [4] has shown that the selfduality equations in four dimensions possess the PP, whereas the pure SU(2) Yang–Mills field equations are not a Painlevé type. t'Hooft [5] has proposed a model for a magnetic monopole which arises as a static solution of the classical SU(2) Yang–Mills–Higg's (YMH) system is a higher dimensional soliton solution of the nonlinear gauge theory. The Lagrangian density for this YMH system is given by,

$$L = -1/4\ F^{\mu\nu a}\ F^a_{\mu\nu} - 1/2 \prod_{\mu}^{\mu a} \prod^{a} + 1/2\mu^2 \phi^a \phi^a - \lambda/4\ (\phi^a \phi^a)^2 \tag{1}$$

where

$$F^a_{\mu\nu} = \partial_\mu A^a_v - \partial_v\ A^a_\mu + e\ \epsilon^{abc} A^b_\mu A^c_v, \tag{2}$$

and

$$\prod_{\mu v}^{a} = \partial_\mu \phi^a + e\ \epsilon^{abc}\ A^b_\mu \phi^c. \tag{3}$$

The time dependent Wu–Yang–t'Hooft–Julia–Zee ansatz [6],

$$\phi^a = \hat{r}^a\ H(r,t)/er, \tag{4}$$

$$A^a_0 = \hat{r}^a\ J(r,t)/er, \tag{5}$$

$$A_i^a = \epsilon_{aij}\ \hat{r}_j[1 - K(r,t)/er, \tag{6}$$

where

$$\hat{r}^a = r^a/r \tag{7}$$

reduces the equations of motion corresponding to the above Lagrangian into two coupled equations

$$r^2(H_{rr} - H_{tt}) = 2HK^2 + (H^3 - C^2r^2H)\lambda/e^2, \tag{8}$$

$$r^2(K_{rr} - K_{tt}) = K(K^2 - 1 + H^2), \tag{9}$$

where $C = \mu e/\lambda$.

Prassed and Sommerfield (PS) [7] were able to find an exact finite energy time independent solution of the above system at a special limit, $\lambda \to 0$. This limit is generally called PS limit. At the PS limit, (8) gives

$$r^2(H_{rr} - H_{tt}) = 2\ HK^2. \tag{10}$$

Some time dependent exact solutions of the above system are known [6,8], but all of them having essential singularities.

In this latter we study the PP analysis of the coupled equations (9) and (10). It is found that this system has no PP. Ten we will use a set of nonlinear transformations by which the static version of the equations (9) and (10) can be reduced into a single nonlinear ordinary differential equation. The PP analysis of this ordinary differential equation gives the Bäcklund transformation for the YMH system. The only solution that we are able to construct is the well known finite energy solution reported by Prasad and Sommerfield [7].

The pair of equation (9) and (10) has the PP when its solution $K(r,t)$ and $H(r,t)$ are single valued about the movable singularity manifolds, determined from the singularity of the Lorentz series expansions

$$K(r,t) = \sum_{j=0}^{\infty} u_j(r,t)\ \phi^{j+\alpha}(r,t), \tag{11}$$

$$H(r,t) = \sum_{j=0}^{\infty} v_j(r,t)\ \phi^{j+\beta}(r,t), \tag{12}$$

where $u_j(r,t)$, $v_j(r,t)$ and $\phi(r,t)$ are the analytic functions in a neighbourhood of the manifold $\phi(r,t) = 0$, The α and β, the least negative integer for which at least two terms of the equations are balanced, are to be determined.

Substitute the Lorentz series expansions (Eqs (11) and (12)) in (19) and (20) and leading order terms analysis gives the values $\alpha = \beta = -1$. The recursion relation for $u_j(r,t)$ and $v_j(r,t)$ are found to be,

$$r^2[u_{j-2,rr} + u_{j-1,rr}(j-2)\ \phi_{,r} + u_j(j-1)(j-2)\ \phi_{,r}^2 + \\ + u_{j-1}(j-1)\ \phi_{,rr} - u_{j-2,tt} - u_{j-1,t}(j-2)\ \phi_{,t} - u_j(j-1)(j-2)\ \phi_{,t}^2 \\ - u_{j-1}(j-2)\ \phi_{,tt}] - 2\sum_{k=0}^{j}\sum_{\ell=0}^{k} v_{j-k}\ v_{k-\ell}\ u_\ell = 0, \tag{13}$$

$$r^2[v_{j-2,rr} + v_{j-1,rr}(j-2)\ \phi_{,r} + v_j(j-1)(j-2)\ \phi_{,r}^2 + v_{j-1}(j-1)\ \phi_{,rr} \\ - v_{j-2,tt} - v_{j-1,t}(j-2)\ \phi_{,t} - v_j(j-1)(j-2)\ \phi_t^2 - v_{j-1}(j-2)\ \phi_{,tt}] \\ - \sum_{k=0}^{j}\sum_{\ell=0}^{k}[v_{j-k}\ v_{k-\ell} + u_{j-k}\ u_{k-\ell}\ v_\ell] + v_{j-2} = 0. \tag{14}$$

For $j = 0$,

$$u_0 = 0, \tag{15}$$

$$v_0^2 = 2/3\ r^2(\phi_r^2 - \phi_t^2). \tag{16}$$

Collecting the coefficients of $u_j(r,t)$ and $v_j(r,t)$ give

$$[3(j-1)(j-2) - 4]u_j = F\ (u_{j-1}, \ldots, \phi_t,\ \phi_r, \ldots), \tag{17}$$

$$[3(j-1)(j-2) - 6]v_j = G\ (u_{j-1}, \ldots, \phi_t, \phi_r, \ldots). \tag{18}$$

Imply that $v_j(r,t)$ are arbitrary for $j = 0, 3$. But the $u_j(r,t)$ are arbitrary for $j = [9 \pm \sqrt{57}]/6$. These values of j are called resonances. Since the resonances of $u_j(r,t)$ are irrational numbers, the system has no PP.

Now we will consider the time independent version of the equations (9) and (10)

$$r^2\ K_{,rr} = K\ (K^2 - 1 + H^2), \tag{19}$$

$$r^2\ H_{,rr} = 2H\ K^2. \tag{20}$$

The PP of these coupled equations (19) and (20) will give the same results as earlier.

We introduce two new nonlinear transformations

$$K = r\, u^{1/2}, \tag{21}$$

$$H = 1 + (r/2u)\,\frac{du}{dr}. \tag{22}$$

Using Eq (21) and (22), the coupled equations (19) and (20) yield a single equation given by

$$u\,\frac{d^2u}{dr^2} - \left(\frac{du}{dr}\right)^2 - 2u^3 = 0. \tag{23}$$

Now we will study the PP of Eq. (23) as earlier. Substitute

$$u = \sum_{k=0}^{\infty} u_k\, \phi^{k+\alpha} \tag{24}$$

in Eq. (23), yields

$$\begin{aligned}
&\sum_{k=0}^{\infty} u_k\, \phi^{k+\alpha}\Big[\sum_{k=0}^{\infty} u_{k,rr}\, \phi^{k+\alpha} + 2\sum_{k=0}^{\infty}(k+\alpha)u_{k,r}\, \phi^{k+\alpha-1}\, \phi_{'r} \\
&+ \sum_{k=0}^{\infty}(k+\alpha)(k+\alpha-1)\, u_k\, \phi^{k+\alpha-2}\, \phi_{'r}^2 + \sum_{k=0}^{\infty}(k+\alpha)\, u_k\, \phi^{k+\alpha-1}\phi_{'rr}\Big] \\
&-\Big[\sum_{k=0}^{\infty} u_{k,r}\, \phi^{k+\alpha} + \sum_{k=0}^{\infty} u_k\, (k+\alpha)\, \phi^{K+\alpha-1}\, \phi_{'r}\Big]^2 \\
&-2\Big[\sum_{k=0}^{\infty} u_k\, \phi^{k+\alpha}\Big]^3 = 0.
\end{aligned} \tag{25}$$

A leading order singularity analysis yields $\alpha = -2$. The resonance is found to be, when $k = 2$. Further, observation will give the following values to $u_j(r)$,

$$u_0(r) = \phi_{'r}^2, \tag{26}$$

$$u_1(r) = -\phi_{'rr}, \tag{27}$$

$$u_1\,\frac{d^2u_1}{d\,r^2} - \left(\frac{d\,u_1}{dr}\right)^2 = 0 \tag{28}$$

and

$$\phi_r^2\ \phi_{rrrr} + \phi_{rr}^3 - 2\ \phi_r\ \phi_{rr}\ \phi_{rrr} = 0. \tag{29}$$

All other values of $u_j(r)$ can be made zero, automatically. Substituting (26) and (27) in (24) and imposing the condition $u_j = 0$ for all $j \geq 2$, yields

$$u(r) = \phi_r^2\ \phi^{-2} - \dot{\phi}_{rr}\ \phi^{-1} \tag{30}$$

as the solution of (24). The $\phi(r)$ is to be obtained from Eqs (27)–(29).

The set of equations (23), (28), (29) and (30) together give a Bäcklund transformation between the equations (23) and (28). Generally, the PP analysis gives auto-Bäcklund transformation, whereas it is interesting to note that we got Bäcklund transformation. Using this Bäcklund transformation, we will construct static solution of YMH system at PS limit.

The particular solution that we found for the system of equations (27)–(29) is given by

$$u_1 = A\ \exp(Br), \tag{31}$$

where A and B are arbitrary constants. Obviously, Eq. (27) gives

$$\phi(r) = -A\ B^{-2}\ \exp(Br) + D - Cr, \tag{32}$$

where C and D are integration constants. Equation (3.2) is consistent with (29) only when $C = 0$, hence the modified form of $\phi(r)$ is given by

$$\phi(r) = -A\ B^{-2}\ \exp(Br) + D. \tag{33}$$

Inserting Eq. (33) in Eq. (30) yields

$$u(r) = ADB^4\ \exp(Br)/[DB^2 - A\ \exp(Br)]^2. \tag{34}$$

Using the nonlinear transformations (21) and (27) we get

$$K(r) = \sqrt{AD}\ B^2\ \exp(Br/2)\ [DB^2 - A\ \exp(Br)]^{-1} \tag{35}$$

and

$$H(r) = 1 + Br[DB^2 + A\ \exp(Br)][2DB^2 - 2A\ \exp(Br)]^{-1}. \tag{36}$$

$DB^2 = A$ yields the well known finite energy solution

$$K(r) = 1/2\ Br\ \sinh\ (Br/2), \tag{37}$$

$$H(r) = 1 + 1/2\ Br\ \coth(Br/2). \tag{38}$$

From the above analysis, it is obvious that the YMH system at the PS limit has no PP. In general the absence of PP implies the nonintegrability. But there are cases when the PP analysis fails [9].

Acknowledgments

The author would like to thank Professor Abdus Salam, the International Atomic Energy Agency and UNESCO for the hospitality at the International Centre for Theoretical Physics, Trieste. This work is partially supported by the Department of Science and Technology, Government of India, under the Project SP/YS/MO9/85.

References

1. J. Weiss, M. Tabor and G. Carnevala, J. Math. Phys., *24*, 522, 1983.
2. A. R. Chowdhury and P.K. Chanda, Phys. Lett., *106A*, 353, 1984.
3. N. Nirmala, M.J. Vedan and B.V. Baby, J. Math. Phys., *27*, 2640, 1986.
4. R.S. Ward, Phys. Lett., *102A*, 279, 1984.
5. G. t'Hooft, Nucl. Phys., *79B*, 276, 1974.
6. W. Mecklenburg and D.F.O. Brien, Phys. Rev., *18D*, 1327, 1978.
7. M.K. Prasad and C.M. Sommerfield, Phys. Rev. Letts., *35*, 760, 1975.
8. K.B. Joseph and B.V. Baby, J. MAth. Phys., *26*, 2746, 1985.
9. J. Weiss, J. Math. Phys., *24*, 1405, 1983.

Acta Physica Hungarica 65 (4), pp. 441 (1989)

ERRATUM

The authors' names of the paper
Residual Resistivity Investigations on High Purity Gallium
(Acta Phys. Hung., *62*, 81, 1987)
correctly read: D. Novák, S. Mészáros, K. Vad and K. Botos

Acta Physica Hungarica 65, 1989
Akadémiai Kiadó, Budapest

Acta Physica Hungarica 65 (4), pp. 448–449 (1989)

BOOK REVIEWS

Localization and Metal-Insulator Transitions

Institute for Amorphous Studies Series. Part 3 of vol.

Festschrift in honor of Sir Nevill Mott on his eightieth birthday.

Edited by: Hellmut Fritzsche and David Adler, Plenum Press, New York and London, 1985, pp. 533 + XIV

The volume is the third part of a book, the previous ones having the titles "Tetrahedrally Bounded Amorphous Semiconductors" and "Physics of Disordered Materials". They were written in honour of N. Mott, who made pioneering work in this field already some fifty years ago and has been its leading expert ever since. The two subjects of the volume are closely interrelated. Localization of conductive electrons arises from local disorder, correlations, electron–phonon coupling; leading to the diminuation of conductivity with weakening of the metallic and strengthening of the insulating properties. This is closely connected with e.g. the increase of the atomic volume in a thermodynamic phase, the electrons having weakened possibility to be free at the larger atomic volumes. This field of science is the subject of rapidly growing interest of experimental and theoretical as well as of technological researchers. The volume is a collection of works of 39 papers of 72 scientists from 11 countries, covering all these three aspects of the problem.

The volume is divided into three parts. *The first* one, containing 15 papers, is devoted to *experimental* studies of metal–semiconductor and metal–insulator transitions. Here the induction of these transitions by the variation of temperature, pressure, compositions (external magnetic field, etc.) is studied mostly on peculiar systems. In these experimental investigations mostly relatively or wholly new experimental techniques, including those of local analysis, are used. *The Second Part*, with 14 papers, deals with the *theoretical* aspects of the problem. The increasing role of *thermodynamic* methods in the description of the behaviour of *real* systems is shown here by the choice of the paper of F. Yonewaza and T. Ogawa, using this method. Here the analysis starts in fact, from the classical theory of *J. W. Gibbs*, explaining phase transitions as consequences of the instability of homogeneous states in certain conditions. This instability (the classical example of which is the behaviour of the Vander-Waals gas in certain circumstances) leads to the existence of two phases instead of a single one, that is, to the onset of phase transition. The metal–insulator transition is described within this framework, by using the earlier theoretical results of Landau and Zeldowitch as well as more recent ones in the very important but by far not closed research of the theory of phase transitions. More detailed but as well more special descriptions are given in the further papers. *The Third Part* contains 10 works on the practically interesting special cases of quasi-one-dimensional and quasi-two-dimensional systems. Examples of these are the grain boundaries of Ge, the layer structures in graphite and metallic oxides, etc.

The volume is interesting to scientists in such different areas as theoretical and mathematical physics, atomic, molecular and chemical physics, physical chemistry, thermodynamics, solid state physics and chemistry, materials science, electronic materials, surface science, etc.

L. Z. Mezey

Concept and Trends in Particle Physics

Proceedings of the "XXV Internationale Universitätswochen für Kernphysik", Schladming, Austria, 1986.

Edited by: H. Latal and H. Mitter, Springer–Verlag, Berlin, Heidelberg, New York, Tokyo, 1987, pp. 325, 48 figures

The Schladming winter school is well known to Hungarian particle physicists. In 1986 the school celebrated the 25th anniversary of its existence. Up till now the school has primarily been devoted to theoretical particle physics although experimentalists have always been invited to lecture on their results.

In view of this, the present book contains lectures on supersymmetry, on superstrings, on the standard model, on QCD, on gauge theory, on the Kaluza–Klein theories. Only a single lecture was devoted to experimental research: this lecture, by L. M. Lederman, was entitled "Experiments Beyond the Standard Model". The lecturers dealing with theory were W. Thirring, J. Wess, W. Kummer, G. Veneziano, G. C. Segre, R. D. Peccei, M. Blau, G. Landi and H. Satz.

The book is of a high level and may first of all reckon on the interest of physicists conversant with theoretical particle physics. The lecturers of the winter school, who are the authors of the individual chapters, discuss their topics in a rather detailed manner. Nevertheless, an amount of basic knowledge is provided, thereby enabling the book to be utilized also by theoretically-inclined, advanced university students who are in possession of certain fundamental concepts.

D. Kiss

Weak and Electromagnetic Interactions in Nuclei

Proceedings of an International Symposium, Heidelberg, 1–5 July 1986.

Edited by: H. V. Klapdor, Springer-Verlag, Berlin, Heidelberg, New York, Tokyo, 1986, pp. 1110, 555 figures

The volume gives a pertinent illustration of the *interdisciplinarity* of modern physics and of the intertwining of the different branches in this field, as well as of the most interesting questions of the adjoining territories of particle physics, nuclear physics, astrophysics and cosmology. The greater part of the book discusses low energy nuclear physical experiments; a comparatively small space is reserved for problems of conventional and traditional nuclear physics. The papers concentrate on experiments of *fundamental* importance.

The volume consists of four main parts followed by a Summary and an Appendix. The first part deals with weak and electromagnetic nuclear properties and excitations; within this field low excitation nuclei, nuclei in highly excited states, high spin states, giant resonances, exotic nuclei, beta decay far from stability, and spin–isospin excitations in nuclei are described.

The second part is reserved for electroweak interactions in nuclei and subnucleonic structure, e. g. the EMC effect, nucleon form factors, etc.

The third part discusses the present status and tests of electroweak theories and of GUT's. Within this field separate papers are dedicated to heavy neutrinos, double beta decay, the beta decay of the neutron, hyperons and hypernuclei, CP violation, lepton number violation, experiments concerning the mass of neutrinos, etc. A separate chapter describes solar neutrinos, including neutrino oscillations, gallium solar neutrino detectors and a further chapter deals with reactor neutrino oscillation experiments.

Muon physics, muon decay, muon capture and μ-atoms have a chapter of their own. Separate papers outline GUT's, supersymmetry theories and superstrings. Within this framework nucleon decay, and neutron–antineutron oscillation experiments for the search of a neutron electric dipole moment are described.

The fourth part, "Weak Interaction in Astrophysics and Cosmology", discusses — among other subjects — the evolution and the structure of the Universe, the inflationary theory and supernovae.

Part 5 is a concise summary of the papers presented at the symposium and of the book itself.

An Appendix, consisting of three chapters is added to the volume. The first of these chapters is dedicated to large scale computing in theoretical physics (example QCD), the second and third outline the history of the University of Heidelberg.

Particle physicists, astrophysicists, cosmologists and nuclear physicists will find this an important and interesting work that gives

a succinct description of the most recent theories and experiments in this field. The book presents a clear survey of the subject and gives an exacting evaluation of the latest results. We would recommend that *theoretical and experimental physicists* read this volume or, at least, partially acquaint themselves with it. The very high scientific level of the book means that it is perhaps not eminently suitable reading for teachers and students of physics — although some chapters may be interesting and understandable for this group of readers, too. The reviewer is pleased to be able to draw the attention of the Hungarian scientific community to this excellent, modern, many-sided book which is exceedingly rich in information.

D. Kiss

G. L. VERSCHUUR: *The Invisible Universe–Revealed (The Story of Radio Astronomy)*

Springer Verlag, Berlin, Heidelberg, New York, London, Paris, Tokyo; 1987.

Radio astronomy is the study of radio waves from space. In the last fifty years it opened a completely new window to the sky and in this way our view and understanding of physical processes in the Universe was basically changed. Of course, radio waves are not visible and therefore radio telescopes can only collect this invisible radiation. With the help of computer image processing, however, radiographs can give us the same impression as photographs about objects never seen before. In the last few decades dozens of new cosmic phenomena have been discovered with the help of radio telescopes and words like quasars, radio galaxies, pulsars, interstellar maser sources etc. have become commonplace but, on the other hand, many of us are rather unfamiliar with the more recently coined words like blazars, radio jets or superluminals.

The 262 page book of Gerrit Verschuur gives a full review of the achievements of radio astronomy written in a nontechnical, easily readable language. It consists of six parts, altogether 18 Chapters and an Appendix. After some short introductory remarks about radio astronomy the story starts with the most distant objects of the known Universe: with quasars and radio galaxies (part 2), it continues with our own Galaxy, the Milky Way, (part 3), and then zooms on to smaller objects like stellar type radio sources and the Solar System (part 4). This approach confronts the reader with the most fascinating (and least understood) problems of radio astronomy just at the start and then proceeds toward the more and more known areas. Part 5 deals partly with radio cosmology and partly with the search for extraterrestrial intelligence. In part 6 the past, the present and the future of radio astronomy is reviewed mostly in terms of instrumentation. Historical material has been kept to a minimum not because it is not important or interesting, but because several books have recently dealt with it. The author is rather concerned about the future of radio astronomy because electromagnetic pollution is a growing problem not only on the Earth, but increasingly so in space. Therefore the book is strongly recommended for those who are involved in communication design and applications.

Instrumentation projects for the next decade are plenty. Very Long Baseline Interferometry (VLBI) will get a dedicated system on the Earth surface (the Very Long Baseline Array – VLBA) in the USA, and also in the space — the QUASAT project, which is a planned orbiting radio telescope.

The emphasis is always on the latest results and on the problems which originate from them. This makes the reading of the book very refreshing even for scientists familiar with the subject.

The book makes the "invisible Universe" visible indeed with the help of magnificent computer processed radiographs. Many of them are from the National Radio Astronomy Observatory (USA) which operates the World's most sophisticated aperture synthesis radio telescope called VLA. The VLA's angular resolution and image quality rivals with that of the best optical telescopes. The text is richly illustrated with photos and drawings from other sources as well, altogether with 108 figures.

This is a completely rewritten version of "The Invisible Universe: the Story of Radio Astronomy" originally published in 1974. It aims at the interested lay person as well as students in high school and colleges. The enthusiastic and sometime lyric style indicates the author's excitement and fascination by this area of science.

I. Fejes

Energy Transfer Dynamics

Studies and Essays in Honor of Herbert Fröhlich on his Eightieth Birthday

Edited by: T. W. Barrett and H. A. Pohl

Springer-Verlag, Berlin, Heidelberg, New York, Tokyo, 1987, pp. 352, 87 figures

The book is a compilation of papers presented at three Conferences in 1985 and 1986 held to honor Prof. Herbert Fröhlich. The topics are related to the main field of his activity, namely to nonthermal energy transfer. It covers phenomena in both physical and biological systems, in the course of which energy is not transferred to chaotic excitation but to selected degrees of freedom of the system. Such effects are of major importance in the fields of dielectrics, quasi periodic solids and surfaces, just like of biological molecules and cells.

The papers are of different character ranging from pure theoretical ideas (soliton theory, chaos, etc.) to problems related to high technology (submicron electronic devices, dielectric spectroscopy). They are connected to each other by the underlying main idea of nonthermal energy transfer.

Therefore, the book can be of high value to researchers in different fields of physics and biophysics related to the above fundamental processes.

P. Richter

Gas Flow and Chemical Lasers

Proceedings of the 6th International Symposium, Jerusalem, September 8–12, 1986

Springer Proceedings in Physics, Volume 15

Edited by: S. Rosenwaks, Springer-Verlag, Berlin, Heidelberg, New York, London, Paris, Tokyo, 1987, pp. 579, 479 figures

This book contains 19 invited and 61 contributed papers and a panel discussion on the prospects for short wavelength chemical lasers, held at the closing session of the Symposium.

The volume is well organised and has 12 separate parts, following from the deductive approach of the Editor. The first chapter gives the introductory concepts of fluid dynamics, and the latest advances in high-speed gas-flow system development are presented. The optics section describes the application of phase conjugation and the design of optical elements.

In the next five chapters the different groups of gas flow and chemical lasers are reviewed, viz. excimer lasers, oxygen–iodine lasers, CO, CO_2 and chemical vibrational transition lasers.

Besides beam diagnostics and propagation, a separate part presents the most important application of these lasers.

The last two chapters show the present state of the topic ("Recent Developments") and the most promising future developments, i.e. the "Short-wavelength Chemical Lasers".

The volume is carefully edited, on 579 pages with 479 figures. It is a valuable summary of recent research results in the field of chemical and gas lasers and their applications.

I. Ketskeméty

Applications of the Monte Carlo Method in Statistical Physics

Edited by: K. Binder (second edition)

Springer-Verlag, Berlin, Heidelberg, New York, Tokyo 1987

This book complements a previous volume with the same title published first in 1979. It contains reviews of recent developments in various fields of statistical physics written by leading experts. Together with the first volume — which was a very successful publication — the two books serve as a useful, comprehensive overview of applications of Monte Carlo simulations in statistical physics, including such diverse topics as ordinary condensed-matter physics, field and elementary particle theory, quantum-mechanical problems, polymer physics, metallurgy and surface physics.

With the appearence of increasingly powerful computers Monte Carlo simulations have become a standard tool in the studies of complex systems leading to many significant results. In addition, simulations are useful for educational purposes, because the general concepts of statistical physics (fluctuations, probability distributions, transition phenomena) can be explicitly demonstrated.

To update the first edition of the second volume (published in 1984) a new chapter "Recent Developments" was added to the original

version, written as a joint effort of all the authors of the book. This chapter contains about 300 most recent references and gives a condensed account of many aspects of this new research. During the past few years the applications of the Monte Carlo method have also become important in the investigations of growth phenomena under far from equilibrium conditions. Since the first edition had appeared before the boom took place in the studies of growth models, this field is not represented in such details as the more traditional ones.

T. Vicsek

P. L. ROSSITER: *The Electrical Resistivity of Metals and Alloys*

Cambridge University Press, Cambridge, New York, Melbourne, 1987, pp. 434

The electrical resistivity of metals and alloys is an important research tool to investigate various microstructural and physical phenomena, including studies of defects, pre-precipitation processes, phase transformation kinetics, etc. The electrical resistivity is also of great practical importance, therefore there is a basic need for the knowledge of the physical processes which determine this property, that is the processes of scattering of conduction electrons in metals and alloys.

As many good books deal with the basic aspects of electrons in solids, the present book is devoted to understanding the electrical properties of real metals and alloys. For this aim the author, whose name is well-known for his work on the electrical resistivity of alloys, assumes that the basic equations concerning electron states in solids are known by the reader and concentrates more on the aspects of electrical conduction, particularly its dependence upon composition and atomic or magnetic structure.

The book consists of eight Chapters. In the first three Chapters the introduction of the basic ideas, the concepts of atomic and magnetic correlations and their microstructural consequences are presented. In Chapter 4 the nearly free electron theory and the pseudopotential approximations are discussed. Based on these concepts Chapter 5 deals with the determination of the electrical resistivity taking into account short and long range atomic correlations as well as the effects of static and dynamic atomic displacements. In Chapter 6 methods appropriate to non-simple metals and alloys are introduced. Chapter 7 discusses the properties of magnetic alloys and finally Chapter 8 deals with miscellaneous phenomena including the properties of amorphous metals.

The book is an excellent up to date review of the present experimental and theoretical knowledge connected with the problem of understanding the electrical properties of concentrated solids. It includes an extensive list of references and is recommended to every theoretical and experimental solid state physicist, metallurgist and material scientist interested in electrical conductivity problems or in the application of resistivity measurements to the study of alloys systems.

I. Kovács

F. IACHELLO and A. ARIMA: *The Interacting Boson Model*

Cambridge Monographs on Mathematical Physics, Cambridge University Press, Cambridge, New York, New Rochelle, Melbourne, Sydney, 1987, pp. x+250

The Interacting Boson Model describes in a unified way the collective properties of the atomic nuclei. It was introduced by the authors of this book in 1974. Since then a great deal of theoretical and experimental efforts have been concentrated on the development and testing of this algebraic theory. The model proved to be very useful in describing a large amount of experimental data, and at the same time its microscopic foundation i.e. a connection to the nuclear shell model was developed. In addition, it has been extended into various directions and, as a result, today there is a whole family of the interacting boson type models.

This well organized volume contains the phenomenological interacting boson model which is applicable to nuclei with even proton and even neutron numbers. In this approach the description of the quadrupole collectivity is based on bosons which are pairs of alike nucleons with angular momenta 0 and 2.

The extension for odd–even nuclei and the microscopic foundation are, according to

the preface, planned to be subjects of subsequent volumes.

The book is divided into three parts. The first one describes the simplest version of the model. The second one deals with the extended version which makes a distinction between protons and neutrons. Both parts contain three chapters according to the internal logic of the theory. They give first the physical operators and the basis states, then the algebraic properties of the model and its applications and finally the geometrical content of this rather abstract approach. The third part briefly reviews some further extensions related to (i) bosons consisting of one proton and one neutron, (ii) bosons with angular momentum 3 and 4, (iii) mixing of boson configurations. It also contains some applications to scattering processes which involve group elements rather than the elements of the corresponding Lie algebras appearing in the previous Chapters.

This nice and concise book gives an elegant description of the mathematical technique used in the interacting boson model, and also gathers a big collection of formulas which serve as a basis for practical applications. Since this model has become, together with the shell model and the collective model, one of the three basis models of nuclear structure, this excellent volume can be recommended not only to nuclear physicists but to students studying nuclear physics as well. The general mathematical framework of Part I can be of interest for experts of other branches of physics, too.

J. Cseh

G. CONTOPOULOS and D. KOTSAKIS: *Cosmology: The Structure and Evolution of the Universe*

Translated from Greek by M. Petrou and P. L. Palmer,

Springer-Verlag, Berlin, Heidelberg, New York, 1987, pp. 235

It would be a remarkable achievement if anyone succeeded in writing a book of less than 240 pages on the structure and evolution of the Universe. The mere attempt arouses the interest of the reader.

This slim volume is divided into three parts beginning with the quite conventional description of the observational results on our Galaxy, galaxies and clusters of galaxies, and the distribution of matter in the Universe. In the first chapter of this part the content (stellar clusters and associations, interstellar medium, gaseous and dust clouds, stellar populations, peculiar objects like pulsars, etc.) and the kinematics (motion of the Sun, distribution of stellar velocities, etc.) of the Galaxy are discussed. The second chapter gives a summary of the present knowledge of galaxies and clusters of galaxies while the third chapter presents the observational facts which are of basic importance in establishing the modern cosmological theories (expansion of the Universe, microwave background radiation, isotropy and homogeneity of the Universe, etc.).

The second part is devoted to the cosmological theories. After the customary introduction (Olbers' Paradox) this part, which is the central one of the book, deals with the theory of general relativity and relativistic cosmology. The concise treatment of non-standard cosmologies is an especially valuable section of the book. The ideas and theories of the evolution of the Universe from the very first stages of the expansion are described and the theories of the formation of protogalaxies and their collapse are also discussed. In recent years much effort has been made to unify the two extreme areas of research, cosmology and microphysics. In the last two decades we have witnessed the great impact of high energy physics on cosmology and the book also directs the reader's attention to this exciting field.

The third and last part of the book includes and expounds several fundamental and unsolved problems connected with the physics of the Universe such as the universality and the uncertainty of physical laws, inflation and causality, space and time at the beginning of the expansion, the cyclic Universe.

The text written, in general, with little mathematics is clear and easy to follow. The treatments are not exhaustive but serve to introduce the main ideas. The book provides a good introduction to cosmology for students starting work in this field and for those from related disciplines who require a concise account of the present status. Luckily, the attentive reader can hardly find any mistakes. I mention only one: It may seem to the reader that G. Abell's fundamental catalogue of clusters of galaxies is only an extract from Shapley and Ames' catalogue (p. 64).

Of course, it is natural to compare such a book with others available in English. The student interested in cosmology may make a choice from among a wide variety of books about cosmology in the English astronomical literature, which is much more extensive than the Greek. Clearly, with library budgets under increasing strain, translating and publishing such a book may seem superfluous. Nevertheless the book can be heartily recommended to all students, even to educated layman with an interest in the subject as a compact, readable and fairly comprehensive account of cosmology.

B. Szeidl

DUGALD MURDOCH: *Niels Bohr's Philosophy of Physics*

Cambridge University Press, Cambridge, 1987, pp. 294

Dugald Murdoch's book presents an excellent exposition and appraisal of Niels Bohr's philosophy of physics.

Starting from the historical background, making use of the material of the Niels Bohr Archive and of the available literature by other scholars, the author highlights the ideas and problems which played a prominent part in the gradual development of Bohr's interpretation of quantum physics. Great emphasis is put on unravelling the realist and non-realist strands in his thinking, and contrasting his views with those of Einstein. Beyond a detailed analysis, Bohr's philosophy is critically assessed.

The book is divided into eleven Chapters:

1. Wave-particle duality
2. Niels Bohr and wave-particle duality
3. From duality to complementarity
4. The meaning of complementarity
5. The foundations of kinematic-dynamic complementarity
6. Bohr's theory of measurement
7. Bohr's theory of properties
8. Einstein versus Bohr
9. The sequel to the Bohr–Einstein debate
10. Bohr's philosophy of physics
11. An appraisal of Bohr's philosophy of physics

A Section of Notes with ample references and an alphabetical Index are also included.

The book can be recommended to specialists in science history and philosophy, but its style, avoiding undue technicalities, makes it accessible for non-specialists as well.

I. Kovács
Department of Atomic Physics
Budapest Technical University

Manuscript received by Akadémiai Kiadó:
19 August 1988
Manuscript received by TYPOTEX GT
for TEX typesetting on 4 May 1989

Date of publication: 20 November 1989

PRINTED IN HUNGARY

Akadémiai Kiadó és Nyomda Vállalat, Budapest

NOTES TO CONTRIBUTORS

I. PAPERS will be considered for publication in Acta Physica Hungarica only if they have not previously been published or submitted for publication elsewhere. They may be written in English, French, German or Russian.

Papers should be submitted to

Prof. I. Kovács, Editor
Department of Atomic Physics, Technical University
1521 Budapest, Budafoki út 8, Hungary

Papers may be either articles with abstracts or short communications. Both should be as concise as possible, articles in general not exceeding 25 typed pages, short communications 8 typed pages.

II. MANUSCRIPTS

1. Papers should be submitted in three copies.
2. The text of papers must be of high stylistic standard, requiring minor corrections only.
3. Manuscripts should be typed in double spacing on good quality paper, with generous margins.
4. The name of the author(s) and of the institutes where the work was carried out should appear on the first page of the manuscript.
5. Particular care should be taken with mathematical expressions. The following should be clearly distinguished, e.g. by underlining in different colours: special founts (italics, script, bold type, Greek, Gothic, etc.); capital and small letters; subscripts and superscripts, e.g. x^2, x_3; small *l* and l; zero and capital O; in expressions written by hand: *e* and *l*, *n* and *u*, *v* and v, etc.

A List of Symbols on a separate sheet should be attached to each paper.

6. References should be numbered serially and listed at the end of the paper in the following form: J. Ise and W. D. Fretter, Phys. Rev., *76*, 933, 1949.

For books, please give the initials and family name of the author(s), title, name of publisher, place and year of publication, e.g.: J. C. Slater, Quantum Theory of Atomic Structures, I. McGraw-Hill Book Company, Inc., New York, 1960.

References should be given in the text in the following forms: Heisenberg [5] or [5].

7. Captions to illustrations should be listed on a separate sheet, not inserted in the text.
8. In papers submitted to Acta Physica all measures should be expressed in SI units.

III. ILLUSTRATIONS AND TABLES

1. Each paper should be accompanied by three sets of illustrations, one of which must be ready for the blockmaker. The other sets attached to the copies of the manuscript may be rough drawings in pencil or photocopies.
2. Illustrations must not be inserted in the text.
3. All illustrations should be identified in blue pencil by the author's name, abbreviated title of the paper and figure number.
4. Tables should be typed on separate pages and have captions describing their content. Clear wording of column heads is advisable. Tables should be numbered in Roman numerals (I, II, III, etc.).

IV. RETURN OF MATERIAL

Owing to high postage costs, the Editorial Office cannot undertake to return *all* material not accepted for any reason for publication. Of papers to be revised (for not being in conformity with the above Notes or other reasons) only *one* copy will be returned. Material rejected for lack of space or on account of the Referees' opinion will not be returned to authors outside Europe.

Periodicals of the Hungarian Academy of Sciences are obtainable at the following addresses:

AUSTRALIA
C.B.D. LIBRARY AND SUBSCRIPTION SERVICE
Box 4886, G.P.O., *Sydney N.S.W. 2001*
COSMOS BOOKSHOP, 145 Ackland Street
St. Kilda (Melbourne), Victoria 3182

AUSTRIA
GLOBUS, Höchstädtplatz 3, *1206 Wien XX*

BELGIUM
OFFICE INTERNATIONAL DES PERIODIQUES
Avenue Louise, 485, *1050 Bruxelles*
E. STORY-SCIENTIA P.V.B.A.
P. van Duyseplein 8, *9000 Gent*

BULGARIA
HEMUS, Bulvar Ruszki 6, *Sofia*

CANADA
PANNONIA BOOKS, P.O. Box 1017
Postal Station "B", *Toronto, Ont. M5T 2T8*

CHINA
CNPICOR, Periodical Department, P.O. Box 50
Peking

CZECHOSLOVAKIA
MAD'ARSKA KULTURA, Národni třida 22
115 66 Praha
PNS DOVOZ TISKU, Vinohradská 46, *Praha 2*
PNS DOVOZ TLAČE, *Bratislava 2*

DENMARK
EJNAR MUNKSGAARD, 35, Nørre Søgade
1370 Copenhagen K

FEDERAL REPUBLIC OF GERMANY
KUNST UND WISSEN ERICH BIEBER
Postfach 46, *7000 Stuttgart 1*

FINLAND
AKATEEMINEN KIRJAKAUPPA, P.O. Box 128
00101 Helsinki 10

FRANCE
DAWSON-FRANCE S.A., B.P. 40, *91121 Palaiseau*
OFFICE INTERNATIONAL DE DOCUMENTATION ET LIBRAIRIE, 48 rue Gay-Lussac
75240 Paris, Cedex 05

GERMAN DEMOCRATIC REPUBLIC
HAUS DER UNGARISCHEN KULTUR
Karl Liebknecht-Straße 9, *DDR-102 Berlin*

GREAT BRITAIN
BLACKWELL'S PERIODICALS DIVISION
Hythe Bridge Street, *Oxford OX1 2ET*
BUMPUS, HALDANE AND MAXWELL LTD.
Cowper Works, *Olney, Bucks MK46 4BN*
COLLET'S HOLDINGS LTD., Denington Estate,
Wellingborough, Northants NN8 2QT
WM DAWSON AND SONS LTD., Cannon House
Folkstone, Kent CT19 5EE
H. K. LEWIS AND CO., 136 Gower Street
London WC1E 6BS

GREECE
KOSTARAKIS BROTHERS INTERNATIONAL BOOKSELLERS, 2 Hippokratous Street, *Athens-143*

HOLLAND
FAXON EUROPE, P.O. Box 167
1000 AD Amsterdam
MARTINUS NIJHOFF B. V.
Lange Voorhout 9–11, *Den Haag*
SWETS SUBSCRIPTION SERVICE
P.O. Box 830, 2160 Sz Lisse

INDIA
ALLIED PUBLISHING PVT. LTD.
750 Mount Road, *Madras 600002*
CENTRAL NEWS AGENCY PVT. LTD.
Connaught Circus, *New Delhi 110001*
INTERNATIONAL BOOK HOUSE PVT. LTD.
Madame Cama Road, *Bombay 400039*

ITALY
D. E. A., Via Lima 28, *00198 Roma*
INTERSCIENTIA, Via Mazzé 28, *10149 Torino*
LIBRERIA COMMISSIONARIA SANSONI
Via Lamarmora 45, *50121 Firenze*
SANTO VANASIA, Via M. Macchi 58
20124 Milano

JAPAN
KINOKUNIYA COMPANY LTD.
Journal Department, P.O. Box 55
Chitose, *Tokyo 156*
MARUZEN COMPANY LTD., Book Department
P.O. Box 5050 Tokyo International, *Tokyo 100-31*
NAUKA LTD., Import Department
2-30-19 Minami Ikebukuro, Toshima-ku, *Tokyo 171*

KOREA
CHULPANMUL, *Phenjan*

NORWAY
TANUM-TIDSKRIFT-SENTRALEN A.S.
Karl Johansgata 43, *1000 Oslo*

POLAND
WĘGIERSKI INSTYTUT KULTURY
Marszalkowska 80, *00-517 Warszawa*
CKP I W, ul. Towarowa 28, *00-958 Warszawa*

ROUMANIA
D. E. P., *Bucuresti*
ILEXIM, Calea Grivitei 64–66, *Bucuresti*

SOVIET UNION
SOYUZPECHAT — IMPORT, *Moscow*
and the post offices in each town
MEZHDUNARODNAYA KNIGA, *Moscow G-200*

SPAIN
DIAZ DE SANTOS Lagasca 95, *Madrid 6*

SWEDEN
ESSELTE TIDSKRIFTSCENTRALEN
Box 62, *101 20 Stockholm*

SWITZERLAND
KARGER LIBRI AG, Petersgraben 31, *4011 Basel*

USA
EBSCO SUBSCRIPTION SERVICES
P.O. Box 1943, *Birmingham, Alabama 35201*
F. W. FAXON COMPANY, INC.
15 Southwest Park, *Westwood Mass. 02090*
MAJOR SCIENTIFIC SUBSCRIPTIONS
1851 Diplomat, P.O. Box 819074,
Pallas, Tx. 75381-9074
READ-MORE PUBLICATIONS, INC.
140 Cedar Street, *New York, N. Y. 10006*

YUGOSLAVIA
JUGOSLOVENSKA KNJIGA, Terazije 27, *Beograd*
FORUM, Vojvode Mišića 1, *21000 Novi Sad*

Index: 26.022